NATIONAL AERONAUTICS AND SPACE ADMINISTRATION

# *The Deep Space Network*
# *Progress Report 42-32*

*January and February 1976*





JET PROPULSION LABORATORY
CALIFORNIA INSTITUTE OF TECHNOLOGY
PASADENA, CALIFORNIA

April 15, 1976

TECHNICAL REPORT STANDARD TITLE PAGE

| 1. Report No. 42-32 | 2. Government Accession No. | 3. Recipient's Catalog No. |
|---|---|---|
| 4. Title and Subtitle<br>THE DEEP SPACE NETWORK PROGRESS REPORT<br>JANUARY AND FEBRUARY 1976 | | 5. Report Date<br>April 15, 1976<br>6. Performing Organization Code |
| 7. Author(s)<br>JPL Staff | | 8. Performing Organization Report No. |
| 9. Performing Organization Name and Address<br>JET PROPULSION LABORATORY<br>California Institute of Technology<br>4800 Oak Grove Drive<br>Pasadena, California 91103 | | 10. Work Unit No.<br>11. Contract or Grant No.<br>NAS 7-100<br>13. Type of Report and Period Covered<br>Progress Report |
| 12. Sponsoring Agency Name and Address<br>NATIONAL AERONAUTICS AND SPACE ADMINISTRATION<br>Washington, D.C. 20546 | | 14. Sponsoring Agency Code |
| 15. Supplementary Notes | | |

16. Abstract

This report describes work performed for the JPL/NASA Deep Space Network (DSN). Progress is presented on DSN supporting research and technology, advanced development and engineering, and implementation, and DSN operations which pertain to mission-independent or multiple-mission development as well as to support of flight projects. Each issue contains a description of the functions and facilities of the DSN.

| 17. Key Words (Selected by Author(s)) | 18. Distribution Statement |
|---|---|
| Ground Support Systems<br>Spacecraft Communications<br>Communications<br>Mathematical and Computer Sciences | Unclassified -- Unlimited |

| 19. Security Classif. (of this report) | 20. Security Classif. (of this page) | 21. |
|---|---|---|
| Unclassified | Unclassified | |

# Preface

Beginning with Volume XX, the Deep Space Network Progress Report changed from the Technical Report 32- series to the Progress Report 42- series. The volume number continues the sequence of the preceding issues. Thus, Progress Report 42-20 is the twentieth volume of the Deep Space Network series, and is an uninterrupted follow-on to Technical Report 32-1526, Volume XIX.

This report presents DSN progress in flight project support, tracking and data acquisition (TDA) research and technology, network engineering, hardware and software implementation, and operations. Each issue presents material in some, but not all, of the following categories in the order indicated.

Description of the DSN

Mission Support
- Ongoing Planetary/Interplanetary Flight Projects
- Advanced Flight Projects

Radio Science

Special Projects

Supporting Research and Technology
- Tracking and Ground-Based Navigation
- Communications—Spacecraft/Ground
- Station Control and Operations Technology
- Network Control and Data Processing

Network and Facility Engineering and Implementation
- Network
- Network Operations Control Center
- Ground Communications
- Deep Space Stations

Operations
- Network Operations
- Network Operations Control Center
- Ground Communications
- Deep Space Stations

Program Planning
- TDA Planning
- Quality Assurance

In each issue, the part entitled "Description of the DSN" describes the functions and facilities of the DSN and may report the current configuration of one of the five DSN systems (Tracking, Telemetry, Command, Monitor & Control, and Test & Training).

The work described in this report series is either performed or managed by the Tracking and Data Acquisition organization of JPL for NASA.

# Contents


## DESCRIPTION OF THE DSN

**Network Functions and Facilities** . . . . . 1
N. A. Renzetti

**DSN Tracking System—Mark III-75** . . . . . 4
W. D. Chaney
NASA Code 311-03-42-95

## MISSION SUPPORT

### Ongoing Planetary/Interplanetary Flight Projects

**Helios B—Deep Space Network Compatibility Test Summary** . . . . 14
A. I. Bryan
NASA Code 311-03-22-10

**Pioneer Venus 1978 Mission Support** . . . . . 25
R. B. Miller
NASA Code 311-03-21-90

**Helios Mission Support** . . . . . 31
P. S. Goodwin, W. G. Meeks, and R. E. Morris
NASA Code 311-03-21-50

## SUPPORTING RESEARCH AND TECHNOLOGY

### Tracking and Ground-Based Navigation

**Atmospheric Water Vapor Calibrations: Radiometer Technique** . . . 38
F. B. Winn, S. C. Wu, G. M. Resch, C. C. Chao, and O. H. von Roos
NASA Code 310-10-60-40

**S- X-Band Experiment: Development and Evaluation of a Set of Group Delay Standards** . . . . . 50
T. Y. Otoshi and R. W. Beatty
NASA Code 310-10-61-13

### Communications—Spacecraft/Ground

**Proposed Modifications to the Wind Loading Specifications Applied to Ground Antennas** . . . . . 65
M. S. Katow
NASA Code 310-20-65-10

**Analysis of Command Detector In-Lock Monitoring** . . . . . 70
R. G. Lipes
NASA Code 310-20-67-09

**Precision Signal Power Measurement Equipment—Radio Frequency Section** . . . . . 74
G. Stevens
NASA Code 310-20-67-03

**Foundation Analysis, Preliminary Investigation** . . . . . 81
H. McGinness and M. S. Katow
NASA Code 310-20-65-02

**Power Spectrum for Binary NRZ Data With Less Than 50% Transitions** . . . . . 86
B. K. Levitt
NASA Code 310-20-67-08

**Precision Signal Power Measurement and Noise-Adding Radiometer Equipment** . . . . . 90
L. C. Constenla
NASA Code 310-20-67-03

**Digital Demodulation With a Non-Ideal Quantizer** . . . . . 100
J. W. Layland
NASA Code 310-20-67-08

**WAVEFRONT Stiffness Matrix Resequencing Program Modifications for the 1108 Computer** . . . . . 106
R. Levy
NASA Code 310-20-65-02

**The Analysis of Microwave Weather Project Data** . . . . . 110
M. S. Reid
NASA Code 310-20-66-06

## Station Control and Operations Technology

**X-Band Reject Filter** . . . . . 118
R. Lay
NASA Code 310-30-69-10

**Two Methods for Reducing the Number of Multiplications in Complex Fast Fourier Transforms** . . . . . 123
D. E. Wallis
NASA Code 310-30-69-08

**An Automated Tracking System for the ARIES Antenna** . . . . . 139
M. W. Sievers
NASA Code 310-30-68-09

**An INTEL 8080 Cross Assembler for the Modcomp II Minicomputer** . . . 151
M. W. Sievers
NASA Code 310-30-68-09

**Theory, Operation, and Computer Programming of the 512-Lag Correlator System** . . . . . 164
R. F. Jurgens
NASA Code 310-30-69-08

## Network Control and Data Processing

**The Analysis of Stuctured Programs—Part I: Kirchhoff's Equations** . . 178
R. J. McEliece
NASA Code 310-40-72-02

**A New Class of Burst-Correcting Cyclic Codes** . . . . . 188
B. Arazi
NASA Code 410-40-70-02

# NETWORK AND FACILITY ENGINEERING AND IMPLEMENTATION

## Network

**An Error-Minimizing Software Audit Technique** . . . . . 201
J. C. Holland and W. O. Paine
NASA Code 311-03-32-20

**Preliminary Results of DSN Performance for Convolutional Codes With a Viterbi Decoder** . . . . . 222
J. M. Urech, L. D. Vit, and B. D. L. Mulhall
NASA Code 311-03-42-95

## Deep Space Stations

**Phase-Stable Receiver Development** . . . . . 241
C. E. Johns
NASA Code 311-03-42-54

**Computer Modeling of a Single-Stage Lithium Bromide/ Water Absorption Refrigeration Unit** . . . . . 247
F. L. Lansing
NASA Code 311-03-44-14

# OPERATIONS

## Network Operations

**DSN Research and Technology Support** . . . . . 258
E. B. Jackson
NASA Code 311-03-14-64

**Analysis of Solar Effects Upon Observed Doppler Noise During the Helios 1 Second Solar Conjunction** . . . . . 262 D26
A. L. Berman
NASA Code 311-03-13-20

**Tracking Operations During the Helios 2 Launch Phase** . . . . . 277 D27
L. E. Bright
NASA Code 311-03-13-20

## Deep Space Stations

**Temperature Effects on Transmission Line Phase and Group Delay** . . 296 D28
H. R. Buchanan and A. L. Price
NASA Code 311-03-14-21

# PROGRAM PLANNING

## TDA Planning

**Life Cycle Costing of Long-Term Capability With a Discount Rate** . . . 301 OMIT
E. C. Posner
NASA Code 311-03-31-30

***Computerizing Goldstone Facility Maintenance Data for Management Decisions*** . . . . . 310 OMIT
F. R. Maiocco and J. P. Hume
NASA Code 311-03-32-10

# Network Functions and Facilities

N. A. Renzetti
Office of Tracking and Data Acquisition

*The objectives, functions, and organization of the Deep Space Network are summarized; deep space station, ground communication, and network operations control capabilities are described.*

The Deep Space Network (DSN), established by the National Aeronautics and Space Administration (NASA) Office of Tracking and Data Acquisition under the system management and technical direction of the Jet Propulsion Laboratory (JPL), is designed for two-way communications with unmanned spacecraft traveling approximately 16,000 km (10,000 miles) from Earth to the farthest planets of our solar system. It has provided tracking and data acquisition support for the following NASA deep space exploration projects: Ranger, Surveyor, Mariner Venus 1962, Mariner Mars 1964, Mariner Venus 1967, Mariner Mars 1969, Mariner Mars 1971, and Mariner Venus Mercury 1973, for which JPL has been responsible for the project management, the development of the spacecraft, and the conduct of mission operations; Lunar Orbiter, for which the Langley Research Center carried out the project management, spacecraft development, and conduct of mission operations; Pioneer, for which Ames Research Center carried out the project management, spacecraft development, and conduct of mission operations; and Apollo, for which the Lyndon B. Johnson Space Center was the project center and the Deep Space Network supplemented the Manned Space Flight Network (MSFN), which was managed by the Goddard Space Flight Center (GSFC). It is providing tracking and data acquisition support for Helios, a joint U.S./West German project; and Viking, for which Langley Research Center provides the project management, the Lander spacecraft, and conducts mission operations, and for which JPL also provides the Orbiter spacecraft.

The Deep Space Network is one of two NASA networks. The other, the Spaceflight Tracking and Data Network, is under the system management and technical direction of the Goddard Space Flight Center. Its function is to support manned and unmanned Earth-orbiting satellites. The Deep Space Network supports lunar, planetary, and interplanetary flight projects.

From its inception, NASA has had the objective of conducting scientific investigations throughout the solar system. It was recognized that in order to meet this objective, significant supporting research and advanced technology development must be conducted in order to provide deep space telecommunications for science data return in a cost effective manner. Therefore, the Network is continually evolved to keep pace with the state of the art of telecommunications and data handling. It was also recognized early that close coordination would be needed

between the requirements of the flight projects for data return and the capabilities needed in the Network. This close collaboration was effected by the appointment of a Tracking and Data Systems Manager as part of the flight project team from the initiation of the project to the end of the mission. By this process, requirements were identified early enough to provide funding and implementation in time for use by the flight project in its flight phase.

As of July 1972, NASA undertook a change in the interface between the Network and the flight projects. Prior to that time, since 1 January 1964, in addition to consisting of the Deep Space Stations and the Ground Communications Facility, the Network had also included the mission control and computing facilities and provided the equipment in the mission support areas for the conduct of mission operations. The latter facilities were housed in a building at JPL known as the Space Flight Operations Facility (SFOF). The interface change was to accommodate a hardware interface between the support of the network operations control functions and those of the mission control and computing functions. This resulted in the flight projects assuming the cognizance of the large general-purpose digital computers which were used for both network processing and mission data processing. They also assumed cognizance of all of the equipment in the flight operations facility for display and communications necessary for the conduct of mission operations. The Network then undertook the development of hardware and computer software necessary to do its network operations control and monitor functions in separate computers. This activity has been known as the Network Control System Implementation Project. A characteristic of the new interface is that the Network provides direct data flow to and from the stations; namely, metric data, science and engineering telemetry, and such network monitor data as are useful to the flight project. This is done via appropriate ground communication equipment to mission operations centers, wherever they may be.

The principal deliverables to the users of the Network are carried out by data system configurations as follows:

- The DSN Tracking System generates radio metric data; i.e., angles, one- and two-way doppler and range, and transmits raw data to Mission Control.
- The DSN Telemetry System receives, decodes, records, and retransmits engineering and scientific data generated in the spacecraft to Mission Control.
- The DSN Command System accepts coded signals from Mission Control via the Ground Communications Facility and transmits them to the spacecraft in order to initiate spacecraft functions in flight.

The data system configurations supporting testing, training, and network operations control functions are as follows:

- The DSN Monitor and Control System instruments, transmits, records, and displays those parameters of the DSN necessary to verify configuration and validate the Network. It provides operational direction and configuration control of the Network, and provides primary interface with flight project Mission Control personnel.
- The DSN Test and Training System generates and controls simulated data to support development, test, training and fault isolation within the DSN. It participates in mission simulation with flight projects.

The capabilities needed to carry out the above functions have evolved in three technical areas:

(1) The Deep Space Stations, which are distributed around Earth and which, prior to 1964, formed part of the Deep Space Instrumentation Facility. The technology involved in equipping these stations is strongly related to the state of the art of telecommunications and flight–ground design considerations, and is almost completely multimission in character.

(2) Ground communications technology supports the Earth-based, point-to-point voice and data communications from the stations to the Network Operations Control Center at JPL, Pasadena, and to the mission operations centers, wherever they may be. It is based largely on the capabilities of the common carriers throughout the world, which are engineered into an integrated system by the Goddard Space Flight Center for support of all NASA programs. We use the term "Ground Communications Facility" for the sets of hardware and software needed to carry out the above functions.

(3) The Network Operations Control Center is the functional entity for centralized operational control of the Network and interfaces with the users. It has two separable functional elements; namely, Network Operations Control and Network Data Processing. The functions of the Network Operations Control are:

- Control and coordination of Network support to meet commitments to Network users.

- Utilization of the Network data processing computing capability to generate all standards and limits required for Network operations.
- Utilization of Network data processing computing capability to analyze and validate the performance of all Network systems.

The personnel who carry out the above functions are located in the Space Flight Operations Facility, where mission operations functions are carried out by certain flight projects. Network personnel are directed by an Operations Control Chief.

The functions of the Network Data Processing are:

- Processing of data used by Network Operations Control for control and analysis of the Network.
- Display in the Network Operations Control Area of data processed in the Network Data Processing Area.
- Interface with communications circuits for input to and output from the Network Data Processing Area.
- Data logging and production of the intermediate data records.

The personnel who carry out these functions are located approximately 200 meters from the Space Flight Operations Facility. The equipment consists of minicomputers for real-time data system monitoring, two XDS Sigma 5s, display, magnetic tape recorders, and appropriate interface equipment with the ground data communications.

# DSN Tracking System—Mark III-75

W. D. Chaney
DSN Systems Engineering Office

*This article provides a description of the DSN Tracking System—Mark III-75 currently in use for multimission support. Tracking functions performed by the Deep Space Stations, Ground Communications Facility, and Network Operations Control Center are given. Changes that were made to the subsystems of the DSN Tracking System—Mark III-73 to implement the DSN Tracking System—Mark III-75 are briefly described.*

## I. Introduction

This article provides a description of the functional capabilities of the DSN Tracking System—Mark III-75 currently in use for multimission support in the generation of radio metric data. The DSN Tracking System—Mark III-75 performs the main functions of radio metric data generation, transmission of data to the Projects and the validation of the tracking system performance. A summary of the functions and data flow is presented in Figure 1.

## II. Key Characteristics

The key characteristics of the DSN Tracking System—Mark III-75 are as follows:

(1) Generation of predictions by DSN Tracking Operations

(2) Real-time reporting of DSN Tracking System status to DSN Operations Control

(3) S-X band doppler and range data generation

(4) Data time tagged to the 10 microsecond level relative to the DSN master clock

(5) Precision control of Block IV receiver and exciter frequencies

(6) Calibration data for the RF transmission media

(7) Use of high-speed data lines for radio metric data and prediction data transmission.

## III. Functional Description

Each 26-meter Deep Space Station (DSS) has the capability of generating one-way, two-way, or three-way doppler and angles from a single spacecraft S-band carrier. Planetary ranging and Differenced Range Versus Integrated Doppler (DRVID) capability can be provided in one 26-meter subnet. Each 64-meter station has the capability of generating one-way, two-way, or three-way doppler simultaneously from two spacecraft carriers within the same beam width, and of obtaining angles,

planetary distance S-X band range, and S-X band DRVID from a single spacecraft. Table 1 summarizes the planned capability for doppler, range, and DRVID.

### A. Data Generation Functions

Functions performed in the generation of radio metric data are:

(1) Tracking predictions generation (Network Operations Control Center (NOCC))

(2) Tracking predictions transmission (Ground Communications Facility (GCF))

(3) Data mode and system configuration selection (Deep Space Station (DSS))

(4) Antenna pointing control (DSS)

(5) Receiver and exciter frequency control (DSS)

(6) Doppler extraction and counting (DSS)

(7) Range and DRVID extraction and measurement (DSS)

(8) Angle readout (DSS)

(9) Interlace partial status, data mode, and system configuration (DSS)

(10) Tracking data handling (DSS)

(11) Original Data Record (ODR) generation (DSS)

(12) Ground weather data and ionosphere data, measurements (DSS)

(13) Open-loop reception and data recording (DSS)

### B. Data Transmission Functions

Functions performed in the transmission of radio metric data are:

(1) Radio metric, ground weather and ionosphere data formatting (DSS)

(2) Radio metric, ground weather and ionosphere data error encoding and transmission (GCF)

(3) Tracking prediction data formatting (NOCC)

(4) Tracking prediction data error encoding and transmission (GCF)

(5) Network Data Log generation (GCF)

(6) Ground Communications error detection (GCF)

### C. Tracking System Validation Functions

Functions performed to accomplish DSN Tracking System validation are:

(1) Transmission of outage alarms to DSN Operations Control (NOCC)

(2) Verification of Tracking System configuration and data mode (NOCC, DSS)

(3) Comparison of radio metric data with predictions (NOCC, DSS)

(4) Transmission of System alarms and status to DSN Operations Control (NOCC)

(5) Display of Tracking System performance and status (NOCC, DSS)

Deep Space Station, Ground Communications and Network Operations control functions are shown in Figures 2, 3 and 4 respectively.

### D. Functional Operation

A brief description of the functional operation of the DSN Tracking System is presented in the remainder of this section. Simplified block diagrams of the 26-m and 64-m stations for Mark III-75 are shown in Figures 5 and 6 respectively.

A spacecraft ephemeris is received from the project, together with standards and limits consisting of spacecraft frequencies, tuning rates, tuning range, data types and rates. DSN tracking predicions are generated from the spacecraft ephemeris ($\phi$ factors) by the Network Operations Control Center Tracking Subsystem. After validation, the predictions are transmitted from the NOCC to the stations via high-speed data line for use in acquiring the spacecraft carriers. The predictions are also used in Tracking System performance validation.

Data mode and system configuration messages are generated for transmission to the stations by high-speed data line or voice, and are used to select the proper data mode and system configuration.

Radio metric data, consisting of angles, range, DRVID, and doppler, together with associated data (i.e., time, frequencies, system configuration, data mode, and status) are measured and sampled by the DSS Tracking Subsystem and are formatted for transmission via high-speed data line. Supplementary data consisting of ground weather data and ionosphere data are also formatted by the DSS Tracking Subsystem for transmission via high-speed data line. An Original Data Record is generated for post-pass recall, if necessary.

The radio metric data are received by the Central Communications Terminal (CCT) and are routed to the Mission Control and Computing Center. A log tape

containing all data received either in real time or by recall is generated by the Central Communications Terminal. Data to fill in gaps in the project data records can be supplied from the Deep Space Station Original Data Record.

The Tracking System performance is validated by the Network Control Tracking Real-Time Monitor processor in response to controls and standards and limits supplied from personnel in the Network Operations Control Area (NOCA). Tracking System alarms, status, and performance data are transmitted from the Network Control Tracking real-time monitor to the Network Control Display Subsystem for display in the NOCA. The Tracking System alarms and status are also transmitted to the Operations Control System for display. A Tracking System Performance Record containing status, alarms, performance data, and radio metric data is maintained for nonreal-time analysis. The Network Control Test and Training Subsystem is used to provide test data to the Tracking System in order to check out the Network Control Tracking Subsystem and to train Network personnel.

## IV. Subsystem Modifications

This section describes the modifications, by subsystem, that were made to the DSN Tracking System—Mark III-73 to produce the Mark III-75 version.

### A. 64-m Deep Space Station Modifications

(1) Antenna Mechanical and Microwave Subsystem. Equipment was added to the antenna mechanical and microwave subsystems to provide the capability of simultaneously acquiring S and X band carriers at 64-m Deep Space Stations.

(2) Receiver-Exciter Subsystem. One Block IV S-band exciter and two Block IV receivers capable of operating at S or X band frequencies were added at the 64-m Deep Space Stations. The Block IV Receiver-Exciter Subsystem was modified to produce biased doppler at 1 MHz rather than 5 MHz, thus improving the doppler resolution for radio science experiments. A second Ranging Demodulation Assembly was added to the Receiver-Exciter Subsystem. These new assemblies produced the capability to generate S and X band doppler and range data simultaneously.

(3) Transmitter Subsystem. A high power amplifier assembly was added at DSS 43 in Australia and 63 in Spain that is capable of transmitting 100 kW at S-band frequencies.

(4) Tracking Subsystem(s). The software for the antenna pointing subsystem was modified to provide precision tracking of the S or X band carriers using conical scan techniques. The Tracking Data Handling Subsystems were modified to provide simultaneous S and X band Doppler counting.

(5) Monitor and Control Subsystem(s). The software for the Digital Instrumentation Subsystem was modified to provide an improved drive tape interface to the Antenna Pointing Subsystem, the one megahertz biased doppler and improved S and X band doppler validation.

(6) Technical Facilities Subsystem. A Meteorological Monitor Assembly was added. This assembly measures and records ground temperature, pressure, relative humidity and ionosphere data. The ionosphere data are measured from tracking the polarization angle of a linearly polarized stationary satellite. These data are recorded on magnetic tape and are transmitted via high speed data lines on a post-pass basis using the Original Data Record recall software.

### B. 26-m Deep Space Stations

(1) Receiver-Exciter Subsystem. A Ranging Demodulator Assembly was added at Goldstone (DSS 11). Switching was provided at DSS 42 in Australia and 61 in Spain to switch the Ranging Demodulator Assemblies from the 64-meter stations to the 26-m stations.

(2) Tracking Subsystem(s). The Antenna Pointing Subsystem software developed for the 64-m stations was also tested and transferred to operations at the 26-m stations. A Planetary Ranging Assembly was added at Goldstone (DSS-11) for ranging data generation. Switching was provided at DSS 42 in Australia and 61 in Spain to switch the Planetary Ranging Assembly from the 64-meter stations to the 26-meter stations.

(3) Monitor and Control Subsystem(s). The software implemented for the 64-meter stations was tested and transferred to operations at the 26-m stations.

### C. Network Operations Control Center

The Tracking System prediction and validation functions were transferred from Mission Support Computers to DSN dedicated computers.

(1) Real Time Monitor Assembly. The real time monitor assembly was developed on a dedicated minicomputer (ModComp II). This assembly validates

tracking system performance for 6 radio metric data streams simultaneously. A System Performance Record is generated for non-real time analysis.

(2) Display Assembly. The display assembly provides cathode ray tube and hard copy displays of performance data for up to 6 radio metric streams simultaneously.

(3) Prediction Assembly. The prediction assembly generates predicted frequencies and angles that are used by the Deep Space Stations for the acquisition and tracking of spacecraft carriers. The prediction assembly operates in a Sigma-5 computer. The predictions are transmitted to the stations via high speed data lines. In addition, the predictions are used to validate the Tracking System performance by comparing observed radio metric data with predicted data.

## V. Summary

The DSN Tracking System—Mark III-75 has been tested in the Network during 1975 and all capabilities except meteorological data have been used for mission support. Complete transfer to operations of the DSN Tracking System—Mark III-75 will occur in the second quarter of CY-1976.

**Table 1. Planned DSS Radio Metric Data Capability**

| Data type | 26-m DSS | 64-m DSS |
|---|---|---|
| Doppler | 1 S-band | 2 S-band or 1 S-X band |
| Range | 1 S-band* | 1 S-band or 1 S-X band |
| DRVID | 1 S-band* | 1 S-band or 1 S-X band |
| Angles | Autotrack or computer aided | Computer aided with conical scan |

*Planetary ranging at DSS 11 and planetary ranging switching capability between DSS 42/43 and DSS 61/63.

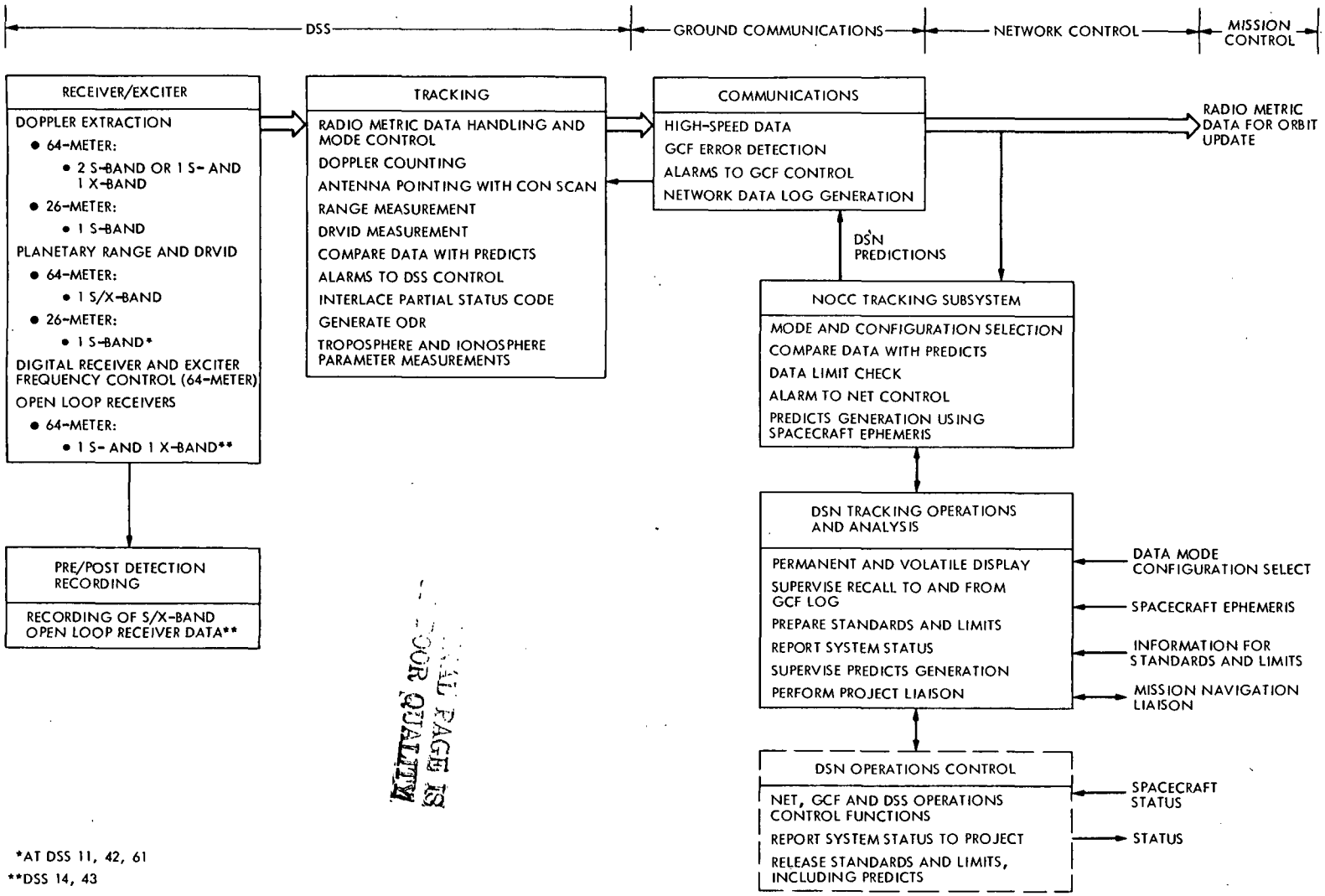




**Fig. 1. DSN Tracking System — Mark III-75 functions**

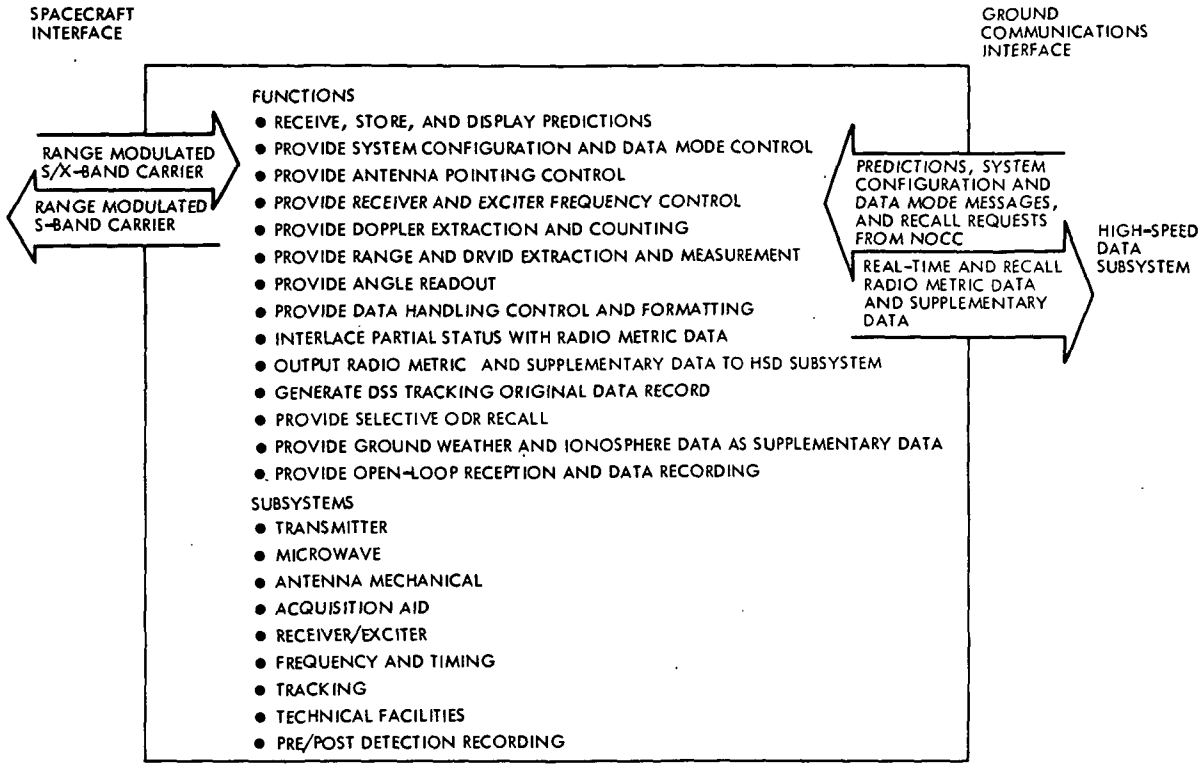


**Fig. 2. DSS tracking functional requirements**

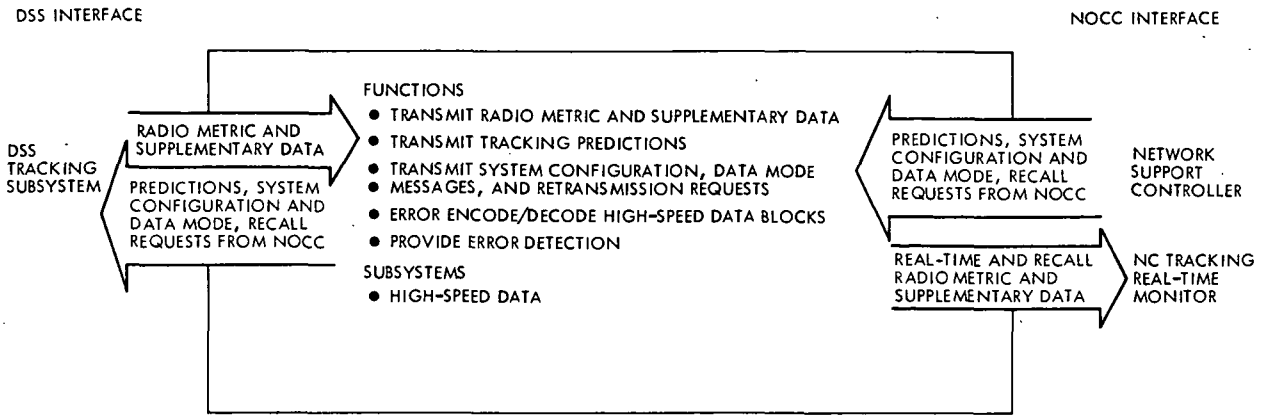


**Fig. 3. Ground communications functional requirements**

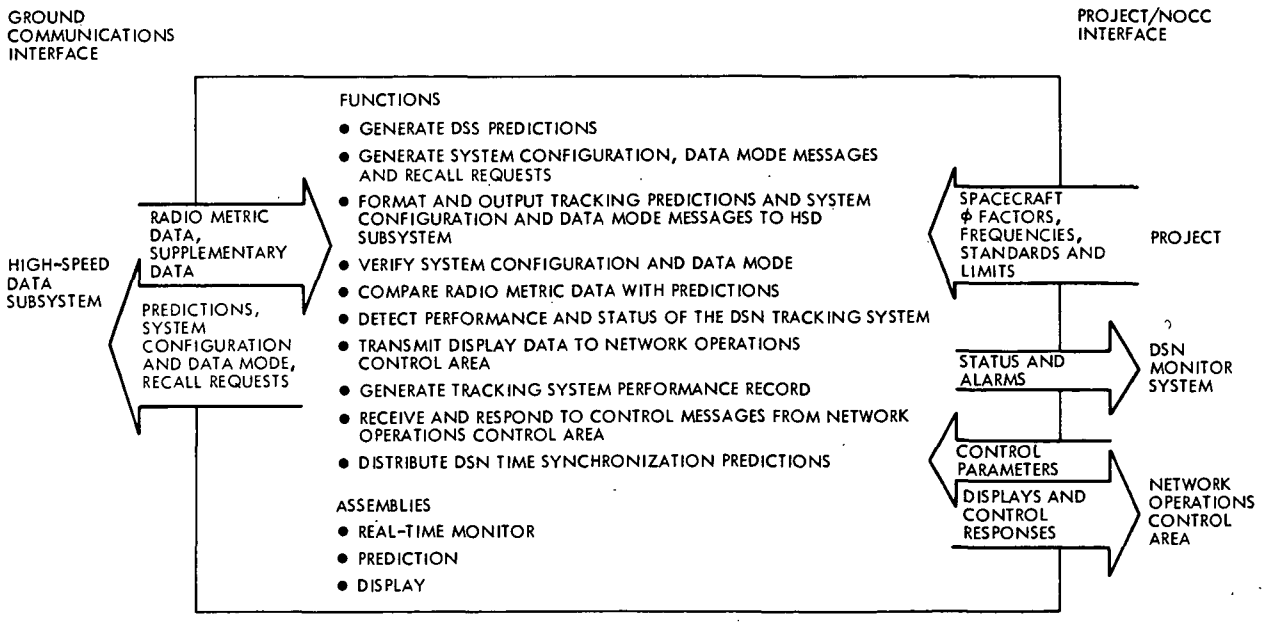


**Fig. 4. NC tracking subsystem functional requirements**

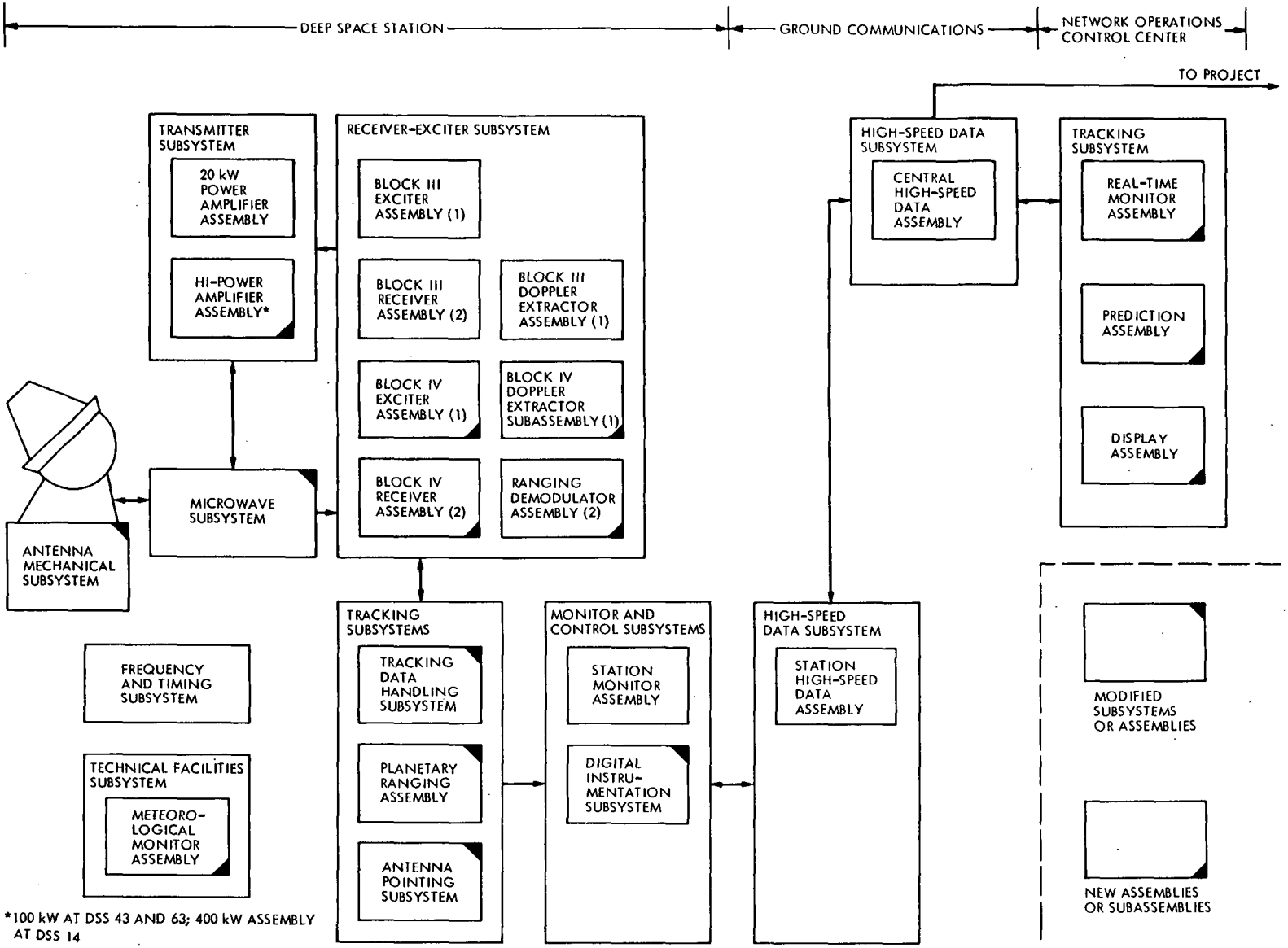


**Fig. 5. DSN Tracking System — Mark III-75 64-m functional block diagram**

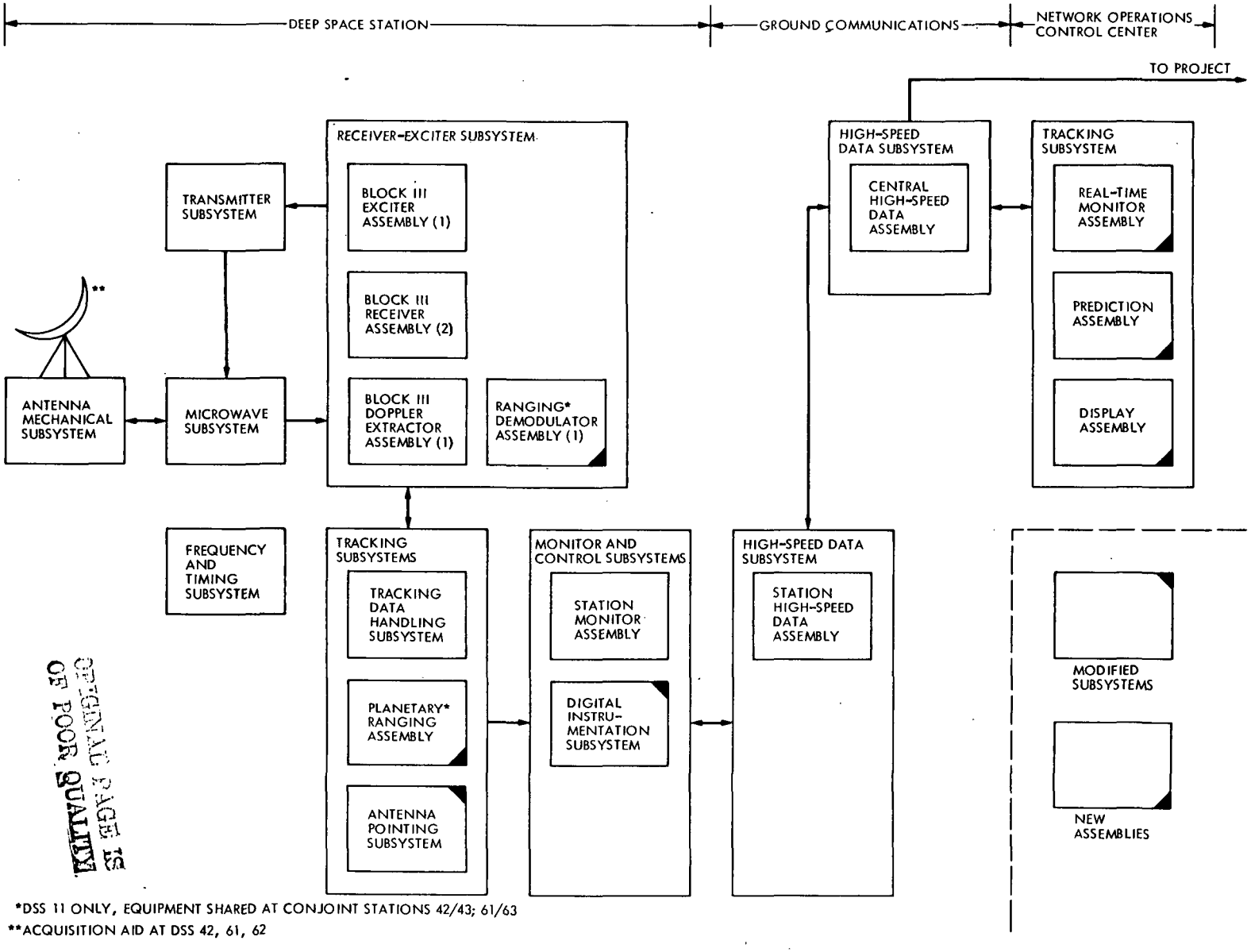




**Fig. 6. DSN Tracking System — Mark III-75 26-m functional block diagram**

# Helios B–Deep Space Network Compatibility Test Summary

A. I. Bryan
DSN Systems Engineering Office

*The DSN–Helios B–compatibility testing followed a very successful three-phase compatibility test program for the Helios prototype and Helios 1 spacecraft. This article covers the tests from arrival of Helios B at Cape Canaveral, Florida through launch. The compatibility tests consisted of (1) DSN–spacecraft radio frequency tests at both weak and strong signal levels, and (2) verification of radio frequency compatibility with the Helios B mated to the launch vehicle at Launch Complex 41.*

## I. Introduction

This report covers the DSN–Helios B compatibility testing that extended over 48 hours from October 31 through November 4, 1975, and for 8 hours on January 10, 1976. The compatibility tests performed during these periods were divided as follows:

(1) DSN–spacecraft radio frequency (RF) tests at both weak and strong signal levels during October 31 through November 4, 1975.

(2) Verification of RF compatibility performed on January 10, 1976, with Helios B mated to the launch vehicle at Launch Complex 41.

The DSN–Helios B compatibility testing followed a very successful three-phase program of compatibility testing between the DSN and the Helios prototype spacecraft (Ref. 1) and Helios 1 (Ref. 2).

## II. Test Report

The DSN–Helios telecommunications compatibility testing utilized a test system that was operationally representative of a standard Deep Space Station (DSS). The test system was under control of a computer to provide appropriate test conditions in an automatic mode of operation.

The spacecraft configurations were agreed upon by the Flight Project and the DSN. Spacecraft modes were selected to exercise a representative subset of all possible configurations and to minimize the time required for completion of an adequate test program.

### A. Telecommunications Compatibility Tests

These tests provided an assessment of telecommunications compatibility status between Helios B and the Network based upon the results obtained between the DSN equipment in the Spaceflight Tracking and Data Network station (STDN MIL 71) and Helios B.

These tests were the final phase of the documented three-phase plan for establishing telecommunications compatibility between the Network and the Helios B spacecraft.

Procedures for conducting the tests were prepared by the DSN. Test parameters and spacecraft design criteria were provided by the Helios spacecraft telecommunications engineers. The final procedures and test plans were approved by the DSN and the Helios Project telecommunications representatives. In particular, the latter personnel provided extensive support during the test procedure preparation and test planning phases. The successful completion of the tests was due in large measure to the excellent support provided by JPL and STDN management and operating personnel.

**1. Test objectives.** A selected set of standard tests for verifying transponder radio frequency, command, telemetry, and metric data compatibility were performed in accordance with the Network Test and Training Plan for the Helios Project.

**2. Test description.** Helios B was configured for flight operations and STDN (MIL 71) was configured to simulate a DSS. The spacecraft was located in the clean room of Building AO, Cape Canaveral Air Force Station, and STDN (MIL 71) is located at Merritt Island, Florida. An S-band radio frequency link of approximately 16 km (10 miles) was used between a 1.85-m antenna at Building AO and a 1.2-m antenna at the STDN station. RF link amplitude variations were 0.5 dB peak-to-peak for the critical tests in telemetry and command.

The STDN station software utilized in performing these tests was supplied by the DSN and was a subset of software officially released to the station for Helios Project support. The programs consisted of:

(1) Telemetry and Command Data Handling Program. This program provides independent control of the commanding and telemetry handling functions. Commands may be controlled manually from the station or automatically from the Mission Control and Computing Center in Pasadena, Calif. Telemetry may be decoded, formatted, and transmitted to the Mission Control and Computing Center for decommutation and display.

(2) Planetary Ranging Assembly Program. This program provides either continuous spectrum or discrete spectrum operation for making very accurate range estimates of a spacecraft at planetary distances.

Tests performed for radio frequency acquisition and tracking performance, telemetry, command and metric data generation are as follows:

Radio Frequency Acquisition and Tracking
- Noncoherent downlink threshold
- Uplink threshold
- Coherent downlink threshold
- Spacecraft maximum sweep and acquisition
- Carrier residual phase jitter
- Subcarrier frequency and phase jitter

Command
- Spacecraft command threshold, 512-Hz subcarrier
- Spacecraft command threshold, 448-Hz subcarrier

Radio Metric
- Ranging channel delay
- Ranging polarity
- Ranging system acquisition time

Telemetry
- Downlink spectrum analysis
- Telemetry bit error rate test
- Telemetry erasure rate

**3. Test results.** Table 1 provides the test results. Significant events and/or other items are discussed below:

(1) During the radio frequency acquisition and tracking tests and radio metric tests, the first downlink threshold measurement was unsuccessful because of excessive RF leakage into the ground receiver. A faulty antenna system was discovered at MIL 71 and replaced. Testing was successfully completed.

(2) Because of ranging channel problems encountered with Helios 1 in October 1975, the radio metric tests performed on Helios B were monitored very closely for any significant deviation from expected performance. There were no anomalies or out-of-tolerance results observed. The spacecraft ranging function performed successfully to all criteria and operating parameters.

(3) In performing the telemetry bit error rate test, it was necessary to modify the procedure. It was noted that large concentrations of low transition densities were present in the data. This condition was manifesting itself in erratic signal-to-noise estimations and bit error counts in the Symbol Synchronizer Assembly. A check with the spacecraft revealed that all experiments were turned off, thereby resulting in no data when these experiments appeared on the spacecraft commutator. By direction of the project, the spacecraft test conductor was not allowed to turn all experiments on. In order to perform the bit error rate tests in the most meaningful manner, it was decided to switch the spacecraft to the coded mode, thereby increasing the data transition density. Therefore, the 8-b/s test was performed at 16 s/s, and the 32-b/s test was performed at 64 s/s. The downlink signal levels were adjusted to correct for the different data rate, and the tests were successfully completed.

### B. Radio Frequency and Data Verification Tests

These tests provided an assessment of telecommunications compatibility status between the DSN, represented by STDN (MIL 71) and Helios B after encapsulation and mating to the launch vehicle. These tests, conducted on January 10, 1976, were a subset of tests performed previously between Helios B and STDN (MIL 71) in October and November 1975.

Procedures for conducting these tests were prepared by the DSN, and spacecraft test parameters and design criteria were provided by the Helios spacecraft telecommunications engineers. The final procedures were approved by the DSN and Helios Project telecommunications representatives.

**1. Test objective.** The objective of the tests was to verify continued compatibility between the DSN and the Helios spacecraft after the spacecraft had been configured for launch operations. All tests were accomplished in accordance with the Network Test and Training Plan for the Helios Project.

**2. Test description.** The Helios spacecraft was in launch configuration, and STDN (MIL 71) was configured to simulate a DSN station. The spacecraft was located at Launch Complex 41, Cape Canaveral Air Force Station, Florida, and STDN (MIL 71) was located at Merritt Island, Florida. An S-band link of approximately 16 km (10 miles) was utilized to establish the spacecraft–ground station interface. The spacecraft transmit–receive function was performed by connecting a test point at the shroud to a 1.2-m antenna connected to the launch service tower.

The ground station software utilized in performing these tests was supplied by the DSN and was a subset of software officially released to the station for Helios Project support. The programs consisted of:

(1) Telemetry and Command Data Handling Program. This program provides independent control of the commanding and telemetry handling functions. Commands may be controlled manually from the station or automatically from the Mission Control and Computing Center in Pasadena. Telemetry may be decoded, formatted, and transmitted to the Mission Control and Computing Center for decommutation and display.

(2) Planetary Ranging Assembly Program. This program provides either continuous spectrum or discrete spectrum operation for determining very accurate range estimates of a spacecraft at planetary distances.

(3) Helios Decommutation and Data Validation Program. This program provides the capability of decommutating spacecraft engineering data and display at the station for verifying spacecraft parameters during compatibility testing.

Tests performed for radio frequency acquisition and tracking performance, telemetry, command and metric data generation are as follows:

Radio Frequency Acquisition and Tracking
- Noncoherent downlink threshold
- Uplink threshold
- Spacecraft maximum sweep and acquisition

Command
- Spacecraft command performance, 512-Hz subcarrier
- Spacecraft command performance, 448-Hz subcarrier

Radio Metric
- Ranging system acquisition time

Telemetry
- Telemetry performance test, 128 b/s
- Telemetry performance test, 1024 b/s

**3. Test results.** Table 2 provides the test results. (Table 3 gives definitions for abbreviations in Tables 1

and 2.) Significant events and/or other items are discussed below:

(1) During the radio frequency acquisition and tracking tests, the initial efforts to perform the spacecraft maximum sweep and acquisition test and the uplink threshold tests were seriously hampered by large fluctuations of the link (5 dB). These fluctuations were isolated to the heavy traffic and activities being conducted on the launch tower by launch vehicle personnel. When that activity ceased, the tests were successfully performed. It is highly recommended that future tests be conducted during periods of minimum activity at the launch vehicle.

(2) No problems were encountered in the command, radio metric, and telemetry tests.

## III. Conclusions

The formal DSN–Helios compatibility program was very successful and terminated in the successful launching of both Helios 1 and Helios 2 spacecraft. Helios 1 was launched on December 10, 1974, followed by Helios 2 on January 15, 1976.

The importance of a formal compatibility test program is clearly demonstrated by the problem areas uncovered, verified and resolved during the DSN–Helios testing. Prominent problem areas discovered and resolved during this test program were:

(1) Deficiencies in the engineering model transponder. The transponder exhibited lack of sensitivity, pushing effects at strong uplink signal levels, instability of the voltage-controlled crystal oscillator, and improper shielding.

(2) Polarity of the ranging channel in the Helios 1 spacecraft was inverted. This condition was different from the prototype spacecraft.

(3) Many hundreds of hours of test time were used at the old DSN station (DSS 71) to determine optimum modulation indices for the Helios Mission. A full description of this testing was published in Ref. 3.

(4) An elaborate test system to simulate uplink and downlink amplitude, phase, and frequency modulation conditions during the spacecraft Step II maneuver was performed. This simulation demonstrated that the spacecraft could be successfully commanded during this very critical phase of flight.

Had these problems remained undetected and unresolved prior to launch, serious operational problems to the Network with the spacecraft in flight would have resulted.

## References


1. Bryan, A. I., "Helios Prototype Spacecraft Deep Space Network Compatibility Test Summary," in *The Deep Space Network Progress Report 42-23*, pp. 22–36, Jet Propulsion Laboratory, Pasadena, Calif., Oct. 15, 1974.

2. Bryan, A. I., "Helios Flight 1 Spacecraft/Deep Space Network Compatibility Test Summary," in *The Deep Space Network Progress Report 42-26*, pp. 27–40, Jet Propulsion Laboratory, Pasadena, Calif., Apr. 15, 1975.

3. Layland, J. W., "DSS Tests of Sequential Decoding Performance," in *The Deep Space Network Progress Report 42-20*, pp. 69–77, Jet Propulsion Laboratory, Pasadena, Calif., Apr. 15, 1974.

| Test date, 1975 | Test title | Test No. | Deep Space Network | | | | | | | | | |
|---|---|---|---|---|---|---|---|---|---|---|---|---|
| | | | RCV | EXC | PRA RNG | CMD | Uplink doppler | Uplink offset | CMA SUBC offset | SDA SUBC offset | CAR SUP | Bit rate |
| 10/10 | SC maximum sweep and acquisition rate | I.1 | Blk IV, 2295.404288 MHz | BLK IV, 2113.65300 MHz | Off | Off | 500 Hz | −30.0 KHz | NA | NA | High | 2048 |
| | | | Same | Same | Off | Off | 500 Hz | +30.0 KHz | NA | NA | High | 2048 |
| | | | Same | Same | Off | Off | 80 Hz | −9.7 KHz | NA | NA | High | 2048 |
| | | | Same | Same | Off | Off | 80 Hz | +9.9 KHz | NA | NA | High | 2048 |
| 11/3 | Downlink spectrum analysis | II.1 | BLK IV, −110 dBm, 2295.369920 MHz, | NA | Off | Off | NA | NA | NA | NA | High | 2048 |
| | | II.2 | Same | NA | Off | Off | NA | NA | NA | NA | High | 128 |
| | | II.3 | Same | NA | Off | Off | NA | NA | NA | NA | Low | 32 |
| | | II.7 | 2295.359896 MHz −79 dBm | 2113.643904 MHz | On (idle seq.) | NA | NA | NA | NA | NA | High | 2048 |
| | | II.10 | Same | Same | On | On | NA | NA | NA | NA | High | 128 |
| 11/31 | Uplink threshold | III.1 | BLK IV, −100 dBm, 2295.369632 MHz | BLK IV, 2113.653000 MHz | Off | Off | NA | NA | NA | NA | High | 128 |
| | | III.2 | Same | Same | On | Off | NA | NA | NA | NA | High | 128 |
| | | III.3 | Same | Same | Off | Off | NA | NA | NA | NA | High | 128 |
| 10/31 | Carrier residual phase jitter | IV.1 | BLK IV, −104 dBm, 2295.369728 MHz | BLK IV, 2113.653000 MHz | Off | Off | NA | NA | NA | NA | High | 2048 |
| | | IV.2 | BLK IV, −100 dBm, 2295.365024 MHz | BLK IV, 2113.653000 MHz | Off | Off | NA | NA | NA | NA | High | 2048 |
| | | IV.3 | BLK IV. −104 dBm, 2295.369728 MHz | BLK IV. 2113.653000 MHz | Off | Off | NA | NA | NA | NA | High | 2048 |
| | | | | | Off | Off | NA | NA | NA | NA | High | 2048 |

Table 1. DSN–Helios B telecommunications test summary

| Spacecraft | | | | | | | | Test data | | Test time | Test Comments |
|---|---|---|---|---|---|---|---|---|---|---|---|
| EXC | RCV | PWR | ANT | TWT | RNG | SC DM | SC FM | Performance | Criteria | | |
| 1 | 1 −102 dBm | HP | MGA | 2 | Off | 0 | 4 | Acquired at −100 dBm; tracked to +65 kHz | Acquire at −100 dBm; track to +32.5 kHz | 2 hr 32 min | Acquired UL at best lock (VCX01) |
| 1 | 1 −102 dBm | HP | MGA | 2 | Off | 0 | 4 | Acquired at −100 dBm; tracked to −32.5 kHz | Acquire at −100 dBm; track to −32.5 kHz | 2 hr 32 min | Acquired UL at best lock (VCX01) |
| 1 | 1 −102 dBm | HP | MGA | 2 | Off | 0 | 4 | Acquired at −141 dBm; tracked to +32.5 kHz | Acquire at −141 dBm; track to +32.5 kHz | 2 hr 32 min | Rcvr 2 OK; Rcvr 1 dropped +7 kHz at −141 ±1; both rcvr's OK at −139 ±1 |
| 1 | 1 −102 dBm | HP | MGA | 2 | Off | 0 | 4 | Acquired at −141 dBm; tracked to −32.5 kHz | Acquire at −141 dBm; track to −32.5 kHz | 2 hr 32 min | Acquired UL at best lock (VCX01) |
| 1 | 1 | HP | MGA | 1 | Off | 0 | 4 | No spurs observed | No spurious signal within 30 dB of the carrier | 9 min | Subcarrier osc No. 2 noncoherent mode |
| 1 | 1 | LP | LGA | NA | Off | 0 | 4 | No spurs observed | No spurious signal within 30 dB of the carrier | 41 min | Subcarrier osc No. 1 noncoherent mode |
| 1 | 1 | LP | LGA | NA | Off | 0 | 4 | No spurs observed | No spurious signal within 30 dB of the carrier | 10 min | Subcarrier osc No. 1 noncoherent mode |
| 1 | 1 −103.5 dBm | LP | LGA | 1 | Off | 0 | 4 | No spurs observed | No spurious signal within 30 dB of the carrier | 22 min | VCX01, coherent (Goldstone first acq.) mode |
| 1 | 1 −103.5 dBm | HP | MGA | 1 | On | 0 | 4 | No spurs observed | No spurious signal within 30 dB of the carrier | 15 min | VCX01, coherent |
| 1 | 1 | HP | MGA | 2 | Off | 0 | 4 | −154.5 dBm | −155.0 ±1.0 dBm | 50 min | Threshold value is average of 3 measurements. Link variations of ±1.5 dB were noted in Subtest 2 |
| 1 | 1 | HP | MGA | 2 | On | 0 | 4 | −153.5 dBm | −155.0 ±1.0 dBm | 31 min | |
| 1 | 2 | HP | LGA | 2 | Off | 0 | 4 | −154.83 dBm | −155.0 ±1.0 dBm | 48 min | |
| 1 | 1 −105 dBm | HP | MGA | 1 | Off | 0 | 4 | 4.93 deg rms | 5.7 deg rms | 16 min | |
| 2 | 1 −102 dBm | HP | MGA | 2 | Off | 0 | 4 | 3.275 deg rms | 5.7 deg rms | 30 min | RF link variation |
| 1 | 1 −104 dBm | HP | MGA | 2 | Off | 0 | 4 | 1.77 deg rms | 2.86 deg rms | 36 min | 10 dB p-p |
| 1 | 1 −104 dBm | HP | MGA | 2 | Off | 0 | 4 | 14.08 deg rms | 22.9 deg rms | | F-2 SC exhibited greater residual phase jitter than F-1 SC because of aux. osc. crystals. Inferior performance not unexpected but still met criteria. |

| Test date, 1975 | Test title | Test No. | Deep Space Network | | | | | | | | | |
|---|---|---|---|---|---|---|---|---|---|---|---|---|
| | | | RCV | EXC | PRA RNG | CMD | Uplink doppler | Uplink offset | CMA SUBC offset | SDA SUBC offset | CAR SUP | Bit rate |
| 10/31 | | IV.4 | BLK IV, −104 dBm, 2295.369728 MHz | BLK IV, 2113.653000 MHz | Off | Off | NA | NA | NA | NA | High | 2048 |
| | | | | | Off | Off | NA | NA | NA | NA | High | 2048 |
| 11/4 | Bit error rate | VIII.1 | BLK IV, −146 dBm, 2295.369774 MHz | BLK IV, 2113.653000 MHz | Off | Off | NA | NA | NA | NA | Low | 8 (coded) |
| | | VIII.2 | BLK IV, −140 dBm | BLK IV, 2113.653000 MHz | Off | Off | NA | NA | NA | NA | Low | 32 (coded) |
| 11/4 | Telemetry erasure rate | IX.1 | BLK IV, −143.5 dBm, 2295.369800 MHz | BLK IV, 2113.653024 MHz | Off | On | NA | NA | NA | NA | High | 128 |
| | | IX.2 | BLK IV, −138 dBm, 2295.369800 MHz | 2113.653024 MHz | On | On | NA | NA | NA | NA | High | 512 |
| | | IX.3 | BLK IV, −134.5 dBm, 2295.369800 MHz | BLK IV, 2113.653024 MHz | Off | On | NA | NA | NA | NA | High | 1024 |
| 10/31 | Subcarrier frequency and phase jitter | X.1 | BLK IV, −104 dBm, 2295.369728 MHz | BLK IV, 2113.653000 MHz | Off | Off | NA | NA | NA | NA | High | 128 |
| | | X.2 | BLK IV. −104 dBm, 2295.369728 MHz | BLK IV, 2113.653000 MHz | Off | Off | NA | NA | NA | NA | High | 128 |
| | | X.3 | Blk IV, −104 dBm, 2295.369728 MHz | BLK IV, 2113.653000 MHz | Off | Off | NA | NA | NA | NA | High | 128 |
| 10/31 | SC command | XI.1 | BLK IV, −100 dBm, 2295.369774 MHz | BLK IV, 2113.653000 MHz | Off | On | NA | NA | NA | NA | High | 128 |
| | | XI.2 | Same | Same | On | On | NA | NA | NA | NA | High | 512 |
| | | XI.3 | Same | Same | Off | On | NA | NA | NA | NA | High | 1024 |

*Block III Receiver I, Exciter 1 used for all tests.*

Table 1 (contd)

| Spacecraft | | | | | | | | Test data | | Test time | Comments |
|---|---|---|---|---|---|---|---|---|---|---|---|
| EXC | RCV | PWR | ANT | TWT | RNG | SC DM | SC FM | Performance | Criteria | | |
| 1 | 2 −104 dBm | HP | LGA | 2 | Off | 0 | 4 | 2.05 deg rms | 2.86 deg rms | 23 min | |
| 1 | 2, −104 dBm | HP | LGA | 2 | Off | 0 | 4 | 14.57 deg rms | 22.9 deg rms | | |
| 1 | 1 −135 dBm | HP | MGA | 2 | Off | 0 | 4 | $1.7 \times 10^{-4}$ | $10^{-4}$ | 2 hr 27 min | Coded mode |
| 1 | 1 −130 dBm | HP | MGA | 2 | Off | 0 | 4 | $1.3 \times 10^{-5}$ | $10^{-4}$ | 3 hr 4 min | Coded mode |
| 1 | 1 −128.1 dBm | HP | MGA | 2 | Off | 0 | 4 | TCP $\alpha = 0$ TCP $\beta = 0$ | $10^{-3}$ | 628 min | |
| 1 | 1 −126 dBm | HP | MGA | 2 | On | 0 | 4 | TCP $\alpha = 0$ TCP $\beta = 0$ | $10^{-3}$ | 115 min | |
| 1 | 1 −133 dBm | HP | HGA | 2 | Off | 0 | 4 | TCP $\alpha = 1.99 \times 10^{-4}$ TCP $\beta = 7.98 \times 10^{-4}$ | $10^{-3}$ | 208 min | |
| 1 | −105 dBm | LP | LGA | NA | Off | 0 | 4 | 0.505 deg rms 32,768 Hz | 1.15 deg rms 32,768 Hz | 38 min | SC DHE osc. No. 1 Chain 1 |
| 2 | NA −105 dBm | LP | LGA | NA | Off | 0 | 4 | 0.505 deg rms 32,768 Hz | 1.15 deg rms 32,768 Hz | 12 min | SC DHE osc. No. 1 Chain 2 |
| 2 | NA −105 dBm | LP | LGA | NA | Off | 0 | 4 | 0.51 deg rms 32,768 Hz | 1.15 deg rms 32,768 Hz | 10 min | SC DHE osc. No. 2 Chain 2 |
| 1 | 1 −144 dBm | HP | MGA | 2 | Off | 0 | 4 | 54 commands accepted and processed | All commands accepted by SC | 37 min | VCOX1, coherent, command SC at 512 Hz |
| 1 | 1 −137 dBm | HP | MGA | | On | 0 | 4 | 54 commands accepted and processed | All commands accepted by SC | 25 min | |
| 1 | 2 −144 dBm | HP | HGA | 2 | Off | 0 | 4 | 54 commands accepted and processed | All commands (continuous) accepted and processed | 38 min | VCX02, coherent, command SC at 448 Hz |

| Test date, 1976 | Test title | Test No. | Deep Space Network | | | | | | | | | |
|---|---|---|---|---|---|---|---|---|---|---|---|---|
| | | | RCV | EXC | PRA RNG | CMD | Uplink doppler | Uplink offset | CMA SUBC offset | SDA SUBC offset | CAR SUP | Bit rate |
| 1/10 | SC maximum sweep and acquisition rate | I.1 | −97 dBm | 2113.621152 MHz to 2113.685856 MHz | Off | Off | 500 Hz | −30 kHz to +32.5 kHz | NA | NA | High | 2048 |
| | | | −97 dBm | 2113.682976 MHz to 2113.618560 MHz | Off | Off | 500 Hz | +30 kHz to −32.9 kHz | NA | NA | High | 2048 |
| 1/10 | Uplink threshold | III.1 | −115 dBm, 2295.368688 MHz | 2113.652000 MHz | Off | Off | NA | NA | NA | NA | High | 2048 |
| | | III.3 | −115 dBm, 2295.368688 MHz | 2113.652000 MHz | Off | Off | NA | NA | NA | NA | High | 2048 |
| 1/10 | Downlink threshold | V.1 | 2295.369056 MHz | 2113.652000 MHz | Off | Off | NA | NA | NA | NA | High | 128 |
| 1/10 | Ranging system acquisition time | VII.1 | −112 dBm, 2295.368688 MHz | 2113.652000 MHz | On | Off | NA | NA | NA | NA | High | 128 |
| 1/10 | Telemetry performance | IX.1 | 2295.368688 MHz | 2113.652000 MHz | Off | On | NA | NA | NA | NA | High | 128 |
| | | IX.3 | −114 dBm, 2295.368688 MHz | 2113.652000 MHz | Off | On | NA | NA | NA | NA | High | 1024 |
| 1/10 | Spacecraft command | XI.1 | −115 dBm, 2295.368688 MHz | 2113.652000 MHz | Off | On | NA | NA | NA | NA | High | 2048 |
| | | XI.3 | −115 dBm, 2295.368688 MHz | 2113.652000 MHz | Off | On | NA | NA | NA | NA | High | 2048 |

Block III Receiver I, Exciter 1 used for all tests.

Table 2. DSN–Helios B–Launch Complex 41 telecommunications test summary

| Spacecraft | | | | | | | | Test data | | Test time | Test Comments |
|---|---|---|---|---|---|---|---|---|---|---|---|
| EXC | RCV | PWR | ANT | TWT | RNG | SC DM | SC FM | Performance | Criteria | | |
| 1 | 1 and 2 −110 dBm | HP | LGA | 2 | Off | 0 | 4 | Acquired and tracked | Acquire at best lock, track to +32.5 kHz | 15 min | 2113.652000 kHz, best lock frequency SC receiver 1/2 |
| 1 | 1 and 2 −110 dBm | HP | LGA | 2 | Off | 0 | 4 | Acquired and tracked | Acquire at best lock, track to −32.5 kHz | | |
| 1 | 1 | HP | LGA | 2 | Off | 0 | 4 | −157.2 dBm | To be measured | 2 hr 4 min | Average of 3 runs, link variance 1.5 dB p-p |
| 1 | 2 | HP | LGA | 2 | Off | 0 | 4 | −157.0 dBm | To be measured | | Average of 2 runs, link variance 1.5 dB p-p |
| 1 | 1 | HP | LGA | 1 | Off | 0 | 4 | −157.5 dBm | −159.0 ±3 dBm | 20 min | Average of 3 runs, link variance 8.0 dB p-p |
| 1 | 1 −116.5 dBm | HP | LGA | 1 | On | 0 | 4 | 1-minute acquisition 98827 RU | TBD | 8 min | 15 components, discrete 1 minute integration time |
| 1 | 1 −113 dBm | HP | LGA | 1 | Off | 0 | 4 | Decommutated data satisfactory | 30 min of decommutated data | 33 min | SDA freq. 131072.0 Hz |
| 1 | 2 −113 dBm | HP | LGA | 1 | Off | 0 | 4 | Decommutated data satisfactory | 30 min of decommutated data | 33 min | SDA freq. 131072.0 Hz |
| 1 | 1 −108 dBm | HP | LGA | 2 | Off | 0 | 4 | All good commands (210 commands) | All commands successfully received by SC | 39 min | Commands 501-506, 512-Hz subcarrier |
| 1 | 2 −108 dBm | HP | LGA | 2 | Off | 0 | 4 | All good commands (210 commands) | All commands successfully received by SC | 42 min | Commands 501-506, 448-Hz subcarrier |

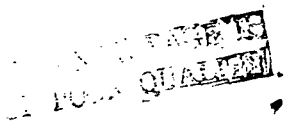

**Table 3. Definitions for Tables 1 and 2**

| | |
|---|---|
| ANT | Spacecraft antenna |
| Bit rate | Clock frequency of the telemetry bit information |
| BLK III exciter | The standard DSN S-band exciter equipment |
| BLK III receiver | The standard DSN S-band receiving equipment |
| CAR SUP | Downlink carrier suppression due to telemetry modulation |
| CMA SUBC offset | Command modulation assembly subcarrier frequency offset relative to nominal |
| CMD | Telemetry and command data handling command modulation |
| EXC | Spacecraft S-band exciter equipment |
| HGA | High-gain antenna |
| LGA | Low-gain antenna |
| MGA | Medium-gain antenna |
| PRA RNG | Planetary ranging assembly modulation |
| PWR | Spacecraft transmitter power mode |
| RCV | Spacecraft S-band receiving equipment |
| RNG | Spacecraft ranging channel |
| SC DHE | Spacecraft data handling equipment |
| SC DM | Spacecraft data mode |
| SC FM | Spacecraft data format |
| SDA SUBC offset | Subcarrier demodulator assembly subcarrier frequency offset relative to nominal |
| TWT | Traveling wave tube amplifier |
| UNC | Uncoded |
| Uplink doppler | Ramp rate of the uplink carrier frequency |
| Uplink offset | Uplink carrier frequency offset relative to the spacecraft receiver rest frequency |

# Pioneer Venus 1978 Mission Support

R. B. Miller
DSN Systems Engineering Office

*The DSN Master Schedule for preparations for the Pioneer Venus 1978 Orbiter and Multiprobe Mission is described.*

## I. Introduction

Accompanying this article is the DSN Major Milestone Schedule (Figs. 1 and 2) for Pioneer Venus 1978 Orbiter and Multiprobe. What follows is a description of the DSN plans for preparing for Pioneer Venus 1978, including current status, using the attached schedule.

A Support Instrumentation Requirements Document (SIRD) for Pioneer Venus 1978 was received in October 1975 and is awaiting NASA Headquarters review and signature. A NASA Support Plan (NSP) will be prepared by the Tracking and Data Systems Manager for Pioneer Project three months after the receipt of a signed Support Instrumentation Requirements Document.

The major mission events for Pioneer Venus are the launch of the Orbiter in May 1978, followed by the launch of the Multiprobe Mission in August 1978. Both launches will utilize an Atlas-Centaur launch vehicle. The Orbiter will go into orbit around the planet Venus on about 1 December 1978, with the Multiprobe entry into the Venusian atmosphere about five days later. The release of the Probes from the Bus spacecraft will take place in late November 1978.

## II. DSN-Spacecraft Compatibility Tests

Deep Space Network-Spacecraft compatibility testing will take place in three phases: weak signal level and strong signal level testing at the Compatibility Test Area (CTA 21) at JPL and compatibility testing at Cape Canaveral using the DSN equipment located at the STDN MIL Station. The weak signal level testing will take place in March 1977 and will utilize breadboard or flight spare spacecraft components which will be brought to CTA 21. It is not currently planned to bring a telemetry subsystem for these tests; however, the Project is planning to provide some means of generating realistic telemetry signals to play through the spacecraft radio system. The weak signal level testing will include X-band tests.

The strong signal level testing will take place in October 1977 for the Orbiter, and in January 1978 for the Multiprobe mission. Strong signal level testing will be accomplished using the actual spacecraft located at Hughes Aircraft Company, with signals relayed via microwave to CTA 21. X-band testing will not be required as it is anticipated the microwave will not support an X-band link.

## III. Mission Operations System Readiness

The Project plans to establish Ground Data System compatibility by testing the Ground Data System in December 1977. For this purpose, the DSN will have at least one station in launch readiness by November 1977. The DSN will have achieved complete launch readiness (at least one 26-meter subnet) by 1 February 1978. The Ground Data System and Near-Earth Readiness dates are the same: 1 April for the Orbiter, and 1 July for the Multiprobe. The Launch Operational Readiness testing will be accomplished in early May for the Orbiter, and early August for the Multiprobe.

The Ground Data System and Mission Operations System encounter readiness date has not yet been established, nor has the DSN encounter readiness date been negotiated with the Project.

## IV. DSN Multimission Implementation Required by Pioneer Venus

Pioneer Venus 1978 will be utilizing new-generation DSN Telemetry and Command Systems that involve replacing the existing XDS-920 computers with minicomputers which separate the telemetry and command functions. Included in this implementation is a minicomputer replacement for the Tracking System hardware at the Deep Space Stations. In addition, a minicomputer will be implemented to control the communications interface with the stations and will also provide a centralized digital Original Data Record. The Multimission schedule for the 920 computer replacement (whose official name is the DSN Mark III Data Subsystems Implementation Project) is shown on Lines 12 and 13 of the schedule (Fig. 1).

The telemetry and command software for Pioneer Venus 1978 will have a two-phase implementation. All of the command software and the telemetry software for interplanetary flight and orbital operations will be delivered in mid-September 1976. The remaining telemetry software for support of the Multiprobe entry will be delivered in mid-March 1977. The second delivery of telemetry software will provide the capability to support the multiple telemetry streams required during the Multiprobe entry as well as the special capability to record the soft decisions out of the Symbol Synchronizer Assembly for two telemetry streams at the Goldstone Mars Station (DSS 14) and the Australia Ballima Station (DSS 43). This latter capability is required because the Multiprobe entry will require the simultaneous reception at each station of four convolutionally coded telemetry streams, whereas the DSN is implementing the capability to decode only two streams in real time.

It is planned to complete the S-X conversion of one 26-meter Deep Space Station prior to the orbital operations of Pioneer Venus. This will require five months of downtime starting 1 July 1978, with full operational status reached by 1 December 1978. This implementation should help alleviate some of the conflicts for 64-meter station coverage during the simultaneous Pioneer Venus orbital operations and Mariner Jupiter–Saturn encounters of the planet Jupiter.

The DSN is converting to 7200-bit-per-second high-speed data blocks in December 1976, which also requires a change of communications equipment at the Ames Research Center's Pioneer Mission Operations Control Center.

Hydogen masers will be operational in the 64-meter subnet by 1 July 1977, and are required to support the Differential Long Baseline Interferometry (DLBI) Wind Measurement Experiment of the Multiprobe Mission.

## V. Receiver Implementation

The remaining part of this article deals with implementation items specifically required for the Multiprobe portion of the Pioneer Venus 1978 mission (see Fig. 2). The first two items listed are additional receivers which are required to support the multiple signals which will be present for the Multiprobe entry. An earlier Progress Report article (Ref. 1) should be consulted for a description of the receiver configuration and analog recording requirements for the Multiprobe entry. Briefly, four Probes will be simultaneously entering the Venusian atmosphere, and the DSN will be required to simultaneously acquire four signals which have not been seen since the spacecraft was launched. An attempt will be made to acquire and maintain in two-way coherent lock one of the four Probes during the Probe entry. Five closed-loop receivers are therefore required to support the Multiprobe entry, which is one more than the usual complement of receivers at a 64-meter station. The fifth receiver is required because an attempt will be made to maintain the large Probe in two-way coherent lock, which could be one-way at any given time during the entry. As a means of recovering data during the time period when the closed-loop receivers have not acquired lock, a pre-carrier detection telemetry recording system is being implemented for Pioneer Venus. This requires four open-loop receivers, one per Probe, which is two additional open-loop receivers compared to the usual 64-meter configura-

tion. These six additional receivers (one closed-loop and two open-loop at both DSS 14 and DSS 43) are being produced by modifying surplus Manned Space Flight Network Block III equivalent receivers. These receivers are to be manufactured by 1 September 1977 and operational by 1 January 1978.

## VI. Predetection Telemetry Recording

The pre-carrier detection telemetry recording to be implemented for Pioneer Venus is also described in Ref. 1. It involves procurement of a new generation of analog recorders to record the output of open-loop receivers with the data from each Probe going on to a separate track of the recorder. These recordings will then be played back through an up-converter into the closed-loop receivers at CTA 21. The necessary up-converters will also be provided to DSSs 14 and 43, but only for the purpose of pre- and post-track validation that the predetection recording equipment is operating properly. A prototype of this recording system is undergoing evaluation which should be completed by 1 July 1976. The operational recorders will be installed at CTA 21 on 1 January 1977, at DSS 14 on 1 June 1977, and at DSS 43 in mid-September 1977.

## VII. Differential Long Baseline Interferometry Wind Measurement

The Differential Long Baseline Interferometry Wind Measurement Experiment for the purpose of measuring the wind velocities in the atmosphere of Venus was described in great detail in Ref. 2. A preliminary plan has been developed for validating the Network's capability of meeting the requirements of this experiment and for developing the necessary calibration and receiver interfaces. This preliminary plan is shown on lines 7 and 8 of Fig. 2. The plan is to develop a preliminary block diagram for the calibrator and receiver interface for the experiment by 1 May 1976, and to have completed the prototype design by 1 July 1976. The prototype should be completed by 1 September 1976. Concurrent with the design and prototype development will be testing in order to determine the Network performance (principally in the area of relative phase stability across the required bandwidth) starting in about June 1976, with a full evaluation of the prototype equipment starting at the completion of the construction of the equipment in September 1976. It is tentatively planned to install the prototype equipment at DSS 14 after the end of the primary Viking Mission in December 1976 and to complete its evaluation by 1 February 1977. The final design of the operational system, based on the experience with the prototype, will start in late-1976 with completion of the operational design by 1 February 1977. Fabrication of the equipment will be completed by 1 September 1977 to achieve an operational capability in the DSN stations by 1 January 1978. The Space Flight Tracking and Data Network (STDN) will be required to develop the receiver interface and calibration system for the STDN stations which will support the Multiprobe entry (Santiago, Chile and Guam). The detailed schedule of the STDN activity and how it will interface with the DSN activity has not yet been negotiated.

The high-rate digital recorders required for the DLBI experiment will undergo testing of the prototype units during 1976, with a target to complete evaluation of the prototypes by 1 October 1976. The DSN is responsible for interfacing the recorder subsystem with the STDN timing and power equipment; the design of these required interfaces is in process with completion targeted for 1 July 1976. Procurement of the operational recorders will start in July 1976, with the completion of manufacture of the recorders targeted for April 1977. The associated monitor and control electronics will be completed by 1 April 1977, with integration to follow with completion in July 1977. It is then planned to have a trial installation for integration test purposes at the STDN station located at Goldstone, California, during August 1977. The original plan was for this integration testing at the STDN station to take place in November 1977, but the date has been moved up to be compatible with the desired operational date at the overseas stations. It is planned to have the Mars station (DSS 14) and the Santiago STDN station operational for the DLBI experiment in January 1978, with DSS 43 and Guam operational in February 1978. The experimenter's schedule for providing the interface at the Massachusetts Institute of Technology for utilizing the high-rate digital recordings produced at the stations has not yet been negotiated, but the Massachusetts Institute of Technology must be capable of receiving tapes to process them for validation purposes by January 1978. Completion of the station's implementation for the DLBI experiment in January and February 1978 will allow ten months of evaluation and testing and training prior to the Multiprobe entry.

## VIII. Multiprobe Entry Simulation and Signal Presence Indicator

Two remaining implementations are planned to support the Multiprobe entry of Pioneer Venus. First is a means of dynamically simulating the signals of the four Probes, both realistically in signal level and doppler. This implementation is felt to be necessary since the DSN will not simultaneously see the four Probe signals until the actual entry event.

The final implementation will be signal presence indicator for DSSs 14 and 43 to be used in real time during the Multiprobe entry. This device will be some type of fast Fourier transform device which will enable taking a spectrum out of the open-loop receiver to determine that all signals are present.

## References


1. Miller, R. B., "Pioneer Venus 1978 Mission Support," in *The Deep Space Network Progress Report 42-27*, pp. 28-35, Jet Propulsion Laboratory, Pasadena, California, June 15, 1975.
2. Miller, R. B., "Pioneer Venus 1978 Mission Support," in *The Deep Space Network Progress Report 42-31*, pp. 11-14, Jet Propulsion Laboratory, Pasadena, California, Feb. 15, 1976.

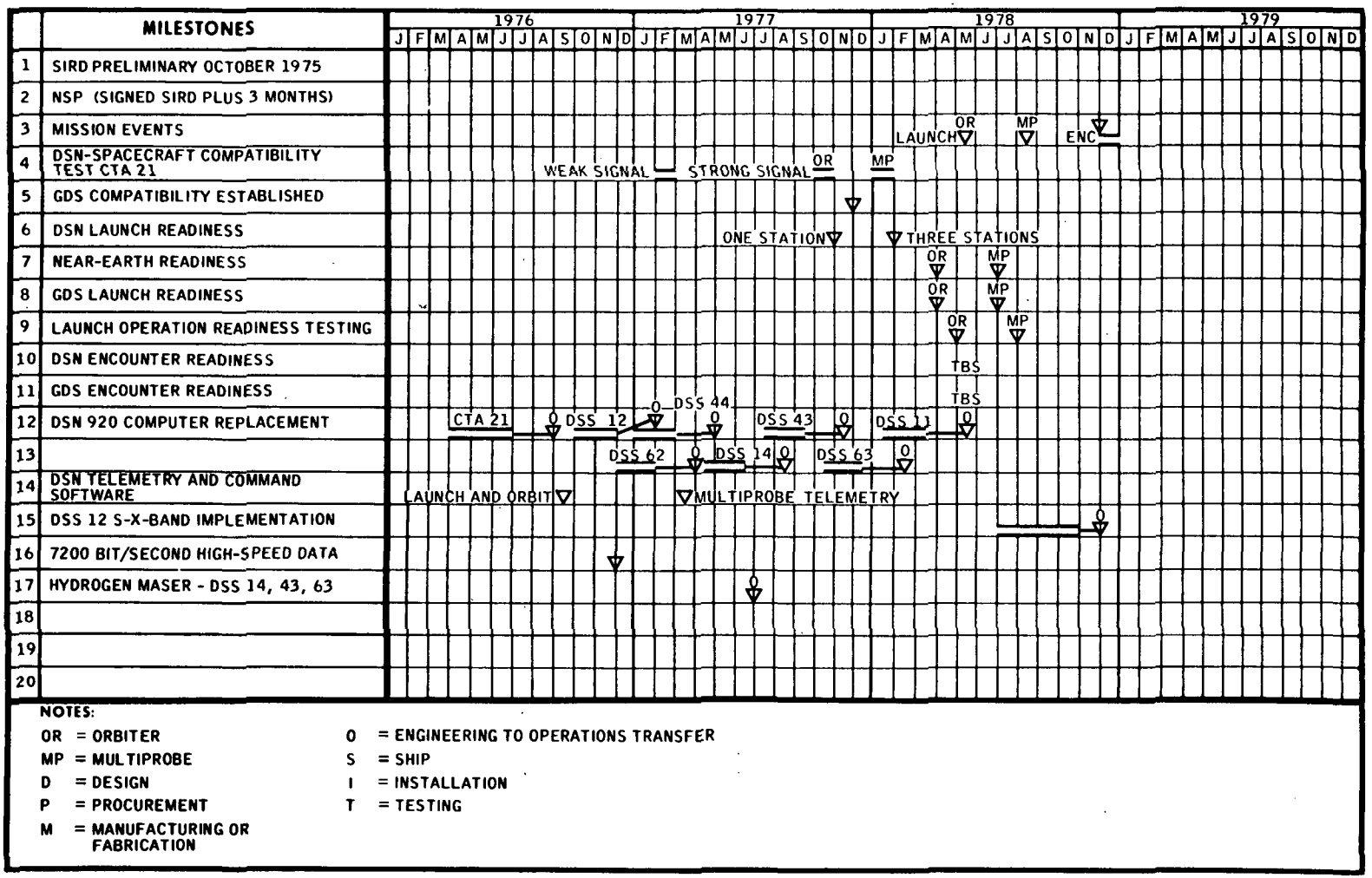


Fig. 1. DSN major milestone schedule for Pioneer Venus 1978 Orbiter and Multiprobe

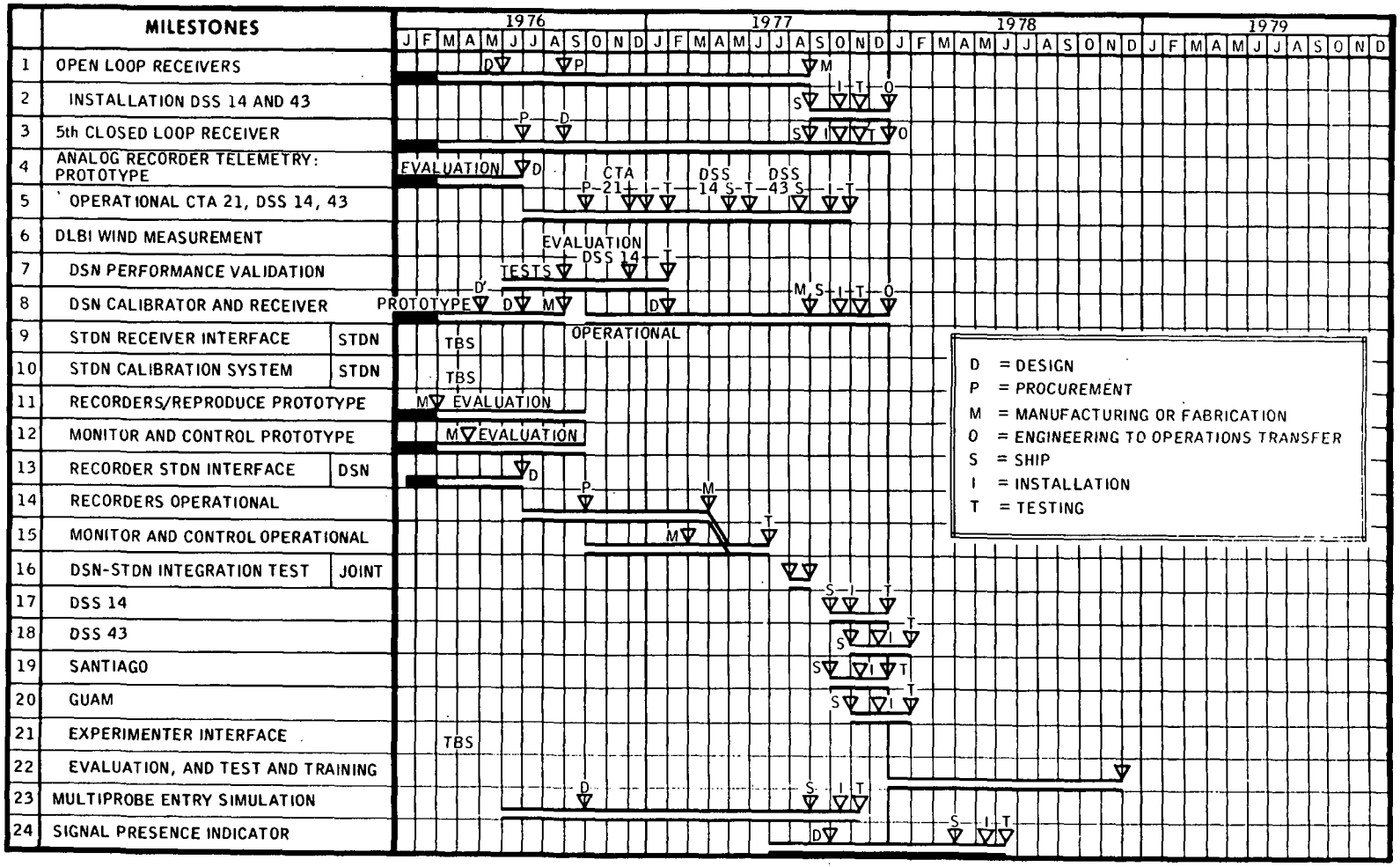


**Fig. 2. DSN major milestone schedule for Pioneer Venus 1978 Multiprobe**

# Helios Mission Support

P. S. Goodwin
DSN Systems Engineering Office
W. G. Meeks and R. E. Morris
Network Operations Office

*The second Helios spacecraft was successfully launched on January 15, 1976. The trajectory will allow inspection of the solar atmosphere at an unprecedented 0.29 astronomical units (AU) distance from the Sun during the Helios-2 perihelion in April 1976. Such a close solar approach will greatly enhance man's knowledge of the inner part of our solar system. This article reports on the prelaunch and launch activities through the first six days of the Helios-2 mission, as well as cruise status of the Helios-1 spacecraft.*

## I. Introduction

This is the eighth article in a series that discusses Helios-1 and -2 mission support. The previous article (Ref. 1) reported on Helios-1 cruise operation between the second perihelion and second aphelion, the traveling-wave tube (TWT) spacecraft anomaly, and Helios-B test and training results. This article covers Helios-B prelaunch and launch activities, Helios-1 cruise status, Helios Deep Space Network (DSN)-Spaceflight Tracking and Data Network (STDN) cross-support and DSN systems performance.

## II. Mission Operations and Status

### A. Helios-B Test and Training

1. DSN tests. Prior to the last Mission Operations System (MOS) test, a DSN Configuration Verification Test (CVT) was performed with each DSN 26-meter station scheduled to support Helios B in order to verify the Network launch configuration. Each CVT was designed to simulate those station activities expected during the first day's coverage of Helios B. The CVTs were scheduled so that each station could maintain its verified Helios-B launch configuration after the completion of the test.

Initial acquisition was simulated at DSS 42 and DSS 44 in Australia. Nominal spacecraft and silent spacecraft acquisition cases were conducted with excellent results from all operational facilities and personnel.

Step II maneuver procedures were practiced with DSS 11 and DSS 12 at Goldstone, since this maneuver is planned during the first pass. All test objectives were met, and the test sequence was completed, free of problems.

Cruise operational procedures were emphasized during the CVT at DSS 61 in Spain. Some contingency procedures, such as manual commanding and an analog tape playback, were included in the CVT. All facets of the test went smoothly, and, upon completion, the station was placed under modified configuration control.

The CVTs brought to a close DSN Helios-B testing. All that remained was the final Operational Readiness Test (ORT) and launch. Subsequent DSN performance during the ORT and the launch phase seem to verify the soundness of the DSN test and training philosophy for Helios B. The plan was for minimal testing of day-to-day Helios operations while concentrating on Helios-B unique operational requirements.

2. Mission Operations System (MOS) tests. To verify the readiness of all systems for mission operations in preparation for the launch of Helios B, an Operational Readiness Test (ORT) was conducted on January 12, 1976. STDN (MIL-71), DSS 42, DSS 44, DSS 61, DSS 11, and DSS 12 participated in this exercise. Viewperiods were simulated so as to allow the launch phase and Step II maneuver to be accomplished in a 12-hour test period. The Helios Math Model was used to simulate the spacecraft from prelaunch through the Step II maneuver. The Mission Control and Computing Center's flight support IBM-360 computer was used to process telemetry, tracking, monitor, and command data, plus the attitude determination programs, providing a realistic atmosphere for the test.

Although a few anomalies occurred during the test, none was serious enough to stop or delay the test. The test was successful, meeting its objectives, demonstrating all systems readiness to support the Helios-B launch.

### B. Helios-B Near-Earth Operations

1. Launch operations. Helios-B launch preparations for a January 15, 1976 liftoff were initiated with the Deep Space Station prelaunch countdowns. Prime Helios-B stations participating in the first pass countdown were the DSN portion of the Spacecraft Compatibility-Monitor Station, Cape Canaveral (STDN (MIL-71)), DSSs 42 and 44 in Australia, DSS 61 in Spain, and DSSs 11 and 12 at Goldstone.

The Helios-B spacecraft was successfully launched on schedule at 05:34:00.36 GMT on January 15, 1976. All Titan-Centaur-Delta launch vehicle stages performed nominally. Data were received from the various down-range, Near-Earth Phase Network (NEPN) stations, and the spacecraft was injected into the desired orbit around the Sun with a preliminary perihelion distance of 0.29 astronomical units (AU) and an orbit period of 185 days. Immediately after solar orbit injection, the Helios-B mission was redesignated Helios 2.

Primary control of Helios-2 post-launch and mission activities resides at the German Space Operations Center (GSOC). The spacecraft team was located at GSOC with a backup team at JPL. Because the launch phase and attitude maneuver computer programs, generated for Helios 1, were available at JPL, the spacecraft attitude and navigation teams were located at JPL for the first weeks of the Helios-2 mission. The interface with STDN (MIL-71) for launch and the down-range stations was handled by the Chief of Mission Operations Support (CMOS). This function was previously handled by the DSN Operations Control Team (OCT).

The German Space Operations Center (GSOC) systems performed very well during the entire launch phase as did the Deep Space Network (DSN) and all other systems at JPL.

2. DSN initial acquisition. DSN initial acquisition by DSSs 42 and 44 in Canberra, Australia, occurred at 06:24 GMT on January 15, 1976. DSS 42 provided the prime source of data with DSS 44 in the role of a redundant backup.

At initial acquisition, the Helios-2 spacecraft transmitted via its low-gain antenna system. This antenna system consists of a linearly polarized dipole element at the top of the spacecraft and a circularly polarized horn antenna at the bottom. The spacecraft radiation pattern boundary between the top dipole antenna and the bottom circular horn antenna element of this omni-antenna system creates an interference region. Approximately five minutes after initial acquisition, the Helios-2 spacecraft aspect angle was such that this interference region was experienced for about three minutes. During the Helios-1 launch phase, this region was predicted to be much longer (approximately 8 minutes) and caused concern as to the quality of telemetry data while in this region. However, during the actual flight of Helios 1 (Ref. 2), the signal degradation caused by this interference region proved to be much less than feared. During the Helios-2 flight, the downlink signal degradation was hardly noticeable at the ground stations.

The establishment of the spacecraft's command uplink followed the end of the interference region. The first of two spacecraft attitude maneuvers was performed during the DSS 42 pass.

3. **Step I maneuver.** The Step I maneuver orients the Helios spacecraft such that its solar panels are evenly illuminated by the Sun, with the spacecraft's spin axis lying essentially in the plane of the ecliptic, i.e., the plane of its injection. This maneuver is required for both electrical power and thermal control. This Helios-2 maneuver was executed completely as planned, and without incident.

4. **Near-Earth experiments turn-on.** Following the Step I maneuver, turn-on of the Near-Earth experiments was executed. During this instrument turn-on and science experiment antennae deployment, the spacecraft telemetry indicated that the cover for Experiment 10 (Micrometeoroid Detector and Analyzer) failed to jettison. However, after careful analysis of other spacecraft instruments, and thermal and attitude parameters, the Project concluded that there is a high probability that the cover did indeed jettison and that the telemetry indicator was faulty. Experiment 10 seems to be functioning normally for this portion of the mission. The data will continue to get careful scrutiny from the Helios spacecraft team as the mission progresses. Spacecraft experiment calibration and memory readouts continued through the first Madrid (DSS 61) pass.

5. **Step II maneuver.** With the Helios-2 spacecraft's first rise over Goldstone, preparation was started for the Step II maneuver. The spacecraft telemetry format was switched from science to engineering data so that more spacecraft parameters could be monitored during the maneuver.

Commands were sent to the Helios-2 spacecraft to calibrate the attitude control gas jets in preparation for the Step II maneuver. This calibration allows more precise control over the spacecraft during the maneuver sequence.

Commands were initiated to pitch the spacecraft such that the antenna mast moved toward the south pole of the ecliptic. This is a deliberate change from Helios 1 in order to provide zodiacal light experiment coverage in the northern ecliptic hemisphere.* Helios 1 will continue to provide zodiacal light sensing in the southern ecliptic hemisphere during its remaining lifetime.

During the Step II maneuver, the spacecraft's attitude is also monitored in the radio metric data as spin modulation on the doppler frequency. As the pitch angle increases, so does the spin modulation. As the spacecraft's attitude is changed, the aspect angle between the DSS and the spacecraft changes, and again the antenna interference region is encountered. To traverse this interference region, two Deep Space Stations (DSSs 11 and 12) were configured to receive linear signals polarized 90 degrees apart. DSS 12 was configured for horizontal antenna polarization with DSS 11 configured for vertical antenna polarization. Telemetry from both stations was supplied via high-speed data lines to the Mission Control and Computing Center (MCCC) at JPL. Telemetry from DSS 12 was selected during the first half of the Step II maneuver, and as the signal level decreased from DSS 12 an increase in DSS 11's signal level followed. When the signal at DSS 11 surpassed that of DSS 12, then DSS 11's telemetry was processed. The degradation of the signal was not severe, so the interference region was traversed without difficulty. Midway through the Step II maneuver, the spacecraft's transmitter was switched to the medium-gain antenna supplying a 6-dB increase in signal level.

During this period, spacecraft temperatures were running low, reaching so-called "soft limits" at various points. This was due to a Project decision to remain in the TWT medium-power mode during this period. To avoid any further decrease of temperatures (caused by gas supply usage), the Project decided to delay the spin-up maneuver.

At the end of the Step II maneuver, the spacecraft had been positioned with the antenna mast aligned toward the south pole of the ecliptic. The medium-gain antenna pattern was close to its peak value, and only minor corrections would be required. Several small trim maneuvers were completed during Goldstone passes 3 and 4 in order to bring the zodiacal light experiment, E-9, into its required attitude to acquire reference stars. Ranging was turned on during the fourth Australian pass. Three good ranging measurements were obtained. The spacecraft spin rate was then stabilized at 60.591 rev/min.

With the completion of the Step II maneuver, the Helios-2 spacecraft had achieved its final orientation, which will be maintained throughout the life of the mission.

### C. Helios-1 and -2 Cruise Operations

1. **Helios 1.** The Helios-1 spacecraft arrived at its second aphelion Christmas Day, December 25, 1975. After 380 days in space, the spacecraft had completed its second orbit around the Sun and was on its way for another. All systems were performing well, but that was not to last.

* The zodiacal light experiment's sensors view the region opposite that of the spacecraft's antenna mast assembly.

On January 28, 1976, while attempting a range measurement over DSS 42 (Australia), the spacecraft's ranging system failed to respond. First thoughts were that perhaps not enough time had been taken in calibrating the DSS ranging equipment because of a "load and go" countdown before the pass. However, on a Viking spacecraft pass following that Helios-1 pass, DSS 42's ranging equipment performed perfectly. Subsequent ranging attempts with the Helios-1 spacecraft have failed to give results. The Helios Project was notified of the problem, and the Project is keeping a very close check on the spacecraft to provide analysis of the failure. Other than the ranging problem, the Helios-1 spacecraft's experiments are performing well, and the spacecraft is in excellent health.

**2. Helios 2.** After six days of initial operation, the Helios-2 spacecraft is now in its cruise phase. All spacecraft systems have been checked out and are providing excellent data. Good downlink power levels and stable spacecraft temperatures prevail. All booms, extendable antennae, and the high-gain antenna (HGA) have been successfully deployed or pointed, and are working as planned. The Helios-2 mission is now well on its way with an expected perihelion of 0.29 AU on April 17, 1976.

On January 30, 1976, the GSOC Helios-2 backup spacecraft team terminated activities at JPL and departed for Germany. According to plan, support by the JPL MOS organization was reduced to the level required for cruise phase. Phase I of the Helios-2 mission has been successfully completed.

### D. Spaceflight Tracking and Data Network (STDN) Cross-Support

On January 15, STDN cross-support for the Helios Mission became operational. This cross-support plan is for the STDN stations (Goldstone and Madrid) to track the Helios-1 and -2 spacecraft and provide analog recordings of telemetry data. These recordings are to be shipped to the STDN (MIL-71) station at Merritt Island, Florida, where they will be played through the DSN telemetry equipment and converted to digital recordings which will subsequently be replayed to JPL via NASCOM high-speed data lines (HSDL). At JPL, the telemetry data will be merged into the Helios Master Data Record (MDR) and shipped to the Project in the normal manner, via existing interfaces. This STDN cross-support provides Helios-1 spacecraft telemetry data that would otherwise be lost because the DSN is scheduled to support other spacecraft, e.g., Helios 2. Approximately 4 passes per week of at least 4 hours each are presently being scheduled at STDN Madrid Station on days when no Helios-1 DSN coverage is scheduled at zero degrees longitude. As of February 16, 15 passes have been recorded by the STDN-Madrid station. The STDN-Goldstone station is presently down for equipment update and is scheduled to become operational and provide Helios support after March 1, 1976.

The timing interface problem reported in the last DSN Progress Report was corrected by the Modified Time Code Translator shipped from JPL to STDN (MIL-71). Several playbacks of the Digital Original Data Record (DODR) produced at STDN (MIL-71) and sent via HSDL to the JPL MCCC have now been made with good results. Blocks of time have been scheduled each week for these playbacks.

The DSN-STDN Interface Agreement regarding cross-support for Project Helios is now in publication and will be ready for review on March 1, 1976. The purpose of this document is to establish the necessary interfaces and operations plans to provide tracking of the Helios-1 and -2 spacecraft by the Spaceflight Tracking and Data Network (STDN) and analog recording of Helios telemetry data.

Figure 1 depicts the milestones associated with the DSN-STDN cross-support effort.

### E. Actual Tracking Coverage Versus Scheduled Coverage

This report covers a 55-day period for Helios-1 tracking coverage, from December 12, 1975 through February 5, 1976, and a 21-day period for Helios-2 tracking coverage, from January 15 through February 5, 1976.

Helios-1 extended mission coverage allocated during this period was 28 percent of the total passes possible. Helios-1 spacecraft received 77 tracking passes and 427 hours of tracking coverage. This is the second reporting period to show a decline in the number of Helios-1 passes, the number of hours tracked, and the percentage of coverage supported. The average pass duration dropped from 7.0 to 5.5 hours. This drop was mainly due to split-pass coverage caused by heavy network activity for other spacecraft and their overlapping viewperiods. During this reporting period, Helios 1 was close to the Earth and could be supported by a 26-meter subnet at high data rates. For this reason, the 64-meter subnet only supported 148.5 hours, a decrease of 81 percent from the last reporting period.

Although declines are shown in most phases of actual coverage of Helios 1, it must be remembered that during the last 21 days of this reporting period Helios 2 was receiving 24 hours a day coverage and most of GSOC's

attention. In addition to this, GSOC can receive data from only one Helios spacecraft at a time.

Helios-2 tracking coverage consists of 68 passes, equalling 817.5 hours. The average pass time was 12 hours. This represents 100 percent coverage by the DSN during this period.

Tracking coverage should pick up from this low point for Helios 1, as the third perihelion will occur during the next reporting period. Scheduled coverage for Helios 2 should remain at 24 hours per day until first occultation.

## III. DSN System Performance for Helios

### A. Command System

With the launch of another Helios spacecraft, a sharp increase in total Helios commands transmitted in December and January was evident. During December, the Helios-1 spacecraft made its first close approach to Earth since launch. A total of 2433 spacecraft commands was transmitted to Helios 1 in December alone. With the launch of Helios B (now identified as Helios 2), tracking opportunities and spacecraft interest shifted to the new flight spacecraft. Many commands are necessary to check out the spacecraft, ready the on-board instruments, adjust the attitude, and in general ready the spacecraft for cruise operations. During the remaining 16 days of January 1976, 2610 spacecraft commands were transmitted. An overall total of 6049 Helios commands were transmitted during the months of December 1975 and January 1976. This was 1380 more than the last period. The cumulative totals at the end of January are: 26,740 commands for Helios 1, and 2610 commands for Helios 2.

One command system abort occurred with Helios 1 on pass 373 over DSS 11 (Goldstone). A command aborted when the Station Monitor & Control Subsystem (DMC) tuned the exciter off the Track Synthesizer Frequency (TSF). The exciter was manually tuned back to the TSF but not before one command abort had occurred. The cumulative total for the Helios-1 Command System aborts was increased to 6, with the System and Project abort total at 14 since the spacecraft launch. No command aborts have been experienced with the Helios-2 spacecraft.

Command System downtime due to equipment problems during this reporting period was 5.06 hours. Only 0.3 hours were lost due to high-speed data line outages. These figures are for both Helios-1 and Helios-2 spacecraft; although the total downtime reflects an increase from last period, considering both spacecraft the increase is not significant.

### B. Tracking System

During this reporting period, two significant ranging anomalies occurred. The first discrepancy was observed on December 12, 1975 while ranging over DSS 42 with Helios 1. When checking the point-to-point consistency of range acquisitions, an unusual pattern was observed in the output of the psuedo-Differenced Range Versus Integrated Doppler (DRVID) program. It was found that periodically one acquisition would differ from the next by approximately 2048 range units. Four other occurrences of this problem have been recorded at different tracking stations. Investigation revealed that each track during which the problem occurred had been preceded by a "load and go" countdown. At this writing, the problem is thought to be procedural in nature, since a similar problem had been observed during Planetary Ranging Assembly testing when the phase relationships were not properly set between the receivers and the Range Demodulator Assembly. Further investigation is underway.

The second ranging problem came to light on January 28, 1976, when the Helios-1 spacecraft failed to respond to a range acquisition over DSS 42. Later attempts have also met with similar results. The Project was informed and is closely monitoring spacecraft conditions to gain insight into the cause.

### C. Telemetry System

Other than the normal weekly telemetry predicts of signal level and signal-to-noise ratio (SNR), no direct support for Helios 1 was required during the first part of this reporting period. With the discovery of a possible Helios-1 spacecraft ranging problem, there has been an extra awareness placed on Helios-1 telemetry by the Helios Project. Certain engineering parameters are being studied by GSOC and compared with the post-analysis of the TWTA 1 failure. To date, none of these data points has repeated itself.

A "load and go" station countdown prepass concept has been initiated in the Network on a trial basis. Although this increases available tracking time, it is causing an increase in the number of out-of-limits residuals. There were nine instances reported for Helios 1 in December alone.

All other projects experienced similar increases. The Data Decoder Assembly again leads the list of telemetry discrepancy reports with 3 of the 6 during Helios tracks.

Several special Telemetry System Analysis Reports were written by the Telemetry Analysis Group. Among them was a Solar Conjunction Report, based on data obtained from the Helios 1 and Pioneer projects. This report provides a cross-correlation on the bit error rate (BER), signal-to-noise ratio (SNR) and system temperature versus the Sun-Earth-probe (SEP) angle.

## IV. Conclusions

The Helios-2 spacecraft has been successfully launched and properly oriented for its mission in space. This achievement culminates the year-long effort between NASA and the Federal Republic of West Germany to place into orbit about the Sun a second Helios spacecraft to further man's knowledge about our solar system.

Helios 2 will travel three million kilometers closer to the Sun than did Helios 1. The orientation of the Helios-2 spacecraft complements that of Helios 1, such that data from both spacecraft may be correlated to prove or disprove theories about the solar system.

Initial control of the spacecraft after being placed into orbit by the Titan-Centaur TE-364-3 launch vehicle was initiated from the German Space Operations Center (GSOC). All JPL-GSOC systems performed as expected and the spacecraft was placed into a 185.67-day-period orbit. The spacecraft will come within 0.29 astronomical units (AU) of the Sun during its perihelion in mid-April 1976. Its inclination to the plane of the ecliptic is 0.0575 degrees.

The DSN will provide continuous coverage of the Helios-2 spacecraft through the first occultation in mid-May 1976. Spaceflight Tracking and Data Network-Deep Space Network cross-support of the Helios spacecraft has been negotiated, and an interface document has been written. This STDN-DSN cross-support is designed to recover data that would otherwise be lost, and will aid in filling the gaps caused by lack of DSN resources to provide continuous coverage of all in-flight spacecraft.

## Acknowledgments

The authors wish to thank the following members of the Network Operations Analysis Group for their contribution of periodic Network Performance Reports: R. Gillette, W. Tucker, and R. Frampton (Command); R. Allis and J. Hendricks (Telemetry); and A. Berman, L. Bright, R. Scharfer, and G. Spradlin (Tracking).

## References

1. Goodwin, P. S., et al., "Helios Mission Support," in *The Deep Space Network Progress Report 42-31*, pp. 15–20, Jet Propulsion Laboratory, Pasadena, Calif., Feb. 15, 1976.

2. Goodwin, P. S., "Helios Mission Support," in *The Deep Space Network Progress Report 42-25*, pp. 43–46, Jet Propulsion Laboratory, Pasadena, Calif., Feb. 15, 1975.

| EVENT | 1975 | | | 1976 | | | | DATE |
|---|---|---|---|---|---|---|---|---|
| | O | N | D | J | F | M | A | |
| STDN (MIL-71) RECORDING TEST | ▲ | | | | | | | OCT. 3, 1975 |
| STDN-GOLDSTONE ENGINEERING TRACK | ▲▲ | | | | | | | OCT. 16, 21, 1975 |
| STDN-MADRID ENGINEERING TRACK | | ▲▲ | | | | | | NOV. 8, 17, 1975 |
| STDN (MIL-71) DATA CONVERSION AND PLAYBACK | | | ▲ | | | | | DEC. 19, 1975 |
| MCCC DATA EVALUATION | | | | ▲ | | | | JAN. 6, 1976 |
| DEMONSTRATION PASS | | | | ▲ | | | | JAN. 9, 1976 |
| INTERIM INTERFACE DOCUMENTATION | | | | ▲ | | | | JAN. 15, 1976 |
| CONDITIONAL TRANSFER TO OPERATIONS | | | | ▲ | | | | JAN. 15, 1976 |
| FINAL TRANSFER TO OPERATIONS | | | | | | △ | | MAR. 15, 1976 |

**Fig. 1. Overall schedule for STDN cross-support**

# Atmospheric Water Vapor Calibrations: Radiometer Technique

F. B. Winn, S. C. Wu, G. M. Resch,
C. C. Chao, and O. H. von Roos
Tracking and Orbit Determination Section

H. S. Lau
Stanford University

*A radiometric technique for determining atmospheric water vapor effects on radiometric range and doppler has been partially evaluated. Empirical test results indicate that the microwave thermal emission from water vapor at 22.2 and 31.4 GHz frequencies can yield line-of-sight electrical phase path calibrations to the centimeter accuracy level.*

## I. Introduction

A radiometric technique for determining atmospheric water vapor effects on radiometric range and doppler has been partially evaluated. Empirical test results indicate that the microwave thermal emission from water vapor at 22.2 and 31.4 GHz frequencies can yield line-of-sight electrical phase path calibrations to the centimeter accuracy level. For range observations acquired at low elevation angles ($< 10$ deg), this represents a 10-fold improvement over alternative calibration techniques.

Atmospheric water vapor imposes a small but important change in the electrical phase path length of signals that propagate through the atmosphere that is of importance to Earth-based ranging systems.

Each space mission/project specifies to the DSN its requirements for atmospheric refraction calibration. Viking 1975 (VK'75) states that the accumulated doppler error (relative range change) over an entire tracking pass (from 6 deg to 6 deg topocentric elevation) is not to exceed 1 meter (1 $\sigma$). Mariner Jupiter/Saturn 1977 (MJS'77) requires the integrated doppler error over a pass (from 10 deg to 10 deg topocentric elevation) not to exceed 0.5 m (1 $\sigma$).

Because of atmospheric refraction, the apparent range of a spacecraft as measured by the Deep Space Network is equal to the geometric range (from the Deep Space Station to the spacecraft) plus $\int_L n(\ell)\, d\ell$, where $n$ is the atmospheric refractive index with the integration extending over the entire ray path.

The range error may be written as $10^{-6}\int_L N\, d\ell$ where $N$, the refractivity, equals $(n\text{-}1)\ 10^6$.

The refractivity due to the dry, predictable component can be separated from the wet component. The wet component, $10^{-6}\ \int_L N_\omega(\ell)\ d\ell$, is not predictable. It must be measured.

## II. "Waterline" Radiometer: Thermal Emission Measurements

A near-linear relationship exists between $\int_L N_\omega(\ell)\ d\ell$ and $\int_L \alpha_\omega(\ell)\ d\ell$ *where* $\alpha_\omega(\ell)$ is the water vapor absorption coefficient for microwave frequencies near 22.2 GHz (the waterline). This relationship holds for the normal atmospheric temperature, pressure, and water vapor concentration levels encountered over DSN Deep Space Stations.

The *Scanning Microwave Inversion Layer Experiment* (SMILE) radiometer (Ref. 1) receives radiation at ~ 22.2 GHz (waterline) and at ~ 31.4 GHz. The measured thermal emission at both frequencies is proportional to the collective amounts of liquid and vapor water within the antenna beam. The brightness temperature at either frequency can be expressed via the radiative transfer equation

$$T_\nu = \int_L T(\ell)\, \alpha\,(\ell,\nu)\, e^{-\tau(\ell)}\, d\ell$$

where

$T(\ell)$ = temperature at $\ell$

$\alpha(\ell, \nu)$ = absorption coefficient at $\ell$ for frequency $\nu$

$\tau(\ell)$ = optical depth at $\ell$

By approximating the atmosphere as isothermal and of small optical depth ($\tau << 1$), Waters (Ref. 2) has shown

$$T_\nu \approx \int_L \alpha(\ell,\nu)\, d\ell$$

which in turn is proportional to the electrical phase path delay $\Delta\rho$ experienced by a radio metric data type.

The thermal emission measured at either frequency is proportional to water in both liquid and vapor states. Electrical phase path delay due to liquid water is orders of magnitude less than the vapor-induced delay. Thus, only the collective amount of water vapor is of interest. To separate the liquid from the vapor, Longbothum[1] matched radiosonde-balloon-data water-vapor assessments to sky temperature brightness measurements via regression analysis:

$$\Delta\rho = a_0 + a_1\, T_{22.2} + a_2\, T_{31.4}$$

where $a_0$, $a_1$ and $a_2$ are regression coefficients resulting from a least squares fit of the sky temperature measurements at the 22.2 and 31.4 GHz frequencies to the radiosonde phase path delay computations. With $a_0$, $a_1$ and $a_2$ estimated, any set of $T_{22}$ and $T_{31}$ measurements yields an estimated $\Delta\rho$.

In the next portion of this article are empirical test results which discuss comparisons of "waterline" radiometer calibrations with calibrations derived from radiosonde, aircraft instrumentation, and models.

## III. Radiometer-Radiosonde Comparison: May 1974

In May 1974, at El Monte, California, Waters showed that such phase delay determinations from SMILE are consistent with radiosonde delay determinations over times of weeks, once the two measurement sets have been matched. The rms discrepancy between the two calibrations for the time period (Fig. 1) is 1.62 cm. The shaded area indicates the radiosonde calibrations and their associated 2-cm (one standard deviation) uncertainty.

A radiosonde, a small electronic instrument, is suspended beneath a weather balloon. As the balloon ascends to 3 km (10,000 ft) or higher, it radios to ground receivers measurements of

absolute pressure $p$, $\sigma_P$ = 2 mb

ambient temperature $T$, $\sigma_T$ = 1°C

relative humidity $RH$, $\sigma_{RH}$ = 5–10% for $RH > 20\%$

= 10–90% for $RH < 20\%$

to the accuracies indicated.

The zenith electrical phase path delay due to water vapor is

$$\Delta\rho = 10^6 \int_0^\infty N_\omega\, dh = k \int_0^\infty \frac{e_v}{(T+273)^2}$$

[1]Private communication (JPL).

from which

$$\Delta\rho = 6.11\,k\sum_i (RH)_i\, 10^{aT_i/(T_i+b)}\,\frac{\Delta h_i}{(T_i+273)^2} \qquad (1)$$

where $\Delta h_i \equiv$ ith altitude increment in meters, $T$ is in °C and $\Delta\rho$ is in cm.

$a \approx 7.5$, $b = 237.3$, $k = 0.373256$ (empirical constants, Ref. 3).

For zenith paths, water vapor calibrations to the 90% accuracy level ($\sigma = 2$ cm) are achieved.

## IV. Radiometer-Aircraft Comparisons: November 1974

In November 1974, over the JPL complex at Pasadena, California, an aircraft owned and operated by Meteorological Research, Inc. (MRI) flew from 900 m to 6 km (3000 to 20,000 ft) in 50 minutes. Pressure, temperature and dewpoint temperature were measured as functions of altitude and time. The aircraft instrumentation measures

absolute pressure $P$, $\sigma_P = 1$ mb

ambient temperature $T$, $\sigma_T = 1$°C

dewpoint temperature $t$, $\sigma_t = 1$°C ($\sigma_{RH} \approx 3\%$)

to the accuracies indicated.

The phase delay is computed

$$\Delta\rho = 6.11\,k\sum_i 10^{at_i/(t_i+b)}\,\frac{\Delta h_i}{(T+273)^2}$$

where $a$, $b$, $k$ were defined in Eq. (1). Along the path the plane traveled, this system can yield approximately 95 percent calibration ($\sigma \lesssim 1$ cm).

Besides two-fold improvement in accuracy over radiosonde balloon zenith calibrations, the aircraft can fly a variety of topocentric elevation paths. This permits line-of-sight calibration for any arbitrary elevation angle.

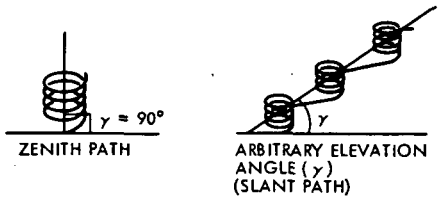


Comparisons of aircraft and SMILE vapor calibrations (Fig. 2) show sub-centimeter agreement between the radiometer and aircraft phase delay computations.

The aircraft dewpoint temperature sensor apparently iced during the morning flight when the aircraft was above 3 km (10,000 ft). Assuming an exponential distribution for the water vapor above 3 km and noting that the aircraft system indicates the water vapor partial pressure to be near 0.1 mb at 3 km, the phase delay due to vapor above 3 km is computed to be $< 0.14$ cm. This small contribution plus the direct calibration derived from the MRI aircraft data below 3 km constitutes the "corrected aircraft" calibration point of Fig. 1.

Although this sample (two points) is not sufficient to permit a definite statement about the relative agreement of these two calibration schemes, it is encouraging. The SMILE regression coefficients, obtained by fitting to radiosonde data in May 1974, still seem valid. This apparent validity persists even though the regression coefficients were derived in May at El Monte by fitting to balloon data and are now being used in November at JPL and compared to aircraft instrument calibrations.

## V. Radiometer-Radiosonde Comparisons: May 1975

In May 1975, at El Monte, California, a second comparison of radiometer–radiosonde calibrations was achieved (Fig. 3). The rms discrepancy between the 2 calibration sets is 1.1 cm. The regression coefficients for SMILE derived a year before at El Monte were used. The regression coefficients still appear valid.

It is of interest to note that on 29 of the 36 radiosonde balloon flights at El Monte, no data above $\sim$ 2.7 km (9000 ft) were acquired. The remaining seven balloon flights produced data to altitudes of 6 km (20,000 ft). The adopted atmospheric water vapor scale height is about 2 km (Ref. 2). In theory, 36 percent of the water vapor medium exists at altitudes above the altitude of the scale height.

The radiosonde devices cannot measure relative humidity below the 20 percent level. Relative humidity is generally less than 20 percent for altitudes greater than 2.7 km. It is observed from balloon data that the relative humidity was about 20 percent at the 2-km altitude over El Monte during May 1975. For those radiosonde flights

to 6 km altitudes where the relative humidity was measured at approximately a constant 20 percent, once the device was above 2 km altitude the electrical phase path delay was overestimated by $\sim$ 10 percent.

Similarly, the phase path delay is underestimated by those balloon flights which terminate at less than 3 km if no effort is made to account for the higher altitude vapor, and no effort was made. The rms uncertainty of the radiosonde calibration with these noted deficiencies present is approximately 2 cm (1 $\sigma$). Thus the radiometer is shown to be at least as accurate as the radiosonde for this test period.

## VI. Radiometer-Aircraft Comparisons: May 1975

In addition to the radiosondes, the aircraft used in November 1974 was also flown during this time. Meteorological data derived from aircraft instrumentation are superior to data obtained from radiosonde balloons. As indicated, the aircraft-based calibrations are 2- to 10-fold more accurate than the balloon-based calibrations. Additionally, the aircraft can sample the atmosphere every few seconds; the aircraft's path is under control, permitting "zenith-spiral ascents" or spiral ascents along varying topocentric elevation angles; and redundant instrumentation can be flown in the aircraft. All of these instrumentation advantages are exploited in this analysis.

There are some disadvantages. The ambient temperature probe has some "thermal inertia." Comparisons of ascent and descent thermal profiles (Fig. 4) show a systematic altitude bias between the ascent–descent thermal profiles. This altitude bias is present in all data. Analysis of all temperature profiles below 3 km indicates that the time delay of the aircraft temperature probe is 20 seconds ($\sigma$ = 9 seconds). The temperatures reported by the instrument were experienced, on the average, 20 seconds earlier. This deficiency is of some consequence in the determination of the collective amount of water vapor along the aircraft's path. The temperature bias is 0.5 K. This translates to 0.2 cm, a 3 percent error, for the average weather conditions of May 1975 at El Monte.

Additionally, there are significant dewpoint temperature measurement errors as shown (Fig. 5). On May 5, for altitudes below 3 km, there appears to be a bias (0.7°C, 17 seconds in time, or 300 meters in altitude). Such a bias amounts to a 0.5-cm error in the phase path delay determination.

As shown in Fig. 4, there is a thermal inversion at approximately 4 km (13,000 ft) that amounts to a 10°C increase between 4 km (13,000 ft) and 4.8 km (16,000 ft). It it in this altitude zone that the "ascent" and descent" profile differs by 3 to 4°C. At these high altitudes, at very low ambient temperatures, the amount of water vapor is quite low, and thus such an inconsistency does not amount to more than 0.1-cm difference in the phase path determination. If such a dewpoint temperature measurement difference exists at low altitudes, at high ambient temperatures, as on May 16 (Fig. 5), the difference in the phase path determination is a few centimeters. Speculation as to which profile is correct, if either, can be obtained by comparing them to the relative humidity profile of the radiosonde of May 16 (Fig. 6). All of the ascent profiles (balloon, aircraft) appear similar, with some variance noted at the thermal inversion altitude. Thus the descent dewpoint profile is suspect.

The dewpoint temperature is measured by observing the temperature at which water vapor condensation occurs on a mirror as it is cooled down. If condensation should collect on the mirror and then freeze (and usually above 1.2 km (4000 ft) ambient temperatures are below the freezing point of water), the dewpoint is not determinable with such a device. This is thought to be the cause of such erroneous dewpoint measurements as do occur.

On the May 14 and 16 flights, two dewpoint devices were simultaneously measuring condensation temperatures at the aircraft. When thermal inversions were traversed on the ascent flights, and during the preponderance of the descent flights, the dewpoint measurements were significantly different (Fig. 7). This inconsistency indicates that some of the measurements are invalid.

On May 5 and 6, when atmospheric conditions were near the ideal (no thermal inversions, no atmospheric turbulence), the aircraft dewpoint temperature measurements were valid.

The rms discrepancy between zenith radiometer and "valid" aircraft calibrations (5 observations) is $<$ 1 cm (Fig. 8). There may be a small positive bias between aircraft and radiometer calibration that may relate to the fact that the May 1974 SMILE regression coefficients do not account for vapor above the radiosonde balloon flight altitudes ($>$ 3 km). However, the 5-point sample is too small to draw any definite conclusions on that point.

## VII. Low Elevation Angle Observations

One of the principal advantages of the radiometer and the aircraft is that the accumulative amounts of water vapor (and thus the phase delay) can be measured not only at zenith as with the balloons but at a variety of different elevation angles.

Figure 9 compares aircraft and radiometer calibrations at an elevation angle of 10 deg. There are three aircraft calibration points denoted by the large circles with the arrows. Circle diameters indicate flight time; the arrows indicate an ascent or descent flight. The radiometer data points are shown as Rs.

During the 6 hours in which radiometer data were acquired on May 6 (Fig. 9) a "diurnal" fluctuation in the water vapor level is evident. From 10:00 (local time) to 14:00, the water-vapor-induced phase delay increased approximately 7 cm along the 10 deg elevation angle path through the atmosphere. The aircraft calibrations tell a consistent story. The indication is that the two systems are providing line-of-sight water vapor calibrations to the centimeter level or better. Figure 10 shows similar quantity comparisons for 20- and 30-deg elevation angle flight paths.

Thus, line-of-sight calibrations for varying elevation angles to better than the 2-cm level have been demonstrated by the radiometer for May 5 and 6, two days of nearly ideal weather, with no clouds, no thermal inversions, and no inhomogeneities apparent.

Less ideal weather was experienced on 14 May, which was the next occasion for the aircraft to acquire data. An overcast existed at the altitude of a rather large thermal inversion. There was a 6°C increase between the 600 m (2000 ft) and 1 km (3300 ft) altitudes. As stated earlier, the aircraft dewpoint temperature data (acquired simultaneously in time and space) did not agree. A similar situation was encountered on May 16, when the plane next operated.

Figure 11 shows aircraft instrument-radiometer calibration comparisons under ideal weather conditions (May 5, 1975) and under adverse weather conditions (May 16, 1975). As indicated, it is the aircraft-based calibration which is of suspect quality. However, the maximum difference, even under the adverse weather is 3 cm along the line of sight. This line-of-sight calibration at a 10-deg elevation angle is nearly an order of magnitude more accurate than the refraction model currently used to support deep space navigation of spacecraft.

## VIII. Seasonal Refraction Model

The current refraction model (Ref. 4) is based on radiosonde balloon data acquired in 1967 and 1968. The two years of data were combined to yield monthly averages for the amount of water-vapor-induced phase path delay. Thus, a standard year for each DSS was defined. The rms discrepancy between the day-to-day fluctuations in the 1967–1968 data base and the monthly mean is approximately 4 cm. This is, of course, at zenith.

## IX. Surface Weather Model

Once high-speed data lines become available, surface weather data from each DSS will be communicated to the Jet Propulsion Laboratory Control Center. Then DSS surface weather data

$$\text{absolute pressure } P,\ \sigma_P = 0.1 \text{ mb}$$

$$\text{ambient temperature } T,\ \sigma_T = 0.1°\text{C}$$

$$\text{dewpoint temperature } t,\ \sigma_t = 1.0°\text{C}$$

acquired to the accuracies indicated will yield water vapor calibrations for phase delay to an 85–90 percent accuracy (2.5 cm – 1 $\sigma$) in the zenith direction (Fig. 12). The model is based on the adiabatic law (Ref. 5).

## X. Electrical Phase Path Delay for Observations at 10 deg Elevation Angle

At zenith, all calibration techniques discussed here—radiometer measurements, radiosonde measurements, aircraft measurements, seasonal model, and surface weather data model—yield one way range calibrations to better than 4 cm ($\sigma$). Inasmuch as the optical depth is 6 times greater at 10 deg than at 90 deg elevation, the zenith calibrations of the radiosonde, the seasonal refraction, and surface weather data models must be multiplied by nearly 6. And, correspondingly, the 1-$\sigma$ uncertainties of each must be so multiplied by 6. At 10 deg, the radiosonde calibration has a 12-cm uncertainty ($\sigma$), while the seasonal model uncertainty is 24 cm and the surface model calibration uncertainty is 15 cm. The uncertainty of the radiometer, a line-of-sight calibration, is thought to be 1–2 cm at 10 deg elevation angle.

Figure 13 shows $\Delta\rho$ for 10-deg elevation angle observations under different weather conditions as derived from the radiosonde, surface weather, aircraft instrumentation, and radiometer. From the May 6 calibrations, subcentimeter agreement between aircraft and radiometer

comparison is exhibited. Both calibrations show the same time history. Radiosonde and surface weather calibrations are centimeters apart from each other as well as from the aircraft and radiometer calibrations. The surface weather measurements indicate a general decrease in the water vapor level while the radiosonde measurements indicate a net increase. However, because of the uncertainties associated with these two "mapped" from zenith to line-of-sight calibrations, the radiosonde and surface weather model indicate temporal changes are not statistically significant.

As the weather conditions deteriorate, the discrepancy between the calibrations increases. This is due to the 6-fold magnification of the zenith errors in the surface data and radiosonde calibrations when those calibrations are "mapped" to 10 deg elevation angle.

## XI. Conclusion

Line-of-sight radiometer calibrations for water vapor effects on range measurements are more accurate than radiosonde and/or surface weather model "mapped" calibrations. They are 5 to 10 times more accurate for range observations at 10 deg elevation angle when ideal weather exists. The performance of radiometers in adverse weather is yet to be determined.

## Acknowledgments

The radiometer evaluated and discussed in this test was loaned to the Atmospheric Research Information Exchange Study (ARIES) Project (JPL) by the Microwave Radiometry Group (JPL), and was maintained and operated by The Space Radar and Microwave Radiometry Section (JPL). The aircraft flight activities were coordinated by Bill Giles of the Caltech Seismology Laboratory. The U.S. Weather Service kindly provided their radiosonde data; we are grateful for the cooperation from Ms. Patricia Burns and Mr. Larry Soussaman of the Weather Service's El Monte office. Dr. Joseph Waters (JPL) originally suggested this type of analysis and provided help and advice throughout the experiment.

## References


1. Staelin, D. H., et al., "The Scanning Microwave Spectrometer (SCAMS) Experiment," *Nimbus 6 User's Guide*, Goddard Space Flight Center, 1975.

2. Waters, J., "Atmospheric Effects on Radio Wave Phase and the Correction of Vapor-Caused Phase Fluctuations by Radiometric Measurements of Water Vapor Emission," *VLA Scientific Memo* No. 8, NRAO, 1967.

3. Bean, B. R., and Dutton, E. J., *Radio Meteorology*, U.S. Dept. of Commerce, NBS, March 1, 1966.

4. Thuleen, K. L., and Ondrasik, V. J., *The Repetition of Seasonal Variations in the Tropospheric Zenith Range Effect*, TR 32-1526, Technical Report 32-1526, Vol. VI, Jet Propulsion Laboratory, Pasadena, Calif., Dec. 15, 1971.

5. Chao, C. C., *New Method to Predict Wet Zenith Range Correction from Surface Weather Measurements*, Technical Report 32-1526, Vol. XIV, Jet Propulsion Laboratory, Pasadena, Calif., Apr. 15, 1973.

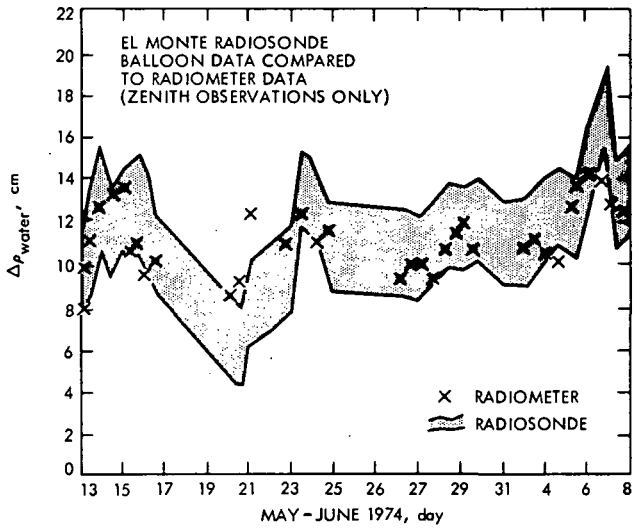


Fig. 1. Comparisons of radiometer/radiosonde/aircraft calibrations, May-June 1974

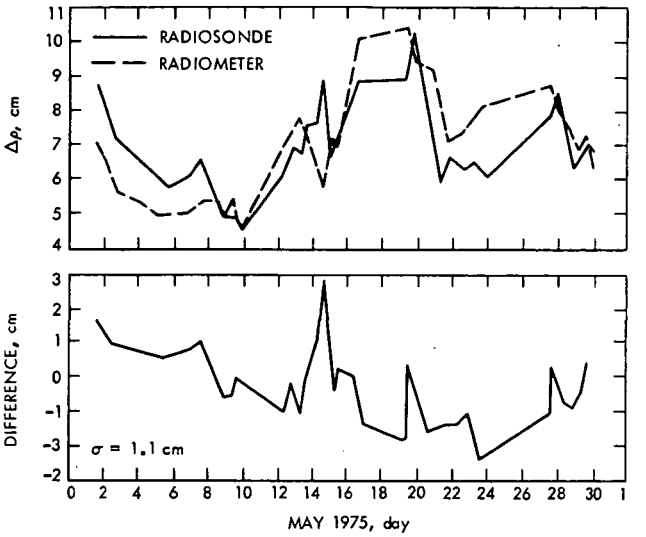


Fig. 3. Comparisons of zenith radiosonde/radiometer calibrations (31 observations), May 1975

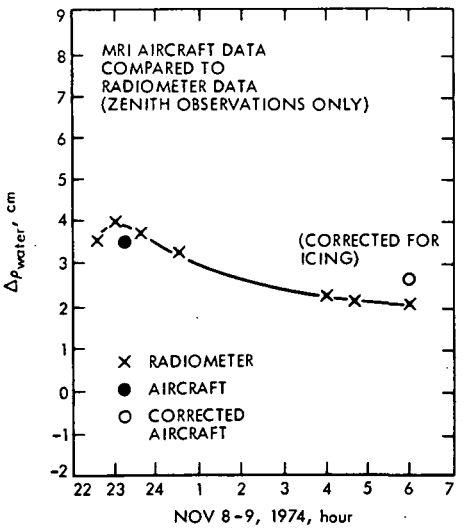


Fig. 2. Comparisons of radiometer/aircraft water vapor calibrations, Nov. 8, 1974

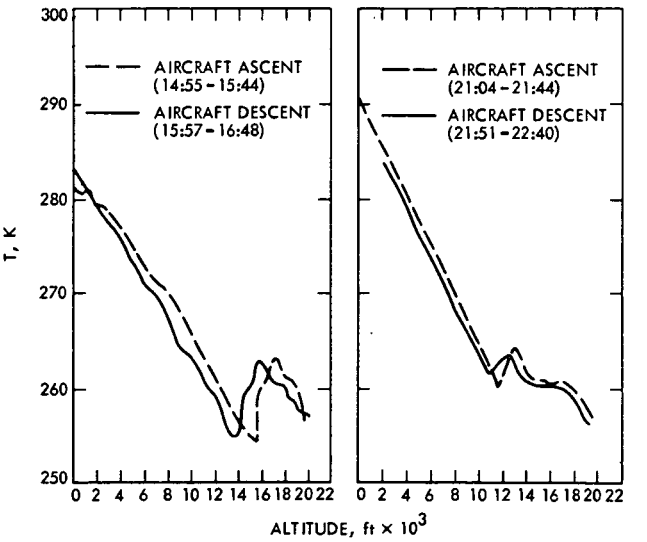


Fig. 4. Evidence of temperature/altitude profile biases, May 5, 1975, El Monte, Calif.

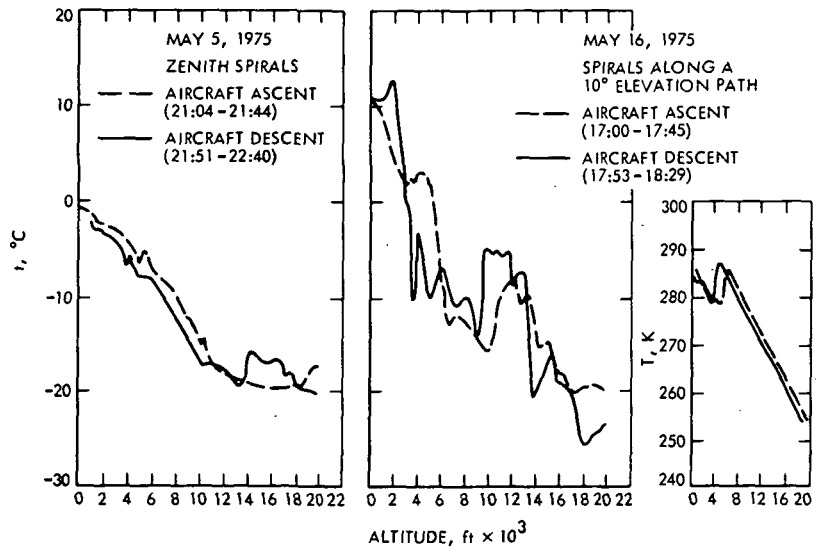


**Fig. 5. Evidence of dewpoint temperature measurement error, El Monte, Calif.**

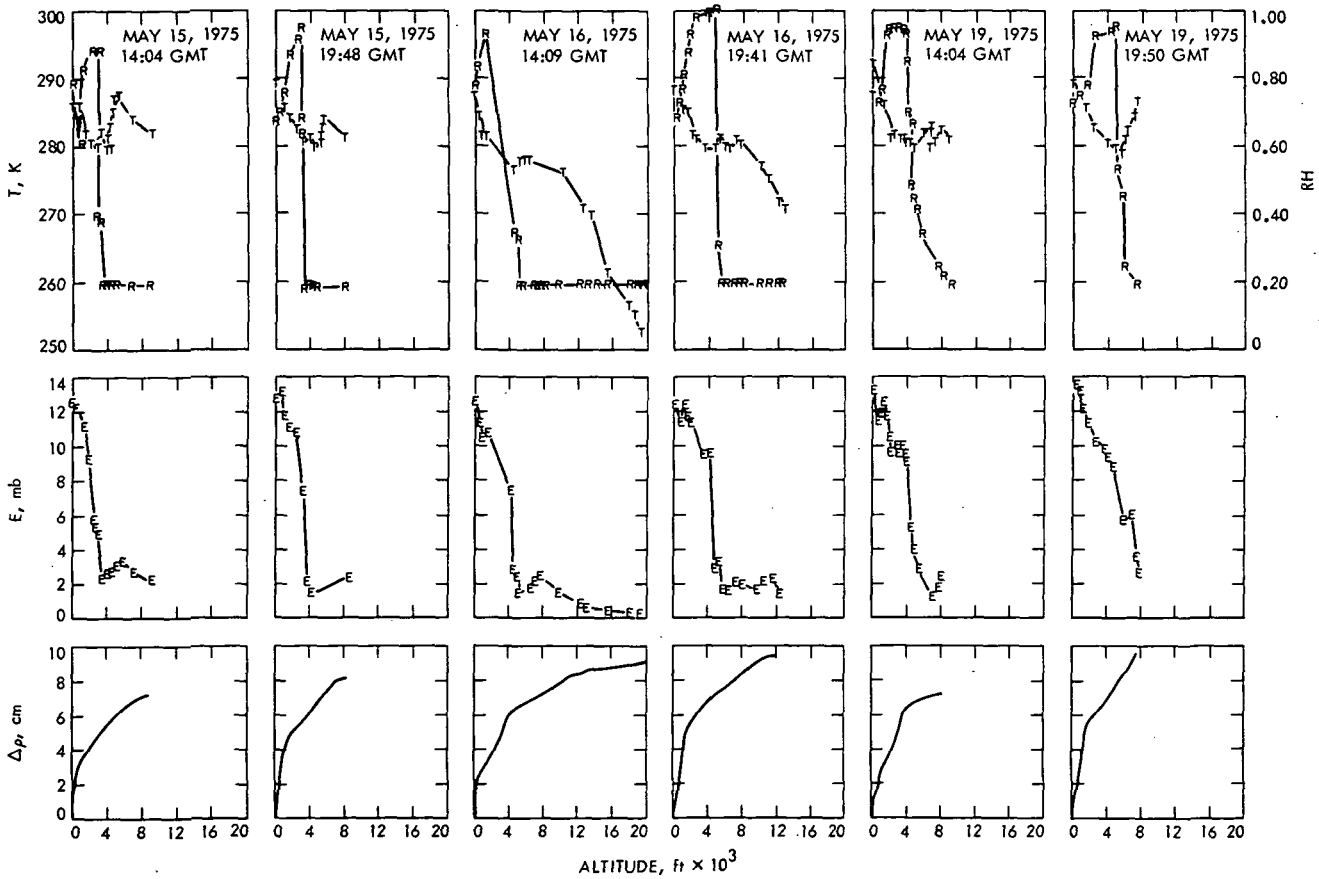


**Fig. 6. Radiosonde variables: vertical gradients, El Monte, Calif. (T = temperature, R = relative humidity, E = refractivity due to water vapor)**

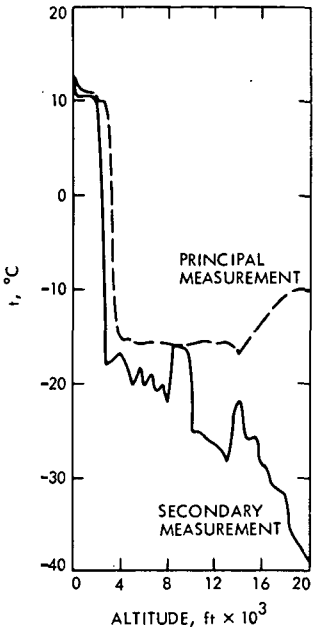


Fig. 7. Inconsistencies of dewpoint temperature/altitude profile

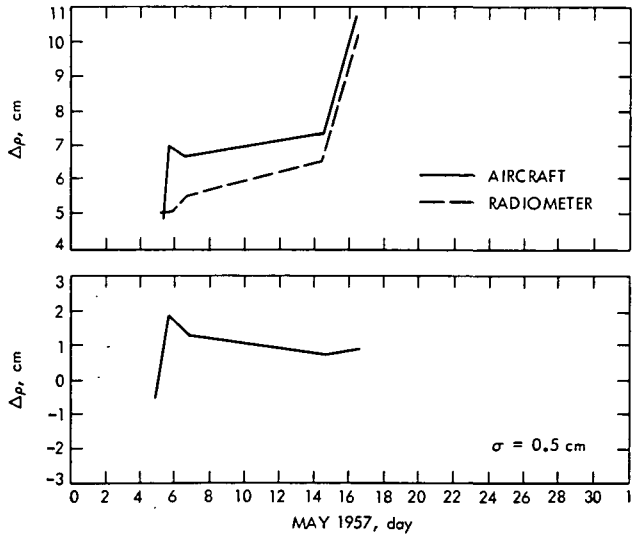


Fig. 8. Comparisons of zenith aircraft/radiometer calibrations (5 observations), May 1975

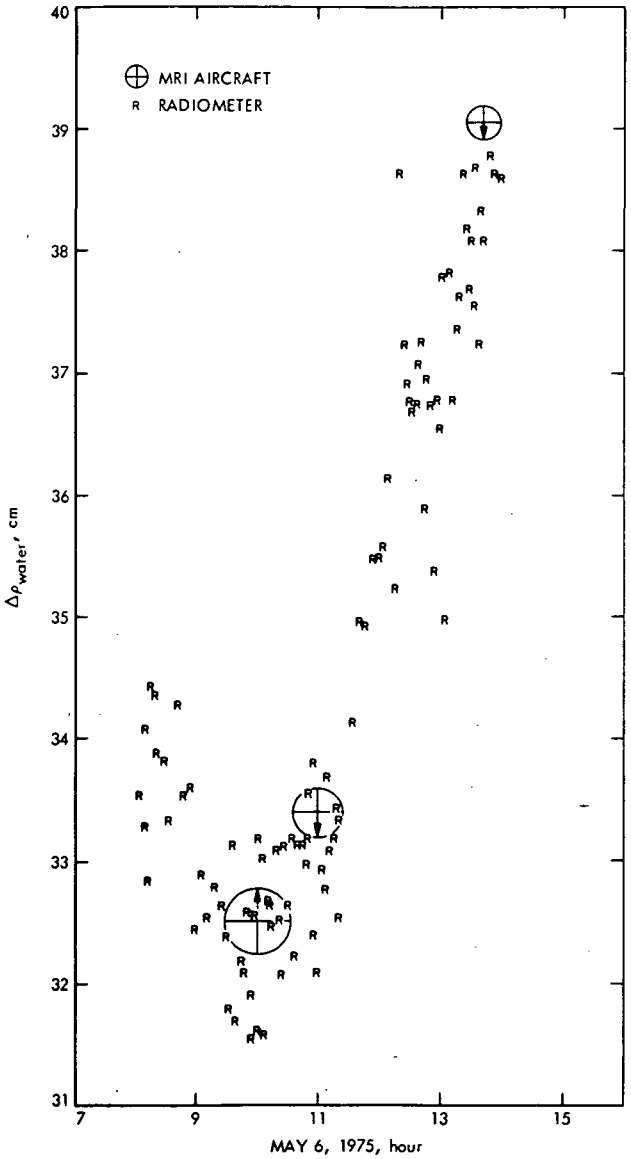


Fig. 9. Comparisons of radiometer/aircraft water vapor phase delay calibrations, line of sight (10° topocentric elevation)

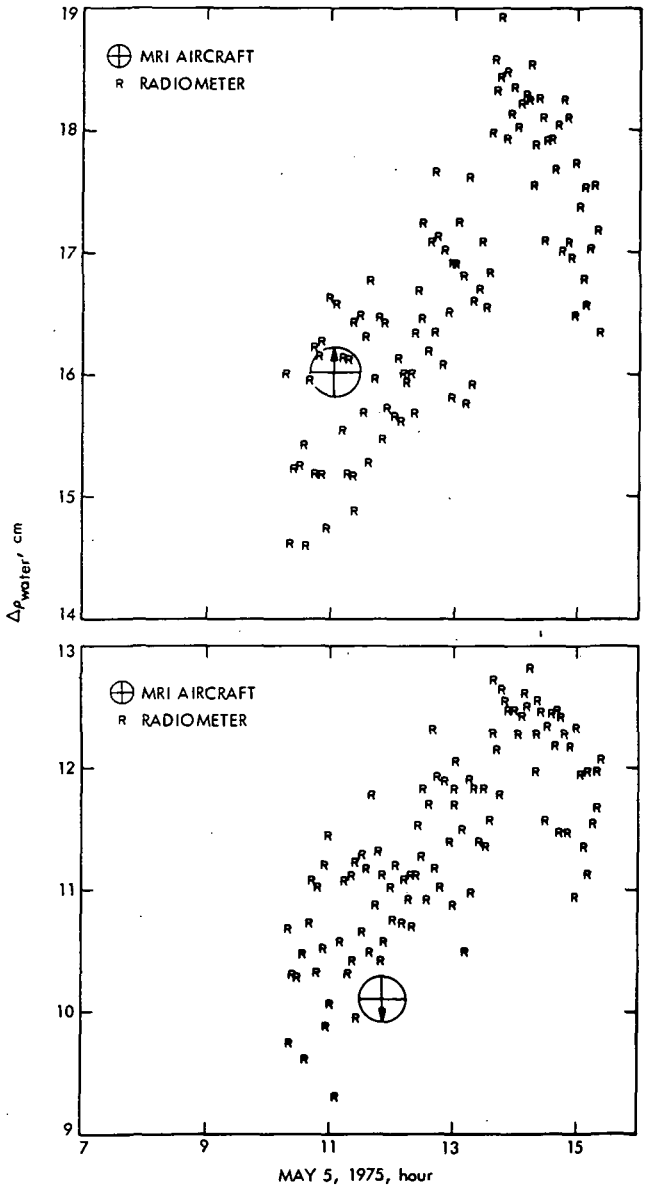


Fig. 10. Comparisons of radiometer/aircraft water vapor phase delay calibrations, line of sight (20 and 30° topocentric elevation angles)

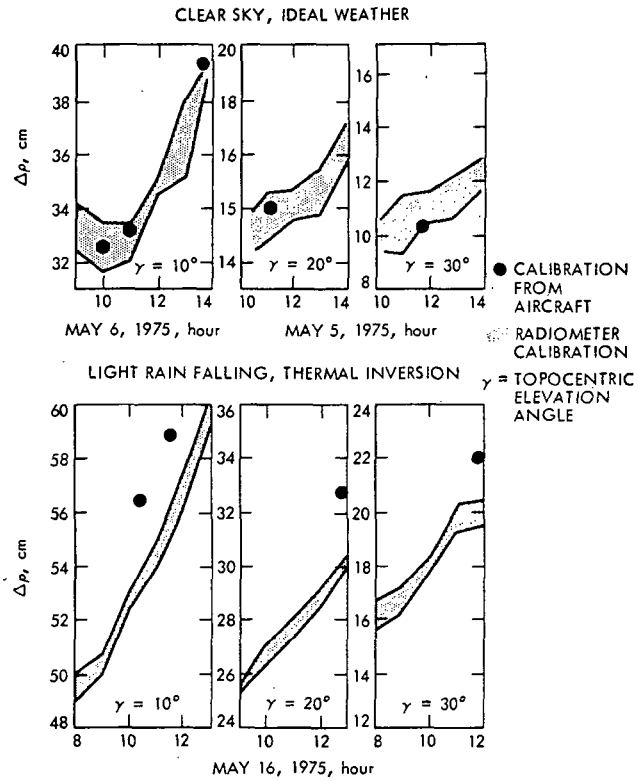


Fig. 11. Comparisons of aircraft instrument and SMILE radiometer calibrations

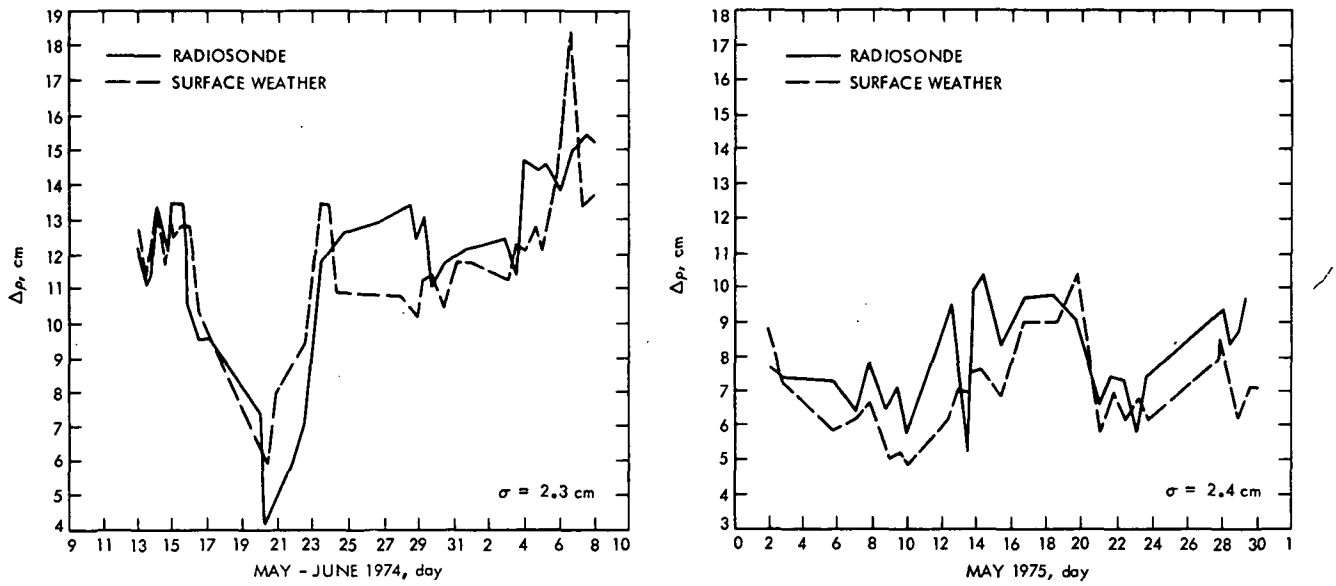


Fig. 12. Comparisons of surface weather data and radiosonde data calibrations, El Monte, Calif.

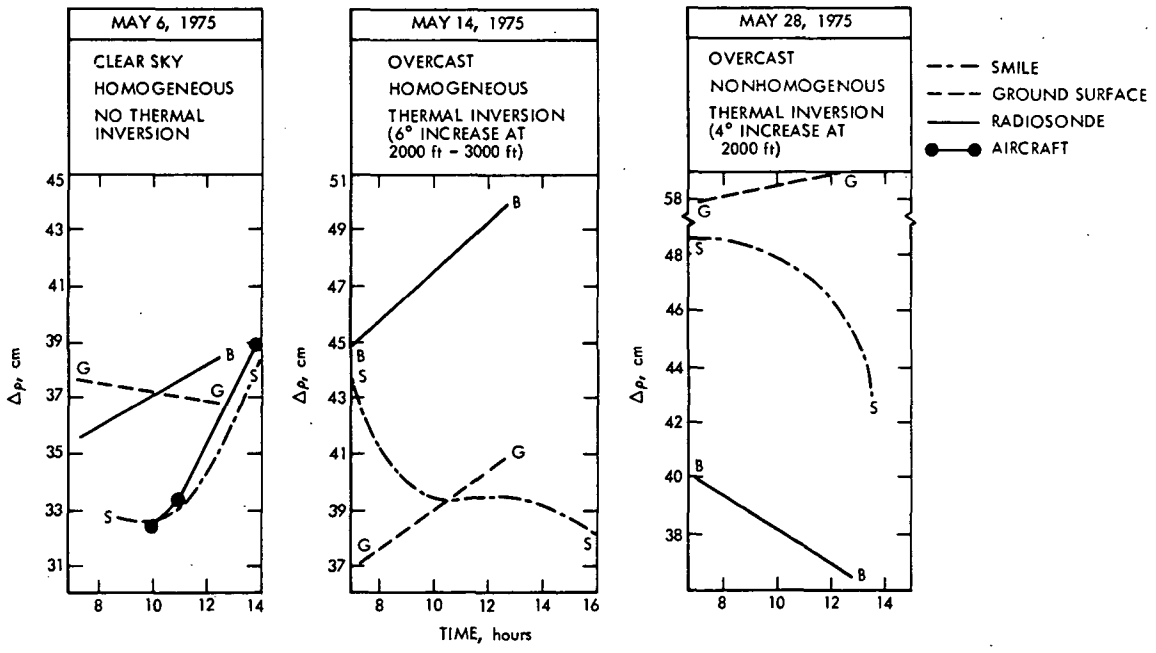


Fig. 13. S-band electrical phase path delay for observation at 10° elevation angle, El Monte, Calif.

# S- X-Band Experiment: Development and Evaluation of a Set of Group Delay Standards

T. Y. Otoshi and R. W. Beatty[1]
Communications Elements Research Section

*Group delay standards of 15, 30, and 60 ns have been developed at JPL with advice and consultation from the U.S. National Bureau of Standards (NBS). Calibration data on the delay standards provided by NBS and others are presented and compared. The effects of dispersion and cable reflections are discussed. Calibrations were performed at the S- X-Band Experiment frequencies of 2113, 2295, and 8415 MHz as well as at the nominal range-code modulation frequency of 500 kHz. The standards will be useful for checking out the JPL ranging system accuracy in measuring delay changes of about 15 to 60 ns.*

## I. Introduction

In 1969, Sokov and Semenova (Ref. 1) proposed a unified system within the USSR for checking group time delay measuring instruments manufactured there. This system was based upon primary group delay standards and working standards consisting of lengths of coaxial cable for small values of delay and helical cables or ultrasonic delay lines for large values of delay in the range of 1 to $10^4$ $\mu$s.

There has been no corresponding system proposed in the USA, but a set of group delay standards having delays in the range of 15 to 60 ns have been designed at JPL with advice and consultation from the U.S. National Bureau of Standards (NBS).

The need for such standards arose at JPL in 1971 for checking the accuracy and precision of the range calibration system installed at a Deep Space Station at Goldstone, California. The system was used in 1973 for the S- X-Band Experiment (Ref. 2) which involved the measurement of differences in the time delays of signals at S- and X-band frequencies (2295 and 8415 MHz) being transmitted from the Mariner 10 spacecraft while in its interplanetary flight to Venus and Mercury.

For the S- X-Band Experiment, it was required that the range measurement system be checked for its accuracy in

[1] Dr. R. W. Beatty, formerly with the National Bureau of Standards, is a private Consulting Electronics Engineer at 2110 Fourth Street, Boulder, Colorado 80302.

the measurement of small, as well as large, changes of time delay. For verifying small delay change measurement accuracy, the development of delay standards was required. It was desirable that a standard delay of about 30 ns be known to within ±0.1 ns, if possible.

After consultation with NBS personnel, JPL wrote specifications and procured three special lengths of cable from the Phelps Dodge Company. These cable lengths had nominal delays of 15, 30, and 60 ns, respectively. In the following, the cables are described and measurements by NBS and others are reported. The uncertainties in the measurements are discussed, and the degree of confidence obtained in the standard delay cables is assessed.

## II. Description of Delay Standards

In order to operate at frequencies up through 8415 MHz without higher mode propagation, and with minimum leakage, the outer conductor of each cable was specified to have an inner diameter of 8.255 mm (0.325 inch), a characteristic impedance of 50 ohms, a solid aluminum outer conductor, and a foam polyethylene dielectric having a nominal permittivity of 1.50. The inner conductor had an outer diameter of 2.972 mm (0.117 inch). The phase-temperature coefficient of this type of cable is about -28 parts per million per °C (-15.6 parts per million per °F) over the temperature range of -46°C (-50°F) to 38°C (100°F) (Ref. 3).

Each cable has Type N male and female connectors conforming to MIL-C-39012. The cables were coiled and potted as shown in Fig. 1, and had the connectors arranged for convenient insertion into a measurement system. Near each cable end there is a transition from the 7-mm 50-ohm line size of the connectors to the cable diameters given above. The transitions plus connectors give rise to small reflections.

The voltage reflection coefficients and characteristic insertion losses or attenuations of the cables at some specific test frequencies are given in Table 1. The effects of reflections and cable attenuations on delays have been analyzed by the authors in another paper (Ref. 4). It was found that cyclical variations of delay with frequency due to reflections will decrease in amplitude as the cable attenuation increases. Thus, even though the reflection coefficients in Table 1 increased with frequency, a corresponding increase in attenuation kept the variation in delay quite low.

## III. Measurement Methods

In the JPL range measurement system for the S- X-Band Experiment, the envelope delays of a square wave (at approximately 500 kHz) modulating S- and X-band carriers are determined. Thus, the quantity of interest in the standard delay cables is the envelope delay or group delay $\tau_g$. In the case of no distortion of the envelope, these are the same, and proportional to the rate of change of phase shift $\phi$ with frequency $f$ (Ref. 5). This relationship is as follows:

$$\tau_g = [-1/(2\pi)](d\phi/df) \quad (1)$$

where $\tau_g$ is in seconds, $\phi$ is in radians, and $f$ is in hertz. If a phase change $\Delta\phi$ is measured over a frequency interval $\Delta f$, then

$$\tau_g \cong [-1/(2\pi)](\Delta\phi/\Delta f) \quad (2)$$

If significant distortion is present, the concept of envelope delay lacks uniqueness and loses significance. The cables were designed to have low dispersion, and measurements of envelope delay and group delay were expected to agree closely.

Several different measurement techniques were employed and measurements were made by JPL, Western Automatic Test Services (WATS), and NBS. The various measurement methods used at each laboratory are listed in Table 2.

In the case of Method 1, a number of impedance measurements were made with Twin-T and Maxwell Bridges at 400, 500, and 600 kHz, and the slopes of the phase shift versus frequency characteristics were calculated at 450 and 550 kHz and averaged to obtain the values given in Table 3. These data were previously reported in Refs. 6 and 7.

In the case of Method 2a, the insertion phase shift of each cable was measured in a phase bridge system tuned to have low reflections at the insertion point at frequencies near the desired frequencies. Group delay was calculated from Eq. (2) and the frequency interval $\Delta f$ over which the data were taken was 2 MHz (Ref. 6).

In the case of Method 2b, the automatic network analyzer was programmed to read out the group delay as calculated from the change in the insertion phase shift between closely spaced frequencies (10 or 15 MHz) near the desired test frequencies. The frequency interval used to calculate group delay from Eq. (2) was 30 MHz for most of the test results to be presented for this method.

In the case of Method 3a, the delays between corresponding maxima on RF bursts (obtained by gating the output of a microwave source) at two points in the system were measured on an X-Y recording of the outputs from a sampling oscilloscope. The gating signal was obtained from a countdown circuit and derived from the microwave signal. For the triangular modulation pulse used, most of the RF energy was contained in a bandwidth of about 400 MHz for test results at 2113 and 2295 MHz, and about 1300 MHz for test results at 8415 MHz (Ref. 6).

A block diagram of the test setup for Method 3b may be seen in Fig. 2. A baseband pulse of 1000-ns width was used to modulate the microwave signal at 2295 MHz. The delay was measured before and after insertion of the cable by means of a computing counter having a resolution of 0.1 ns (Ref. 8). Data were not obtained at 2113 MHz or 8415 MHz due to difficulty in obtaining low reflection coefficients at the insertion point with system components that were available in the laboratory.

In Method 4, the JPL Mu-ranging system (Refs. 9 and 10) generates a range code of approximately 500 kHz, which phase modulates an uplink RF carrier of 2113 MHz. The ground station transmits this modulated carrier to a target transponder for retransmission back to the ground station at coherent downlink frequencies of 2295 and 8415 MHz. The ground station receiver extracts the range-code modulation, and the ranging system measures the phase difference between the transmitted and received range codes by use of correlation techniques. The measured phase shifts enable determination of round-trip propagation delays. The total system delays were measured before and after insertion of the delay standards at different points in the ground station S- or X-band ranging paths. Additional details of the particular JPL Mu-ranging system, receiver subsystems, and test setup that were used may be found in Ref. 11.

## IV. Results

A summary of the measured results are given in Table 3. The values shown for each method represent an averaging and condensation of more extensive data. To enable comparisons of the various methods, a weighted overall average was obtained at each test frequency for each of the delay standards. The weighted averages were obtained in a straightforward manner using weighting factors inversely proportional to the square of the estimated limits of uncertainty for each measurement method. The estimated error limits as well as deviations from the weighted average are shown in Table 4.

Examination of the data in Table 4 shows that the discrepancies between the measured results and the weighted averages are nearly all within the estimated limits of error. The main examples where this is not true are in Method 3a for the 30-ns cable at 2113 MHz (0.13 versus ±0.08 ns) and 2295 MHz (0.14 versus ±0.08 ns). The lack of agreement is within 0.06 ns, and this could be due to failure to include errors due to reflection interactions in the estimated limits of uncertainty. As will be discussed later, the effect of reflections from discontinuities at the cable ends should be considered in estimating the error limits of each of the measurements, since this effect is significant compared with other sources of error. This was not done for any of the measurement methods because the results of the analysis of Ref. 4 were not known at the time the measurements were made.

In Table 4 the estimated error limits for the JPL ranging system (Method 4) are not shown, and the Method 4 results were not included in obtaining the weighted averages shown in Table 3. The reason for this is that the magnitudes of various errors for this measurement method were not sufficiently well known. After the measurements reported in this article were made, it was found that the ranging system measurement error is a function of waveform distortions and total system delay (Ref. 10) and also of changes in received signal levels. The calibration data required to refine the results were not later retrievable, and it was not feasible to repeat the measurements.

The JPL ranging system is presently not capable of subnanosecond-type accuracy, since it was designed primarily to enable accurate measurements of large time delays of weak signals (such as would be received from a distant spacecraft) in the presence of noise. The results from this system (Method 4) were presented mainly to illustrate the usefulness of group delay standards for testing small delay change measurement accuracy of an actual operational system for measuring time delay.

## V. Discussion of Error Sources

### A. Dispersion

Dispersion is an important consideration in the JPL ranging system measurements because it is necessary to avoid distortion of the square wave envelope to keep errors in delay measurements from this source small. For example, if one needs to consider 11 harmonic components of the 500-kHz square wave to accurately represent a square wave for purposes of delay measurement, then

sidebands ±5.5 MHz of 2113, 2295, and 8415 MHz must be free of distortion due to dispersion.

Figures 3, 4, and 5, respectively, show the results of measurements obtained with an automatic network analyzer at frequencies from 2000 to 2500 MHz, 5825 to 6775 MHz, and 8000 to 9000 MHz. The data in these figures show that at these microwave frequencies the group delays are essentially constant with frequency to within ±0.1 ns. Therefore, the effects of dispersion in the standard cables would be insignificant for a square wave modulated carrier at 2113, 2295, and 8415 MHz.

Dispersion effects near 500 kHz are also of considerable interest because the delay standards will be inserted into the baseband ranging path as well as into the intermediate frequency (IF) and radio frequency (RF) portions of the JPL ranging system to help determine the location of error sources. To determine whether or not significant dispersion effects were near 500 kHz, data were obtained at 400, 500, and 600 kHz using Method 1.

The results in Table 5 at 400, 500, and 600 kHz (Ref. 7) show that a small, but significant, dispersion effect is present at these frequencies. The dispersion is due to changes in skin effect in the conductors. It has been noted (Ref. 12) that at frequencies below, say, 10 MHz, a decrease in frequency produces a significant increase in the inductance per unit length without greatly affecting the capacitance, such that the (phase) velocity of propagation decreases. At higher frequencies, the skin depth remains small compared with the cross-sectional dimensions of the cable, and changes in skin depth do not produce significant dispersion effects. This is borne out by the data shown in Figs. 3–5 at microwave frequencies.

### B. Internal Reflections

The effect of reflections upon the variation with frequency of group delays of standard cables can be assessed with reference to the data in Table 1 and the analysis and graph of Ref. 4. These effects are small (less than 0.3 ns) for the conditions usually encountered here, but in developing confidence in the standards and the measured results, it is necessary to show this.

Reflections at the ends of the cable will interact, going in and out of phase as the frequency changes, and produce cyclical changes in the group delay. The magnitude of the effect depends upon the magnitudes of the reflections and the attenuation of the cable. The reflections can be due to system mismatches, discontinuities of connector pairs where the cables are connected into the system, and discontinuities between the cables and the connectors due to changes in conductor diameters. At the insertion point, it is possible to tune the measurement system to reduce mismatches or to use isolators and connectors having low reflections. Then any residual reflection interactions will be due primarily to discontinuities internal to the cable.

Figure 6 shows the type of variation obtained where large discontinuities were placed at the ends of a 30-ns coaxial cable. The cyclical variations in group delay were purposely made large to illustrate the effect. It is clear that the group delay varies with frequency about an average value near 30 ns. The cyclical variation due to reflections from discontinuities at the ends of the cable has a period of about $1/(2\tau_p)$, where $\tau_p$ is the nominal phase delay of the cable, and for a low dispersion cable $\tau_p$ may be replaced by $\tau_g$. In Fig. 6, it can be seen that for the 30-ns delay standard, a full period of cyclical variation occurs in a frequency interval of 16.7 MHz.

If one measures the group delay of a 30-ns standard by measuring phase shifts at the ends of a large frequency interval (large enough to encompass several cycles of the cyclical variation which occurs in phase shift as well as in group delay), one will obtain a value of group delay close to the average value of 30 ns. However, if one uses the same method with a frequency interval much smaller than a period of the cyclical variation, one will obtain a value of group delay which lies somewhere on the cyclically varying curve of Fig. 6.

When the cable reflection coefficients are reduced to the values shown in Table 1, from 0.02 to 0.07, it can be demonstrated that the cyclical changes in group delay with frequency are small for the standard cables. Suppose we assume that the input reflection coefficient of 0.07 shown in Table 1 is the result of discontinuities at each end of the 30-ns cable having reflection coefficients of 0.05. This is a reasonable assumption since the wave reflected from the opposite end discontinuity is attenuated by the cable loss but can combine in phase with the wave reflected from the discontinuity at the input side. Applying this reflection coefficient of 0.05 and an attenuation of 4.13 dB (at 8415 MHz) in the graph (Fig. 5 of Ref. 4), the cyclical variation of group delay with frequency is found to be $(30/100)(\pm 0.19) = \pm 0.06$ ns. Although the amplitude of this delay variation is very small compared with the nominal delay of 30 ns, it is significant when compared with the limits of uncertainties of the various measurement methods shown in Table 4.

## VI. Conclusions

The results show that the standard cables are suitable for the intended application, and that the different measurement methods of independent laboratories generally agree within estimated limits of error. Two of the major sources of errors that can cause discrepancies between various measurement methods have been investigated. These error sources are dispersion and internal reflections.

It was found that although significant dispersion was observed at frequencies near 500 kHz, there was no significant effect observed at tested microwave frequency bands between 2000 to 9000 MHz. These results indicate that the most accurate measurements of group delay can probably be made by measuring phase shift variation with frequency using a fairly wide frequency interval, say, 100 MHz or so, provided the phase shift varies linearly with frequency over that range. This was substantially the case for the standard delay cables at the microwave frequencies.

Cyclical variations of phase can occur as a function of frequency due to reflections from small discontinuities at the ends of the cables where dimensional changes occur going into the connectors. These phase deviations from linearity give rise to small cyclical variations of group delay with frequency. If the cyclical variation in group delay has an amplitude that is negligible compared with the error limit in measurement, then one should use a wide frequency interval so as to obtain an accurate value for the average group delay. However, if the cyclical variation in group delay has an amplitude that is larger than the error limit in measurement, then a small frequency interval should be used in order to measure the amount the group delay is above or below the average value at the particular frequency of interest.

## Acknowledgments

The authors thank the following persons who contributed to the development and testing of the group delay standards. At the Jet Propulsion Laboratory, L. J. Derr, P. D. Batelaan, and R. B. Lyon contributed during the initial development phase and performed measurements. Dr. C. T. Stelzried and G. S. Levy encouraged and supported the development of the delay standards for the S- X-Band Experiment. At Phelps Dodge Communications Company, W. Meola and H. Edwards were involved in the design and fabrication. At Western Automatic Test Services, measurements were performed by A. Rosenzweig and M. Culbertson. At the National Bureau of Standards, K. C. Roe, R. N. Jones, and P. A. Simpson performed the NBS measurements, while A. Estin contributed to the initial development work and provided administrative support.

## References

1. Sokov, I. A., and Semenova, V. P., "Measurement of the Group Time Delay and Checking on Group Time Delay Measurement Devices," *Measurement Techniques*, Vol. 14, No. 9, Sept. 1971, pp. 1387-1390. Translated from Izmeritel'naya Tekhnika, No. 9, pp. 63-65, Sept. 1971. Original article submitted Nov. 27, 1969.
2. Levy, G., Dickinson, R., and Stelzried, C., "RF Techniques Research: S/X-Band Experiment," JPL Space Programs Summary 37-61, Vol. III, pp. 93-95, Feb. 20, 1970.
3. Meola, W., "Phase-Temperature Coefficient of Phelps Dodge FXA 38-50 Semirigid Cable," Engineering Report 162, Phelps Dodge, North Haven, Connecticut, Jan. 9, 1970.

4. Beatty, R. W., and Otoshi, T. Y., "Effect of Discontinuities on the Group Delay of a Microwave Transmission Line," *IEEE Trans. Microwave Theory Tech.*, Vol. MTT-23, No. 11, pp. 919–923, November 1975.

5. *IRE Dictionary of Electronics Terms and Symbols*, Inst. of Radio Engineers, N.Y., 1961. See p. 53, Envelope Delay; p. 104, Phase Delay.

6. Roe, K. C., *Delay Line Measurements*, NBSIR 73-332, National Bureau of Standards, Boulder, CO, August 3, 1973, 10 pages.

7. Estin, A. J., and Jones, R. N., private correspondence (additional test data from National Bureau of Standards, Boulder Laboratories, were given in letter dated May 13, 1975).

8. Gordon, G. B., and Reeser, G. A., "Introducing the Computing Counter," *Hewlett-Packard Journal*, Vol. 20, No. 9, pp. 2–8, May 1969.

9. Martin, W. L., and Goldstein, R. M., "Binary Coded Sequential Acquisition Ranging System," U.S. Patent 3,659,292, April 25, 1972.

10. Martin, W. L., "System Performance of the Dual-Channel Mu-II Sequential Ranging," *The Deep Space Network Progress Report 42-26*, pp. 54–68, April 15, 1975.

11. Otoshi, T. Y., ed., *A Collection of Articles on S/X-Band Experiment Zero Delay Ranging Tests*, Tech. Memorandum 33-747, Vol. I, Jet Propulsion Laboratory, Pasadena, CA, pp. 23–32, November 1, 1975.

12. Anderson, A. R., and McCraven, M. R., *Changes in Coaxial Cable Delay with Temperature and Frequency*, Engineering Report No. E-131, Phelps Dodge, North Haven, Connecticut, May 31, 1967.

**Table 1. Measured voltage reflection and loss characteristics of group delay standards**

| Nominal delay of standard cable | Input voltage reflection coefficient magnitude | | | Characteristic insertion loss, dB | | |
|---|---|---|---|---|---|---|
| | 2113 MHz | 2295 MHz | 8415 MHz | 2113 MHz | 2295 MHz | 8415 MHz |
| 15 ns | 0.02 (M)[a]<br>0.02 (F)[b] | 0.02 (M)<br>0.02 (F) | 0.06 (M)<br>0.05 (F) | 0.82 | 0.87 | 2.04 |
| 30 ns | 0.01 (M)<br>0.01 (F) | 0.02 (M)<br>0.02 (F) | 0.06 (M)<br>0.07 (F) | 1.63 | 1.75 | 4.13 |
| 60 ns | 0.02 (M)<br>0.02 (F) | 0.03 (M)<br>0.02 (F) | 0.05 (M)<br>0.07 (F) | 3.29 | 3.49 | 8.26 |

[a]Denotes male connector input side.

[b]Denotes female connector input side.

**Table 2. List of measurement methods and laboratories**

| Method | Laboratory | Description of method |
|---|---|---|
| 1 | NBS | Measure open- and short-circuit impedances at 400, 500, and 600 kHz, and calculate phase constants of cables. Then group delay is calculated from the range of change of phase shift with frequency. |
| 2a | NBS | Measure phase shift versus frequency at frequencies near 2113, 2295, and 8415 MHz using phase bridge. |
| 2b | WATS | Measure rate of change of phase shift with frequency with HP 8542A automatic network analyzer system at frequencies near 2113, 2295, and 8415 MHz. |
| 3a | NBS | Measure time delay between corresponding peaks of an RF pulse burst at frequencies near 2113, 2295, and 8415 MHz. |
| 3b | JPL | Measure time delay of a baseband pulse at a repetition rate of 500 kHz, using an HP 5360A computing counter. The baseband pulse modulates the microwave frequency of 2295 MHz. |
| 4 | JPL | Measure the phase shift of a 500-kHz modulating envelope on RF carrier frequencies of 2113, 2295, and 8415 MHz using the JPL Mu-ranging system. |

**Table 3. Summary of measured group delays in nanoseconds**

| Frequency | Laboratory | Method (see Table 2) | Nominal group delay of cable | | |
|---|---|---|---|---|---|
| | | | 15 ns | 30 ns | 60 ns |
| 500 kHz | NBS | 1 | 15.20 | 30.34 | 60.88 |
| 2113 MHz | NBS | 2a | 15.09 | 30.01 | 59.94 |
| | NBS | 3a | 14.95 | 30.18 | 60.07 |
| | WATS | 2b | 15.04 | 29.98 | 59.97 |
| | JPL | 4 | 16.51[a] | 31.28[a] | 61.11[a] |
| | Weighted average | | 15.00 | 30.05 | 59.98 |
| 2295 MHz | NBS | 2a | 15.09 | 29.96 | 59.98 |
| | NBS | 3a | 15.04 | 30.21 | 59.82 |
| | WATS | 2b | 14.98 | 30.02 | 59.99 |
| | JPL | 3b | 15.01 | 30.03 | 60.08 |
| | JPL | 4 | 16.51[a] | 31.28[a] | 61.11[a] |
| | Weighted average | | 15.02 | 30.07 | 59.97 |
| 8415 MHz | NBS | 2a | 15.10 | 30.12 | 60.03 |
| | NBS | 3a | 15.03 | 29.90 | 59.91 |
| | WATS | 2b | 15.03 | 30.03 | 60.08 |
| | JPL | 4 | — | 29.84 | 57.67 |
| | Weighted average | | 15.03 | 30.03 | 60.06 |

[a]A cable standard was inserted into a common transmit/receive signal path of the JPL ranging system. This insertion caused the total measured delay change to be the sum of the cable delay at 2113 and 2295 MHz. It was not possible to determine the cable delay at the individual frequencies from these data. However, since the two frequencies were reasonably close together, it was assumed that the delay at each frequency was the same and therefore equal to the total measured delay change divided by 2.

**Table 4. Deviations from average and estimated limits of uncertainty**

| Frequency, MHz | Laboratory | Method | Nominal group delay of cable | | | | | |
|---|---|---|---|---|---|---|---|---|
| | | | 15 ns | | 30 ns | | 60 ns | |
| | | | Dev. from avg., ns | Est. error limit, ns | Dev. from avg., ns | Est. error limit, ns | Dev. from avg., ns | Est. error limit, ns |
| 2113 | NBS | 2a | 0.09 | ±0.13 | −0.04 | ±0.13 | −0.04 | ±0.13 |
| | NBS | 3a | −0.05 | ±0.05 | 0.13 | ±0.08 | 0.09 | ±0.14 |
| | WATS | 2b | 0.04 | ±0.06 | −0.07 | ±0.06 | −0.01 | ±0.06 |
| | JPL | 4 | 1.51 | — | 1.23 | — | 1.13 | — |
| 2295 | NBS | 2a | 0.07 | ±0.13 | −0.11 | ±0.13 | 0.01 | ±0.13 |
| | NBS | 3a | 0.02 | ±0.05 | 0.14 | ±0.08 | −0.15 | ±0.14 |
| | WATS | 2b | −0.04 | ±0.06 | −0.05 | ±0.06 | 0.02 | ±0.06 |
| | JPL | 3b | −0.01 | ±0.30 | −0.04 | ±0.30 | 0.11 | ±0.30 |
| | JPL | 4 | 1.49 | — | 1.21 | — | 1.14 | — |
| 8415 | NBS | 2a | 0.07 | ±0.13 | 0.09 | ±0.13 | −0.03 | ±0.13 |
| | NBS | 3a | 0.00 | ±0.05 | −0.13 | ±0.13 | −0.15 | ±0.27 |
| | WATS | 2b | 0.00 | ±0.04 | 0.00 | ±0.04 | 0.02 | ±0.06 |
| | JPL | 4 | — | — | −0.19 | — | −2.39 | — |

**Table 5. Measured phase and group delay of standard cables at frequencies near 500 kHz (Method 1)**

| Frequency, kHz | Nominal delay in nanoseconds of standard cable | | |
|---|---|---|---|
| | 15 | 30 | 60 |
| | Phase delay in ns | | |
| 400 | 15.44 | 30.85 | 61.70 |
| 500 | 15.39 | 30.75 | 61.52 |
| 600 | 15.36 | 30.68 | 61.43 |
| | Group delay in ns | | |
| 450 | 15.18 | 30.35 | 60.77 |
| 500 | 15.20 | 30.34 | 60.88 |
| 550 | 15.23 | 30.33 | 60.99 |

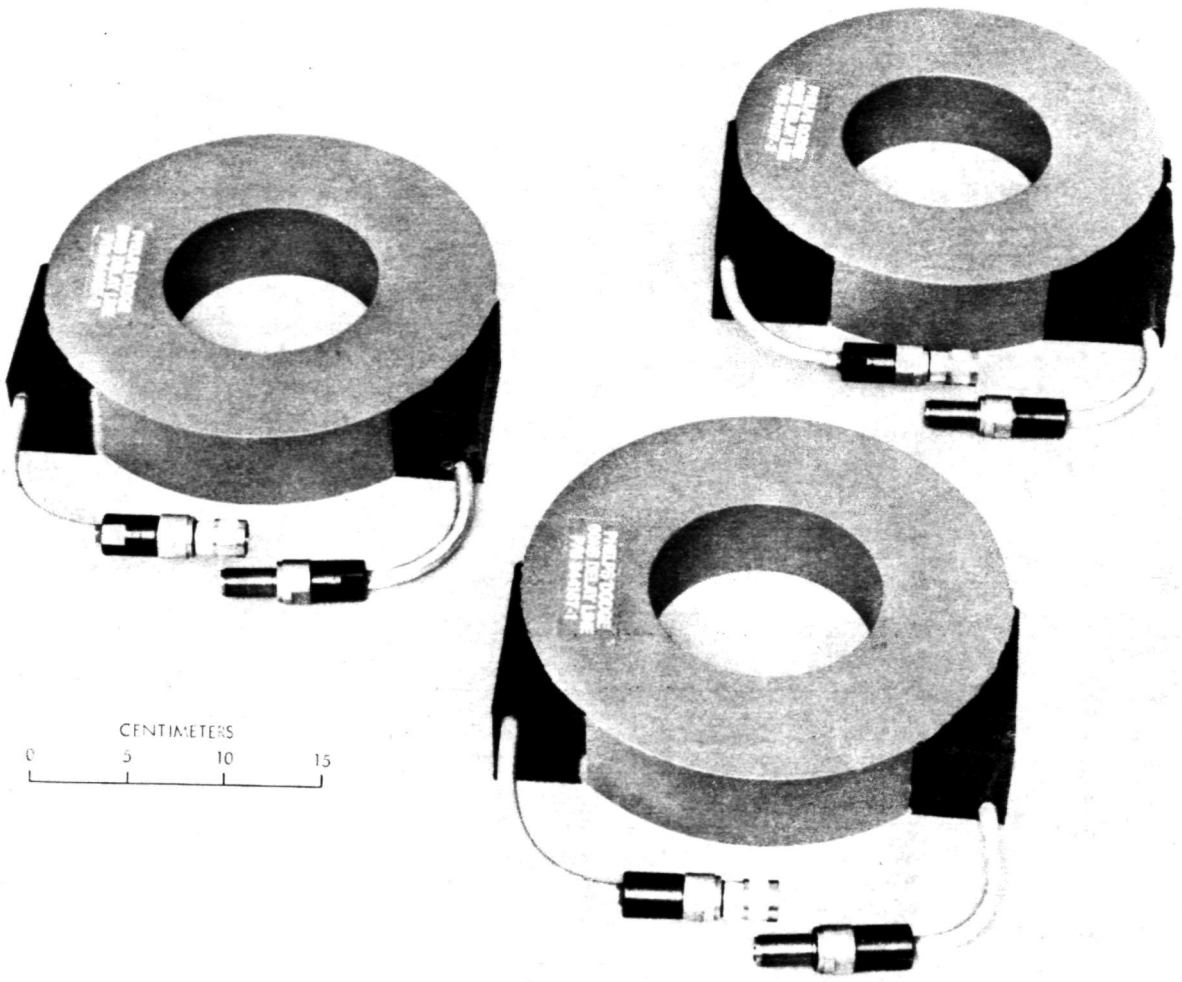


Fig. 1. Group delay standards of 15, 30, and 60 ns

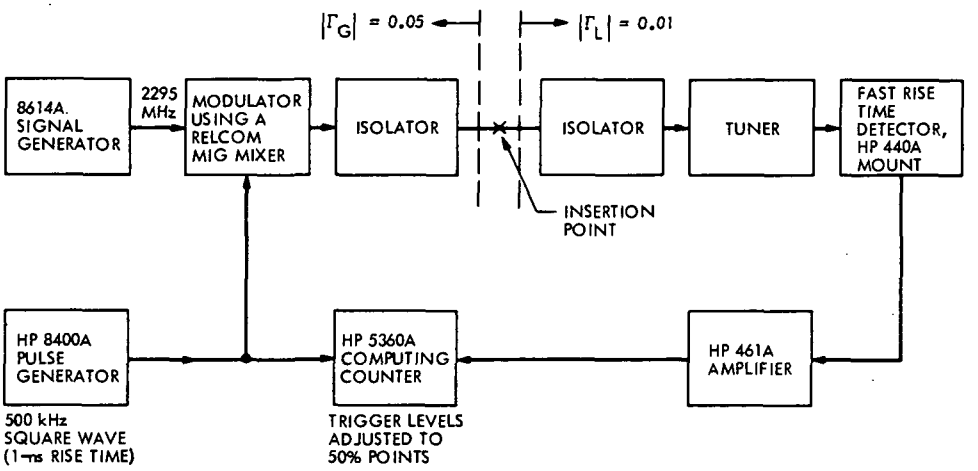


Fig. 2. Block diagram of delay measurement method utilizing a computer counter

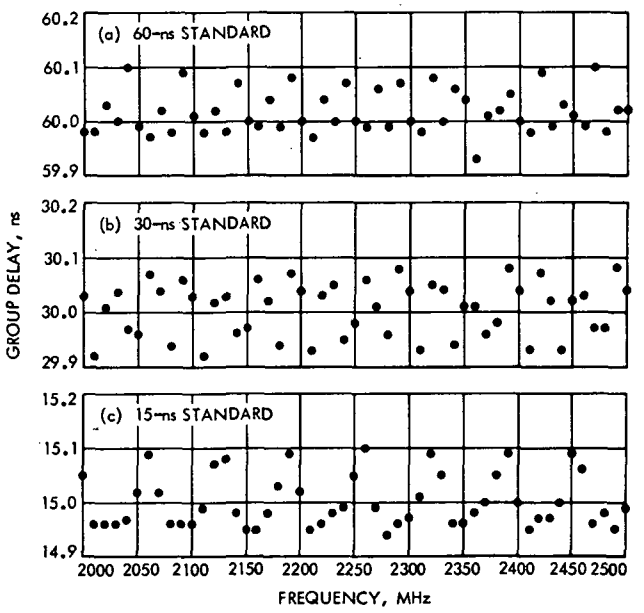


Fig. 3. Measured group delays of 15, 30, and 60 ns standards in the frequency range of 2000 to 2500 MHz (frequency interval associated with each data point was 20 MHz)

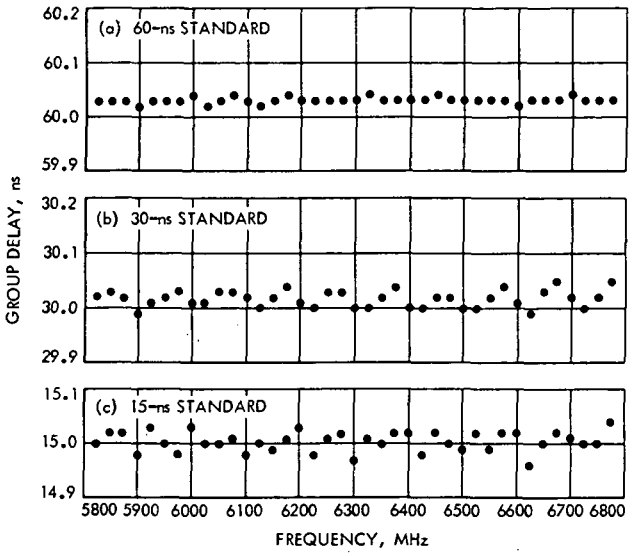


**Fig. 4. Measured group delays of 15, 30, and 60 ns standards in the frequency range of 5775 to 6775 MHz (frequency interval associated with each data point was 50 MHz)**

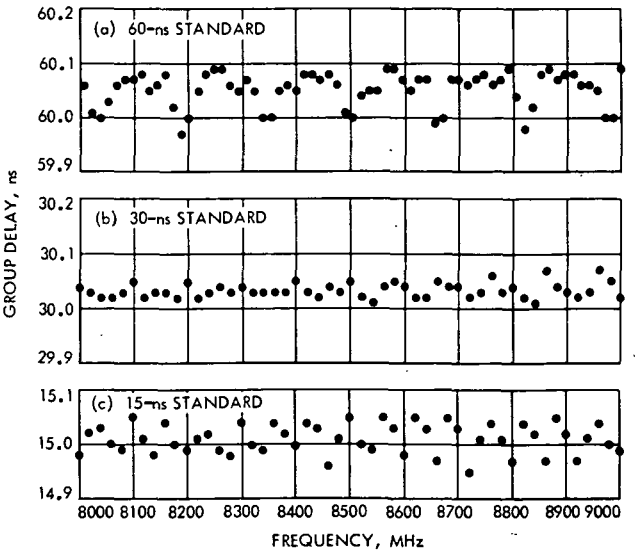


**Fig. 5. Measured group delays of 15, 30, and 60 ns standards in the frequency range of 8000 to 9000 MHz (frequency interval associated with each data point was 40 MHz for 15 and 30 ns cables and 30 MHz for the 60 ns cable)**

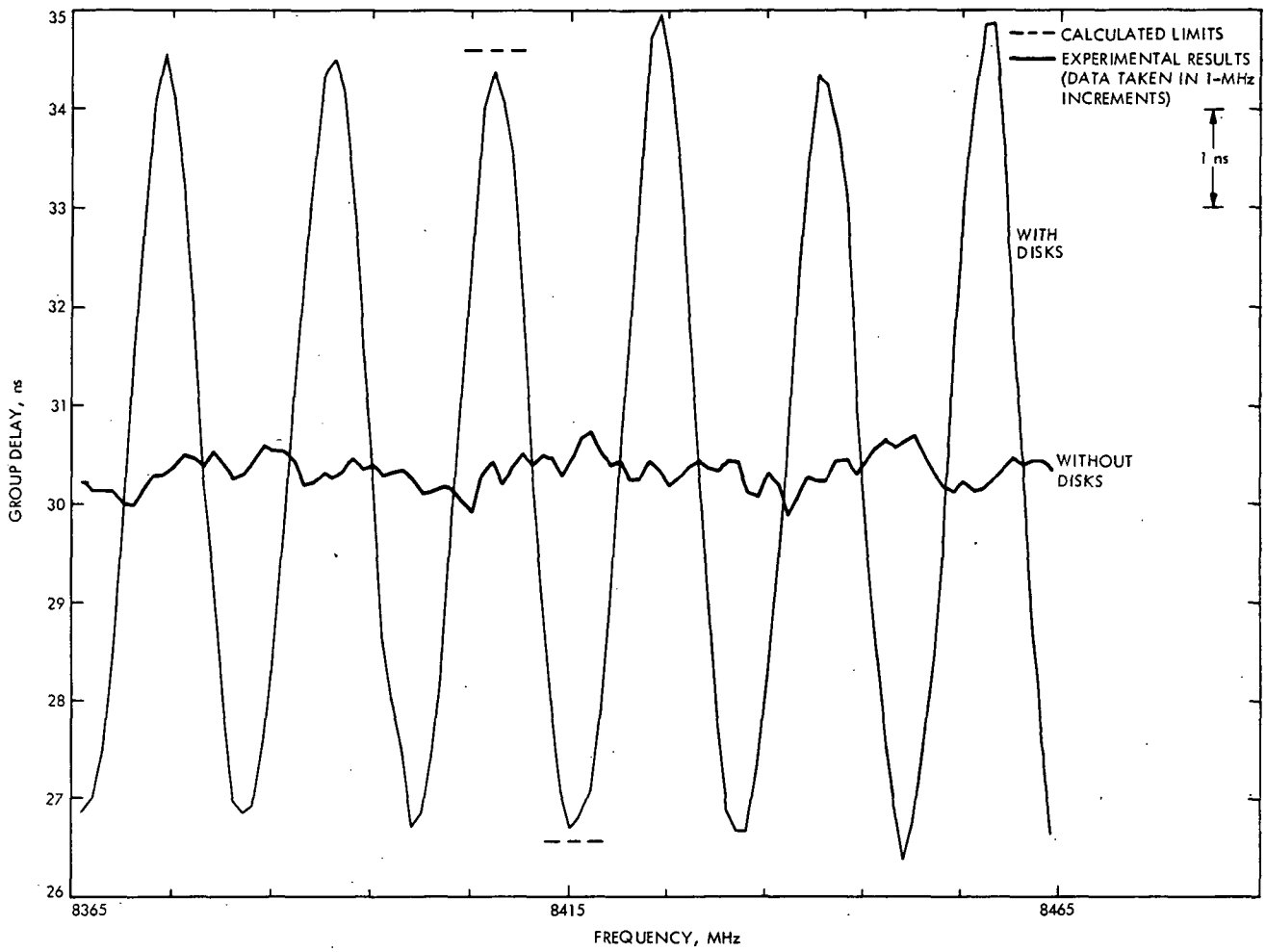


**Fig. 6. Measured group delay of a 30-ns standard transmission line plus short end sections of 7-mm lines with and without 6.12-mm (0.241 in.) diam disks**

# Proposed Modifications to the Wind Loading Specifications Applied to Ground Antennas

M. S. Katow
DSN Engineering Section

*As the survival wind velocity specification mainly controls the final weight of the reflector structure of a ground antenna, this reporting of a study of the latest wind data shows that the survival specification can be lowered, and therefore the weight can be lowered, from 53.0 m/s (120 mi/h) to less than 44.1 m/s (100 mi/h). The results are based on analysis methods as recommended by the existing design guides. However, the next study reporting will be based on considerations of the dynamic action of wind, which is the upgraded analysis method described in the literature.*

## I. Introduction

During the design period of the 64-m antenna, the two specifications that controlled the minimum weight of the antenna structure were (1) the requirement to satisfy the minimum natural frequency of vibration of 1.5 Hz, which mainly affected the weight of the alidade and the elevation wheel assembly of the reflector, and (2) the requirement to survive in a 53.0 m/s (120 mi/h) wind in stow configuration, which controlled the weight of the reflector structure. In the truss type of structure used for antenna assemblies, the weight is closely proportional to the cross-sectional areas of the bar elements of the truss, which directly reflects its stiffness and strength.

This article describes the results of a study made to redefine the survival wind velocity based on recent wind data and the use of the latest engineering methods to resolve the actual wind loadings on the antenna structure by the environmental winds at the Goldstone Deep Space Communications Complex.

This report describes the wind data and calculations for wind loadings based on existing design guides (Refs. 1 and 2) published by the American Society of Civil Engineers. A future report will describe the application of formulations based on statistical concepts of random vibrations pioneered by Davenport (Ref. 3).

## II. Discussion

To determine the stow wind pressures on the antenna, it is necessary first to select the design velocity, which is the maximum average wind velocity for a selected time period that is proper for the locality. Gust pressures

must be included. Gusts are relatively short-period horizontal and vertical fluctuations of the wind, but are of sufficient extent to envelop the antenna and permit the corresponding aerodynamic effects to develop.

At Goldstone, we can eliminate consideration of tornadoes, hurricanes and icing. The storms which generate the high winds here are described as "extratropical cyclones" (Ref. 2) that cross the United States at a rate of about 2 cyclones per week.

Thom (Ref. 4) of the U.S. Department of Commerce, published results of wind data taken throughout the United States by the U.S. Weather Bureau which were statistically analyzed and resolved in maps showing contours of the annual fastest mile of wind in miles per hour at 30 feet above ground. The 100-yr Probable Period of Recurrence Map is reproduced as Fig. 1. This mile of wind velocity is computed as: Velocity (mph) = 1/Time, in hours, of passage of one mile of wind, and is also the average velocity for the measured time period.

The Task Committee on Wind Forces of the Society of Civil Engineers (ASCE) (Ref. 2) recommends the use of a basic velocity from the 50-yr period of recurrence for all permanent structures except those that, in the judgment of the engineer, have a high degree of wind sensitivity and an unusually high degree of hazard to life and property in case of failure. The ground antenna is judged to be in the latter classification. The wind speeds in Fig. 1 have the probability of being exceeded of 0.01. For the U.S., these speeds are, on the average, 1.08 times the corresponding speeds for the 50-yr winds.

The location of the Goldstone Deep Space Communications Complex is indicated by the X on Fig. 1. The wind velocity is 32.63 m/s (73 mi/h) at 9.14 m (30 ft) height above ground. This recommendation (Ref. 2) is based on conditions in open, level country as a standard of reference also described as exposure "C," and the influence of shielding or of deflections and channelling due to unusual topography or to large obstructions is expected to be separately evaluated. The present Mars 64-m antenna location is judged to be in open country because of the long stretch of smooth terrain approaching the location in the high wind direction. Figure 2 shows a plot of the 1/7 power-law curve common to open country or exposure "C" going through the 15.9-m (52-ft) height measured 5-min average wind speed with the measured simultaneous values for 45.7-m (150 ft) and 87.1-m (286 ft) heights placed on the graph. A good fit of the measured data to the 1/7 power curve results.

In stow configuration the 64-m antenna height is 51.82 m (170 ft). Based on the 1/7 power curve, the 32.63-m/s (73-mi/h) velocity at 9.14 m (30 ft) translated to 40.3-m/s (93.5-mi/h) velocity by Eq. (1) at a height of 51.82 m (170 ft) equals:

$$V_z = V_{9.14}\left(\frac{Z}{V_{9.14}}\right)^{1/m}$$

$$V_{51.82} = 32.63\left(\frac{51.82}{9.14}\right)^{1/7} = 41.8 \text{ m/s } (93.5 \text{ mi/h}) \quad (1)$$

where

$V_z$ = velocity at height $Z = 51.82$ m

$V_{9.14}$ = basic velocity at 9.14-m (30-ft) height

$m$ = exponent

If we follow the recommendations of the Task Committee on Wind Forces of ASCE (2), a gust factor in terms of a multiplier to the extreme wind speed must be developed.

The Task Committee recommends the use of a curve from (5) which defines the gust factor (gust velocity ÷ 5 min average velocity) in terms of the gust duration. The curve may be expressed by a fitted equation

$$Y = \left(\frac{300}{D}\right)^{0.0399}$$

$Y$ = gust factor (2)

$D$ = gust duration

The gust duration is the time the basic velocity takes to travel 6 to 8 times the longitudinal length of the object or antenna. This, in fact, defines the "minimum effective gust size" required to envelop and develop the incremental aerodynamic pressures (Ref. 5).

If we use the conservative recommendations in Ref. 6 of 4 times the smallest of the height and the longitudinal length, we have

Wind velocity at 51.82 m = 41.8 m/s

Gust duration $D = \dfrac{4 \times 51.82}{41.8} = 4.96$, say 5 sec

Since the gust factors of Ref. 5 are based on the 5-min average wind velocity, a conversion is required from the mile of wind velocity. This may be done by Fig. 3 which

is reproduced from Ref. 6 and is based upon the results of a statistical analysis of data obtained in strong winds over flat, unobstructed terrain. Figure 3 shows, for a given period of $t$ seconds used to average a wind speed, the factor $F$, the ratio of the average probable maximum wind speed to the mean hourly speed.

First, the averaging period $t$ for the fastest mile of wind is from (Ref. 6)

$$t = \frac{3600}{V_f} \text{ s}$$

$V_f$ = the fastest mile velocity in mph
for 41.8 m/s (93.5 mi/h) $t = 3600/93.5 = 38.5$ s

$F$ from Fig. 3 for $t = 38.5 = 1.29$

$F$ from Fig. 3 for $t = 300 = 1.10$
($t = 300$ for 5-min average)

$$\text{5-min average wind speed} = \frac{41.8 \times 1.10}{1.29} = 35.6 \text{ m/s}$$

From Eq. (2)

$$\text{Gust factor} = \left(\frac{300}{D}\right)^{0.0399}$$

$$= \left(\frac{300}{5}\right)^{0.0399}$$

$$= 1.177$$

Maximum design
wind velocity = 5-min average speed × gust factor

$$= 35.6 \times 1.177 = 41.9 \text{ m/s (95.1 mi/h)}$$

which is only 0.1 m/s over the extreme mile of wind speed at a height of 51.82 m (170 ft).

## III. Conclusions

The results of this study using the recommendations from the design guides show that the extreme mile of wind speed at the top height of the stowed 64-m antenna represents the maximum design wind velocity, since the effects of gusts are shown to be negligible for the size of the 64-m antenna.

The exposure of the antenna location is based on a terrain classified as flat, open, grassland country. As shown in Fig. 2, the actual measured wind speeds on the 91-m (300-ft) tower near the Mars station at Goldstone show a close fit to the 1/7 power velocity curve of this type of exposure.

The actual measured extreme wind speeds during the period from September 1966 to August 1967 on the tower at the 15.2-m (50-ft) height was in the range of 17.0–18.3 m/s (56–60 mi/h) in January 1967 and at the 45.7-m (150-ft) height was 21.6–22.9 m/s (71–75 mi/h). These wind speeds were lower than that predicted by Fig. 1.

## References


1. Task Committee on Tower Design, "Electrical Transmission Line and Tower Design Guide," Journal of the Structural Division, *Proc. ASCE*, Vol. 93, No. ST4, Aug. 1967, pp. 245–282.
2. Task Committee on Wind Forces, "Wind Forces on Structures," *Trans. ASCE*, Vol. 126, Part II, 1961, pp. 1124–1198.
3. Davenport, A. G., "The Application of Statistical Concepts to the Wind Loading of Structures," *Proc. ICE*, London, Vol. 19, 1961, pp. 449–472.
4. Thom, H. H. S., "New Distributions of Extreme Winds in the United States," Journal of the Structural Division, *Proc. ASCE*, Vol. 94, No. ST7, July 1968, pp. 1787–1801.
5. Sherlock, R. H., "Gust Factors for the Design of Buildings," International Association for Bridge and Structural Engineering, Zurich, Switzerland, 1947, pp. 207–236.
6. Vellozzi, J., and Cohen, E., "Gust Response Factors," Journal of the Structural Division, *Proc. ASCE*, Vol. 94, ST6, June 1968, pp. 1295–1313.

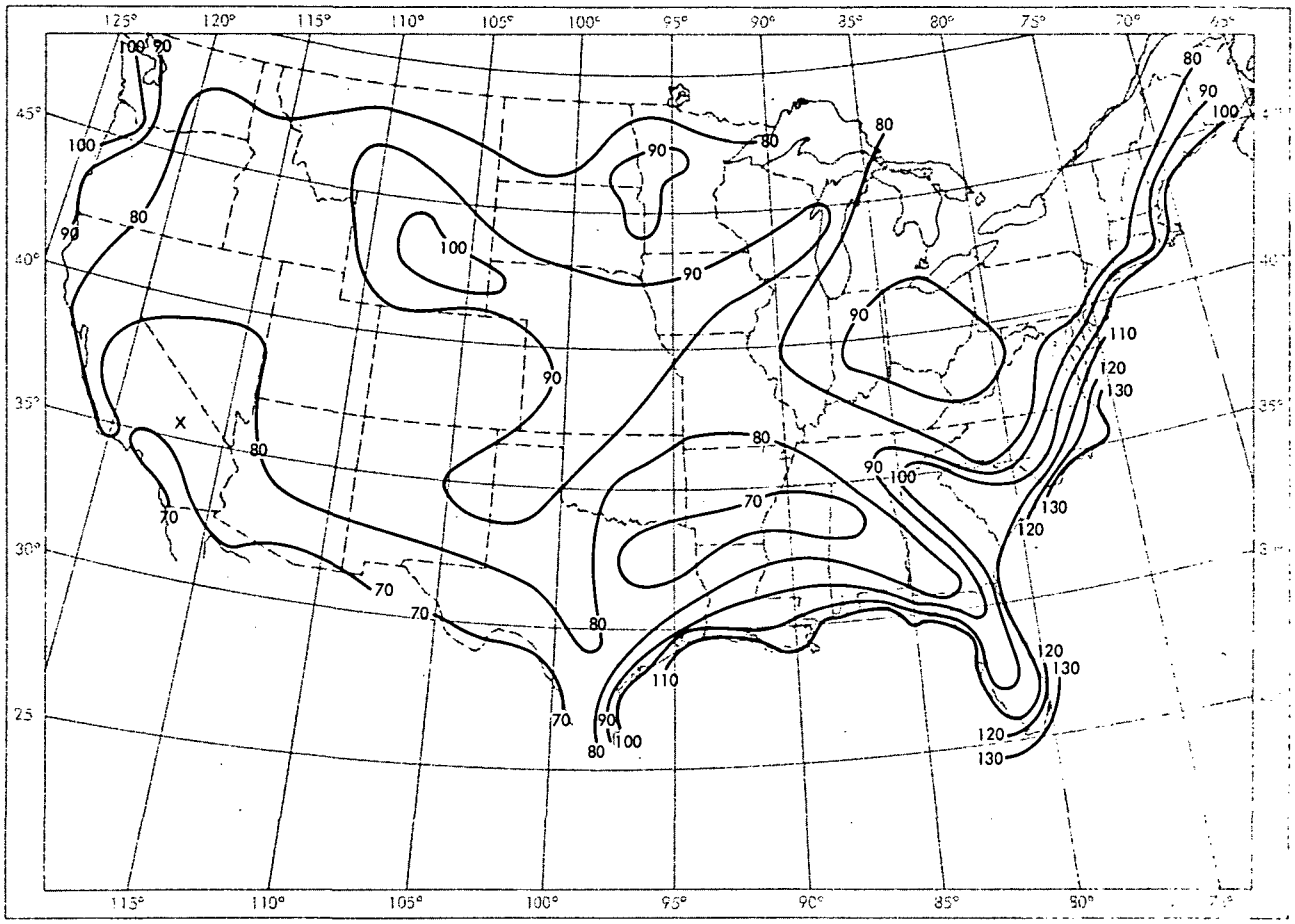


**Fig. 1. Wind speed (mi/h): annual extreme-mile 30 ft above ground, 100-yr mean recurrence interval (from Ref. 4)**

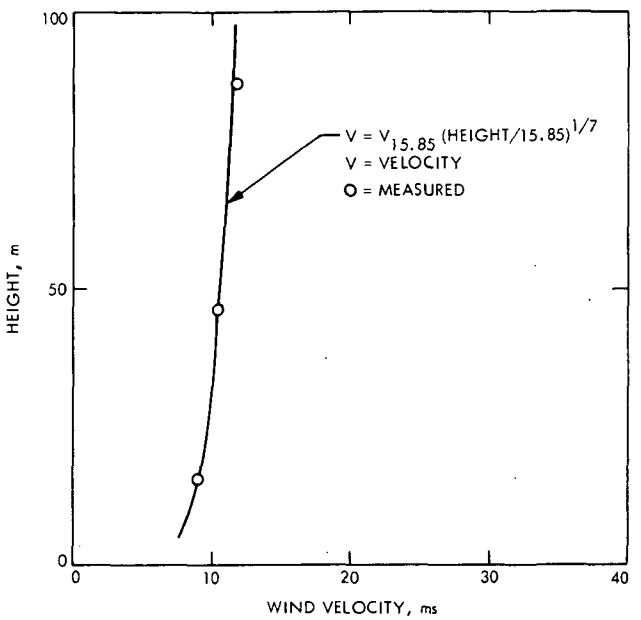


Fig. 2. Wind velocity vs height at Mars site

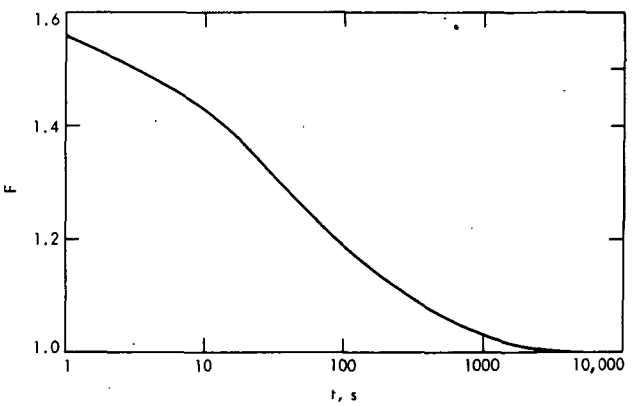


Fig. 3. Ratio *F* of probable maximum speed averaged over period *t* to that averaged over 1 hour (exposure C)

# Analysis of Command Detector In-Lock Monitoring

R. G. Lipes
Communications Systems Research Section

*We have investigated a command detector in-lock monitoring strategy that uses* N *estimates of* $(SNR)^{1/2}$ *each composed of* M *samples from both data and error channel outputs. The detector recognizes only two states (in-lock and out-of-lock) and indicates state transition when* N *successive* $(SNR)^{1/2}$ *estimates violate a threshold. We give the probabilities of indicating in-lock given the detector is out-of-lock and out-of-lock given in-lock as a function of threshold for* (N,M) = *(1,10), (2,5), (5,2), (10,1). From these probabilities a threshold compatible with design requirements can be determined.*

## I. Introduction

A command detector being developed for NASA uses signal-to-noise ratio (SNR) estimates to monitor operations of the detector. An important monitoring function is to determine whether or not the detector is in-lock. The purpose of this article is to investigate how well the monitoring function can be performed using a particular set of strategies that can be relatively easily implemented.

In Section II we will detail the particular set of strategies we wish to pursue. We will measure their performance in terms of the conditioned probabilities of indicating in-lock, given the detector is out-of-lock, and indicating out-of-lock, given in-lock. In Section III, we will develop expressions for those conditional probabilities whose evaluation requires numerical integration. In Section IV, we will present the results of the numerical evaluations for strategies that appear most relevant to present design plans for the command detector.

## II. Statement of Command Detector Strategy

In a previous DSN article (Ref. 1), we analyzed a method for estimating the square root of the SNR rather than the SNR itself. This method involved obtaining $(SNR)^{1/2}$ from the ratio of an average of $M$ absolute values of data (in-phase) channel integrated outputs to an average of $M$ absolute values of error (quadrature) channel integrated outputs. The strategy for using this $(SNR)^{1/2}$ estimate as an in-lock indicator is the following: We consider the command detector as being in one of two states: in-lock or out-of-lock. Initially, before the command is acquired, the detector is out-of-lock. We define transition to the in-lock state as occurring after $N$ consecutive independent $(SNR)^{1/2}$ estimates are each above a threshold $T_0$. Once the in-lock state is reached, we define transition to the out-of-lock state as occurring after $N$ consecutive independent $(SNR)^{1/2}$ estimates are each below a threshold $T_0$. Since $NM$ samples of both data and error channels are required for the in-lock monitoring function, we will

consider schemes for which the product of $N$ and $M$ is constant. The performance of a set with constant $NM$ will be determined by considering the conditional probabilities of indicating in-lock, given out-of-lock, and of indicating out-of-lock, given in-lock.

## III. Derivation of Expressions for the Conditional Probabilities

### A. Expression for a Useful Probability

The following have been demonstrated in a previous DSN Progress Report (Ref. 1). The in-phase channel integrated output samples $X_i$ are independent random variables identically distributed with probability density

$$P_X(\alpha) = \begin{cases} \frac{1}{(2\pi\sigma^2)^{1/2}} \left\{ \exp\left[ -\frac{1}{2\sigma^2}(\alpha - AT)^2 \right] \right. \\ \left. + \exp\left[ -\frac{1}{2\sigma^2}(\alpha + AT)^2 \right] \right\}, & \alpha \geq 0 \\ 0, & \alpha < 0 \end{cases} \tag{1}$$

where $A$ is the signal amplitude, $T$ is the integration time, and $\sigma^2 = N_0 T/2$ with $N_0/2$ the two-sided power spectral noise density. The error channel integrated output samples $Y_i$ likewise are independent identically distributed random variables with probability density given by Eq. (1) with $A = 0$. The actual SNR is

$$\text{SNR} = \tfrac{1}{2}(AT/\sigma)^2 \tag{2}$$

and the command detector estimate $W$ of (SNR)½ is

$$W = (\pi)^{-1/2} \frac{1}{M} \sum_{i=1}^{M} X_i \left[ \frac{1}{M} \sum_{i=1}^{M} Y_i \right]^{-1} \tag{3}$$

For the present investigation we need to calculate the probability that $W < T_0$ when actual SNR is, say, $S_0^2$. Define random variables $\nu,\Delta$ equal to

$$\frac{1}{M}\sum_{i=1}^{M} X_i, \quad \frac{1}{M}\sum_{i=1}^{M} Y_i$$

respectively. Then, the needed probability $P(M,T_0,S_0^2)$ is

$$P(M,T_0,S_0^2) \equiv \iint d\alpha_1\, d\alpha_2\, P_\nu(\alpha_1)\, P_\Delta(\alpha_2)\, \theta\left( \sqrt{\pi}\, T_0 - \frac{\alpha_1}{\alpha_2} \right) \tag{4}$$

where the $\theta$-function, which is one if its argument is greater or equal to zero, and zero otherwise, has the integral representation

$$\theta(\beta) = \lim_{\epsilon \to 0} -\frac{1}{2\pi i} \int_{-\infty}^{\infty} \frac{dY}{Y + i\epsilon} \exp(-i\beta Y) \tag{5}$$

Substituting this into Eq. (3) and interchanging order of integration gives

$$P(M,T_0,S_0^2) = \lim_{\epsilon \to 0} -\frac{1}{2\pi i} \int_{-\infty}^{\infty} \frac{dY}{Y + i\epsilon} M_\nu(Y)\, [M_\Delta(\sqrt{\pi}\, T_0 Y)]^* \tag{6}$$

where $M_\nu(\alpha)$, $M_\Delta(\alpha)$ are the characteristic functions of $\nu,\Delta$ respectively. Using Eq. (1) and the independence of the $X_i$, we have

$$M_\nu(\alpha) = \left\{ \frac{1}{2} \exp\left( -\frac{\sigma^2\alpha^2}{2M^2} \right) \left[ \exp\left( i\frac{AT\alpha}{M} \right) \operatorname{erfc}\left( -\frac{AT}{\sqrt{2}\sigma} + i\frac{\sigma\alpha}{\sqrt{2}M} \right) + \exp\left( -i\frac{AT\alpha}{M} \right) \operatorname{erfc}\left( \frac{AT}{\sqrt{2}\sigma} + \frac{i\sigma\alpha}{\sqrt{2}M} \right) \right] \right\}^M \tag{7}$$

where $\operatorname{erfc}(x)$ is the complement of the error function:

$$\operatorname{erfc}(x) = 1 - \frac{2}{\sqrt{\pi}} \int_0^x e^{-u^2} du.$$

We obtain $M_\Delta(\alpha)$ from $M_\nu(\alpha)$ when $A = 0$, so

$$M_\Delta(\alpha) = \left\{ \exp\left( -\frac{\sigma^2\alpha^2}{2M^2} \right) \operatorname{erfc}\left( i\frac{\sigma\alpha}{\sqrt{2}M} \right) \right\}^M \tag{8}$$

With a change of variable $u = [(1 + \pi T_0^2)/2M]^{1/2}\, \sigma Y$ and using the symmetry relations of erfc $(x)$ (Ref. 2) we have, from Eq. (6):

$$P(M,T_0,S_0^2) = \frac{1}{2} + \frac{1}{\pi} \int_0^\infty \frac{du}{u} \exp(-u^2) \times Im[g(u) \operatorname{erfc}(-i\sqrt{\pi}\,\gamma\, T_0 u)]^M \tag{9}$$

where $Im$ means "imaginary part of," $\gamma = [M(1 + \pi T_0^2)]^{1/2}$, and we have defined the function $g(u)$:

$$g(u) \equiv \exp(-i\, 2\gamma S_0 u) - i \times Im[\exp(-i\, 2\gamma S_0 u) \operatorname{erfc}(S_0 - i\,\gamma u)] \tag{10}$$

Eqs. (9) and (10) use $S_0^2$ for the actual SNR $= \tfrac{1}{2}(AT/\sigma)^2$.

### B. Probabilities Involved in In-Lock Indicator Performance

In Eq. (9) we give an expression for the probability that the $(SNR)^{1/2}$ estimate $W$ is less than $T_0$ given actual SNR equals $S_0^2$. To evaluate the schemes proposed in Section II we need to relate actual SNR to the in-lock and out-of-lock states. We will assume the in-lock state exists when actual SNR is above command detector design point of $S_0^2 = 11.22$ (corresponding to 10.5 dB) and the out-of-lock state exists when actual SNR equals $S_0^2 = 0$. With these assumptions, we have for the conditional probability of indicating in-lock given out-of-lock:

$$P(IN|OUT) = [1 - P(M,T_0,0)]^N \tag{11}$$

and for the conditional probability of indicating out-of-lock given in-lock:

$$P(OUT|IN) \leq [P(M,T_0,11.22)]^N \tag{12}$$

## IV. Results and Conclusions

Present design plans for the command detector commit 10 data and error output samples for in-lock indication monitoring. This means the product $NM$ must be 10. There are, of course, four ways to accomplish this: $(N,M) = (1,10)$, $(2,5)$, $(5,2)$, and $(10,1)$. We wish, therefore, to have the probabilities of Eqs. (11) and (12) for these four possibilities as a function of $T_0$.

The required probabilities require numerical evaluation of Eq. (9). While conceptually straightforward, this integration requires some care, since the integrand is oscillatory, so the integral achieves a small value from cancelling contributions. For example, Eq. (9) immediately suggests Hermite integration. However, the required values of $N$ and $M$ cause oscillations of the integrand too rapid to be reliably approximated by Hermite polynomials of degree $\leq 20$, which is the highest degree with tabulated roots and weights (Ref. 3). Instead, we used the transformation $u = \tan^{-1} v$, divided the interval $[0, \pi/2]$ into equal intervals, and used 8-point Gaussian quadrature in each interval. The value of the integrals was insensitive to the number of partitioning intervals when the number exceeded 175. For the erfc functions of complex argument we used approximations depending upon the magnitude of the argument[1] to insure accuracy and rapid convergence of the summations involved. Since we could calculate analytically

$$P(1,T_0,0) = \frac{2}{\pi} \tan^{-1}(\sqrt{\pi}\, T_0),$$

we checked the numerical integration in this case and obtained agreement to 5 significant decimal figures for $P(IN|OUT) = [1 - P(1,T_0,0)]^{10}$.

The results of numerical evaluation of Eqs. (11) and (12) for the four possibilities as functions of $T_0^2$ (the equivalent threshold SNR) are presented in Fig. 1. From these curves one can establish a threshold to meet design requirements. If, for example, the requirements are $P(IN|OUT) < 10^{-3}$ and $P(OUT|IN) < 10^{-9}$, then we see that $(N,M) = (5,2)$ with $1 < T_0^2 < 1.7$ will be adequate.

[1]When the complex argument of the erfc-function had a squared magnitude less than 26 we used the approximation of Eq. 7.1.29 on p. 299 of Ref. 2. When the squared magnitude was greater than 26 we utilized the relation between the erfc-function and the confluent hypergeometric function to develop a 10-term asymptotic expansion for erfc derived from Eq. 13.5.1 of Ref. 2. The value 26 was chosen to insure rapid convergence of summations involved. Both representations of erfc agreed to 5 significant decimal figures for squared magnitudes between 20 and 26.

## References


1. Lipes, Richard G., "Analysis of Command Detector Signal-to-Noise Estimator," in *The Deep Space Network Progress Report 42-31*, pp. 75–83, Jet Propulsion Laboratory, Pasadena, Calif., Feb. 15, 1976.
2. Abramowitz, M., and Stegun, I., *Handbook of Mathematical Functions*, National Bureau of Standards, p. 297.
3. Krylov, V. I., *Approximate Calculations of Integrals*, Macmillan Co., New York, 1962; also Ref. 2, p. 924.

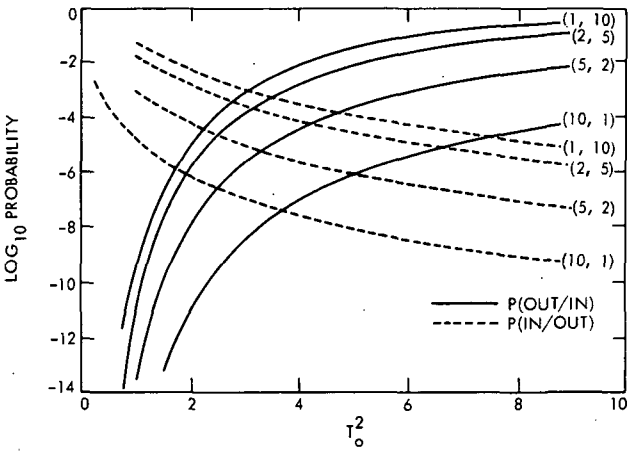


**Fig. 1. Plot of conditional probabilities as a function of threshold for strategies (*N*,*M*) = (1,10), (2,5), (5,2), (10,1). *N* is the number of estimates of $(SNR)^{1/2}$ and *M* is the number of samples in each estimate.**

# Precision Signal Power Measurement Equipment—Radio Frequency Section

G. Stevens
Communications Systems Research Section

*The Precision Signal Power Measurement (PSPM) equipment has been installed at the Goldstone Mars Station, DSS 14. The PSPM equipment features a highly flexible radio frequency (RF) section providing amplification, frequency translation, filtering, sampling and analog to digital (A-D) conversion of the 50 MHz Block III Receiver or 55 MHz Block IV Receiver intermediate frequency (IF) signals. Remote control of gain, tuning and filter selection permits hands-off operation of the RF section of the equipment. This article describes the RF section of the PSPM equipment.*

## I. Introduction

The Precision Signal Power Measurement (PSPM) equipment has been installed in the Mars Station (DSS 14) at Goldstone. An integral part of the PSPM hardware is a radio frequency (RF) section which translates a narrow slice of the receiver's 50 MHz (Block III) or 55 MHz (Block IV) intermediate frequency (IF) spectrum to baseband. Sampling and A-D conversion of the baseband signal are also provided in the RF section. The baseband data are then submitted to the digital section of the PSPM system for spectral analysis and signal-to-noise ratio (SNR) formulation. A second channel in the RF section measures the total IF bandwidth power. This channel consists of a broadband square law detector (Ref. 1) and an A-D converter, and is used with a calibrated noise adding diode to accurately and continuously measure system temperature. This article describes the RF section of the PSPM equipment. The balance of the PSPM equipment and its operation are described in Reference 2.

## II. RF Section Requirements

The PSPM equipment is designed to operate over a wide dynamic range of signal level conditions, processing the IF signals from either Block III or Block IV receivers, while simultaneously measuring system temperature. The RF section satisfies the following requirements:

(1) It is tunable to the 50 MHz IF of the Block III receiver or to the 55 MHz IF of the Block IV receiver.

(2) It provides a tuning range of ±1 MHz about either of these IFs to permit precise power level measure-

ments of individual sideband components of the signal.

(3) It provides three selectable sampling bandwidths and filters for extended strong signal measurement capability.

(4) Its RF attenuators, 50/55 MHz preselector tuning and baseband filter selection are remotely controlled by the PSPM MAC-16 computer.

(5) It provides signal level monitors at key points in the RF chain to alert system users to improper operation, loss of signal or equipment malfunction.

(6) It provides a noise adding radiometer (NAR) channel which measures the total IF bandwidth power.

(7) It provides 12-bit A-D conversion for signal and NAR channels.

## III. System Description

Figure 1 is a simplified block diagram of the PSPM RF section showing its connections to the DSN receivers. The IF signals from Receivers 1 through 4 are buffered by a set of R&D isolation amplifiers and are then supplied to the PSPM equipment. Within the PSPM RF section, the selected receiver's signal is split and simultaneously applied to the signal channel and NAR channel inputs. Signal data and noise data are supplied to the PSPM digital section.

A detailed block diagram of the PSPM RF section is shown in Figure 2. The signal channel consists of four modules, while the NAR channel uses only one module plus the broad band square law detector.

### A. Power Splitter Module

The power splitter module is the first module in the signal channel. This module amplifies the 50 MHz or 55 MHz IF signal of the selected receiver, provides four isolated output ports, and exhibits a maximum gain of 34 dB. The gain of this module is controllable over a 31.5 dB range, in increments of 0.5 dB. The programmable attenuator providing the gain control is driven by a set of six optocouplers.

### B. Tunable IF Module

The function of the tunable IF module is to translate the 50 MHz or 55 MHz IF signal to 10 MHz (less a small offset frequency), bandpass filter the 10 MHz signal, and provide controllable gain.

The tunable IF module receives its input from the power splitter module. The signal is bandpass filtered, amplified and fed to the input of the PSPM first mixer. The voltage-tuned bandpass filter prevents noise folding in the first mixer by providing approximately 30 dB of attenuation at the image frequency (20 MHz below the input frequency). One digital control line, optocoupled to a precision voltage generator, tunes the filter to 50 MHz or 55 MHz. Local oscillator (LO) drive for the first mixer is provided by a saturated amplifier driven by a Hewlett Packard frequency synthesizer. Since this RF system employs a fixed frequency (10 MHz) LO for the second mixer, the frequency offsets must be computed and entered in the first LO. The correct LO frequency is determined by first subtracting 10 MHz from the incoming frequency and then adding an offset frequency whose value is equal to one half of the corner frequency of the baseband module's selected low pass filter. For example, consider a carrier power measurement of a signal supplied to the PSPM equipment by a Block III receiver. For this example, assume that the 25 Hz low-pass filter has been selected. The carrier supplied to the PSPM equipment will be at precisely 50 MHz, locked there by the Block III receiver's RF loop. The LO frequency of the PSPM equipment must be:

$$50\ \text{MHz} - 10\ \text{MHz} + (25\ \text{Hz})/2 = 40{,}000{,}012.5\ \text{Hz}$$

This LO frequency will yield a baseband module output with the received signal exactly centered in its 25 Hz power spectrum.

After being translated to the 10 MHz IF by the PSPM first mixer, the signal is narrow band filtered, amplified and passed through a programmable attenuator. This attenuator adjusts the gain of the tunable IF module from -0.5 dB to +30 dB.

### C. Baseband Module

The 10 MHz IF signal supplied to the baseband module is amplified and fed to a two-way power splitter. One output of the power splitter leads to the baseband mixer, while the other drives a power level detector. A meter connected to the detector output yields a continuous indication of the 10 MHz IF power level. The second mixer translates the 10 MHz IF signal to baseband. A 5 MHz frequency doubler and saturated amplifier supplies LO drive to the baseband mixer. Following the baseband mixer is a low-noise 26 dB gain amplifier which drives the three low-pass filters. These active low-pass filters were designed to exhibit 6-pole Chebyshev response with passband ripple of 0.1 dB. Corner frequencies of 22 Hz, 220 Hz and 2.2 kHz were chosen to prevent frequency aliasing

when using sampling bandwidths of 25 Hz, 250 Hz and 2.5 kHz, respectively. In-band power gain of each filter is inversely proportional to its bandwidth, making the output noise power independent of which sampling bandwidth and low-pass filter is selected. A set of remotely controlled relays couple the baseband signal through the output buffer and direct-current blocking capacitor to the module output. Since the three low-pass filters have different gains, module gain is a function of filter selection. The baseband module's gain is 71.6 dB with the 25 Hz filter, 61.6 dB with the 250 Hz filter, and 51.6 dB with the 2.5 kHz low-pass filter. The output level capability of this module is compatible with the ±10-volt input range of the signal A-D converter module.

### D. Signal and Noise A-D Converter Modules

The signal and noise A-D converter modules are very similar in design. Both modules use modular sample and hold amplifiers and 12-bit A-D converters. Differentially arranged transistor-transistor logic (TTL) drivers buffer the data and status lines, driving optocoupled receivers in the digital section of the PSPM equipment. Sampling pulses generated within the digital section are received by optocouplers in the two A-D modules. The sampling rate in the NAR channel is 500 samples/second. In the signal channel, Nyquist sampling rates of 50 Hz, 500 Hz and 5 kHz are used with their respective 25 Hz, 250 Hz and 2.5 kHz low-pass filters. The signal A-D converter is wired to accept input voltages of ±10 volts peak, with negative values coded in two's complement. The noise A-D converter is wired for unipolar operation, receiving its 0- to +10-volt input from the broadband square law detector. Contained within the signal A-D converter module is a peak-reading meter circuit. A meter connected to this detector allows the equipment operator to monitor the signal level at the input of the signal A-D converter.

## IV. Packaging

The PSPM technique of signal power measurement is based on the comparison of signal and noise powers in known bandwidths. To make accurate signal power measurements of weak signals it is essential to preserve the power spectrum of the received signal, and not corrupt the power spectrum by allowing stray RF leakage into the signal channel. Carrier power measurements are susceptible to RF leakage because the signal frequency is either 50 MHz or 55 MHz and is therefore harmonically related to most standard frequencies and timing signals distributed throughout the tracking station. Signal contaminants, along with the received signal, are amplified by the PSPM equipment's high gain which, at maximum, is approximately 136 dB.

The RF hardware is packaged in five modules which provide adequate isolation and shielding. Internal cavities are machined into the modules to accommodate individual circuit boards and RF components. Cover plates are secured on both sides of each module, ensuring an RF-tight enclosure. Three-terminal voltage regulators provide local power supply regulation within each module. Radio frequency decoupling of sensitive components is provided in the power supply lines by using inductance-capacitance (LC) filters as cavity wall feedthroughs. Optocouplers provide RF isolation from control and data lines entering the modules. Input and output signals are passed through coaxial connectors on the module front panels, while control lines, data lines and power supplies connect through multi-pin connectors on the rear of the RF modules. Figures 3 and 4 show the left and right sides of the baseband module with the covers removed. Similar construction techniques were used in the other four modules.

The five RF modules are housed in one rack-mounted cage. Engagement of the module connectors to mating connectors in the cage is automatic when the modules are inserted into the cage and secured in place by tightening two thumbscrews in each module's front panel. Figure 5 shows the RF cage (with the modules inserted) and the square law detector. The coaxial cables which interconnect the modules were removed for this photograph.

## V. Summary

The RF section shown in Figure 2 has been constructed and installed as part of the PSPM equipment at the Goldstone Mars Station, DSS 14. The PSPM equipment has been used to simultaneously measure system temperature and carrier power during actual spacecraft tracks, rendering data which were in close agreement with operationally observed values.

## References


1. Reid, M. S., Gardner, R. A., and Stelzried, C. T., *A New Broadband Square Law Detector*, Technical Report 32-1599. Jet Propulsion Laboratory, Pasadena, Calif., Sept. 1, 1975.
2. Constenla, L. C., "Precision Signal Power Measurement and Noise-Adding Radiometer System," in this issue.

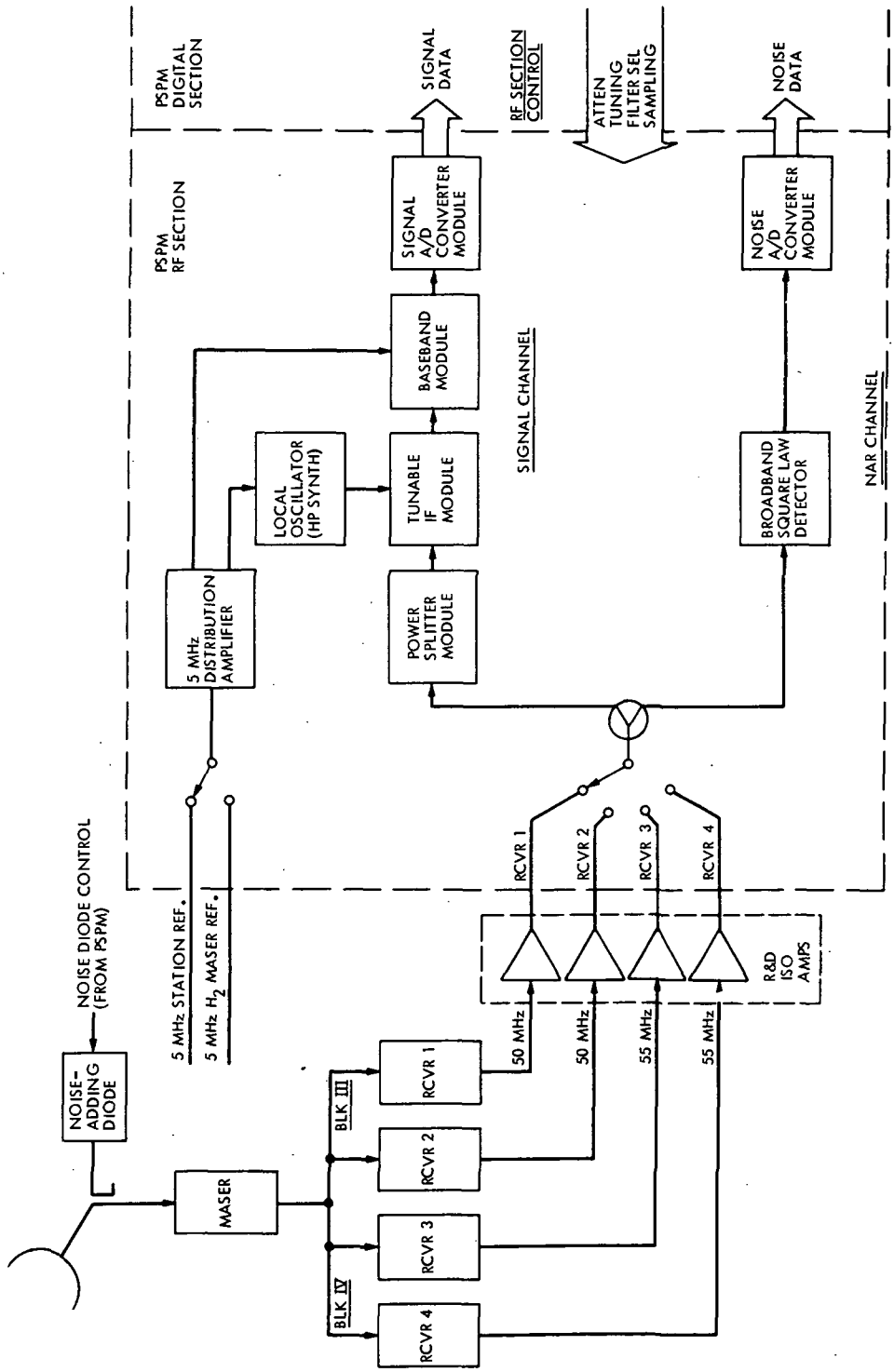


Fig. 1. PSPM equipment RF section, simplified block diagram

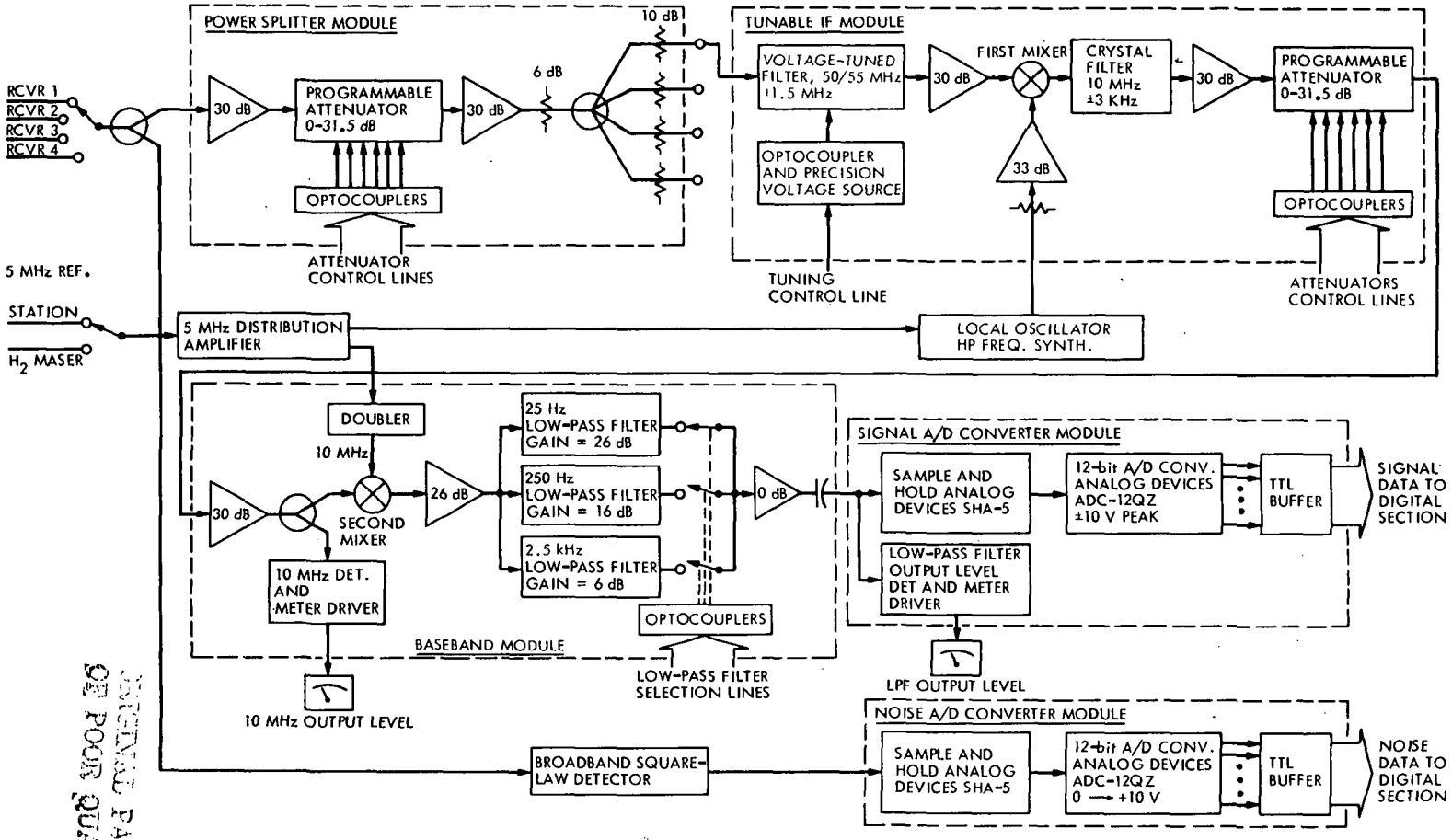


Fig. 2. PSPM equipment RF section, detail block diagram

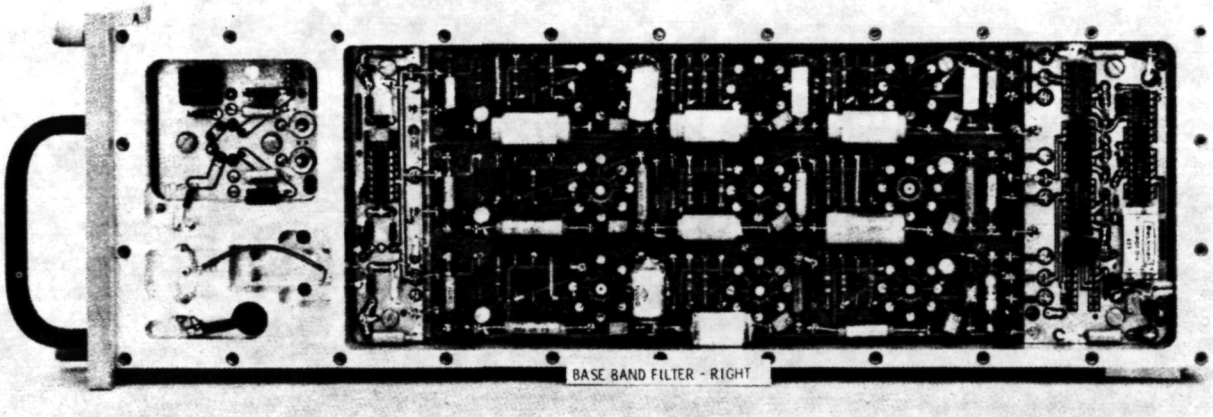


Fig. 3. Baseband module, right side

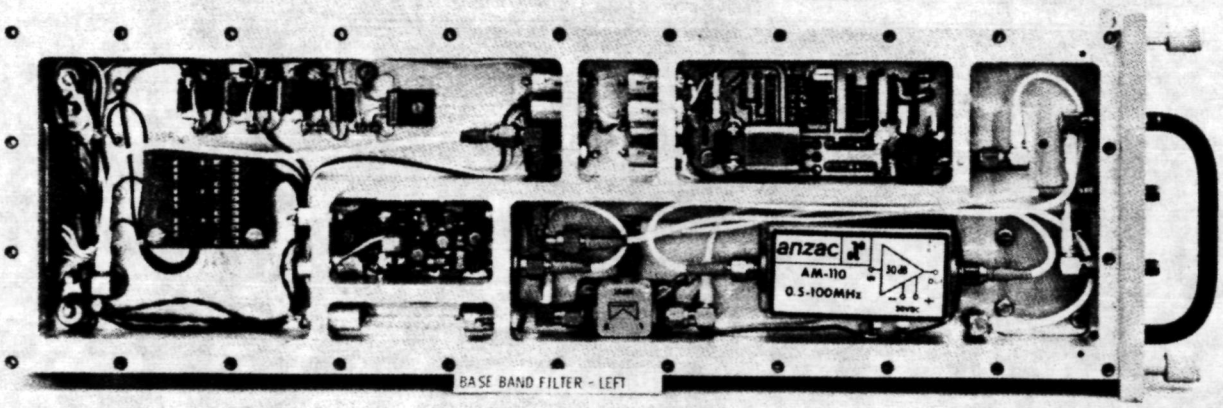


Fig. 4. Baseband module, left side

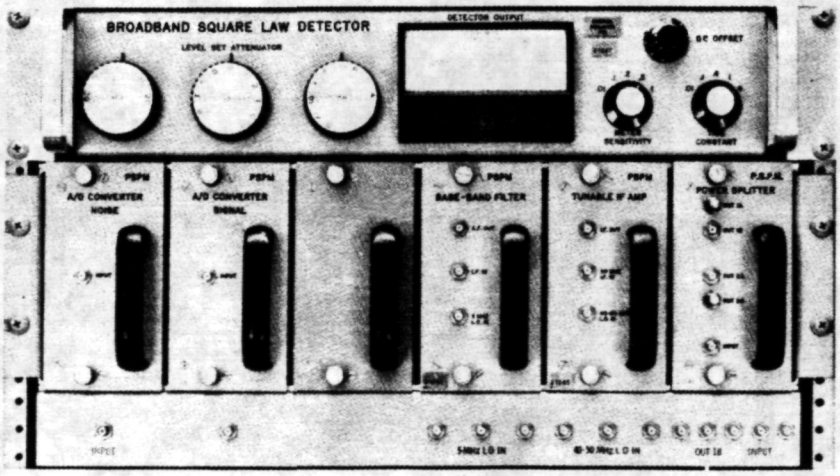


Fig. 5. Broadband square law detector and RF cage

# Foundation Analysis, Preliminary Investigation

H. McGinness and M. S. Katow
DSN Engineering Section

*The known solution of a semi-infinite plate with normal forces on its edge is compared to the computed results of an assembly of solid finite elements in Nastran.*

## I. Introduction

The azimuth bearing of large antennas is usually an annular runner for hydrostatic support pads or a circular track for support wheels. In either case the foundation for the bearing is a cylindrical concrete pedestal or footing which supports the whole weight of the antenna. During construction, the runner or track is positioned accurately a few centimeters above the foundation, and then the intervening space is packed with grout or other suitable stable substance. It is desirable to have good estimations for both the deflection of the bearing and for the maximum compressive stress in the supporting grout. Rigorous analyses of these quantities have been difficult in the past. Current general-purpose structural analysis programs, such as Nastran, have the capability of modeling the problem with an assembly of finite element plates.

In an attempt to ascertain the fineness of the grid point spacing required to give acceptable results, a relatively simple problem was modeled which has a known closed form solution. By comparing the results of a few models of different fineness to the exact solution, the fineness required to produce satisfactory results can be determined because this problem is intimately related to the real azimuth bearing configuration.

## II. The Related Simple Problem

The relatively simple problem is the determination of the deflection and stresses in a semi-infinite plate having a uniformly distributed pressure applied over a finite length of its edge. Since the pads or wheel groups of the real bearing are spaced far apart on a large radius, it is believed that the semi-infinite plate approximates the real problem insofar as vertical deflections are concerned. A discussion of the maximum grout stresses when a runner or track is interposed between the applied load and grout will appear in a subsequent report.

In Fig. 1 is shown the pressure loading $p$ on the semi-infinite plate. The origins of the spacial coordinates $Y$ and $R$ are the edge of the undeflected plate and the center of the loaded area, respectively. The vertical deflections $V$ of the edge of the plate parallel to coordinate $Y$ are derived by a coordinate transformation of the equations of Ref. 1, page 92, and are as follows:

$$V_c = \frac{2ap}{\pi E}[(1-\nu) + 2\ln\zeta - (1-\lambda)\ln(1-\lambda) - (1+\lambda)\ln(1+\lambda)], \quad \lambda \leq 1 \tag{1}$$

$$V_0 = \frac{2ap}{\pi E}[(1-\nu) + 2\ln\zeta + (\lambda-1)\ln(\lambda-1) - (\lambda+1)\ln(\lambda+1)], \quad \lambda \geq 1 \tag{2}$$

where

$V_c$ is the surface deflection under the loaded area of length $2a$

$V_0$ is the surface deflection outside the loaded area

$p$ is the applied uniform pressure load

$E$ is the modulus of elasticity of the semi-infinite plate

$\nu$ is Poisson's ratio

$\zeta = d/a$ where $d$ is the vertical distance beneath the center of the loaded area at which the deflection is assumed to be zero

$\lambda = R/a$, where $R$ is the horizontal coordinate

Equations (1) and (2) may be evaluated conveniently over a large range of $\lambda$ by the following single equation:

$$V = \frac{2ap}{\pi E}[(1-\nu) + 2\ln\zeta + f(\lambda)] \tag{3}$$

where the value of $f(\lambda)$ is given by the curve of Fig. 2. This curve represents the relative deflections of points on the edge of the plate.

The first and second derivatives of the vertical displacements are as follows:

$$\frac{dV_c}{dR} = \frac{2p}{\pi E}[\ln(1-\lambda) - \ln(1+\lambda)], \quad \lambda < 1 \tag{4}$$

$$\frac{d^2V_c}{dR^2} = \frac{2p}{\pi aE}\left[\frac{-2}{1-\lambda^2}\right], \quad \lambda < 1 \tag{5}$$

$$\frac{dV_0}{dR} = \frac{2p}{\pi E}[\ln(\lambda-1) - \ln(\lambda+1)], \quad \lambda > 1 \tag{6}$$

$$\frac{d^2V_0}{dR^2} = \frac{2p}{\pi aE}\left[\frac{2}{\lambda^2-1}\right], \quad \lambda > 1 \tag{7}$$

The horizontal displacements at the surface are:

$$U_c = -\frac{(1-\nu)}{E}pR, \quad R \leq a \tag{8}$$

$$U_0 = -\frac{(1-\nu)}{E}pa, \quad R \geq a \tag{9}$$

The principal stresses are derived from Ref. 1, pages 89–92. Figure 3 defines the two principal directions, namely, radial and tangential, The principal stresses at any point $P$ are:

$$\sigma_{radial} = \frac{-p}{\pi}(\alpha + \sin\alpha) \tag{10}$$

$$\sigma_{tangential} = \frac{-p}{\pi}(\alpha - \sin\alpha) \tag{11}$$

For points a distance $d$ beneath the center of the loaded area, the radial (vertical) principal stress is

$$\sigma_{radial} = \frac{-p}{\pi}\left[2\arctan\frac{a}{d} + \sin\left(2\arctan\frac{a}{d}\right)\right] \tag{12}$$

## III. Finite Element Model

The finite element model was built up of solid hexahedron isoparametric elements, each element having 12 straight edges and eight corners attached to grid points. A one-element-thick layered model, as shown in Fig. 4, was built up using a simple computing program to generate all of the necessary input data.

Symmetric plane constraints were generated for the centerline and one side of the plane of elements to simulate a plate. Ground constraints were attached to the bottom nodes (points of zero vertical deflections). An alternate solution used additional side constraints to simulate a two-dimensional problem.

Two mesh patterns were used. The finer mesh configuration used the finest mesh size $E$ equal to $a/4$. As the distance increased from the load point and the centerline, the element size for one dimension was increased along both the horizontal and vertical direction; that is, the

aspect ratio increased. The coarse mesh configuration started with $E$ equal to $a/2$.

The computed results are presented in dimensionless units. For the Y deflection along the top surface in Fig. 5, the constant in Eq. (3) was transposed and $V\pi E/2ap$ was plotted against the horizontal distance $R/a$. The exact solution using Eq. (3) is shown as the solid line, and the fine mesh model answers with one-sided constraints are shown by the dotted line.

Compressive stresses on the vertical centerline are compared in Fig. 6. The exact solution for stress calculation uses a model infinitely deep while the finite element model has a fixed depth of 14.5a. The stresses at the center of the hexahedron elements are compared to the exact solution on the centerline for the same depth.

## IV. Conclusions

1. The vertical deflections comparison along the horizontal line using the one-sided constraints in the finite element model shows an adequate match for practical use. With the alternate two-dimensional constraint use, the match was closer. Our second thoughts are that the alternate model is a closer simulation to the exact model, as the stresses are constant throughout the cross section for this model.

2. The compressive stress comparisons using the computed center stresses in the isoparametric hexahedron element show a good match of the results even though the finite element model must be cut off at a definite depth. The coarse mesh model has adequate accuracy.

## Reference

1. Timoshenko, *Theory of Elasticity*, 1st ed., p. 92, McGraw-Hill, New York, 1934.

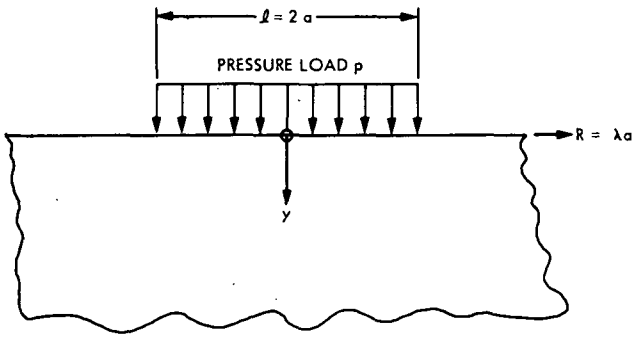


Fig. 1. Configuration of loading on semi-infinite plate

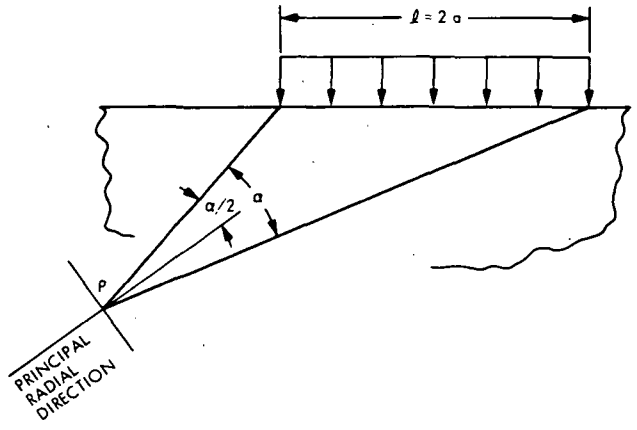


Fig. 3. Principal stress directions

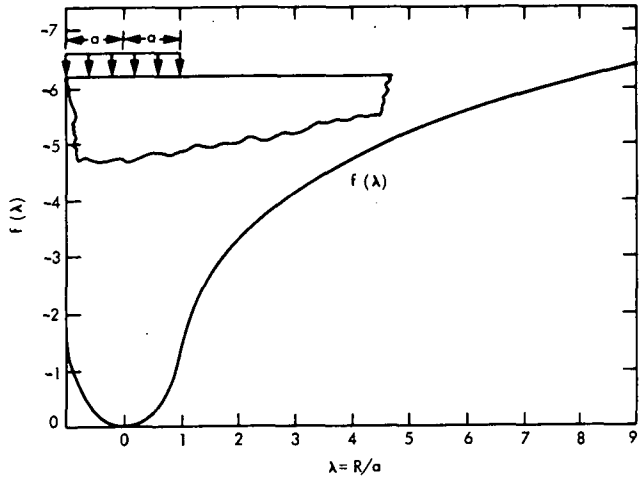


Fig. 2. Relative deflections of points on edge of plate

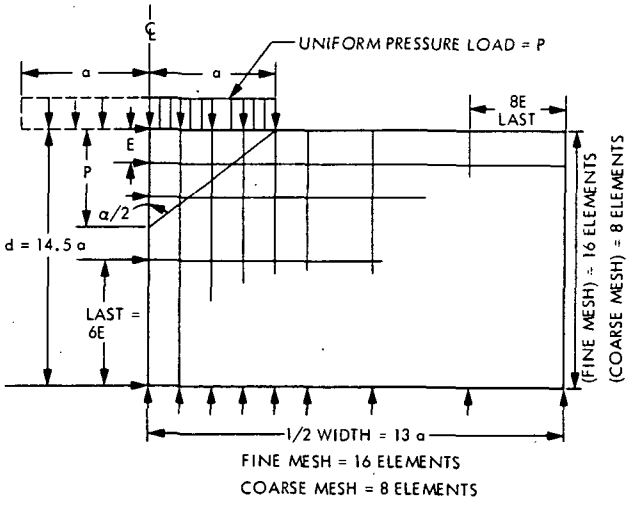


Fig. 4. Configuration of finite elements

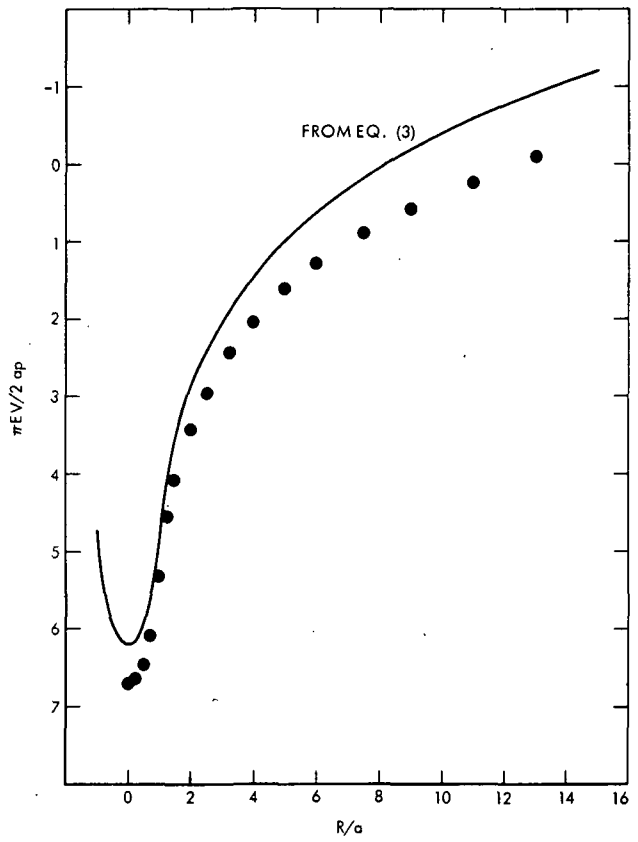


Fig. 5. Vertical deflections vs horizontal distance

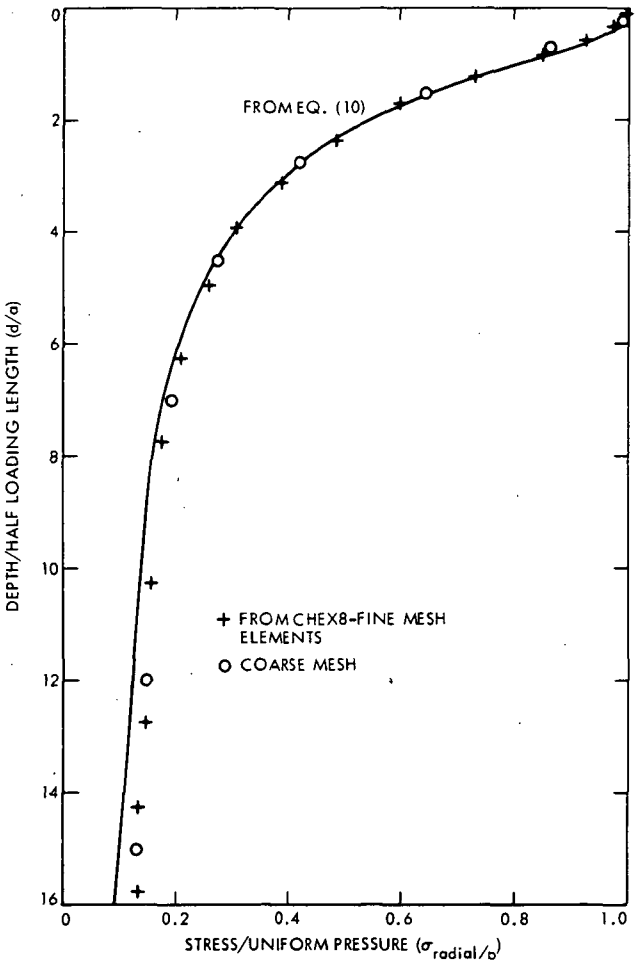


Fig. 6. Compressive stress at the vertical centerline

# Power Spectrum for Binary NRZ Data With Less Than 50% Transitions

B. K. Levitt
Communications Systems Research Section

*Spacecraft-to-ground telemetry received by the DSN can often be modelled as binary NRZ data with independent transitions of probability* p ≤ ½. *In this paper, a simple expression is derived for the power spectrum of this type of data modulation; this formula is used to investigate how rapidly the data bandwidth decreases as* p *gets smaller.*

## I. Introduction

The performance of a coherent communication link will be degraded by data modulation that falls within the carrier tracking loop bandwidth. Satellite telemetry links must operate under imposed bandwidth constraints. Crosstalk can occur when two adjacent data channels overlap in the frequency domain. With these considerations in mind, a space telecommunications designer is interested in determining the power spectra of his transmitted data.

For many deep space telemetry links supported by the DSN, the data modulation is in a binary NRZ format, and the data source suggests an independent transition model. When the transition rate is ½, it is well known (e.g., Ref. 1) that the data power spectrum is given by

$$S_d(f) = \frac{1}{R}\left[\frac{\sin(\pi f/R)}{\pi f/R}\right]^2 \tag{1}$$

where $R$ is the data rate. In this paper, a simple expression is derived for the data power spectrum when the transition rate is less than ½; this formula is then used to measure the data bandwidth dependence on the transition rate.

## II. Derivation of Data Power Spectrum

Consider the unit-amplitude, binary NRZ data stream $d(t)$, shown in Fig. 1. The data is assumed to be generated by a Markov source: data transitions occur independently, with stationary probability $p$. That is,

$$Pr[d_i = -d_{i-1}] = p, \forall_i. \tag{2}$$

As a preliminary step to computing the power spectrum of $d(t)$, we can calculate its autocorrelation function

$$R_d(\tau) \equiv \overline{d(t)\,d(t+\tau)} \tag{3}$$

It is easy to show that for $k/R \leq |\tau| \leq (k+1)/R$, $k = 0,1,2,\ldots$

$$R_d(\tau) = (1-2p)^k\,[(1+2kp) - 2p|\tau|R] \tag{4}$$

which yields the piecewise-linear function of Fig. 2. For example, using Fig. 3 for $1/R \leq |\tau| \leq 2/R$, it is evident that

$$R_d(\tau) = \left(\frac{\frac{2}{R} - |\tau|}{\frac{1}{R}}\right) \cancel{d_i d_{i+1}}^{(1-p)-p} + \left(\frac{|\tau| - \frac{1}{R}}{\frac{1}{R}}\right) \cancel{d_i d_{i+2}}^{(1-p)^2+p^2-2p(1-p)}$$

$$= (1-2p)\,[(1+2p) - 2p|\tau|R] \tag{5}$$

The data power spectrum $S_d(f)$ is simply the Fourier transform of $R_d(\tau)$. Using the construction diagram of Fig. 4, we can write

$$R_d(\tau) = \sum_{k=1}^{\infty} R_k(\tau) \quad \Updownarrow \quad S_d(f) = \sum_{k=1}^{\infty} S_k(f) \tag{6}$$

The parameters $a_k$ and $b_k \equiv a_{k-1} - a_k$ in Fig. 4 are specified by

$$a_k = (k+1)\,q^k - kq^{k+1}$$

$$b_k = kq^{k-1}(1-q)^2 \tag{7}$$

where

$$q \equiv 1 - 2p.$$

But $R_k(\tau)$ is the autocorrelation function of binary NRZ data with 50% transitions and data rate $R/k$; modifying Eq. (1), we have

$$S_k(f) = \frac{Rb_k}{k}\left[\frac{\sin(k\pi f/R)}{\pi f}\right]^2 = \frac{Rq^k(1-q)^2\,[1-\cos(2k\pi f/R)]}{2(\pi f)^2} \tag{8}$$

$$\therefore S_d(f) = \frac{R(1-q)^2}{2q(\pi f)^2}\left[\sum_{k=1}^{\infty} q^k - \sum_{k=1}^{\infty} q^k \cos(2k\pi f/R)\right] \tag{9}$$

where $\frac{q}{1-q}$ and $\frac{q(\cos 2\pi f/R - q)}{1 - 2q\cos 2\pi f/R + q^2}$ are the last summation is found in Ref. 2. Simplifying Eq. (9) yields the power spectrum formula[1]

$$S_d(f) = \frac{1}{R}\left[\frac{\sin(\pi f/R)}{\pi f/R}\right]^2 \times \left[\frac{1-(1-2p)^2}{1-2(1-2p)\cos(2\pi f/R) + (1-2p)^2}\right] \tag{10}$$

## III. Results

Normalized data power spectra are plotted in Fig. 5 for several transition rates $p \leq \frac{1}{2}$, using Eq. (10). As expected, the bandwidth narrows as $p$ decreases. The functional dependence of the one-sided bandwidth $BW$ on $p$ is illustrated in Fig. 6 for cases where 90% and 95% of the total data power lies in the frequency domain $(-BW, BW)$.

[1]Equation (10) agrees with a prior unpublished result obtained by M. K. Simon of JPL Section 339 following an entirely different approach based on Chapter 1 of Ref. 1.

## References


1. Lindsey, W. C., and Simon, M. K., *Telecommunication Systems Engineering*, Prentice-Hall, Inc., Englewood Cliffs, N. J., 1973, Eq. 1-21.
2. Gradshteyn, I. S., and Ryzhik, I. M., *Table of Integrals, Series, and Products*. Academic Press, New York, New York, 1965, p. 40.

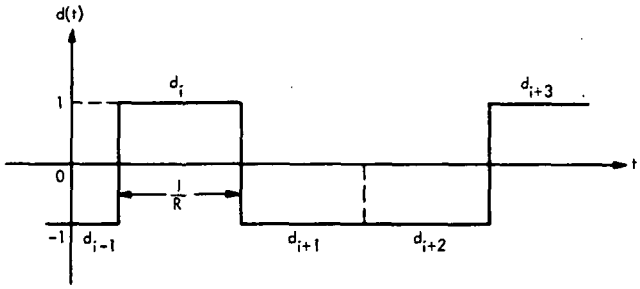


Fig. 1. Unit-amplitude, binary NRZ data

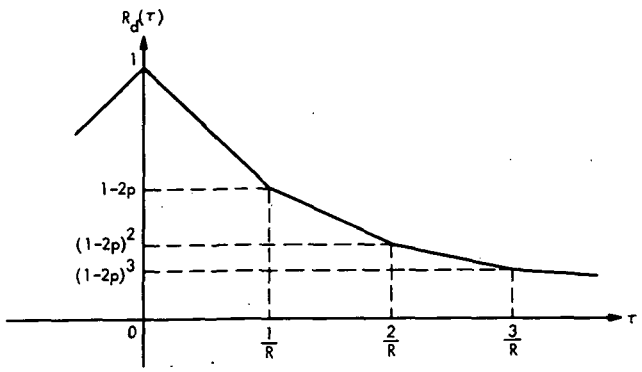


Fig. 2. Autocorrelation function of $d(t)$, with transition probability $p$

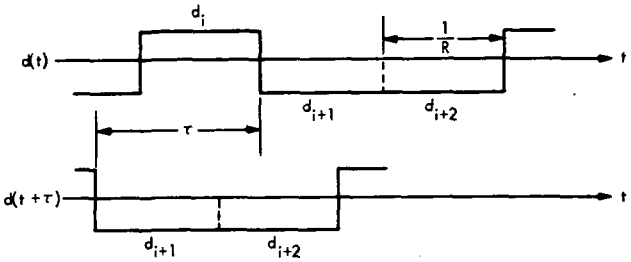


Fig. 3. Comparison of $d(t)$ and $d(t + \tau)$ for $1/R \leq \tau \leq 2/R$

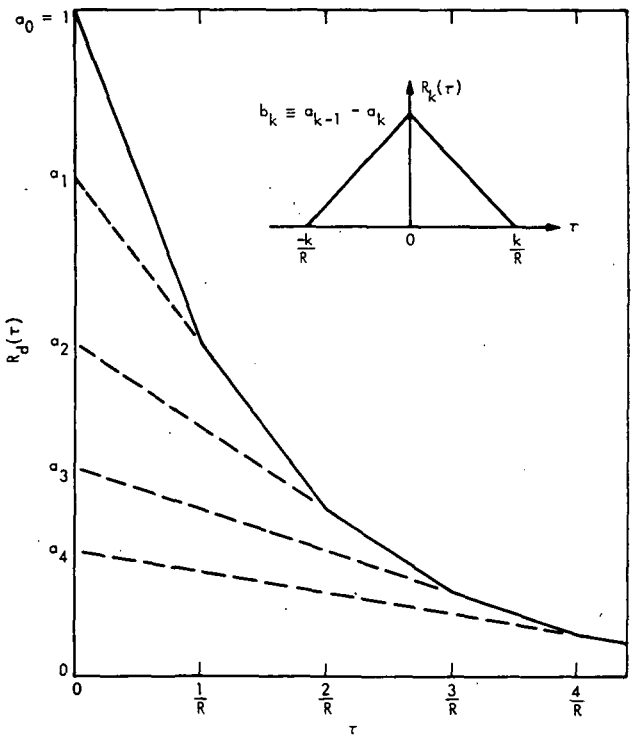


Fig. 4. Decomposition of $R_d(\tau)$ into $\sum_{k=1}^{\infty} R_k(\tau)$

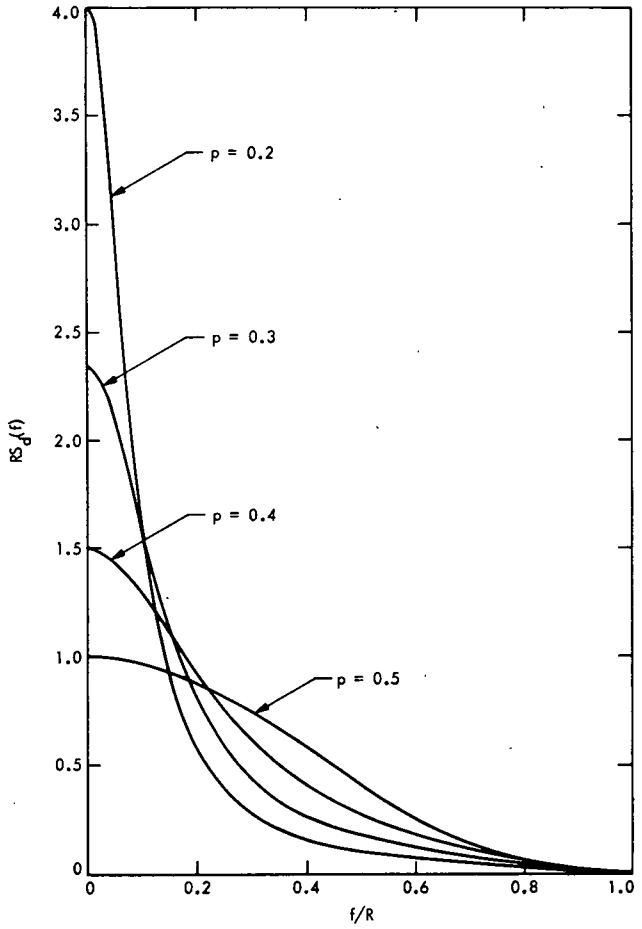


Fig. 5. Normalized power spectra of $d(t)$ vs transition probability $p \leq \frac{1}{2}$

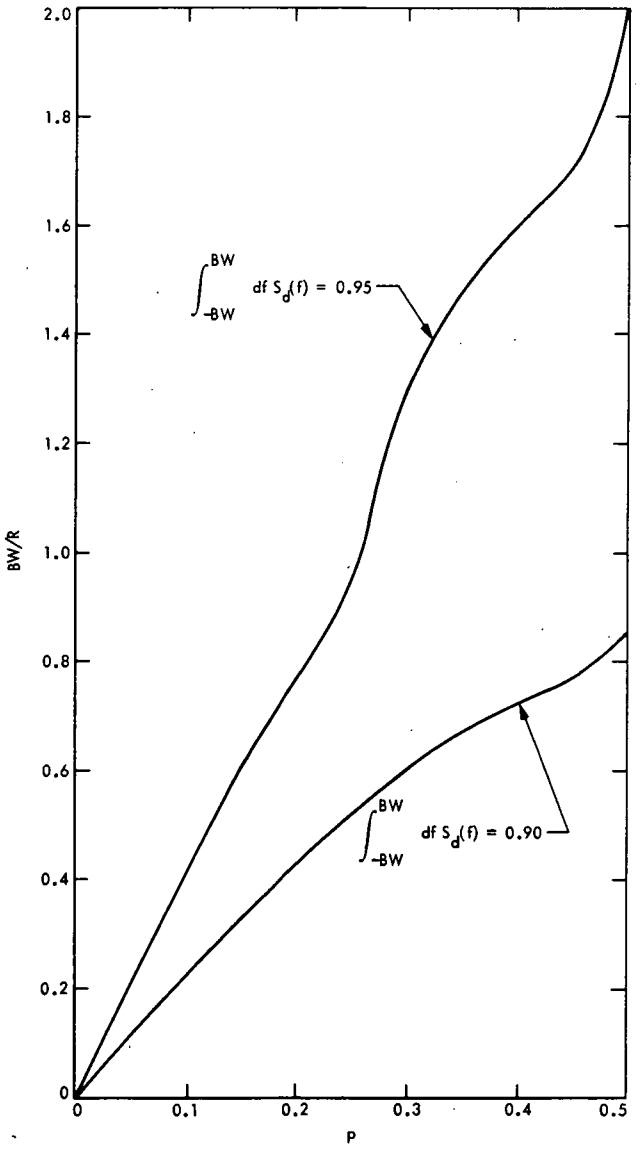


Fig. 6. Functional behavior of one-sided bandwidth $BW$ of $d(t)$ vs transition probability $p$, for 90% and 95% of total data power contained in $(-BW, BW)$

# Precision Signal Power Measurement and Noise-Adding Radiometer Equipment

L. C. Constenla
Communications Systems Research Section

*A new Precision Signal Power Measurement equipment incorporating a Noise-Adding Radiometer technique has been developed for precise measurement of spacecraft signal power returns. This equipment continuously measures the receiver system noise temperature, signal-to-noise ratio, and received signal power in real time during actual spacecraft tracking. The operation of this system requires that a precisely known amount of noise be switched on and off at the receiver input. This increase in noise is detected and used as a reference in the determination of the receiver system noise temperature. In turn, the system temperature is used to calculate the received signal power.*

*The Precision Signal Power Measurement equipment is presently installed in the Pedestal Room of the DSN 64-m-diameter antenna at the Mars Deep Space Station (DSS 14). The system was successfully tested during the Helios track on 2 October 1975, recording an averaged received carrier power of -140.6 dBm, which was in close agreement with the calibrated automatic gain control (AGC) method used by the station.*

## I. Introduction

A new single-rack stand-alone Precision Signal Power Measurement (PSPM) and Noise-Adding Radiometer (NAR) equipment was built and installed in the Pedestal Room at the Mars Deep Space Station. This system digitally measures the receiver system noise temperature, signal-to-noise ratio (SNR), and received signal power in real time during spacecraft tracking. The equipment is permanently connected through isolation amplifiers to the BLOCK III receivers 1 and 2, and BLOCK IV receivers 3 and 4, 50- and 55-MHz intermediate frequencies (IF), respectively. The NAR operation makes use of the existent noise diode boxes installed in the antenna S- and X-band feedcones.

The PSPM system is designed to be operated either locally as a stand-alone unit or remotely under control of a supervisory computer via a Network Operations Control

Center (NOCC) Standard Interface. Once in operation, all processing and control are done locally by a dedicated minicomputer that is part of the system.

The measured parameters are automatically displayed on a front panel read-out as well as printed on a teletypewriter (TTY) and/or sent to the supervisory computer for further processing and storage. The system is capable of measuring signal power levels between −125 and −190 dBm with an rms error less than 0.2 dBm for signals stronger than −175 dBm.

## II. PSPM and NAR Equipment

A simplified block diagram of the equipment used to implement the PSPM and NAR techniques is shown in Fig. 1. Any one of the four available receiver IF signal channels can be selected as input to the equipment. Table 1 shows the characteristics of these IF signal channels. The signal selected is then split into the NAR and PSPM sections of the equipment.

The NAR portion of the equipment uses a new Broadband Square Law Detector (Ref. 1) as a total-power radiometer detector. The analog voltage output of this device is sampled at a 500-Hz rate by an A-D converter and entered in the computer as data. The NAR scheme also requires that a constant amount of noise be added to the receiver input. This is accomplished by switching a reference noise diode source on and off under computer control as shown.

In the PSPM section of the equipment, the signal is first bandpassed by a 50/55-MHz tunable filter and then mixed down to 10-MHz IF and filtered again. A second mixer translates the IF signal to baseband, which is then fed into the low-pass filters.

A set of three 6-pole active low-pass Chebyshev filters with a 0.1-dB ripple in the passband and cutoff frequencies of 22, 220, and 2200 Hz is provided as anti-aliasing filters for the PSPM power spectrum operation. Its outputs are sampled at rates of 50, 500, and 5000 Hz, respectively, by the A-D converter and entered via direct memory access (DMA) in the computer as a table of data points. The first and second local oscillators (LO) and the sampling frequencies of both A-D converters are coherent with respect to the receiver reference frequency. A small CRT display unit connected to the computer is used as a monitor for the power spectrum operation. Further details of the radio frequency portion of the PSPM are given in Ref. 2.

## III. Principle of Operation

The Precision Signal Power Measurement technique is based on the determination of the SNR from a digitally computed narrow-band spectrum analysis of the received signal (Refs. 3, 4, 5, and 6). Since the computed SNR relates the strength of the signal to that of the noise at the input of the receiver, knowledge of the noise power entering the receiver is essential to calculate the signal power. Thus, concurrently with the spectrum analysis process, a Noise-Adding Radiometer process is used to measure the noise temperature of the receiver front end (Ref. 1). The signal power is then calculated from the combined results of these two asynchronous processes.

The Fast Fourier Transform (FFT) method is used to compute the power spectrum of the received signal from its digitally stored samples. Since the sampling process of the signal is coherent with the receiver reference frequency, the location of the signal within the spectrum is precisely known. Furthermore, the tracking action of the receiver causes the signal to appear stationary in frequency.

After accumulating the power spectra of the sampled data for a predetermined amount of time, the computer proceeds to normalize the resulting power spectrum. The principal requirement for the SNR calculation is that the noise be equally distributed throughout the resulting power spectrum, except for the low and high end roll-off regions. The SNR is determined by summing the individual spectral power points in two equivalent regions of the spectrum with one of the regions containing the additional signal power contribution. The detail analysis of the PSPM technique is presented in Ref. 4.

The system temperature is calculated from voltage samples taken from the Broadband Square Law Detector output that is part of the NAR equipment. The detector output voltage $V$ is proportional to the system noise temperature $T_{op}$ as given by

$$V = GKT_{op}$$

where $G$ is the system gain, and $K$ is a scaling factor. The operation begins by turning the noise reference source on and accumulating sample readings for a predetermined period of time. With the noise reference source off, an equal number of readings are taken, and a ratio of output powers ($Y$ factors) is calculated:

$$Y = GK(T_{op} + T_N)/GK(T_{op})$$

where $T_N$ is the equivalent noise temperature of the noise reference diode. The Y factor operation is repeated a given number of times and an average value $\overline{Y}$ is computed. Thus, solving for $T_{op}$

$$T_{op} = T_N/(\overline{Y} - 1)$$

where $T_N$ is a known constant value, typically around 0.5 K. The noise reference source is measured off-line before tracking, and its value is entered in the computer as an equivalent noise temperature.

## IV. Hardware Configuration

A detailed block diagram of the PSPM and NAR equipment hardware configuration is shown in Fig. 2. This diagram shows the interrelation between the PSPM and NAR hardware and the dedicated minicomputer as well as the optional remote control function provided by the supervisory computer.

The final PSPM and NAR implementation was influenced by the on-going effort on the part of JPL to automate the DSN stations. To this effect the equipment was designed to use the recently adopted NOCC Standard Interface to communicate with the station supervisory computer. A second NOCC Standard Interface link between the PSPM and NAR hardware and the dedicated minicomputer is provided for greater system integration flexibility.

The PSPM and NAR hardware uses a PSPM-NAR digital controller to communicate with the dedicated minicomputer via a Standard Interface Adapter (SIA) port. The function of the digital controller is to decode the commands and data sent by the control computer and direct the information to the RF and A-D converters, PSPM control and display front panel, and CRT display unit. Another function of this controller is to send device status, PSPM and NAR data to the control computer.

A Lockheed Electronics Company MAC-16 minicomputer (Ref. 7), modified to include a two-port SIA digital controller, is used as the control computer. This built-in controller connects the two SIA ports to the minicomputer DMA channel, programmed data channel (PDC), and interrupt system. In addition, several of the minicomputer front panel control switches are connected to the SIA port that communicates with the supervisory computer. This provides for complete remote operation of the MAC-16 computer by the supervisory station control computer.

DSN station time is brought into the control computer by means of a NASA 36-bit 1-s time code translator built as part of the digital controller. An ASR 33 teletypewriter is used by the operator to communicate with the PSPM and NAR real-time program.

Any computer having an SIA port, sufficient memory, and one magnetic tape transport can be used as a supervisory computer. Presently, the Pedestal Room XDS 930 computer connected to a 900-series SIA (Ref. 8) is being used as the supervisory computer.

Figure 3 shows the picture of the PSPM and NAR equipment rack. From the picture, some of the main components can be readily identified. At the top of the rack there is a chassis containing all the power supplies used to power the digital controller cage and RF cage. Below is the MAC-16 minicomputer power supply. The Broadband Square Law Detector is used by the NAR equipment for the determination of the system temperature. The RF cage contains the RF and A-D converter modules for the PSPM operation and the A-D converter module for the NAR operation.

The PSPM-NAR digital controller cage contains all necessary controls for the RF cage equipment, digital controller front panel display and control switches, and CRT display unit. Also, the digital controller cage contains the SIA port to communicate with the dedicated MAC-16 minicomputer. The CRT display unit is used as a monitor for the real-time logarithmic display of the calculated received signal power spectra.

The MAC-16 minicomputer is a 16-bit parallel processor with 8000 words of core memory, and 16 levels of interrupt. This minicomputer is used for PSPM-NAR hardware control and PSPM and NAR calculations, as was explained above. A Hewlett-Packard 5100A frequency synthesizer is used as the PSPM equipment first local oscillator. At the bottom of the rack there is the receiver selection patch panel and the rack ac power panel.

## V. System Software

The Precision Signal Power Measurement and Noise-Adding Radiometer system software is a real-time program written in MAC-16 LEAP 8 (Ref. 9) assembly language. The entire program, consisting of a main control program, the PSPM and NAR subprograms, and all the working tables, is contained in 8000 words of core memory. Double and triple precision fixed-point math routines were either created or modified to maximize the program speed.

During the system design phase, careful attention was given to the hardware-software interaction to achieve an optimum balance. To this effect, many of the control functions were implemented in hardware, including all the data multiplexing and the entire SIA control function.

## VI. Test Results

The PSPM and NAR equipment was tested for the first time during the Helios track on 2 October 1975. For this experiment a measured 0.46-kelvin equivalent noise temperature reference diode was used to calculate the system temperature. The noise diode reference was switched on and off by the equipment at two-second intervals. Every four seconds, a new $Y$ factor ratio was obtained, and these ratios averaged for a period of five minutes. The NAR operation then calculated the average system temperature for that five-minute interval.

Measurements of the received signal power were completed every 3.5 minutes from the combined results of the SNR and system temperature. Figure 4 shows a two-hour plot of the measured receiver system temperature. The decrease in average system temperature results from an increasing antenna elevation angle. The standard deviation, $\sigma_T$, computed from a cubic approximation obtained by a least square regression, is 0.168 K, which is equivalent to 0.029 dBm.

The received signal power estimates calculated by the PSPM using a 250-Hz sampling bandwidth and filter is shown in Fig. 5. The standard deviation, $\sigma_P$, is 0.064 dBm. The averaged received power remains constant at -140.6 dBm, which was expected from the Helios spacecraft.

## VII. Conclusion

An automatic real-time PSPM and NAR equipment is presently installed in the Pedestal Room at DSS 14. The equipment is capable of measuring the receiver-system temperature to a resolution of a few millikelvins and the received signal power from -125 dBm to below receiver detection threshold with a standard deviation of $< 0.2$ dBm. Initial tests have demonstrated that the system is very accurate, requiring no calibration except for the precise off-line measurement of the noise source diode used as a reference. The equipment built for research, development, and demonstration can be easily interfaced to the station equipment via an SIA.

## References


1. Reid, M. S., Gardner, R. A., and Stelzried, C. T., *A New Broadband Square Law Detector*, Technical Report 32-1599, Jet Propulsion Laboratory, Pasadena, Calif., Sept. 1, 1975

2. Stevens, G., "Precision Signal Power Measurement Equipment—Radio Frequency Section," in this issue.

3. Newton, J. W., "Precise Measurement of Spacecraft Signal Power," in *The Deep Space Network*, Space Programs Summary 37-58, Vol. II, pp. 42-50, Jet Propulsion Laboratory, Pasadena, Calif., July 31, 1969.

4. Winkelstein, R., "Precision Signal Power Measurement," in *JPL Quarterly Technical Review*, Vol. 2, No. 2, pp. 18-24, Jet Propulsion Laboratory, Pasadena, Calif., July 1972.

5. Emerson, R. F., "Precision Signal Power Measurement System Using Central Computing," in *The Deep Space Network*, Technical Report 32-1526, Vol. XV, pp. 116-127, Jet Propulsion Laboratory, Pasadena, Calif., June 15, 1973.

6. Newton, J. W., "Precise Measurement of Spacecraft Signal Power," in *The Deep Space Network*, Technical Report 32-1526, Vol. XVII, pp. 104-107, Jet Propulsion Laboratory, Pasadena, Calif., Oct. 15, 1973.

7. *MAC-16 Computer Reference Manual*, Lockheed Electronics Company, Los Angeles, Calif., Dec. 1971.

8. Lushbaugh, W., "An NCS Standard Interface for the XDS 900 Series Computers," in *The Deep Space Network Progress Report 42-26*, pp. 168–174, Jet Propulsion Laboratory, Pasadena, Calif., Apr. 15, 1975.

9. *MAC-16 Leap Assembler Manual*, Lockheed Electronics Company, Los Angeles, Calif., Dec. 1970.

**Table 1. Receiver IF channel characteristics**

| | |
|---|---|
| **Block III receivers (S-band)** | |
| IF | 50 MHz |
| BW | $\approx$ 10 MHz @ −3 dB |
| $P_N$ | $\approx$ −30 dBm for $T_{op}$ = 20 K |
| **Block IV receivers (S, X-band)** | |
| IF | 55 MHz |
| BW | $\approx$ 36 MHz @ −3 dB |
| $P_N$ | $\approx$ −35 dBm for $T_{op}$ = 20 K |

NOTE: $P_N$ = available noise power at power splitter input
$T_{op}$ = system noise temperature

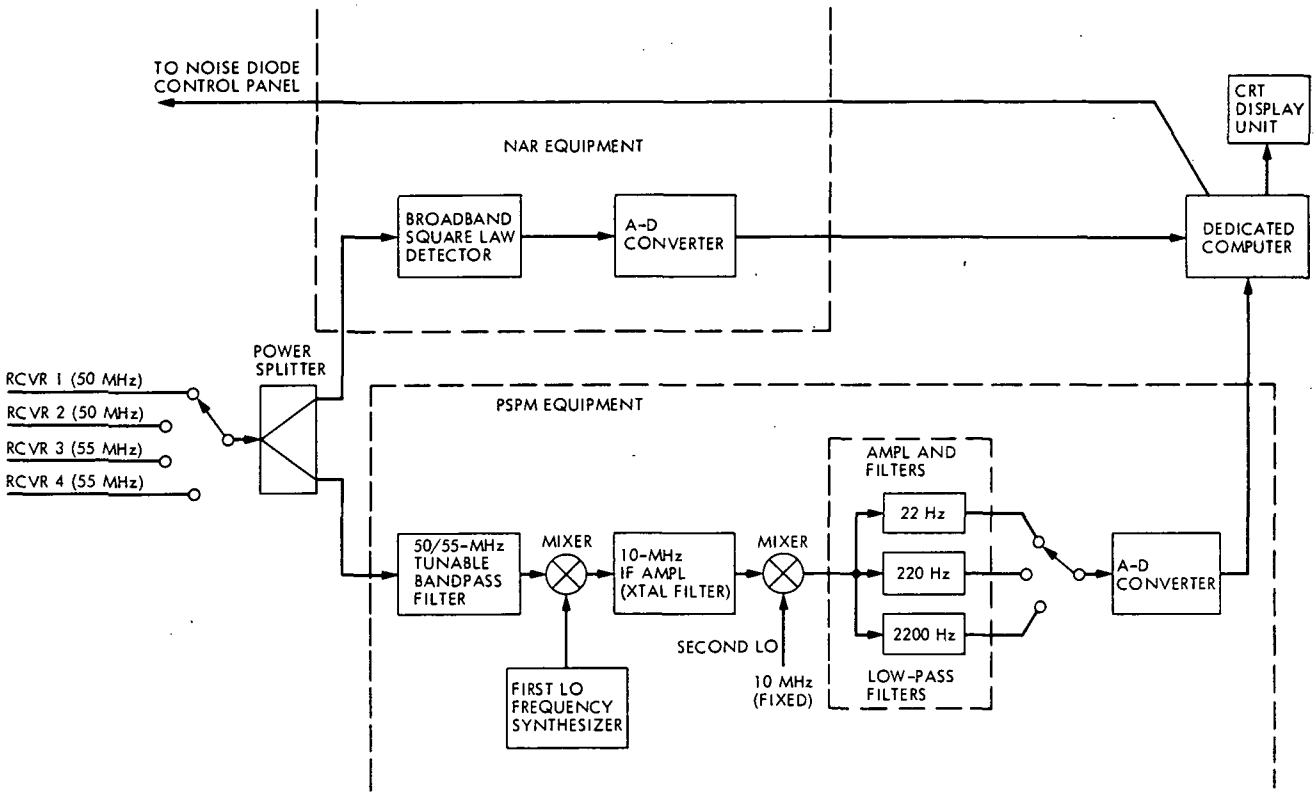


**Fig. 1. PSPM and NAR system block diagram**

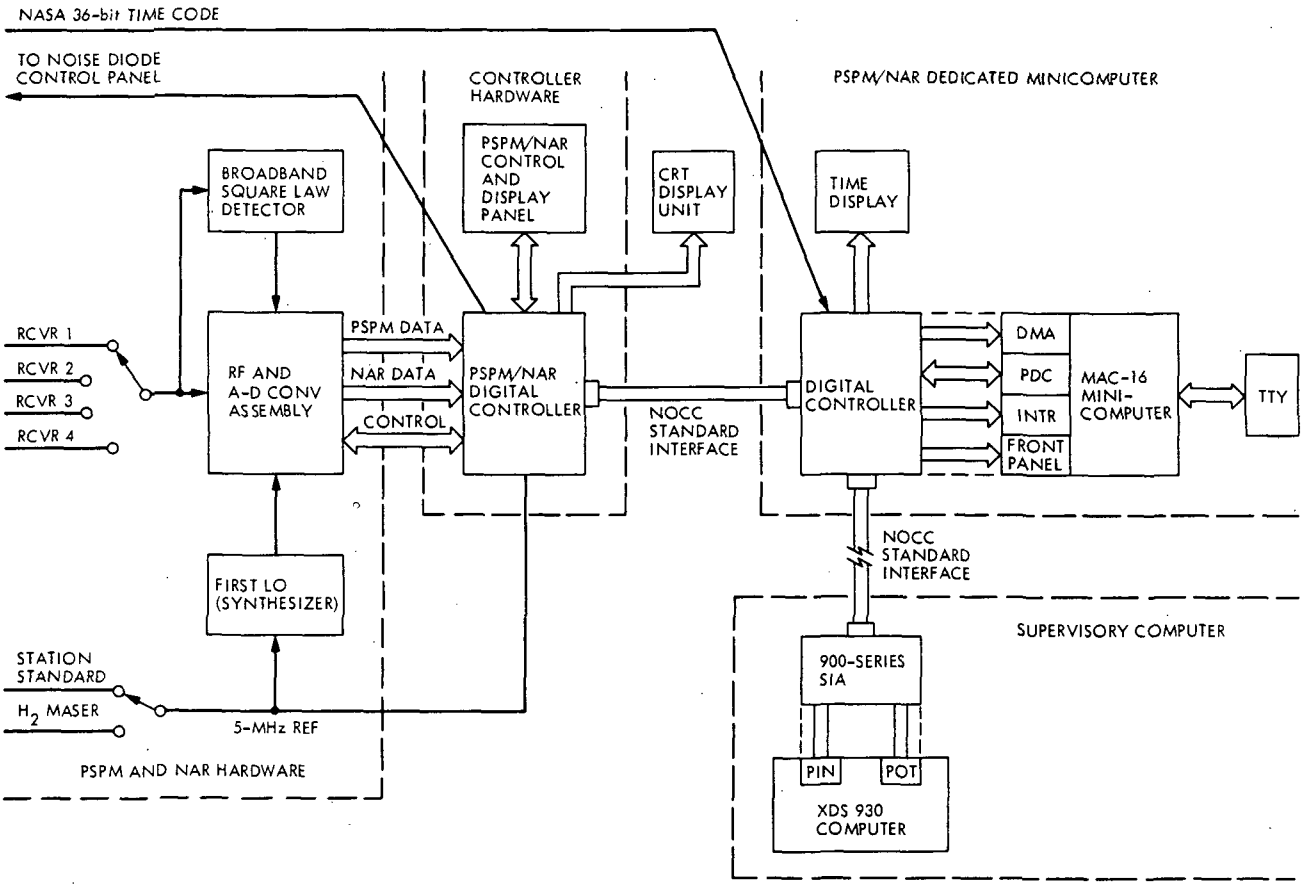


**Fig. 2. PSPM and NAR hardware configuration block diagram**

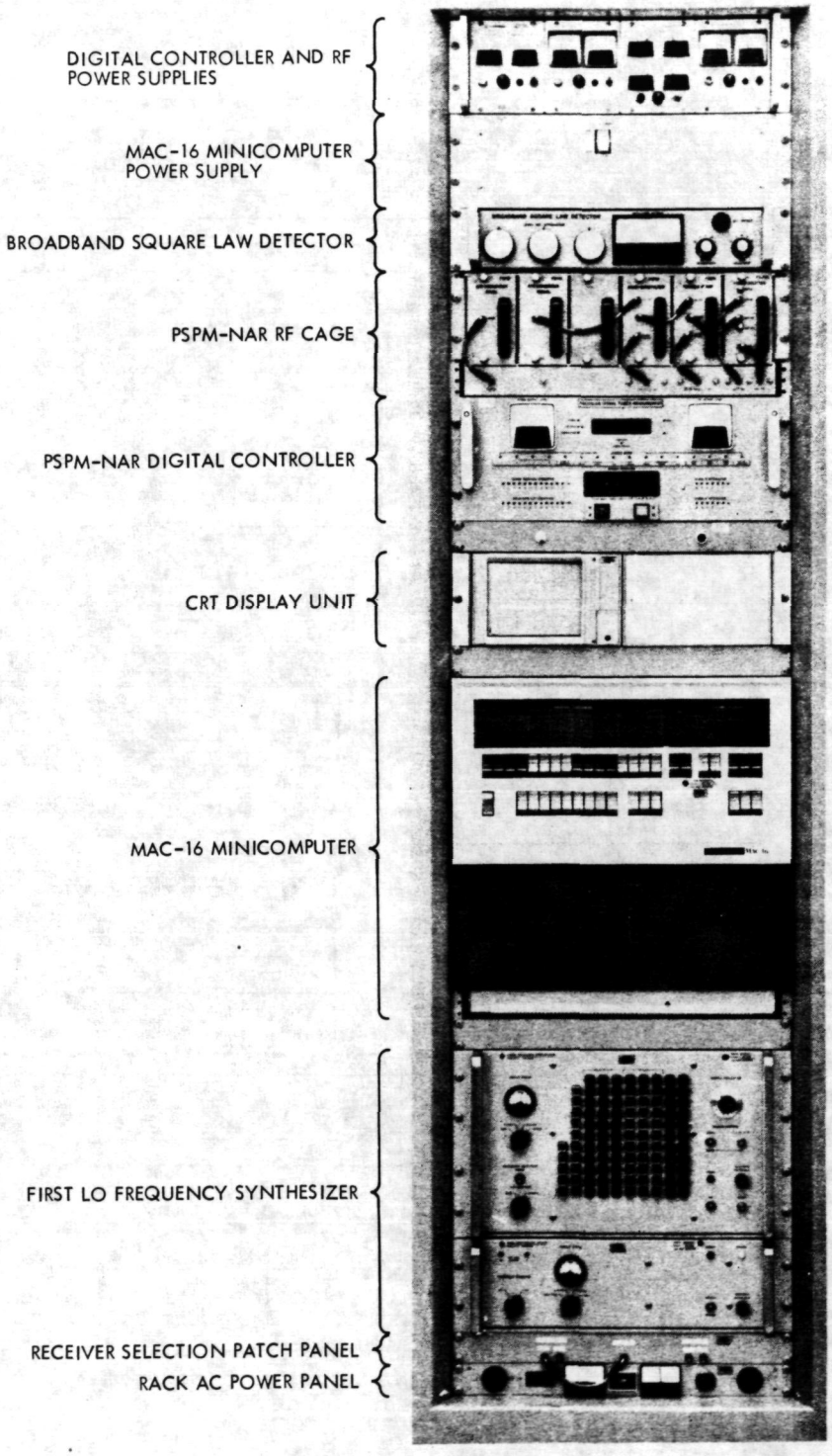


Fig. 3. PSPM and NAR equipment rack

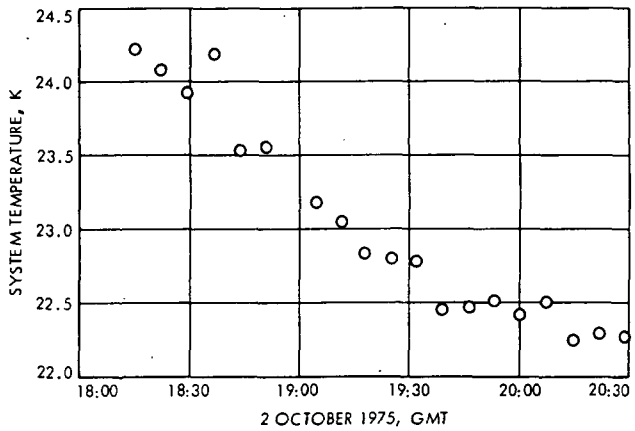


Fig. 4. System temperature measurement

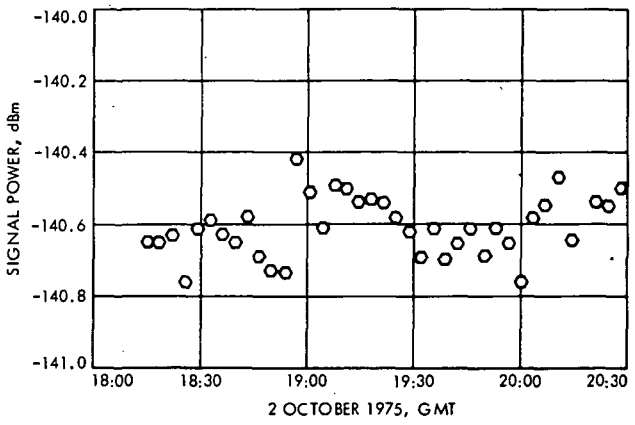


Fig. 5. Received signal power measurement

# Digital Demodulation With a Non-Ideal Quantizer

J. W. Layland
Communications Systems Research Section

*The use of digital demodulation techniques, or the conversion from analog to digital signal domains before data are demodulated from a radio frequency (RF) carrier, has become increasingly more feasible in recent years as logic circuit speeds have increased. This feasibility has been demonstrated by use in the Dual-Channel (Mu-II) Sequential Ranging System. Further use is contemplated in the telemetry stream, or integrated into the phase-tracking receiver. This article reviews some of the properties which must be considered in the analog-to-digital (A-D) converter to be used in these applications. In particular, the loss to be expected with an A-D unit built from current circuitry is calculated.*

## I. Introduction

The use of digital demodulation techniques, or the conversion from analog to digital signal domains before data are demodulated from an RF carrier, has become increasingly more feasible in recent years as logic circuit speeds have increased. This feasibility has been demonstrated by use in the Dual-Channel (Mu-II) Sequential Ranging System (Refs. 1 and 2). Further use is contemplated in the telemetry stream, or integrated into the phase-tracking receiver. This article reviews some of the properties which must be considered in the A-D converter to be used in these applications. In particular, the loss to be expected with an A-D unit built from current circuitry is calculated.

## II. Quantizer Design Considerations

Analog-to-digital converters for digital demodulation must be fast enough to respond to signals at a reasonable intermediate frequency (IF), say, 10 MHz, and precise enough that a tolerably small degradation is introduced. The speed requirement implies that conversion is performed "in parallel" instead of serially by successive approximation. This in turn imposes a constraint on the precision of the quantizer since a quantizer with $b$-bits of precision resolves a signal into $2^b$ separate levels and requires $2^b - 1$ threshold elements. Quantizers with 3 to 4 bits seem relatively uncomplex. Quantizers with 6 or more bits, over half a hundred threshold elements, seem complex enough to be impractical. Fortunately, as

calculations to be displayed later show, a 4-bit quantizer appears adequate for this application.

The signal to be quantized consists of Gaussian noise, white over the band of interest, together with a sinusoidal signal. This sinusoid in turn is phase modulated by a square-wave signal, either containing data, a data subcarrier, or a range code. The phase angle of modulation may be rather large, near $\pi/2$, for a data signal, or exceedingly small, less than 0.1 radian, for a ranging code. The sampling of this signal is performed in phase synchronism with this carrier frequency, and at a rate equal to four times that frequency. The phase of the sampling clock is controlled so that the (unmodulated) carrier component of the signal is sampled at its zero-crossings and peaks. Samples at the carrier zero-crossings correspond directly to the modulation which is in quadrature to that carrier. Alternatively, one could leave the phase of the samples and carrier random, and reconstruct the modulation by appropriate weighting of all samples, as was done in the Mu-II Ranging System. We assume that the bandwidth of the noise is wide enough that each sample of that additive noise is independent. This assumption considerably simplifies quantizer analysis.

## III. Quantizer Behavior

An ideal quantizer is a memoryless nonlinear device which is subject to straightforward calculation of input-output relationships. The threshold elements which make up a real quantizer are not memoryless but exhibit hysteresis, i.e., the output will not change state from "above" to "below" until the input has dropped to some specific non-zero level $-\delta$ *below* the threshold, and will not change state from "below" to "above" until the input has climbed to $+\delta$ *above* the threshold. Furthermore, this means that the input could be initially above the threshold, and then drop to slightly below the nominal threshold, but not $-\delta$ below that threshold, and yet continually indicate "above." This is a complicating feature for the calculation of the quantizer input-output characteristic, since if the quantizer input is within $\pm\delta$ of a threshold, the quantizer output depends upon what that output was previously. Assuming that the noise is independent from sample-to-sample, and that the input signal has a short period (4 here) makes the problem tractable for computer solution. For a $b$-bit quantizer, we calculate $2^{2b} - 1$ probabilities for each of the four samples, which correspond to the probability that a sample falls solidly within one of the $2^b$ output levels, or in the hysteresis gap within $\pm\delta$ of the $2^b - 1$ thresholds. Whenever a sample is in a hysteresis gap, the output can be associated to the output level either above or below that threshold, depending upon quantizer output for the previous sample. The probability distribution of the previous sample in turn depends upon the sample previous to it, and so on, until the cycle closes at the period of the input wave, and the calculation can be completed.

Subjectively, a quantizer with hysteresis, given an input of a small amplitude sine wave plus larger-power Gaussian noise, produces an output whose expected value is a phase-shifted sine wave. The amount of phase shift depends upon the width of the hysteresis gap, $\delta$, and upon the relative phase of the sine wave and sampling clock, as is shown in Fig. 1 for total input power equal to 5 (quantizer-steps-squared), and input SNR ($\rho$) of 1 and 5 dB. Figure 1a for $\rho = 1$ seems representative of low SNR behavior where the noise effectively "dithers" the signal through several quantization steps. Figure 1b only hints at the erratic behavior which appears as the SNR before quantization increases to the point where the additive noise is insufficient to smooth the step between quantization levels.

## IV. Calculated Performance

The loss in signal-to-noise ratio for demodulated data extracted from a sine wave carrier in noise has been calculated and is displayed below for a quantizer of the type used in the Mu-II Ranging System (Refs. 1 and 2). This quantizer is a 4-bit, 15-level device with outputs from -7 to +7. A zero input corresponds to mid-range on the zero-output level, and numerical output values "make sense" as an approximation to the input voltage. The stepsize between thresholds is 100 mV, and the hysteresis bias $\delta$ is specified by the manufacturer as 10 mV maximum for the threshold elements used. The quantizer is preceded by an automatic gain-control amplifier which maintains total signal-plus-noise power constant. Since signal-to-noise ratio is small in the unprocessed samples, this device seems to be a valid approximation to the optimum linear quantizer for decoding (see, e.g., Ref. 3). Figure 2 shows the detected signal SNR loss in dB as a function of sample SNR for various values of total input power for modulation angles of 0.3 radians (Fig. 2a) and 1.5 radians (Fig. 2b) and no hysteresis. Input "power" in this case is actually mean-square input signal level, defined relative to output level number, and represents $\sigma_n^2 + A^2/2$, where $A$ is sine-wave amplitude. A low data rate is assumed so that the quantizer is essentially in steady-state.

Figure 3 shows detected signal SNR loss in dB for modulation angles of 0.3 radians (Fig. 3a) and 1.5 radians (Fig. 3b) and hysteresis $\delta$ of 0.1, corresponding directly to

worst-case component values for the Mu-II quantizer. In both Figs. 2 and 3, degradation can be held to less than 0.1 dB over most of the range for power levels in the neighborhood of 5. Hysteresis effects, the motivator for the study described here, seem to contribute at most a few hundredths of a dB degradation in excess of an ideal quantizer at low SNR, and perhaps 0.2 dB at high SNR. The increasing degradation at higher SNRs can be rationalized in that such levels would seldom, if ever, be encountered in the DSN. For example, we could expect a −5-dB predetection SNR for a $10^6$-bit/s data stream at $10^{-5}$-bit error rate. Higher SNRs could be expected only with higher data rates and correspondingly stronger signals.

Figure 4a-e shows the effect of varying the hysteresis gap width on quantizer loss for several values of modulation angle, and a fixed power level of 5. For low predetection SNR, the effect is relatively insensitive to modulation angle. For hysteresis gap widths up to that encountered in practice, the quantizer degradation remains below 0.1 dB throughout the expected operating range. However, rapid deterioration appears with larger hysteresis gap widths.

## V. Conclusions

Digital demodulation of spacecraft radio signals appears viable. No serious distortion problem is evident, and quantizers can be fabricated with existing components which degrade the subsequently detected signal by less than 0.1 dB over the expected operating ranges. Furthermore, it should be noted that a single quantizer used in the receiver replaces several nonlinear analog components which can induce distortion in the current receiver-demodulator implementation.

## References


1. Martin, W. L., "System Performance of the Dual-Channel Mu-II Sequential Ranging," in *The Deep Space Network Progress Report 42-26*, pp. 54–68, Jet Propulsion Laboratory, Pasadena, Calif., Apr. 15, 1975.
2. Martin, W. L., and Zygielbaum, A. I., *Mu-II Ranging*, Technical Memorandum 33-768, Jet Propulsion Laboratory, Pasadena, Calif. (to be published).
3. Wax, J., "Quantizing for Minimum Distortion, *IRE Trans. Info. Theory*, Vol. IT-6, pp. 7–12, March 1960.

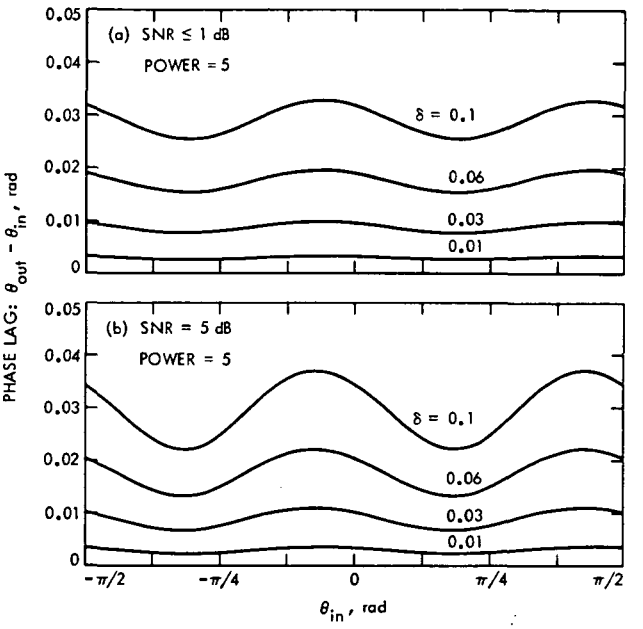


Fig. 1. Phase lag of quantizer with hysteresis as a function of sample phase for several hysteresis gap sizes

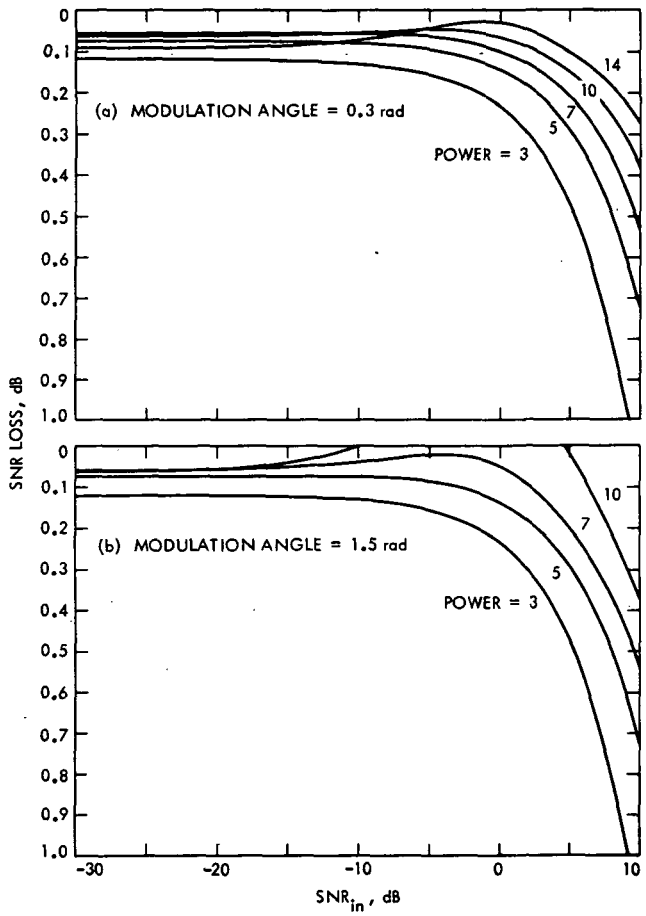


Fig. 2. Quantizer degradation vs input SNR for several input power levels, no hysteresis

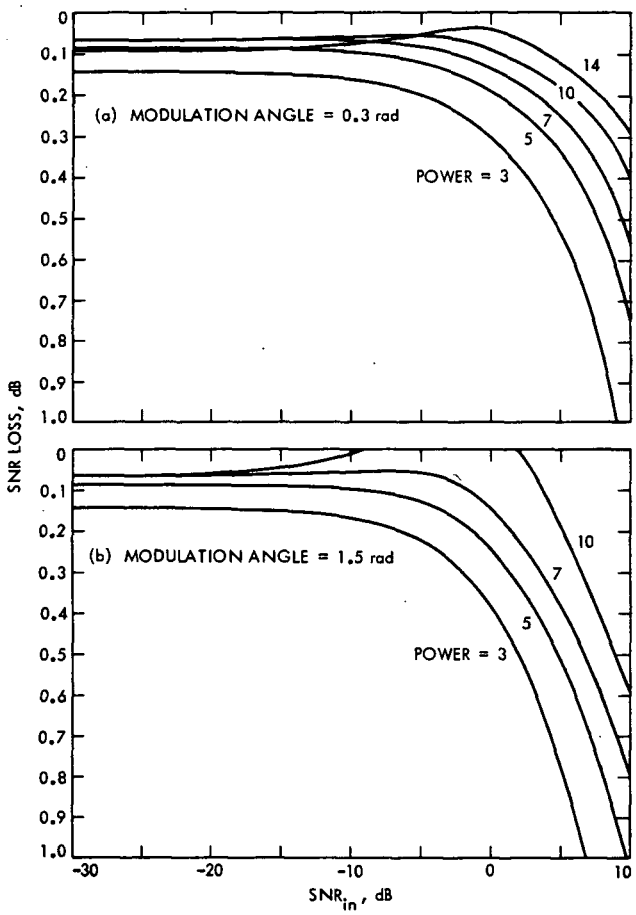


Fig. 3. Quantizer degradation vs input SNR for several input power levels, hysteresis gap = 0.1

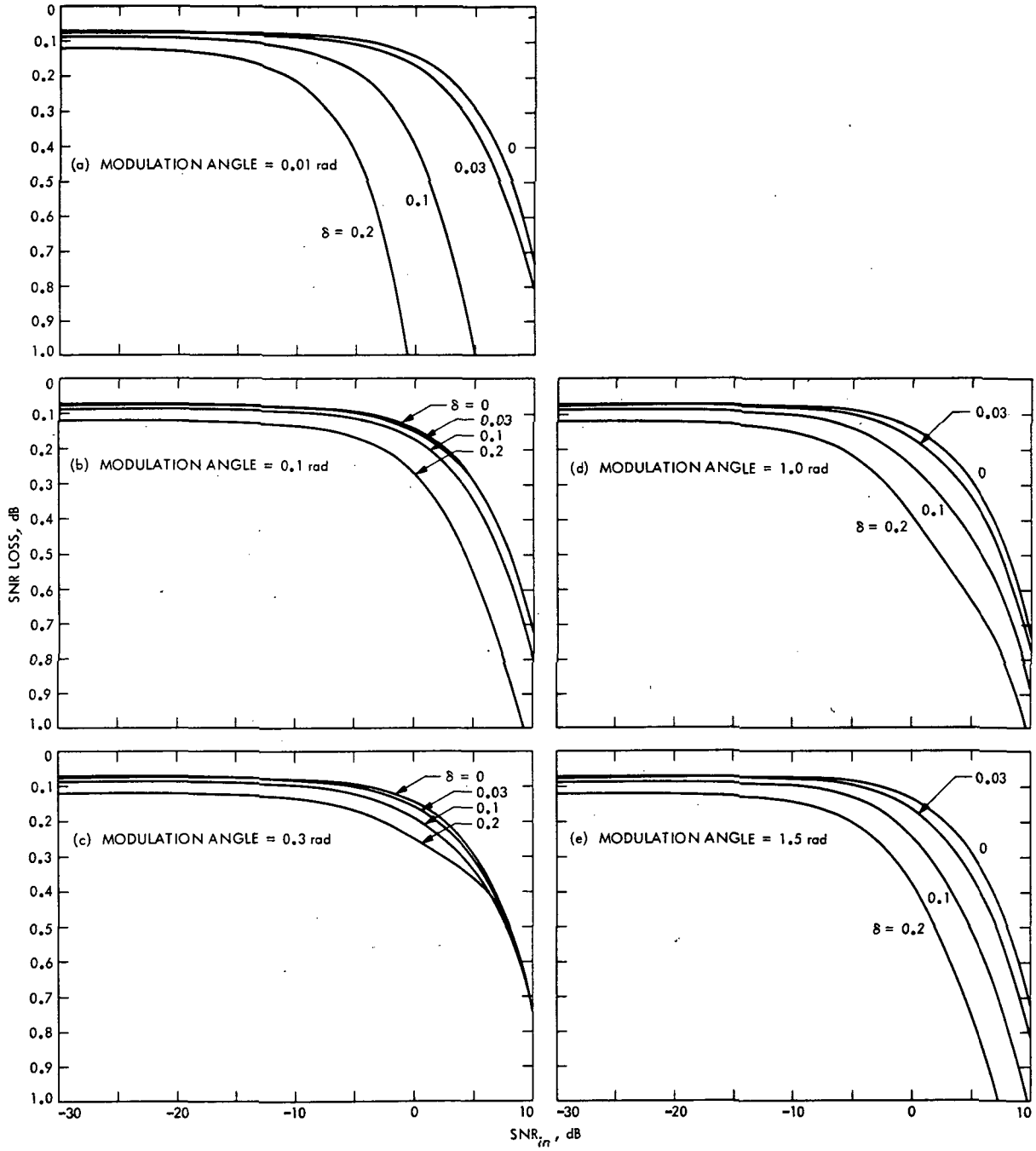


Fig. 4. Quantizer degradation vs input SNR for several values of hysteresis threshold gap, input power = 5

# WAVEFRONT Stiffness Matrix Resequencing Program Modifications for the 1108 Computer

R. Levy
DSN Engineering Section

*WAVEFRONT is a preprocessor computer program that provides resequencing to expedite decomposition of the structural stiffness matrix within the NASTRAN analysis system. Modifications described here improve WAVEFRONT by reducing core requirements, speeding the execution, and extending the acceptable categories for input data.*

## I. Introduction

WAVEFRONT (Refs. 1,2) is a preprocessor computer program that provides a resequencing of the structural stiffness matrix nodes for more efficient processing during structural analysis. The objective of WAVEFRONT is to provide a reordered nodal sequence to reduce the maximum stiffness matrix wavefront during decomposition. Input to and output from the program are designed for compatability with the NASTRAN structural analysis system. The present modifications of WAVEFRONT are designed to extend its present capabilities and to improve its execution efficiency. The present resequencing strategy, however, will remain almost unchanged.

## II. Resequencing for the NASTRAN Program

Heretofore both the BANDIT (Ref. 3) and the WAVEFRONT programs have been found to be effective resequencing preprocessors. Current versions of NASTRAN (release Level 15 and earlier) employ a mixed bandwidth/active column algorithm during decomposition of the stiffness matrix. BANDIT attempts to reduce the matrix bandwidth by means of the Cuthill-McKee algorithm (Ref. 4) independently of the numbers of active columns. WAVEFRONT ignores the bandwidth and operates to reduce the number of active columns, which then become equivalent to the wavefront. For applicability to future releases of the NASTRAN program (beginning with Level 16), which will employ a pure wavefront decomposition algorithm, BANDIT has been amended (Ref. 5) to include new options developed by Gibbs, Poole and Stockmeyer (Ref. 6).

Recently a promising approach has been developed by Gibbs (Ref. 7) and will possibly be included in BANDIT. This is a hybrid method that incorporates both a new

algorithm to develop a starting point and an existing algorithm of King (Ref. 8) to continue the resequencing process beyond this starting point. Although developed independently, the underlying strategy for resequencing within WAVEFRONT is closely related to King's strategy. It is quite likely, however, that the relative effectiveness of these, or other methods that may yet appear, is problem-dependent. Nevertheless, it appears to the writer that BANDIT may be preferable for regular structures with clearly defined and relatively smooth connectivity grids, while WAVEFRONT may be best suited to highly irregular structures of complex connectivity. Confirmation of this assessment of course awaits the dissemination of the new NASTRAN program and testing on a variety of diverse problems.

## III. WAVEFRONT Modifications

The purpose of these modifications is to improve program execution and scope of application, rather than to provide algorithm changes that affect the results produced. These modifications take advantage of special features specifically available on the Univac 1108, Exec 8 computer. It could require substantial coding changes to incorporate equivalent features that may be available on other computers. The modifications are in three categories:

(1) Reduction of core storage and adding the capability of handling larger sized problems than heretofore.

(2) Improvement of execution speed.

(3) Extension of the type of NASTRAN connection cards that can be interpreted and processed.

### A. Core Storage Reduction

The previous version of the program required storage for six arrays equal in size to the maximum number of connectivity matrix nodes and five arrays equal to the maximum number of connection edges linking pairs of nodes. It was also necessary to anticipate the upper bounds of this storage at compilation time. The modified version requires four vectors of node size and one vector of connectivity edge size and will automatically adjust to this size without recompilation. As an example, a problem previously compiled for 1200 nodes and 8000 edges that required 47.2K words of array storage would now require 12.8K storage locations. In addition to array storage, about 17K words of storage are required for code, fixed-size data blocks, and the program control table, so that for the example described the total core would now be about 30K, while formerly it would have been about 60K. If two 65K banks of core are available, a problem of about 10,000 nodes and 65,000 edges could be resequenced.

This storage reduction has been achieved by elimination or equivalencing of storage arrays that were found to be redundant, and by use of the Fortran V Field (FLD) function, which allows packing of independent information within partial (half word) locations.

### B. Execution Speed

Several of the subroutines were recoded to improve execution speed. Additional sorting operations were included by means of a more efficient sorting subroutine, and binary search algorithms were coded in-line to expedite locating particular elements within arrays. The time required for processing the input data appears to be less than half of that formerly required. After input is processed, the time required to perform a cycle of matrix nodal resequencing has been reduced by 30 to 40 percent. The typical time required for a complete program execution tends to be slightly more than half of the former time.

### C. NASTRAN Connection Card Processing

NASTRAN connection card types are identified by the first three characters of the mnemonic appearing in the first three card columns. Twelve mnemonic types can now be recognized, while previously only eight were possible. The following three-character identifiers are now accepted:

| | | |
|---|---|---|
| CBA | CQU | CTR |
| CHE | CRO | CTU |
| CON | CSH | CTW |
| CQD | CTE | CWE |

Only the integer labels of the connected node labels are read on these connections. These node labels must be placed in the proper NASTRAN 8-column card field but need not be right- or left-adjusted within the field. Up to two independent connections can be supplied on the CROd and CTUbe cards, but if only one connection is supplied it must appear in the left-most set of fields. The CHE (hexahedron elements) cards, which include a continuation card to supply the labels for the seventh and eigth nodes, require that the continuation card follow immediately after the associated mnemonic card.

The connectivity edges developed from these connection cards consist of all combinations that can be formed

from the set of associated node labels. In the case of the hexahedron and wedge connections, the present form of the NASTRAN element stiffness matrix will not develop all of these edges, but this is expected to have a minor influence on the sequencing produced.

## IV. Input Data Deck and Runstream

The form of the bulk data consisting of a set of NASTRAN GRID cards followed by the connection cards is similar to that in previous versions of WAVEFRONT. However, as a new alternative, an existing set of NASTRAN SEQGP cards can be inserted in place of the GRID cards. These will redefine the initial nodal sequencing for attempts at improvement. Otherwise the initial sequence is established by the submitted order of the grid cards. A restriction on the SEQGP cards requires that all integer data on these cards be right-adjusted in their 8-column card fields. A set of SEQGP cards produced by a prior sequencing run on WAVEFRONT will meet this requirement. A mixture of GRID and SEQGP cards can also be supplied, providing that they generate a unique set of all of the nodes that are referenced by the connection cards. User-option parameters to control the manner of execution are supplied by a new namelist form that replaces and extends the previous fixed format option card. The optional data on this namelist "INPUT" are:

KCYCLE The number of cycles of resequencing cycles to be performed. Default = 1.

ROWA Integer row number of the initial sequence at which the first resequencing cycle should start. If this is not supplied, the first cycle will begin at a row of minimum connectivity. For subsequent cycles, the first row will be picked at random from the set of rows that do not have more than the median number of connections.

IREP The program will terminate if IREP consecutive cycles do not produce a reduction of the maximum wavefront. Default = 8.

IPCH For a cycle that successfully reduces the current maximum wavefront, SEQGP cards will be punched only if the new maximum wavefront is less than IPCH. Default = 5000. To prevent ever punching SEQGP cards, supply IPCH = 0.

NPRT If any non-zero integer is supplied, a connectivity table of the input sequence is printed. This table gives the row connectivities in terms of nodal sequence number and external label. Default = 0.

NEWCNT If any non-zero integer is supplied, a row-by-row wavefront table and summary statistics will be printed for any sequencing cycle that produces a wavefront reduction. The statistics are useful for estimating the time that will be required to decompose the stiffness matrix.

MGRIDS This is an upper bound estimate of the maximum number of nodes. The default value is 4000, and since this affects only one storage vector, there is little reason to supply a lower number if the problem is appreciably smaller. If the number of nodes is larger than the default value, an estimated upper limit must be supplied.

MSHIFT This controls the magnitude of the steps in core size to accommodate the actual problem. While the connection cards are being read in, core is increased in jumps of MSHIFT to accommodate these connections. The default value of 1536 has been proposed, as reasonable and moderate changes in this would have little effect on execution efficiency.

IDEBUG If any non-zero integer is supplied, a very large amount of programmer debugging information will be supplied. The default value of 0 should not be changed.

As an example, for a problem estimated to contain less than 4000 nodes, where four sequencing cycles are to be attempted and no SEQGP cards are desired unless the wavefront is less than 40 nodes, the following cards could be supplied:

```
b$INPUT    KCYCLE = 4,    IPCH = 40,
   NEWCNT = 123456,    $END
```

The modified program is cataloged on the JPL 1108 A computer. A sample runstream is supplied below:

```
@RUN .....
@ASG,A 52219*RIL.
@HDG,P optional heading
@XQT 52219*RIL.WAVE/TRIAL
```

Title Card, Format (80A1) For problem identification and echo

b$INPUT

..... optional input parameters as described

b$END

Header Card, Format (12A6) This will be echoed

Package of GRID, SEQGP, or a combination of these cards

Blank Card (at least the first 16 card columns must be blank)

Header Card, Format (12A6) This will be echoed

Package of connection cards, containing any of the 12 3-word mnemonics in the first three columns or one continuation card following each CHE card

Blank Card (at least the first 3 card columns must be blank)

@FIN

## References


1. Levy, R. "Resequencing of the Structural Stiffness Matrix to Improve Computational Efficiency" in *Quarterly Technical Review*, Vol. I, No. 2, pp. 61–70, Jet Propulsion Laboratory, Pasadena, Calif., July 1971.
2. Levy, R. "Structural Stiffness Matrix Resequencing Program (WAVEFRONT)," *COSMIC Report*, NPO-13322, Computer Program Abstracts Vol. 5, No. 2, July 15, 1973.
3. Everstine, G. C., "The BANDIT Computer Program for the Reduction of Matrix Bandwidth for NASTRAN," *Computation and Mathematics Department Research and Development Report 3827*, Naval Ship Research and Development Center, Bethseda, Md., March 1972.
4. Cuthill, E., and McKee, S., "Reducing the Bandwidth of Sparse Symetric Matrices," *Applied Mathematics Laboratory* Technical Note, AML-40-69. Naval Ship Research and Development Center, Washington, D.C., June 1969.
5. Everstine, G. C., "Recent Improvements to BANDIT," *NASTRAN: User's Experiences*, NASA TM X-3278, pp. 511–521, Sept. 1975.
6. Gibbs, N. E., Poole, W. G., Jr., and Stockmeyer, P. K., "An Algorithm for Reducing the Bandwidth and Profile of a Sparse Matrix," *Institute for Computer Applications in Science and Engineering (ICASE) Report*, Hampton, Virginia, July 1974.
7. Gibbs, N. E., "A Hybrid profile Reduction Algorithm," *Technical Report II*, Mathematics Department, College of William and Mary, Williamsburg, Va., Aug. 1975.
8. King, I. R., "An Automatic Reordering Scheme for Simultaneous Equations Derived from Network Systems," *Int. J. Numer, Meth. Eng.*, Vol. 2, pp. 523–533, 1970.

# The Analysis of Microwave Weather Project Data

M. S. Reid
Communications Elements Research Section

*The Microwave Weather Project forms part of an overall Radio Systems Development Project which seeks to optimize the spacecraft-to-ground communications link. Statistical correlations of weather and communications capability at X- and K-bands are needed to provide practical statistical prediction of the performance of the Deep Space Network at X-band and, in the future, at K-band. A previous article discussed the general approach of the project, the measurements, calibrations, equipment, and methods. This article summarizes the results of the Weather Project for 1971 through 1974. Computed results of increases in system temperature due to atmospheric effects are plotted as functions of time, frequency, elevation angle, etc. Comparisons are made with theoretical predictions derived from a contractor report submitted to JPL, which calculated signal attenuation due to cloud cover from meteorological measurements.*

## I. Introduction

The Microwave Weather Project forms part of an overall Radio Systems Development Project which seeks to optimize the spacecraft-to-ground communications link. Statistical correlations of weather and communications capability at X- and K-bands are needed to provide practical statistical prediction of the performance of the DSN at X-band and, in the future, at K-band. A previous article (Ref. 1) discussed the general approach of the project, the measurements, calibrations, equipment, and methods. Problems encountered were also discussed as well as their possible solutions. This article summarizes the results of the Weather Project for calender years (CY) 1971 through 1974. Comparisons are made with theoretical predictions derived from a contractor report submitted to JPL, which calculated signal attenuation due to cloud cover from meteorological measurements (Ref. 2).

## II. Equipment, Measurements, and Methods

A previous article (Ref. 1) discussed the equipment, the calibrations, the measurements, and the methods. For most of the recording period, CY 1971-1974, the

equipment used was the X- and K-band total power radiometers in the Multiple-Frequency X- and K-Band (MXK) feed cone and the S-band total power radiometers in the S-Band Megawatt Transmit (SMT) or Polarization Diversity S-Band (PDS) feed cones. These radiometers were operated for the Microwave Weather Project on a continuous basis, except for periods when it was not possible to operate and record data.

Time, antenna elevation angle, and system operating noise temperature were recorded once per minute for each frequency. The analysis of the data consisted of sorting the recorded information into elevation angle ranges (6–15, 25–45, and 45–90 deg) and into time periods (years, quarter years (seasons), and months), and computing percent of time that the system operating noise temperature was above a baseline for each frequency and for each time period and elevation angle range. The baseline noise temperature for each frequency is defined as that system operating noise temperature expected in clear, dry weather at any given antenna elevation angle. The baseline is thus the lowest system temperature that can be measured with a given instrumentation in a given configuration as a function of elevation angle.

All recorded data were carefully quality controlled. Data suspected of contamination with interference or with errors due to equipment or recording problems were excluded from the data set. Thus, as far as it was possible to ensure, all computed excess system temperatures (defined as recorded system temperature minus the baseline system temperature for the given elevation angle) were due to weather effects only. Certain contaminating effects, such as some station maintenance procedures on the antenna, minor detuning of receivers, etc., were difficult to distinguish from atmospheric effects, and therefore perfect data quality control cannot be guaranteed. However, as far as was possible to determine, no real weather effects were excluded and no extraneous effects were included.

## III. Results

Figure 1 is a summary of the entire data set for S-, X- and K-bands for the calender year period 1971 through 1974. This is a probability distribution of the relative increase in system temperature and is averaged over all antenna elevation angles. The relative increase in system temperature (excess system temperature) is plotted in kelvins against percent of time. The reference system temperature against which the excess was measured was the baseline profile for each frequency, as discussed above.

The baseline was an average profile for each frequency, measured and computed over the several possible antenna and other equipment configurations. This has been discussed in detail elsewhere (Ref. 1). Different system configurations yielded different baselines, and as it was not possible to record all equipment interchanges and configuration changes, an average baseline over the time period was computed and used in the data analysis. The effect of using an average baseline rather than a measured baseline for each configuration was to reduce the resolution on excess system temperature measurement. The figure shows that the best resolution was 10 K at any elevation angle. The zenith values for the baseline were 25 K at S-band, 27.5 K at X-band, and 36 K at K-band.

Figures 2 through 5 show the same data separated by calender years. These four figures show the variable nature of atmospheric effects. Goldstone had a particularly bad year in 1971 with an unusually heavy and protracted snowstorm, while 1972 was a mild year from the point of view of atmospheric degradation.

Other effects must be taken into account when examining the results. Not only were different amounts of data recorded at the different frequencies but different amounts of data were recorded in different calender years as well. Furthermore, data at the different frequencies were not necessarily recorded at the same time. On the average, S-band and K-band data were simultaneously recorded with X-band data between 30 percent and 40 percent of the time.

Figures 6 through 8 present the same data separated by frequency and calender year.

In order to separate the different magnitudes of atmospheric noise temperature degradation by season, the data were plotted by frequency and quarter. Figure 9 shows the probability distribution of relative increase in system temperature for S-Band, averaged over all elevation angles and averaged over calender years 1971 through 1974, but separated into quarters. Figures 10 and 11 are similar plots for X-band and K-band, respectively.

Figure 12 shows a comparison between theoretical and measured X-band system temperature degradations as a function of elevation angle for one percent probability conditions. The dashed curves have been taken from the theoretical study of cloud effects referred to above (Ref. 2). The solid curves are taken from measured zenith elevation angle X-band data for Goldstone, averaged over calender years 1971 through 1974. These zenith, X-band data for one percent probability conditions were plotted

as a function of elevation angle by the cosecant law. (The theoretical curves were also plotted by the cosecant law.) It may be seen from the figure that the spread of the measured data is greater than the spread of the theoretical data. It must be noted, however, that the theoretical data are for clouds only, whereas the measured data were taken in all possible weather conditions.

The average number of events per year is plotted in Fig. 13 for the S-, X-, and K-bands. An event is a degradation in system operating noise temperature due to atmospheric effects. A system temperature degradation of 3 dB, for example, indicates that the system temperature doubled. The degradation of system temperature in kelvins is therefore a function of elevation angle. The curves in Fig. 13 are averaged over all elevation angles and over calender years 1971 through 1974. They show, for example, that a 3 dB degradation in system temperature, at any elevation angle, occurs an average 3 times per year at S-band, 6.7 times per year at X-band, and 52 times per year at K-band.

Figure 14 shows the average time duration in minutes of system temperature degradation events. The data in Fig. 14 are averaged for 1971 through 1974 and averaged over all elevation angles.

The same cautions should be observed with Figs. 13 and 14 as were noted with all the previous figures.

Figures 15 and 16 show the probability distributions of relative increase in system temperature as a function of antenna elevation angle at S- and X-bands, respectively. These curves are averaged over 1971 through 1974 and show the differences in degradation effects at different elevation angle ranges.

## IV. Conclusions

The results show that higher resolution is a desirable goal. The lack of resolution is due to the averaging of the baselines. An average baseline was mandatory because of a lack of recording capability on configuration changes. These configuration changes included subreflector position, diplexed or low noise operation, reflex or retracted microwave optics, receiver bandwidth changes and operating frequency changes. Most, but not all, X-band data were taken at 7840, 8415, or 8448 MHz. Most, but not all, K-band data were taken at 14.5, 14.7, or 15.3 GHz. Other effects, which led to reduced resolution due to the introduction of contaminated data, were fourth harmonic interference at X-band by the S-band transmitter breakthrough, receiver tests injecting a continuous-wave (CW) signal level in the intermediate frequency (IF) pass-band, maser gain drifts, etc.

In order to acquire high resolution data, a noise-adding radiometer system at X-band has been built and installed at the Goldstone Venus Station (DSS 13) for the recording of weather data. This is a gain-stabilized system with careful temperature control on all sensitive components and which operates continuously supplying data to an automatic data acquisition system (Ref. 3). This X-band radiometer system has been described in detail elsewhere (Ref. 4) and will be supplemented by a K-band (15 GHz) system in the near future.

## References


1. Reid, M. S., "A Description of the Weather Project," in *The Deep Space Network Progress Report*, Technical Report 32-1526, Vol. X, pp. 116–122, Jet Propulsion Laboratory, Pasadena, Calif., Aug. 15, 1972.
2. Smith, T. B., and Chien, C. W., *Cloud Cover Effects on Signal Attenuation at DSN Sites*, Subcontract No. 952757, Meteorology Research Inc., Altadena, Calif., Apr. 1970.
3. Reid, M. S., and Gardner, R. A., "A Versatile Data Acquisition System for Goldstone," in *The Deep Space Network Progress Report 42-30*, pp. 132–143, Jet Propulsion Laboratory, Pasadena, Calif., Dec. 15, 1975.
4. Reid, M. S., Parham, O. B., and Gardner, R. A., "An X-Band Radiometer for the Microwave Weather Project" in *The Deep Space Network Progress Report 42-29*, pp. 54–59, Jet Propulsion Laboratory, Pasadena, Calif., Oct. 15, 1975.

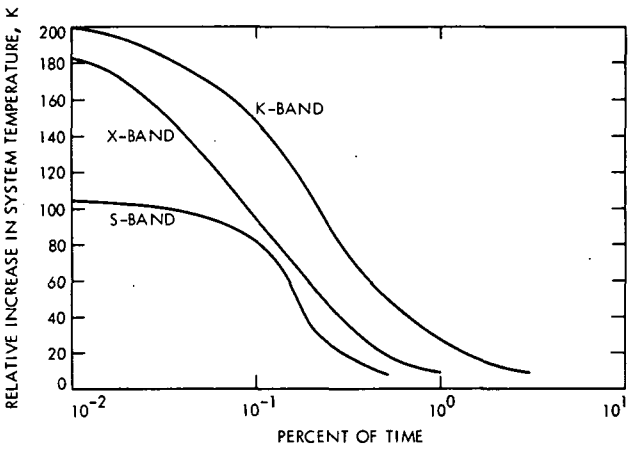


*Fig. 1. Probability distribution of relative increase in system temperature: 1971 through 1974 averages for S-, X-, and K-bands*

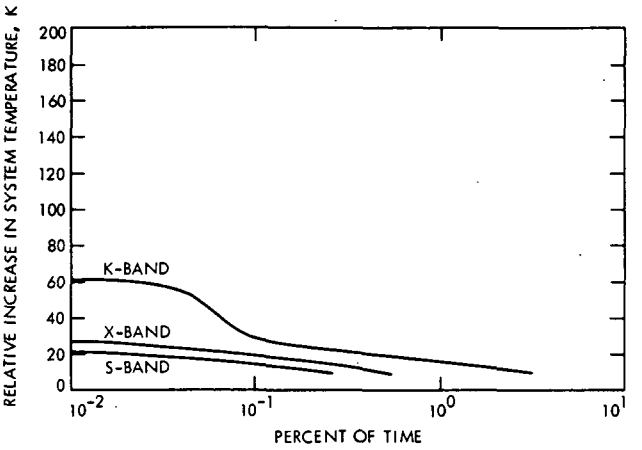


*Fig. 3. Probability distribution of relative increase in system temperature for calendar year 1972*

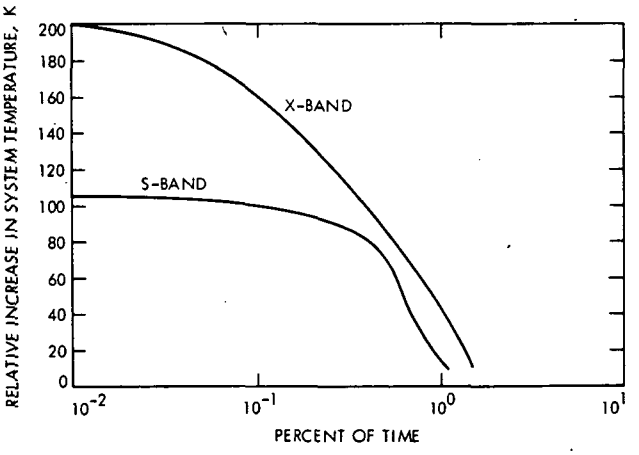


**Fig. 2. Probability distribution of relative increase in system temperature for calendar year 1971**

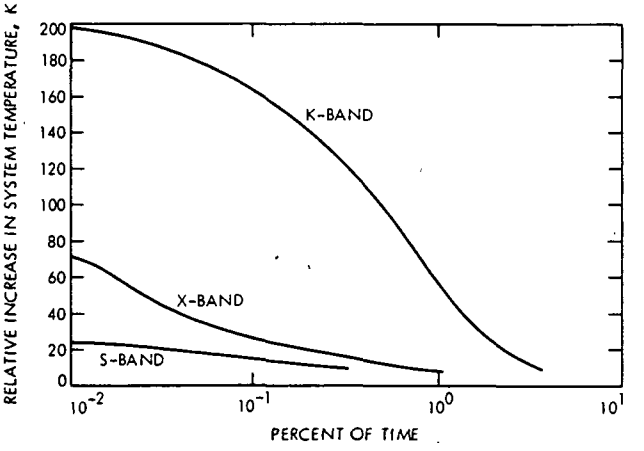


**Fig. 4. Probability distribution of relative increase in system temperature for calendar year 1973**

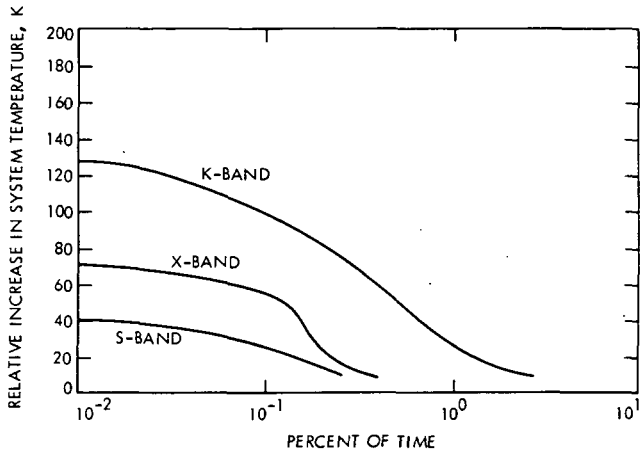


Fig. 5. Probability distribution of relative increase in system temperature for calendar year 1974

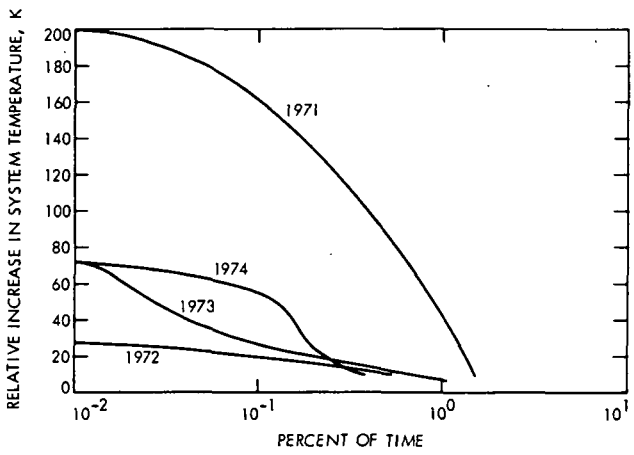


Fig. 7. Probability distribution of relative increase in system temperature for X-band for calendar years 1971 through 1974

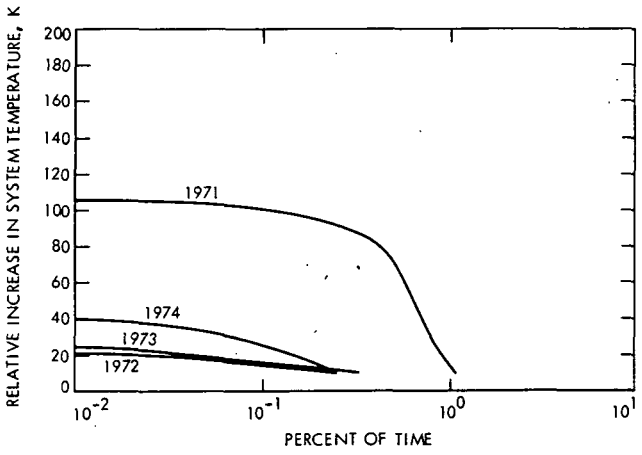


Fig. 6. Probability distribution of relative increase in system temperature for S-band for calendar years 1971 through 1974

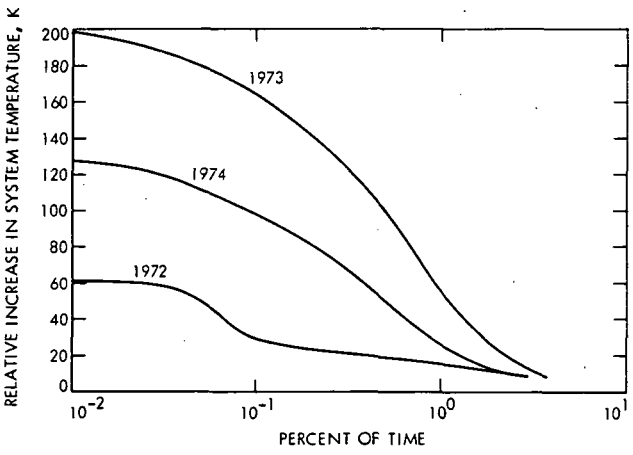


Fig. 8. Probability distribution of relative increase in system temperature for K-band for calendar years 1972 through 1974

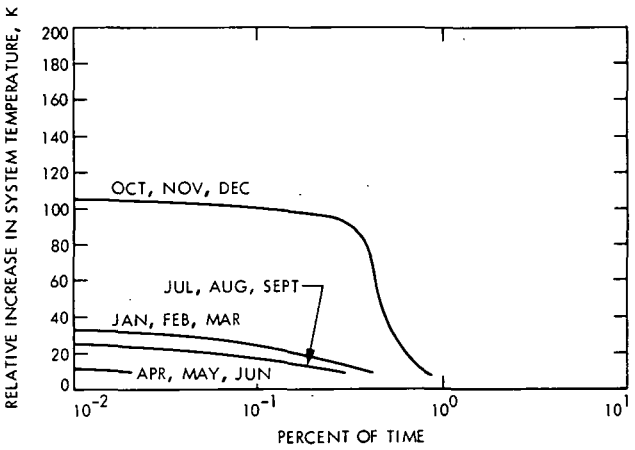


Fig. 9. Probability distribution of relative increase in system temperature for S-band by season

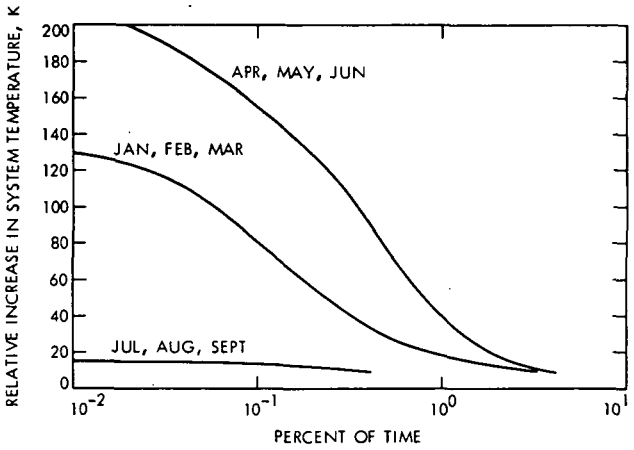


Fig. 11. Probability distribution of relative increase in system temperature for K-band by season

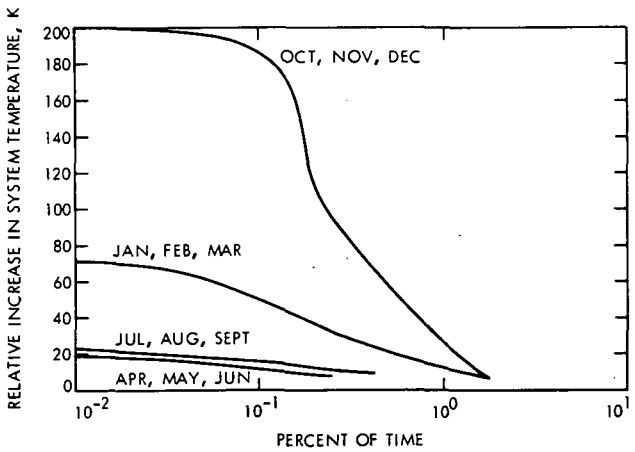


Fig. 10. Probability distribution of relative increase in system temperature for X-band by season

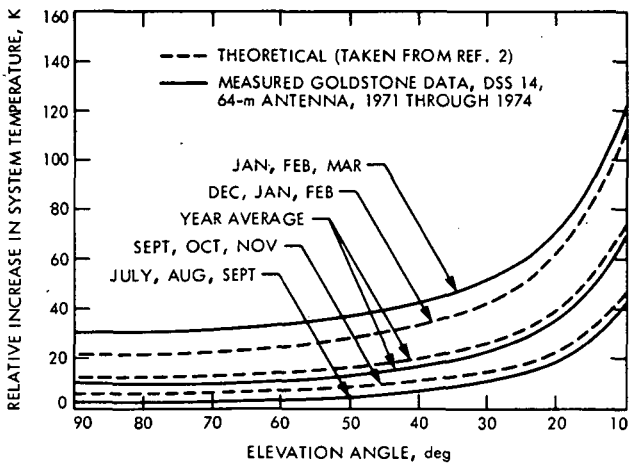


Fig. 12. Theoretical and measured relative increase in system temperature at X-band due to the atmosphere at Goldstone for one percent probability conditions

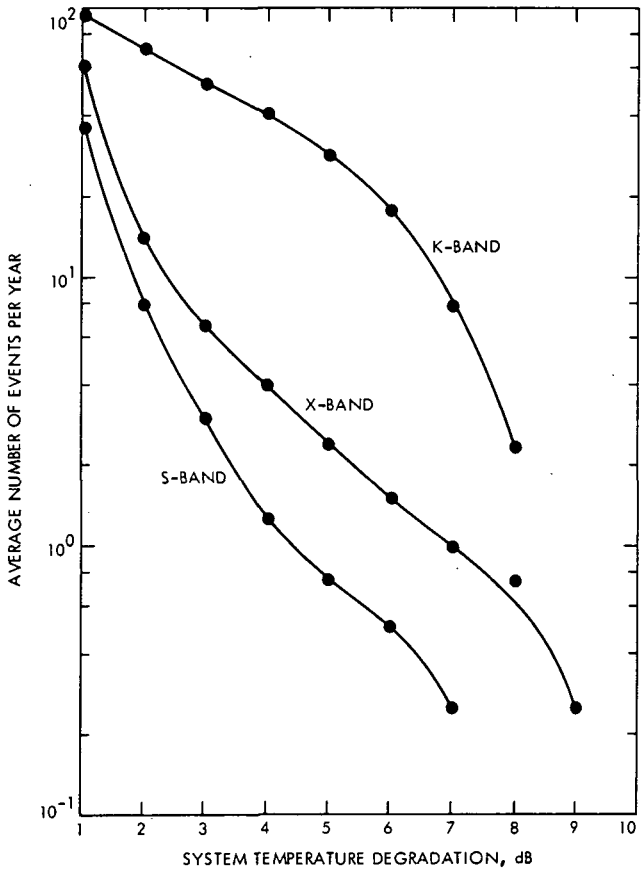


Fig. 13. Average number of system temperature degradation events per year for S-, X-, and K-bands

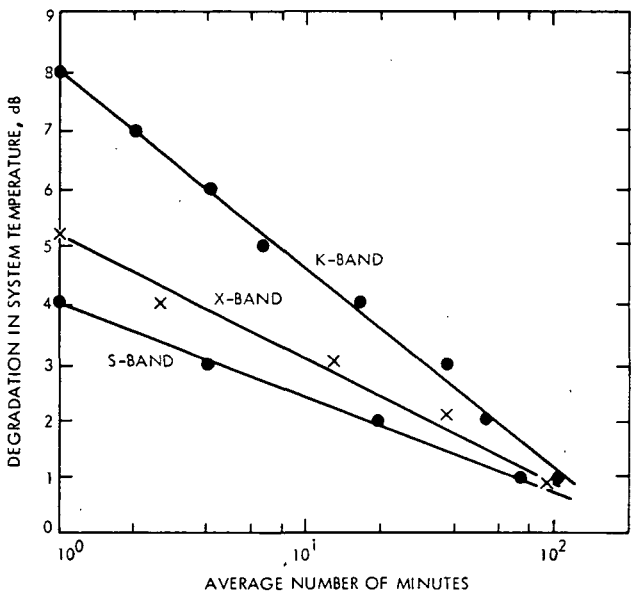


Fig. 14. Average time duration of system temperature degradation events for S-, X-, and K-band

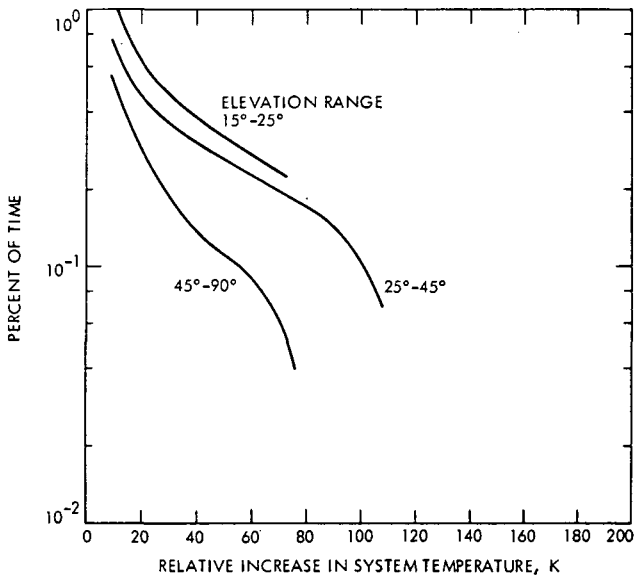


Fig. 15. Probability distribution of relative increase in system temperature for S-band as a function of elevation angle

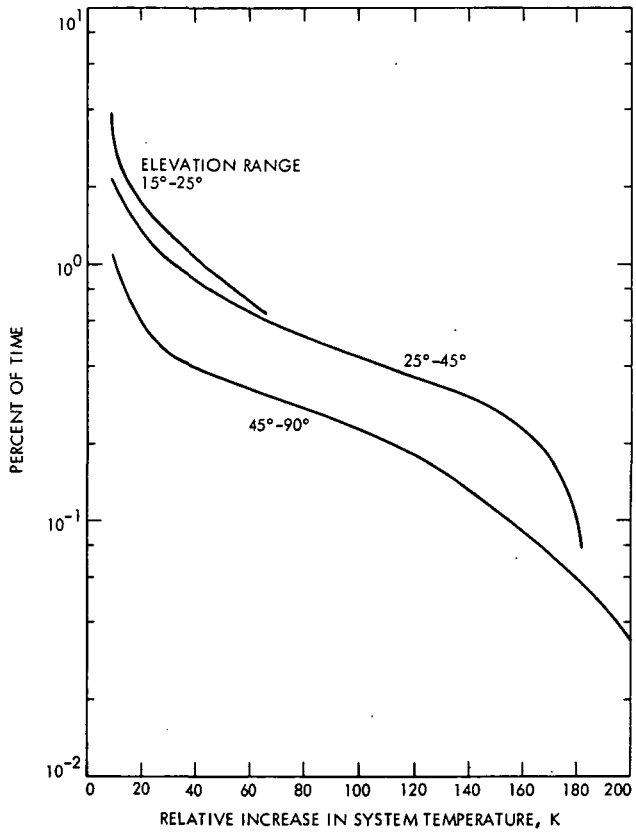


Fig. 16. Probability distribution of relative increase in system temperature for X-band as a function of elevation angle

# X-Band Reject Filter

R. Lay
R. F. Systems Development Section

*In support of an effort to isolate any receive band components of transmitter noise being received at the X-band maser, a one-cavity band reject filter has been fabricated and tested. The goal was to develop a series of cavity band reject filters capable of providing a rejection of 100 dB in the passband of the receiver.*

## I. Introduction

The need for an X-band transmit frequency filter at the DSN tracking stations is to isolate any receive band components of transmitter noise being received at the receiver. This X-band transmit frequency filter, when placed between the transmit arm of the diplexer and the transmitter, will allow signals from the transmitter to go through at 7192 MHz and reject any components of the transmitter noise falling within the passband of the receiver (8400–8450 MHz). As part of an effort to achieve a rejection of 100 dB in the passband of the receiver, a band reject filter with one cavity has been developed.

## II. Theory of Operation

The single cavity reject filter is shown in Figure 1. A portion of the main WR125 waveguide signal is coupled to an H-plane WR125 waveguide cavity by means of a rectangular aperture in the side wall of the main waveguide. The power level coupled into the cavity is controlled by the size of this rectangular aperture. The resonant frequency of the cavity is determined by the cavity length. The size of the rectangular aperture used for the single cavity reject filter was calculated to be 0.789 × 1.588 cm (0.350 × 0.625 in.) with a cavity length of 1.905 cm (0.750 in.) (Figure 2). The theoretical attenuation of the waveguide band reject filter derived from the low pass prototype circuit is calculated from Reference 1 and was approximately 24.5 dB.

## III. Test Results

Resonance of this single cavity reject filter occurred at a frequency of 9240 MHz (Figure 3). By use of the tuning screw this resonance frequency was tuned to the receive frequency of the receiver (Figure 4). The actual measured attenuation of this filter is 19 dB. The agreement between the theoretical and the measured attenuation is accepta-

ble. The discrepancy was caused by the difficulty in calculating the Q value accurately. Mismatches at the receive frequency in the main waveguide resulting from the aperture were reduced using a matching septum plate 0.546 × 1.588 cm (0.215 × 0.625 in.) with its edges parallel to the electric field (Figure 2). The voltage standing wave ratio (VSWR) was between 1.03 and 1.06 measured at the passband of the receiver (7155–7240 MHz) (Table 1).

## IV. Future Plans

From the testing, it was apparent that the tuning screw was very lossy. Thus, to overcome this problem the tuning screw will not be included in the next test sample. The cavity length will be changed to enable resonance to occur at the receive frequency. Also, the number of resonators used will be increased to achieve the desired rejection of 100 dB at the receive frequency.

## References


1. Matthaei, G. L., Young, L. and Jones, E. M. T., *Microwave Filters, Impedance-Matching Networks, and Coupling Structures*, McGraw-Hill Book Company, New York, 1964, pp. 156–161, pp. 229–242, pp. 725–771.
2. Marcuvitz, N., *Waveguide Handbook*, Dover Publications, Inc., New York, 1951, pp. 224–227.
3. Buchanan, H. R., "Variable S-Band High Power Tuner," *DSN Progress Report*, Technical Report 32-1526, Vol. XIX, pp. 176–177, Jet Propulsion Laboratory, Pasadena, Calif., Feb. 15, 1974.

Table 1. VSWR at transmit frequency band

| Frequency | VSWR |
|---|---|
| 7150 | 1.060 |
| 7155 | 1.040 |
| 7160 | 1.035 |
| 7165 | 1.035 |
| 7170 | 1.030 |
| 7175 | 1.050 |
| 7180 | 1.060 |
| 7185 | 1.050 |
| 7190 | 1.040 |
| 7195 | 1.030 |
| 7200 | 1.040 |
| 7205 | 1.050 |
| 7210 | 1.060 |
| 7215 | 1.050 |
| 7220 | 1.055 |
| 7225 | 1.040 |
| 7230 | 1.050 |
| 7235 | 1.050 |
| 7240 | 1.060 |
| 7245 | 1.040 |
| 7250 | 1.060 |

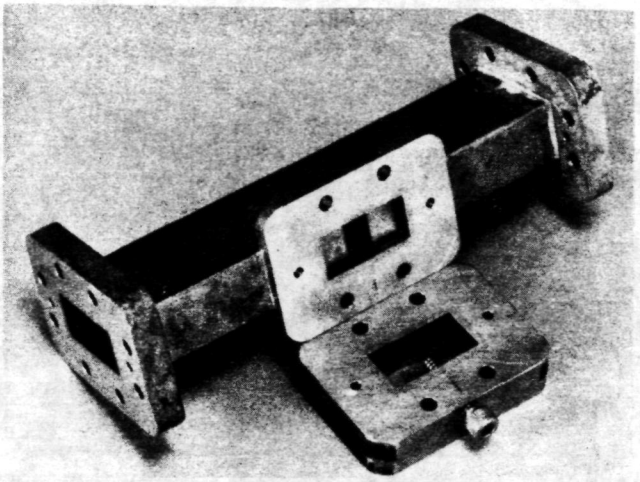

Fig. 1. X-Band reject filter

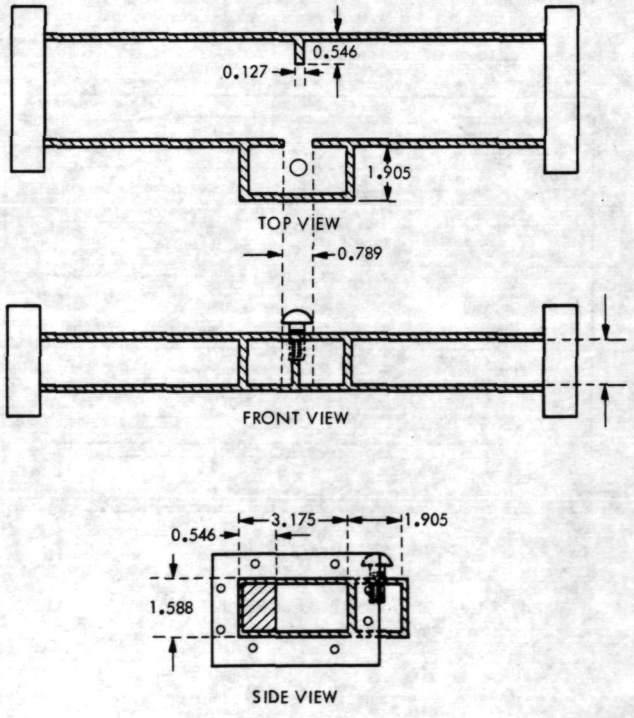


Fig. 2. Mechanical parameters

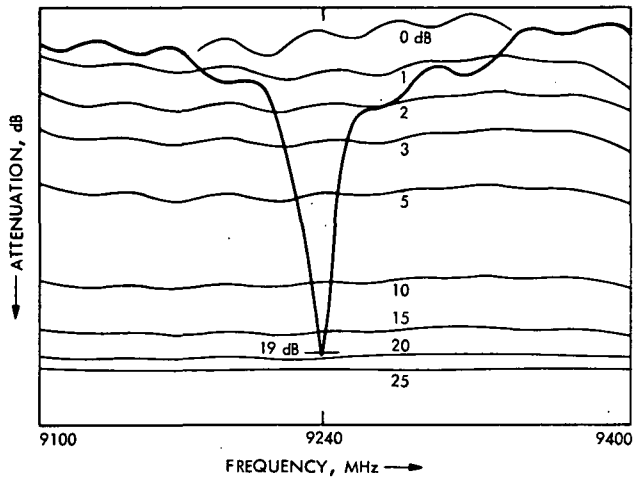


Fig. 3. Filter response without tuning screw

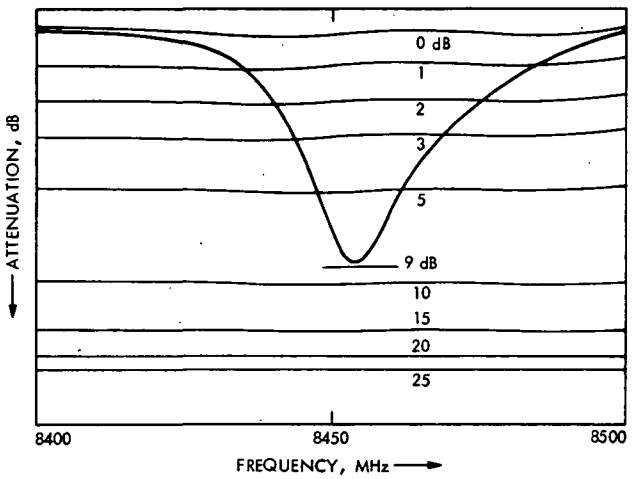


Fig. 4. Filter response tuned to receive frequency band

# Two Methods for Reducing the Number of Multiplications in Complex Fast Fourier Transforms

D. E. Wallis
Communications Systems Research Section

*Computational savings in hardware and software mechanizations of the Fast Fourier Transform (FFT) can be obtained by two methods: the first method, generalizable for N a power of 2, exploits the intrinsic simplicity of multiplication by j (unit imaginary), in addition to the periodicity and half-period negation identities usually employed. The second method, outlined for the case N = 16 only, exploits the quadrantal symmetries of the real cosine and sine functions in an implementation of the complex FFT which uses only real multiplications. The first method requires N/2 log$_2$ N/8 + 2 nontrivial complex multiplications, or 10 complex multiplications at N = 16. The second method requires only 12 real-coefficient multiplications at N = 16 to achieve the same result, but a generalization to higher N is not presently known.*

## I. Introduction

The conventional Fast Fourier Transform (FFT), of Refs. 1 and 2, is a highly efficient means of accomplishing the discrete Fourier transform. The current versions of the FFT for $N$ (number of tabular points in the discrete function to be transformed) equal an integer power of 2 are based on matrix factorization and exploitation of the two complex-exponential identities

$$\text{(periodicity)} \quad e^{-j\,2\pi/N\,nm} \equiv e^{-j\,2\pi/N\,(mn \bmod N)} \quad N,m,n \text{ integers} \tag{1}$$

$$\text{(half-period negation)} \quad e^{-j\,2\pi/N\,(n+N/2)} \equiv -e^{-j\,2\pi/N\,n} \quad N \text{ even} \tag{2}$$

to which might be added (as done in this report) the identity

$$\text{(identification of } -j\text{)} \quad e^{-j\,2\pi/N\,(N/4)} \equiv -j \tag{3}$$

The result is often expressed as a signal flowgraph in which the number of complex additions (subtractions)

and complex multiplications is seen to be enormously reduced relative to the number of such operations which would be required in executing the transform verbatim from its usual $N \times N$-matrix-times-$N$-vector definition.

The objective of this report is to present two methods for reducing still further the number of multiplications required to implement the FFT. The derivation of the first method (FFT) exploits (3) to obtain a favorable grouping of the multiplications by $j$. The derivation of the second method—real FFT (RFFT)—exploits four additional identities:

(frequency aliasing)
$$e^{-j\,2\pi/N\,mn} \equiv e^{+j\,2\pi/N\,m\,(N-n)} \tag{4}$$

(definition of complex exponential)
$$e^{-j\,2\pi/N\,mn} \equiv \left(\cos\frac{2\pi}{N}mn\right) - j\left(\sin\frac{2\pi}{N}mn\right) \tag{5}$$

(cosine in terms of sine)
$$\cos\left[\frac{2\pi}{N}n\right] \equiv \sin\left[\frac{2\pi}{N}\left(n+\frac{N}{4}\right)\right] \tag{6}$$

(sine of full period in terms of quarter period, with symmetry)
$$\begin{cases} \sin\left[90^\circ + \frac{2\pi}{N}n\right] \equiv \sin\left[90^\circ - \frac{2\pi}{N}n\right] \\ \sin\left[-\frac{2\pi}{N}n\right] \equiv -\sin\left[\frac{2\pi}{N}n\right] \end{cases} \tag{7}$$

The derivations for both methods follow parallel developments based on matrix partitioning. The resulting transforms are expressed as flowgraphs for comparison of the methods. At $N = 16$, the RFFT requires 12 real-coefficient multiplications, 72 additions, and 7 *trivial* multiplications by $j$ (or $-j$), the unit imaginary, to accomplish the transform, as opposed to the 10 complex-coefficient multiplications, 64 additions, and 7 multiplications by the unit imaginary required by the FFT.

It is not presently known whether the savings in multiplications of the RFFT over the FFT for $N = 16$ can be obtained in general. The complex FFT used in the comparison is possibly a new form in that its flowgraph has exactly $(N/2)\log_2(N/8) + 2$ nontrivial multiplications (with $N \log_2 N$ additions) as compared with $(N/2)\log_2(N/2)$ multiplications usually quoted in the literature. The savings thereby obtained are, however, implicit (if not easily recognized) in other standard forms of the FFT.

## II. Discussion of FFT and RFFT Flowgraphs

Flowgraphs for the FFT and RFFT are given for the case $N = 16$ in Figs. 1 and 2, respectively. In both flowgraphs, the complex-valued data vector to be transformed is $(x_0, x_1, \cdots, x_{15})$, and the complex-valued transform of the data is the vector $(s_0, s_1, \cdots, s_{15})$. Nodes of the graphs having two input signal lines are *summing nodes*: Any signal brought to a summing node via a solid line is added, and any signal brought on a dashed line is subtracted. The signal resulting from the summation (or differencing) operation then flows to subsequent nodes. An integer $n$ appearing inscribed in a node of the FFT (Fig.1) implies that the result of summation is to be multiplied by the *complex* scalar coefficient $\exp[-j(2\pi/N)n]$ which is, for $N = 16$, $\exp[-j(2\pi/16)n]$. Somewhat correspondingly, an integer $n$ appearing inscribed in a node of the RFFT (Fig. 2) implies multiplication by the *real* scalar coefficient $\sin[(2\pi/N)n]$, which is $\sin[(2\pi/16)n]$ when $N = 16$. It was not possible, in drawing the RFFT diagram, to associate all of the required multiplications with specific nodes. To accommodate this (unexpected) exigency, the square/diamond symbol containing an inscribed integer is used to associate a multiplication with a *path* rather than a node.

Multiplications by the unit imaginary ($+j$, or $-j$ as appropriate) appear in both the FFT and RFFT diagrams. It has seemed reasonable to count such multiplications separately from those multiplications involving a general complex coefficient, because multiplication of a complex number by $j$ is accomplished by a *complementary swap*, i.e., swap the real and imaginary parts, then negate one of them, as shown in (8).

$$j(a + jb) \equiv -b + ja \qquad a,b \text{ real.} \tag{8}$$

Thus, it may be appreciated that multiplication by $j$ is actually a simpler operation than multiplication by a general complex coefficient, and is, in fact, simpler than a complex addition. This is the reason underlying the choice of version of the FFT selected for comparison with the RFFT, since other FFT versions would appear to have *more* complex multiplications, and thus compare less favorably with the RFFT.

The main advantage that might be claimed for the RFFT is reduction of the number of multiplication operations required to implement the transform. That the use of multiplication by real coefficients (as in the RFFT) constitutes a saving over the use of multiplication by complex coefficients is apparent: Since the data to be transformed are assumed complex (worst case for the RFFT), it requires four real multiplications to implement

complex-coefficient multiplication, but only two real multiplications when the coefficient is *a priori* known to be only real-valued. Thus, the 12 real-coefficient multiplications of the RFFT of Fig. 2 represent considerably fewer multiplications than the 10 complex-coefficient multiplications of the FFT of Fig. 1. It is also true that multiplication of a complex number by a complex coefficient requires the equivalent of a complex addition, i.e., $(a + jb)(c + jd) \equiv (ac - bd) + j(bc + ad)$. Thus, even though the RFFT uses 72 additions and the FFT uses 64 additions, it appears that the excess of additions in the RFFT is balanced in the comparison by the fact that 12 additions are implicit in the 12 complex-coefficient multiplications in the FFT.

The FFT of Fig. 1 is of that class of FFTs in which normally ordered data are transformed into a *shuffled-order* transform; i.e., the resulting elements of the transform do not come out in the natural order of their subscripts. (The shuffled-order form of output is one of the accepted canonical forms, cf. Ref. 2.) It will be seen that the RFFT of Fig. 2 also has a shuffled-order output, which has been arranged to show some (incomplete) similarity to the FFT output in Fig. 1. A general rule for the RFFT output arrangement awaits development.

A curious phenomenon of the RFFT which occurs by design is the fact that the coefficients of the conventional discrete Fourier analysis (Ref. 3) in terms of sines and cosines is obtained at intermediate points of the flowgraph: The cosine-harmonic amplitudes are $a_0, a_1, a_2 \cdots, a_6, a_7, a_8$ and the sine-harmonic amplitudes are $b_1, b_2, \cdots, b_6, b_7$ ($b_0$ and $b_8$ are never present), where the subscript indicates the frequency or *harmonic number*. Thus, the RFFT (suitably truncated) provides a "fast" method for obtaining the Fourier analysis.

## III. Derivation of the Comparison FFT by Matrix Partitioning

The complex-valued discrete Fourier transform (DFT) is usually defined by the matrix-vector product (9):

$$\begin{bmatrix} s_0 \\ s_1 \\ \vdots \\ s_{N-1} \end{bmatrix} = \frac{1}{N} \begin{bmatrix} & & \\ & e^{-j\,2\pi/N\,mn} & \\ & & \end{bmatrix} \begin{bmatrix} x_0 \\ x_1 \\ \vdots \\ x_{N-1} \end{bmatrix}$$

$N$ = dimension of transform matrix

$m$ = row index ("frequency")

$n$ = column index ("time") (9)

In (9), the column vector $\{x\}$ on the right is a complex-valued time series of $N$ points (equally spaced in time) which is to be transformed by the indicated product to produce the column vector $\{s\}$, which is called the discrete Fourier transform (DFT) of $\{x\}$. The transform $\{s\}$ is, however, seldom computed by the direct application of the product (9). This is because combinational schemes, called "fast" Fourier transforms (FFT) exist which can compute the DFT with far fewer multiplications and additions than are indicated in (9). One such FFT will be derived in this section.

### A. Notation

It is customary in DFT derivations to suppress the factor $1/N$ appearing in (9) and to focus attention on the exponents of the exponential elements of the DFT matrix in (9). Consider the case $N = 16$ to be used in the derivation. The $16 \times 16$ DFT can be indicated as shown in Fig. 3a, in which the elements of the matrix (9) are replaced by the exponents $mn$ of the matrix elements which were of the form $[\exp - j(2\pi/16)]^{mn}$, with application of the periodicity identity (1).

The elements of the transform $\{s\}$ can, of course, be computed in any desired order by permuting the order in which the rows of exponents appear in the transform matrix. A convenient arrangement of the rows is that shown in Fig. 3b. This arrangement gives the elements of $\{s\}$ in the so-called "shuffled" order (Ref. 2). The shuffling procedure may be derived by inspection, noting that all rows having 0 in column 8 are sorted into a group at the top of the matrix, so that the remaining rows having 8 in column 8 are sorted to the bottom. The top and bottom halves are then regarded as independent submatrices, and these are further sorted to group together those rows having identical elements in column 4, then column 2. This row sorting operation may be called an "even-odd sort on identical column keys."

### B. Derivation

The sorting operation positions the elements of the $16 \times 16$ DFT matrix so that the relationships $A_{12} = A_{11}$ and $A_{22} = -A_{21}$ hold among the four $8 \times 8$ partition-block submatrices. That $A_{22} = -A_{21}$ follows from the negation identity (2); i.e., if 8 is added to the exponents of $A_{21}$ (modulo 16, of course), the exponents of $A_{22}$ result. Application of the distributive law causes the DFT of Fig. 3b to be reduced to the form shown in Fig. 4. This reduction is accomplished at a cost of 8 additions and 8 subtractions (called 16 "additions"). The reduction leaves two $8 \times 8$ matrix multiplications as the indicated operations to be

carried out to complete the transform. But it turns out that these indicated matrix multiplications can themselves be reduced by a procedure essentially the same as that already applied. Thus, the matrix multiplications remaining at each step of reduction are never actually carried out explicitly.

Before continuing to the next step of reduction, it may be noted by inspection of the matrix for the half-transform $(s_1, s_9, \cdots, s_7, s_{15})$ that if exponent 4 is factored from the last four columns, then relationships similar to the $A_{12} = A_{11}$ and $A_{22} = -A_{21}$ of the preceding step hold among the $4 \times 4$ partition-blocks. The factoring is most efficiently accomplished by multiplying the last four elements of the column vector by $\{\exp[-j(2\pi/16)]\}^4 = -j$, as indicated schematically by the circle symbol ④, and subtracting 4 from the elements of the last four matrix columns. It may now be seen that column vectors on the right in Fig. 4 are precisely those available at the first echelon of nodes in the FFT flowchart of Fig. 1. The principle of factoring entire columns of matrix elements by means of multiplication of the corresponding vector elements is the key also to the RFFT derivation given in the next section. In the present example, the fact that exponents of 0 and 8 remain in column four after the factorization causes no difficulty, since exponent 0 is *unity* and exponent 8 is *negation*, as used in the first reduction step. To avoid carrying unduly complicated notation to the next reduction step, the vectors on which matrix operations are indicated are redesignated as $\{y\}$, is shown in Fig. 4.

Figure 5 gives the remaining reduction steps. The procedure is the same as for the first reduction step. At each step, the notations for vectors representing intermediate computations are redefined to simplify the notation for the next step. The result is shown in the FFT flowchart of Fig. 1. It is seen that $N$ ($N = 16$ in the example) additions are required at each step of the reduction, and that exactly $N \log_2 N$ additions (if $N$ is a power of 2) are required. (Here, $N \log_2 N = 64$). The number of multiplications by a complex scalar coefficient is 10 if multiplications by $-j$ (unit imaginary) are not counted (as indicated in the preceding section); otherwise, the total number of multiplications is 17.

### C. Theorem

*The count $C$ of nontrivial multiplications by complex coefficients in an FFT flowchart based on the described DFT reduction scheme for $N$ a power of 2 is*

$$C = \frac{N}{2}\log_2\frac{N}{8} + 2 \qquad 2 \leq N$$

The proof is by inspection. Temporarily assume $8 \leq N$. The number of echelons, or reduction steps is $\log_2 N$. The first echelon requires no nontrivial multiplications, and the last echelon requires no multiplications at all. Therefore, only $E = (\log_2 N - 2) = \log_2 (N/4)$ intermediate echelons require multiplication.

There are always less than $N/2$ multiplications in each echelon: Inspecting the $E$ intermediate echelons, it may be seen that the lower half of the first (intermediate) echelon requires multiplication at half its nodes. Then, the lower 3/4 of the next echelon requires multiplication at half its nodes. Then the lower 7/8 of the next echelon requires multiplication at half its nodes, etc. Since the width of the echelon is $N$, the number of multiplications in the flowchart is, assuming the induction,

$$C = \frac{1}{2}N\left(\frac{1}{2} + \frac{3}{4} + \frac{7}{8} + \cdots\right)_{E\ terms}$$

Complementing the indicated summation gives

$$C = \frac{1}{2}N\left[E - \left(\frac{1}{2} + \frac{1}{4} + \frac{1}{8} + \cdots\right)_{E\ terms}\right]$$

$$= \frac{1}{2}N\left[E - \frac{1}{2}\left(1 + \frac{1}{2} + \frac{1}{4} + \cdots\right)_{E\ terms}\right]$$

Summing the indicated geometric series to $E$ terms yields

$$C = \frac{1}{2}N\left[E - \frac{1}{2}\left(\frac{(1/2)^E - 1}{(1/2) - 1}\right)\right] = \frac{1}{2}N\left[E - 1 + (1/2)^E\right]$$

Substituting $E = \log_2 (N/4) \geq 1$, the theorem is proved for $8 \leq N$. Construction of the flowgraph for the simple cases $N = 2$ and $N = 4$ establishes that the formula is valid for $2 \leq N$.

## IV. Derivation of the RFFT

In this section, the RFFT is derived from the DFT definition (9), with factor $1/N$ suppressed. This is done by reducing the matrix in (9) to real terms to a maximum extent, introducing explicit factors of $j$ where required, and then reducing the indicated real matrix operations by application of the distributive law and scalar factorization of matrix columns, similarly to what was done in the preceding section.

### A. Notation

The matrix (9) for the DFT is reduced to real terms as shown schematically in Fig. 6. The matrix (9) is ex-

pressed directly in Fig. 6a. Through application of the aliasing identity (4), the positive-frequency exponentials in the frequency range $(N/2) + 1$ to $N - 1$ are expressed in terms of negative-frequency exponentials in the frequency range $-[(N/2) - 1]$ to $-1$, as shown in Fig. 6b, for general $N$ (even). (This modification has been applied to the lower $(N/2) - 1$ rows). Without loss of generality, application of the definition (5) to the matrix of Fig. 6b produces, for $N = 16$, the matrix of Fig. 6c. It may be observed that there are no sine terms at frequencies 0 and 8. Also, the elements of the row for $\cos[(2\pi/16)\,0n]$ are all equal to unity (real) and the elements of the row for $\cos[(2\pi/16)\,8n]$ are alternating $+1, -1, +1, -1, \ldots$ (real).

It appears then that the complex DFT can be written in terms of a real sine-cosine matrix, with the aid of a simple factorization, as shown in Fig. 7a. The product of the sine-cosine matrix times the data vector $\{x\}$ can itself be regarded as a transform. This transform will be called the *discrete Fourier analysis* (DFA), and is seen to be a matrix formalism for conventional discrete Fourier analysis (Ref. 3). The coefficients $a_0, a_1, a_2, \cdots, a_6, a_7, a_8$ and $b_1, b_2, \cdots, b_6, b_7$ are, respectively, the discrete Fourier cosine and sine amplitude coefficients. These coefficients are real if the data vector $\{x\}$ is real, and complex if $\{x\}$ is complex. The DFA matrix elements are, of course, strictly real-valued.

The notation to be used may now be introduced: Each element of the DFA matrix is a value of a sine or cosine function at some value of argument. These values will be indicated by a simple *code* which will express every value in the matrix in terms of the sine function tabulated for the first quadrant of its argument. The code is, for $N = 16$,

| Code | | Value |
|---|---|---|
| numerals | 0 | $\sin\left(\frac{2\pi}{16}0\right) = 0$ |
| | 1 | $\sin\left(\frac{2\pi}{16}1\right)$ |
| | 2 | $\sin\left(\frac{2\pi}{16}2\right)$ |
| | 3 | $\sin\left(\frac{2\pi}{16}3\right)$ |
| letter | I | $\sin\left(\frac{2\pi}{16}4\right) = 1$ |

It will be necessary to show negation of the encoded sine values, and this can conveniently be done by underlining. This notation may then be applied to the DFA matrix of Fig. 7b, with the aid of identities (6) and (7), to obtain the DFA matrix form shown in Fig. 8a.

### B. Derivation

The RFFT is defined as the "fast" computational organization of the operations indicated in matrix form in Fig. 7a. Since the transformation matrix on the left in Fig. 7a can be accomplished with but 7 trivial multiplications by $j$ (or $-j$) and 14 additions, this transformation is already in "fast" form. Thus, it will be necessary only to derive a "fast" version of the DFA of Fig. 7b. This will be done using the notation of Fig. 8a.

As was done in the derivation of the FFT in Section III, the outputs of the DFA in Fig. 8a will be *shuffled* by permuting the rows of the DFA matrix to the form shown in Fig. 8b. The shuffling is done to enhance symmetries among the $8 \times 8$ partition blocks. Application of the distributive law to the partition blocks of the matrix of Fig. 8b yields the reduced transform of Fig. 9a. It may be observed that the sums and differences of $x_i$ appearing on the right hand side of Fig. 9a are precisely the quantities available at the first echelon of nodes in the RFFT flowchart of Fig. 2. These sums and differences are redesignated as $\{y\}$ to simplify the notation for the second reduction step, shown in Fig. 9b.

The reduction from the lower $8 \times 8$ matrix of Fig. 9a to the two lower $4 \times 4$ matrices of Fig. 9b departs somewhat from the straightforward application of the distributive law, as do the subsequent reduction steps, in that *folding* about the pivotal elements $y_8$ and $y_{12}$ is required. What is meant by folding can be inferred from the lower two $4 \times 4$ matrix operations in Fig. 9b, which recognize the odd symmetry which holds among the columns of rows 0 through 3 and the even symmetry which holds among the columns of rows 4 through 7, respectively, in the lower $8 \times 8$ matrix of Fig. 9a. Before proceeding to the third reduction step, the value $\sin[(2\pi/16) \cdot 2]$ is factored from the third column of the two lower $4 \times 4$ matrices in Fig. 9b, and is applied as indicated by the ② symbol to the corresponding column-vector elements. The column vector notation is then changed to $\{z\}$ to simplify the notation for subsequent steps.

In the third reduction step, shown in Fig. 10, the distributive law is applied directly to the matrix operations for $a_0, a_8, a_4$, and $b_4$. The matrix rows for $a_2, a_6$ are folded to exploit odd column symmetry, and the rows for $b_2, b_6$ are folded to exploit even column symmetry with

column factorization applied. The matrix operations for the pairs $(a_1,a_7)$, $(a_5,a_3)$, $(b_1,b_7)$, and $(b_5,b_3)$ are reduced, as shown in Fig. 10, by matrix partitioning and column factorization.

The fourth (final) reduction step can be done by inspection, and so is not shown in matrix form. All of the reduction steps are, of course, equivalent to the DFA portion of the RFFT flowgraph of Fig. 2, to which has been added the transformation which converts the DFA to the RFFT.

## V. Concluding Remarks

The code notation for the sine function, used in the RFFT derivation, has turned out to be similar to that used in Ref. 4. A distinction, however, is in the fact that the sine code used in the present report is *value*-oriented, and has been applied to give the cosine as well as the sine, tabular values. Indeed, the results of row shuffling, as in Fig. 8a, show that the sine and cosine amplitude coefficients are most efficiently obtained when interspersed to some extent, and the value notation gives the *sorting keys* for doing this.

An unelaborated comment in Ref. 5 suggested that the complex exponentials of the FFT matrix be expressed in real form, to minimize the number of real multiplications. The RFFT derivation realizes such a minimization. Also suggested in Ref. 5 was the possibility of regarding the unit imaginary $j$ as a "special element" to be exploited in FFT matrix factorization schemes, and this has been done to a maximum extent in the derivation of the comparison FFT. The importance of $j$ is not, of course, its use as a pivotal element of the factorization, but rests rather with the fact that multiplication by $j$ is a trivial complex multiplication, to be exploited in the actual computations.

## References


1. Cooley, J. W., and Tukey, J. W., "An algorithm for the machine calculation of complex Fourier series," *Math. Comput.*, Vol. 19, pp 297–301, Apr. 1965.
2. Cochran, W. T., et al., "What is the fast Fourier transform?," *IEEE Trans. Audio and Electroacoust.*, Vol. AU-15, No. 2, pp. 45–55, June 1967.
3. Korn, G. A., and Korn, T. M., *Mathematical Handbook for Scientists and Engineers*, McGraw-Hill Book Company, New York, 1961.
4. Danielson, G. C., and Lanczos, C., "Some improvements in practical Fourier analysis and their application to X-ray scattering from liquids," *J. Franklin Inst.*, Vol. 233, pp. 365–380, Apr. 1942.
5. Gentleman, W. M., "Matrix multiplication and fast Fourier transforms," *Bell Sys. Tech. J.*, Vol. 47, pp. 1099–1103, July 1968.

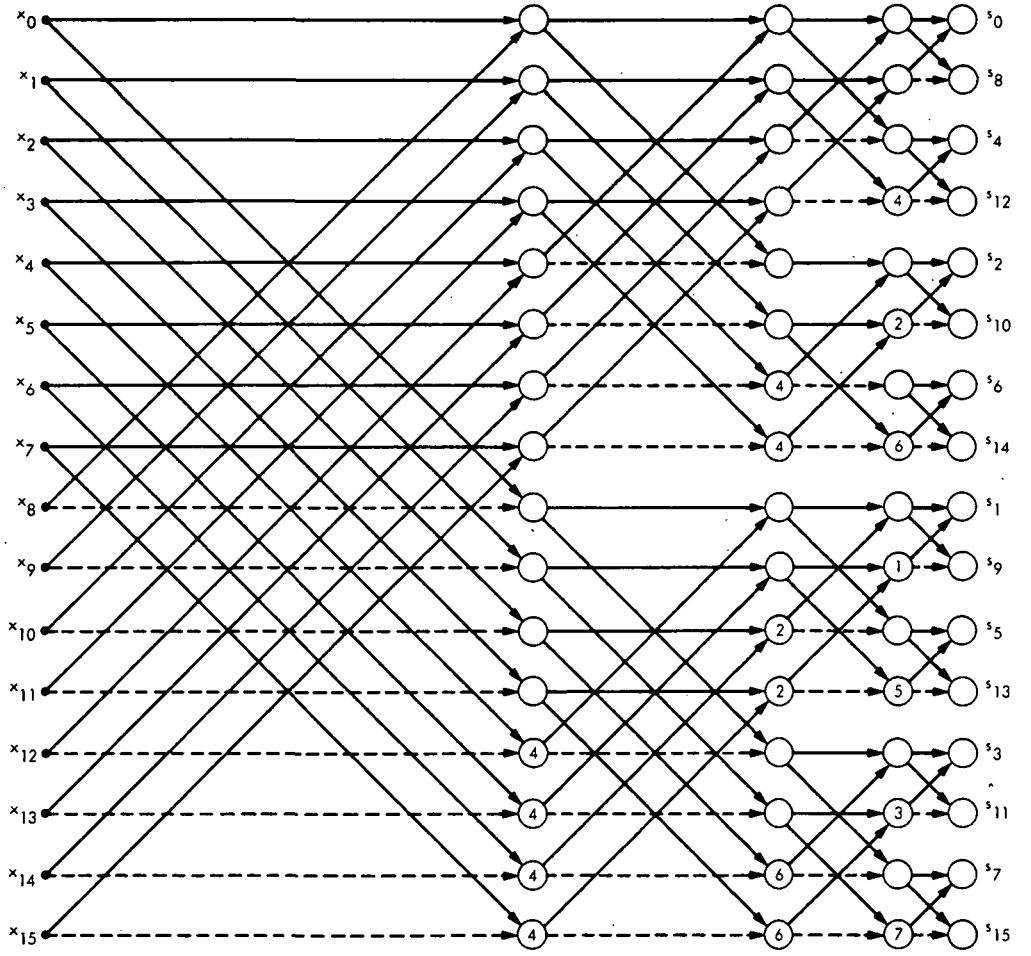


Fig. 1. Flowchart for conventional Fast Fourier Transform ($N = 16$)

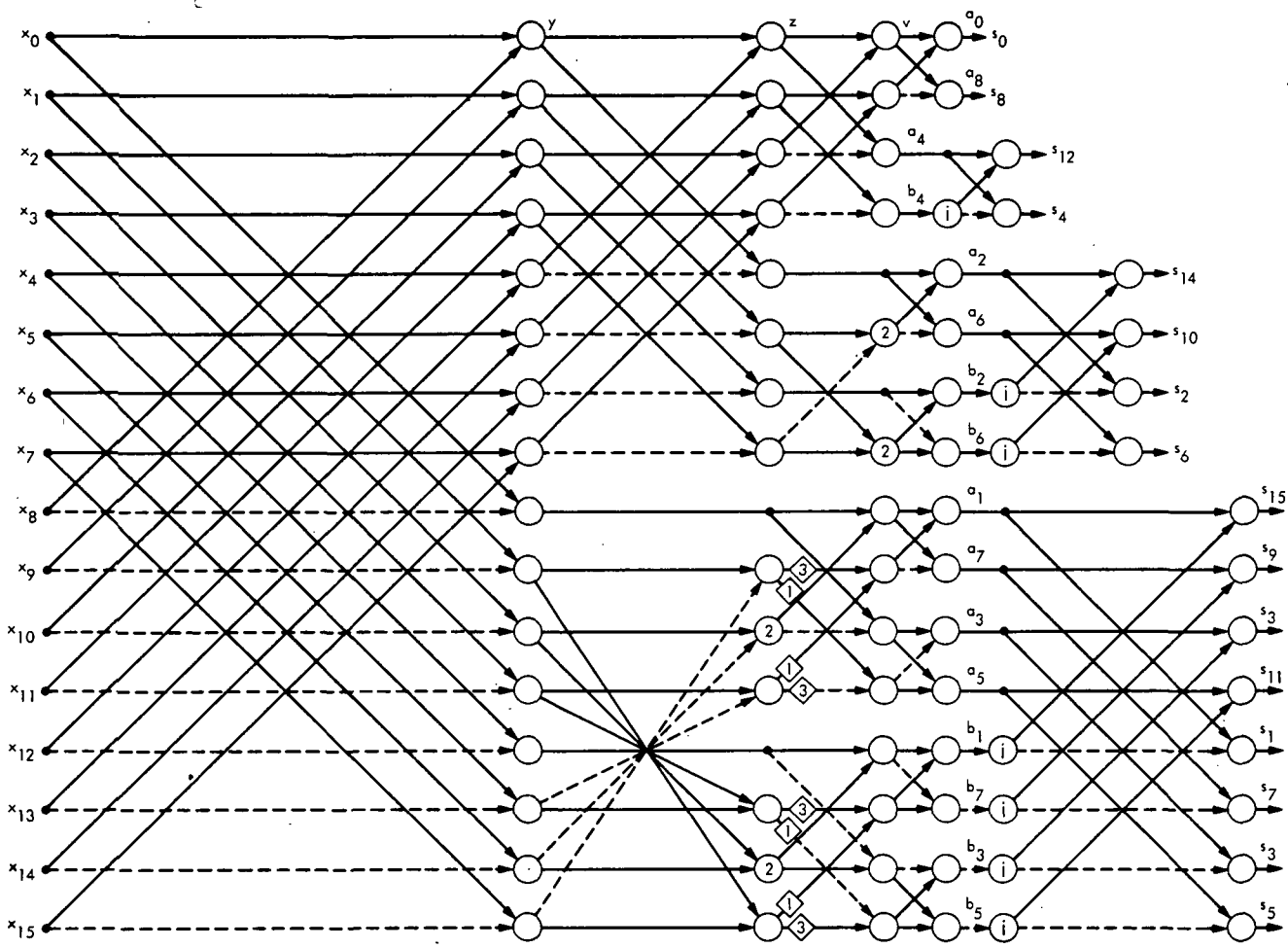


Fig. 2. Flowchart for RFFT

$$
\begin{bmatrix} s_0 \\ s_1 \\ s_2 \\ s_3 \\ s_4 \\ s_5 \\ s_6 \\ s_7 \\ s_8 \\ s_9 \\ s_{10} \\ s_{11} \\ s_{12} \\ s_{13} \\ s_{14} \\ s_{15} \end{bmatrix} = \begin{bmatrix}
0 & 0 & 0 & 0 & 0 & 0 & 0 & 0 & 0 & 0 & 0 & 0 & 0 & 0 & 0 & 0 \\
0 & 1 & 2 & 3 & 4 & 5 & 6 & 7 & 8 & 9 & 10 & 11 & 12 & 13 & 14 & 15 \\
0 & 2 & 4 & 6 & 8 & 10 & 12 & 14 & 0 & 2 & 4 & 6 & 8 & 10 & 12 & 14 \\
0 & 3 & 6 & 9 & 12 & 15 & 2 & 5 & 8 & 11 & 14 & 1 & 4 & 7 & 10 & 13 \\
0 & 4 & 8 & 12 & 0 & 4 & 8 & 12 & 0 & 4 & 8 & 12 & 0 & 4 & 8 & 12 \\
0 & 5 & 10 & 15 & 4 & 9 & 14 & 3 & 8 & 13 & 2 & 7 & 12 & 1 & 6 & 11 \\
0 & 6 & 12 & 2 & 8 & 14 & 4 & 10 & 0 & 6 & 12 & 2 & 8 & 14 & 4 & 10 \\
0 & 7 & 14 & 5 & 12 & 3 & 10 & 1 & 8 & 15 & 6 & 13 & 4 & 11 & 2 & 9 \\
0 & 8 & 0 & 8 & 0 & 8 & 0 & 8 & 0 & 8 & 0 & 8 & 0 & 8 & 0 & 8 \\
0 & 9 & 2 & 11 & 4 & 13 & 6 & 15 & 8 & 1 & 10 & 3 & 12 & 5 & 14 & 7 \\
0 & 10 & 4 & 14 & 8 & 2 & 12 & 6 & 0 & 10 & 4 & 14 & 8 & 2 & 12 & 6 \\
0 & 11 & 6 & 1 & 12 & 7 & 2 & 13 & 8 & 3 & 14 & 9 & 4 & 15 & 10 & 5 \\
0 & 12 & 8 & 4 & 0 & 12 & 8 & 4 & 0 & 12 & 8 & 4 & 0 & 12 & 8 & 4 \\
0 & 13 & 10 & 7 & 4 & 1 & 14 & 11 & 8 & 5 & 2 & 15 & 12 & 9 & 6 & 3 \\
0 & 14 & 12 & 10 & 8 & 6 & 4 & 2 & 0 & 14 & 12 & 10 & 8 & 6 & 4 & 2 \\
0 & 15 & 14 & 13 & 12 & 11 & 10 & 9 & 8 & 7 & 6 & 5 & 4 & 3 & 2 & 1
\end{bmatrix} \begin{bmatrix} x_0 \\ x_1 \\ x_2 \\ x_3 \\ x_4 \\ x_5 \\ x_6 \\ x_7 \\ x_8 \\ x_9 \\ x_{10} \\ x_{11} \\ x_{12} \\ x_{13} \\ x_{14} \\ x_{15} \end{bmatrix}
$$

(a) NORMAL-ORDER DFT FOR N = 16

$$
\begin{bmatrix} s_0 \\ s_8 \\ s_4 \\ s_{12} \\ s_2 \\ s_{10} \\ s_6 \\ s_{14} \\ \hline s_1 \\ s_9 \\ s_5 \\ s_{13} \\ s_3 \\ s_{11} \\ s_7 \\ s_{15} \end{bmatrix} = \left[\begin{array}{cccccccc|cccccccc}
0 & 0 & 0 & 0 & 0 & 0 & 0 & 0 & 0 & 0 & 0 & 0 & 0 & 0 & 0 & 0 \\
0 & 8 & 0 & 8 & 0 & 8 & 0 & 8 & 0 & 8 & 0 & 8 & 0 & 8 & 0 & 8 \\
0 & 4 & 8 & 12 & 0 & 4 & 8 & 12 & 0 & 4 & 8 & 12 & 0 & 4 & 8 & 12 \\
0 & 12 & 8 & 4 & 0 & 12 & 8 & 4 & 0 & 12 & 8 & 4 & 0 & 12 & 8 & 4 \\
0 & 2 & 4 & 6 & 8 & 10 & 12 & 14 & 0 & 2 & 4 & 6 & 8 & 10 & 12 & 14 \\
0 & 10 & 4 & 14 & 8 & 2 & 12 & 6 & 0 & 10 & 4 & 14 & 8 & 2 & 12 & 6 \\
0 & 6 & 12 & 2 & 8 & 14 & 4 & 10 & 0 & 6 & 12 & 2 & 8 & 14 & 4 & 10 \\
0 & 14 & 12 & 10 & 8 & 6 & 4 & 2 & 0 & 14 & 12 & 10 & 8 & 6 & 4 & 2 \\
\hline
0 & 1 & 2 & 3 & 4 & 5 & 6 & 7 & 8 & 9 & 10 & 11 & 12 & 13 & 14 & 15 \\
0 & 9 & 2 & 11 & 4 & 13 & 6 & 15 & 8 & 1 & 10 & 3 & 12 & 5 & 14 & 7 \\
0 & 5 & 10 & 15 & 4 & 9 & 14 & 3 & 8 & 13 & 2 & 7 & 12 & 1 & 6 & 11 \\
0 & 13 & 10 & 7 & 4 & 1 & 14 & 11 & 8 & 5 & 2 & 15 & 12 & 9 & 6 & 3 \\
0 & 3 & 6 & 9 & 12 & 15 & 2 & 5 & 8 & 11 & 14 & 1 & 4 & 7 & 10 & 13 \\
0 & 11 & 6 & 1 & 12 & 7 & 2 & 13 & 8 & 3 & 14 & 9 & 4 & 15 & 10 & 5 \\
0 & 7 & 14 & 5 & 12 & 3 & 10 & 1 & 8 & 15 & 6 & 13 & 4 & 11 & 2 & 9 \\
0 & 15 & 14 & 13 & 12 & 11 & 10 & 9 & 8 & 7 & 6 & 5 & 4 & 3 & 2 & 1
\end{array}\right] \begin{bmatrix} x_0 \\ x_1 \\ x_2 \\ x_3 \\ x_4 \\ x_5 \\ x_6 \\ x_7 \\ \hline x_8 \\ x_9 \\ x_{10} \\ x_{11} \\ x_{12} \\ x_{13} \\ x_{14} \\ x_{15} \end{bmatrix}
$$

(b) SHUFFLED-ORDER DFT FOR N = 16, OBTAINED BY PERMUTING THE ROWS OF THE MATRIX IN (a).

Fig. 3. Discrete Fourier transforms for $N = 16$ using integer exponents as symbolic representations of matrix elements

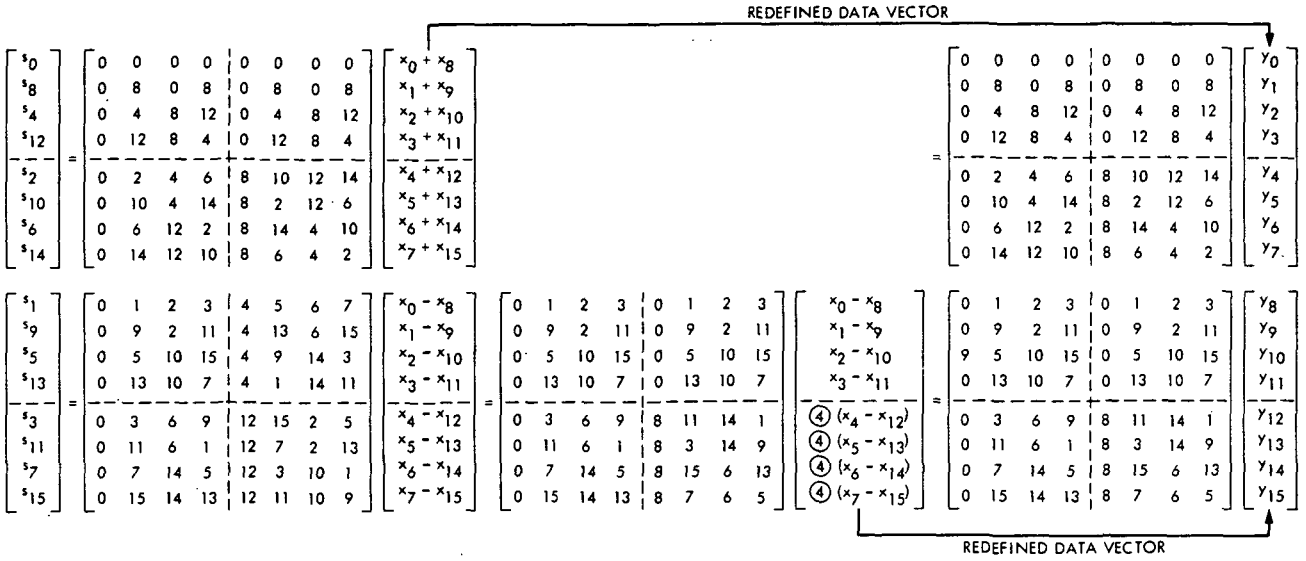


Fig. 4. First step of reduction of DFT of Fig. 3

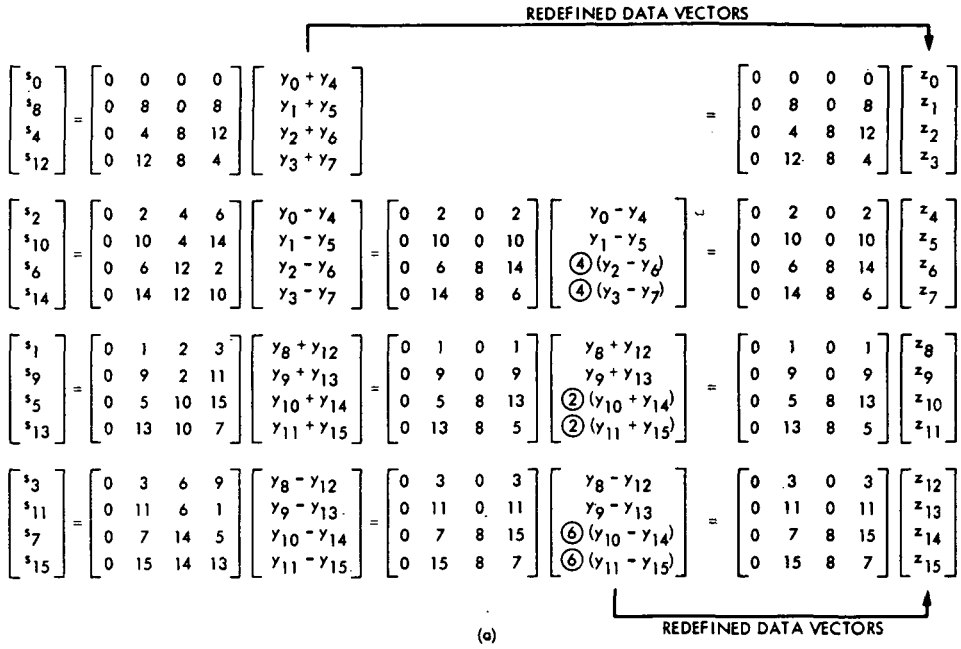


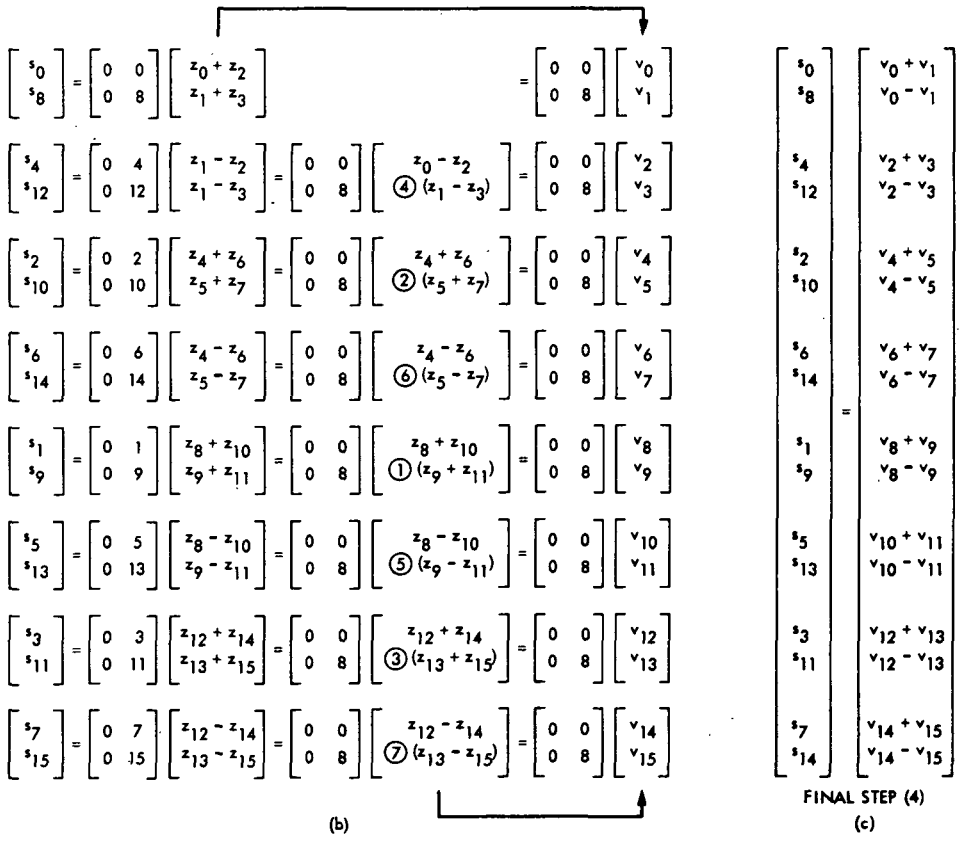


Fig. 5. Steps 2, 3, and 4 of reduction of DFT

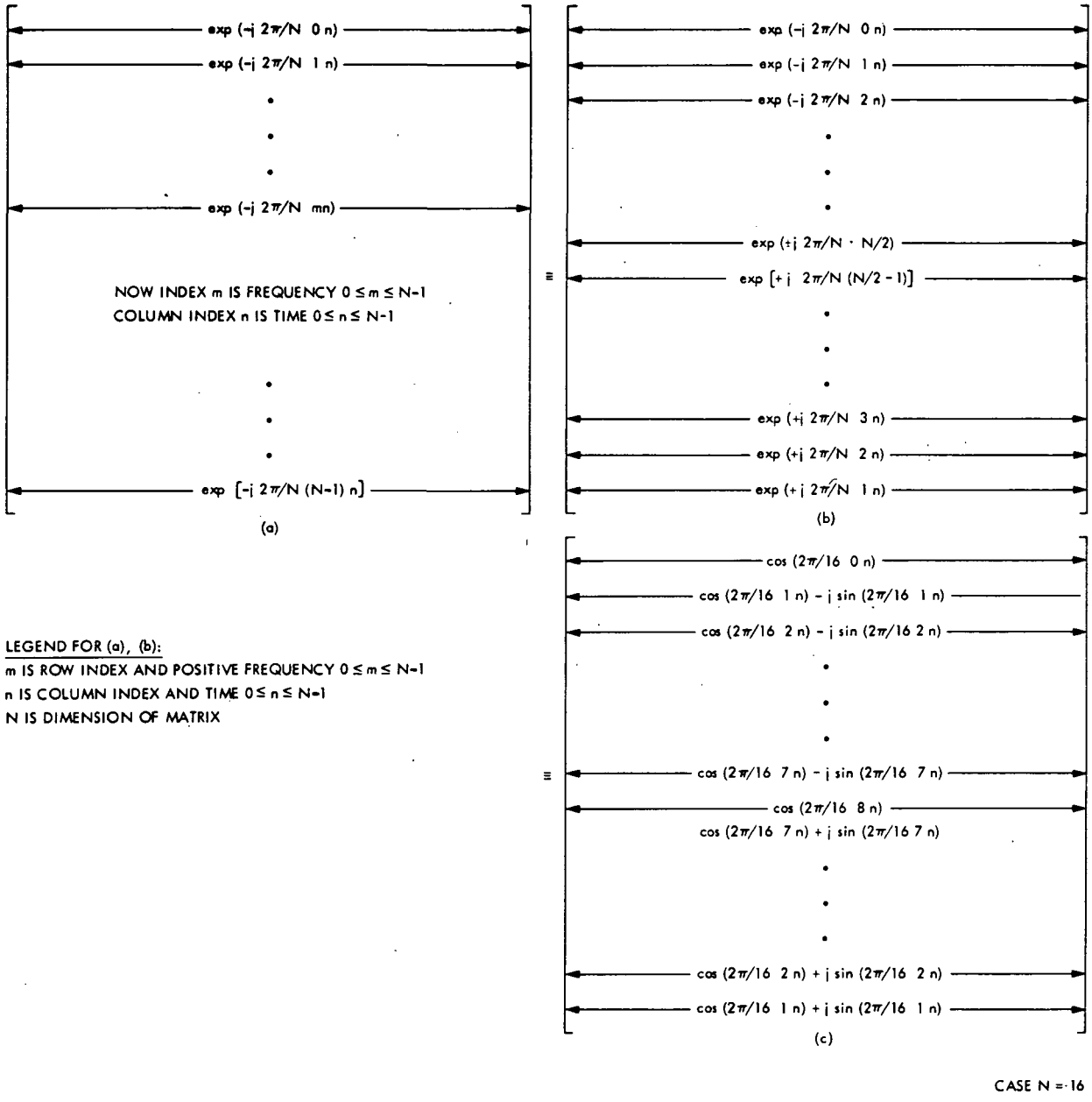


Fig. 6. Reduction of DFT matrix to sine-cosine form

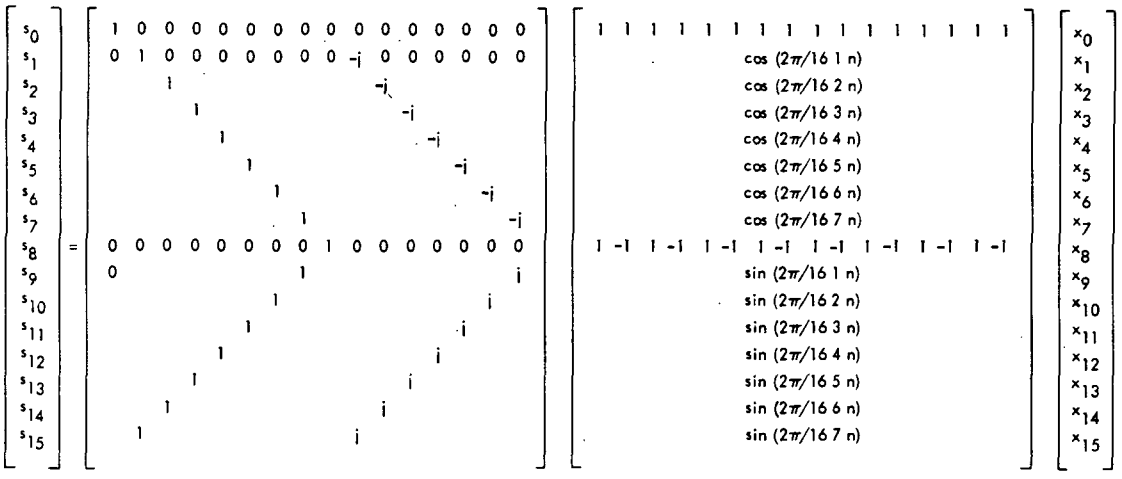


Fig. 7. Representation of DFT in terms of real DFA matrix

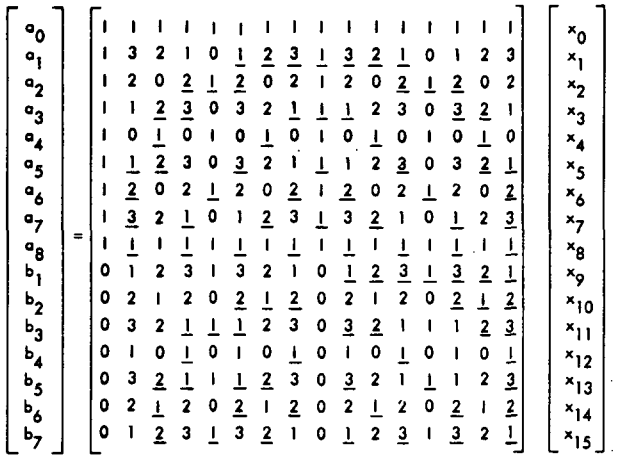


(a) NORMAL-ORDER DFA

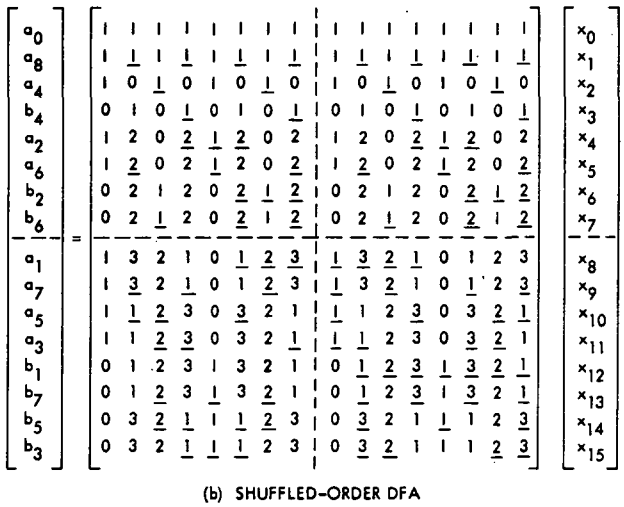


(b) SHUFFLED-ORDER DFA

**Fig. 8. Discrete Fourier analysis (DFA) for $N = 16$ using integer code for quadrantal sine tabular values**

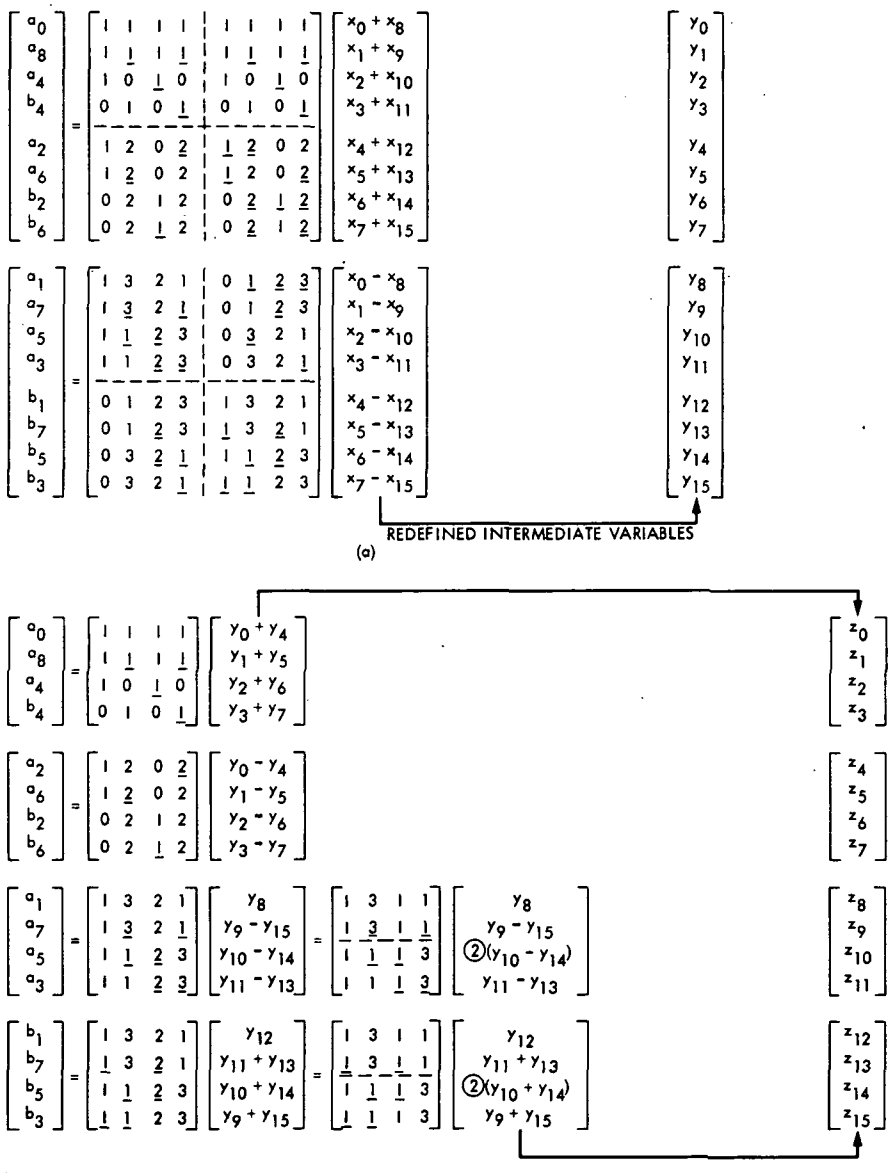


**Fig. 9. First and second reduction steps of the DFA for $N \approx 16$**

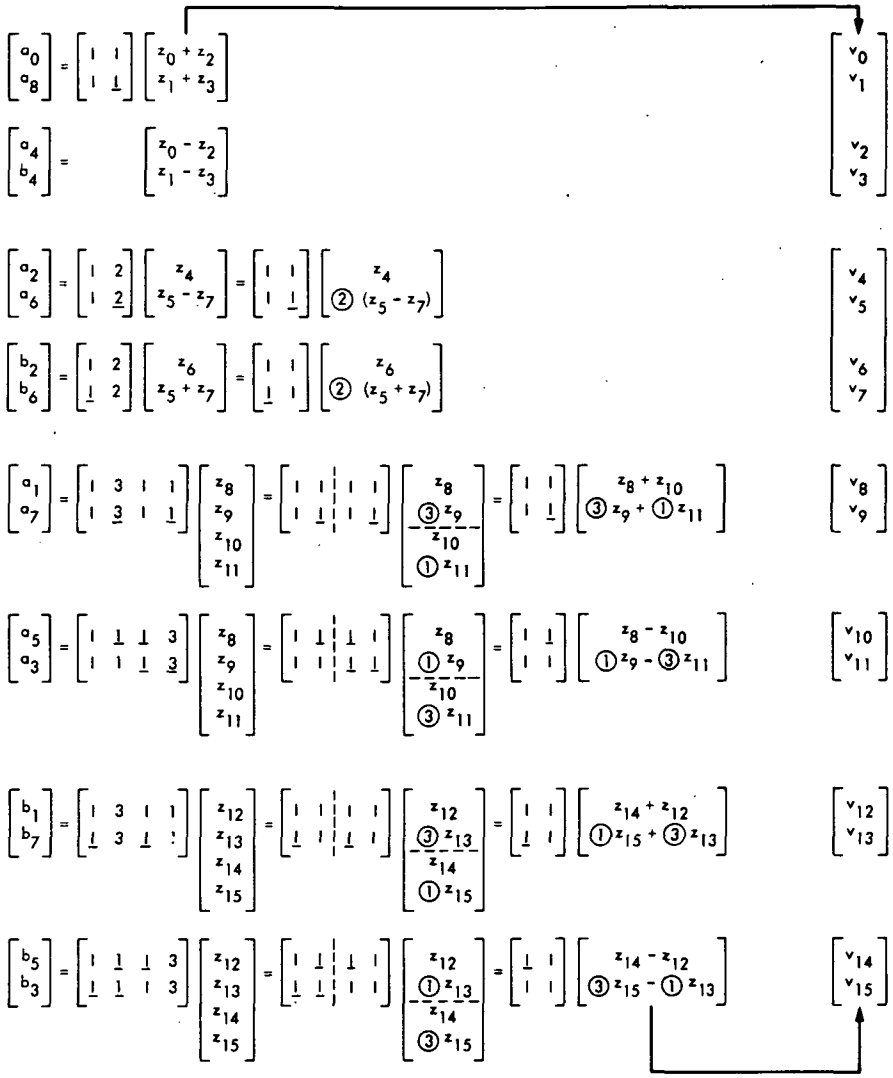

Fig. 10. Third reduction step of the DFA for $N = 16$

# An Automated Tracking System for the ARIES Antenna

M. W. Sievers
Communications Systems Research Section

*A miniprocessor-based tracking system has been developed for the Astronomical Radio Interferometric Earth Surveying (ARIES) antenna. The system is a servo loop in which tracking errors and correction commands are calculated in software.*

## I. Introduction

An automated tracking system based on a Modcomp II miniprocessor has been developed for the ARIES antenna. The miniprocessor executes a real-time program that calculates antenna position as a function of time and source coordinates entered at a teletype. An error is determined by subtracting the calculated antenna position from the actual position as determined by sensors on the antenna. The error is translated into rate commands, which are sent to the antenna azimuth and elevation motors. An operator may communicate with the program via sense switches and teletype input/output.

## II. System Hardware

Figure 1 is a block diagram of the ARIES tracking system. The Universal Time Generator produces 30-bit binary-coded decimal (BCD) Universal Time (UT) and two pulse trains having rates of one and sixty pulses per second. The 1-pulse/s pulses are synchronous with UT, and the 60-pulse/s pulses are synchronous with the 1-pulse/s pulses. These pulses are used as interrupts to drive the real-time tracking program.

The ARIES tracking program is executed by a 16-bit Modcomp II miniprocessor. The Modcomp is configured with 32 k words of memory, a dual digital-to-analog converter (DAC), a teletype, a high-speed paper tape reader, eight Modcomp 1121 digital input ports and five Modcomp 1131 digital output ports.

Modcomp's 1121 input port is a 16-bit parallel transistor-transistor logic (TTL) device. It gates data at its inputs to an internal data bus when the Modcomp executes an input data instruction addressing it. A Modcomp 1131 output port is also a 16-bit parallel TTL device. It will strobe data into an output register when the Modcomp executes a data output instruction addressing it. Data in an 1131 output register will not change until they are over-written by another output data instruction. Neither device is capable of handshaking, and therefore

input-output (I-O) synchronization is left to interrupts and software manipulation of I-O ports. In this system, UT input is synchronized by the 1-pulse/s interrupt, and control of the Angle Encoder Interface (AEI), discussed below, requires an 1121 for input and 1131 for control.

A dual DAC develops analog rate signals for the azimuth and elevation motors. Each DAC is a 12-bit device capable of producing voltages in the range ±10 V dc. The DAC pair has a single device address; selection of a particular DAC is via a bit in the data word sent to the pair. In the 16-bit data word sent the pair, bit 0 (the most significant bit) determines the sign of the output voltage, and bit 1 selects the DAC. Bits 5 through 15 contain the digital information to be converted to an analog voltage, and bits 2, 3 and 4 are ignored.

Output voltages developed by the DACs are amplified by operational amplifiers (op amps) and applied to the azimuth and elevation motors. There are no integrators in the system, so it is not necessary for the tracking program to remember the previous commands it sent to the antenna. Antenna motors are geared such that peak output from a DAC will produce a maximum velocity of 0.6 degree/second in either azimuth or elevation.

Antenna position is sensed by four transducers mounted on the antenna. Two of these transducers generate analog voltage equivalents of azimuth and elevation position in fractions of a circle. The remaining transducers produce two switch closures, indicating that the antenna is sensed to be in either the left or right wrap-up region. The switch closures are input directly into an 1121 input port for interrogation by the tracking program.

An NPL Angle Encoder converts the analog position voltages into 18-bit binary azimuth words and 17-bit binary elevation words. Decimal equivalents of binary positions are calculated in the angle encoder and used for display purposes. Analog position data are continuously sampled by the angle encoder, and the binary and equivalent decimal results of analog to digital conversions are stored in four accumulators. Data in an accumulator may be transferred to one of four latching output registers by applying a negative INTERROGATE pulse to the register. INTERROGATE signals are angle encoder inputs; there is one INTERROGATE line for each of the output registers. Data are held constant in an output register until the receipt of the next INTERROGATE pulse.

An angle encoder interface (AEI) was designed to convert 18-bit azimuth words and 17-bit elevation words into a Modcomp 1121 16-bit format. The interface is driven by commands sent via a Modcomp 1131 output port. These commands control the selection of portions of the angle encoder words that are connected to an 1121 input port. Additionally, one bit in the command word is buffered in the interface and connected to the azimuth and elevation INTERROGATE lines. The bit is toggled in software to produce a negative pulse as required by the angle encoder.

Figure 2 illustrates the AEI. The interface is composed of eight 74153 dual four-line to one-line data selectors. The inputs of these gates are connected directly to the binary output registers of the angle encoder. Data selection is determined by two bits in the Modcomp 1131 output port. Note that the AEI separates each angle encoder word into two left-justified 16-bit words with trailing zeros inserted.

## III. Software System

The real-time ARIES tracking program was written in Modcomp's Fortran IV using inline assembly code as necessary for driving non-standard interfaces. The paper tape environment of the ARIES Modcomp necessitated developing all software on a disk environment system and transferring the linked object to paper tape. The linked object tape is not stand-alone executable because Fortran calls system services which are expected to be core resident. For this reason an operating system tape must be loaded prior to the ARIES tracking program. The tracking program is loaded and executed via the $EXECUTE command.

The ARIES program is interrupt driven, i.e., most program action is in response to an interrupt. The 1-pulse/s interrupt sets a flag that is tested in the background, and establishes parameters for the 60-pulse/s routine, which is given higher priority than the 1-pulse/s interrupt. In response to a 60-pulse/s interrupt, the program examines current antenna position and sends commands to the antenna. The time when no interrupts are being processed (background) is used for operator communication, diagnostic routines, and calculation of instructed antenna position. The flag set by the 1-pulse/s interrupt routine informs the background that it must calculate a new instructed position.

Calculation of instructed position in the background is necessitated by the non-re-entrancy of Modcomp's Fortran. A decision was made to avoid re-entrancy conflicts and keep the ARIES program a single task rather than to divide the program into several separate tasks.

Although the Modcomp operating system is multi-tasking, the additional core requirements of multiple tasks are prohibitively large for the ARIES configuration. The ARIES Modcomp, being a paper tape system, cannot support real-time program swapping in and out of core; thus the decision to have a single task.

## IV. Program Modes

The ARIES program operates in two basic modes. In the tracking mode, the operator inputs the right ascension (RA) and declination (DEC) of a source at the teletype. Program action is to slew the antenna to the azimuth and elevation calculated as a function of time and source coordinates subject to wrap-up and elevation limitations (elevation must be in the range 6.0 deg $\leq$ EL $\leq$ 90 deg). The source is then tracked at the sidereal rate. An on-source message is typed at the teletype when the antenna is positioned within 0.05 degrees of the instructed position. The program endeavors to track with zero error and will inform the operator when the actual antenna position is outside of the 0.05-degree tolerance. Tracking continues until the antenna is stopped or until a new source is entered (see discussion below).

A subset of the tracking mode permits the operator to select a scan procedure. A scan is executed by positioning the antenna a specified offset in azimuth and/or elevation from the source. At a given time, the antenna is swept past the source at a specified rate. Offsets, rates, and start scan times are inputs supplied by the operator.

A local or non-tracking mode is provided in which the operator specifies coordinates in azimuth (AZ) and elevation (EL). In this mode, the antenna is moved to the instructed AZ and EL and stopped. This mode may be used to stow the antenna or position it for maintenance purposes.

An operator may enter new source coordinates, a scan request and scan parameters, position offsets, or request a diagnostic test by a combination of sense switch settings and teletype input-output. Sense switches are used as break points in the program to initiate the input-output routines desired by the operator. Diagnostics are included with the ARIES program that relate to hardware peculiar to the pointing system, e.g., a UT diagnostic, and an angle encoder diagnostic.

Several means have been provided to stop the antenna. Panic stops may be performed via a sense switch. This switch is tested in the 60-pulse/s routine and when set will cause a zero-rate command to be sent to the antenna motors. Antenna motion resumes when this switch is reset. Additionally, each time the operator sets the sense switch signaling the desire to enter new source coordinates, the antenna is stopped. Antenna motion resumes when a new source has been entered. Completion of a scan will also stop the antenna and requires that the operator enter a new source. Finally, should the coordinates of a newly entered source correspond to an elevation below the horizon, the source is checked to determine whether or not it is rising. A rising source will be followed in azimuth and tracked when it appears above the horizon. If the source is determined to be setting, the antenna is stopped and a message typed at the teletype. The operator must then enter a new source.

## V. Program Structure

Figure 3 is a simplified flowchart of the ARIES background routine. Several subroutines are called to initialize interrupts and constants, and to check for operator input-output requests. At several points, the background checks a 1-pulse/s flag. This flag is set by the 1-pulse/s interrupt routine to indicate to the background that it must calculate new antenna positions. Variable ISTOP is used as a flag to indicate that a source has been entered. When ISTOP is positive, the 60-pulse/s interrupt routine may move the antenna. Variables ION and ISLEW are used in a software flip-flop to indicate when the antenna is on or off source. When the antenna is off source, ISLEW is set to 1 and ION to 0. The flip-flop is changed when the antenna has moved on source. On and off source is determined by parameters IAZON and IELON, which are set in the 60-pulse/s routine.

Details of the 1-pulse/s routine, ONEPPS, are shown in Figure 4. This routine is entered either by a 1-pulse/s interrupt or by a call from the background routine to calculate new positions. ONEPPS maintains two sets of position parameters. A "current" set describes the antenna position (AZ,EL) and rates (DAZ,DEL) during the current second. A "next" set describes antenna motion and position during the next second (AZN, ELN,DAZN,DELN). "Next" values are calculated when ONEPPS is called from the background routine. When entered by an interrupt, ONEPPS sets the "next values" equal to the "current" values and sets the 1-pulse/s flag.

The 60-pulse/s routine is illustrated in Figure 5. This routine begins by checking ISTOP. If ISTOP is negative, zero rate commands are sent to the antenna. For ISTOP positive, PPS60 reads the actual antenna position and wrap-up conditions. DAZ and DEL are added to AZ and EL to update the instructed position. Commands AZCOM

and ELCOM are determined by subtracting the instructed positions from the actual positions. The commands are scaled and AZCOM is adjusted as necessary to compensate for wrap-up conditions. For AZCOM and/or ELCOM less than 0.05 degrees, IAZON and/or IELON are set to 1. Subroutine IFIX is called to change AZCOM and ELCOM to IAZCOM and IELCOM. Although changing floating point numbers to integers is a FORTRAN function, its use would cause a re-entrancy problem. IFIX was written in assembly language and called by a branch and link (BLM) instruction. Finally, IAZCOM and IELCOM are output to the dual DACs.

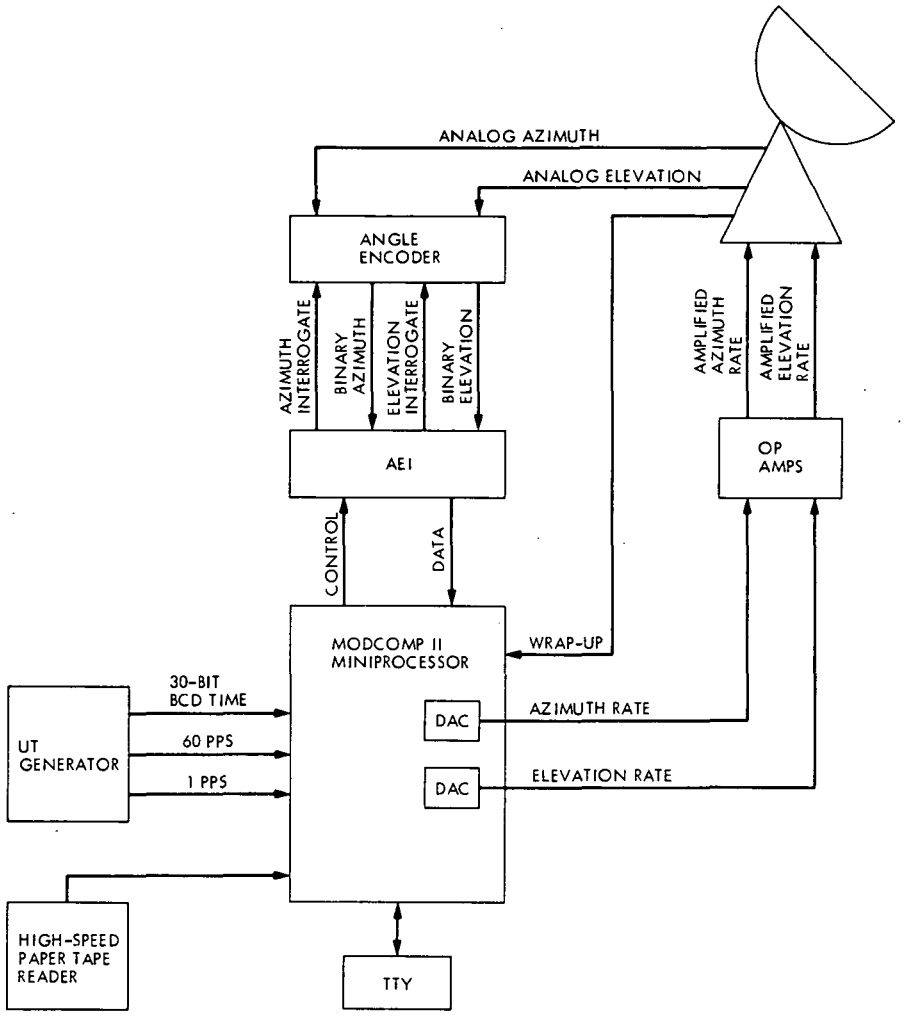


Fig. 1. ARIES automated tracking system

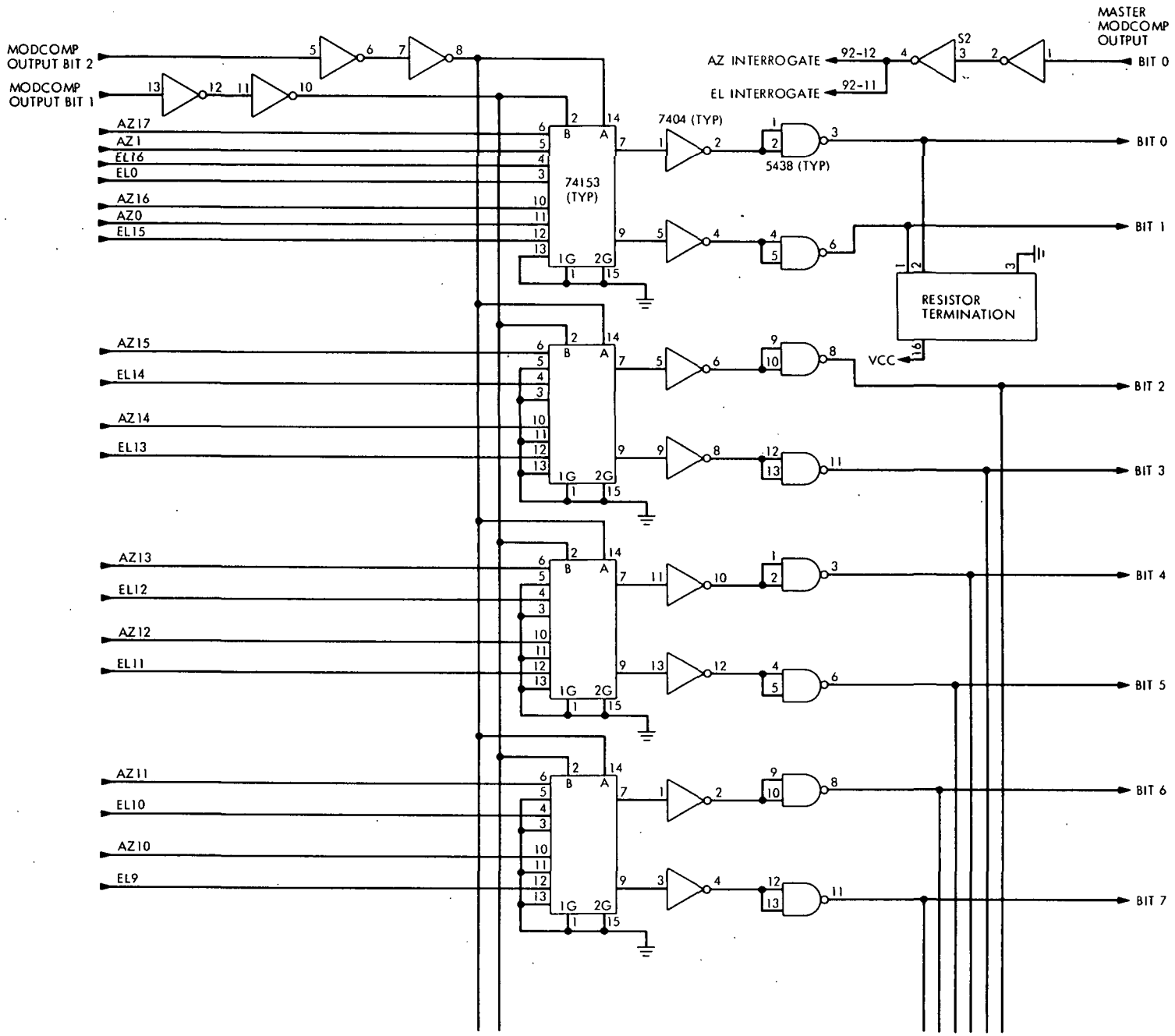
MODCOMP OUTPUT BIT 2
MODCOMP OUTPUT BIT 1
AZ17
AZ1
EL16
EL0
AZ16
AZ0
EL15
AZ15
EL14
AZ14
EL13
AZ13
EL12
AZ12
EL11
AZ11
EL10
AZ10
EL9
74153 (TYP)
7404 (TYP)
5438 (TYP)
AZ INTERROGATE
EL INTERROGATE
92-12
92-11
S2
MASTER MODCOMP OUTPUT
BIT 0
BIT 0
BIT 1
RESISTOR TERMINATION
VCC
BIT 2
BIT 3
BIT 4
BIT 5
BIT 6
BIT 7

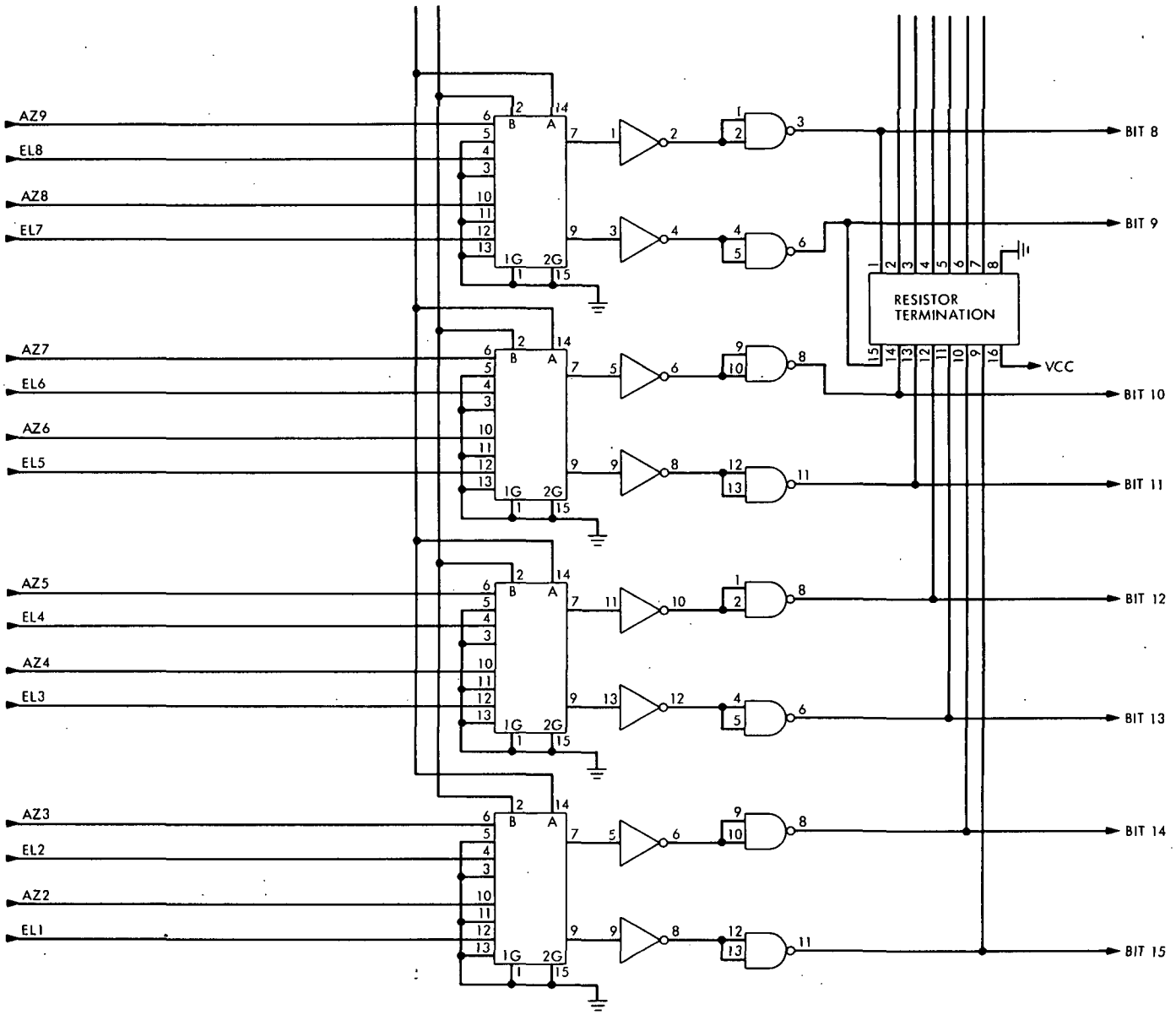


Fig. 2. Angle encoder interface

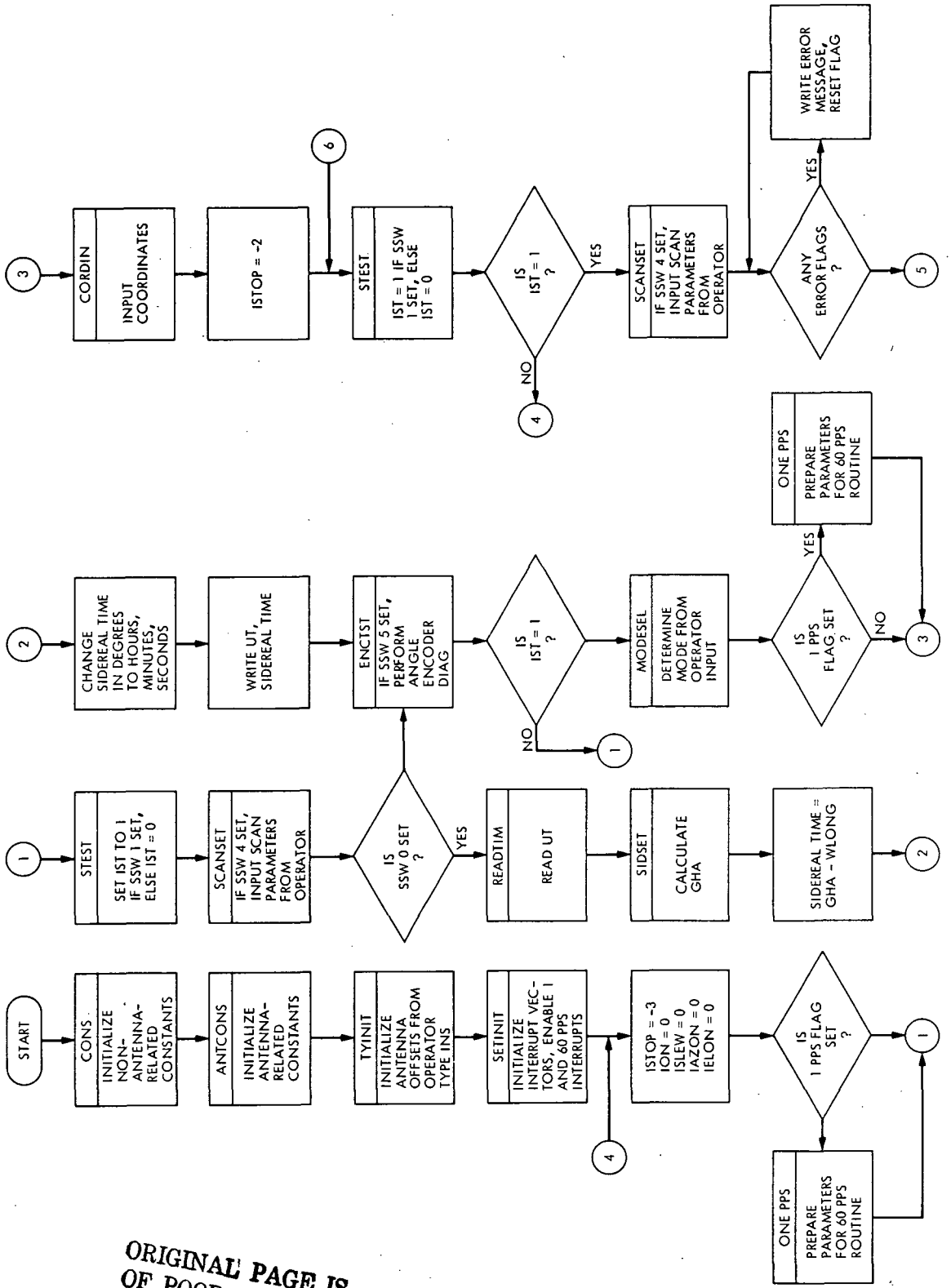


Fig. 3. Background routine

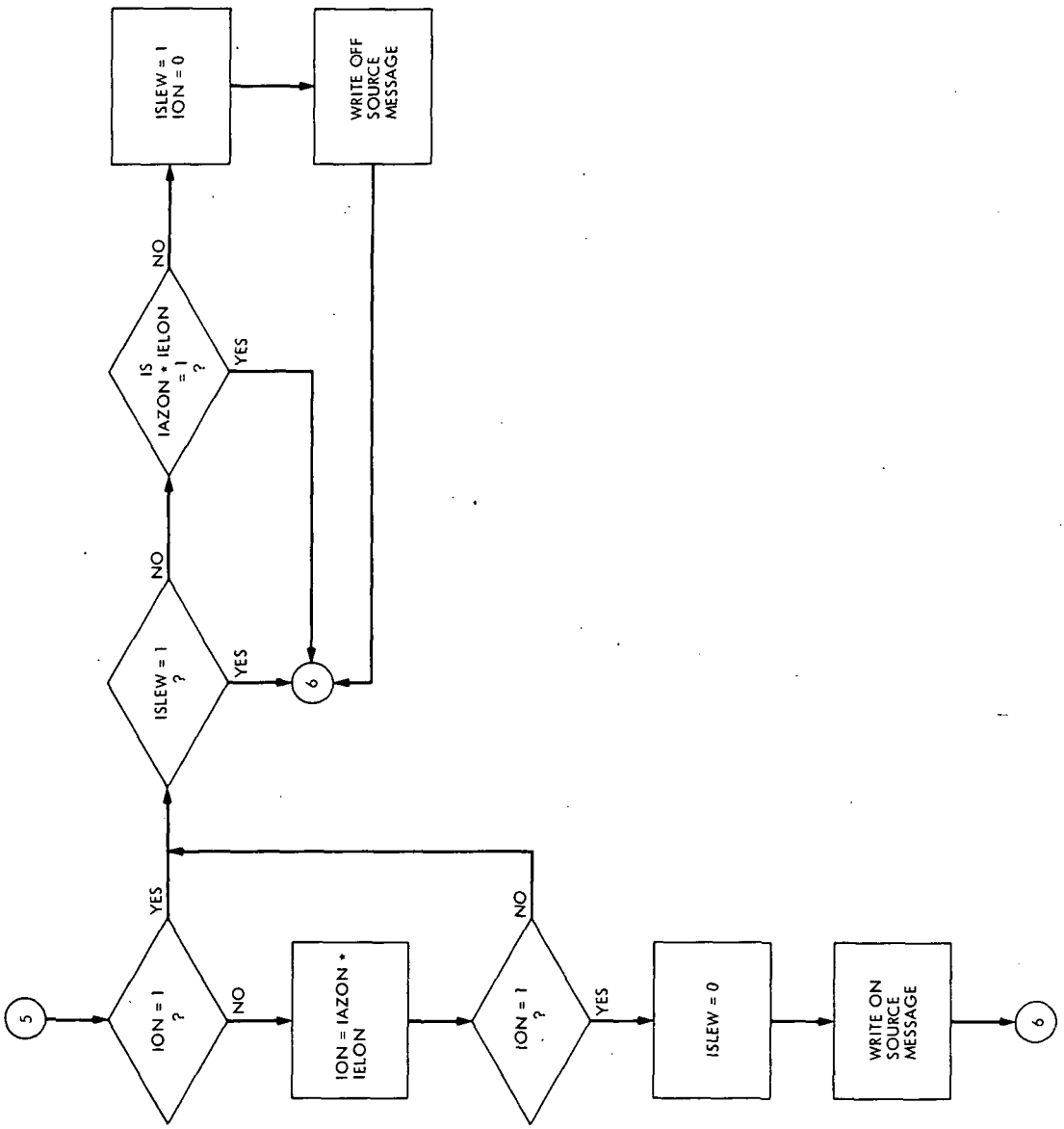




Fig. 3 (contd)

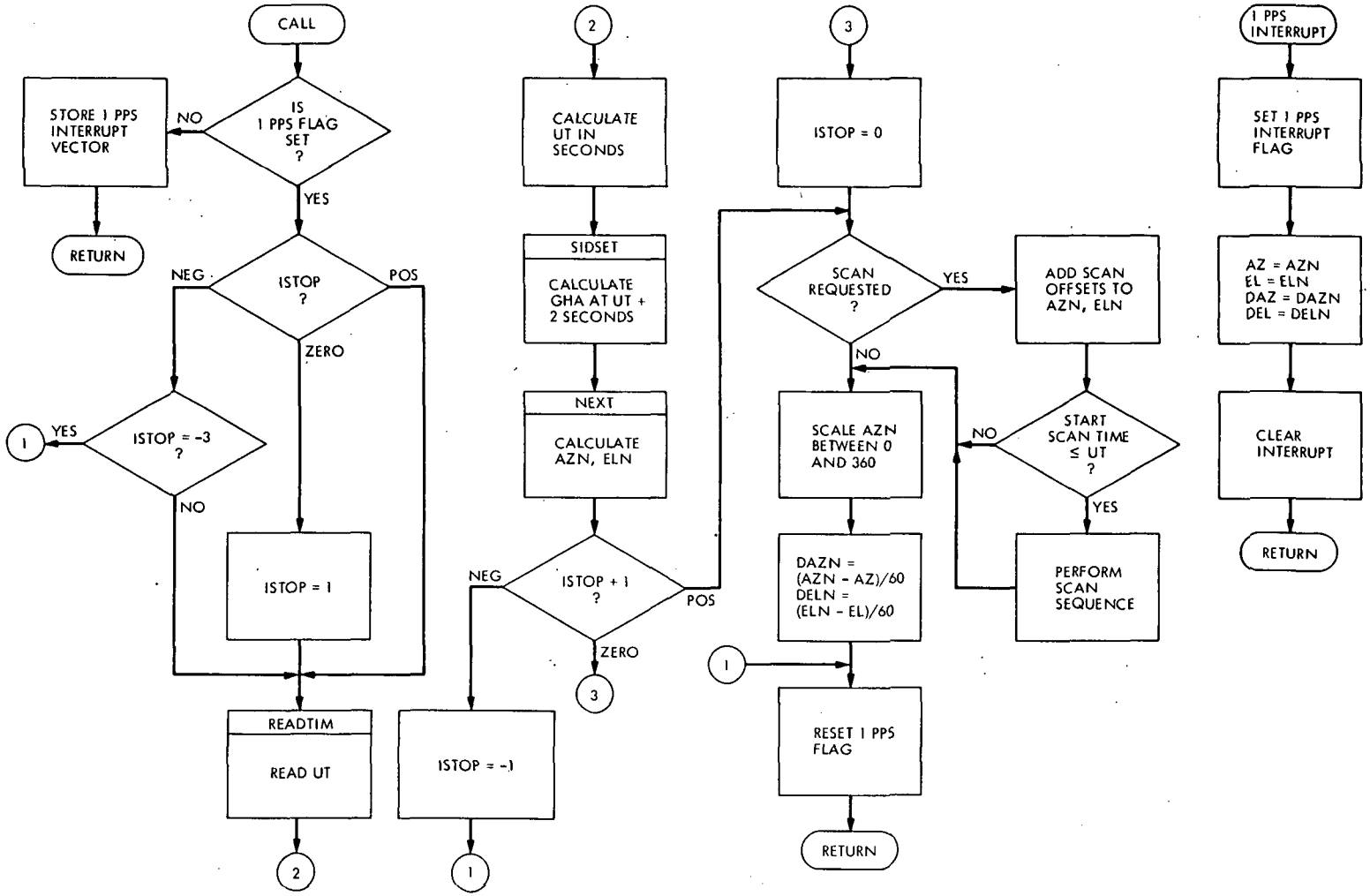


Fig. 4. One-PPS routine

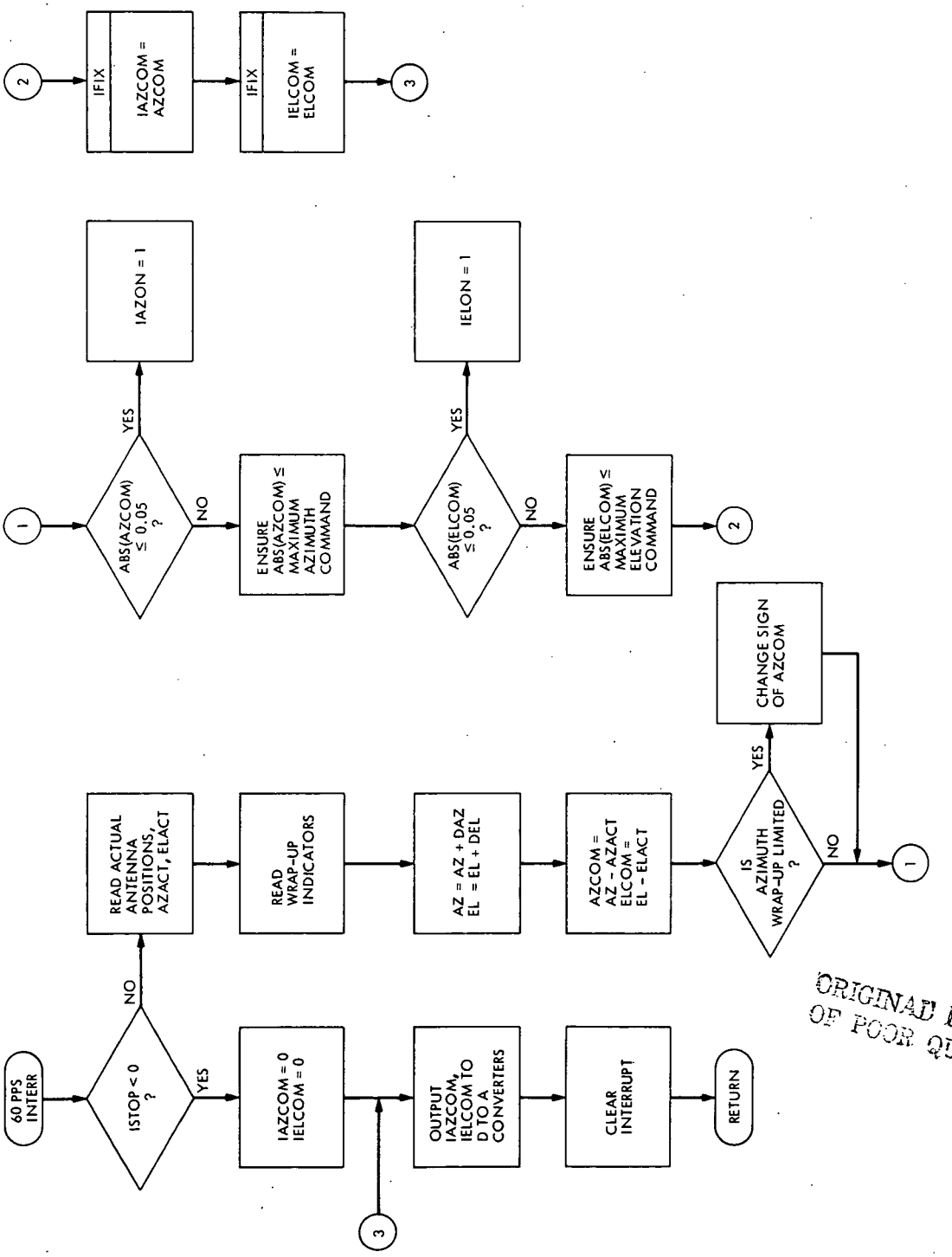


Fig. 5. Sixty-PPS routine

# Appendix

Calculation of azimuth and elevation from right ascension and declination requires four subroutines. Subroutine READTIM reads the current UT from the UT generator. The program calculates "next" AZ and EL values for two seconds from the current time. Thus, when the 1-pulse/s interrupt occurs, e.g., at T(0), the values of AZN and ELN which are set equal to AZ and EL were calculated at T(-2), and the values of AZN and ELN calculated at T(0) will be used as the current values at T(2). Subroutine SIDSET, which calculates the Greenwich hour angle (GHA), therefore adds two seconds to the time read by READTIM. The formula used to calculate GHA is GHA = (IDAYS-1) * SOLSID + GHO + TIME* SIDRAT, where TIME is UT in seconds, IDAYS is the day number from January 1, SOLSID is the solar to sidereal constant (= 0.98564540 deg/day), GHO is the Greenwich hour angle on January 1 (= 100.02578 deg for 1975), and SIDRAT is the sidereal rate (= 0.004178074622 deg/sec).

After determining the value of GHA in SIDSET, subroutine NEXT is invoked. NEXT computes the local hour angle (HA) from GHA, RA, and the west longitude (WLONG) of the antenna position; HA = GHA - WLONG - RA. Subroutine CORCON (not shown) is called by subroutine NEXT to perform the coordinate conversions. CORCON uses the following equations:

$$HAR = HA * DEGRAD$$
$$COSH = COS(HAR)$$
$$SINH = SIN(HAR)$$
$$DECR = DEC * DEGRAD$$
$$COSD = COS(DECR)$$
$$SIND = SIN(DECR)$$
$$X1 = -COSD * SINH$$
$$X2 = SIND * COSL - COST * SINL * COSH$$
$$X3 = SIND * SINL + COSD * COSL * COSH$$
$$X4 = SQRT(X1 * X1 + X2 * X2)$$
$$AZN = ATAN2(X1, X2) * RADDEG$$
$$ELN = ATAN2(X3, X4) * RADDEG$$

where

$$DEGA = \pi/180$$
$$RADDEG = 180/\pi$$
$$COSL = COS(ALAT)$$
$$SINL = SIN(ALAT)$$
$$ALAT = LAT * DEGRAD$$

and LAT is the latitude of the antenna position.

CORCON returns AZN, and ELN to NEXT, which then scales AZN to fall in the range $0 \leq AZN \leq 360$. Subroutine REFR (not shown) is then called to compute the refraction correction to be added to ELN as follows:

$$ZD = 90.0 - ELN$$
$$ANUM = ((P3 * Z1) + P2) * ZD + P1) * ZD + P0$$
$$DEN = (Q2 * ZD + Q1) * ZD + Q0$$
$$ELN = ELN + RCON * ANUM/DEN$$

where

$$P0 = 0.00010076196$$
$$P1 = 0.00025124078$$
$$P2 = -0.44557132 \times 10^{-5}$$
$$P3 = 0.18838847 \times 10^{-5}$$
$$Q0 = 1.0$$
$$Q1 = -0.022050589$$
$$Q2 = 0.00012174320$$
$$RCON = P/760.0$$
$$P = 657.0$$

# An INTEL 8080 Cross Assembler for the Modcomp II Minicomputer

M. W. Sievers
Communications Systems Research Section

*The flexibility of Modcomp's macro assembler has been exploited to implement an INTEL 8080 cross assembler. This simple implementation is very powerful, allowing, for example, macro definitions, and declaration of common and external labels. The cross assembler may be executed on any Modcomp II minicomputer.*

## I. Introduction

A macro assembler is a special type of assembler that permits the definition of prototype constructs or macros. Each macro prototype is labeled and may consist of other macro references, argument paraforms and/or assembly language code. A macro is referenced by its label; each reference is usually followed by an argument list. During pass 1 of the macro assembler, macro prototypes are placed in a prototype table. Each time the macro assembler recognizes a macro label in the op code field of a source statement, it fetches the prototype for that macro from the table and replaces argument paraforms with arguments from the argument list. The resultant construct is then inserted into the source after the statement in which it was referenced. After completing pass 1, the usual second assembler pass is invoked which produces a complete binary object file.

The flexibility of macro assemblers can be exploited to generate cross assemblers for virtually any machine with minimal effort. A cross assembler can be implemented by defining a set of macro prototypes whose labels correspond to the mneumonics in the target assembly language. Once these prototypes have been defined, assembly directives for the target machine may be assembled by the host machine's macro assembler.

Binary object produced by the cross assembler described above is not necessarily directly transferable to the target machine. For example, differences may arise in word length or byte ordering. These differences can be resolved by a loader routine. The complexity of the loader naturally depends on the complexity of the differences which it must resolve. It can be expected however, that a loader routine will in general be far simpler to write than an assembler that generates directly transferable object.

This paper will describe an INTEL 8080 cross assembler and loader that executes on a Modcomp II minicomputer. The cross assembler is very flexible

allowing, for example, the definition of macro prototypes, and the declaration of common and external labels. If desired by the user, the loader can write binary output onto paper or magnetic tape for easy transport to an 8080 microcomputer.

## II. 8080 Assembler

An 8080 cross assembler has been implemented as described above by defining a collection of macro prototypes written in Modcomp's macro assembly language (ref. section VIII of Modcomp's Assembler Reference Manual, TM16094). These macros are labeled with 8080 mneumonics and collectively stored on disk under the label ASM8080. ASM8080 macros are inserted into an 8080 source program at assembly time via the INSERT directive (ref. section IV, TM16094, for a discussion of the INSERT directive). Once ASM8080 has been inserted, Modcomp's macro assembler can assemble 8080 source code.

Four macro prototypes found in ASM8080 are shown below. The first three macros define, respectively, one-, two-, and three-byte 8080 instructions. The fourth macro is a special address macro which is referenced by triple byte instruction macros (see below).

```
*SINGLE BYTE MACRO
HLT MAC
    DFC #76
    EMP
*DOUBLE BYTE MACRO
IN MAC
    DFC #DB
    DFC %1
    EMP
*TRIPLE BYTE MACRO
CALL MAC
    DFC #CD
    ADDR %1,%2
    EMP
*SPECIAL ADDRESS MACRO
ADDR MAC
    IFM %2,A
    DFC %1,%2
    EXM
A AOP
    DFC #FFFF, %1
    EMP
```

The single byte macro above is typical of all single byte 8080 instruction macros. It consists of a label, in this case HLT (HALT), which corresponds to an 8080 mneumonic, and a DFC (DEFINE CONSTANT) statement. The DFC defines a constant equal to the value of the operation code for the mneumonic.

The macro for the IN (INPUT) instruction shown above is a typical double byte instruction macro. Two DFC statements define, respectively, the operation code for the IN mneumonic and an argument paraform for its operand. As mentioned previously, the argument paraform is replaced by an actual argument at assembly time.

The CALL (CALL SUBROUTINE) macro is a typical three-byte instruction macro. In addition to defining an operation code constant, the address macro ADDR is referenced. ADDR examines the address field of the 8080 source statement. If the address field contains two address bytes, ADDR creates a DFC that defines the values of these bytes. If the address field contains a single address word, ADDR creates a DFC which defines a hexadecimal FFFF and the address word. The hexadecimal FFFF is a flag recognized by the loader which signals it to exchange the bytes in the address.

The 8080 cross assembler is a subset of Modcomp's macro assembler and as such contains the macro assembler's inherent flexibility and limitations. It is permissible therefore to use any of the macro assembler's pseudo operations, such as ORG (ORIGIN), COM (COMMON), RES (RESERVE), DFC (DEFINE CONSTANT), EXT (EXTERNAL), and INT (INTERNAL) to specify program origin, define blocks of common, reserve areas in core and prepare subroutines for subsequent storage in a subroutine library. The reader should refer to Section IV of Modcomp's Assembler Reference Manual for a discussion of these pseudo directives and rules governing their use. Note that Modcomp macro assembler restrictions require that the 8080 source format resemble Figure 1.

A sample cross assembly is shown in Figure 2. As already mentioned, 8080 assembly source statements are constrained to conform to all rules and limitations governing writing in Modcomp's macro assembly language. In addition to these requirements, there are the following nuances particular to this 8080 cross assembler:

(1) When using 8080 assembly directives that require a register pair, it is necessary to include both register names in the operand field. For example, PUSH B is not acceptable; PUSH BC must be used.

(2) A special macro called REGDEF is included in the ASM8080 prototype collection. This macro is used to define the value of 8080 registers and register pairs via EQUATE statements. It must be referenced in the 8080 source after all macro prototypes and common definitions but prior to any reference to 8080 registers or register pairs (ref. Figure 1).

(3) Since the register names (A, B, C, D, E, H, L, M) and register pairs (BC, DE, HL) are defined by EQUATE statements in REGDEF, register names and register pair names may not be used as labels.

(4) The dollar sign ($), when used in the operand field of a statement, refers to the current contents of the program counter plus 1.

## III. Loader

The purpose of the loader is to compress binary files produced by the cross assembler and to reorder address bytes to be in the order expected by the 8080. The loader may be executed only after all addresses and common have been resolved. Modcomp's link editor should be used as required to perform the resolution function.

The loader is catalogued as a background overlay under the alias LDR. It reads data from the file assigned to BI and writes to the file assigned to BO. Since BI and BO may be assigned to any valid Modcomp file, it is possible for example, to read BI from disk and write BO onto paper tape. This facilitates producing transportable binary object. The BI and BO files must be assigned prior to executing the loader.

The loader recognizes special function codes inserted into the binary output of a cross assembly by the macro assembler. These codes inform the loader, for example, to reserve an area in core and initialize that area to a given value, or exchange the bytes in a word. Additionally, the loader recognizes the codes for origin directive and end of object. When one of these codes is found, control is passed to a routine in the loader that handles the particular code. With the exception of the code for exchanging bytes, the function codes are discussed in an appendix of the Modcomp Macro Assembler Reference Manual.

The other function performed by the loader is that of compressing the object file by removing extraneous zero high-order bytes. These bytes are inserted by the macro assembler because it expects to assemble sixteen-bit Modcomp words and not eight-bit 8080 words. Refer to the sample assembly in Figure 2.

Figures 3 through 6 illustrate the flowchart for the loader. The main routine (Figure 3) recognizes the special function codes described above and determines what routine to execute. Subroutine GTRCRD (Figure 4) reads records from the BI file into a core buffer called IBUFF. Subroutine GETWORD (Figure 4) fetches words out of IBUFF and stores them in buffer INEXT. If GETWORD is asked to fetch a word beyond the last word in IBUFF, it calls GTRCRD. Subroutine SCAN (Figures 5 and 6) scans portions of the input buffer for the exchange byte code. If that code is found, SCAN replaces the code with the low-order byte of the next word and shifts the high-order byte of the next word into its low-order byte. Subroutine COMPRESS (Figure 6) examines portions of the input buffer for extraneous zero high-order bytes. If one is found, COMPRESS shifts the next non-extraneous byte into it, thereby removing it. Finally, subroutine PUTWORD (Fig. 5) places words into an output buffer called OBUFF. PUTWORD will write the output buffer to the BO file when it is full or when an end of object has been found in the input buffer. Figure 7 illustrates the binary produced by the loader.

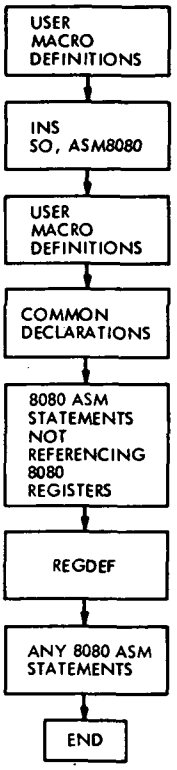


Fig. 1. Generalized 8080 source format



```
MODCOMP MACRO ASSEMBLY (X)#H  DATE  STANDARD-O/S
  SAMPLE 8080 PROGRAM


  2                         *
  3                         *   THIS IS A SAMPLE INTEL 8080
  4                         *   ASSEMBLY  LANGUAGE PROGRAM
  5                         *
  6                               PGM   SAMPLE
  7                         STOP  MAC
  8                               HLT
  9                               EMP
 10                         LOOP  MAC
 11                               NOP
 12                               JNC   $-2
 13                               EMP
 14                               INS SO,ASM8080
316                         COM   COM   100
317          C 0000         COM1  CEQ   COM
318          C 0001         COM2  CEQ   COM+1
319          C 0002         COM3  CEQ   COM+2
320                               REGDEF
321          A 0007         A     EQU   7
322          A 0000         B     EQU   0
323          A 0001         C     EQU   1
324          A 0002         D     EQU   2
325          A 0003         E     EQU   3
326          A 0004         H     EQU   4
327          A 0005         L     EQU   5
328          A 0006         M     EQU   6
329          A 0000         BC    EQU   0
330          A 0001         DE    EQU   1
331          A 0002         HL    EQU   2
332          A 0003         SP    EQU   3
333          A 0003         PSW   EQU   3
334          A 0500               ORG   #500
335    0500  A 0019               RES   10,25
336                               EXT   SUBR
337                         START CALL  SUBR
338    050A  A 00CD               DFC   #CD
339    050B  A FFFF               DFC   #FFFF,SUBR
       050C  X 0001
340                               JNC   $
341    050D  A 00D2               DFC   #D2
342    050E  A FFFF               DFC   #FFFF,$
       050F  R 050E
343                               MOV   A,B
344    0510  A 0078               DFC   8*A+B+#40
345                               XCHG
346    0511  A 00EB               DFC   #EB
347                               LOOP
348    0512  A 0000               DFC   0
349    0513  A 00D2               DFC   #D2
350    0514  A FFFF               DFC   #FFFF,$-2
       0515  R 0512
351                         LABLE NOP
352    0516  A 0000               DFC   0
353                               JC LABLE
354    0517  A 00DA               DFC   #DA
355    0518  A FFFF               DFC   #FFFF,LABLE
       0519  R 0516
356                               JZ    #18,#60
357    051A  A 00CA               DFC   #CA
358    051B  A 0018               DFC   #18,#60
       051C  A 0060
359                               STOP
360    051D  A 0076               DFC   #76
361          A 0550               ORG   #550
362                               LDA   COM1
363    0550  A 003A               DFC   #3A
364    0551  A FFFF               DFC   #FFFF,COM1
       0552  C 0000
365                               PUSH  PSW
366    0553  A 00F5               DFC   16*PSW+#C5
367                               PUSH  BC
368    0554  A 00C5               DFC   16*BC+#C5
369    0555  A 5448         TEXT1 DFC   "THIS IS SAMPLE TEXT"
       0556  A 4953
       0557  A 2049
       0558  A 5320
       0559  A 5341
       055A  A 4D50
       055B  A 4C45
       055C  A 2054
       055D  A 4558
       055E  A 5420
370    055F  A 534F         TEXT2 DFC   "SO IS THIS"
       0560  A 2049
       0561  A 5320
       0562  A 5448
       0563  A 4953
371    0564  R 050A               END   START
$$
```

Fig. 2. Sample assembly

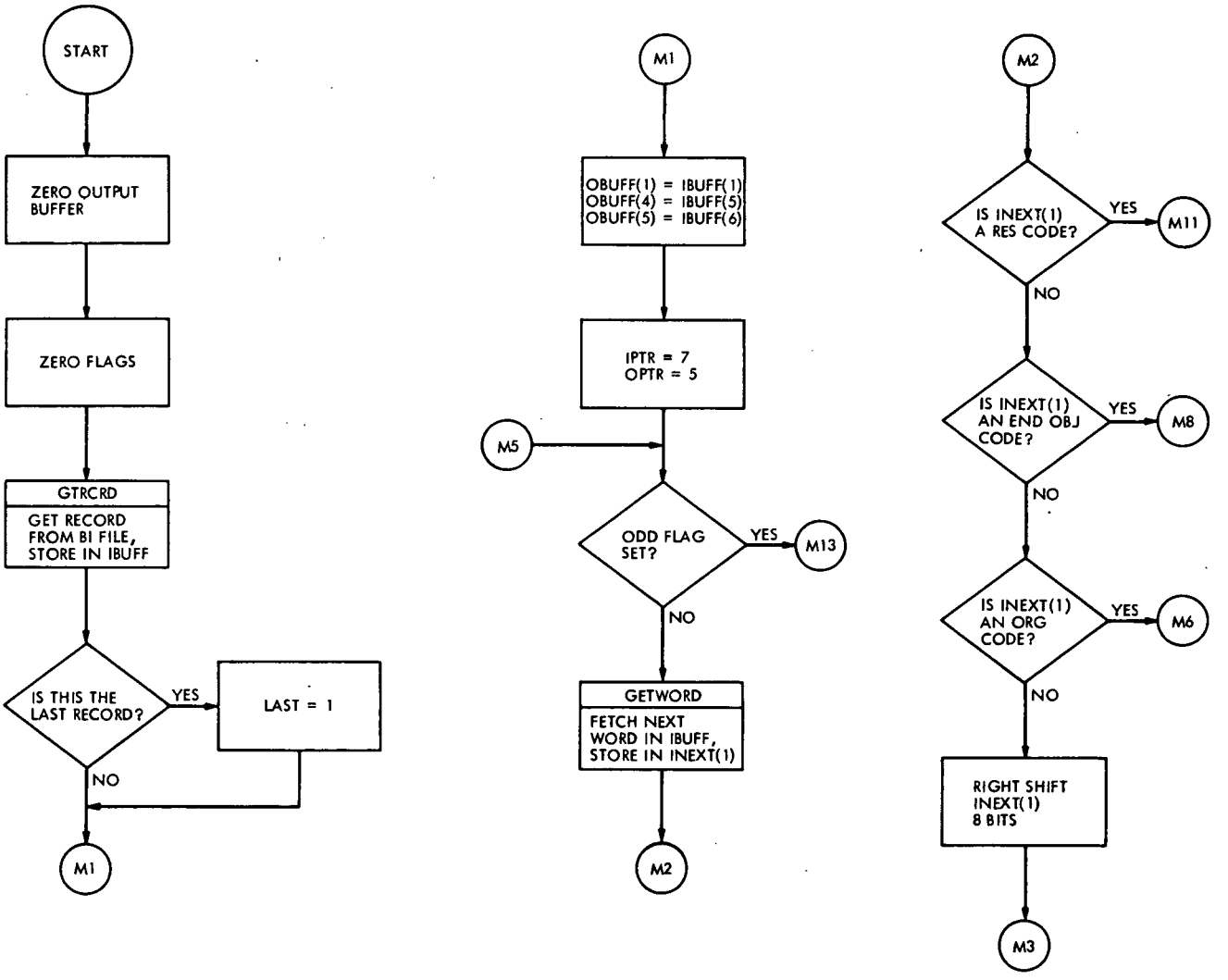


Fig. 3. 8080 loader main program

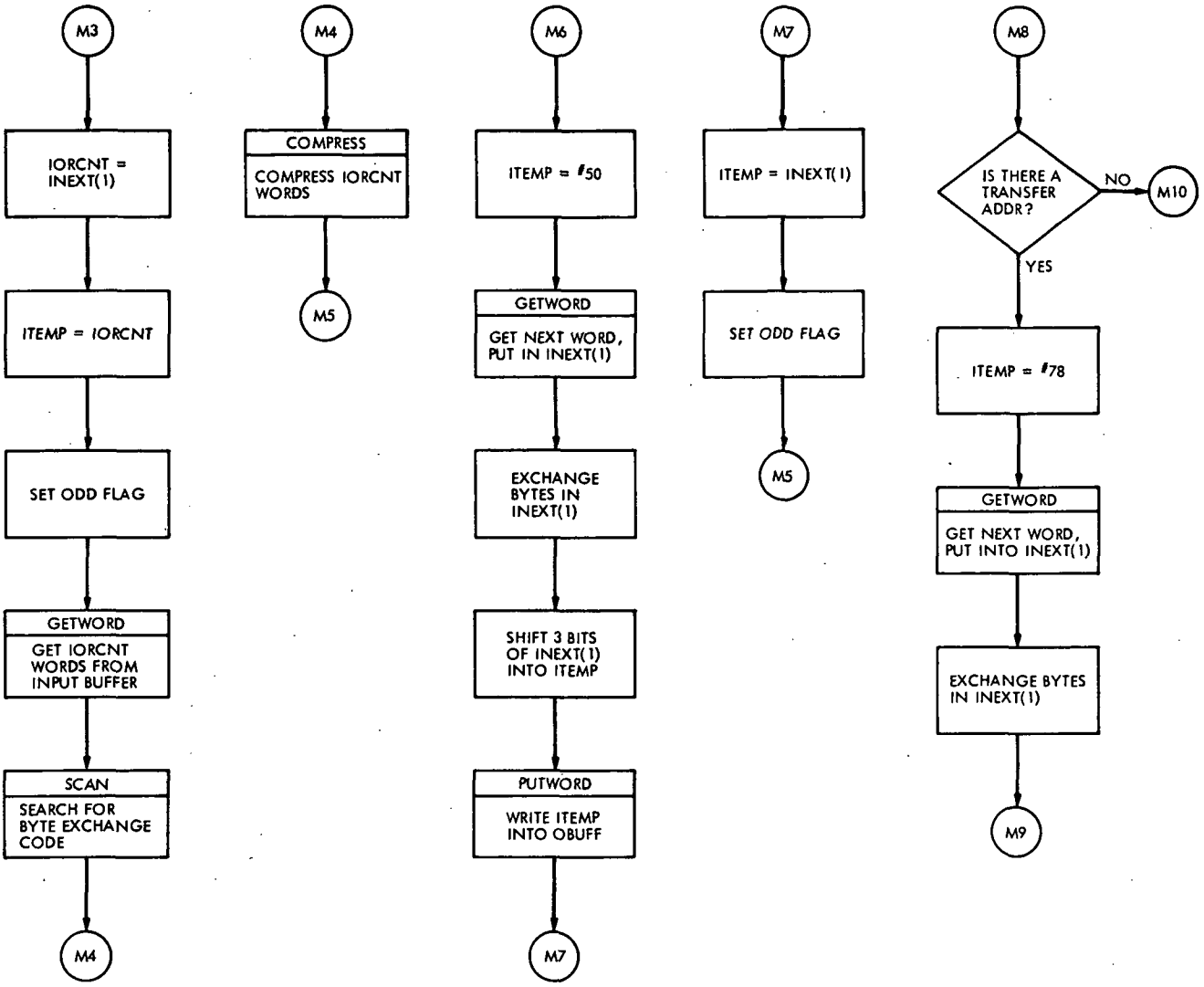
M3
IORCNT = INEXT(1)
ITEMP = IORCNT
SET ODD FLAG
GETWORD
GET IORCNT WORDS FROM INPUT BUFFER
SCAN
SEARCH FOR BYTE EXCHANGE CODE
M4
M4
COMPRESS
COMPRESS IORCNT WORDS
M5
M6
ITEMP = #50
GETWORD
GET NEXT WORD, PUT IN INEXT(1)
EXCHANGE BYTES IN INEXT(1)
SHIFT 3 BITS OF INEXT(1) INTO ITEMP
PUTWORD
WRITE ITEMP INTO OBUFF
M7
M7
ITEMP = INEXT(1)
SET ODD FLAG
M5
M8
IS THERE A TRANSFER ADDR?
NO
M10
YES
ITEMP = #78
GETWORD
GET NEXT WORD, PUT INTO INEXT(1)
EXCHANGE BYTES IN INEXT(1)
M9

Fig. 3 (contd)

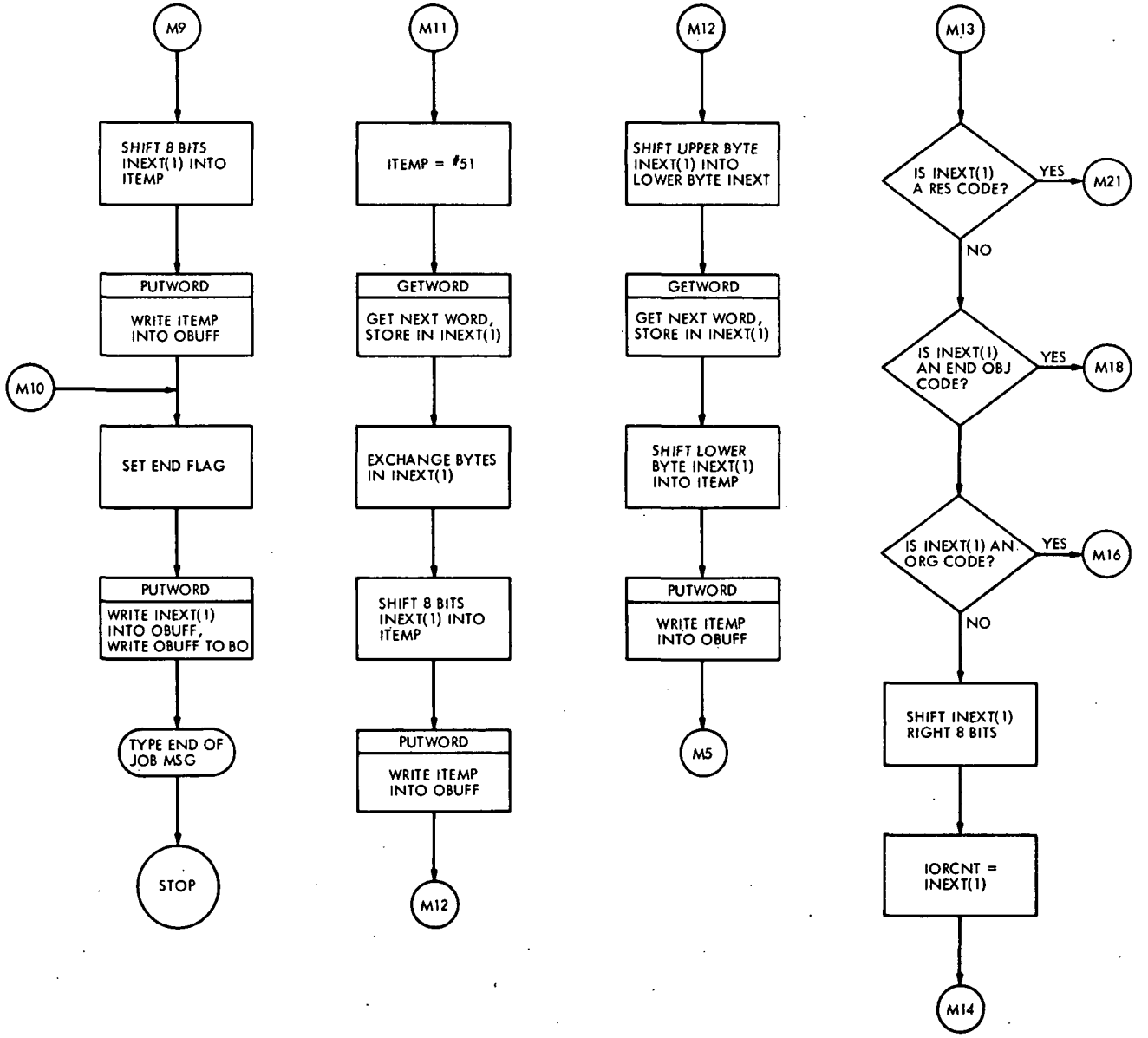




Fig. 3 (contd)

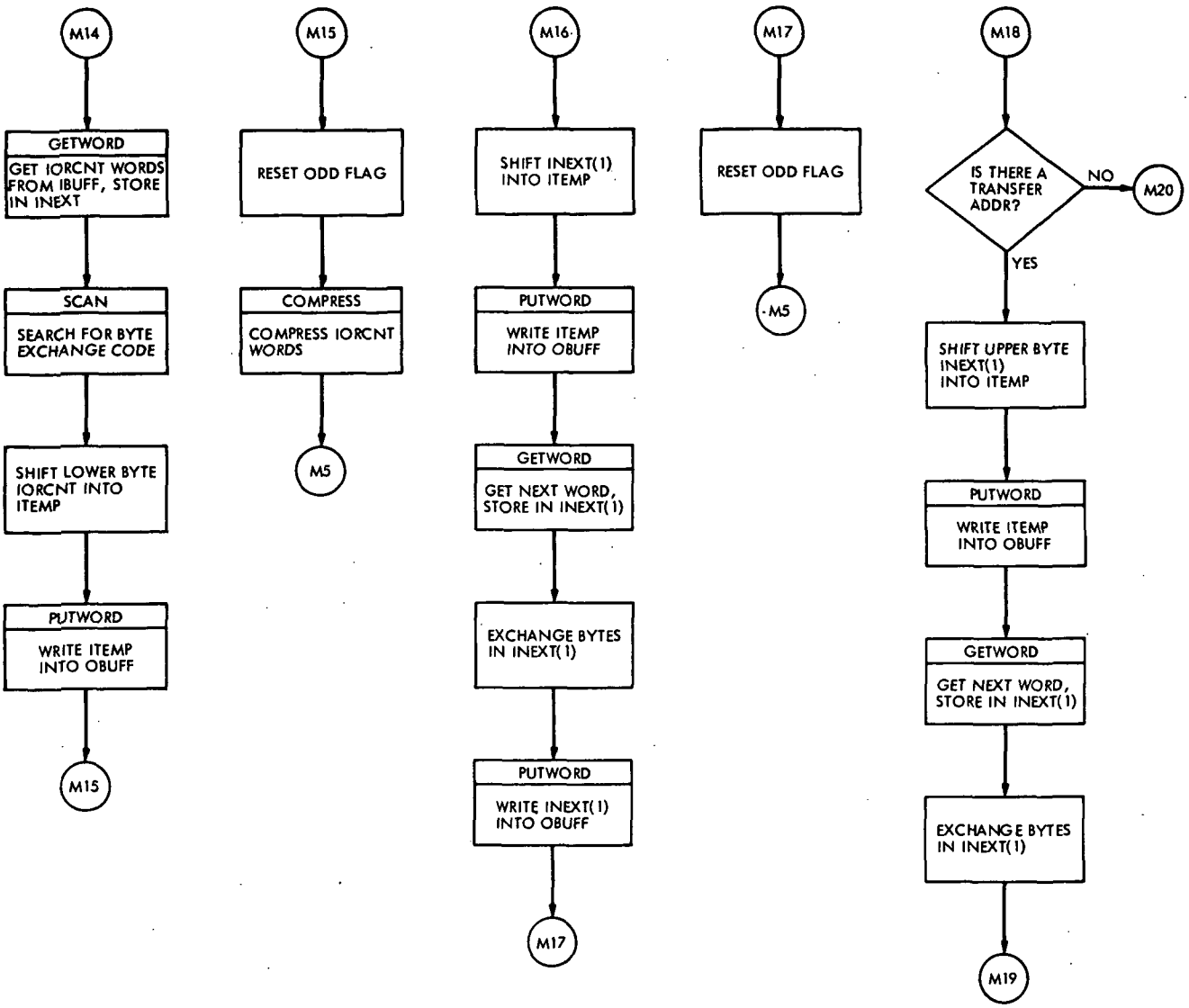
M14
GETWORD
GET IORCNT WORDS FROM IBUFF, STORE IN INEXT
SCAN
SEARCH FOR BYTE EXCHANGE CODE
SHIFT LOWER BYTE IORCNT INTO ITEMP
PUTWORD
WRITE ITEMP INTO OBUFF
M15
M15
RESET ODD FLAG
COMPRESS
COMPRESS IORCNT WORDS
M5
M16
SHIFT INEXT(1) INTO ITEMP
PUTWORD
WRITE ITEMP INTO OBUFF
GETWORD
GET NEXT WORD, STORE IN INEXT(1)
EXCHANGE BYTES IN INEXT(1)
PUTWORD
WRITE INEXT(1) INTO OBUFF
M17
M17
RESET ODD FLAG
M5
M18
IS THERE A TRANSFER ADDR?
NO
M20
YES
SHIFT UPPER BYTE INEXT(1) INTO ITEMP
PUTWORD
WRITE ITEMP INTO OBUFF
GETWORD
GET NEXT WORD, STORE IN INEXT(1)
EXCHANGE BYTES IN INEXT(1)
M19

Fig. 3 (contd)

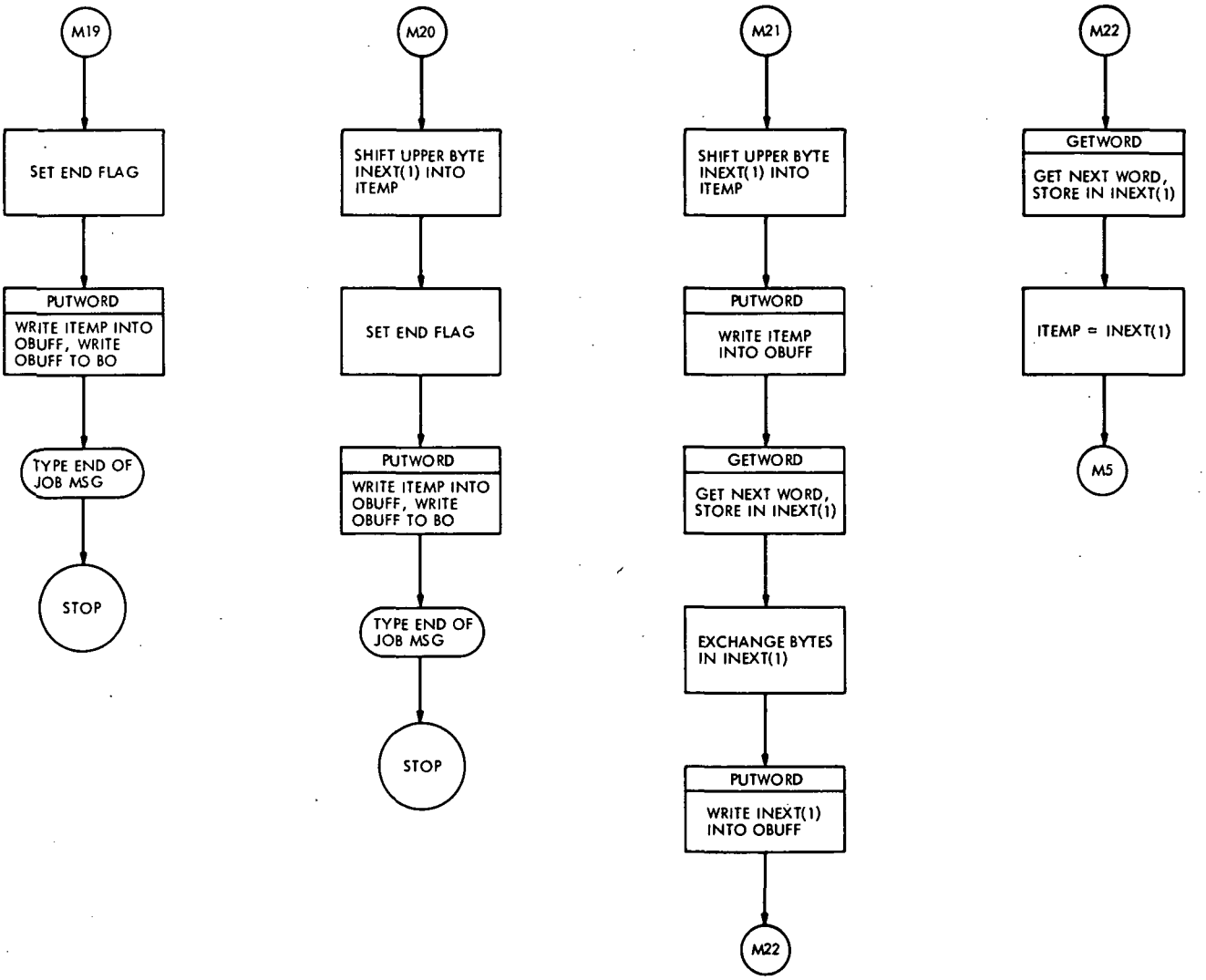


Fig. 3 (contd)

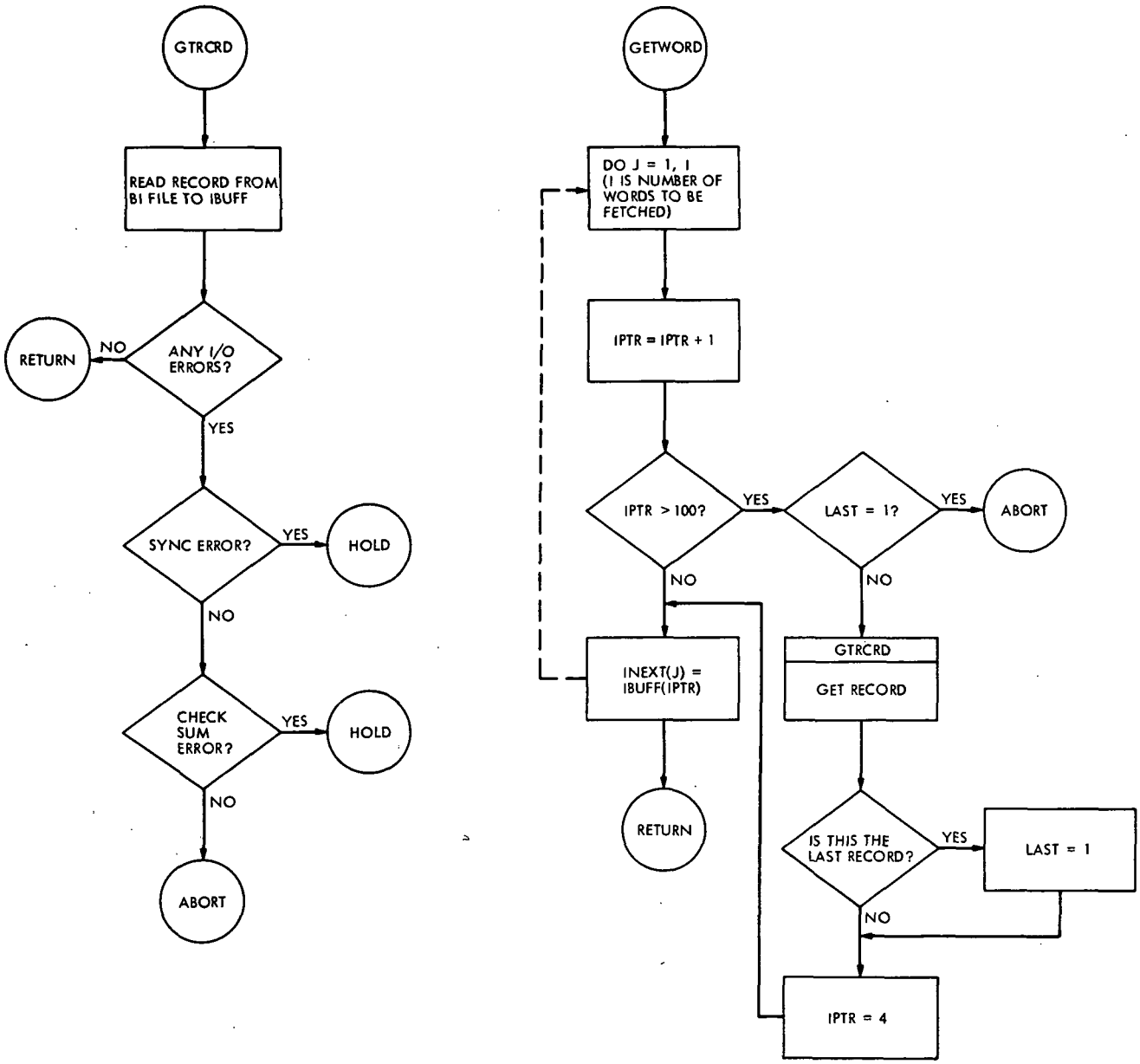


Fig. 4. 8080 loader subroutine GTRCRD, subroutine GETWORD

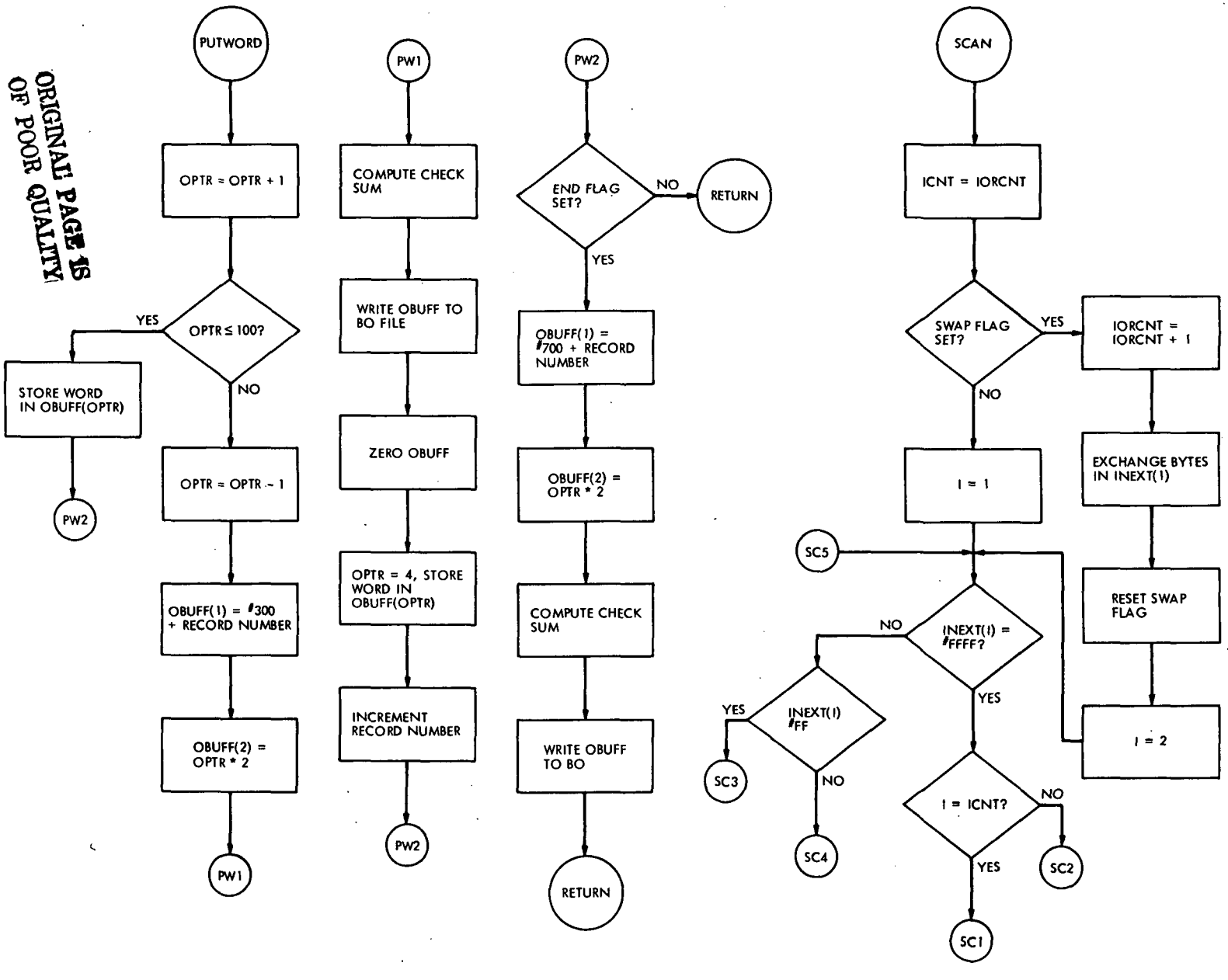


Fig. 5. 8080 loader subroutine PUTWORD, subroutine SCAN

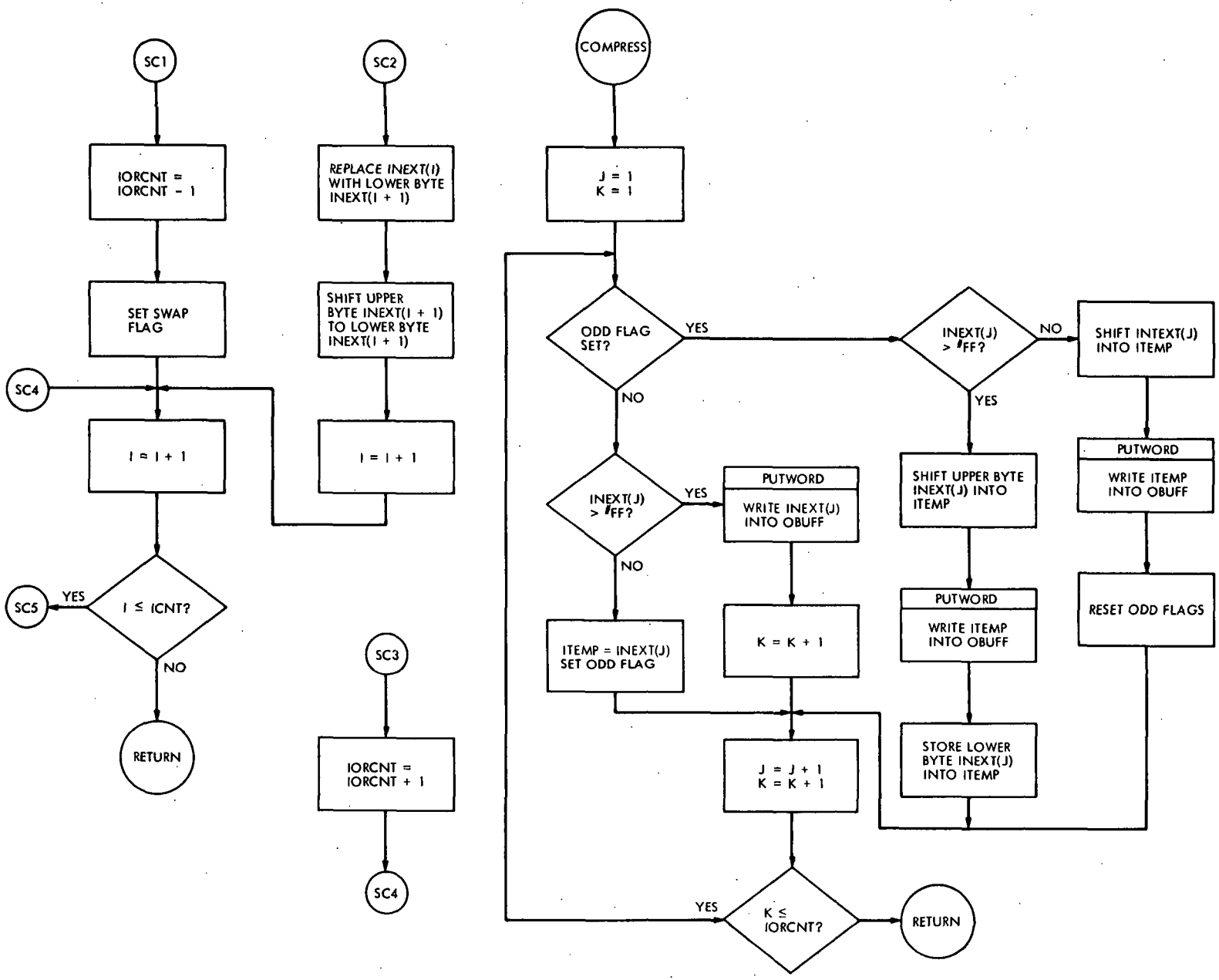


Fig. 6. 8080 loader subroutine SCAN, subroutine COMPRESS

FIRST RECORD

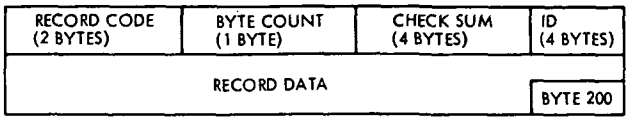


SECOND AND SUBSEQUENT RECORDS

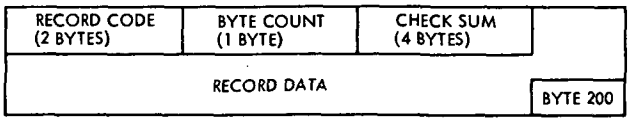


RECORD CODE: $3XX_{16}$ INDICATES $XX^{TH}_{16}$ RECORD

$7XX_{16}$ INDICATES $XX^{TH}_{16}$ RECORD; THIS ONE IS THE LAST RECORD

RECORD DATA

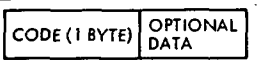


CODES: $51_{16}$ = RESERVE, DATA CONTAINS RES VALUE

$50_{16}$ = ORIGIN, DATA IS ORIGIN

$70_{16}$ = END OF OBJECT, NO DATA PRESENT

$78_{16}$ = END OF OBJECT, DATA = TRANSFER ADDR

ANYTHING ELSE = BYTE COUNT OF DATA BEFORE NEXT CODE

**Fig. 7. Loader format**

# Theory, Operation, and Computer Programming of the 512-Lag Correlator System

R. F. Jurgens
Communications Systems Research Section

*The theory, operation, and computer programming of the JPL–Haystack autocrosscorrelator system is described. This system provides 512 channels with a basic bandwidth of 10 MHz and has provisions for multilevel sampling, oversampling, and bandwidth multiplication by factors of 2 and 4. The system controller features automatic word extension to 40 bits, precise control of the zero lag counter, and computer-enabled run or start commands.*

## I. Theory and Operation of JPL–HAC Correlator System

### A. General Description of the Autocorrelator and Controller

The JPL–HAC 512 channel correlator is a high-speed digital signal processor designed to measure auto- and crosscorrelation functions. The discrete Fourier transforms of these functions are power spectra and cross power spectra, respectively, when certain corrections for the digital quantizing of the signals have been made. In particular, the correlation function $R_{xy}(\tau_n)$ may be formed from sample functions of the signals $x(t)$ and $y(t)$, where $x$ and $y$ are real or complex as shown below:

$$R_{xy}(\tau_k) = \sum_{n=1}^{N} x(\tau_n)y^*(\tau_{n+k})$$

The samples of $x(t)$ and $y(t)$ are usually assumed to be zero mean, gaussian random variables generated from two ergodic processes. In this case, the values of $y(\tau_{n+k})$ are assumed to exist for all values of $n + k$ for which there is interest. For digital processing, $x$ and $y$ are quantized variables. The most crude approximation results

when only two levels are preserved, i.e., only the sign of the variable is measured and is represented by binary levels 0 and 1. Other quantizing systems are possible, however. Measurements of power spectra obtained from the two-level processing (one-bit correlations) are degraded in signal-to-noise ratio by only a factor of $\pi/2$ relative to the signal-to-noise ratio obtained from continuous variables. This mode is particularly easy to implement since the product can be formed by simple correlation matching using an exclusive OR gate. Specifically, the quantized signals $x_n$ and $x_{n+k}$ are the present and delayed samples of two real processes $x(t_n)$ and $y(t_{n+k})$,

$$\bar{x}_n \oplus y_{n+k}$$

where $\bar{x}_n$ is the logically inverted signal and $\oplus$ indicates the exclusive OR operation. A logic 1 state from this gate represents a correlation match and is counted for each n in the sequence.

The JPL–HAC 512 channel autocorrelator is an implementation of one half of the 1024 channel autocorrelator designed by Jim Levine for use at the Haystack Observatory. The JPL autocorrelator system has been modified slightly to provide a precisely measured run time that is programmable by the control computer.

The autocorrelator system consists of the 512-channel autocorrelator (8 subsystem units with one spare unit), a control unit and computer interface module, a data sampler and signal drive unit, a PDP-11/20 control computer, and a direct memory access (DMA) link to the SDS-930. A block diagram of the system configuration is shown in Fig. 1.

Special features of the system presently include a computer controlled run or start, 16-bit word extension by automatic DMA from the controller permitting integration times as long as 10 hours at the maximum clock rate, program controlled bypassing of defective autocorrelator units, and data unloading and restarting in less than 30 ms for 512 channels.

### B. Autocorrelator Operation Modes

The sensitivity of the usual 1-bit (2 × 2 level) autocorrelator can be improved by sampling faster than the Nyquist rate or by extending the number of quantizing levels of the signal (multilevel correlation). Table 1 shows some degradation factors relative to a continuous system (no quantizing) for various possible systems.

The table indicates that not much is gained beyond double sampling or 3 × 3 levels. The JPL–HAC autocorrelator ultimately may be operated in the modes indicated by Table 2.

The unmodified autocorrelator cards also permit 3 × 5 level processing in some modes. However, this facility has been eliminated temporarily in order to provide an extended run gate which permits the autocorrelator to properly complete the overflow scanning sequence.

The simplest mode of operation is the (2 × 2) level mode with sampling at the Nyquist rate. Figure 2 shows diagram of the autocorrelator in this mode where the FF indicates a delay flipflop and X designates exclusive OR gates.

A significant improvement in the degradation factor can be made by using the oversample mode when full bandwidth capability is not required. In this case the sample clock runs at 4 × B Hz. The autocorrelator contains an extra delay flipflop between each lag processor to permit one-half delay interval averaging. Figure 3 shows a block diagram of this configuration.

The 3 × 2 level autocorrelator requires a sampler that distinguishes three levels with properly selected thresholds and a two-level sampler identical to the previous system. The three-level signal can be thought of as containing levels −1, 0, and 1 and the two-level signal as containing −1 and 1. The autocorrelator counts the coincidence of delayed two-level samples with the −1 and 1's of the three-level present sample and inhibits the count when the present sample is zero.

Figure 4 shows an implementation of this scheme including the oversampling flipflops.

The combination of the (3 × 2) level sampling and oversampling yields an improvement in signal-to-noise ratio over the (2 × 2) level sampler operating at the Nyquist rate of 1.27. If this improvement were to be made up in observing time, a 60 percent increase would be required.

Further improvement of the signal-to-noise ratio can be achieved by using (3 × 3) level multiplication. However, the implementation of this feature results in one-half the number of channels. The oversample mode may still be used and results in a reduction in observing time by about a factor of 1.9 for equivalent signal-to-noise ratios relative

to the (2 × 2) level system sampled at the Nyquist rate. In this case the multiplication matrix is as shown below.

| | −1 | 0 | 1 |
|---|---|---|---|
| −1 | 1 | 0 | −1 |
| 0 | 0 | 0 | 0 |
| 1 | −1 | 0 | 1 |

or

| | −1 | 0 | 1 |
|---|---|---|---|
| −1 | 2 | 1 | 0 |
| 0 | 1 | 1 | 1 |
| 1 | 0 | 1 | 2 |

In the first case an up-down counter could be used, but the borrow or negative counts create a large problem with respect to the word extension of the counter in memory. The second matrix requires different gating levels.

The implementation of the first matrix in this autocorrelator is accomplished by dividing each module in half and tallying separate parts of the matrix in each half such that the results can be assembled by the computer after the data are read out. In any case it is necessary to provide a delayed sample "zero" source. This source is used to inhibit the accumulators so that the zeros in the matrix are taken care of. The present sample line drives the first half of the unit while the complement of this sequence drives the second half and accumulates the −1's in the matrix. The proper autocorrelation function may be computed by subtracting the second set of accumulators from the first. Figure 5 shows a block diagram of the implementation of the logic including the gates for oversampling.

### C. Bandwidth Doubling Modes

One of the features of the JPL–HAC autocorrelator is its ability to process signals having bandwidths greater than the maximum logic frequency. The machine is structured such that this can be done in two ways. The most obvious way is to operate the autocorrelator as a number of parallel units each accepting data from differing IF amplifiers and samplers. The system could be configured to drive each of the 8 units having 64 lags from separate IF amplifiers giving a total bandwidth of 80 MHz with a frequency resolution of 156.25 kHz. In this way resolution may be traded directly against bandwidth, permitting the following possible configurations (Table 3):

The second procedure that may be used, suggested by Art Shalloway, requires a single sampler operating at 2 or 4 times the 20-MHz sampling clock. The sequence of samples is separated into series containing every other or every fourth sample. For example, consider the simple bandwidth doubling mode. Let S be a series of samples numbered 1, 2, 3, 4, . . . which is broken into two new series containing the even and odd numbered samples. A contains 1, 3, 5, . . . and B contains 2, 4, 6, 8, . . . . The desired autocorrelation function $R_{ss}(n)$ is formed from the original sequence as shown in Eq. (1).

$$R_{ss}(n) = \sum_{k=1}^{N} (k,n+k) \tag{1}$$

where $(k,n+k)$ indicates the sample pairs used in the product and $N$ is the total number of counts or clock pulses. Four correlation functions may be formed from the sequences $A$ and $B$; these are $R_{AA}$, $R_{BB}$, $R_{AB}$, and $R_{BA}$. It is easy to show that $R_{ss}$ can be formed by properly combining the four correlation functions by first separating Eq. (1) into even and odd summations as shown in Eq. (2).

$$R_{ss}(n) = \sum_{k=1,3,5}^{N} (k,n+k) + \sum_{k=2,4,6}^{N-1} (k,n+k) \tag{2}$$

Here, $N$ has been assumed to be odd but results in no loss of generality as the upper limits of the sums can be interchanged if $N$ is even. Now let $\ell$ be an even index 0, 2, 4, 6, . . . and $m$ be an odd index 1, 3, 5, . . . and evaluate $R_{ss}(n)$ for each case.

$$R_{ss}(\ell) = \sum_{k=1,3,5}^{N} (k,\ell+k) + \sum_{k=2,4,6}^{N-1} (k,\ell+k)$$

$$= R_{AA}\frac{\ell}{2} + R_{BB}\frac{\ell}{2} \tag{3}$$

The odd lags may be evaluated in the same way resulting in Eq. (4).

$$R_{ss}(m) = \sum_{k=1,3,5}^{N} (k,m+k) + \sum_{k=2,4,6}^{N-1} (k,m+k)$$

$$= R_{AB}\left(\frac{m-1}{2}\right) + R_{BB}\left(\frac{m+1}{2}\right) \tag{4}$$

If 512 channels are available, 256 lags may be evaluated.

A similar analysis holds for sampling at 4 times the correlator rate and requires 16 correlation functions. This mode is more difficult to accomplish when only 8 units are available since each unit must be partitioned into half units. This may be accomplished by operating each unit

in the "complex" mode. The complex mode permits each unit to use a second source for the delayed data stream to the second bank of 32 correlation channels. Thus each unit can form an autocorrelation function in the first bank if the data and multiplier lines contain identical data and a cross correlation against the data on the multiplier lines if the data line contains a different source in the second bank. If the data and multiplier lines on the first bank contain different data sources, two crosscorrelation functions may be formed in a single unit.

If the original sequence S is separated into four sequences *A*, *B*, *C*, and *D*, the following correlation functions can be set up in the units indicated. The second subscript is always a permutation beginning with the first which is always an autocorrelation function. This allows a simple scheme to be used to determine which part of memory contains the particular function desired to reconstruct $R_{ss}$. Note that 3 × 3 level processing is not possible since the correlator units are divided into the smallest banks that have been provided (Table 4).

### D. Complex Autocorrelation Functions

The previous discussion indicates that crosscorrelation functions are easily accomplished since the delayed data lines and multiply lines are separate. The autocorrelation function of a complex function requires the formation of crosscorrelation functions between the real and imaginary parts of the complex signal.

If the autocorrelation function of a complex signal $s(t)$ is $R_{ss}$, then $R_{ss}$ can be formed from the real and complex parts of s in the following manner:

$$R_{ss}(n) = R_{s_R s_R}(n) + R_{s_I s_I}(n) + j\left[R_{s_I s_R}(n) - R_{s_R s_I}(n)\right]$$

The autocorrelation must be partitioned into four sections each containing 2 units. Any modes of operation that can be implemented with 2 units can be used. Bandwidth doubling could be implemented by using half units.

### E. Crosscorrelation Functions

Crosscorrelation functions of real data can be measured with any of the modes of Table 2 by providing separate data and multiplier samplers. Complex crosscorrelation functions may be measured in the same manner as complex autocorrelation functions by partitioning the correlator into 4 banks.

### F. Autocorrelator Controller

The control unit for the autocorrelator system acts as a two-way interface between the autocorrelator and the PDP-11 control computer. It also greatly reduces the software support required to operate the system by keeping track of the overflows from the 24-bit counters internal to the autocorrelator. This is accomplished by supplying an overflow array address to the controller as well as a good-unit's control word that programs the sequence of unit addresses called by the controller to supply a display of the 24th bit of all lags. The PDP-11 memory is incremented by direct memory access when respective overflows occur. This procedure also frees the PDP-11 for other data reduction chores during the "run" cycle.

The end of the "run" cycle is indicated by a controller-generated interrupt that may be used to inform the PDP-11 to unload the data or to continue to some other task. A fairly complete description of the operation of the controller is given in Section II on commands and programming. The controller is capable of establishing all possible operation modes of the autocorrelator.

### G. Interim Sampler Module

The present sampling unit consists of a two-level sampler having a digital direct current (dc) removal system that feeds back a reference signal to a comparator in order to maintain the average number of 1's and 0's equal (Ref. 2). With the present configuration, only the first two autocorrelator units may be driven from the sampler. The sampler is also wired to permit only autocorrelation; that is, the data and multiplier lines are supplied with the same signal. The sampler unit also distributes the master clock, the run, and extended run signals to the first two units. This configuration permits bypassing unit 1 should it fail to operate properly. All other units presently may be driven from unit $N - 1$ or $N - 2$. No provisions are available for bandwidth doubling or multilevel sampling at the present time.

## II. Control, Operation, and Test Software for the JPL–HAC Autocorrelator

This section describes the procedure for controlling the JPL–HAC autocorrelator via the PDP-11/20 computer. Descriptions of the controller registers and required function codes are given with examples shown in PAL-11 code. The appendix section shows an example of a subroutine written in the Sigma 5 metasymbol code for the PDP-11 cross assembler (Ref. 3). Examples of the register loading, data readout sequence, and run cycle commands are given.



C-3

### A. Autocorrelator Controller Registers

Operation of the autocorrelator requires that the controller be properly initialized. This consists of loading the first six internal registers of the controller from a list called the control register vector (CRV). Figure 6 shows the configuration for the CRV. The first 5 registers (0 through 4) contain 16-bit words while the 6th register contains the most significant byte (8 bits) of the 40-bit zero lag counter. The zero lag counter must be loaded with the 1's complement of the true number of counts desired following the commencement of the run command and must be reset prior to each run command if a precise run length is desired. Registers 0, 1, and 2 need not be reset. Control register 1 contains the good-units word. This register may have a maximum of 9 bits set in the locations 0 through 8. Each bit set corresponds to an operating unit. Thus, if the first four units are to be operated, $17_8$ would be transferred to this register. Unit 2 could be bypassed by sending $25_8$ to this register. In this case, more advanced software could establish that unit 1 is to be driven from the data sampler, unit 3 from unit N − 2, and units 4 and 5 from units N − 1.

Control register 2 contains the starting address of the array in which overflow incrementing is to begin for each channel of all operating units. The overflow array provides a 16-bit extension to the 24-bit counters internal to the autocorrelator. Normally no more than 8 units will be operated so that the array need contain only $1000_8$ words. Control register 5, which contains the most significant 8 bits of the zero lag counter, will return zeroes in the upper byte of the word when read back irrespective of what is written there. Since the controller does not respond to byte transfers from the PDP-11, a MOVB instruction may not be used to transfer data to this register. A MOVB used to read CDR-6 will always return the lower byte and will respond only to the even address boundary $164002_8$.

Registers 6 and 7 are used for data communication between the autocorrelator and the control computer (PDP-11/20). The selection of a particular register is made by sending the register number to the status and control register (SCR) located at address $164000_8$. This establishes the multiplexing of the 6 CRV words into the proper controller data register (CDR) located at $164002_8$. As an example, loading the interrupt vector address is accomplished by the following instructions:

SCR = 164000

CDR = 164002

| | |
|---|---|
| MOV #0,SCR | select register 0 |
| MOV #270,CDR | write interrupt vector address in register 0 |
| CMP CDR,#270 | check register 0 |
| BNE ERROR | go to error routine |

Each autocorrelator unit contains a bus function register (BFR) consisting of 12 bits that establish the signal source configuration and operation mode. These data are passed through CDR #6 by selecting register 6 along with a unit address to which the data are to be transmitted. Unit addresses 1 through $11_8$ are legal and address $17_8$ addresses all units. The "all units" address may be used to set identical data in the BFRs of all units but obviously cannot be used to read data from all units.

### B. Controller Status and Control Register Configuration

In order to load the BFRs, the status and control register must be properly programmed. The bit configuration of this register is shown in Fig. 7.

Bits 0–2 point to the controller data register.

Bits 3–4 normally contain zeroes, but are used in the data readout sequence.

A one placed in bit 3 will lock out or protect the data register from further write commands to location $164002_8$.

Bits 5–6 specify the interrupt priority level of the correlator when the interrupt is generated at the end of the run.

Bits 7–10 specify the unit address as discussed earlier.

Bits 11–12 correspond to the bus control function codes of the autocorrelator.

00 = connect

01 = load bus function register

10 = data reset

11 = initialize

Bit 13 is a computer operated run control.

1 = run

0 = stop

Bit 14 is a run status flag.

Bit 15 indicates a time out if a correlator unit does not respond within 10 $\mu$s.

### C. Bus Function Register Configuration

Figure 8 shows the Bus Function Register configuration internal to each autocorrelator unit.

The bit assignments for the Bus Function Register are as follows:

| | | |
|---|---|---|
| Bits 0–1 | Signal source | 0 — from stage N − 1<br>1 — from stage N − 2<br>2 — from data sampler<br>3 — from auxiliary unit |
| Bits 2–3 | Data type | 0 — real two level<br>1 — real three level<br>2 — complex two level<br>3 — complex three level |
| Bits 4–5 | Multiplier type | 0 — 2 level<br>1 — 3 level<br>2 — 4 level<br>3 — 5 level |
| Bit 6 | Oversample | 0 — Nyquist rate<br>1 — 2x Nyquist rate |
| Bit 7 | Overflow read | 0 — data read mode<br>1 — overflow read mode |
| Bit 8 | Low-speed clock | 0 — high-speed clock<br>1 — low-speed clock |
| Bit 9–11 | Test mode | 0 — operate<br>1 — disable data bus<br>2 — bus transmit 1's<br>3 — bus transmit 0's<br>4 — memory load 1's<br>5 — memory load 0's<br>6 — spare<br>7 — fault indicator on |

Suppose 8 units are to be operated in the simplest mode (real-two level data, two level multiply). $\#13606_8$ sent to the SCR selects the data transfer register, CDR-6, selects write mode on all units, and prepares for the loading of the bus function register. $\#200_8$ may be sent to the CDR to specify that all units are to be driven from unit N − 1, and the overflow read mode is set by bit 8. Since unit 1 has no source unit, the data and run command signals must be sent from the controller and data sampler. This is accomplished by sending $\#10206_8$ to the SCR followed by $\#202_8$ to the CDR.

### D. Initialize and Data Reset

The initialize command resets the entire correlator and generates a data reset which clears the low order 8-bit counters and prepares the 16-bit memory for clearing when the run command is sent. Approximately 4 $\mu$s is required to clear the memory. The initialize also clears the Bus Function Register, which must be reprogrammed prior to the run command. The data reset command clears the low order 8-bit counters and prepares the 16-bit counters for clearing upon sending the run command. The data reset signal also resets the memory address sequencer to zero. Since the data in the memory are not destroyed until the run is enabled, the memory can be reread repeatedly. However, the low order 8 bits will read zero for one cycle and a checkerboard test pattern for all successive read cycles. The initialize signal is also generated during the power-up cycle and insures that all counters and control memory devices are in the initialized state. These commands may be sent to all units simultaneously by using the all-units address code. The codes follow:

```
MOV    #3606,SCR    Initialize all units
CLR      CDR
MOV    #7606,SCR    Data reset all units
CLR      CDR
```

### E. Run Control

Presently, the autocorrelator may be set in the run mode by sending a $\#34000_8$ to the SCR. This enables the run bit and sets the connect code so that subsequent overflow read requests generated by the controller are recognized by any unit that is addressed. The run command may be removed before the zero lag counter has finished and the interrupt is fired. This feature permits the aborting of a long run that is discovered to be defective for any reason, but because the zero lag counter is halted, the overflow scan cycle is prematurely terminated. Therefore, some overflows may not have been tallied, and reading the data from the autocorrelator may not be useful.

Because the run control is computer-actuated, the exact starting time is not exactly known. Future modifications will permit the computer to generate a run enable signal, which will permit an external clock to generate the run command at a precise time.

### F. Data Read Mode

The interrupt service routine, which is initiated once the countdown of the zero lag counter is completed, generally initiates a data unloading sequence. The low-order bytes and medium-order words are generally loaded into separate arrays, as this can be accomplished more quickly

than the packing of the data into 40-bit words. The packing could be done once the next run is initiated if time permits. The read request sequence requires that the autocorrelator be in the connect mode and that a read request be generated by the controller. The order of reading CDR 6 and 7 is unimportant; however, bit 5 of the SCR must be set during the first read and reset to zero during the second read. The toggling of bit 5 actually establishes the read request to the autocorrelator and increments the memory address. The autocorrelator is first set in the data read mode as follows:

```
MOV     #13606,SCR      Set data read mode
CLR       CDR           On all units
```

It is convenient to take advantage of the autoincrement addressing modes of the PDP-11 while unloading the data. If MOWA and LOBA are the first address locations of the medium-order word array and the low-order byte array, then a simple program to unload unit 1 might be written as:

```
MOWA = 3000₈
LOBA  = 3200₈
        MOV     LOBA,R1       Put array addresses
        MOV     MOWA,R2       in registers 1 and 2
        MOV     #101,RO       Initialize loop
                              counter
LOOP    DEC     RO            Decrement loop
                              index
        BEQ     EXIT          Go to exit if index
                              is zero send
                              connect, lockout
                              write mode
        MOV     #14236,SCR    Send read request
                              and select CDR 6
        MOVB    CDR,(R1)+     Read CDR 6
        MOV     #14217,SCR    Lock out write
                              mode send connect
                              toggle bit 5
                              select CDR 7
        MOV     CDR,(R2)+     Read CDR 7
        BR      LOOP          Continue loop
EXIT - - - - -
```

The medium-order words now fill $100_8$ words and the low-order bytes fill $40_8$ words, beginning at these respective addresses. The overflow array also fills $100_8$ words. These three arrays comprise the entire data output. If it is known that the zero lag counter contains less than a 16-bit count, the MOV CDR,(R2)+ instruction may be replaced with a MOVB to cut the MOWA in half. In the case of very long runs, the least significant bits do not have to be read, but the toggle of bit 5 must be sent to the SCR.

The appendix shows an example of a subprogram to unload $N$ good units as specified by the good units word (GUW).

### G. Test Modes

The autocorrelator may be operated in five test modes. These permit the computer to execute a number of diagnostic tests to determine if a particular unit is operating properly. These tests are not exhaustive, and complete testing requires the operation of the autocorrelator with certain test signals for which the exact autocorrelation function is known. These test signals are exact square waves counted down digitally from the master clock and are available behind the data sampler module.

1. Test mode 1 (disable data bus). Test mode 1 may be established by loading the BFR with $1000_8$. This mode disables the tristate bus driver, and subsequently reads from the data bus should return $177777_8$ through the CDR.

2. Test mode 2 (bus transmit 1's). Test mode 2 is established by loading the BFR with $2000_8$. This mode disables the tristate drivers of the memory multiplexer bus that feeds the output bus. A series of 64 read requests will cycle through the entire multiplex sequence, insuring that the multiplex bus is free in all address modes if $177777_8$ is returned through the CDR. The lower 8 bits also transmit 1's through the data bus in this mode.

3. Test mode 3 (bus transmit 0's). Test mode 3 transmits zeroes to the output bus by disabling the memory output lines. These lines are inverted and passed through the multiplex bus. Therefore, the inverters as well as the memory disable may be tested. The low-order 8 bits also will indicate zeroes when read, since test modes 1 and 3 generate a data reset signal that clears the 8-bit counters. This test mode assures that the 8-bit counters clear if all 64 reads indicate zeroes.

4. Test mode 4,5 (memory transmit 1's, memory transmit 0's). Test modes 4 and 5 are somewhat more difficult

to set up and require that a large amount of the autocorrelator be operating properly. In particular, the memory scan circuits must be operating properly. Since the memory scanning does not operate unless the autocorrelator is in the "run" mode, a short run cycle must be executed to cause the memories to clear all addresses. This requires about 4 $\mu$s. In test mode 4, the memories are cleared and decremented so that all 1's are presented to the multiplex bus. Test mode 5 is identical except that the decrement signal is not generated. The low-order 8-bit data bus will read the contents of the 8-bit counters. A data reset command will clear these counters and insure that zeroes will be read in either test mode 4 or 5. The ability of these counters to load 1's and 0's may be tested by repeating the read sequence. During the first read sequence the data latches of these counters are filled with an alternating 1-0 pattern so that an 8 × 64 checkerboard pattern exists. During the second read cycle, the 16-bit memory will repeat the original data, as these data are not destroyed during the readout. The 8 low-order bits will alternately read $125_8$ and $252_8$.

In order not to have to set up the interrupt instructions, it is convenient to use the manual run mode to provide the run signal. Clearing the zero lag counter will insure that no interrupt can happen for roughly 8 hours. An example of a program to check test mode 4 is shown below.

```
MOV #3, SCR          Clear zero lag counter
CLR CDR
MOV #4, SCR
CLR CDR
MOV #5, SCR
CLR CDR
MOV #206, SCR        Initialize unit 1
CLR CDR
MOV #10206, SCR      Select load bus function
MOV #4002, CDR       Select test mode 4
                     and drive unit from
                     data sampler
MOV #34000, SCR      Run
NOP                  Wait 4 microseconds
NOP
NOP
CLR SCR              Stop run
MOV #1, GUW          Set good units word
JSR R5, UNLDAC       Unload unit 1
WORD GUW, MOWA, LOBA
```

Arrays located at MOWA and LOBA now contain the results of the test. The 16-bit MOWA should contain $177777_8$ in all 64 words, and the 8-bit LOBA should contain 1's in all 64 locations. A second call to the unload routine will cause the checkerboard pattern to be loaded into the LOBA.

Test mode 6 is unimplemented, and test mode 7 causes the fault lamp to operate.

### H. Reading the BFR

The first 8 bits of the Bus Function Register may be read on the 8-bit data bus when the autocorrelator is in the overflow read mode. In order to accomplish this, the autocorrelator must be placed in the run mode long enough for the controller to issue an overflow read request. A countdown from $2^{24}$ in the zero lag counter is adequate for this purpose. It is not possible to know which unit was read last at the finish of the run cycle. Therefore, this test requires that the good-units word, GUW, contain only one set bit; i.e., only one unit is operated at a time. As a result, the reading of the BFR is generally useful only for test purposes and not for verifying the operational configuration.

## References


1. Bowers, F. K., and Klinger, R. J., *Quantization Noise of Correlation Spectrometers*, Department of Electrical Engineering, University of British Columbia, Vancouver, British Columbia.

2. Brokl, S. S., and Hurd, W. J., "Digital DC Offset Compensation of Analog-to-Digital Converters," in *The Deep Space Network*, Technical Report 32-1526, Vol. XVII, Jet Propulsion Laboratory, Pasadena, Calif., Oct. 15, 1973.

3. Erickson, D. E., "The SAPDP Program Set for Sigma 5 Assembly," in *The Deep Space Network*, Technical Report 32-1526, Vol. VII, Jet Propulsion Laboratory, Pasadena, Calif., Feb. 15, 1972.

**Table 1. Degradation factors (Ref. 1)**

| Levels | Nyquist | 2 × Nyquist | 3 × Nyquist |
|---|---|---|---|
| 2 × 2 | 1.57 | 1.35 | 1.29 |
| 2 × 3 | 1.39 | 1.24 | 1.19 |
| 3 × 3 | 1.23 | 1.13 | 1.11 |
| 3 × 5 | 1.15 | 1.09 | 1.07 |
| 4 × 4 | 1.13 | 1.07 | 1.06 |

**Table 2. Operation modes**

| Signal bandwidth, MHz | Signal levels | Sampling rate | Channels available |
|---|---|---|---|
| 40 | 2 × 2, 3 × 2 | Nyquist | 128 |
| 20 | 2 × 2, 3 × 2 | Nyquist | 256 |
| 20 | 3 × 3 | Nyquist | 128 |
| 10 | 2 × 2, 3 × 2 | Nyquist | 512 |
| 10 | 3 × 3 | Nyquist | 256 |
| 5 | 2 × 2, 3 × 2 | Nyquist | 512 |
| 5 | 2 × 2, 3 × 2 | 2 × Nyquist | 512 |
| 5 | 3 × 3 | Nyquist | 256 |
| 5 | 3 × 3 | 2 × Nyquist | 256 |

**Table 3. Bandwidth vs resolution using multiple IF amplifiers**

| Total BW, MHz | Number of IFA | Number of lags/IF | Resolution, kHz |
|---|---|---|---|
| 80 | 8 | 64 | 156.25 |
| 40 | 4 | 128 | 78.125 |
| 30 | 3 | 192 | 52.0833[a] |
| 20 | 2 | 256 | 39.0625 |
| 10 | 1 | 512 | 19.53125 |

[a]Using spare unit to yield 3 banks of 3 units.

**Table 4. Signal drive sources for bandwidth quadrupling mode**

| Unit | $R_1$ | $R_2$ | Mul | $D_1$ | $D_2$ |
|---|---|---|---|---|---|
| 1 | $R_{AA}$ | $R_{AB}$ | A | A | B |
| 2 | $R_{AC}$ | $R_{AD}$ | A | C | D |
| 3 | $R_{BB}$ | $R_{BC}$ | B | B | C |
| 4 | $R_{BD}$ | $R_{BA}$ | B | D | A |
| 5 | $R_{CC}$ | $R_{CD}$ | C | C | D |
| 6 | $R_{CA}$ | $R_{CB}$ | C | A | B |
| 7 | $R_{DD}$ | $R_{DA}$ | D | D | A |
| 8 | $R_{DB}$ | $R_{DC}$ | D | B | C |

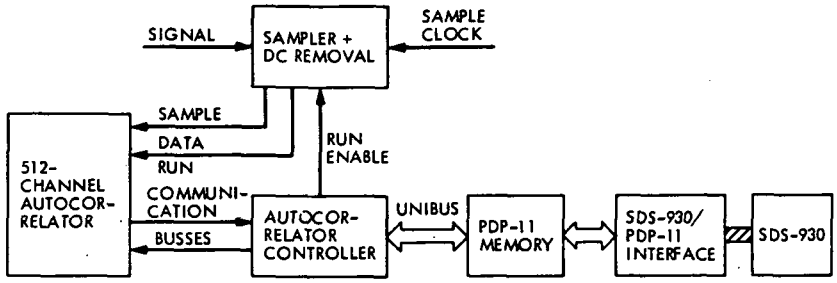


Fig. 1. Block diagram of the autocorrelator system

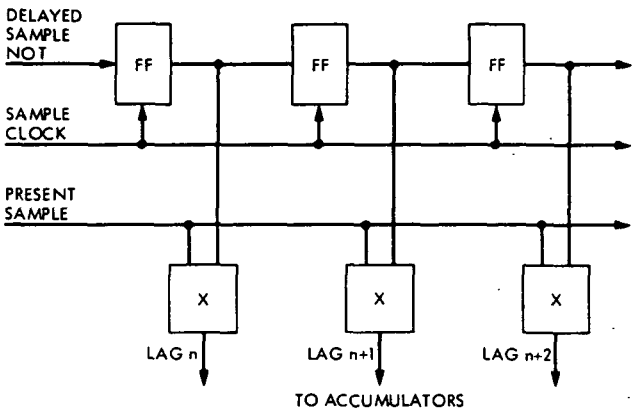


Fig. 2. Two-level autocorrelator at Nyquist rate

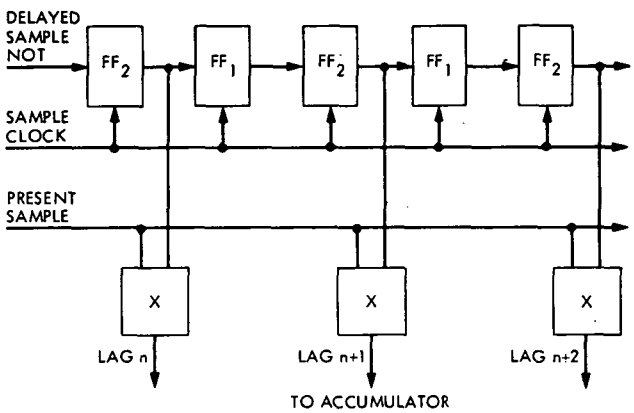


Fig. 3. Oversample mode in 2 × 2 levels

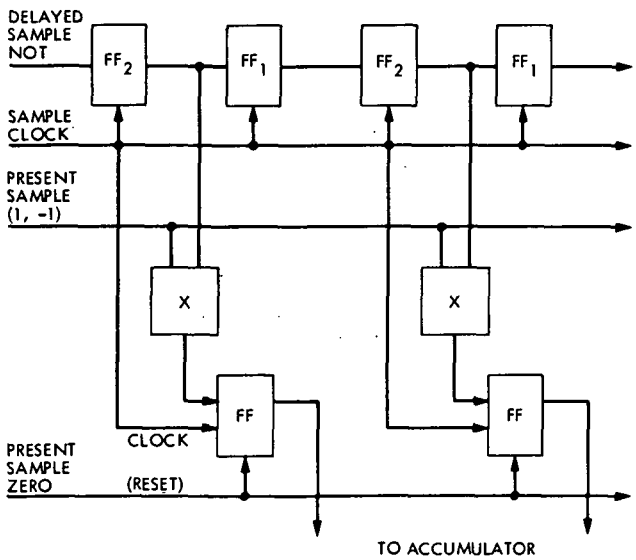


Fig. 4. Autocorrelator with oversampling, (3 × 2) level

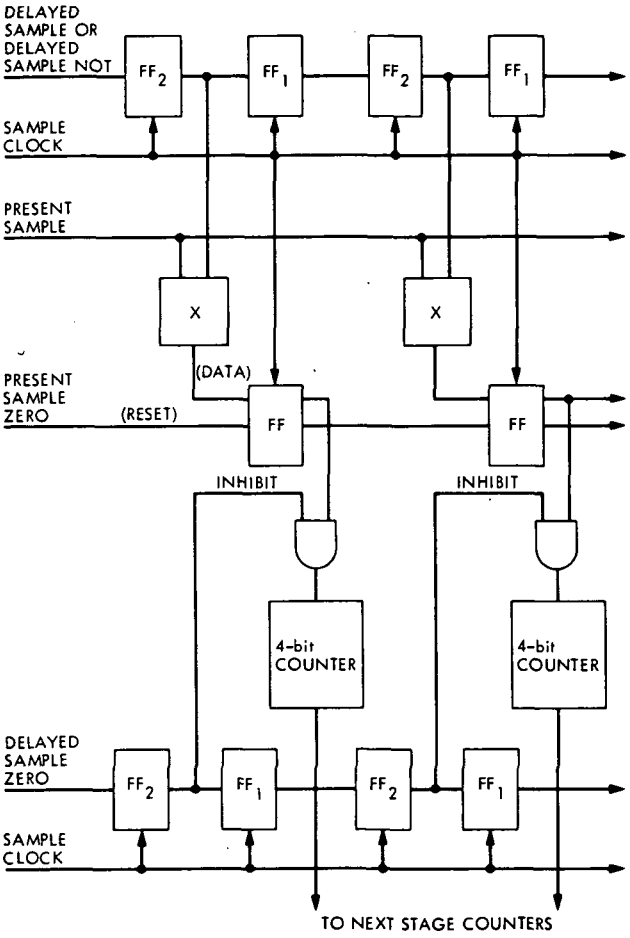


Fig. 5. Autocorrelator with oversampling, (3 × 3) level

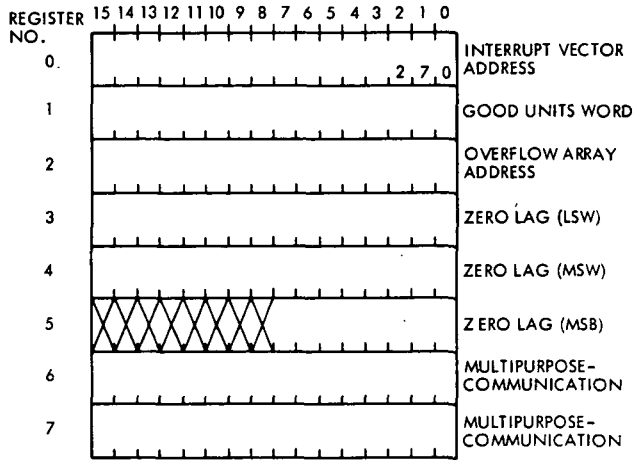


Fig. 6. Control register vector

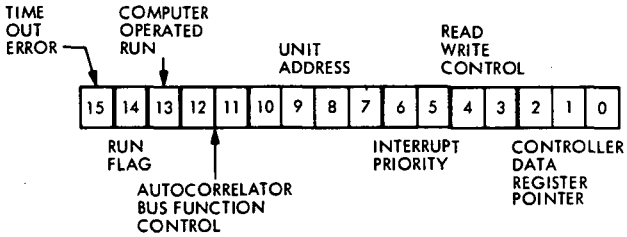


Fig. 7. Status and control register configuration

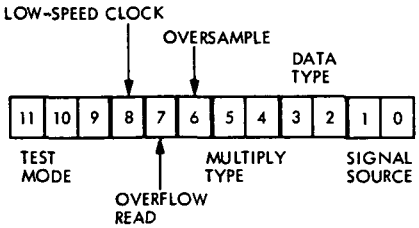


Fig. 8. Bus function register configuration

# Appendix

## Subroutine for unloading N units

```
 13:31 FEB 19,'76 ID=00CF=F00
 JOB AUTOCOR,JURGENS
METASYM SI,LP,SB

HDU   13:31  FEB 19, '76                                SYSTEM PDP11                                    1
      1   01 00000                          BRG,1   8'1000'
      1   01 00080

HDU   13:31  FEB 19, '76                                SYSTEM PDP11                                    2
      2                                          SYSTEM  PDP11
      3                                  *  SUBROUTINE TO UNLOAD MAC-JPL AUTOCORRELATOR
      4                                  *  CALLING SEQUENCE:  JSR  5, UNLDAC
      5                                  *                      WORD  GUM,MOWA,LOBA
      6                                  *
      7                                  *  R.F.JURGENS  7  JAN 76
      8                                  *
      9   01 00080    09F70C5C  A    UNLDAC JSR      7,SAVREG
     10   01 00081    15F71786  N           MOV      (#,8'13606'),ZSCRA  SET DATA READ MODE
                      E5F6
     11   01 00082 2  0A37E5F4  N           CLR      ZDRA
     12   01 00083 2  1777004A  A           MOV      *(5,8),UNLDGU       PICK UP GOOD UNITS WORD
     13   01 00084 2  1742      A           MOV      *(5,8),2            PICK UP MOWA
     14   01 00085    1741      A           MOV      *(5,8),1            PICK UP LOBA
     15                                  *  INITIALIZE READ REQUEST CODES
     16   01 00085 2  15C3181E  A           MOV      (#,8'14036'),3      UNIT 0 LOB READ REQUEST CODE
     17   01 00086 2  15C418CF  A           MOV      (#,8'14317'),4      UNIT 0 MOW READ REQUEST CODE
     18                                  *  UNIT LOOP
     19   01 00087 2  15F70C0A  A           MOV      (#,10),UNLDNW       INITIALIZE UINT COUNTER
                      003A
     20   01 00089    0AF70C36  A    UNLD1  DEC      UNLDNW              DEC UNIT COUNTER
     21   01 0008A    0316      A           BEQ      UNLD3
     22   01 0008A 2  65C3D08D  A           ADD      (#,8'203'),3        INCREMENT UNIT ADDRESS CODES
     23   01 0008B 2  65C40D8D  A           ADD      (#,8'203'),4
     24   01 0008C 2  0C37DC26  A           ROR      UNLDGU              ROTATE GOOD UNIT BIT INTO CARRY
     25   01 0008D 2  83F6      A           BCC      UNLD1
     26                                  *  LAG LOOP
     27   01 0008E    15C00041  A           MOV      (#,65),0            INITIALIZE LAG COUNTER
     28   01 0008F    0ACC      A    UNLD2  DEC      0                   LAG COUNT LOOP
     29   01 00090 2  03F2      A           BEQ      UNLD1
     30   01 00090    10F7E5BC  N           MOV      3,ZSCRA             READ LOB
     31   01 00091    10D1E5BA  N           MOV      ZDRA,(1,8)
     32   01 00092    1137E5B4  N           MOV      4,ZSCRA             READ MOW
     33   01 00093    10D2E5B2  N           MOV      ZDRA,(2,8)
     34   01 00094    00A0      A           NOP
     35   01 00094 2  00A0      A           NOP
     36   01 00095    01F3      A           BR       UNLD2

HDU   13:31  FEB 19, '76                                SYSTEM PDP11                                    3
     37   01 00095 2  09F70C14  A    UNLD3  JSR      7,RESREG
     38   01 00096 2  0085      A           RTS      5
     39   01 00097                UNLDGU RES,2    1                   GOOD UNITS SCANNER WORD
     40   01 00097 2              UNLDNW RES,2    1                   NUMBER OF UNITS INDEX
     41        0000E5C0           ZSCRA  EQU     8'164C00'
     42        0000E5C2           ZDRA   EQU     8'164002'
     43                                  *
     44                                  *
     45                                  *  SUBROUTINE SAVREG
     46                                  *  CALLING SEQUENCE  JSR  7,SEVREG
     47                                  *  SUBROUTINE TO SAVE GENERAL REGISTERS ON STACK WHEN R5 IS USED AS
     48                                  *  A SUBROUTINE LINKAGE REGISTER.   R0 TO R4 ARE SAVED.
     49                                  *  CALL TO SAVEREG MUST BE FIRST INSTRUCTION IN SUBROUTINE TO INSURE
     50                                  *  THAT NO OTHER DATA IS PLACED ON THE STACK.
     51                                  *
     52   01 00098    1126      A    SAVREG MOV      4,(8,6)             PUT REGISTERS 0 TO 4 ON STACK
     53   01 00098 2  10E6      A           MOV      3,(8,6)
     54   01 00099    10A6      A           MOV      2,(8,6)
     55   01 00099 2  1066      A           MOV      1,(8,6)
     56   01 0009A    1026      A           MOV      0,(8,6)
     57   01 0009A 2  007E000A  A           JMP      *(10,6)             RETURN TO SUBROUTINE
     58                                  *
     59                                  *
     60                                  *  SUBROUTINE RESREG
     61                                  *  CALLING SEQUENCE:    JSR  7,RESREG
     62                                  *  SUBROUTINE TO RESTORE REGISTERS AT EXIT OF SUBROUTINE  WHICH CALLED
     63                                  *  SAVREG AS FIRST INSTURCTION.   RESREG MUST BE CALLED BEFORE THE
     64                                  *  RTS 5  AT THE EXIT OF THE SUBROUTINE
     65                                  *
     66   01 00098 2  1536000A  A    RESREG MOV      (6,8),(10,5)        MODIFY LINKAGE RETURN ADDRESS
     67   01 0009C 2  1580      A           MOV      (6,8),0             RESTORE REGISTERS 0 TO 4
     68   01 0009D    1581      A           MOV      (6,8),1
     69   01 0009D 2  1582      A           MOV      (6,8),2
     70   01 0009E    1583      A           MOV      (6,8),3
     71   01 0009E 2  1584      A           MOV      (6,8),4
     72   01 0009F    005E      A           JMP      *(6,2)              RETURN TO NEW LINKAGE ADDRESS
     73                                  *
```

```
HOU   13:31  FEB 19, '76                          SYSTEM PDP11                          4
      74                                  END
 CONTROL SECTION SUMMARY: 01 0009F 2 PT 0

HOU   13:31  FEB 19, '76                          SYSTEM PDP11                          5
*    SYMBOL VALUES
        ANSI:CII/LIST          A1/LIST              A2/LIST              J/00000001
        L/00000000             M/LIST               RESREG/01 00098      SAVREG/01 00098
        UNLDAC/01 00080        UNLDGU/01 00097      UNLDNW/01 00097      UNLD1/01 00089
        UNLD2/01 0008F         UNLD3/01 00095       WC/00000000          ZDMA/0000E802
        ZSCRA/0000E800         #/00000000           $/00000000           %%/00000000
        @1/00000000
* NO EXTERNAL DEFINITIONS
* NO PRIMARY REFERENCES
* NO SECONDARY REFERENCES
* NO UNDEFINED SYMBOLS
*    ERROR SEVERITY LEVEL: 0
* NO ERROR LINES

 LOAD (BIAS,0),(MAP),(NOSYSLIB),(NOTCB),(ABS),(LMN,PDPL),(GE),(SL,1)

* * ALLOCATION SUMMARY * *
  PROTECTION      LOCATION   PAGES

DATA (00)                      1
PROCEDURE (01)      200        1

CSEC          0
                    DATA
          A0        SIZE
         200        PROCEDURE
          16        SIZE

ASSIGN MIPS,(DEVICE,PPA01),(OUT)
ASSIGN MIE17,(FILE,PDPL)
RUN (LMN,SLOAD,IDSN)
```

# The Analysis of Structured Programs—Part I: Kirchhoff's Equations

R. J. McEliece
Communications Systems Research Section

*In this article we show that the analysis of a structured computer program is in some ways much easier than the analysis of an unstructured one. This is in contrast to the usual argument, which is that the synthesis of a structured program is easier than the synthesis of an unstructured one.*

## I. Introduction

It is often necessary to make a careful analysis of an existing computer program—for example, in order to obtain precise timing information. In this article we will show that if the program is *structured* (in a sense to be made precise in Section II), an important part of this analysis can be done by merely inspecting the program documentation; but if the program is not structured, the analysis is much harder.

Let us begin with an example.[1] Figure 1, which is taken from Tausworthe (Ref. 2, pp. 5–33), is the flowchart for a simple *unstructured* program.

Each box in Fig. 1 represents a program step, and the letter inside the box represents the number of times the corresponding step is performed during one run of the program. While of course these numbers in general depend on the details of the program and the program's

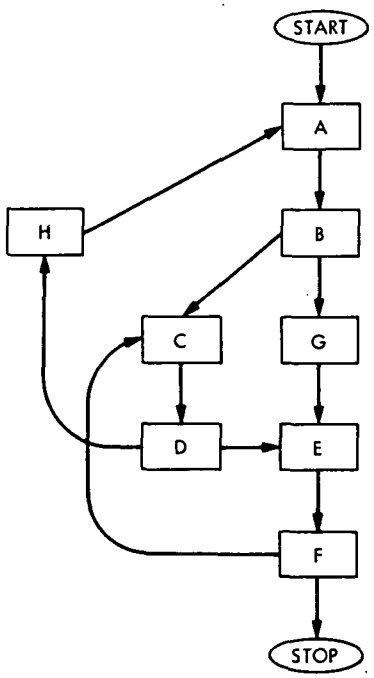


Fig. 1. An unstructured flowchart

[1]The discussion which follows is largely taken from Knuth (Ref. 1, pp. 364–369).

input, there is a considerable amount that can be learned directly from the flowchart. To glean this information, let us draw the flowchart in a more abstract form (Fig. 2), in which the branches are labeled $e_1, e_2, \cdots, e_{12}$.

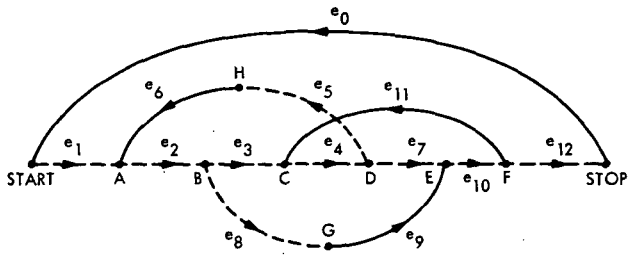


**Fig. 2. Flowchart with branches labeled**

Let $E_j$ (called a *branch variable*) denote the number of times branch $e_j$ is taken during the program run. Then since the number of times each program step is entered is the same as the number of times it is exited, for each program step we get a linear equation involving the branch variables. These are called Kirchhoff's equations, since if we were considering electrical networks instead of program flowcharts, and if $E_j$ represented the current along the edge $e_j$, Kirchhoff's current law would yield the same set of equations. Thus we obtain 8 equations in the 12 branch variables:

$$E_1 + E_6 = A = E_2$$

$$E_2 = B = E_3 + E_8$$

$$E_3 + E_{11} = C = E_4$$

$$E_4 = D = E_5 + E_7$$

$$E_7 + E_9 = E = E_{10}$$

$$E_{10} = F = E_{11} + E_{12}$$

$$E_8 = G = E_9$$

$$E_5 = H = E_6.$$

The fictitious edge $e_0$ has been added so that Kirchhoff's laws will also hold for the START and STOP nodes; i.e.,

$$E_0 = E_1 \quad \text{(START)}$$

$$E_{12} = E_0 \quad \text{(STOP)}$$

Since START and STOP are executed exactly once in each program run, we have the boundary condition $E_0 = 1$. From now on, we will focus our attention on the branch variables $E_0, \cdots, E_{12}$ rather than the step variables $A, \cdots, H$.

At this point we could apply classical linear algebra and "solve" our system of equations, but there is another technique which can be used and which takes advantage of the combinatorial structure of the flowchart.

The first step in this procedure is to find a *free subtree* in the flowchart graph. A free subtree is a connected subgraph which contains each node and has no cycles. In our case the dotted branches $e_1$, $e_2$, $e_3$, $e_4$, $e_5$, $e_7$, $e_8$, $e_{10}$, $e_{12}$ of Fig. 2 form a free subtree. The remaining branches, $e_0$, $e_6$, $e_9$, $e_{11}$ are called *fundamental branches*. If we add one of the fundamental branches to the free subtree, the resulting graph contains a unique cycle, called a *fundamental cycle*. For example, the fundamental cycle containing $e_9$ is $e_9$, $e_7$, $e_4$, $e_3$, $e_8$. However, in this cycle the branches $e_7$, $e_4$, $e_3$ must be traversed in the direction opposite the arrows, so we denote this cycle by $e_9 - e_7 - e_4 - e_3 + e_8$. In this way we list the four fundamental cycles of our flowchart:

$$C_0: + e_0 + e_1 + e_2 + e_3 + e_4 + e_7 + e_{10} + e_{12}$$

$$C_6: + e_2 + e_3 + e_4 + e_5 + e_6$$

$$C_9: - e_3 - e_4 - e_7 - e_8 - e_9$$

$$C_{11}: + e_4 + e_7 + e_{10} + e_{11}$$

The matrix of coefficients of these cycles contains the same information in more compact form:

$$C = \begin{array}{c} \\ 0 \\ 6 \\ 9 \\ 11 \end{array} \begin{array}{c} \begin{array}{cccccccccccc} 0 & 1 & 2 & 3 & 4 & 5 & 6 & 7 & 8 & 9 & 10 & 11 & 12 \end{array} \\ \begin{bmatrix} 1 & 1 & 1 & 1 & 1 & 0 & 0 & 1 & 0 & 0 & 1 & 0 & 1 \\ 0 & 0 & 1 & 1 & 1 & 1 & 1 & 0 & 0 & 0 & 0 & 0 & 0 \\ 0 & 0 & 0 & -1 & -1 & 0 & 0 & -1 & 1 & 1 & 0 & 0 & 0 \\ 0 & 0 & 0 & 0 & 1 & 0 & 0 & 1 & 0 & 0 & 1 & 1 & 0 \end{bmatrix} \end{array}$$

It turns out (see Knuth, Ref. 1, p. 366) that the rows of C form a basis for the set of solutions to Kirchhoff's equations; i.e., a vector $\mathbf{E} = [E_0, E_1, \cdots, E_{12}]$ satisfies Kirchhoff's equations if and only if E is a linear combination of the rows of C. Consequently, the four branch variables $E_0$, $E_6$, $E_9$, $E_{11}$, can be taken as independent, and the remaining 9 can be expressed in terms of them simply by reading off the appropriate columns of C:

$$E_1 = E_0$$

$$E_2 = E_0 + E_6$$

$$E_3 = E_0 + E_6 - E_9$$

$$E_4 = E_0 + E_6 - E_9$$

$$E_5 = E_6$$

$$E_7 = E_0 - E_9 + E_{11}$$

$$E_8 = +E_9$$

$$E_{10} = E_0$$

$$E_{12} = E_0$$

Finally, we use our "boundary condition" $E_0 = 1$ and obtain the following values for our original set of unknowns $A, B, \cdots, H$:

$$A = 1 + E_6$$

$$B = 1 + E_6$$

$$C = 1 + E_6 - E_9$$

$$D = 1 + E_6 - E_9$$

$$E = 1 + E_{11}$$

$$F = 1 + E_{11}$$

$$G = +E_9$$

$$H = +E_6$$

This set of equations expresses the number of times each program step is executed in terms of the number of times the three fundamental branches $e_6$, $e_9$, $e_{11}$ are traversed. This is as far as Kirchhoff's equations can take us, and to proceed further it is necessary to know more about the program itself. Our point is merely that solving Kirchhoff's equations for an arbitrary (unstructured) flowchart requires a considerable amount of work: the fastest known algorithm for finding a set of fundamental cycles for a directed graph requires $0(n^\gamma)$ arithmetical operations, where $n$ is the number of nodes and $\gamma$ is an integer between 2 and 3 which depends on the "fine structure" of the graph (Ref. 3, pp. 280–284). Thus the "worst case" performance of this algorithm is $0(n^3)$, which is the same as if we had used ordinary Gaussian elimination on Kirchhoff's equations.

In the next section we show that for structured programs, the situation is much simpler.

## II. Structured Programs

In a computer program, it is often helpful to have certain program steps called *subprograms*, and to give details of these subprograms elsewhere. For example, a program flowchart could look like this (Fig. 3):

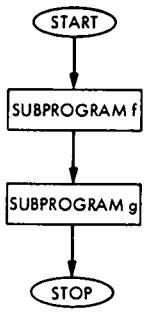


**Fig. 3. Program flowchart**

and the subprogram flowcharts might look like this (Fig. 4):

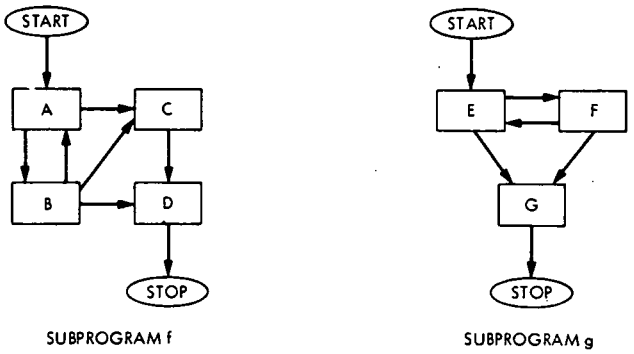


**Fig. 4. Subprogram flowchart**

This program and its subroutines could be combined into the following flowchart (Fig. 5):

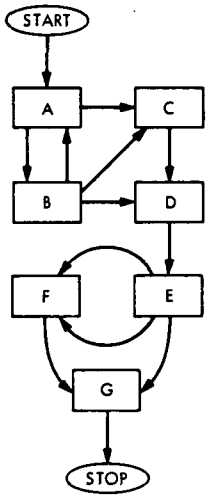


**Fig. 5. Program and subroutine flowchart**

In general, the subroutines could themselves contain subroutines containing further subroutines, etc. In this way, a very large and complex flowchart can be built up from simple components. The basic idea of *structured programming* is to build up program flowcharts in this way from a small collection of "basic" allowable flowcharts.

Let us now formally define a program *flowchart* as a set of *steps* and a set of *branches*, each branch leading from a step $a$ to a step $b$, and denoted pictorially by $a \rightarrow b$ . This branch is called an *exit* from $a$ and an *entrance* to $b$. A flowchart must always have two special steps called START and STOP such that there is only one exit from START, and no entrances, and only one entrance to STOP, no exits. Furthermore, a flowchart step with exactly one entrance and exit can be designated a "subprogram," and will refer to another flowchart, as in the above example.

A few important flowcharts which have been given "names" for reference are shown in Fig. 6.

It is common to employ different symbols in order to distinguish various kinds of program steps. Thus in Ref. 2 a step with one entrance and several exits is called a *decision* node and denoted by a lozenge; one with one exit and several exits is called a *collecting* node and denoted by a circle; and one with one entrance and one exit is called a *process* node and denoted by a rectangle.

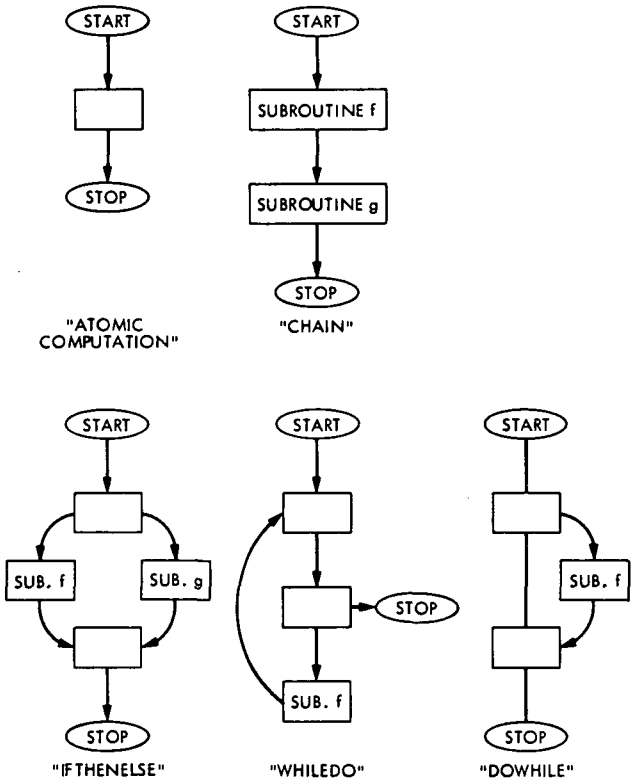


**Fig. 6. Some important flowcharts**

We come now to the definition of a *structured* program flowchart. If $\mathcal{B} = \{F_1, F_2, \cdots\}$ is a set of flowcharts—called $\mathcal{B}$-flowcharts—another flowchart is said to be *$\mathcal{B}$-structured* if it is either an *atomic computation*, or if it is a $\mathcal{B}$-flowchart, all of whose subprograms are $\mathcal{B}$-structured.

It is known (Ref. 2, ch. 5) that any program[2] can be rewritten in such a way that its flowchart is $\mathcal{B}$-structured if $\mathcal{B} = \{\text{CHAIN,IFTHENELSE,DOWHILE}\}$.

Since structured program flowcharts with many levels of subprograms are hard to draw, it is convenient to have a compact pictorial description of them. One such description is the *program tree*, in which each $\mathcal{B}$-flowchart is represented by a program tree *module*, consisting of a box labeled with the flowchart name, and descending arrows corresponding to the subprograms. For example, the modules for CHAIN, IFTHENELSE, DOWHILE, and WHILEDO look like this (Fig. 7):

[2]Actually this result holds only for *proper* programs; for definitions, see Ref. 2.

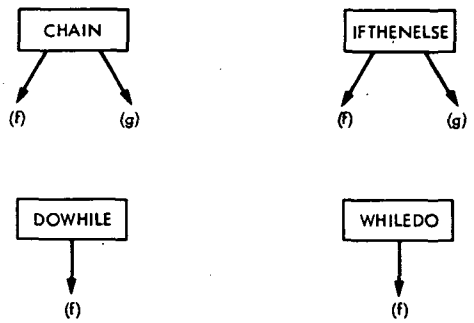


**Fig. 7. Some program tree modules**

The module for the special flowchart "atomic computation" is the symbol "≡".

Given a $\mathcal{B}$-structured flowchart, its program tree is defined as "≡", if it is an atomic computation, or if it is a $\mathcal{B}$-flowchart with subprograms, as the program tree module of the $\mathcal{B}$-flowchart, with the program trees of its subprograms attached to the appropriate arrows of the module We define the *level* of the first (top) $\mathcal{B}$-flowchart as 1, and for the other flowcharts as one more than its "parent" flowchart in the program tree. For example, here is the program tree of a {CHAIN,IFTHENELSE,DOWHILE}-structured program, with the level numbers written in parentheses to the right of the flowchart modules (Fig. 8):

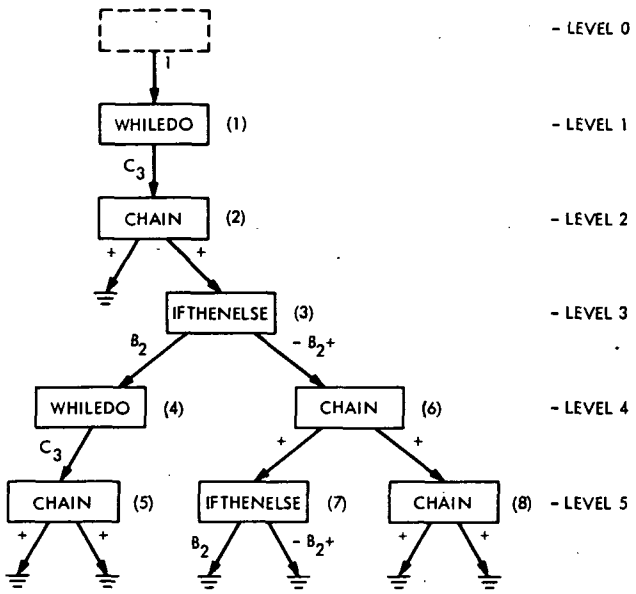


**Fig. 8. A program tree for a structured flowchart**

(The dummy module at level 0 and the labels on the arrows will be explained in Section III; for now they should be ignored.) If expanded into one flowchart, it would look like this (Fig. 9):

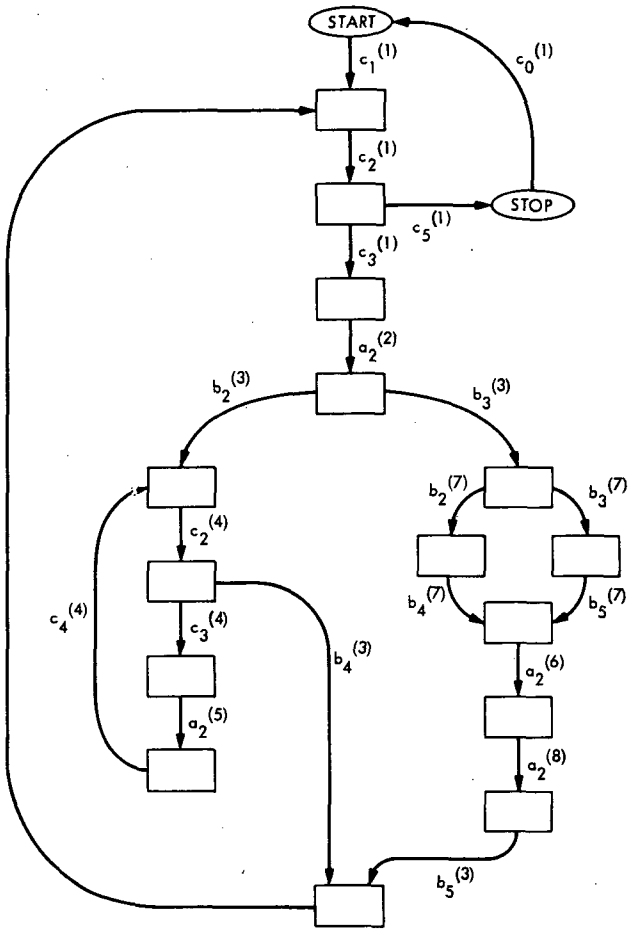


**Fig. 9. Flowchart represented by the tree of Fig. 8**

(This is the same as the flowchart in Figure 5.1.2 in Ref. 2; the branch labels will be explained in Section III.)

## III. Solving Kirchhoff's Equations for Structured Flowcharts

In this section we will show that for a $\mathcal{B}$-structured program flowchart, Kirchhoff's equations can be solved by a simple *inspection* of the program tree. Throughout, we will illustrate the ideas with the $\mathcal{B}$-structured program of Figs. 8 and 9, with $\mathcal{B}$ = {CHAIN, IFTHENELSE, WHILEDO}.

The first step is to solve Kirchhoff's equations in each of the $\mathcal{B}$-flowcharts. This can be done by the method described in Section I, and it may take a lot of work if $\mathcal{B}$ contains many complicated flowcharts. The point is, however, that once this is done we will be prepared to solve Kirchhoff's equations for *any* $\mathcal{B}$-structured program with essentially no additional work.

For example, if $\mathcal{B}$ = {CHAIN, IFTHENELSE, WHILEDO}, a set of solutions to Kirchhoff's equations is given in Fig. 10 (cf. Fig. 6; the edges are labeled with lower-case a's, b's, and c's, and the upper-case letters denote the corresponding branch variables.)

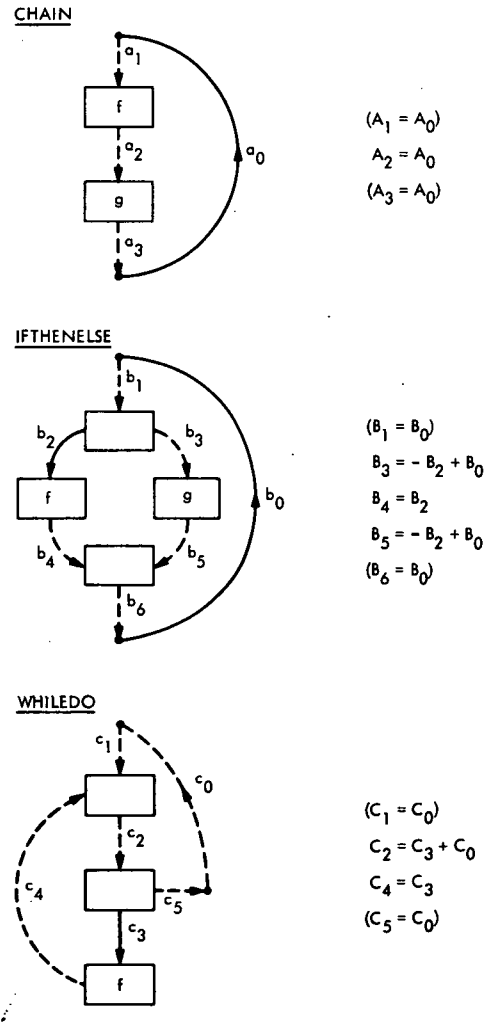


**Fig. 10. Structured program flowchart**

(Appendix A contains the solutions to Kirchhoff's equations for four more simple flowcharts which may be encountered as $\mathcal{B}$-flowcharts.)

Having done this preliminary work, we are prepared to solve Kirchhoff's equations for any $\mathcal{B}$-structured flowchart. Our first step is to assign *labels* to the branches in the component $\mathcal{B}$-flowcharts. To do this, we assign an identifying number to each flowchart and use that number as a superscript on the branch variables, so that identical $\mathcal{B}$-flowcharts which appear in different places in the program tree can be distinguished. For example in the flowchart of Fig. 8, the branch variables of WHILEDO Flowchart 1 will be denoted by $c_i^{(1)}$, and those of Flowchart 4 by $c_i^{(4)}$.

It is important to notice that except for the top (level 1) flowchart, not all of the flowchart branches need be considered. For example, in Fig. 8, in CHAIN Flowchart 2, branch $a_1^{(2)}$ is the entrance from WHILEDO Flowchart 1 and so it is identical to $c_3^{(1)}$. Similarly $a_3^{(2)}$ is identical to $c_4^{(1)}$. Because of this, in each $\mathcal{B}$-flowchart except the top one, the exit from START, the entrance to STOP, and the fictitious branch from STOP to START will all be missing. In the example of Fig. 8 there will be 20 labeled branches; these have been indicated in Fig. 9, although we emphasize that it will not be necessary to draw the complete flowchart in order to solve Kirchhoff's equations.

The next step is to observe that within each component $\mathcal{B}$-flowchart, *Kirchhoff's equations remain valid*, except that a special interpretation must be given the fictitious STOP → START branches. For example, in the WHILEDO Flowchart 4 in Fig. 8, the branch $c_0^{(4)}$ represents the "boundary" between this flowchart and the rest of the program. Thus $C_0^{(4)}$ is the number of times the WHILEDO Flowchart 4 is entered, and so the "boundary condition" is $C_0^{(4)} = B_2^{(3)}$, since every time the branch $b_2^{(3)}$ in IFTHENELSE Flowchart 3 is traversed, the flowchart WHILEDO Flowchart 4 is entered.

In this way we can express every branch variable in the $\mathcal{B}$-structured flowchart in terms of the *fundamental* branch variables of the component $\mathcal{B}$-flowcharts, as follows. Given a branch in one of the component $\mathcal{B}$-flowcharts, use Kirchhoff's equations within the flowchart to express the corresponding branch variable in terms of the fundamental branch variables in the *same* $\mathcal{B}$-flowchart, together with a branch variable in a $\mathcal{B}$-flowchart at a higher level. This new branch variable, if not itself fundamental, is then subject to the same procedure, until eventually the top flowchart is reached.

For example the edge $b_3^{(7)}$ in Figs. 8 and 9 yields the following series of equations:

$$B_3^{(7)} = -B_2^{(7)} + B_0^{(7)}$$
$$B_0^{(7)} = A_1^{(6)}$$
$$A_1^{(6)} = B_3^{(3)}$$
$$B_3^{(3)} = -B_2^{(3)} + B_0^{(3)}$$
$$B_0^{(3)} = A_2^{(2)}$$
$$A_2^{(2)} = A_0^{(2)}$$
$$A_0^{(2)} = C_3^{(1)}$$

Thus finally we get the equation $B_3^{(7)} = -B_2^{(7)} - B_2^{(3)} + C_3^{(1)}$, which expresses $B_3^{(7)}$ in terms of the fundamental branch variables $B_2^{(7)}$, $B_2^{(3)}$, $C_3^{(1)}$.

We can avoid this "unraveling" procedure by observing that in the above procedure we "bubble-up" through the program tree, picking up fundamental branch variables as we go. This suggests that we should label the arrows in the program tree with information that will tell us which branches to "pick up" in our rise to the top. The simplest such scheme is to label each program tree arrow with the formula which expresses the corresponding $\mathcal{B}$-flowchart branch variable in terms of the fundamental branch variables, perhaps omitting the fictitious branch variables, but retaining their signs[3]. Thus the modules in Fig. 7 would appear as this (Fig. 11):

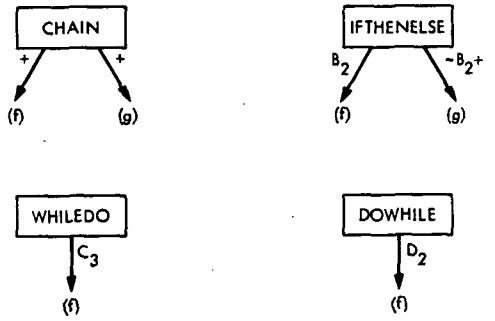


**Fig. 11. Modules of Fig. 7**

[3]It is possible that some branch variables will occur on the fundamental cycle which includes the fictitious branch with a minus sign. However, for any flowchart which corresponds to a realizable computer program, there will always be a properly oriented path from START to STOP, which we can take as part of this fundamental cycle. This means that we can always assume that the fictitious branch variable occurs with a "+" sign in Kirchhoff's equations.

Assuming that the program tree has been built from these arrow-labeled modules, the expression of a given branch variable (b.v.) in terms of the fundamental branch variables (f.b.v.'s) can be obtained as follows. First, express the given b.v. in terms of f.b.v.'s in its own (local) $\mathcal{B}$-flowchart. If the fictitious b.v. does not occur in this expression, we are through, since these local f.b.v.'s are global f.b.v.'s as well. If, however, the fictitious b.v. does appear, it must be expressed in terms of fundamental b.v.'s at higher levels. This is done by "climbing" the program tree, picking up arrow labels along the way, and stopping as soon as an arrow without a "+" is reached. (To be completely systematic, we should add a dummy module at level 0, whose arrow is labeled "1", so that the fictitious b.v. at level 1 will be assigned the value 1 by this procedure. This has been done in Fig. 8).

For example, using this technique on the program tree of Fig. 8, we express $B_3^{(7)}$ in terms of f.b.v.'s as follows:

$B_3^{(7)} = -B_2^{(7)} + B_0^{(7)}$ (Solution to Kirchhoff's equations in IFTHENELSE flowchart; see Fig. 10.)

$B_0^{(7)} = -B_2^{(3)} + C_3^{(1)}$ (From labeled program tree; see Fig. 8.)

In this way we obtain the following complete solution to Kirchhoff's equations for the flowchart of Figs. 8 and 9:

| Flowchart number | Solution |
|---|---|
| 1 | $C_1^{(1)} = 1$ |
| | $C_2^{(1)} = C_3^{(1)} + 1$ |
| | $C_3^{(1)} =$ fundamental |
| | $C_4^{(1)} = C_3^{(1)}$ |
| | $C_5^{(1)} = 1$ |
| 2 | $A_2^{(2)} = C_3^{(1)}$ |
| 3 | $B_2^{(3)} =$ fundamental |
| | $B_3^{(3)} = -B_2^{(3)} + C_{(1)}^3$ |
| | $B_4^{(3)} = B_2^{(3)}$ |
| | $B_5^{(3)} = -B_2^{(3)} + C_3^{(1)}$ |
| 4 | $C_2^{(4)} = C_3^{(4)} + B_2^{(3)}$ |
| | $C_3^{(4)} =$ fundamental |
| | $C_4^{(4)} = C_3^{(4)}$ |
| 5 | $A_2^{(5)} = C_3^{(4)}$ |
| 6 | $A_2^{(6)} = -B_2^{(3)} + C_3^{(1)}$ |
| 7 | $B_2^{(7)} =$ fundamental |
| | $B_3^{(7)} = -B_2^{(7)} - B_2^{(3)} + C_3^{(1)}$ |
| | $B_4^{(7)} = B_2^{(7)}$ |
| | $B_5^{(7)} = -B_2^{(7)} - B_2^{(3)} + C_3^{(1)}$ |
| 8 | $A_2^{(8)} = -B_2^{(3)} + C_3^{(1)}$. |

In this way we have expressed each of the 20 branch variables in terms of the four fundamental branch variables $C_3^{(1)}$, $B_2^{(3)}$, $C_3^{(4)}$, $B_2^{(7)}$.

In summary, we have seen that in order to solve Kirchhoff's equations for a $\mathcal{B}$-structured program, it is first necessary to solve Kirchhoff's equations in the $\mathcal{B}$-flowcharts, and also to label the arrows of the program tree modules. Once this is done the solution to Kirchhoff's equations can be read directly from the program tree. Since the program tree is generally available anyway—it is part of the program documentation—once the solutions to Kirchhoff's equations for the $\mathcal{B}$-flowcharts are available, the solution of Kirchhoff's equations in an arbitrary $\mathcal{B}$-structured flowchart becomes trivial. For this reason, we have listed in the appendix seven flowcharts which are likely to appear in $\mathcal{B}$, together with their fundamental cycles, solutions to Kirchhoff's equations, and program tree modules.

## References


1. Knuth, Donald, *The Art of Computer Programming, Vol. 1: Fundamental Algorithms*, Addison-Wesley, Reading, Mass., 1969.
2. Tausworthe, Robert, *Standardized Development of Computer Software*, SP 43-29, Jet Propulsion Laboratory, Pasadena, Calif. (to be published).
3. Deo, Narsingh, *Graph Theory, with Applications to Engineering and Computer Science*, Prentice-Hall, Englewood Cliffs, N. J., 1974.

# Appendix A

## Some Basic Flowcharts

In the flowchart diagram, *solid* branches are fundamental, *dotted* branches are not. Equations in parentheses involve branch variables whose branches are "connections" to the overall flowchart and which will not occur except at the top of the program tree.

CHAIN

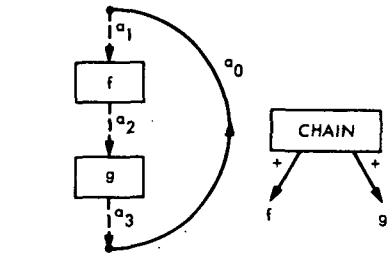


FUNDAMENTAL CYCLES

$a_0 + a_1 + a_2 + a_3$

KIRCHHOFF'S EQUATIONS

$(A_1 = A_0)$

$A_2 = A_0$

$(A_3 = A_0)$

IFTHENELSE

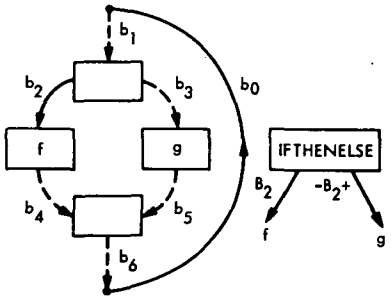


FUNDAMENTAL CYCLES

$b_0 + b_1 + b_3 + b_5 + b_6$

$b_2 + b_4 - b_5 - b_3$

KIRCHHOFF'S EQUATIONS

$(B_1 = B_0)$

$B_2$ = FUNDAMENTAL

$B_3 = -B_2 + b_0$

$B_4 = B_2$

$B_5 = -B_2 + B_0$

$(B_6 = B_0)$

WHILEDO

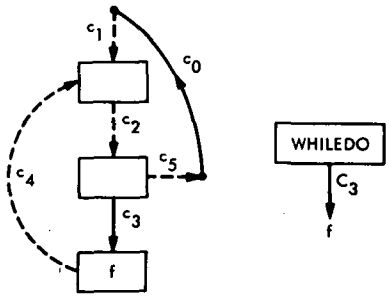


FUNDAMENTAL CYCLES

$c_0 + c_1 + c_2 + c_5$

$c_3 + c_4 + c_2$

KIRCHHOFF'S EQUATIONS

$(C_1 = C_0)$

$C_2 = C_3 + C_0$

$C_3$ = FUNDAMENTAL

$C_4 = C_3$

$(C_5 = C_0)$

DOWHILE

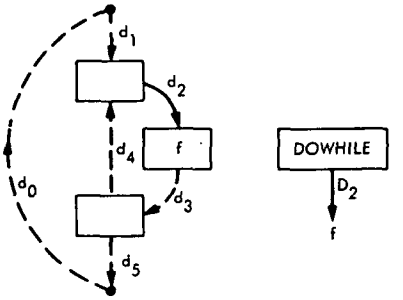


FUNDAMENTAL CYCLES

$d_0 + d_1 - d_4 + d_5$

$d_2 + d_3 + d_4$

KIRCHHOFF'S EQUATIONS

$(D_1 = D_0)$

$D_2$ = FUNDAMENTAL

$D_3 = D_2$

$D_4 = D_2 - D_0$

$(D_5 = D_0)$

REPEAT

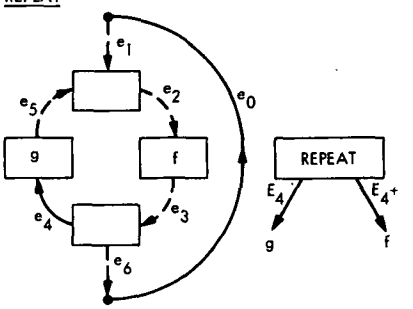


FUNDAMENTAL CYCLES

$e_0 + e_1 + e_2 + e_3 + e_6$

$e_4 + e_5 + e_2 + e_3$

KIRCHHOFF'S EQUATIONS

$(E_1 = E_0)$

$E_2 = E_4 + E_0$

$E_3 = E_4 + E_0$

$E_4$ = FUNDAMENTAL

$E_5 = E_4$

$(E_6 = E_0)$

CHAIN (n)

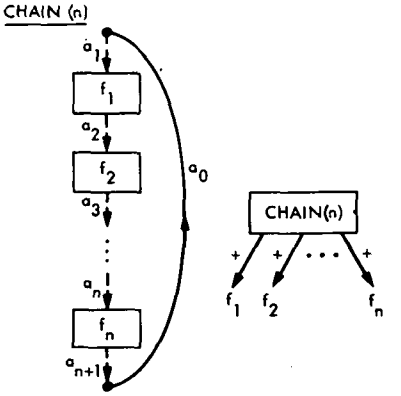


FUNDAMENTAL CYCLE

$a_0 + a_1 + a_2 + \ldots + a_{n+1}$

KIRCHHOFF'S EQUATIONS

$(A_1 = A_0)$

$A_2 = A_0$

$(A_{n+1} = A_0)$

CASE(n)

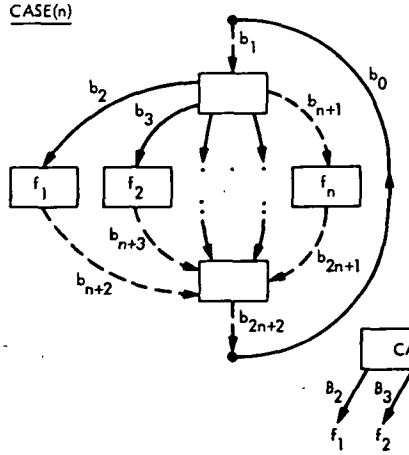


FUNDAMENTAL CYCLES

$b_0 + b_1 + b_{n+1} + b_{2n+1} + b_{2n+2}$

$b_i + b_{n+i} - b_{2n+1} = b_{n+1}$

$(i = 2, 3, \ldots, n)$

KIRCHHOFF'S EQUATION

$(B_1 = B_0)$

$B_{n+1} = B_{2n+1} = -B_2 - \ldots - B_n + B_0$

$B_{n+i} = B_i \quad (i = 2, \ldots, n)$

$B_{2n+2} = B_0)$

# A New Class of Burst-Correcting Cyclic Codes

B. Arazi[1]
Communications Systems Research Section

*In many DSN communication systems (the GCF, computer-computer data transfer, etc.) transmission errors tend to occur in intermittent bursts. In this article a new class of burst-error-correcting codes, potentially applicable to DSN systems, is described. Many of these codes are superior to any previously known.*

## I. Introduction

A systematic way of constructing burst-correcting cyclic codes is presented. If the length of the burst and the length of the codeword are denoted by $b$ and $n$, respectively, then for $b \geq 30$ and $b/n \leq 5$ percent, these codes outperform the most efficient burst-correcting codes known, in most cases. (For the same $b$ and $n$, the rate of the suggested code is higher.)

The main advantage of the suggested code lies in the simple hardware implementation of both encoder and decoder. The encoder uses a feedback shift register with a simple structure of feedback connections. The decoder uses only two end-around shift registers.

## II. Presentation

*Theorem*

(1) Let $q$ be a prime and let $q > p$, where $p$ is a positive integer. The polynomial $g(X) = (X^q + 1)(X^p + 1)/(X + 1)$ generates a cyclic code. The length of a codeword is $q \cdot p$.

(2) The code is capable of correcting any error burst of length $p - 1$ or less iff $p - n(q-p)$ is prime for $n = 0,1,2, \cdots, [p/(q-p)]$.

(3) Let $b$ denote the length of an error burst.

(a) If $b \leq \max(p + 1, q - p + 1)$ the error is detected.

[1]Visiting from the National Electrical Engineering Research Institute, South Africa.

(b) If $\max(p + 1, q - p + 1) < b < q$ then the probability of not detecting an error is less than $p \cdot 2^{p-q-1}$.

The proof is given in the Appendix.

Table 1 shows some cases where such a code can be used. (The efficiency is defined as $(2b + 2)/(n - k)$. The numerator is the minimum theoretical number of parity bits needed for correcting a burst of length $b$ or less and detecting all bursts of length $b + 1$ and $b + 2$. The denominator is the actual number of parity bits used. The efficiency is an important feature of a code. (If a shortened version of the code is used, the higher the efficiency the higher the rate is.) These codes are suitable for correcting long bursts inside relatively long codewords. (If $t \leq b < u - 1$, where $t$ and $u$ are two successive primes, that code is selected which corrects a burst of length $u - 1$ or less.)

For those cases where $b \geq 30$ and $b/n \leq 5$ percent, these codes outperform the known codes in most of the cases (higher rate and higher efficiency). A list of the known codes is given in Ref. 1. "These codes and the codes derived from them by interlacing (interleaving) are the most efficient single burst error correcting codes known."

Table 2 compares the performance of the suggested code and the known codes for the same values of $b$ and $n$. (In order to achieve the specified values of $b$ and $n$, the known codes were interleaved. Both codes were shortened when necessary. Table 2 demonstrates how, in most cases, the suggested code outperforms slightly the most efficient codes known. Its main importance lies, however, in the simplicity of the hardware implementation of both encoder and decoder.

The encoder of a cyclic code consists of a shift register and a feedback loop to which some stages are connected (via an exclusive OR gate), according to the coefficients of the generator polynomial. In our case,

$$\begin{aligned} g(X) &= (X^q + 1)(X^p + 1)/(X + 1) \\ &= (X^q + 1)(X^{p-1} + X^{p-2} + \cdots + 1) \\ &= X^{q+p-1} + X^{q+p-2} + \cdots + X^q \\ &\quad + X^{p-1} + X^{p-2} + \cdots + 1 \end{aligned}$$

It follows that the encoder consists of a shift register with $q + p - 1$ stages from which the first and last $p - 1$ stages are all connected to the feedback loop.

After considering the structure of the parity check matrix $H$ given in the proof of the theorem, it follows that the decoding operation which is performed by multiplying $H$ by the received message, can have a simple form, which is shown in Fig. 1.

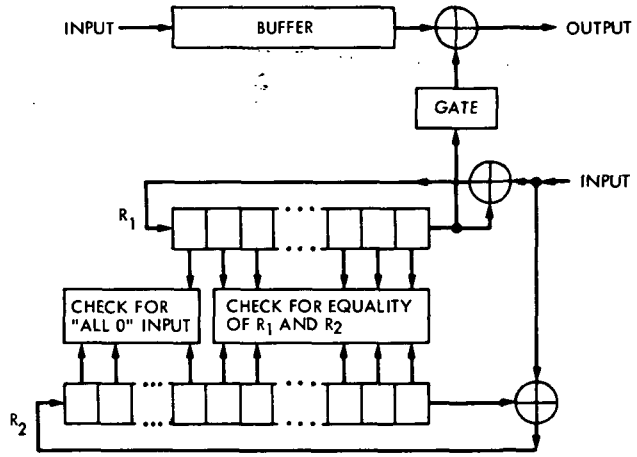


**Fig. 1. The decoder**

The received message is shifted into a buffer, and also into registers $R_1$ and $R_2$, which are a $p$-stage and a $q$-stage register, respectively. After the complete message has been received, a check is made to determine whether the content of the registers is "all 0." If this is the case, no error has been detected and the received message is shifted out of the buffer without any correction.

If an error is detected, the content of the last stage of $R_1$ (counting from the right), as well as the last $(q - p + 1)$ stages of $R_2$ are checked as to being "all 0." At the same time the contents of the $i$th stages of $R_1$ and $R_2$, $1 \leq i \leq p - 1$, are checked for being identical. If either one of the two checks described fails, the bits stored in the buffer are shifted out one at a time, while the gate is closed. For each bit leaving the buffer, both registers are shifted cyclically by one place (the input is constantly logic 0) and the checks described are performed for each shift.

When both checks have been satisfied (one check shows "all 0" input and the other shows identity of the content of the first $p - 1$ stages) the gate is opened and the content of $R_1$ is added bit by bit to the bits shifted out of the buffer and the correction is completed.

The advantage of the described decoder lies in the fact that it does not use feedback connections at all. On the

other hand, when implementing the decoder of the known cyclic codes, some complicated feedback connections are made according to the coefficients of the generator polynomial.

The theorem considers also the case where $q - p + 1 > p + 1$, which means that $q > 2p$. Notice that if $p$ and $q$ are primes where $q > 2p$ it follows from the theorem that the code generated by $(X^p + 1)(X^q + 1)/(X + 1)$ is capable of correcting any error burst of a length $p - 1$ or less.

Clarifying the concept of error detection is also worthwhile. An error is detected when the decoder detects the existence of an error, together with the fact that it is uncorrectable, such that no false attempt is made to correct the error. Referring to the described decoder, an error is detected when either one of the two checks performed is not satisfied by the time the message is shifted completely out of the buffer.

The following demonstrates the ability of the code for the case where $p = 31$ and $q = 101$:

(1) Any error burst of length 30 or less is corrected.

(2) Any error burst of length 71 or less is detected.

(3) The probability of not detecting an error of a length between 72 and 100 is less than $10^{-20}$.

(4) By keeping $p = 31$ and changing $q$, it is possible to achieve almost any desirable error detection capability.

The theorem states that the condition posed on the values of $p$ and $q$ is also a necessary condition. It is worthwhile demonstrating why it is not enough to require that $p$ and $q$ should be prime.

Let $X$ be a set of positive integers which are the locations of the erroneous bits inside the received message. Let $A$ and $B$ be the sets of residues of the elements of $X$ modulo $p$ and $q$, respectively. It follows from the structure of the decoder that by the time the received message is stored completely in the buffer, the locations of the 1 elements in $R_1$ and $R_2$ are the elements of $A$ and $B$, respectively.

An error burst cannot be corrected uniquely if a set $Y$, which is different from $X$, produces the same residue sets $A$ and $B$. Two such sets $X$ and $Y$ can exist although $p$ and $q$ are primes. For example: $p = 11$, $q = 13$.

$$X = \{11,12,14,15,19,20\}, \quad Y = \{58,59,63,64,66,67\}$$

$$A = \{1,3,4,8,9,11\}, \quad B = \{1,2,6,7,11,12\}$$

The elements in both $X$ and $Y$ are confined to 10 successive places since the error burst is of length $p - 1$ or less.

## Reference

1. Lin, S., *Introduction to Error Correcting Codes*, Prentice-Hall, Inc., Englewood Cliffs, N.J., 1970.

# Appendix

# Proof of the Theorem

*Step 1:* Proof of part (1) of the theorem

The greatest common divisor of $X^p + 1$ and $x^q + 1$ is $X^{(q,p)} + 1 = X + 1$. Since $X^p + 1$ and $X^q + 1$ are both divisors of $X^{q \cdot p} + 1$, the polynomial $g(X) = (X^p + 1)(X^q + 1)/(X + 1)$ is also a divisor of $X^{q \cdot p} + 1$, which is a necessary and sufficient condition for $g(X)$ to generate a cyclic code of length $p \cdot q$.

*Step 2:* Finding a parity check matrix

Let us define a polynomial $h(X)$,

$$h(X) = (X^{q \cdot p} + 1)/g(X)$$

$$= [(X^{p \cdot q} + 1)(X + 1)]/[(X^p + 1)(X^q + 1)].$$

The rows of the parity check matrix $H$ consist of multiples of $h(X)$ (a polynomial is regarded as the row of a matrix when its coefficients form the elements of the row). In our case, $p + q - 1$ rows should be linearly independent. (Usually the number of rows of a parity check matrix equals the number of independent parity checks. However, if some extra rows which are a linear combination of the independent ones are added, the obtained matrix is still a parity check matrix in the sense that a syndrome S is defined as $H$ X = S where X is the received message. The syndrome S is the "all 0" vector iff X is a transmitted codeword.)

Let $m_i(X) = h(X) \cdot X^i \cdot (X^q + 1)/(X + 1) = X^i(X^{q \cdot p} + 1)/(X^p + 1) = X^i(X^{(q-1)p} + X^{(q-2)p} + \cdots + X^p + 1)$ $i = 0,1, \cdots, p - 1$.

$s_i(X) = h(X) \cdot X^i(X^p + 1)/(X + 1) = X^i(X^{q \cdot p} + 1)/(X^q + 1) = X^i(X^{(p-1)q} + X^{(p-2)q} + \cdots + X^q + 1)$ $i = 0,1, \cdots, q - 1$.

Let the first $p$ rows of a matrix $H$ consist of the polynomials $m_i(X)$ and let its last $q$ rows consist of the polynomials $s_i(X)$. This matrix can be described in a very simple way. Its first $p$ rows consist of the unity matrix of order $p \times p$ written successively $q$ times. A similar description applies for the last $q$ rows.

For example, for $p = 2$, $q = 3$,

$$H = \begin{bmatrix} 1 & 0 & 1 & 0 & 1 & 0 \\ 0 & 1 & 0 & 1 & 0 & 1 \\ 1 & 0 & 0 & 1 & 0 & 0 \\ 0 & 1 & 0 & 0 & 1 & 0 \\ 0 & 0 & 1 & 0 & 0 & 1 \end{bmatrix}$$

The sum of the rows of $H$ is the "all 0" vector, which means that any particular row equals the sum of all the other rows. In view of the structure of $H$ it is obvious that if one row is omitted, the rest $q + p - 1$ rows are linearly independent and $H$ is therefore a parity check matrix of the code.

*Step 3:* Analyzing the syndrome

Let X be a codeword generated by $g(X)$ and let Y = X + N be the received message where N is an error burst of length $p - 1$ or less. Let $E$ be a vector of length $p - 1$ whose elements are the error pattern, where its first element is 1. (If the burst is of length $d < p - 1$, the last $p - 1 - d$ elements of $E$ are 0). Let $E_1$ and $E_2$ be two binary vectors of length $p$ and $q$ respectively. The first $p - 1$ bits of both vectors equal the vector $E$, and the rest of their elements are 0.

Let $E_1^{(j)}$ and $E_2^{(j)}$ denote the vectors obtained from $E_1$ and $E_2$ by shifting them cyclically for $j$ places. If the first erroneous bit of the error burst is in the $j$th place of the received message, then in view of the construction of $H$, the first $p$ bits of the syndrome are the vector $E_1^{(j)}$ and its last $q$ bits are the vector $E_2^{(j)}$. The error burst cannot be corrected iff there exists an error burst pattern $F$ which starts at the $k$th place of the received message and which produces the same syndrome, where $F \neq E$ or $j \neq k$ (or both).

3.1 $F \neq E, j = k$. Such a case is impossible. (Two different error patterns which occur at the same place in the received message cannot produce the same syndrome.)

3.2 $F = E, j \neq k$. Since the same syndrome is produced it follows that $E_1^{(j)} = E_1^{(k)}$ and $E_2^{(j)} = E_2^{(k)}$. A vector can equal a cyclic shift of itself if all its elements equal each other. Such a case is impossible here since both $E_1$ and $E_2$ start with a 1 and end with a 0. Since the length of $E_2$ is prime, the last two equalities are possible iff $j - k$ is divisible by $r \cdot q$, where $r$ is a divisor of $p$. (Generally, $r$ can also be a product of $p$, but this is impossible here since $0 < j, k \leq p \cdot q$.) It follows that $p$ must be factorized.

3.3 $F = E, j \neq k$. The theorem deals with error bursts of length $p - 1$ or less. The length of $F$ is therefore $p - 1$ where $F$ starts with a 1. (If the length of the burst whose pattern is represented by $F$ is less than $p - 1$, the last elements of $F$ are 0.) Let $F_1$ and $F_2$ be binary vectors of length $p$ and $q$, respectively, both equal in their first $p - 1$ places to the vector $F$. The rest of their elements are 0. Since the same syndrome is produced by $E$ and $F$ it follows that $E_1^{(j)} = F_1^{(k)}$ and $E_2^{(j)} = F_2^{(k)}$.

Let $i \equiv j - k \pmod{p}$ and $m \equiv j - k \pmod{q}$. It follows that $F_1 = E_1^{(i)}$ and $F_2 = E_2^{(m)}$. If either $i = 0$ or $m = 0$ it will follow that $E = F$. Such a case was treated above. The rest of the proof will show that it is possible to have $F_1 = E_1^{(i)}$ and $F_2 = E_2^{(m)}$ where $i, m > 0$ iff $p - n(q - p)$ is factorized for some $n$.

The vectors $E_2$ and $F_2$ both start with a 1 and have $q - p + 1$ zeroes at the end. In order for $F_2$ to be obtained from $E_2$ by a cyclic shift, $E_2$ must have somewhere in it $q - p + 1$ successive zeroes (which are transferred to its end by the cyclic shift that produces $F_2$). These zeroes are followed by a 1 (which is transferred to the beginning of $F_2$) and therefore cannot be part of the last $q - p + 1$ zeroes at the end of $E_2$. It follows that $E_2$ has in it $q - p + 1$ successive zeroes confined to the first $p$ places, which means that $E_1$ contains $q - p + 1$ successive zeroes.

The vectors $E_1$, $E_2$, $F_1$ and $F_2$ have therefore the following form.

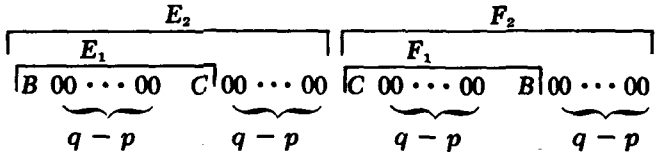


where $B$ and $C$ are two vectors starting with a 1 and ending with a 0.

*Step 4:* A general description of the proof

Let $D$ denote an "all 0" vector of length $s = q - p$. Let the length of the vectors $B$ and $C$ obtained in the previous step be denoted by $r$ and $t$, respectively.

Assuming that $F_1 = E_1^{(i)}$, steps 5 through 11 of the proof analyze the value of $p$ for all possible positive values of $i$. The various values of $i$ are related to $r$, $s$ and $t$.

It is shown that for each relation among $t,r,s$ and $t$ a certain vector $V_i$ has two different structures which can exist simultaneously iff $p - n \cdot s$ is factorized for some $n$.

Figure A-1 describes how each step of the proof follows from the previous one. (The number near each branch refers to the corresponding step.) Consulting this drawing might simplify the reading of the proof.

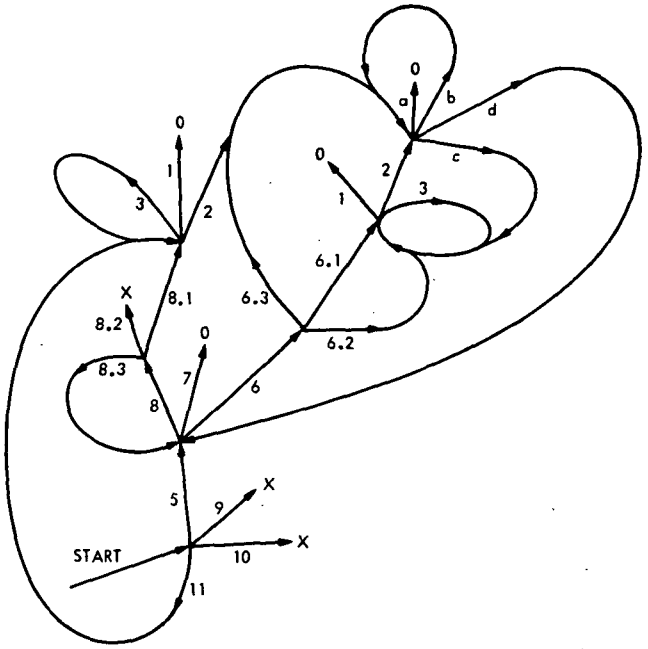


**Fig. A-1. Description of the proof**

The vector treated at the starting point is $F_1$. A last branch in a path (which is terminated by 0 or X for reasons explained later) corresponds to the structure of a certain vector $V_i$, and the path which starts with the starting point and ends with that last branch, shows the way by which $V_i$ is obtained from $F_1$.

The vector whose structure corresponds to a last branch in a path is denoted by $V_i$ if the path which connects the starting point to that branch connects on its way $i$ branches to branches with a lower index. This excludes the case where step 11 continues with step 8.1. (If this connection is the only backwards connection in the path, the vector treated in the last branch is still $V_0$.)

When a branch is terminated with an $X$ it means that a contradiction is met and the vector $V_i$, whose structure corresponds to this branch, cannot exist.

If a branch ending with a 0 corresponds to the structure of a vector $V_0$ whose length is $d_0$, it is proved that $d_0 - m \cdot s$ is factorized for some $m$.

When a branch in Fig. A-1 is connected to a branch with a lower index, it means that the proof arrives at an intermediate vector $V$ whose structure is identical to that

of a vector $V'$ treated previously, and the proof should therefore follow the same lines from that step on. (Within the proof, this reference to a previous step is of the form "continue with Eq. X." The equation preceding such a statement and Eq. X, are of the same form.)

*Conclusion 1.* It is enough to prove that $d_0 - m \cdot s$ is factorized for all possible $V_0$ in order to prove that $d_i - m \cdot s$ is factorized for all possible $V_i$ ($m$ does not have the same value for all $V_0$, but it is always some integer).

The factorization of $d_i - m \cdot s$ is in the sense that $V_i$ consists of a set of subvectors. Of these subvectors $m$ subvectors equal the vector $D$ and the rest equal a vector $A$ whose length is at least 2.

While reading the proof and observing the way by which the possible vectors $V_1$ are obtained (a vector $V_1$ is obtained when there is only one branch in the path which generates $V_1$ which is connected to a branch with a lower index), it is important to notice that if $V_1$ consists of subvectors which are either $D$ or $A$, so does the vector $V_0$, which corresponds to the same last branch as $V_1$. This means that if $d_1 - m \cdot s$ is factorized, so is $d_0 - n \cdot s$, where $m$ and $n$ are positive integers.

The last statement can be extended by induction in the sense that $V_{i+1}$ and $V_1$ can be treated as $V_1$ and $V_0$, respectively. It should also be noticed that $d_0 = p$.

*Conclusion 2.* If $d_i - m \cdot s$ is factorized for some $V_i$, so is $p - n \cdot s$.

Conclusion 3 follows from conclusions 1 and 2.

*Conclusion 3.* It is enough to prove that $d_0 - m \cdot s$ is factorized for all possible $V_0$, in order to prove that $p - n \cdot s$ is factorized for every possible structure of $F_1$ (assuming that $F_1 = E_1^{(i)}$ for $p > i > 0$).

Within the proof, the 4 different vectors $V_0$ are referred to as $F_1$ (since $V_0$ is the same vector treated at the starting point). However, in view of conclusion 3 it is enough to prove that $p - m \cdot s$ is factorized for those 4 vectors $F_1$ ($p = d_0$) in order to prove that $p - n \cdot s$ is factorized for all possible vectors $F_1$, where $m$ and $n$ are some integers.

*Remark:* In view of Fig. A-1, it might appear as if there are cases where a path enters an infinite loop and a terminating point is never reached. However, each time the path goes back to a step with a lower index, a shorter vector is treated. Since $F_1$ (which is the original vector treated) has a finite length, it is impossible to have an infinite loop.

(The case where step 11 continues with step 8.1 leaves the length of the vector unchanged. However, such a case can happen in one path only once.)

*Notation:* Throughout the proof, an equation of the type $X = HIJ$ means that a vector $X$ consists of the vectors $H$, $I$, and $J$ written successively. For example,

$$H = (abc), I = (de), J = (fgh), X = (abcdefgh)$$

Using this notation, $E_1 = BDC$ and $F_1 = CDB$.

*Step 5:* Assume $F_1 = E_1^{(i)}, 0 < i < t$

$E_1 = BDC_1C_2$ where the length of $C_2$ is $i$.

$F_1 = C_2BDC_1$, but $F_1 = C_1C_2DB$. It follows that

$$C_2BDC_1 = C_1C_2DB \tag{A-1}$$

where $B$, $C_1$, and $C_2$ all start with a 1 and end with a 0. (This statement follows from the fact that each one of the three vectors either starts or terminates $E_1$ or $F_1$.)

Let the length of $C_1$ be denoted by $u (u = t - i)$.

*Step 6:* Assume $F_1 = E_1^{(i)}, 0 < i < t, u < r$

6.1 $i > u$

The two arrangements of $F_1$ shown in Eq. (A-1) can be described by the following drawing (Fig. A-2):

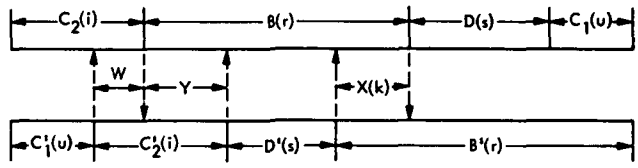


**Fig. A-2. The two arrangements of $F_1$**

The figures in the brackets denote the length of each vector. The vectors in the bottom drawing are denoted by "'," although they are identical to the corresponding ones in the upper drawing. According to the drawing it appears that $r > s+u$. This must be the case since it is assumed that $r > u$. The vector $B'$ starts with a 1 which must fall outside $D$ (which is the "all 0" vector). A vector $X$ whose length is $k = r - (s+u)$ is therefore obtained.

The following two equations follow from the drawing

$$B' = XDC_1$$

$$B = YD'X$$

It follows that

$$XDC_1 = YDX. \tag{A-2}$$

Three different cases should be observed. These cases are: (1) $k < u + s$ and $u < k + s$. (2) $u > k + s$. (3) $k > u + s$. Any other relation among $k$, $u$ and $s$ involves an immediate correspondence between the first element of $X$ or $C_1$ and an element in $D$, which is impossible since $X$ and $C_1$ start with a 1, and $D$ is the "all 0" vector.

It is assumed that such a consideration is well understood and therefore when a similar case occurs later in the proof it will not be analyzed.

(1) $k < u + s, u < k + s$

The following drawings are the structures of B′ and B shown in Fig. A-2.

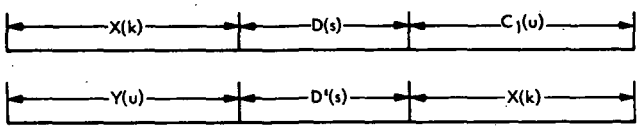


It follows that $k = u$ and therefore $X = Y = C_1$. Referring back to Fig. A-2 we observe: $C_2Y = C_1'C_2'$. It follows that $C_1C_2 = C_2C_1$. The last equation is possible only if both $C_1$ and $C_2$ consist of a subvector $A$ which repeats itself (i.e., $C_1 = AA \cdots A$, $C_2 = AA \cdots A$). The vector $A$ starts with a 1 and ends with a 0, which means that it has at least two elements. Since $F_1 = C_2YDXDC_1$, it follows that $p - 2s$ is factorized. ($p$ is the length of $F_1$. After deleting from it twice the vector $D$ the rest consist of a repetition of $A$.)

(2) $u > k + s$

It is observed in Fig. A-2 that both $C_1$ and $X$ terminate either $B'$ or $B$, and they both are preceded by $D$. Since $u > k + s$, it follows that $C_1$ is terminated by $DX$ which means that $C_1 = ZDX$.

$$B' = XDC_1 = XDZDX$$

$$B = YD'X \text{ and therefore } Y = XDZ$$

$$C_2 = C_1'W = ZDXW, C_2' = WY = WXDZ$$

and therefore

$$ZDXW = WXDZ \tag{A-3}$$

Four different cases should be considered.

(a) In the two versions of $C_2$, the vector $D$ coincides with itself.

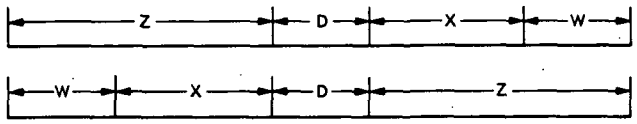


It follows that $WX = XW = Z$ and therefore $W$, $X$ and $Z$ have the form $AA \cdots A$.

$$F_1 = C_2YD'XDC_1 = ZDXWXDZDXDZDX.$$

It follows that $p - 5s$ is factorized. (After deleting $D$ five times, the rest is a repetition of $A$.)

The other three cases for the possible construction of $C_2$ are those where $D$ is completely contained in Z, $X$ or W. (Any other possibility results in an immediate correspondence between the first element of any of these three vectors and an element in $D$.)

(b) $D$ is completely contained in Z.

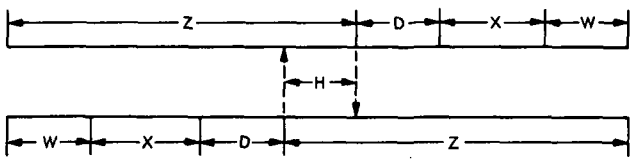


It follows that $WXDH = HDXW$ (both equal Z). Continue with Eq. (A-3).

(c) $D$ is completely contained in $X$.

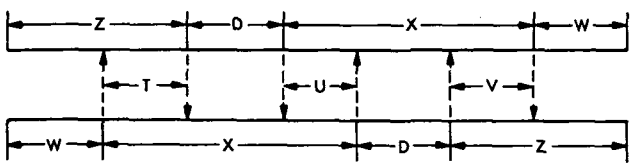

It follows that $TDU = UDV$ (both equal X). Continue with Eq. (A-2).

(d) $D$ is completely contained in $W$.

Eq. (A-3) states that $ZDXW = WXDZ$. Suppose that $D$ in the left side of the equation is contained in $W$ on the right side. (This assumption is always true for $D$ contained in $W$ since it holds iff $D$ on the right side of the equation is contained in $W$ on the left side.) It follows that $W$ has the form $ZDV$. Eq. (A-3) has now the form $ZDXZDV = ZDVXDZ$. It follows that $XZDV = VXDZ$. Continue with Eq. (A-1).

(3) $k > u + s$.

Both $C_1$ and $X$ terminate either $B'$ or $B$ (as shown in Fig. A-2). It follows that X has the form $ZDC_1$.

$$B' = XDC_1 = ZDC_1DC_1$$

$$B = YD'X = YDZDC_1$$

It follows that $ZDC_1 = YDZ$. Continue with Eq. (A-2).

6.2 $i = u$.

Referring to Eq. (A-1), the two arrangements of $F_1$ can be described as follows:

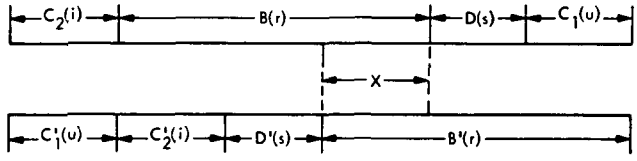


It follows that $C_1 = C_2$ and therefore $C_1DX = XDC_1$. (Both equal either $B$ or $B'$.) Continue with Eq. (A-2).

6.3 $i < u$.

$F_1$ has the following two arrangements.

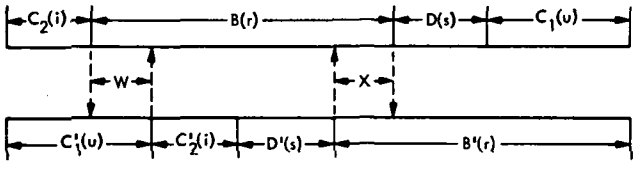


$C'_1 = C_2W$

$B' = XDC_1 = XDC_2W$

$B = WC'_2D'X$

It follows that $XDC_2W = WC_2DX$. Continue with Eq. (A-3).

The final conclusion from step 6 is that for $0 < i < t$ and $u < r$ it is possible to have $F_1 = E_1^{(i)}$ only if $p - n \cdot s$ is factorized for some $n$.

*Step 7*: Assume $F_1 = E_1^{(i)}, 0 < i < t, u = r$

Since $F_1 = C_2BDC_1 = C_1C_2DB$, where the length of $C_1$ and $B$ is $u$ and $r$, respectively, it follows that $C_1 = B$ and therefore $C_1C_2 = C_2C_1$. It follows that $C_1, C_2$ and $B$ all have the form $AA \cdots A$ and $p - s$ is therefore factorized.

*Step 8*: Assume $F_1 = E_1^{(i)}, 0 < i < t, u > r$

8.1 $u < r + s + i$

The two arrangements of $F_1$ are described as follows:

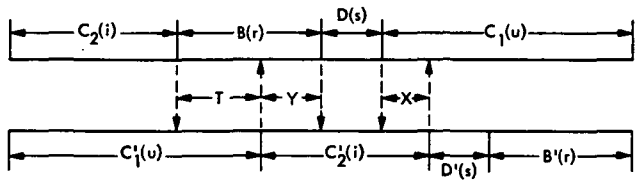


$C'_1 = C_2T$

$C'_2 = YDX$

It follows that $C_1$ = YDXT.

$C_1 = XD'B'$

$B = TY$

It follows that $C_1 = XDTY$ and therefore

$$YDXT = XDTY \qquad \text{(A-4)}$$

Three cases are observed now.

(1) $X = Y$.

It follows that $XT = TX$ which means that Y, X and T all have the form $AA \cdots A$. $F_1 = C_2TYDXD'B' = YDXTYDXDTY$. It follows that $p - 3s$ is factorized.

(2) $Y > X$.

It follows from Eq. (A-4) that Y has the form $XDV$. Equation (A-4) therefore has the form

$$XDVDXT = XDTXDV.$$

It follows that $VDXT = TXDV$. Continue with Eq. (A-3).

(3) $X > Y$.

It follows from Eq. (A-4) that X has the form $YDV$. Equation (A-4) therefore has the form

$$YDYDVT = YDVDTY$$

It follows that YDVT = VDTY. Continue with Eq. (A-4).

8.2 $u = r + s + i$

It follows from Eq. (A-1) that $C_2DB = C_2BD$, which means that $DB = BD$, which is impossible (1 in $B$ corresponds to 0 in $D$).

8.3 $u > r + s + i$

The two arrangements of $F_1$ are described as follows:

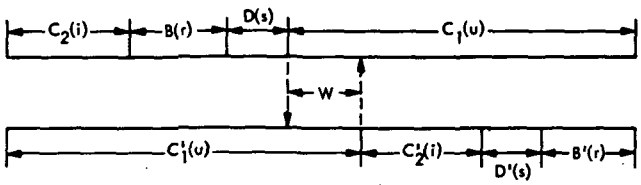


It follows that $C_2BDW = WC_2'D'B'$. (Both equal either $C_1'$ or $C_1$.) Continue with Eq. (A-1).

The conclusion drawn from steps 5 to 8 is that for $0 < i < t$ it is possible to have $F_1 = E_1^{(i)}$ only if $p - n \cdot s$ is factorized for some $n$.

*Step 9:* Assume $F_1 = E_1^{(i)}$ where $i = t$

It follows that $CBD = CDB$, and therefore $DB = BD$, which is impossible since $D$ starts with a 0 and $B$ starts with a 1. The same applied for $i = t + s$.

*Step 10:* Assume $F_1 = E_1^{(i)}$ for $t < i < t + s$

$E_1 = BD_1D_2C$ where the length of $D_2C$ is $i$.

$F_1 = D_2CBD_1 = CD_1D_2B$, which is impossible since $F_1$ starts once with a 1 and once with a 0.

*Step 11:* Assume $F_1 = E_1^{(i)}$ for $t + s < i$

$E_1 = B_1B_2DC$ where the length of $B_2DC$ is $i$.

$F_1 = B_2DCB_1$

$F_1 = CDB_1B_2$. It follows that $B_2DCB_1 = CDB_1B_2$. Continue with Eq. (A-4).

*Step 12:* Conclusion of the proof of part (2) of the theorem.

It has been shown in step 3.2 and in steps 5 to 11 that if $F_1 = E_1^{(i)}$ for $p > i > 0$ then $p - n \cdot s$ is factorized for some $n \geq 0$. This means that it is sufficient to require that $p - n \cdot s$ should be primes for $n = 0,1,2, \cdots [p/]$ in order for the code to be able to correct any error burst of length $p - 1$ or less. (For values of $n$ higher than $[p/s]$ the value of $p - n \cdot s$ is negative.)

On the other hand, for every $n$, $0 \leq n \leq [p/s]$ it is possible to find a vector $F_1$ such that $F_1 = E_1^{(i)}$ ( $p > i > 0$) provided that $p - n \cdot s$ is factorized.

$$\text{For } n = \begin{Bmatrix} 0 \\ 1 \\ 2 \\ 3 \\ 5 \end{Bmatrix} \text{ the vector } F_1 \text{ is described in step } \begin{Bmatrix} 3.2 \\ 7 \\ 6.1.(1) \\ 8.1.(1) \\ 6.1(2)(a) \end{Bmatrix}$$

The following describes a systematic way by which a vector $F_1$ can be obtained such that $F_1 = E_1^{(i)}$ ($p > i > 0$) and $p - n \cdot s$ is factorized, for every value of $n$, $1 \leq n \leq [p/s]$.

If steps 5, 7 are performed, the result is that $p - s$ is factorized. If a vector $V_1$ whose length is $d_1$ is obtained by performing steps 5,8, 8.3, 7, then $d_1 - s$ is factorized. If $F_1$ is now reconstructed in terms of the subvectors of $V_1$, the result is that $p - 2s$ is factorized. Generally, if $V_1$ is obtained by doing the steps 5, $(8,8.3)^i$, 7, then by reconstructing $F_1$ in terms of the subvectors of $V_i$ the result is that $p - (i + 1) \cdot s$ is factorized.

It can be concluded that the condition stated in the theorem is sufficient and necessary, and by this part (2) of the theorem is proved.

*Step 13:* Proof of part (3) of the theorem

13.1 $b = p$.

It has been shown that if $F_1 = E_1^{(i)}$ for some $0 < i < p$, then $p - n \cdot s$ is factorized for some $n$. By this the validity of the code is proved, since it is enough to require that $p - n \cdot s$ should be prime.

The result that $p - n \cdot s$ is factorized followed from the fact that $F_1$ consists of $n$ subvectors $D$ (an "all 0" vector of length $s = q - p$), and the rest consists of repetition of a subvector $A$ whose length is at least 2. The last result followed from the fact that $b \leq p - 1$.

If $b = p$, the repeated vector $A$ can consist of one element. This means that it is possible to have $F_1 = E_1^{(i)}$ although $p - n \cdot s$ is prime, provided that $F_1$ consists of $n$ subvectors $D$ and $p - n \cdot s$ elements of value 1, where each pair of subvectors $D$ is separated by at least one 1 element. It follows that $F_1$ — or any cyclic shift of it — do not have $q - p + 1$ successive zeroes. This means that the check for "all 0" input performed by the decoder (and demonstrated in Fig. 1.) is never satisfied. It follows that if $b = p$, the error is always detected.

13.2 $b = p + 1$

The first and last elements of the error burst are $p$ places apart. In view of the construction of the first $p$ rows in the parity check matrix $H$, it follows that if $H$ is multiplied by the received erroneous message, the number of 1 elements in the first $p$ places of the syndrome will be less by 2 from the corresponding number in the last $q$ places of the syndrome, and an uncorrectable error is detected. Hardwarewise, no match is possible between the content of the first $p - 1$ stages of $R_1$ and $R_2$, where the rest of the stages contain 0. (This comment refers to Fig. 1 which describes the decoder.)

13.3 $p + 1 < b \leq q - p + 1$.

Let $G$ be a vector of length $q$ whose first $b$ elements are the error pattern and the rest of its elements are 0. The last $q$ elements of the syndrome consist of a cyclic shift of $G$.

Referring to the description of the decoder (Fig. 1) it is seen that in order for an error to be corrected the content of the last $q - p + 1$ stages of register $R_2$ is required to be all 0 in order to correct the error. The content of $R_2$ is a cyclic shift of $G$. This vector has a 1 element in its first place and $b$th place where $p + 1 < b \leq q - p + 1$. No cyclic shift of $G$ can have $q - p + 1$ successive zeroes at its end. Since one of the necessary conditions for correcting the error is never met, an uncorrectable error pattern is detected.

It can be concluded from steps 13.1 to 13.3 that if $b \leq \max(p + 1, q - p + 1)$ the error is detected.

13.4 Proof of error detection probability

It is assumed here that the noise source which produces the error burst is of such a type that all transmitted information is lost during the interruption time. It is therefore assumed that the error burst has an equal probability of having any particular pattern. The probability of not detecting an error is defined as the number of undetectable patterns divided by the total number of possible patterns.

If $q - p + 1 < p + 1 < b$ or $p + 1 < q - p + 1 < b$ then for both cases the vector $G$ (defined in section 13.3) cannot have at its end $q - p + 1$ successive zeroes. In order for a cyclic shift of it to have this number of zeroes at its end, the vector $G$ must have $q - p + 1$ successive zeroes within the first $b$ places. This group of zeroes can start anywhere between the second place and the $b - (q - p + 1)$ place. (The first and $b$th elements must be 1). These zeroes have therefore less than $p$ different places to start with. It follows that the probability of having an undetectable error is less than $p \cdot 2^{b-2-(q-p+1)}/2^{b-2} = p \cdot 2^{p-q-1}$. The proof of the theorem is thus completed.

**Table 1. Some suggested burst-correcting cyclic codes**

| Burst-correcting ability $b$ | $(n,k)$ | Rate, % | Efficiency, % | $q$ | $p = b+1$ |
|---|---|---|---|---|---|
| 22 | (667,616) | 93.4 | 90.2 | 29 | 23 |
| 30 | (1333,1260) | 94.5 | 84.9 | 43 | 31 |
| 40 | (2173,2080) | 95.7 | 88.2 | 53 | 41 |
| 52 | (4399,4264) | 96.9 | 78.5 | 83 | 53 |
| 60 | (6283,6120) | 97.4 | 74.8 | 103 | 61 |
| 66 | (6499,6336) | 97.4 | 82.2 | 97 | 67 |
| 72 | (7519,7344) | 97.7 | 83.4 | 103 | 73 |
| 82 | (9379,9184) | 97.9 | 85.1 | 113 | 83 |
| 96 | (12139,11916) | 98.2 | 87 | 127 | 97 |
| 100 | (13231,13000) | 98.3 | 87.4 | 131 | 101 |
| 126 | (19939,19656) | 98.6 | 89.8 | 157 | 127 |
| 148 | (29353,29008) | 98.8 | 86.4 | 197 | 149 |
| 250 | (78061,77500) | 99.3 | 89.5 | 311 | 251 |

**Table 2. Comparing some codes**

| $b$ | $n$ | Suggested code | | "Most efficient code" | | |
|---|---|---|---|---|---|---|
| | | $k$ | Rate, % | Original code | $k$ | Rate, % |
| 30 | 1,000 | 927 | 92.7 | (121,112) | 910 | 91 |
| 40 | 1,000 | 907 | 90.7 | (164,153) | 890 | 89 |
| 40 | 2,000 | 1,907 | 95.3 | (290,277) | 1,896 | 94.8 |
| 50 | 2,000 | 1,865 | 93.2 | (290,277) | 1,870 | 93.5 |
| 50 | 4,000 | 3,865 | 96.6 | (290,277) | 3,844 | 96.1 |
| 65 | 3,000 | 2,837 | 94.5 | (290,277) | 2,861 | 95.3 |
| 65 | 6,000 | 5,837 | 97.2 | (511,499) | 5,796 | 96.6 |
| 80 | 4,000 | 3,805 | 95.1 | (290,277) | 3,792 | 94.8 |
| 80 | 9,000 | 8,805 | 97.8 | (511,499) | 8,760 | 97.3 |
| 100 | 5,000 | 4,769 | 95.3 | (290,277) | 4,740 | 94.8 |
| 100 | 10,000 | 9,769 | 97.6 | (511,499) | 9,700 | 97 |

# An Error-Minimizing Software Audit Technique

J. C. Holland and W. O. Paine
Quality Assurance—DSN and Mechanical Hardware Section

*This article presents a method for systematizing a software code-design audit, using principles of set theory to delineate, with a minimum of effort and a maximum of error-detecting capability, the various individual discrepancies present in the software.*

This analysis outlines the methodology of an auditing technique for evaluating computer software, which minimizes the effort involved, maximizes the information obtained from an audit, and minimizes auditing errors.

The process of uncovering discrepancies of whatever type between documentation of computer software systems and listings of software source programs is one of regarding labels and the sections of logic[1] so labeled (both in the assembly listing and in the documentation) as members of sets. Clearly, labels either agree (aside from typographical errors) or they do not. The situation is less clear when comparing sections of logic, which may be further subdivided, when necessary, into smaller sections—those which agree between the documentation and the source program, and those which do not. We may repeatedly subdivide sections of logic, as required, until we reach the point at which individual executable statements are compared. The "sections of logic," then, are simply collections of consecutive executable statements, separated from one another by whatever condition is encountered which creates a natural boundary. This may be the beginning or end statements of a subroutine or control program, a label, or an encounter with statements in the logic of the documentation or the source program which have no counterpart in the other.

These collections of consecutive executable statements (of whatever extent) and labels are thought of as the elements of sets. By the process of finding the intersections of these sets and their complements we may then establish various categories of discrepancies. This approach of uncovering discrepancies has three very powerful advantages over the examination of each labeled section of logic in the assembled program or in the documentation on an individual basis:

(1) By treating whole classes of labels or sections of logic having the same characteristics as a single

[1] Here, and elsewhere in this article, the phrase "section of logic" is taken to mean any set of consecutive executable statements regardless of their extent.

entity, we avoid overlooking some of the (otherwise) harder-to-identify discrepancies. We also avoid describing them incorrectly because of failure to notice some of of their characteristics.

(2) It is inherent in the process described below that it proceeds much more rapidly than an individual item-by-item examination and description.

(3) The use of set-theoretic processes has extremely powerful self-inductive properties. We get more out of the process than we put in. The completion of each step in the described procedure immediately suggests ways to use information already obtained in other ways.

One may regard the universe of elements being treated by the logical model as consisting of all labels and all sections of logic, both in the documentation and in the assembled program. These four categories, or sets, intersect in a manner shown in Fig. 1, the various subsets of which—intersections and their complements—are labeled with Roman numerals and subsequently described.

I. *Complete correspondence*—A logic section is found both in the documentation and the source program listing and is labeled the same in both. The logic completely agrees between the two. This corresponds to ABCD of Figure 1.

II. *Dummy section of labeled assembly-listing logic*—The labels in the source listing and the documentation agree and the documentation logic is given, but the source listing has plugged-up, or non-existent, logic. Note that this condition corresponds to $ABC\overline{D}$ (A and B and C and NOT-D) and immediately reveals its characteristic—unimplemented logic—by being inside circles (sets, that is) A, B, and C, but outside D.

III. *Undocumented label*—The logic exists both in the documentation and source listing, but is labeled only in the source listing. This corresponds logically to $\overline{A}BCD$.

IV. *Undocumented logic section*—This label exists both in the source listing and in the documentation (by reason of being the title of a program block within a subroutine or control program but not the title of a separate flow chart or section of flow chart) and corresponds to a section of logic in the source listing. This is, of course, $A\overline{B}CD$.

V. *Unlabeled or incorrectly labeled section of code in the source listing*—The logic is in the documentation, where it is labeled, and in the source listing, where it either is an unlabeled section of code embedded in another program section, or has a different label. This corresponds to $AB\overline{C}D$.

VI. *Documented, labeled code not in the source listing at all*— Unimplemented code not represented by a labeled program stub or dummy. This is $AB\overline{C}\overline{D}$.

VII. *Documented logic, unlabeled, in the source listing as a label only, no logic*—This is a strange case, but it could happen. The nature of the logic (and the names used) in the documentation could be so unique that the dummy label in the source program could correspond *only* to that section of logic in some undefined way. Comments in both places could also correspond. This is one example of how the set-theoretic approach gives us more than we asked for, and is identified as $\overline{A}BC\overline{D}$.

VIII. *Source listing logic; labeled, not documented*—Self-explanatory. Corresponds to $\overline{A}\overline{B}CD$.

IX. *Documented label (no documented logic) corresponds to an unlabeled section of source listing logic*—This, by the way, is the complement of case VII. Here the nature of the operations being performed in the source program logic is so unique (or accompanied by comments) as to identify them with the label in the documentation (in a logic-block label within another subroutine, say), even though that logic is never documented. This is $\overline{A}\overline{B}C\overline{D}$.

X. *Documented label only, no documented logic and no such label or logic in the source program*—This is the case where a single logic block in a documented subroutine or control program has a label which is found nowhere else—neither in the documentation nor the source program. This is identified logically as $\overline{A}\overline{B}C\overline{D}$.

XI. *Documented section of logic, unlabeled, unimplemented*—Here is the case where (as, for example, in a control program originated in the lower memory) no label is attached, and the program does not exist in the source Program. This is $\overline{A}BC\overline{D}$.

XII. *Dummy source listing label*—No documentation logic or label and no corresponding section of logic as such in the source program. Corresponds to $\overline{A}\overline{B}CD$.

XIII. *Unlabeled source listing section of logic, undocumented*—Could indicate revision of program since documentation was last updated. This is $\overline{A}\overline{B}C\overline{D}$.

Considering that the above classification rests upon the basis of set-intersections and their complements, one should proceed to classify the various elements (labels and sections of logic) by beginning with the most inclusive, as

well as most easily managed—by reason of being alphabetically ordered—set, the Autoflow[2] label index, and the set of documentation flow charts. Matching and nonmatching labels will then constitute separate categories which may further be subdivided by the identification of label index entries as undocumented subroutines, control programs or unidentified sections of implemented logic, and the matching of flow chart logic in the documentation with some sections of labeled or unlabeled logic in the source program.

Thus the repeated subdivision of the largest categories of labels and sections of logic into their various subsets produces the various categories of discrepancies without redundancy and with minimum effort.

The following is a complete description of the process of obtaining an audit by this method:

(1) Using the Autoflow flow chart set and its label index, mark each label in the index which corresponds to the name of a subroutine or (apparently, judging by comments or (later) by documentation flow charts) control programs.

(2) Collate the documentation flow charts with the Autoflow label index, putting the names which match on a given list (call it List 1) if the label index entry is marked (indicating a subroutine or control program) and on List 2 if the label index entry is unmarked. Place the names of unmatched documentation flow charts on List 3. Additionally, we have the unmatched labels of the Autoflow label index which are also unmarked; call them List 4. These lists are illustrated in Figure 2.

(3) Compare the logic of the source programs on List 1 with the logic of the corresponding documentation flow chart. One of three conditions should be observed:

(a) Complete agreement between the two. *This is Category I* of the preceding classification.

(b) Agreement between the two except for isolated discrepancies (individual steps omitted from one or the other, incorrect order of steps, lack of YES/NO labeling on decision steps, etc.). These will be *reported on the Discrepancy List of the audit report.*

(c) Entire sections of logic (labeled or unlabeled) existing in one of the two, but not the other. *Mark the extent of this logic block* on the Autoflow chart or documentation chart, wherever it occurs. Put its beginning label (if any) or location on a separate list as noted below.

We have now separated List 1 into four sublists, shown in Figure 3.

(4) Compare the logic of the source programs and subroutines on List 2 with the documentation flow charts having the same labels. This will have the effect of separating this list into sublists in a manner similar to that used to partition List 1. This breakdown is shown in Figure 4.

(5) Compare the extraneous blocks of logic whose beginning addresses are found in Lists 1C and 2C with the unmatched documentation flow charts found in List 3. The various outcomes are shown in Figure 5.

(6) Using the Autoflow label index and concordance, place those labels not already marked on List 6A if they are entirely unreferenced (in the concordance), on List 6B if they are only internally referenced (according to the concordance). Additionally, an examination of the Autoflow charts will reveal a certain number of initial points in lines of flow that are unlabeled and reveal no apparent method of access. Since these may conceivably be reached by an indexed branching instruction, this condition should be checked for. If it cannot be determined that this is the case and, labeled or unlabeled, there seems to be no way to reach these sections of logic, their initial locations should be entered on List 6C. The results are shown in Figure 6.

(7) Compare the logic blocks found only in the documentation flow charts (Lists 1D and 2D) with the unmatched sections of source program logic from Lists 5D and 6A, B and C. The various outcomes are presented in Figure 7.

(8) Finally, make lists of documentation labels which are unaccompanied by corresponding logic (e.g., being representative of some undefined program stub) and source program labels unaccompanied by logic (perhaps representing dummy sections of unimplemented source program code). Compare the documentation labels with unidentified sections of source program logic from Lists 6A, B and C, in the sense that unique identifiers may appear in the comments of both or in the names of operands used in the source program logic. Compare the source program labels from above with the extraneous logic blocks from Lists 7A and B in the sense that the two

[2] Registered trademark of Applied Data Research, Inc. (Ref. 1).

may use the same unique identifiers or correspond with respect to their comments. The outcomes of these comparisons are shown in Figure 8.

From all of the above classifications of errors, the software discrepancy audit report may be written, treating entire classes rather than individual errors, the exception being the descrepancy list, in which the differences between individual blocks or labels in the source program and documentation are discussed in detail.

As an example of the foregoing analysis, we consider the two flow charts of Figures 9 and 11, headed by the entry points labeled "RQSTCK" and "STOPCK," respectively:

(1) In step 1 of the previously described procedure no such labels as RQSTCK or STOPCK were encountered in the Autoflow label index nor, of course, in the Autoflow charts themselves. A label, CONTRL, which matched a subroutine, was found and marked.

(2) In step 2 of the procedure it was noted that the documentation flow charts for RQSTCK and STOPCK were unmatched by corresponding labels in the Autoflow label index, and therefore these two flow chart names were placed on List 3.

    The documentation flow chart for CONTRL, being matched by an Autoflow chart and marked label in the label index, was placed on List 1.

(3) In step 3 of the above-described procedure, the logic of the documentation flow chart CONTRL was compared block-by-block with the logic of the Autoflow chart headed by the same label—CONTRL. The points at which the logic of the documentation flow chart for CONTRL failed to agree with that of the Autoflow chart were marked for future reference. Sizeable sections of the Autoflow logic were found to have no counterpart in the documentation flow chart. Their extent was marked, as in step 3c. There was no beginning label.

(4) Step 4 of the procedure was not involved in this case.

(5) In step 5 of the procedure, a match was found between the logic of two of the flow charts on List 3—STOPCK and RQSTCK—and parts of the unmatched logic of the CONTRL Autoflow chart. The match was in both cases less than perfect. At this point the logic blocks which did match between CONTRL and either STOPCK or RQSTCK were marked, and a line-by-line examination of the source program code and the unmatched logic (or missing logic, as the case may be) of the documentation was undertaken to pinpoint the differences. The documentation flow charts were corrected accordingly, as shown in Figures 10 and 12.

    In both cases (STOPCK and RQSTCK) the differences in logic between the documentation flow charts and source program code were noted in the discrepancy list, and the fact that these so-called "subroutines" were in reality sections of unlabeled code embedded in another program was indicated by their presence on the List 5B, which is reported by classification in the audit. The annotated source program code and Autoflow charts are given in Figures 13 and 14, respectively.

## Reference

1. *Map Autoflow II Assembly Series Reference Manual*, Applied Data Research, Inc. (Copyright January 1974 by Applied Data Research, Inc.).

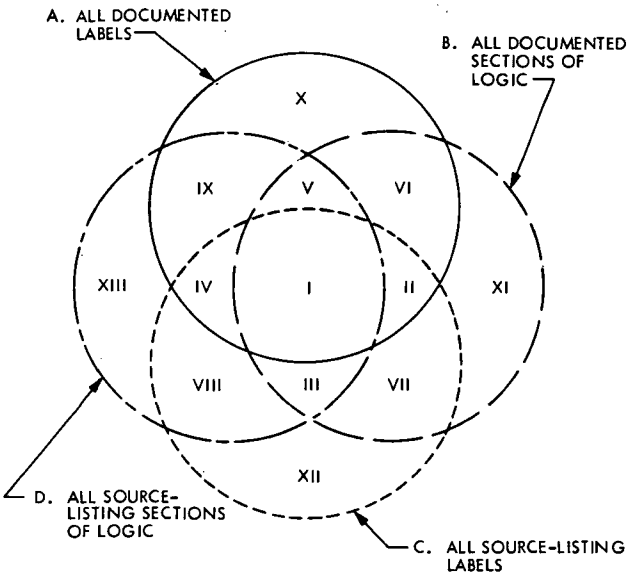


Fig. 1. A Venn Diagram of the sets of labels and logic sections, and their intersections



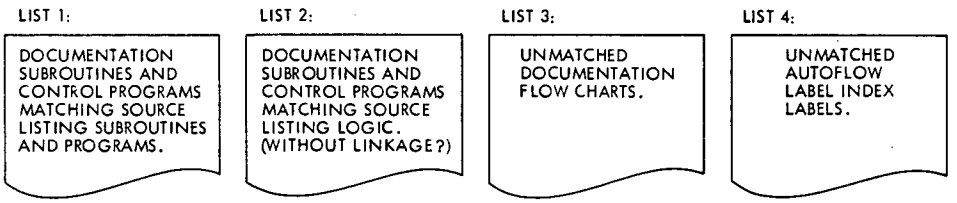


Fig. 2. An initial breakdown of matching and non-matching labels

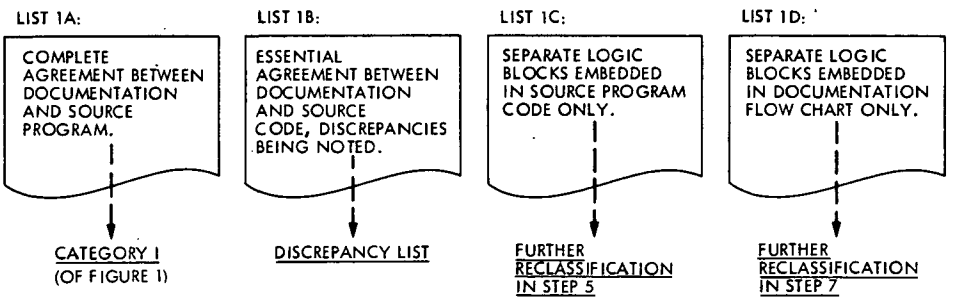


Fig. 3. A breakdown of matching and non-matching sections of logic between similarly labeled program sections

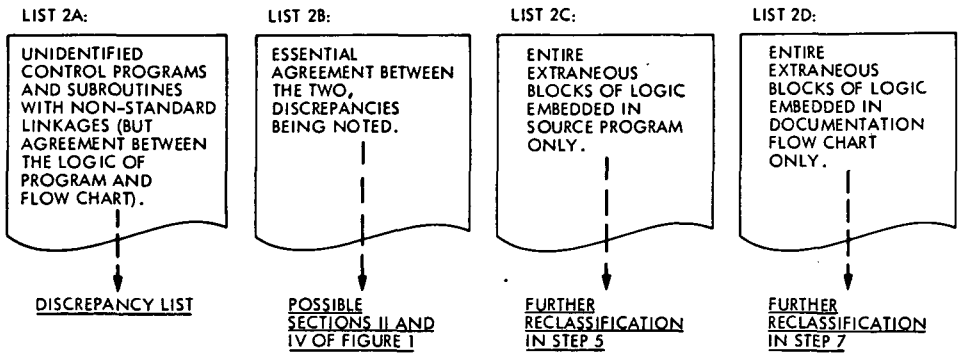


Fig. 4. A breakdown of matching and non-matching sections of logic between dissimilarly labeled program sections

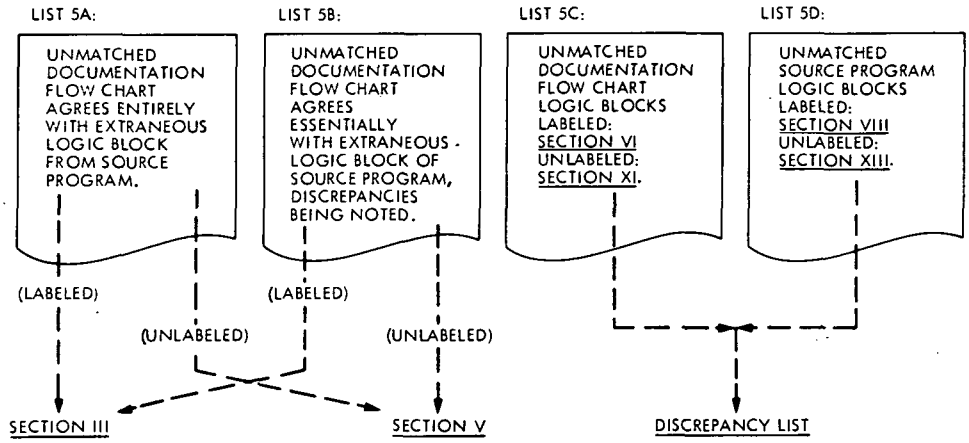


Fig. 5. A breakdown of matching and non-matching sections of logic between unmatched flowcharts and extraneous source-program logic



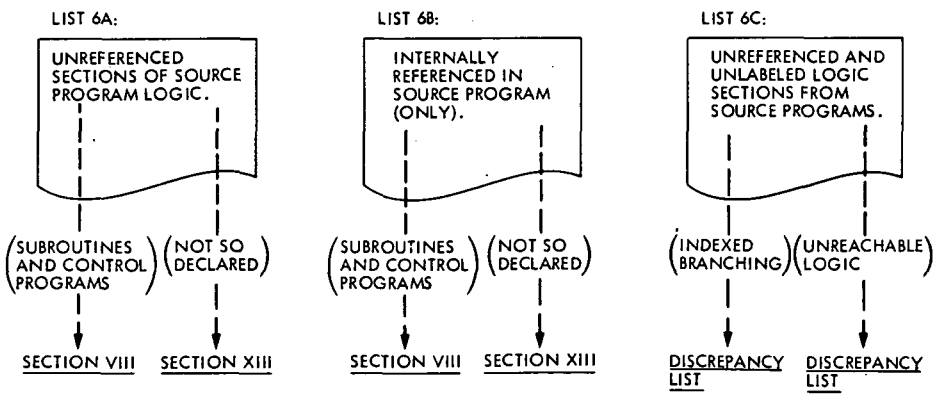


*Fig. 6. Completely unreferenced sections of flow chart or source program logic*

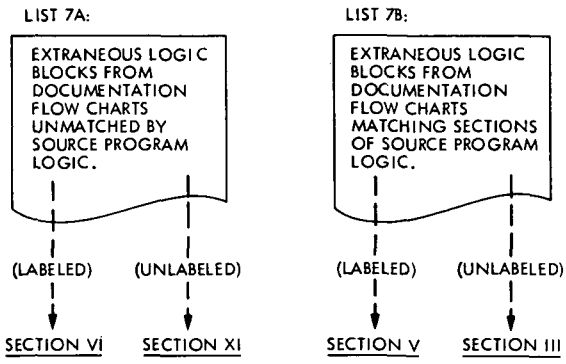


Fig. 7. Collation of unreferenced logic sections from flow charts and source program

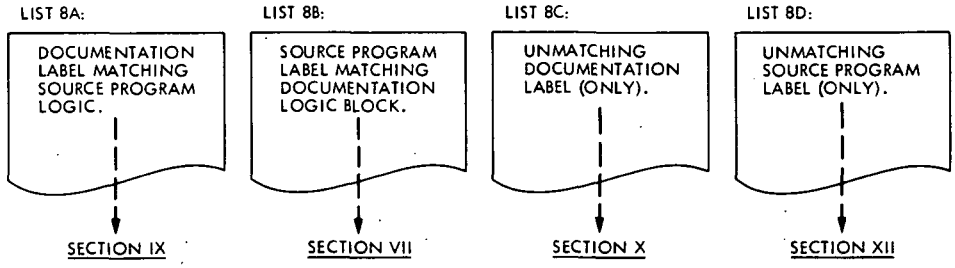


Fig. 8. A breakdown of matching label/logic block pairs and unmatching labels

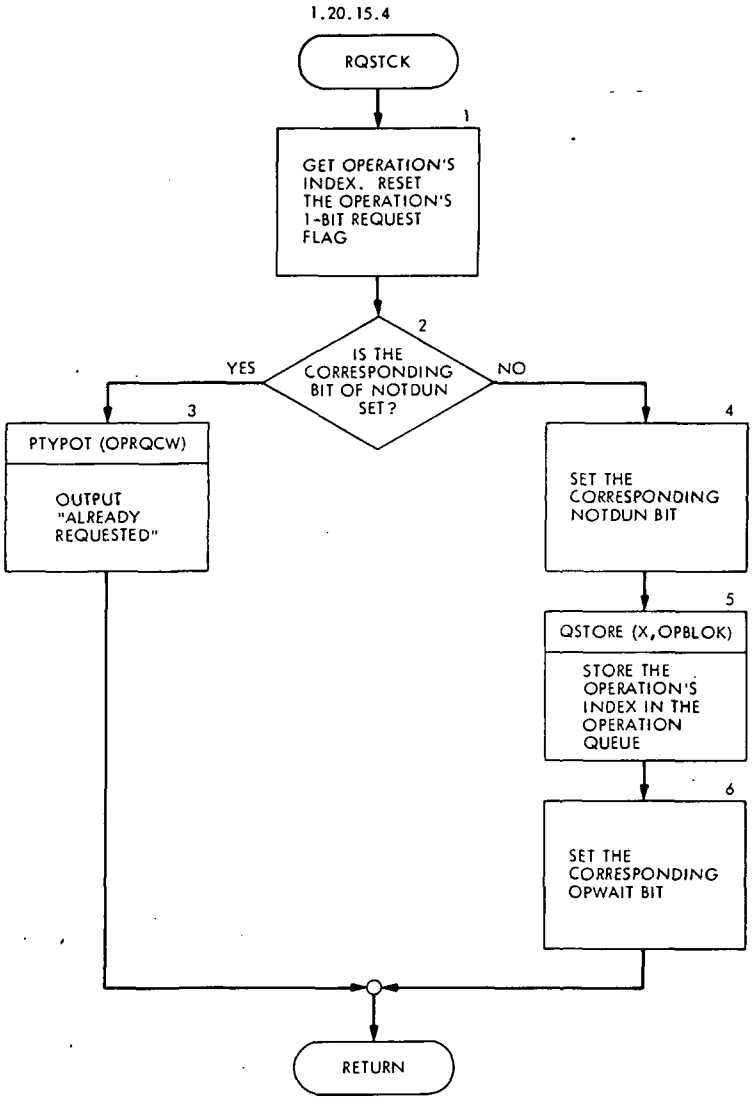


*Fig. 9. Original flow chart from documentation*

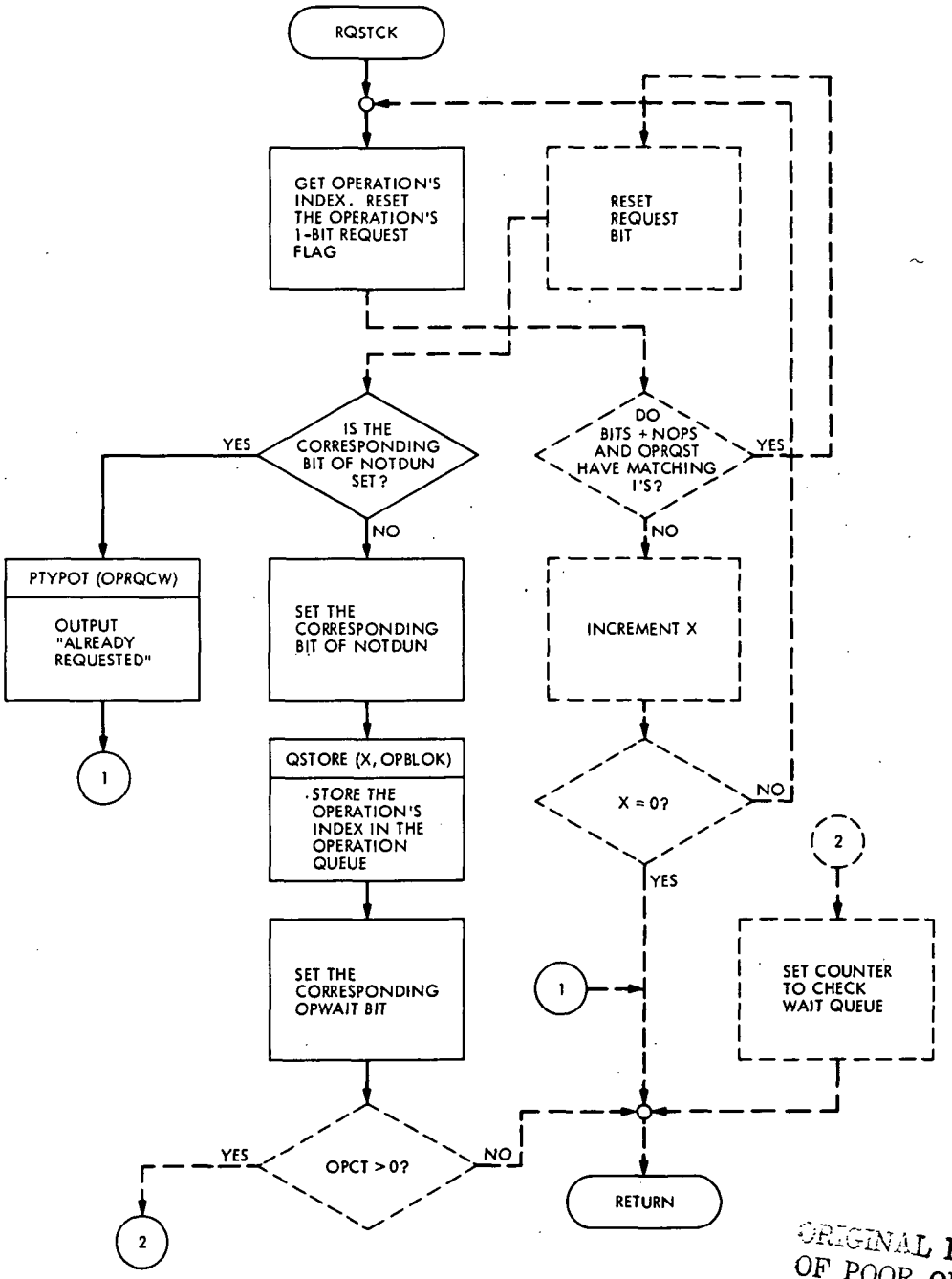




Fig. 10. Corrected flow chart agreeing with source program

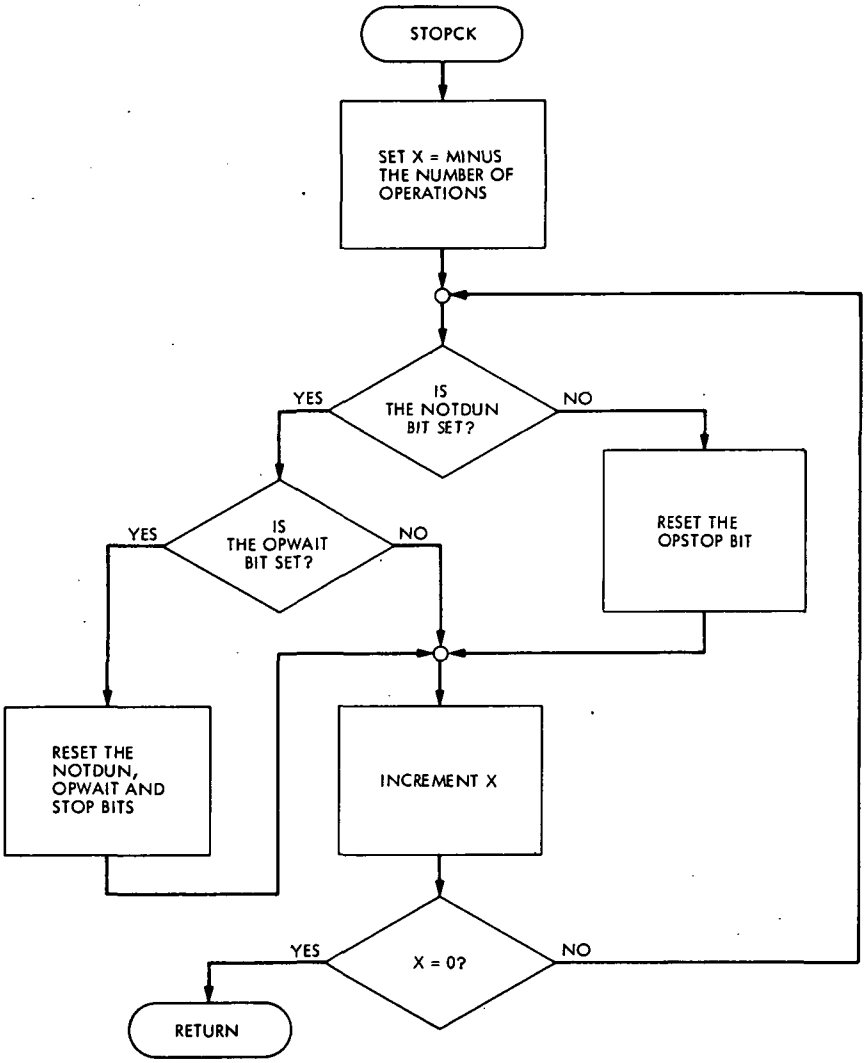


**Fig. 11. Original flow chart from documentation**

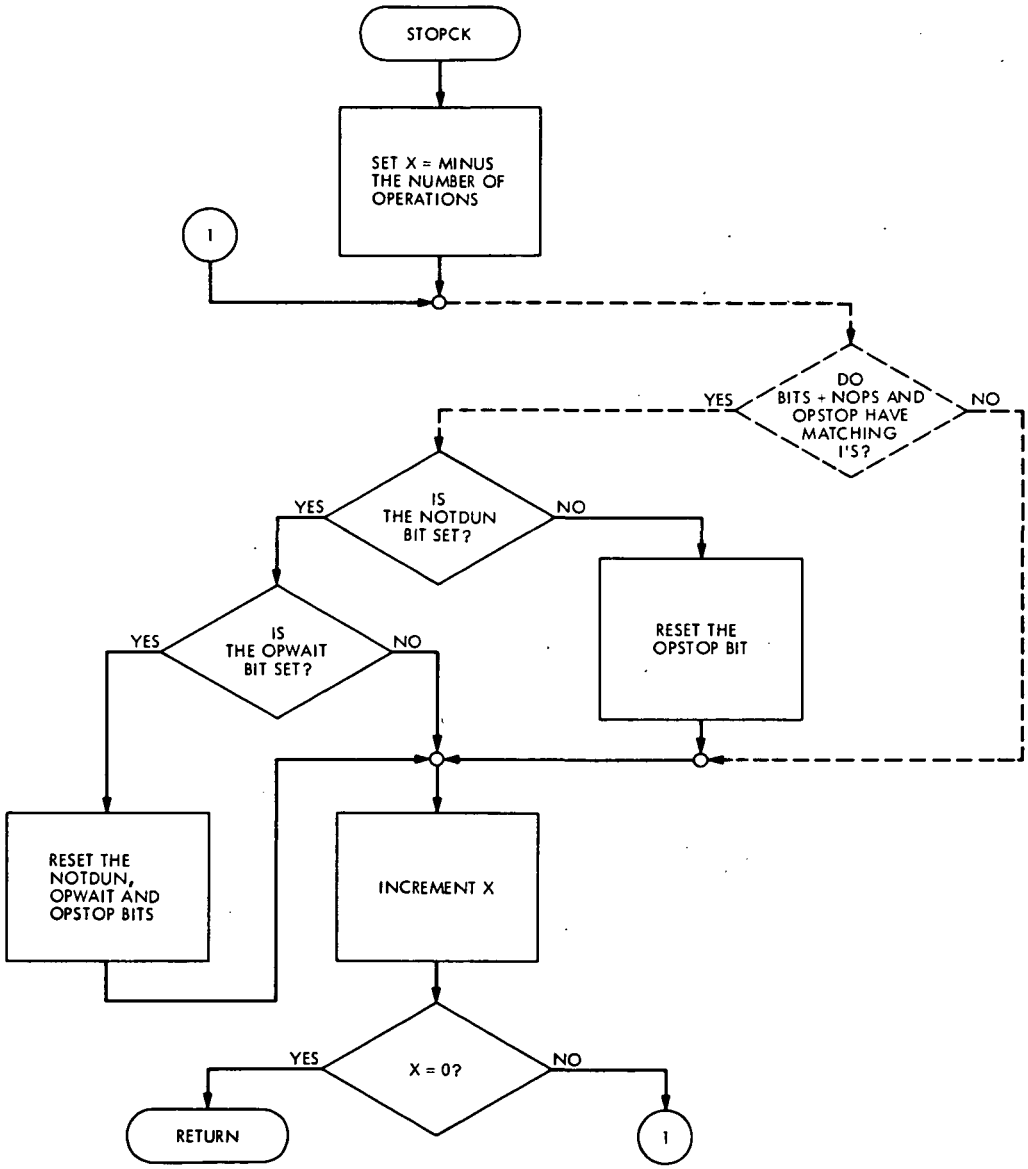


Fig. 12. Corrected flow chart agreeing with source program

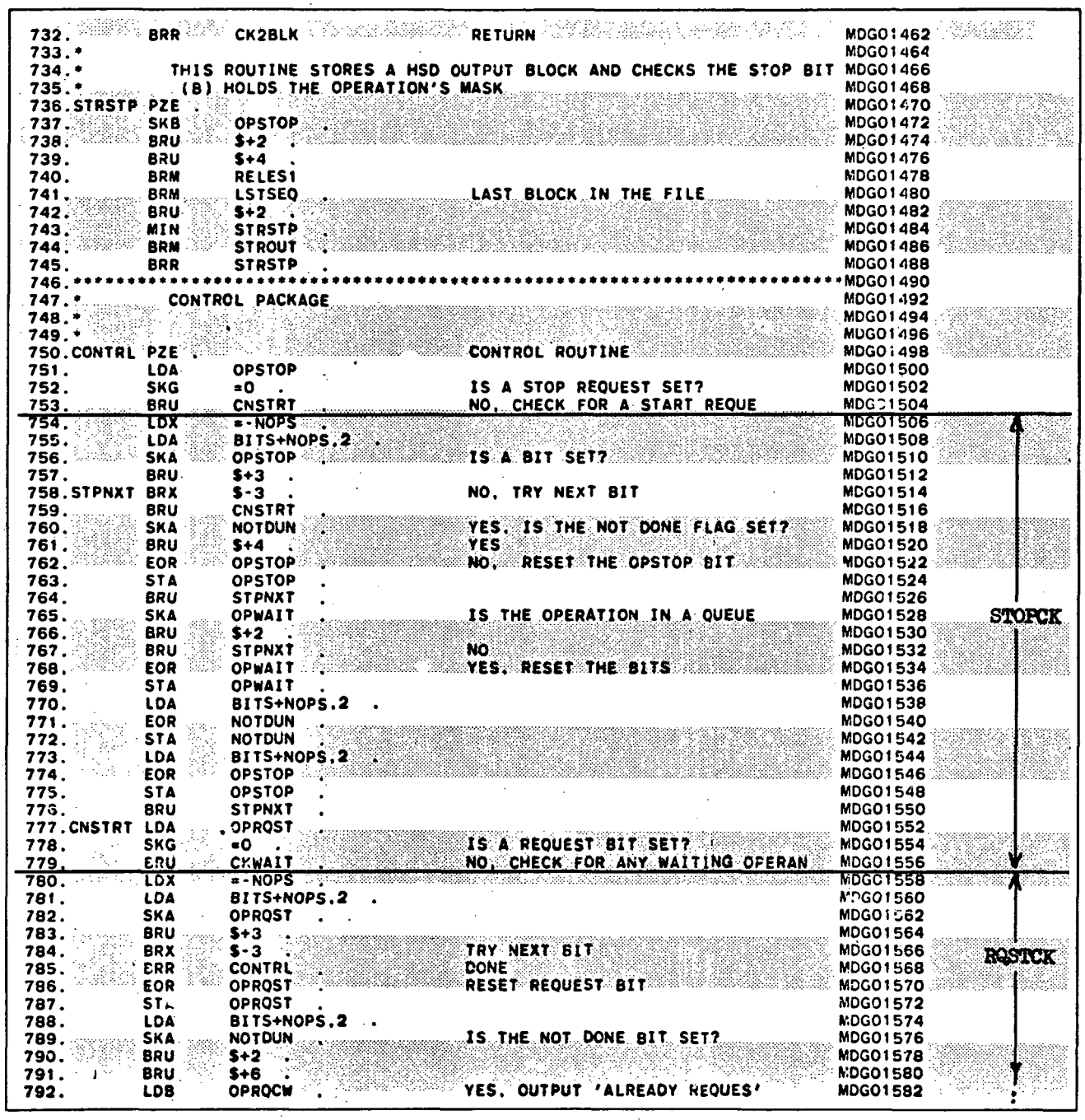


```
732.          BRR     CK2BLK          RETURN                                  MDG01462
733.*                                                                         MDG01464
734.*       THIS ROUTINE STORES A HSD OUTPUT BLOCK AND CHECKS THE STOP BIT    MDG01466
735.*         (B) HOLDS THE OPERATION'S MASK                                  MDG01468
736.STRSTP PZE  .                                                           MDG01470
737.          SKB     OPSTOP  .                                             MDG01472
738.          BRU     $+2     .                                             MDG01474
739.          BRU     $+4     .                                             MDG01476
740.          BRM     RELES1                                                MDG01478
741.          BRM     LSTSEQ  .       LAST BLOCK IN THE FILE                MDG01480
742.          BRU     $+2     .                                             MDG01482
743.          MIN     STRSTP  .                                             MDG01484
744.          BRM     STROUT  .                                             MDG01486
745.          BRR     STRSTP  .                                             MDG01488
746.**********************************************************************MDG01490
747.*       CONTROL PACKAGE                                                 MDG01492
748.*                                                                       MDG01494
749.*                                                                       MDG01496
750.CONTRL PZE  .               CONTROL ROUTINE                             MDG01498
751.          LDA     OPSTOP  .                                             MDG01500
752.          SKG     =0      .       IS A STOP REQUEST SET?                MDG01502
753.          BRU     CNSTRT  .       NO, CHECK FOR A START REQUE           MDG01504
754.          LDX     =-NOPS  .                                             MDG01506
755.          LDA     BITS+NOPS,2     .                                     MDG01508
756.          SKA     OPSTOP  .       IS A BIT SET?                         MDG01510
757.          BRU     $+3     .                                             MDG01512
758.STPNXT BRX     $-3     .       NO, TRY NEXT BIT                      MDG01514
759.          BRU     CNSTRT  .                                             MDG01516
760.          SKA     NOTDUN  .       YES, IS THE NOT DONE FLAG SET?        MDG01518
761.          BRU     $+4     .       YES                                   MDG01520
762.          EOR     OPSTOP  .       NO,  RESET THE OPSTOP BIT             MDG01522
763.          STA     OPSTOP  .                                             MDG01524
764.          BRU     STPNXT  .                                             MDG01526
765.          SKA     OPWAIT  .       IS THE OPERATION IN A QUEUE           MDG01528
766.          BRU     $+2     .                                             MDG01530
767.          BRU     STPNXT  .       NO                                    MDG01532
768.          EOR     OPWAIT  .       YES, RESET THE BITS                   MDG01534
769.          STA     OPWAIT  .                                             MDG01536
770.          LDA     BITS+NOPS,2     .                                     MDG01538
771.          EOR     NOTDUN  .                                             MDG01540
772.          STA     NOTDUN  .                                             MDG01542
773.          LDA     BITS+NOPS,2     .                                     MDG01544
774.          EOR     OPSTOP  .                                             MDG01546
775.          STA     OPSTOP  .                                             MDG01548
776.          BRU     STPNXT  .                                             MDG01550
777.CNSTRT LDA     OPRQST  .                                             MDG01552
778.          SKG     =0      .       IS A REQUEST BIT SET?                 MDG01554
779.          BRU     CKWAIT  .       NO, CHECK FOR ANY WAITING OPERAN      MDG01556
780.          LDX     =-NOPS  .                                             MDG01558
781.          LDA     BITS+NOPS,2     .                                     MDG01560
782.          SKA     OPRQST  .                                             MDG01562
783.          BRU     $+3     .                                             MDG01564
784.          BRX     $-3     .       TRY NEXT BIT                          MDG01566
785.          ERR     CONTRL  .       DONE                                  MDG01568
786.          EOR     OPRQST  .       RESET REQUEST BIT                     MDG01570
787.          STA     OPRQST  .                                             MDG01572
788.          LDA     BITS+NOPS,2     .                                     MDG01574
789.          SKA     NOTDUN  .       IS THE NOT DONE BIT SET?              MDG01576
790.          BRU     $+2     .                                             MDG01578
791.          BRU     $+6     .                                             MDG01580
792.          LDB     OPRQCW  .       YES, OUTPUT 'ALREADY REQUES'          MDG01582
```

Fig. 13. Source program coding showing extent of unlabeled and improperly linked "subroutines" RQSTCK and STOPCK

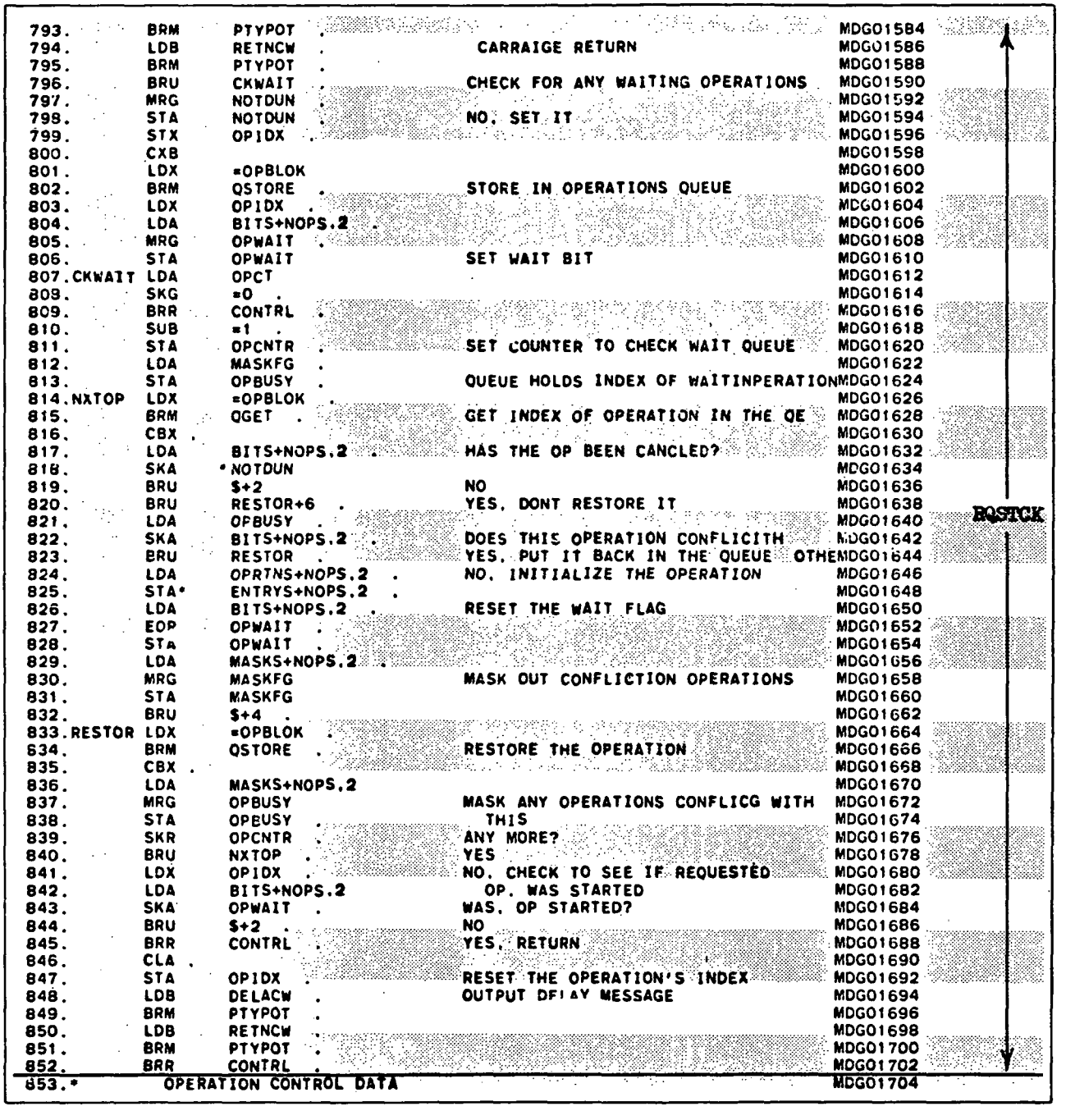

```
793.        BRM     PTYPOT   .                                    MDGO1584
794.        LDB     RETNCW   .        CARRAIGE RETURN            MDGO1586
795.        BRM     PTYPOT   .                                    MDGO1588
796.        BRU     CKWAIT   .        CHECK FOR ANY WAITING OPERATIONS  MDGO1590
797.        MRG     NOTDUN   .                                    MDGO1592
798.        STA     NOTDUN   .        NO, SET IT                  MDGO1594
799.        STX     OPIDX    .                                    MDGO1596
800.        CXB                                                   MDGO1598
801.        LDX     =OPBLOK                                       MDGO1600
802.        BRM     QSTORE   .        STORE IN OPERATIONS QUEUE   MDGO1602
803.        LDX     OPIDX    .                                    MDGO1604
804.        LDA     BITS+NOPS,2   .                               MDGO1606
805.        MRG     OPWAIT   .                                    MDGO1608
806.        STA     OPWAIT            SET WAIT BIT                MDGO1610
807.CKWAIT  LDA     OPCT                                          MDGO1612
808.        SKG     =0   .                                        MDGO1614
809.        BRR     CONTRL   .                                    MDGO1616
810.        SUB     =1   .                                        MDGO1618
811.        STA     OPCNTR   .        SET COUNTER TO CHECK WAIT QUEUE  MDGO1620
812.        LDA     MASKFG   .                                    MDGO1622
813.        STA     OPBUSY   .        QUEUE HOLDS INDEX OF WAITINPERATIONMDGO1624
814.NXTOP   LDX     =OPBLOK  .                                    MDGO1626
815.        BRM     QGET     .        GET INDEX OF OPERATION IN THE QE  MDGO1628
816.        CBX  .                                                MDGO1630
817.        LDA     BITS+NOPS,2   .   HAS THE OP BEEN CANCLED?    MDGO1632
818.        SKA     *NOTDUN                                       MDGO1634
819.        BRU     $+2               NO                          MDGO1636
820.        BRU     RESTOR+6  .       YES, DONT RESTORE IT        MDGO1638
821.        LDA     OPBUSY   .                                    MDGO1640
822.        SKA     BITS+NOPS,2   .   DOES THIS OPERATION CONFLICITH  MDGO1642
823.        BRU     RESTOR   .        YES, PUT IT BACK IN THE QUEUE  OTHEMDGO1644
824.        LDA     OPRTNS+NOPS,2  .  NO, INITIALIZE THE OPERATION  MDGO1646
825.        STA*    ENTRYS+NOPS,2  .                              MDGO1648
826.        LDA     BITS+NOPS,2   .   RESET THE WAIT FLAG         MDGO1650
827.        EOP     OPWAIT   .                                    MDGO1652
828.        STA     OPWAIT   .                                    MDGO1654
829.        LDA     MASKS+NOPS,2  .                               MDGO1656
830.        MRG     MASKFG            MASK OUT CONFLICTION OPERATIONS  MDGO1658
831.        STA     MASKFG                                        MDGO1660
832.        BRU     $+4   .                                       MDGO1662
833.RESTOR  LDX     =OPBLOK  .                                    MDGO1664
834.        BRM     QSTORE   .        RESTORE THE OPERATION       MDGO1666
835.        CBX  .                                                MDGO1668
836.        LDA     MASKS+NOPS,2                                  MDGO1670
837.        MRG     OPBUSY            MASK ANY OPERATIONS CONFLICG WITH  MDGO1672
838.        STA     OPBUSY   .          THIS                      MDGO1674
839.        SKR     OPCNTR   .        ANY MORE?                   MDGO1676
840.        BRU     NXTOP    .        YES                         MDGO1678
841.        LDX     OPIDX    .        NO, CHECK TO SEE IF REQUESTED  MDGO1680
842.        LDA     BITS+NOPS,2         OP, WAS STARTED           MDGO1682
843.        SKA     OPWAIT   .        WAS, OP STARTED?            MDGO1684
844.        BRU     $+2   .           NO                          MDGO1686
845.        BRR     CONTRL   .        YES, RETURN                 MDGO1688
846.        CLA  .                                                MDGO1690
847.        STA     OPIDX    .        RESET THE OPERATION'S INDEX  MDGO1692
848.        LDB     DELACW   .        OUTPUT DELAY MESSAGE        MDGO1694
849.        BRM     PTYPOT   .                                    MDGO1696
850.        LDB     RETNCW   .                                    MDGO1698
851.        BRM     PTYPOT   .                                    MDGO1700
852.        BRR     CONTRL   .                                    MDGO1702
853.*         OPERATION CONTROL DATA                              MDGO1704
```



Fig. 13 (contd)

CHART TITLE - DIS/MSD DOI-5468-SP 1/8/76

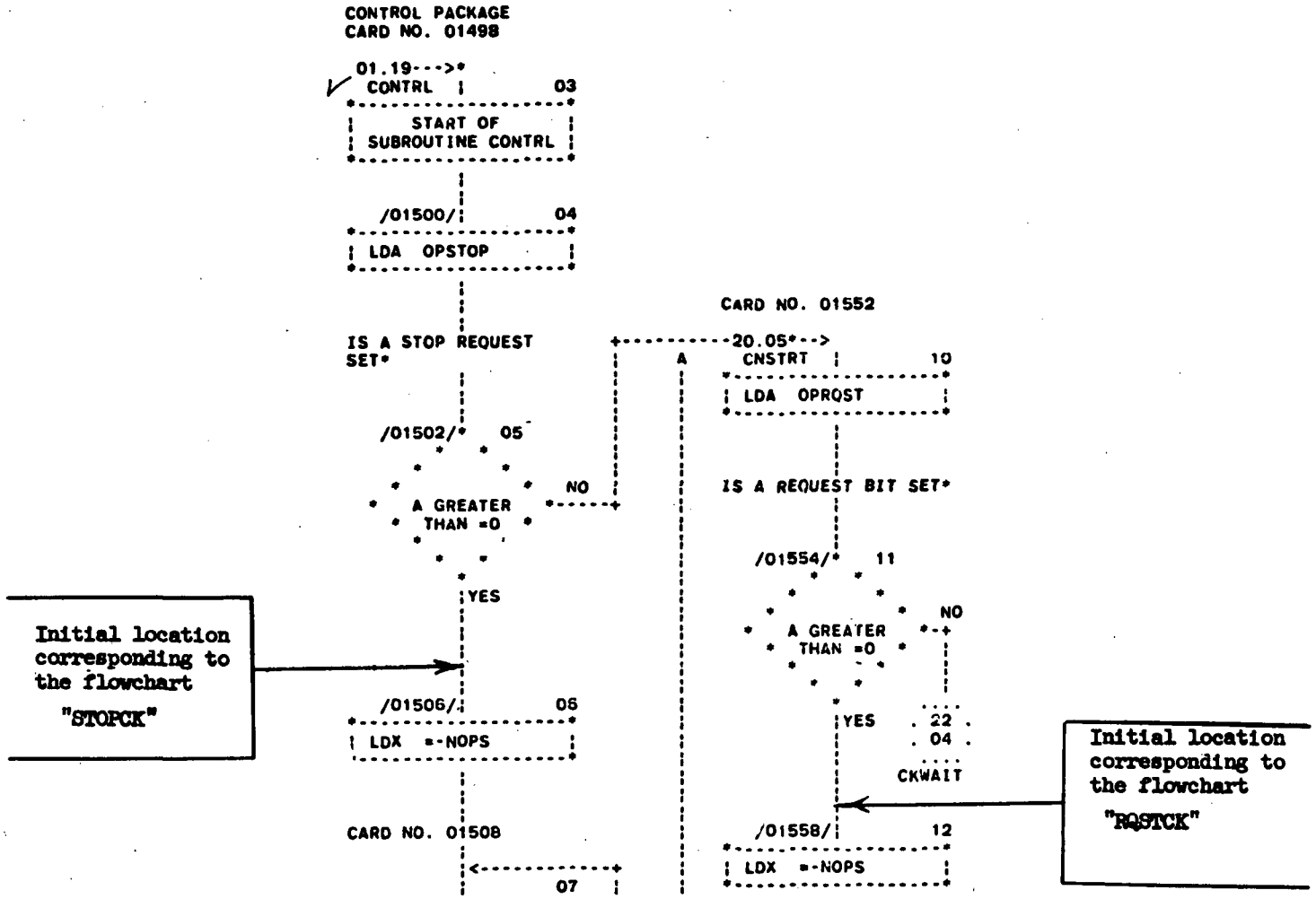

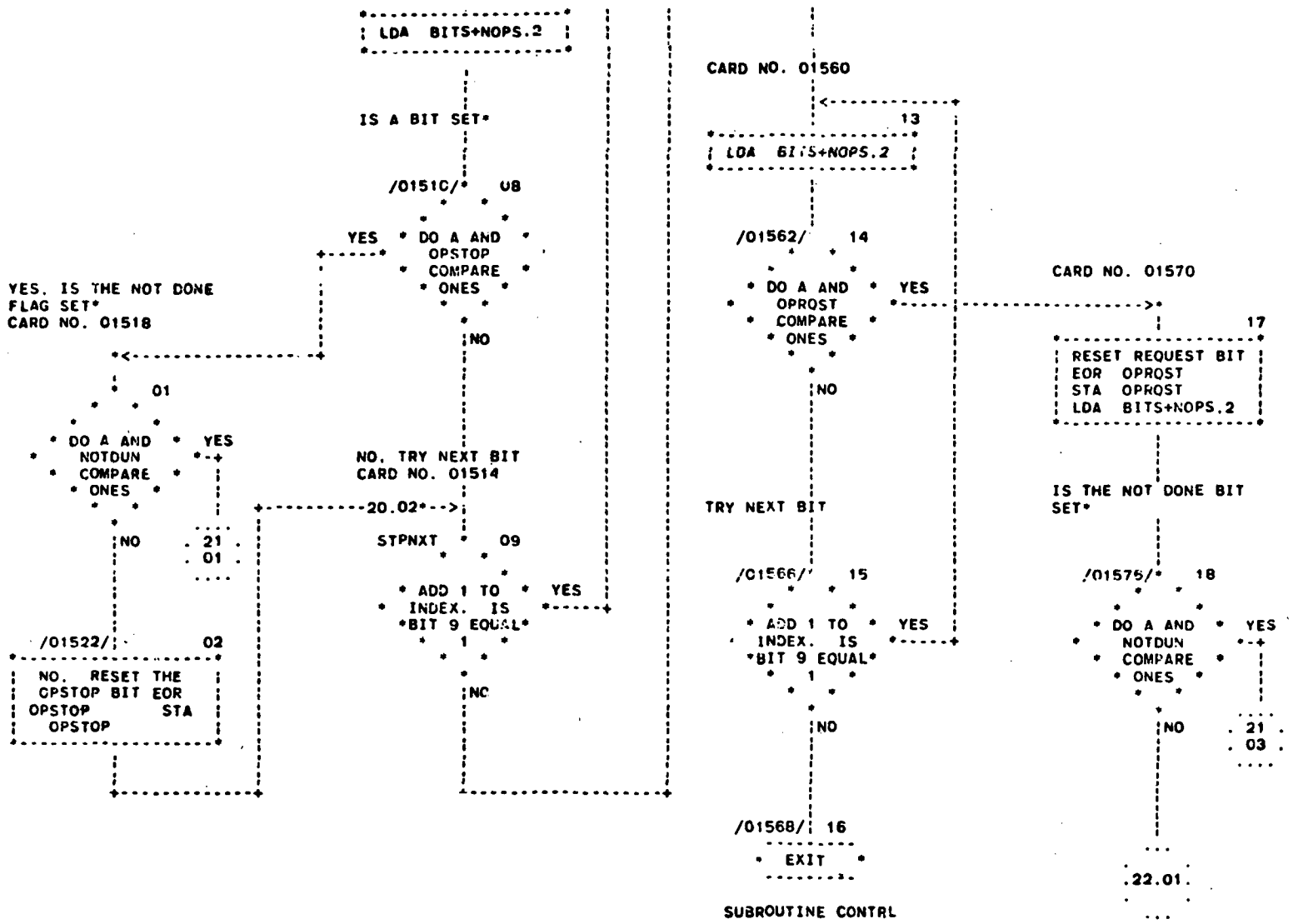


Fig. 14. Autoflow charts for the subroutines CONTRL, STOPCK, and RQSTCK

CHART TITLE - DIS/HSD DOI-5468-SP 1/6/76

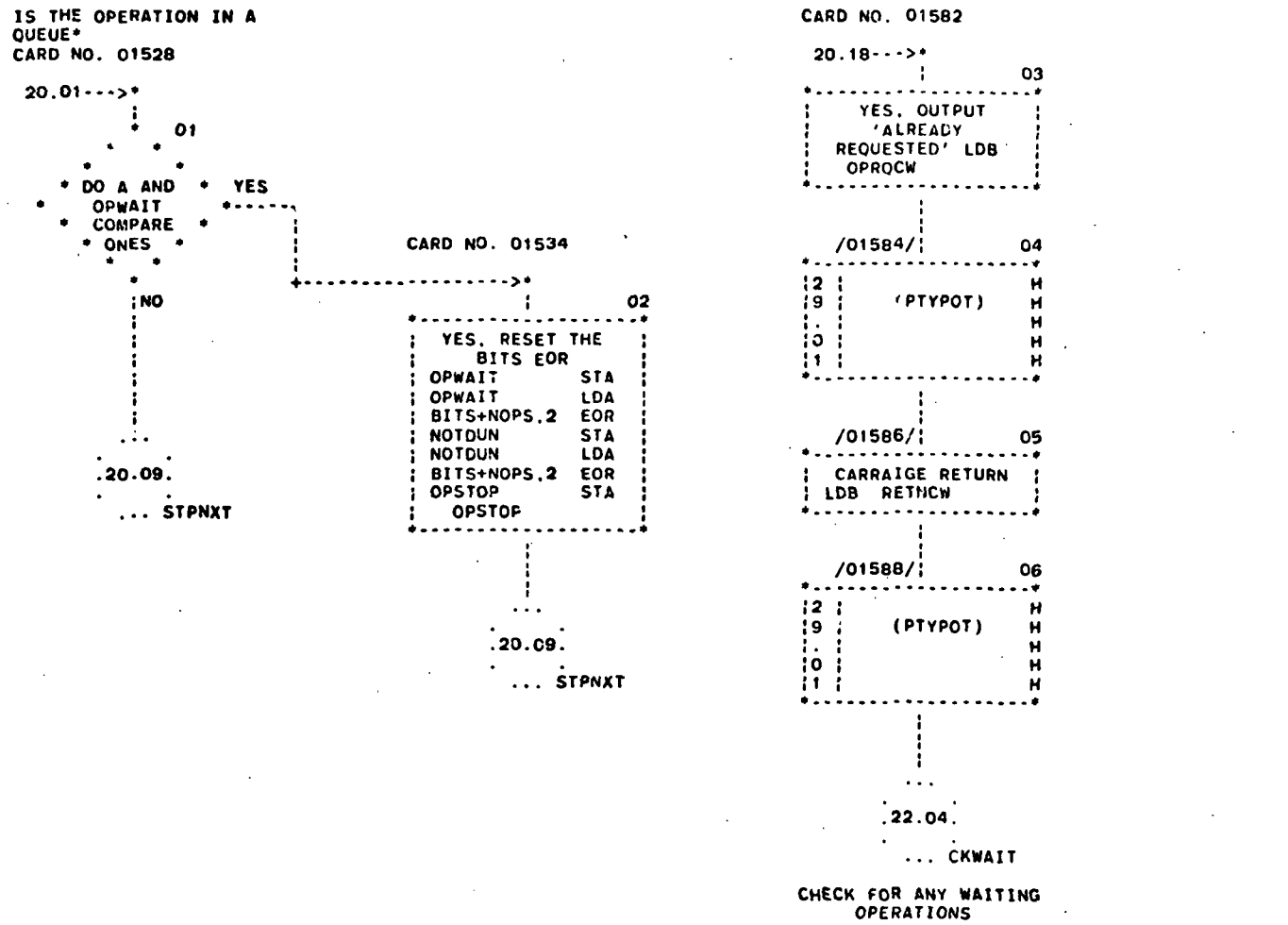


Fig. 14 (contd)

CHART TITLE - DIS/HSD DOI-5468-SP :/6/76

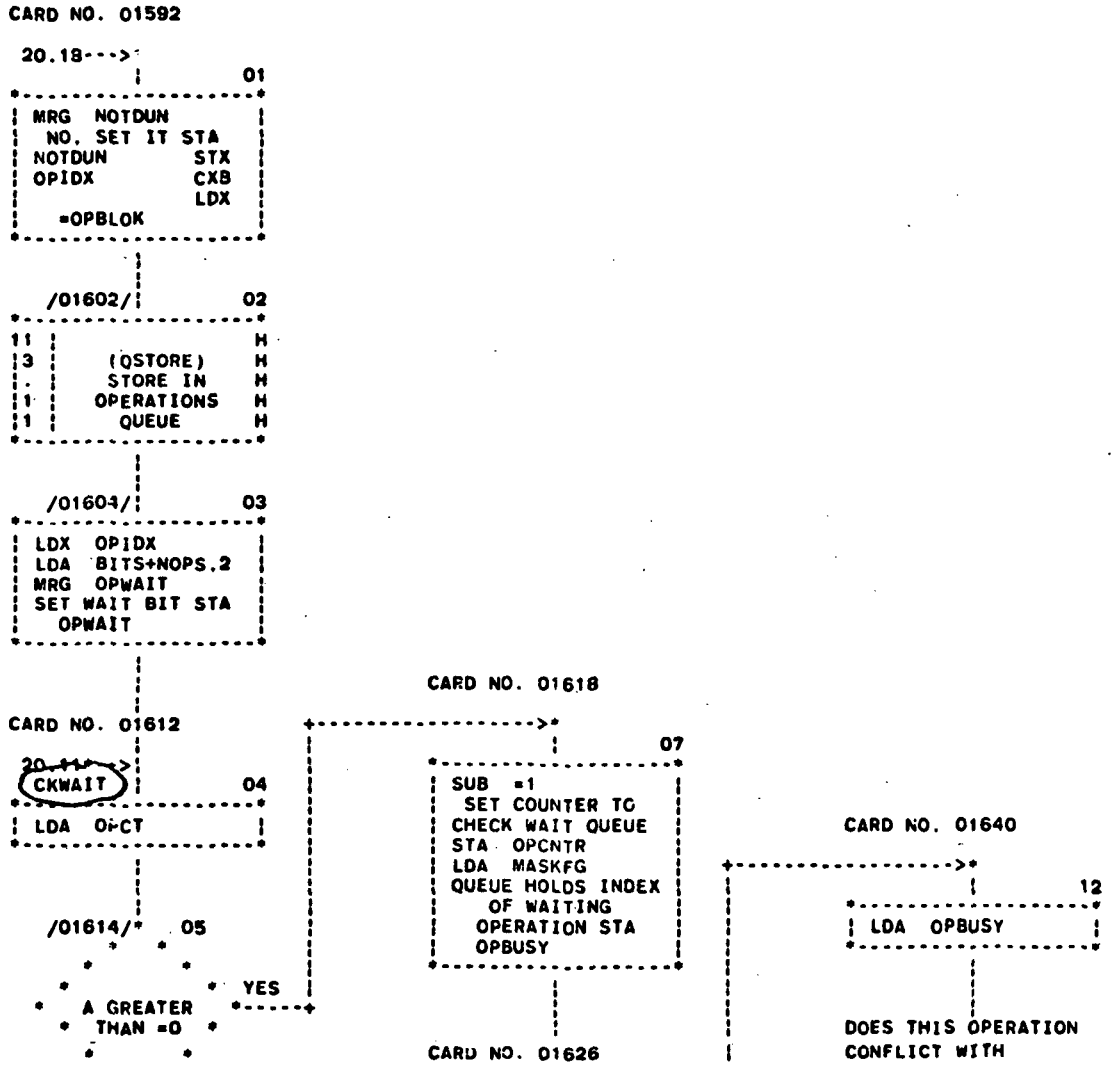

Fig. 14 (contd)

CHART TITLE - DIS/HSD DOI-5468-SP 1/6/76

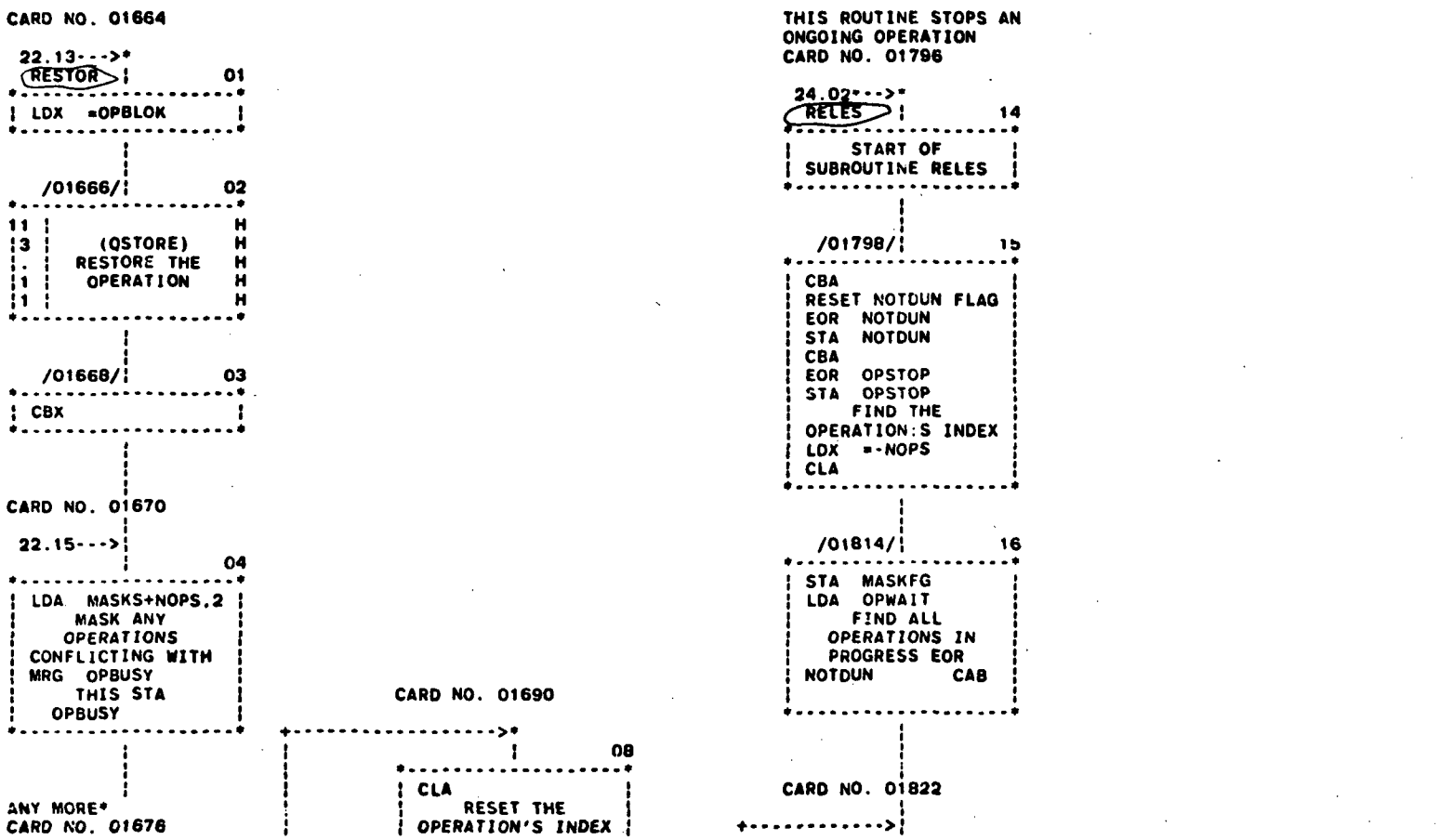

Fig. 14 (contd)

# Preliminary Results of DSN Performance for Convolutional Codes With a Viterbi Decoder

J. M. Urech
Station Director, Cebreros, Spain

L. D. Vit
Operations Manager, Robledo Station

B. D. L. Mulhall
DSN Systems Engineering Office

*To determine DSN Telemetry System performance when maximum-likelihood convolutional decoding is employed, testing is being undertaken at DSS 62, Madrid, Spain. Testing hardware and software have been developed to evaluate the performance of the DSN in the Viterbi mode with the LV7015 model. Since the bit errors at the decoder output occur in bursts, the test program includes a series of statistical analyses in runs of correct bits and bursts of bits in error.*

## I. Introduction

This is the first report on the Madrid DSN engineering task "DSN Performance for Convolutional Decoding," undertaken by DSSs 61/62 in a joint effort with the JPL DSN Systems Engineering Office. The objectives of this task are to determine telemetry system performance with maximum-likelihood convolutional decoding using the Viterbi algorithm. Specifically, bit error rate, burst error statistics, and performance monitor capability are objectives.

The task requires the integration of a maximum-likelihood convolutional Viterbi encoder/decoder (model LINKABIT LV7015) into the DSN Telemetry and Command Data Subsystem (TCD) as well as the evaluation of decoder performance. Since the LV7015 is functionally equivalent to the Maximum Likelihood Convolutional Decoder (MCD) being implemented in the Network (with two small exceptions which will be discussed later), performance of the LV7015 can be used to predict DSN Telemetry System performance for flight operations. It also includes the development of the appropriate testing software and a real-time performance evaluator algorithm.

The task began with the receipt of the LV7015 unit at the end of June. This article covers the integration phase and the preliminary results that have been obtained thus

far. For clarification purposes, it has been divided into the following sections:

*Hardware integration.* Describing the hardware changes that were required to interface the decoder with the system and the implementation of the normalization rate counter and sync status bit.

*Software integration.* Describing the operational software modifications required for operating in the Viterbi mode, formatting of data flow, and processing of sampled parameters (normalization rate and sync status).

*System calibration and preliminary evaluation.* Describing the system parameters which affect decoder performance and the *theoretical evaluation of the normalization rate values.*

*Testing software.* Describing the test software development to analyze and evaluate the tests to be performed.

## II. Hardware Integration

The LV7015 has been installed within the Data Decoder Assembly (DDA), as shown in Fig. 1. The idea behind this integration scheme has been to minimize the amount of modifications or additions required to incorporate the high-rate convolutional decoder into any of the existing Multimission Telemetry (MMT) strings. Furthermore, the modifications introduced in the operational equipment have been made, seeking a total compatibility with both operational software and hardware.

All the hardware modifications have been incorporated into a single DDA interface board, known as the Symbol Synchronizer Assembly–Block Decoder Assembly/DDA (SSA–BDA/DDA) coupler. The modifications are described in four different sections, according to the following criteria:

(1) Quantization scheme modification.

(2) Viterbi serial data input to DDA, and formatting modification.

(3) Normalization rate counter implementation.

(4) Viterbi decoder sync condition monitoring.

### A. Quantization Scheme Modification

There exists an 8-level quantization scheme, already implemented within the SSA–DDA coupler, which is used by the firmwired sequential convolutional decoder of the DDA (Fano algorithm). The 8-level quantization scheme required by the Viterbi decoder is slightly different, as depicted in Fig. 2.

The conversion from the DDA 8-level scheme into the LV7015 scheme is accomplished by exclusive-oring the sign bit with the two magnitude bits to obtain the new magnitude bits. The sign bit remains unchanged.

*Example:* Convert DDA level 5 (binary 101) into LV7015 equivalent level.

| | Fano's | | | | Viterbi's |
|---|---|---|---|---|---|
| Sign bit | 1 | → | Unchanged | → | 1 |
| Magnitude 1 | 0 | → | 0 ⊕ 1 | → | 1 |
| Magnitude 2 | 1 | → | 1 ⊕ 1 | → | 0 |
| | | | Mag ⊕ Sign | | |
| Octal | 5 | | ——→ | | 6 |

(Symbol ⊕ denotes exclusive-or operation.)

### B. Viterbi Serial Data Input to DDA and Formatting Modification

To accept the Viterbi decoded data into the SSA–DDA coupler, a new operation mode of this coupler has been devised, maintaining some of the peculiarities of the convolutional decode mode (such as the 8-level quantization scheme). The new operation includes a full uncoded mode using as a serial data input the decoded data output from the Viterbi decoder.

The new operating mode is characterized by a simultaneous setting of both the uncoded mode (UCM1) and the convolutional mode (CCM1) in the corresponding initialization command memory. This is accomplished by modifying the SSA coupler command in the operational software. At the same time, the old uncoded and convolutional code mode indicators have to be modified accordingly so as not to create confusion in the existing hardware. For this reason, three new modes of operation are formed with two command control logic signals, as follows (the dot represents a logic AND operation):

| *Mode* | *Controlled by* |
|---|---|
| Uncoded | UCM1 · CCM0 |
| Convolutional (not Viterbi) | UCM0 · CCM1 |
| Viterbi | UCM1 · CCM1 |

The serial data input of the uncoded data formatting registers is modified to accept either uncoded data from the SSA (existing capability retained), or decoded data from the Viterbi decoder. The clock accompanying the data is modified in the same way.

The modification includes the generation of the new operating modes and their incorporation into the applicable parts of the existing circuitry.

### C. Normalization Rate Counter Implementation

The behavior of the Viterbi decoder may be known dynamically by observing the so-called "normalization rate." A normalization process takes place whenever a path global metric exceeds a fixed threshold established in the decoder circuitry as part of its memory overflow-protection scheme. When this happens, a normalization pulse is generated and sent to the appropriate decoder section to subtract a fixed quantity and thus reduce the metric to a value below the threshold.

To take advantage of this mechanism, a copy of the normalization pulses is used to feed a counter, which is periodically read by the operational software. In this way, a normalization rate can be computed and further utilized as an estimator of the signal-to-noise ratio of the signal processed by the decoder (see Section III).

The implementation of this counter requires the deletion of a test input monitoring not used at present either in the operational or in the test software.

### D. Viterbi Decoder Sync Condition Monitoring

When the normalization rate exceeds a hardwired limit (which corresponds roughly to a symbol error rate greater than 11 percent), the Viterbi decoder declares itself out-of-sync. The monitoring of a condition to determine the in- or out-of-sync was implemented.

## III. System Calibration and Preliminary Evaluation

After the integration of the Linkabit LV7015 into the existing multimission telemetry equipment, a series of tests was performed to determine the optimum system calibration and to evaluate its performance.

Theoretical documents concerning the Viterbi decoding algorithm are numerous but frequently ignore the effect of elements such as the receiver or demodulator. In addition, the information provided by the decoder manufacturer was insufficient in this respect, and did not include areas of interest for this study. It was, therefore, necessary to deduce specific operating characteristics from direct observations and many hours of testing. To this end the following lines of action were established:

(1) The decoding function was verified at high signal-to-noise ratio (SNR) using a simple test pattern.

(2) The Viterbi mode of operation explained in Section II was checked and found to be compatible with other operational modes.

(3) As explained elsewhere, the normalization rate counter is periodically transferred to the operational software for further processing. The different normalization criteria presented in available literature did not precisely match the LV7015 normalization scheme. Therefore, the normalization mechanism was studied and evaluated by forcing specific error patterns into otherwise error-free data and correlating the expected values with the actual normalization counter readings. The use of the normalization counter as a system performance evaluator will be explained in Subsection B.

(4) The next testing was aimed at studying the basic system calibration as explained in Subsection A.

### A. System Calibration

Among the known degradation factors that take place along the system configuration, the Subcarrier Demodulator Assembly–Symbol Synchronizer Assembly (SDA–SSA) interface calibration plays a most significant role. In the soft quantization mode, the SSA integrator output is converted into a 3-digit binary number that constitutes a fundamental element in the decoding process. This analog-to-digital correspondence at the SSA integrator output is influenced by the relationship

$$K = \frac{\text{integrator mean (mV)}}{\text{quantization interval (mV)}} \qquad (1)$$

The quantization intervals have been represented in Fig. 2, Subsection II-A, and the integrator mean is actually the average of the integrated symbols. In a standard calibration procedure, given an arbitrary telemetry modulation index, the SDA output is adjusted to provide 280 mV to the SSA input. This is done by means of a set of attenuators (modulation index (MI) attenuators that will compensate different modulation indexes to have a relatively constant integration mean at the SSA output).

However, this standard procedure must be proven to be optimum for the Viterbi decoding algorithm at different SNRs. In other words, it is necessary to find an optimum $K$ and its influence on the decoding behavior.

*Although the specific purpose of the* MI *attenuators is to compensate different modulation indexes, they will be used here as a way of controlling the integrator output relative to the quantization intervals.* (These quantization intervals are fixed and hardwired to 312 mV).

By definition, the optimum $K$ will be such as to provide the minimum bit error rate at the decoder output as a function of the SDA output signal level. Consequently, the SDA output was varied in 2-dB steps and the bit error rate (BER) measured at each point. Figure 3 shows this relationship for three different energy per symbol-to-spectral noise density ratios. The reference value of 0 dB selected was that resulting from the standard setup procedure, i.e., 280 mV at the SDA output.

Figure 3 then shows that the bit error rate goes through a minimum for a determined SDA-SSA adjustment and this holds at different energy-per-symbol-to-noise-spectral density ($ST_S/N_0$) values for a specific test configuration. However, we are actually interested in the corresponding value of $K$ which comes in terms of SSA output values, while Fig. 3 was obtained in terms of SDA output values. Since the value of $K$ cannot be determined easily as a function of the SDA calibrations, it was evaluated by experimental testing and was found that:

$$\{\text{SDA output: } 280 \text{ mV}\} \approx \{K : 2.5\} \qquad (2)$$

The value of $K$ may vary, however, from 2 to 3 depending upon the degree of accuracy in the setup calibrations.

In general then, it can be said that the standard setup procedure (280 mV into the SSA) is valid for the Viterbi decoding algorithm and holds for different signal-to-noise ratios. As the MI setting attenuators are used very frequently as an operational parameter in any system configuration, care must be taken to select the proper value to avoid the degradations that would result (Figs. 3, 4, and 5).

It must be noted that a change of 1 unit in the SDA attenuator corresponds to a change of 2 dB in the SSA output signal power for a constant signal-to-noise ratio. Therefore:

(1) If the MI attenuators are *decreased* by *one* step,

$$\Delta\,(\text{MI}): -1 = \Delta\,(M^2): +2 \text{ dB}$$

From Eq. (1),

$$\Delta\,(\text{MI}) = 10 \log \left(\frac{K_1 \cdot Q}{K_0 \cdot Q}\right)^2 = 2$$

Thus,

$$\Delta\,(\text{MI}) = \frac{K_1}{K_0}\,(\text{ratio}): \log^{-1}(2/20): 1.258$$

(2) If the MI attenuators are *increased* by *one* step, then

$$\Delta\,(\text{MI}) = \frac{K_1}{K_0} : 1/1.258 \text{ (see Figs. 4 and 5)}$$

where $M^2$ represents the signal power at the SSA output, $Q$ is the quantization interval and the built-up MI steps of 2 dB are a system characteristic.

Expression (2) was found experimentally. However, it will be justified in Subsection III-B-3 when analyzing the normalization rate parameter. Parameters $\overline{N}_b$ ( ) in Figs. 4 and 5 will be explained in Subsection III-B-3.

## B. System Performance Evaluator

It is convenient to derive the system performance evaluation from some parameter directly related to the decoder operation, and the only parameter that may be made available to the operational program is the normalization counter, as already explained. The following presentation justifies the use of the normalization values as a performance evaluator.

**1. Normalization rate.** The Viterbi decoder algorithm behaves basically as a progression along the trellis by pairwise comparisons of paths and the elimination of less probable paths, following a metric criterion. The pairwise comparisons are made at each bit time and the metric values are derived from the channel symbol quantizations provided by the Symbol Synchronizer Assembly and the branch symbols hypothesized by the so-called "normalization rate" mechanism. The normalization rate will then be used to evaluate decoder performance.

The normalization mechanism may be visualized as being composed of a set of 4-stage buffers that, at each bit time, are incremented by a metric value and then compared pairwise as per the trellis structure. To simplify the scheme it may be assumed that the path holding the

lowest metric is considered to be the "best path." However, during the decoding process all paths including the "best path" will accumulate metric values so as to saturate their corresponding buffers (assuming a significant noise level). In the decoding range of operation the "wrong" paths will nevertheless accumulate at a much faster rate than the "best" path. Therefore, the decoder logic must detect the fact that the "wrong" paths are going to be saturated and that the "best" path is growing over a preestablished threshold. It must be noted that at low SNRs the estimated "best path" may actually be in error due to the channel noise, but as will be shown later, the fact that bit errors occur does not seem to disturb the metric accumulation rates. A *normalization* occurs when the logic detects that all the "wrong" paths have a high metric ($m >> 4$) and that the best path has just reached or surpassed a threshold of 4. At this time all the buffers are reduced (normalized), and this fact (normalization) is registered in a counter. The normalization counter is made available to the operational program through the SSA coupler.

**2. Theoretical model.** Figure 6 represents two superimposed Gaussian probability density curves $p(Z)$ that correspond to the integrations of the telemetry symbols performed by the SSA. These integrations will have averages of $M_0$ and $M_1$, respectively. The channel noise causes the integrated output to vary around $M_0$ or $M_1$ with a normal distribution. A positive integration corresponds to a logical "0" while a negative integration represents a logical "1." The dotted lines in Fig. 6 represent the quantization intervals $Q_i$ and reproduce the intervals shown in Fig. 2. Therefore, any voltage at the integrator output, when sampled at the end of a symbol time, represents the integration of a symbol and this sampled value is converted into a binary number. A symbol error occurs when a "0" falls on the negative side; or alternatively, when a "1" falls on the positive side. In other words, if for instance a "1" is sent through the channel and is received as any of the quantized values that correspond to ($Q_0$, $Q_1$, $Q_2$, or $Q_3$), a symbol error has occurred.

Regarding Fig. 6, it must be noted that the curves are assumed to be normalized ($\sigma = 1$) and the random variables or output voltages are expressed as Z from the respective origins $M_0$ and $M_1$. From all these considerations we can express the symbol error probability as:

$$P_e(\text{"0"}) = \int_{-\infty}^{-M_0} p(Z')\, d_Z' \text{ for a "0"}$$

$$P_e(\text{"1"}) = \int_{M_1}^{\infty} p(Z)\, d_Z \text{ for a "1"}$$

Since the two superimposed curves are symmetrical and two consecutive symbols are independent of each other, our analysis can be focused on the equivalent representation shown in Fig. 7, which will be valid either for a "0" or a "1."

It was stated in Subsection III-B-1 that the normalization mechanism is mainly governed by the metric evolution along the "best path."

For a normalization to occur, metrics (positive values) must equal or be greater than 4 in the best path. But at the same time this metric accumulation must represent a symptom that there is a certain degree of difficulty when trying to decode the received data. In other words, the normalization rate must behave so as to give an estimate of the channel noise level, which is equivalent to estimating symbols in error. Intuitively, at each bit time the global metric along the best path must increase when the hypothesized branch symbols have corresponding symbol quantizations of opposite sign (see Fig. 7). The higher the excursion over the error side, the higher the metric increment. It follows then that the criteria for selecting the metric values introduce a weight for each quantization interval that is inversely proportional to its probability of occurrence. The metric criteria used in the LV7015 model are summarized in Table 1.

For instance, if (1, 1) is the hypothesized branch symbol pair and the received quantization pair is (5, 1) (see Fig. 2) then the metric increment in this bit time for all paths having this particular hypothesis will be (0 + 2): 2. In general, in terms of separate symbols, for a hypothetical symbol $X$ the metric increment will be $m(Q_i/X)$ when $Q_i$ is the corresponding quantized value. The values are tabulated in Table 1.

It should now be clear that from the normalization point of view we are interested only in those increments such that

$$m(Q_i/X) \neq 0$$

and which affect the "best path" (wrong paths are assumed to be saturated or nearly saturated). These increments are precisely the weights that have been assigned to the quantized symbol values (Fig. 7).

The above considerations were verified for the LV7015 unit through simulation by inserting specific and repetitive errors into an otherwise error-free data stream, and by observing the normalization counter.

As a summary it will thus be assumed that:

(1) The best path metric is a direct consequence of the channel symbol error rate.

(2) The wrong-path metrics build up very quickly (for a moderate error rate once the decoder is in sync) while the "best path" builds up its metric at a much lower rate.

(3) The normalization rate is due to the necessity of normalizing the best path global metric thus avoiding values over or equal to 4.

***Important:*** The present approach is valid and intuitive for a moderate symbol error rate but must certainly be verified to hold for low values of $ST_S/N_0$ where the noisy channel causes bit errors at the decoder output and "wrong paths" become more "competitive."

A mathematical model was elaborated from assumptions (1), (2), and (3), above and was then compared with the experimental results, especially at low $ST_S/N_0$ near the decoder threshold.

**3. Mathematical model.** In Fig. 7 it is seen that a metric increment $m(Q_i)$ will be added to the global metric with relative frequency $p_i$.

In general the normalization per symbol pair (i.e., per bit) for an arbitrary path length of $n$ symbols can be expressed by:

$$\text{normalization} \times \text{bit}^{-1} = N_b = 1/4 \left(2 \times \frac{\text{global metric along best path}}{n \text{ symbols}}\right)$$

(where the numerator is the best path global metric that would be subsequently accumulated if no normalizations occurred). The average value of $N_b$ is

$$\bar{N}_b = 1/2 \sum_i p_j \cdot m(Q_j) \qquad j = 1, 2, 3, 4 \qquad (3)$$

From Fig. 7,

$$p_1 = \int_{z_0}^{z_1} p(Z)\, dz = P_e(Z_0) - P_e(Z_1)$$

$$p_2 = \int_{z_1}^{z_2} p(Z)\, dz = P_e(Z_1) - P_e(Z_2)$$

$$p_3 = \int_{z_2}^{z_3} p(Z)\, dz = P_e(Z_2) - P_e(Z_3)$$

$$p_4 = \int_{z_3}^{\infty} p(Z)\, dz = P_e(Z_3)$$

Substituting in Eq. (3):

$$\bar{N}_b = 1/2(P_e(Z_0) + P_e(Z_1) + P_e(Z_2) + P_e(Z_3))$$

where $P_e(Z_i)$ represents the error probability which corresponds to variable $Z_i$

$$P_e(Z_i) = \int_{z_i}^{\infty} p(Z)\, dZ$$

An alternate expression for Eq. (3) is:

$$\bar{N}_b = 1/2 \sum_i \text{erf}\, Z_i \qquad i = 0,1,2,3$$

For practical purposes it is interesting to express the above relationship in terms of $ST_S/N_0$ and also in terms of the parameter $K$, which was introduced in Subsection III-A.

$$K = \frac{M}{Q} \left.\begin{matrix} \\ \end{matrix}\right\} \begin{matrix} M = \text{integration mean} \\ Q = \text{quantization interval} \end{matrix}$$

$$\text{But } Z_i = M + i.Q \text{ or } Z_i = M\left(1 + \frac{Q.i}{M}\right)$$

$$Z_i = M\left(1 + \frac{i}{K}\right) \text{ for } i = 0, 1, 2, 3$$

Since

$$\left(\frac{Z_i}{Z_0}\right)^2 = (1 + i/K)^2$$

it follows that

$$(ST_{Si}/N_0 - ST_0/N_0)\ \text{dB} = 20 \log(1 + i/K); \quad i = 0, 1, 2, 3$$

Equation (3) can thus be written:

$$\overline{N}_b = 1/2\left[+P_e(ST_{s0}/N_0) + P_e(ST_{s0}/N_0 + 20\log\left(1+\frac{1}{K}\right)\right) + P_e\left(\frac{ST_{s0}}{N_0} + 20\log\left(1+\frac{2}{K}\right)\right) + P_e\left(\frac{ST_{s0}}{N_0} + 20\log\left(1+\frac{3}{K}\right)\right)\right] \quad (4)$$

where $P_e(X)$ represents the probability of symbol error at an $ST_{s0}/N_0$ of $X$ dB, which is the actual channel energy per symbol-to-spectral density, and corresponds to the value $Z_0$.

Thus, expression (4) relates the normalization rate per bit to the $(ST_s/N_0)$dB in the channel and also includes the parameter $K$, which will determine the optimum calibration point in the SSA integrator.

Equation (4) has been numerically determined for a wide range of $(ST_s/N_0)$dB and three values of $K$ (see Table 2 and Fig. 8).

At this point several considerations arise:

(1) For an $ST_s/N_0 \geq 5$ dB, the mathematical mode may be approximated by:

$$\overline{N}_b \approx 1/2\, P_e$$

where $P_e$ is the channel symbol error probability. This can be justified by the fact that at these values of $ST_s/N_0$ the excursions beyond $Z_1$ (Fig. 7) have very low probability of occurring.

(2) $\overline{N}_b$ is a monotonic function of $K$ for constant $ST_s/N_0$ and is bounded below by $1/2\, P_e$ as already stated in (1).

(3) There is no considerable influence of $K$ on the normalization rate.

Now the question arises: will the model depart from experimental results at low $ST_s/N_0$ when the bit error rate is significant? How will the model be adapted to the system operating conditions? To answer these questions a series of tests was run with a standard configuration, sampling the normalization counter for different $ST_s/N_0$ and assuming a value of $K$ corresponding to the optimum SDA/SSA setting of 280 mV.

**4. An algorithm for performance evaluation.** The mathematical model developed in the preceding section seems to be accurate enough to constitute the basis for a performance evaluator. The requirements may be summarized as a need to evaluate decoder performance (or the system performance) from the normalization rate. A convenient performance estimator could be one that would evaluate the bit error rate or, more simply, the energy per bit-to-spectral noise density. In our case the problem will be reduced to relating the normalization counter values to the bit energy-to-spectral noise density $(ST_b)/N_0$ dB.

Let expression (4) be represented by:

$$\overline{N}_b = f(ST_s/N_0)$$

where parameter $K$ has been substituted by its optimum numerical value. Since $\overline{N}_b$ is the actual variable and the image should be $ST_b/N_0$ rather than $ST_s/N_0$, we first must find $f^{-1}(\,)$ and then introduce the change

$$(ST_b/N_0)\text{ dB} = (ST_s/N_0)\text{ dB} + 3\text{ dB}$$

where it has been assumed that the code rate (symbols per bit) is 2 and that all the degradation effects will be reflected by the normalization rate with no impact on the symbol-to-bit relationship.

Therefore, $f^{-1}(\,)$ was first determined by graphically finding the inverse of $f(\,)$, and then the corresponding values of $ST_s/N_0$ were incremented by 3 dB. However, since the normalization counter is transferred to the operational program every 192 bits, it was thought that it would be preferable to use normalization counts $(\overline{N}_c)$ instead of the normalization rate $(\overline{N}_b)$ as the variable. Thus, a final change was made where

$$\overline{N}_c = 192 \times \overline{N}_b$$

and finally

$$(ST_b/N_0)\text{ dB} = g(\overline{N}_c)$$

was obtained. As stated previously, $f^{-1}(\,)$ was found graphically. For the practical purposes of using the relationship as a computerized algorithm, a polynomial was fitted to the numerical values of $g(\,)$ by using the least squares criterion. The final expression adopted for the algorithm was then:

$$(ST_b/N_0)\,dB = \frac{2.9664}{\overline{N}_c + 0.08} + 5.1218 - 0.2252\,\overline{N}_c \quad (5)$$

This expression will, therefore, convert the normalization counts as transferred from the decoder into the corresponding channel $(ST_b/N_0)$ dB.

Figure 9 is a plotting of expression (5) and is compared to the values of $g(\ )$. The fit has an error lower than 0.3 dB in the range $1 < \overline{N}_c < 15$.

Although $g(\ )$ could theoretically reach very high values for values of $\overline{N}_c$ in the vicinity of 0, this is an impractical approach since the corresponding high values of $ST_b/N_0$ are useless. The criterion was then adopted to saturate the conversion on the order of 35 dB. At the same time the fit accuracy is worse at that end because of the low $ST_b/N_0$ values. Note that the statistics become very poor at $ST_b/N_0$ over 7 dB since extremely few normalizations will occur and the conversion into $ST_b/N_0$ becomes less relevant.

Finally, Fig. 10 is a plotting of BER versus the corresponding values of $ST_b/N_0$ measured with the algorithm directly from the normalization counter. Also shown is $\overline{N}_b$ versus $ST_b/N_0$.

**5. Conclusions regarding normalization rate.** The normalization rate mechanism has been analyzed in terms of its capability to provide a system performance evaluation. In summation, it has been found that:

(1) *The normalization rate behavior is similar to channel symbol error behavior.* In fact, at values of $ST_s/N_0$ about or above 5 dB, both functions may be closely approximated and differ only by a constant.

(2) *$\overline{N}_b$ is quite insensitive to the presence of decoded bits in error and does not significantly depart from the theoretical model.*

(3) When compared to the bit error probability, the normalization function varies at a much lower rate. The $\overline{N}_b$ global derivative function is considerably lower than the BER global derivative and, therefore, a significant BER increment will not be reflected by a significant $\overline{N}_b$ change.

(4) $\overline{N}_b$ is a monotonic function of $K$ where $K$ was defined in Eq. (1) and represents a basic parameter in the SDA/SSA setup. The lower the value of $K$, the lower the normalization rate. However, it does not follow that the lower the $K$ the lower the BER. *Consequently, $\overline{N}_b$ cannot be used to determine the optimum channel operating conditions.*

(5) A relationship between $ST_b/N_0$ and $\overline{N}_c$ was found from a theoretical model based on heuristic considerations. The mathematical model and the experimental results seem to match quite well. However, from (1) to (2) above it follows that the evaluation algorithm is useful only if the system has been properly calibrated or when any existing degradation directly affects the channel error probability by a measurable amount. For a given $ST_b/N_0$, an incorrect calibration (typically a higher MI setting) *may yield such a $\overline{N}_b$ as to induce an estimated BER better than the actual value.*

Therefore, it must be concluded that the system performance evaluator algorithm derived from the normalization rate is valid under certain conditions. It will be further analyzed and evaluated during the forthcoming testing phase as described in Section VIII.

## IV. Differences Between the MCD and the LV7015

As previously stated, there are two minor differences in the functional capability between the DSN Maximum Likelihood Convolutional Decoder being implemented in the Network and the commercially available LV7015 Viterbi decoder. First, the MCD inverts alternate coded symbols to assure sufficient transition density, while the LV7015 does not; second, the MCD has a memory path length of 64 bits, while the LV7015 has a 36-bit memory path length.

The first difference is insignificant. The second difference results in an improvement in decoder performance for the longer memory path length. Based on Linkabit reports and a simulation in which over 200,000 bits were decoded, the difference in performance for the 64-bit memory over the 36-bit memory is undetectable at error rates of $10^{-5}$ (Ref. 1). Consequently, the results reported here are not affected since these tests are designed to investigate performance at this error rate.

Testing using the LV7015 to simulate the MCD at error rates of $10^{-3}$ will have to be adjusted by about 0.1 dB.

## V. Test Plan

Table 3 lists the tests to be carried out. This general test plan includes Block III and Block IV receivers, different SDA bandwidths, and different modulation indexes. Those modulation indexes and the signal power levels included in the plan intend to cover a wide operating

range to determine the optimum channel utilization of the MJS-77 mission.

The test objectives are aimed at the evaluation of the bit error characteristic at the decoder output. Namely:

(1) Estimate the bit error rate.

(2) Determine the statistical behavior of the error bursts.

(3) Evaluate the estimated channel SNR from the normalization rate scheme.

## VI. Bit Error Characteristics

The Viterbi decoding algorithm does not proceed on a per block basis like the Fano algorithm and does not reconsider past bit decisions. The decoded bits may be in error in a certain path length and yet be able to remerge with the good path at a certain mode and remain correct thereafter. Therefore, the decoder always proceeds forward and may depart from the correct path occasionally, depending on channel noise characteristics. The symbol errors occur in bursts whose characteristics are to be determined for the testing conditions. The burst approach suggests two definitions:

(1) An "error burst" (burst) is defined as a sequence of decoded bits that begins with a bit in error, ends with a bit in error, and has fewer than 6 consecutive correct bits within the burst. In general for a constraint length of $K$, the number of consecutive correct bits within the burst must be $K$-2 at most.

(2) An "error free run" (runs) is a sequence of consecutive correct bits including correct bits within a burst. Even runs of length 0 (two consecutive errors) are considered.

The main point thereafter is to identify the bits in error, proceed with their classification into bursts and then analyze the clustering of errors and correct bits within the bursts.

To handle the previously exposed conditions, the following approach was chosen. A bit error pattern is obtained by direct comparison of the original data and the decoded bits. Therefore, the ones in this pattern represent bits in error in the decoded data. Instead of operating directly with this binary error pattern, a preprocessing step is first carried out. The number of consecutive ones and consecutive zeros in the error pattern are counted. The binary pattern is consequently converted into a sequence of integers where the terms of *odd* order correspond to consecutive *ones* in the error pattern, while terms of *even* order correspond to consecutive *zeros* in the error pattern. This preprocessing greatly reduces the data storage required, the search time, and also simplifies the statistical evaluation.

Given then an error pattern of the form:

$$\cdots \underbrace{1\cdots1}_{K_1} \quad \underbrace{0\cdots0}_{K_2} \quad \underbrace{1\cdots1}_{K_3} \quad \underbrace{0\cdots0}_{K_4}$$

the corresponding sequence of integers would be

$$\cdots K_1, K_2, K_3, K_4 \cdots \qquad K_i \in N$$

In general then, the runs of ones and the runs of zeros are transformed into a sequence of integers

$$(a_i)_i \in N$$

where the subsequence of odd terms

$$(a_i)_i = 2K - 1 \qquad K = 1, 2 \cdots$$

represents the respective lengths of the runs of *ones*, and the subsequence of even terms

$$(a_i)_i = 2K \qquad K = 1, 2 \cdots$$

represents the respective lengths of the runs of zeros.

All the considerations concerning error bursts or runs of correct bits (zeros in the error pattern) are done directly from the sequence $(a_i)_{i \in N}$. For instance, an error burst always starts with a term of subindex

$$i = (2K_0 - 1) \qquad \text{if } a_2(K_0 - 1) \geq 6$$

This would mean that $a_{2(K_0-1)}$ is not a run within a burst.

The burst will end when a run of zeros (from burst start) equals or exceeds 7; that is, the end of a burst occurs at certain $K_1$ for which

$$a_{2K_1} \geq 6$$

Then for a burst beginning with term

$$a_{(2K_0-1)}$$

and ending at term $a_{(2K_1-1)}$ with $K_0 < K < K_1$, those terms of the form $a_{2K}$ for $K_0 < K < K_1$ must be

$$a_{2K} < 6$$

We may identify a burst by the pair

$$(K_1, K_2)$$

where $a_{2(K_1-1)}$ is the first term in the burst sequence, and $a_{2(K_2-1)}$ is the last term in the burst sequence. Note that the burst is 1 bit long, and $K_1 = K_2$. The number of ones in a burst $(K_1, K_2)$ may be found by

$$\sum_{K_1}^{K_2} a_{2K-1}$$

For the number of zeros in a burst $(K_1, K_2)$

$$\sum_{K_1}^{K_2-1} a_{2K}$$

The total burst length is $(2K_2 - 1) - (2K_1 - 1) + 1 = 2(K_2 - K_1) + 1$. Any $K$ defines a pair of terms of $(a_i)$ where

$$a_{2K-1} \equiv \text{a run of ones}$$

$$a_{2K} \equiv \text{a run of zeros}$$

For any $K$ such that $a_{2K} \geq 6$, $a_{2K-1}$ is the end of a burst and $a_{2K+1}$ is the beginning of a burst. For instance, for a pattern:

1,0000000011010000011111000000 • • •

$(a_i) \equiv 1, 8, 2, 1, 1, 5, 5, 7$ • • •

For $K = 1$, $a_2 > 6$ then $a_1$ is the end of a burst, $a_2$ is a run out of a burst and $a_3$ the beginning of a new run. Then

$$\text{burst } (1, 1) \equiv 1, \text{ number of ones} = 1, \text{ number of zeros} = 0$$

$$\text{burst } (2, 4) \equiv (2, 1, 1, 5, 5)$$

$$\text{burst length} \equiv 2(4 - 2) + 1 = 5 \text{ [in terms of elements of } (a_i)]$$

$$\text{number of ones} = \sum_{2}^{4} a_{2K-1} = 2 + 1 + 5 = 8$$

$$\text{number of zeros} = \sum_{2}^{4-1} a_{2K} - 1 + 5 = 6$$

## VII. Testing Program Algorithms

The program will analyze the previously presented sequence $(a_i)$ and other complementary parameters within the high-speed data blocks to provide:

(1) The test signal level average and standard deviation in dBm, and the number of samples.

(2) The SSA $ST_B/N_0$ in dB (average and $\sigma$) and number of samples.

It must be noted that this is the standard value processed by the SSA and is biased for values below 4 dB. This should be taken into account when comparing this parameter to the $ST_B/N_0$ derived from $\bar{N}_c$.

(3) Normalization per bit value $\bar{N}_b$ (average and $\sigma$) and number of samples.

(4) The runs length average and $\sigma$, i.e., the statistic on the correct bits, and the total number of runs processed. (Note that correct bits within a burst are also considered.)

(5) The burst length average and $\sigma$, i.e., the statistic on the error bursts and the total number of bursts processed.

(6) The $ST_b/N_0$ (dB) estimation from the normalization count $\bar{N}_c$. The program computes:

$$\frac{ST_b}{N_0}\,\text{dB} = g(\bar{N}_c)$$

as

$$\frac{ST_b}{N_0}\,(\text{dB}) = \frac{a}{\bar{N}_c + K} + b + c\bar{N}_c$$

where

$\bar{N}_c = 192\,\bar{N}_b$ (from item 3 above) and constants $a$, $b$, $c$, specified in Subsection III-B-4.

An estimate of $\sigma(ST_b/N_0)$ is obtained by computing:

$$\left.\begin{aligned} m_1 &= (\bar{N}_b + \sigma_{N_b})\,192 \\ m_2 &= (\bar{N}_b - \sigma_{N_b})\,192 \end{aligned}\right\} \frac{ST_b}{N_0}$$

$$= \frac{|g(\bar{N}_c) - g(m_1)| + |g(\bar{N}_c) - g(m_2)|}{2}$$

(7) The total number of bits processed.

(8) The total burst length i.e., $\sum$ (burst lengths) in bits.

(9) The bit error rate i.e., the relationship:

$$\text{BER} = \frac{\text{ones in the error pattern}}{\text{total no. of bits processed}}$$

(10) The probability that a bit within a burst is in error. Note that since runs of zeros in the error pattern of length $R < 6$ are possible, these bits are actually correct bits within a burst.

(11) The bit error in the average burst length, that is, average burst length × bit error in a burst.

(12) Finally the program tabulates the following statistics:

For bursts ($B$):

The density function $p(B = L) \equiv$ relative frequency of a burst of length $= L$ ($L = 1, 2, 3, \cdots, 100$), and for bursts of length $L$: the average number of error bits per burst and their standard deviation. The distribution function $p(B \geq L)$.

For runs ($R$):

The density function $p(R = L) \equiv$ relative frequency of a run $= L$ ($L = 0, 1, 2, \cdots$), and the distribution function $p(R \geq L)$.

## VIII. General Conclusions

The statistical analysis of the bit error patterns is performed in terms of bursts and runs. The system characteristics will then be determined through the statistical behavior of these parameters. Also, the system performance is evaluated with the normalization rate parameter that has been developed in Section III.

This preliminary report does not consider actual results that will be included in a future document. Also, at the time of this report, the software program is already in use for test evaluation, but still requires modification in a few operating procedures. A full program description and handling procedure will also be presented in a future report.

## Reference

1. Benjauthrit, B. D., Mulhall, D. L., and Wong, J. S., "A Viterbi Decoding Program for DSN Telemetry System Analysis," in *The Deep Space Network Progress Report 42-28*, pp. 5–10, Jet Propulsion Laboratory, Pasadena, Calif., Aug. 15, 1975.

# Bibliography


Gilhousen, K. S., "Coding Systems Study For High Data Rate Telemetry Links," Linkabit Corp., NASA CR-114278, Jan. 1971.

Heller, J., and Jacobs, I., "Viterbi Decoding For Satellite And Space Communication," *IEEE Trans. Commun. Tech.*, Vol. COM-19, No. 5 Oct. 71.

"Instruction Manual LV7015 Convolutional Encoder Viterbi Decoder," Linkabit Corp., 1972.

Maximum Likelihood Convolutional Decoder MCD," Technical Requirement Document 338-256, 10 Jul 1974 Rev B. 12-13-74. Jet Propulsion Laboratory, Pasadena, Calif., July 10, 1974 (Rev. B, Dec. 13, 1974) (an internal document).

"Telemetry Coding Study for the International Magnetosphere Explorers," NASA-CR-132880, Vol. I, Sections 3.2.1 through 3.2.4.

Viterbi, A., "Convolutional Codes and Their Performance In Communications Systems." *IEEE Trans. Commun. Tech.*, Vol. COM-19, No. 5 Oct. 71.

Weber, C. L., "Notes On Convolutional Codes," Gaylord K. Huth, Axiomatic Corp.

**Table 1. Metric criteria**

| Symbol | $m(Q_3)$ | $m(Q_2)$ | $m(Q_1)$ | $m(Q_0)$ | $m(Q_4)$ | $m(Q_5)$ | $m(Q_6)$ | $m(Q_7)$ |
|---|---|---|---|---|---|---|---|---|
| 0 | 0 | 0 | 0 | 0 | 1 | 2 | 3 | 4 |
| 1 | 4 | 3 | 2 | 1 | 0 | 0 | 0 | 0 |

**Table 2. Signal-to-noise ratio vs decoder normalization rate**

| dB | Z | $P_e(Z)$ | $N_b$ | | |
|---|---|---|---|---|---|
| | | | $K=2$ | $K=2.5$ | $K=3.0$ |
| −1.5 | 1.189912 | 0.117040 | 0.082154 | 0.092719 | 0.102841 |
| −1.25 | 1.224658 | 0.110352 | 0.075857 | 0.085422 | 0.094688 |
| −1.00 | 1.260419 | 0.103759 | 0.069882 | 0.078498 | 0.086935 |
| −0.75 | 1.297224 | 0.097277 | 0.064221 | 0.071942 | 0.079585 |
| −0.50 | 1.335104 | 0.090921 | 0.058870 | 0.065752 | 0.072636 |
| −0.25 | 1.374089 | 0.084707 | 0.053822 | 0.059923 | 0.066088 |
| 0.00 | 1.414214 | 0.078650 | 0.049070 | 0.054447 | 0.059936 |
| 0.25 | 1.455509 | 0.072764 | 0.044605 | 0.049317 | 0.054175 |
| 0.50 | 1.498011 | 0.067065 | 0.040421 | 0.044524 | 0.048797 |
| 0.75 | 1.541754 | 0.061567 | 0.036510 | 0.040059 | 0.043794 |
| 1.00 | 1.586774 | 0.056282 | 0.032862 | 0.035913 | 0.039155 |
| 1.25 | 1.633108 | 0.051223 | 0.029470 | 0.032073 | 0.034868 |
| 1.50 | 1.680796 | 0.046401 | 0.026325 | 0.028530 | 0.030922 |
| 1.75 | 1.729876 | 0.041826 | 0.023418 | 0.025271 | 0.027303 |
| 2.00 | 1.780389 | 0.037506 | 0.020741 | 0.022284 | 0.023997 |
| 2.25 | 1.832378 | 0.033448 | 0.018283 | 0.019558 | 0.020990 |
| 2.50 | 1.885884 | 0.029655 | 0.016036 | 0.017079 | 0.018266 |
| 2.75 | 1.940953 | 0.026132 | 0.013989 | 0.014835 | 0.015810 |
| 3.00 | 1.997630 | 0.022878 | 0.012113 | 0.012814 | 0.013606 |
| 3.25 | 2.055962 | 0.019893 | 0.010439 | 0.011001 | 0.011639 |
| 3.50 | 2.115997 | 0.017173 | 0.008940 | 0.009385 | 0.009893 |
| 3.75 | 2.177785 | 0.014711 | 0.007603 | 0.007951 | 0.008352 |
| 4.00 | 2.241377 | 0.012501 | 0.006418 | 0.006680 | 0.007000 |
| 4.25 | 2.306827 | 0.010532 | 0.005374 | 0.005556 | 0.005822 |
| 4.50 | 2.374187 | 0.008794 | 0.004461 | 0.004596 | 0.004803 |
| 4.75 | 2.443515 | 0.007272 | 0.003665 | 0.003767 | 0.003923 |
| 5.00 | 2.514866 | 0.005953 | 0.003017 | 0.003086 | 0.003183 |
| 5.25 | 2.588302 | 0.004822 | 0.002437 | 0.002484 | 0.002554 |
| 5.50 | 2.663882 | 0.003862 | 0.001947 | 0.001979 | 0.002029 |
| 5.75 | 2.741668 | 0.003056 | 0.001538 | 0.001559 | 0.001593 |
| 6.00 | 2.821727 | 0.002388 | 0.001200 | 0.001213 | 0.001236 |
| 6.25 | 2.904122 | 0.001841 | 0.000924 | 0.000932 | 0.000948 |
| 6.50 | 2.988924 | 0.001399 | 0.000701 | 0.000707 | 0.000717 |
| 6.75 | 3.076203 | 0.001048 | 0.000525 | 0.000528 | 0.000534 |
| 7.00 | 3.166029 | 0.000772 | 0.000386 | 0.000388 | 0.000392 |
| 7.25 | 3.258479 | 0.000560 | 0.000280 | 0.000281 | 0.000283 |
| 7.50 | 3.353628 | 0.000398 | 0.000199 | 0.000200 | 0.000201 |
| 7.75 | 3.451556 | 0.000278 | 0.000139 | 0.000139 | 0.000140 |
| 8.00 | 3.552343 | 0.000190 | 0.000095 | 0.000095 | 0.000096 |
| 8.25 | 3.656074 | 0.000128 | 0.000064 | 0.000064 | 0.000064 |
| 8.50 | 3.762833 | 0.000083 | 0.000042 | 0.000042 | 0.000042 |
| 8.75 | 3.872710 | 0.000053 | 0.000027 | 0.000027 | 0.000027 |
| 9.00 | 3.985795 | 0.000033 | 0.000016 | 0.000016 | 0.000016 |
| 9.25 | 4.102182 | 0.000020 | 0.000010 | 0.000010 | 0.000010 |
| 9.50 | 4.221968 | 0.000012 | 0.000006 | 0.000006 | 0.000006 |
| 9.75 | 4.345252 | 0.000006 | 0.000003 | 0.000003 | 0.000003 |
| 10.00 | 4.472135 | 0.000003 | 0.000002 | 0.000002 | 0.000002 |

**Table 3. Test conditions**

| Run | Symbol/sec, SPS (BPS) | RCV BLK No., BW | SDA BLK No., BW | $P_T$, $N_0$ db | $Eb/N_0$ db | Mod index, deg | Carrier suppression, db | Duration of test, h | No. of bits $\times 10^6$ | No. of bit errors expected | Max. No. [a] of bit bursts expected |
|---|---|---|---|---|---|---|---|---|---|---|---|
| M1 | 5120 (2560) | III, N 12 Hz | III, N | 39.67 | 3.8549 | 55 | 4.828 | 1.0 | 9.216 | 460.8 | 121.26 |
| 2 | | | | | 4.7331 | 65 | 7.481 | 1.0 | 9.216 | 460.8 | 121.26 |
| 3 | | | | | 4.9906 | 69 | 8.913 | 1.0 | 9.216 | 460.8 | 121.26 |
| 4 | | | | | 5.0473 | 70 | 9.319 | 2.0 | 18.432 | 921.6 | 242.42 |
| 5 | | | | | 5.0799 | 70.6[b] | 9.573 | 2.0 | 18.432 | 921.6 | 242.42 |
| 6 | | | | | 5.1010 | 71 | 9.747 | 2.0 | 18.432 | 921.6 | 242.42 |
| 7 | | | | | 5.1517 | 72 | 10.200 | 1.0 | 9.216 | 460.8 | 121.26 |
| 8 | | | | | 5.1995 | 73 | 10.681 | | | | |
| 9 | | | | | 5.2444 | 74 | 11.193 | | | | |
| 10 | | | | | 5.3257 | 76 | 12.326 | | | | |
| 11 | | | | | 5.3957 | 78 | 13.642 | | | | |
| 12 | | | | | 5.4546 | 80 | 15.207 | | | 460.8 | |
| N1 | 5120 (2560) | IV, N 3 Hz | IV, N | 39.67 | 3.8549 | 55 | 4.828 | | | 921.6 | |
| 2 | | | | | 4.7331 | 65 | 7.481 | | | 921.6 | |
| 3 | | | | | 4.9906 | 69 | 8.913 | 1.0 | 9.216 | 921.6 | 121.26 |
| 4 | | | | | 5.0473 | 70 | 9.319 | 2.0 | 18.432 | 460.8 | 242.42 |
| 5 | | | | | 5.0799 | 70.6[b] | 9.573 | 2.0 | 18.432 | 460.8 | 242.42 |
| 6 | | | | | 5.1010 | 71 | 9.747 | 2.0 | 18.432 | 460.8 | 242.42 |
| 7 | | | | | 5.1517 | 72 | 10.200 | 1.0 | 9.216 | 921.6 | 121.26 |
| 8 | | | | | 5.1995 | 73 | 10.681 | | | | |
| 9 | | | | | 5.2444 | 74 | 11.193 | | | | |
| 10 | | | | | 5.3257 | 76 | 12.326 | | | | |
| 11 | | | | | 5.3957 | 78 | 13.642 | | | | |
| 12 | | | | | 5.4546 | 80 | 15.207 | 1.0 | 9.216 | 921.6 | 121.26 |
| G1 | 5120 (2560) | 12 Hz | III, M | 40.26 | 4.4449 | 55 | 4.828 | 1.0 | 9.216 | 460.8 | 121.26 |
| 2 | | | | | 5.3231 | 65 | 7.481 | | | | |
| 3 | | | | | 5.5806 | 69 | 8.913 | | | | |
| 4 | | | | | 5.6373 | 70 | 9.319 | 1.0 | 9.216 | 460.8 | 121.26 |
| 5 | | | | | 5.6910 | 71 | 9.747 | 5.0 | 46.08 | 2304 | 606.32 |
| 6 | | | | | 5.7417 | 72[b] | 10.200 | 5.0 | 46.08 | 2304 | 606.32 |
| 7 | | | | | 5.7895 | 73 | 10.681 | 5.0 | 46.08 | 2304 | 606.32 |
| 8 | | | | | 5.8344 | 74 | 11.193 | 1.0 | 9.216 | 460.8 | 121.26 |
| 9 | | | | | 5.8765 | 75 | 11.740 | | | | |
| 10 | | | | | 5.9857 | 78 | 13.642 | | | | |
| 11 | | | | | 6.0446 | 80 | 15.207 | | | | |
| H1 | 5120 (2560) | 12 Hz | III, N | 39.67 | 3.8549 | 55 | 4.828 | | 9.216 | | |
| 2 | | | | | 4.7331 | 65 | 7.481 | | 9.216 | | |
| 3 | | | | | 4.9906 | 69 | 8.913 | 1.0 | 9.216 | 460.8 | 121.26 |
| 4 | | | | | 5.0473 | 70 | 9.319 | 5.0 | 46.08 | 2304 | 606.32 |
| 5 | | | | | 5.0799 | 70.6[b] | 9.573 | 5.0 | 46.08 | 2304 | 606.32 |
| 6 | | | | | 5.1010 | 71 | 9.747 | 5.0 | 46.08 | 2304 | 606.32 |
| 7 | | | | | 5.1517 | 72 | 10.200 | 1.0 | 9.216 | 460.8 | 121.26 |
| 8 | | | | | 5.1995 | 73 | 10.681 | | | | |
| 9 | | | | | 5.2444 | 74 | 11.193 | | | | |
| 10 | | | | | 5.3257 | 76 | 12.326 | | | | |
| 11 | | | | | 5.3957 | 78 | 13.642 | | | | |
| 12 | | | | | 5.4546 | 80 | 15.207 | | | | |
| I1 | 5120 (2560) | 12 Hz | III, M | 39.77 | 3.9549 | 55 | 4.828 | 1.0 | 9.216 | 460.8 | 121.26 |

Table 3 (contd)

| Run | Symbol/sec, SPS (BPS) | RCV BLK No., BW | SDA BLK No., BW | $P_T$, $N_0$ db | $Eb/N_0$ db | Mod index, deg | Carrier suppression, db | Duration of test, h | No. of bits $\times 10^6$ | No. of bit errors expected | Max. No. [a] of bit bursts expected |
|---|---|---|---|---|---|---|---|---|---|---|---|
| 12 | 5120 (2560) | 12 Hz | | | 4.8331 | 65 | 7.481 | 1.0 | 9.216 | 460.8 | 121.26 |
| 3 | | | | | 5.0906 | 69 | 8.913 | 1.0 | 9.216 | 460.8 | 121.26 |
| 4 | | | | | 5.1473 | 70 | 9.319 | 5.0 | 46.08 | 2304 | 606.32 |
| 5 | | | | | 5.1852 | 70.7[b] | 9.616 | 5.0 | 46.08 | 2304 | 606.32 |
| 6 | | | | | 5.2010 | 71 | 9.747 | 5.0 | 46.08 | 2304 | 606.32 |
| 7 | | | | | 5.2517 | 72 | 10.200 | 1.0 | 9.216 | 460.8 | 121.26 |
| 8 | | | | | 5.2995 | 73 | 10.661 | | | | |
| 9 | | | | | 5.3444 | 74 | 11.193 | | | | |
| 10 | | | | | 5.4257 | 76 | 12.326 | | | | |
| 11 | | | | | 5.4957 | 78 | 13.642 | | | | |
| 12 | | | | | 5.5546 | 80 | 15.207 | 1.0 | 9.216 | 460.8 | 121.26 |
| J1 | 5120 (2560) | 12 Hz | III, W | 39.82 | 4.0049 | 55 | 4.828 | 1.0 | 9.216 | 460.8 | 121.26 |
| 2 | | | | | 4.8831 | 65 | 7.481 | 1.0 | 9.216 | 460.8 | 121.26 |
| 3 | | | | | 5.1406 | 69 | 8.913 | 5.0 | 46.08 | 2304 | 606.32 |
| 4 | | | | | 5.2405 | 70.8[b] | 9.660 | 5.0 | 46.08 | 2304 | 606.32 |
| 5 | | | | | 5.2510 | 71 | 9.747 | 5.0 | 46.08 | 2304 | 606.32 |
| 6 | | | | | 5.3017 | 72 | 10.200 | 1.0 | 9.216 | 460.8 | 121.26 |
| 7 | | | | | 5.3495 | 73 | 10.681 | | | | |
| 8 | | | | | 5.3944 | 74 | 11.193 | | | | |
| 9 | | | | | 5.4757 | 76 | 12.326 | | | | |
| 10 | | | | | 5.5457 | 78 | 13.642 | | | | |
| 11 | | | | | 5.6046 | 80 | 15.207 | | | | |
| K1 | 5120 (2560) | 12 Hz | III, M | 41.26 | 5.4449 | 55 | 4.828 | | | | |
| 2 | | | | | 6.3231 | 65 | 7.481 | 1.0 | 9.216 | 460.8 | 121.26 |
| 3 | | | | | 6.7417 | 72 | 10.200 | 5.0 | 46.08 | 2304 | 606.32 |
| 4 | | | | | 6.8123 | 73.5[b] | 10.933 | | 46.08 | 2304 | 606.32 |
| 5 | | | | | 6.8344 | 74 | 11.193 | | 46.08 | 2304 | 606.32 |
| 6 | | | | | 6.8765 | 76 | 11.740 | 1.0 | 9.216 | 460.8 | 121.26 |
| 7 | | | | | 6.9157 | 76 | 12.326 | | | | |
| 8 | | | | | 6.9521 | 77 | 12.958 | | | | |
| 9 | | | | | 7.0446 | 80 | 15.207 | 1.0 | 9.216 | 460.8 | 121.26 |
| L1 | 5120 (2560) | 12 Hz | III, M | 42.76 | 6.9449 | 55 | 4.828 | 1.0 | 9.216 | 460.8 | 121.26 |
| 2 | | | | | 7.8231 | 65 | 7.481 | | | | |
| 3 | | | | | 8.2895 | 73 | 10.681 | | | | |
| 4 | | | | | 9.3344 | 74 | 11.193 | 1.0 | 9.216 | 460.8 | 121.26 |
| 5 | | | | | 8.3765 | 75 | 11.740 | 5.0 | 46.08 | 2304 | 606.32 |
| 6 | | | | | 8.3845 | 75.2[b] | 11.854 | 5.0 | 46.08 | 2304 | 606.32 |
| 7 | | | | | 8.4157 | 76 | 12.326 | 5.0 | 46.08 | 2304 | 606.32 |
| 8 | | | | | 8.4521 | 77 | 12.958 | 1.0 | 9.216 | 460.8 | 121.26 |
| 9 | | | | | 8.4857 | 78 | 13.642 | 1.0 | 9.216 | 460.8 | 121.26 |
| 10 | | | | 42.76 | 8.5446 | 80 | 15.207 | 1.0 | 9.216 | 460.8 | 121.26 |

[a]Based on Linkabit's average number of errors per burst of 3.8 bits at about BER = $5 \times 10^5$.

[b]Theoretical optimal value.

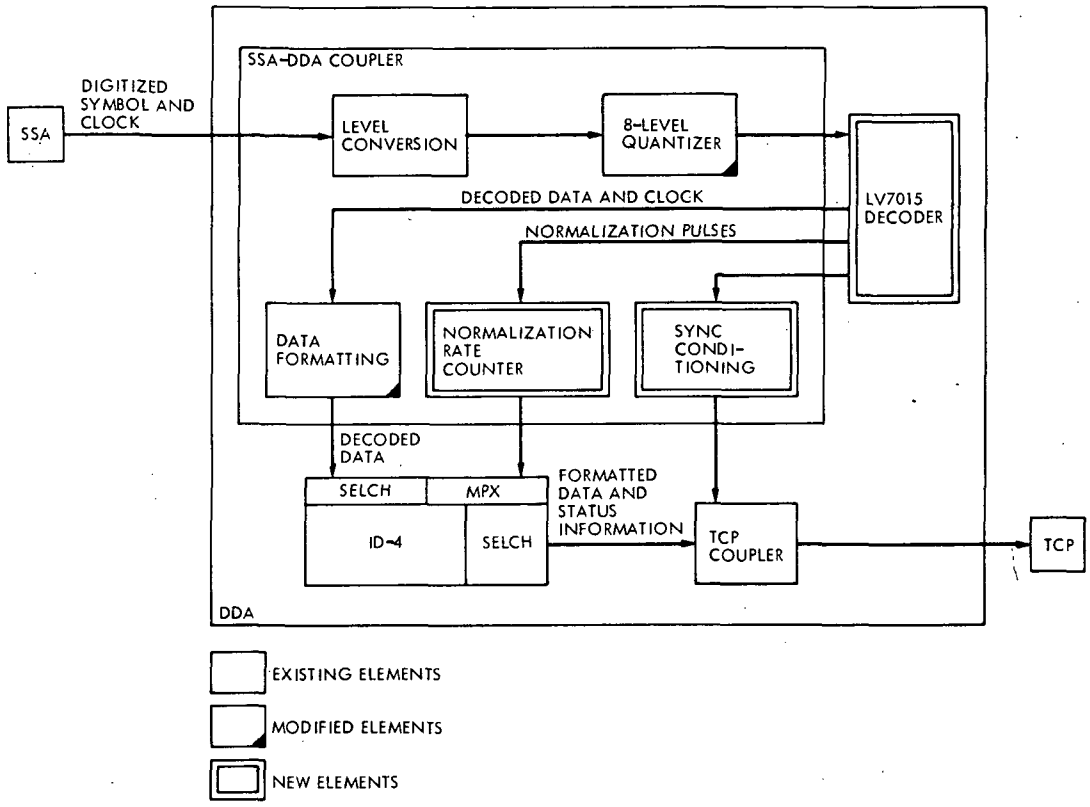


Fig. 1. LV7015 integration

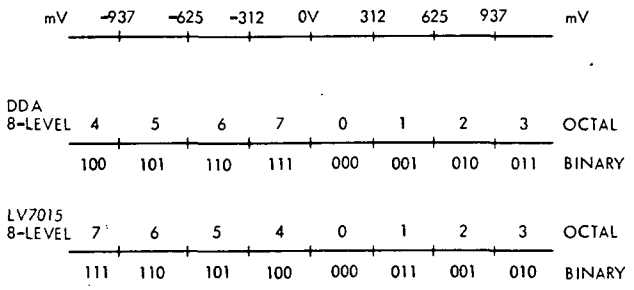


Fig. 2. SSA analog-to-digital conversion levels

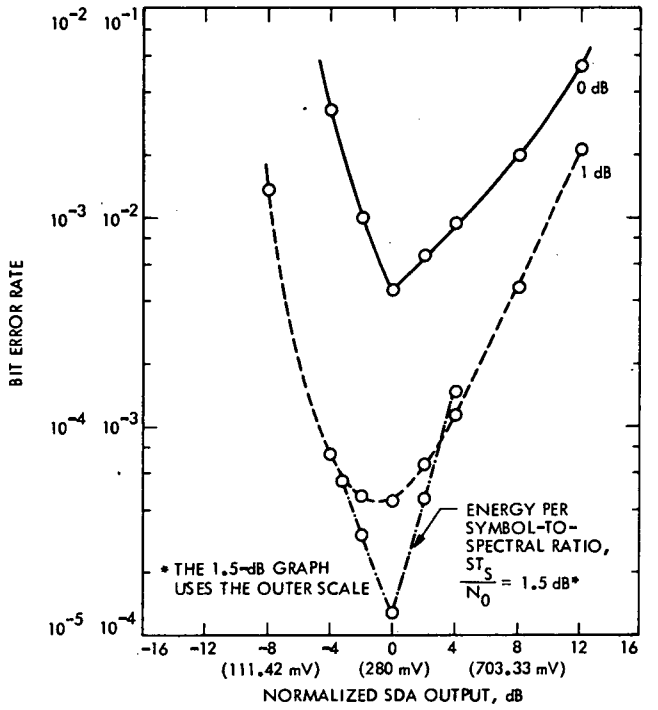


**Fig. 3. Bit error rate vs SDA output for $ST_S/N_0$ = 0, 1, and 1.5 dB**

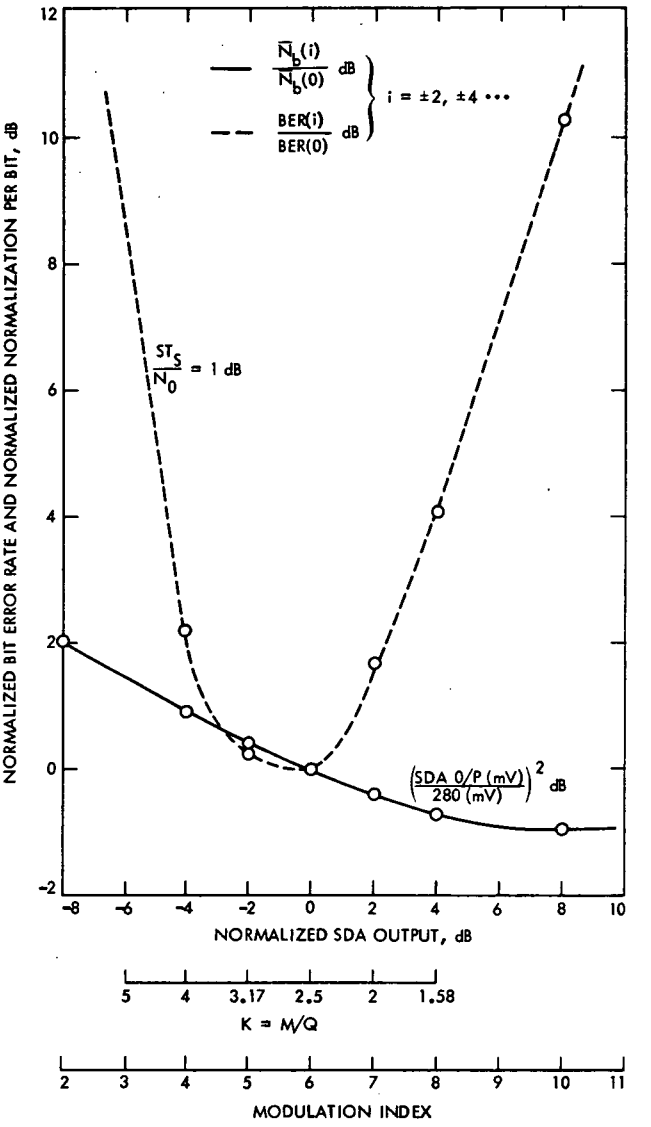


**Fig. 4. Bit error rate vs SDA output and normalization rate vs modulation index ($ST_S/N_0$ = 1 dB)**

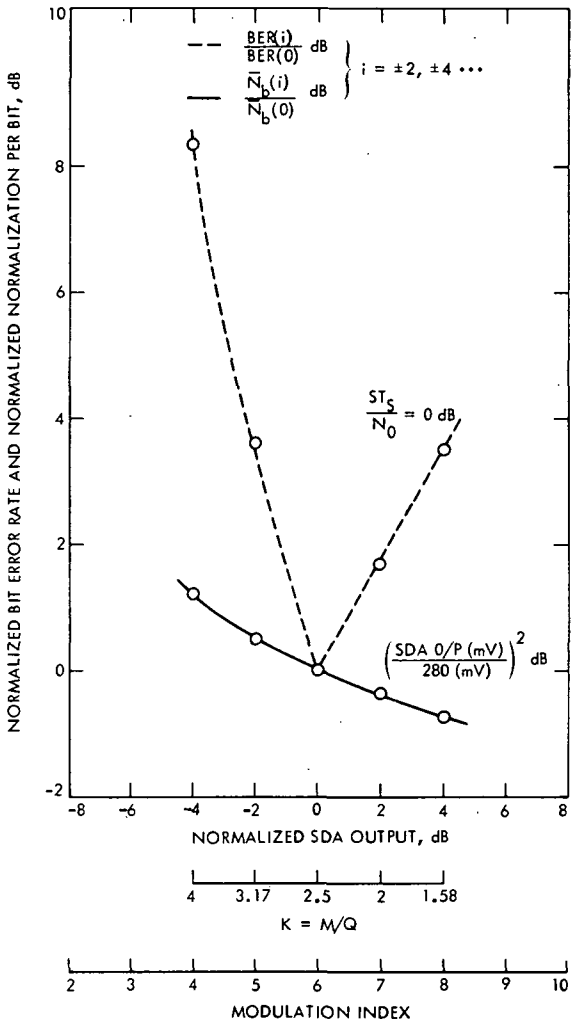


Fig. 5. Bit error rate vs SDA output and normalization rate vs modulation index ($ST_S/N_0$ = 0 dB)

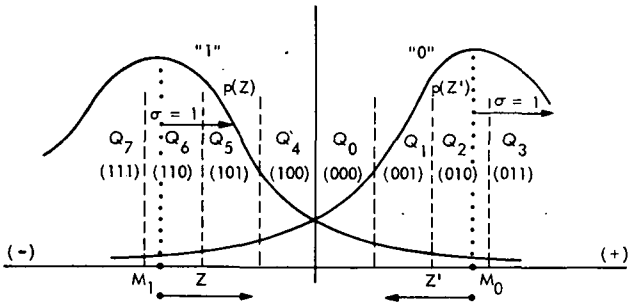


Fig. 6. Two superimposed gaussian probability density curves, p (Z)

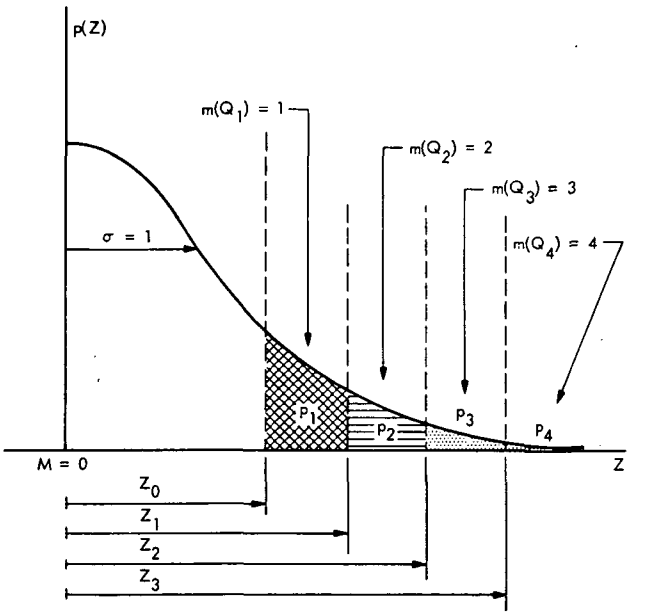


Fig. 7. An equivalent representation of two superimposed gaussian probability density curves

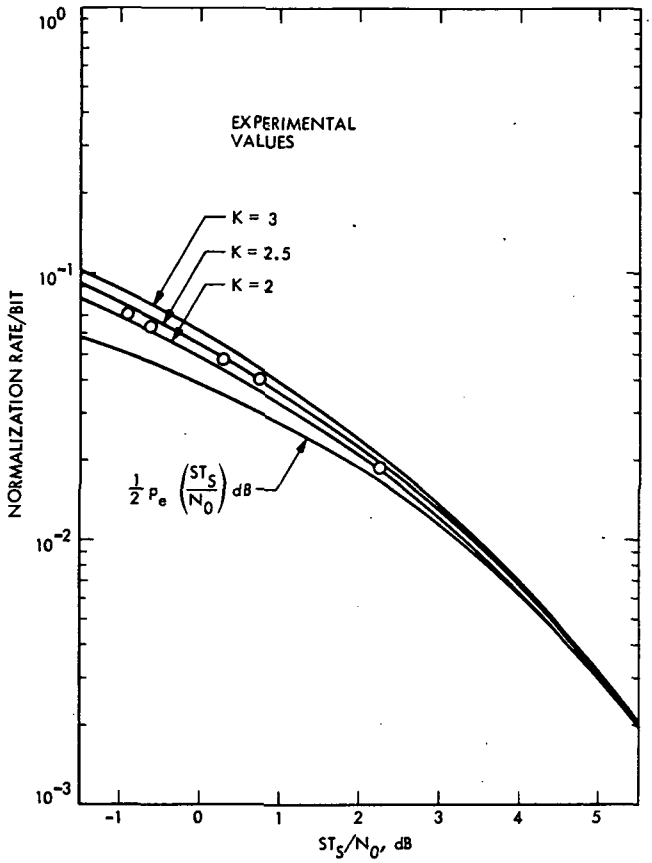


**Fig. 8. Normalization rate per bit $N_b$ vs energy per symbol-to-spectral noise density ratio $ST_S/N_0$, dB**

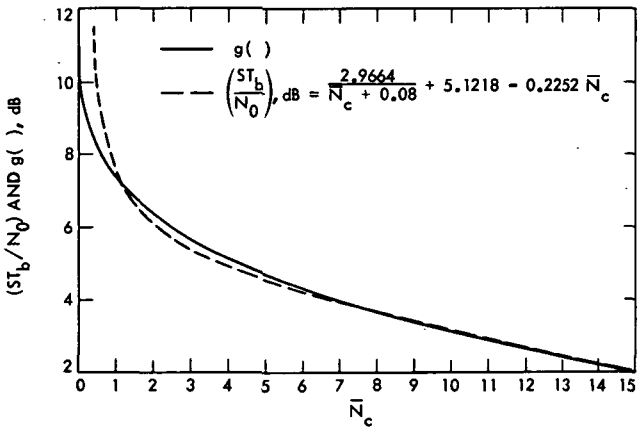


*Fig. 9. $ST_S/N_0$ and g ( ) vs normalization counts $N_c$*

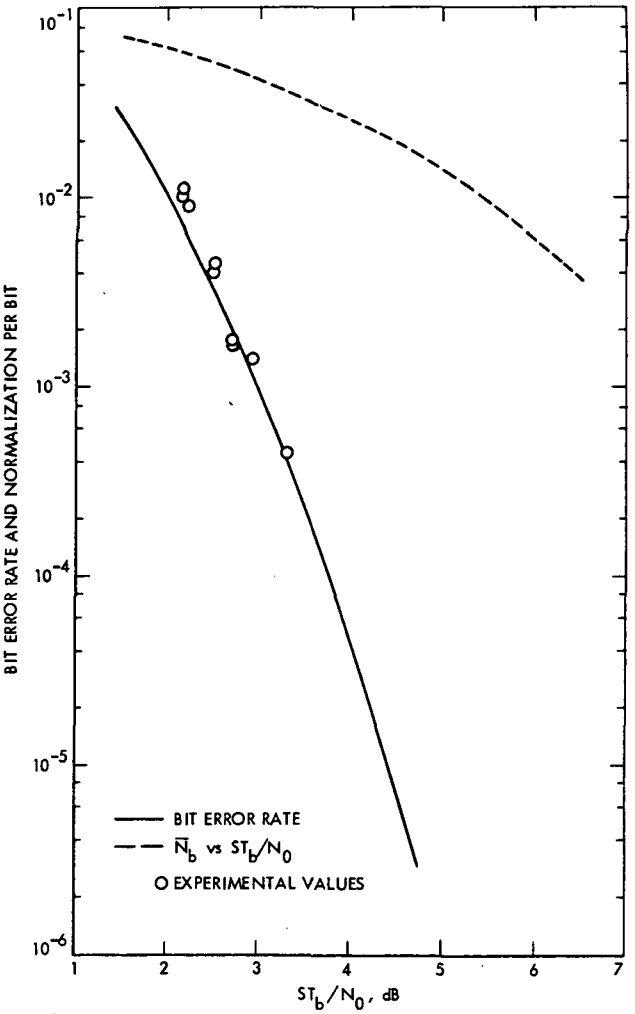


**Fig. 10. Baseband performance characteristics of K = 7 rate 1/2 convolutional code, Viterbi coding, soft quantized, Q = 3**

# Phase-Stable Receiver Development

C. E. Johns
RF Systems Development Section

*Physical changes in coaxial cable parameters cause corresponding phase variations to RF signals being transmitted through them. In some types of receivers these variations directly affect the information signal. A phase-correcting circuit has been developed which greatly reduces the cable effects upon an RF signal. This article describes two types of correcting loops and test results from breadboard units.*

## I. Introduction

Stable reference frequencies, such as those generated by atomic standards, are being incorporated as local oscillators within newer receiver subsystems where the phase stability of the detected signal is directly affected by the phase stability of the reference signals. One example of a system in this category is a very-long baseline interferometry (VLBI) type receiver.

Maintaining a constant reference phase becomes difficult to achieve where long coaxial cables are used between the reference source and other remote locations, such as between the control room and the antenna at a DSS. Temperature, humidity, cable flexure and other effects cause cable properties to change, creating a corresponding variation in its electrical length. Methods have been devised (Refs. 1 and 2) to compensate for phase delay variations over very long distances, such as between two tracking stations, where transmission losses are large. Because of the transmission loss, these have been sophisticated systems and very costly.

To reduce the cost for a single cable phase control circuit, the use of a simple phase-correcting loop, rather than a phase-locked loop, was investigated. The phase-correcting loop utilizes a simple voltage-variable phase shifter instead of a crystal voltage-controlled oscillator. Two such types of control loops were investigated.

## II. Type 1 Loop

The block diagram of the first type of loop constructed is shown in Fig. 1. It closely resembles one of the block diagrams suggested by J. W. MacConnell and R. L. Sydnor

(Ref. 1) in that it utilizes two phase detectors whose dc outputs are summed, filtered and then applied to the phase-variable element within the loop.

Figure 2 shows a mathematical model of the Type 1 loop using Laplace notation. When the loop is in operation, the phase-correcting signal at point A of Fig. 2 is

$$\text{Phase correction} = \frac{-2K\theta_B(S)}{2K+1} \tag{1}$$

where $K$ is the total loop gain and $\theta_B(S)$ is the cable phase variation. The signal output phase, at point $B$, is the summation of the signal phase variation, due to cable perturbations, and the phase correcting signal at point A:

$$\text{Output phase} = \theta_B(S) - \frac{2K\theta_B(S)}{2K+1} = \frac{\theta_B(S)}{2K+1} \tag{2}$$

Therefore, phase variations for this type of loop can be greatly reduced by using a high loop gain.

The loop gain $K$ is the product of the phase detector constant $K_D$ in volts/degree, the dc amplifier gain $G_A$ in volts/volt and the voltage variable phase shifter gain $K_\phi$ in degrees/volts; i.e.:

$$K = K_D \cdot G_A \cdot K_\phi \tag{3}$$

The breadboard unit was designed for a loop gain of 20. To assure correct phase compensation, the phasing of the 100-MHz reference signals into the phase detectors (D1 and D2) and the detector gains must be carefully adjusted. Gain and phasing adjustments on the breadboard unit proved to be difficult, but once achieved, the unit performed nearly as predicted.

To test the circuit, a line stretcher was inserted into the line at point X in Fig. 2. The unit was aligned by phasing the 100-MHz reference signals into the phase detectors, and the detector gains were equalized by varying the line stretcher while adjusting the detector gains until the phase variation between the input to the control room unit and the output of the antenna unit was minimized. With the loop inoperative (open-loop) the total phase deviation supplied by the line stretcher was approximately 14 deg. With the loop operating (closed-loop), the total phase deviation was reduced to about 0.4 deg, which is a correction factor (CF) of 35; i.e.,

$$\text{CF} = \frac{\Delta\phi \text{ open-loop}}{\Delta\phi \text{ closed-loop}} \tag{4}$$

Using the design value of $K = 20$, the calculated value of the output phase, for a 14-degree cable variation, is

$$\text{Output phase} = \frac{14}{2 \times 20 + 1} = \frac{14}{41} = 0.34 \text{ deg} \tag{5}$$

and the calculated correction factor is

$$\text{CF} = \frac{\Delta\phi \text{ open-loop}}{\Delta\phi \text{ closed-loop}} = \frac{14}{0.34} = 41.2 \tag{6}$$

The difference between the calculated and measured correction factors is due to alignment tolerances and mismatches at the cable ends. Signal reflections, due to these mismatches, add to the desired signals, thus altering the original phase variation caused by cable.

## III. Type 2 Loop

Because of the difficulty in aligning the Type 1 loop design, the possibility of using a single phase detector circuit was investigated. Several block diagrams of this type are shown in Fig. 3. A breadboard of the type shown in Fig. 3a has been constructed. Figure 4 shows the signal phases within the loop.

Ideally, the Type 2 correction loop can be adjusted to completely compensate a coaxial cable. To explain the loop action, refer to Fig. 4. Point A will be designated the correcting phase $\theta_C(S)$. The total phase at point $E$ is the sum of this correcting phase and twice the cable error:

$$\textit{Phase}_E = \theta_C(S) + 2\theta(S) \tag{7}$$

The point A and E phases are differenced in the phase detector, yielding a dc error voltage of

$$\textit{Error}_{dc} = \theta_C(S) - [\theta_C(S) + 2\theta(S)] = -2\theta(S) \tag{8}$$

This dc error is multiplied by the loop gain $K$, as previously defined, causing a phase change at the phase shifter output:

$$\theta_C(S) = -2K\theta(S) \tag{9}$$

In order to obtain an output phase equal to the input phase,

$$\theta_C(S) = -\theta(S) \tag{10}$$

Therefore,

$$K = \frac{1}{2} \tag{11}$$

Thus when the total loop gain is exactly 1/2, complete cable compensation is attained, but due to alignment tolerances and impedance mismatches at the cable ends, it is not possible to achieve 100% compensation. The measured correction factor (CF) of the loop evaluated in the lab was 70.

To assure that the compensating loop does not contribute to the phase error, the hardware must be packaged in temperature-stable enclosures both in the antenna and control room.

## IV. Conclusion

The feasibility of using simple phase-correcting loops for compensation of cable drifts has been successfully demonstrated. It is planned to use this type of loop for stabilizing the local oscillator frequencies within the Pioneer Venus differential long baseline interferometry (DLBI) receiver to permit accurate system calibrations. Also, a loop will be used at the Goldstone Mars Station (DSS 14) for generating a stable X-band reference signal to allow making phase stability measurements on the Block IV X-band local oscillator, to determine if the Block IV meets the Viking VLBI requirements.

## References


1. MacConnell, J. W., and Sydnor, R. L., "A Microwave Frequency Distribution Technique for Ultra Stable Standard Frequencies," in *The Deep Space Network Progress Report 32-28*, pp. 34–41, Jet Propulsion Laboratory, Pasadena, Calif., Aug. 15, 1975.
2. Chernoff, R. C., "Large Active Retrodirective Arrays for Space Applications," to be published.

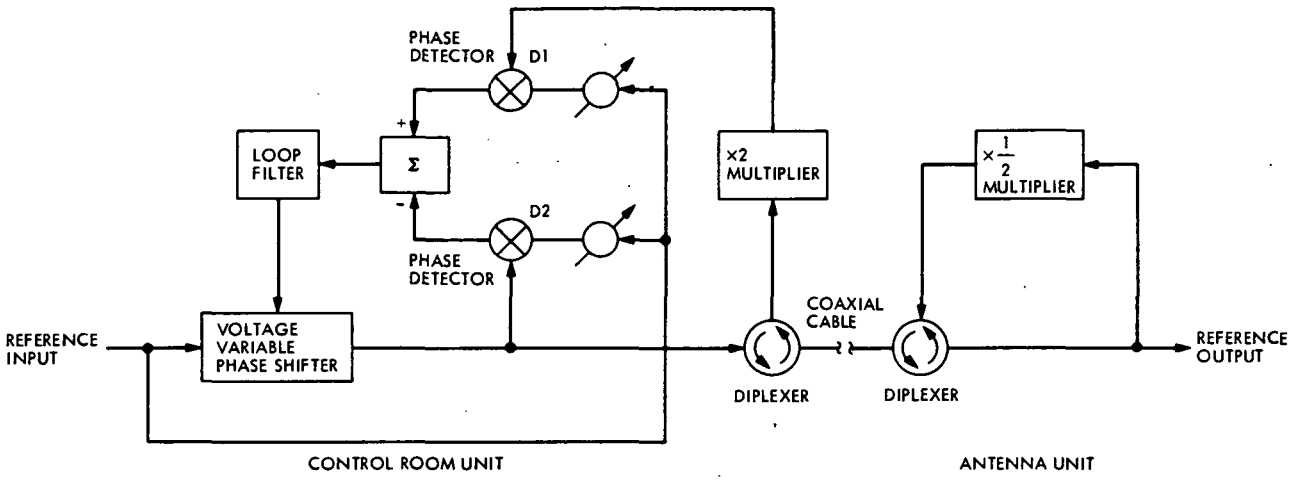


Fig. 1. Type 1 phase-correcting loop

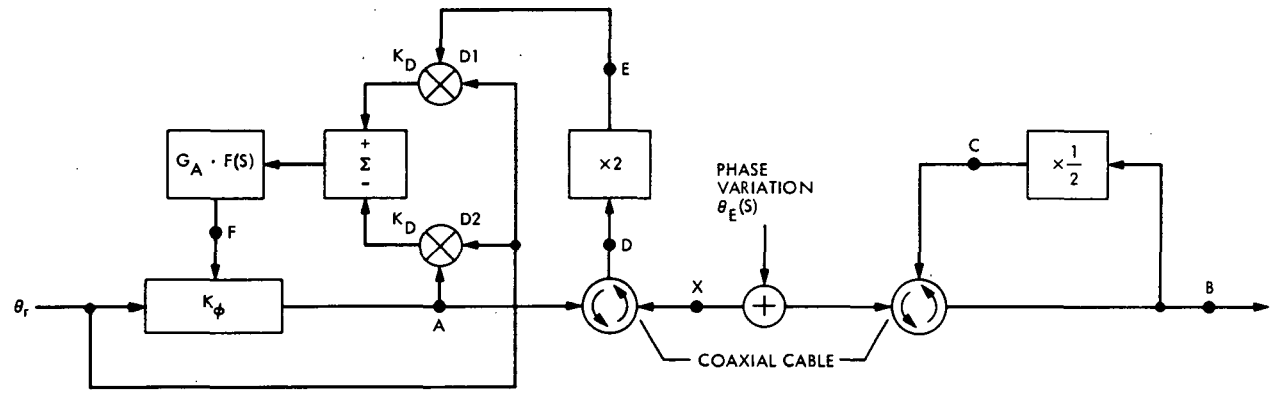


NOMENCLATURE

$K_\phi$, VOLTAGE VARIABLE PHASE SHIFTER GAIN, deg/V

G · F(S), ACTIVE LOW-PASS FILTER WITH DC GAIN, V/V

$K_D$, PHASE DETECTOR GAIN, V/deg

$\theta_r(S)$, INPUT REFERENCE PHASE

$\theta_E(S)$, SIGNAL PHASE VARIATION DUE TO CABLE

K, TOTAL LOOP GAIN = $K_D \cdot G \cdot K_\phi$

LOOP SIGNAL PHASES

A. $\frac{-2K\theta_E(S)}{2K+1}$, PHASE CORRECTING SIGNAL

B. $\frac{\theta_E(S)}{2K+1}$, SIGNAL OUTPUT PHASE

C. $\frac{\theta_E(S)}{2(2K+1)}$, $\frac{1}{2}$ SIGNAL OUTPUT PHASE

D. $\theta_E(S)$, RETURNED SIGNAL PHASE

E. $2\theta_E(S)$, 2 × RETURNED SIGNAL PHASE

F. $\frac{2\theta_E(S)}{K_\phi(2K+1)}$, DC PHASE ERROR/$K_\phi$

Fig. 2. Type 1 phase-correcting loop, signal phases

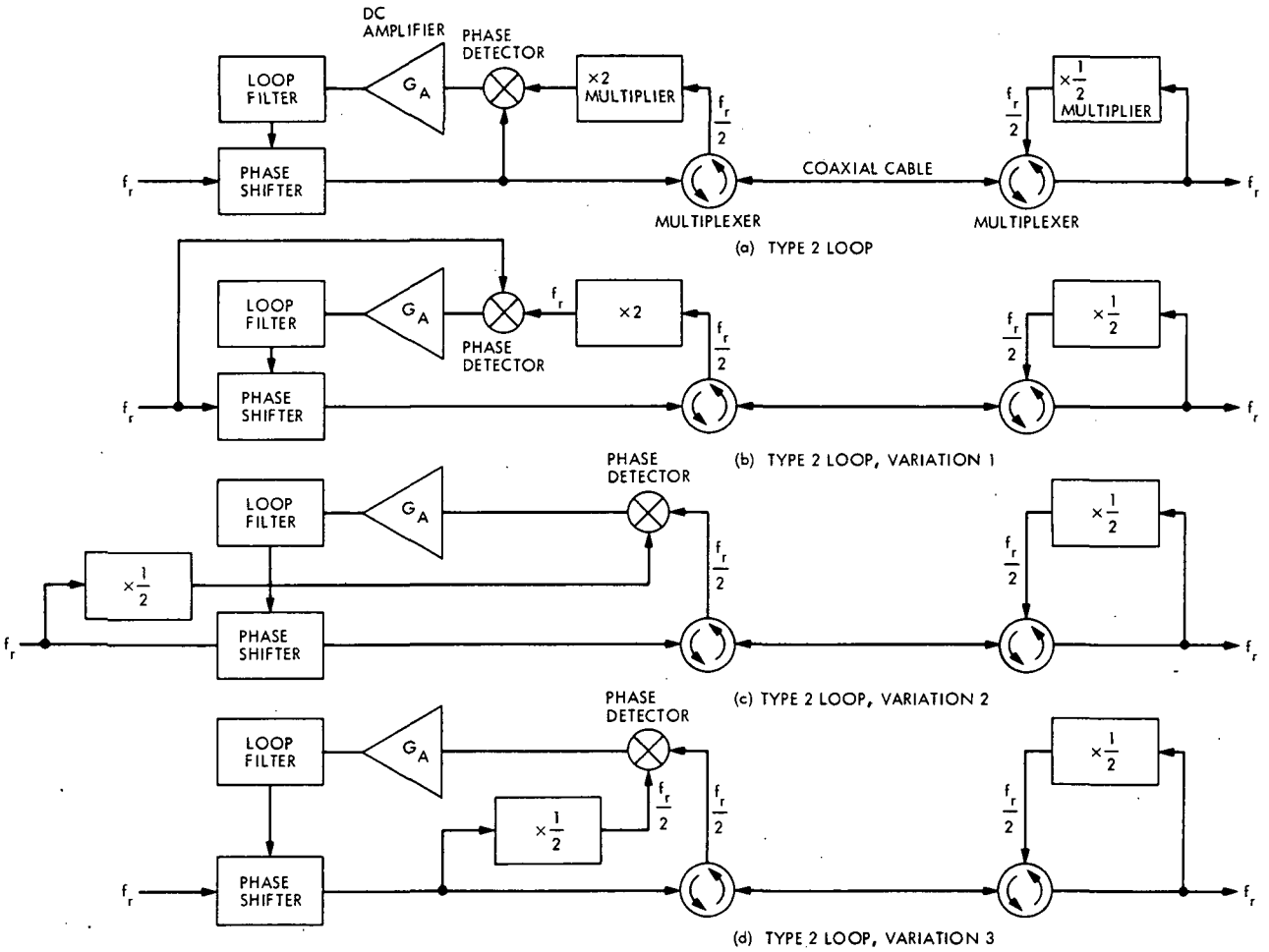


**Fig. 3. Type 2 phase-correcting loops**

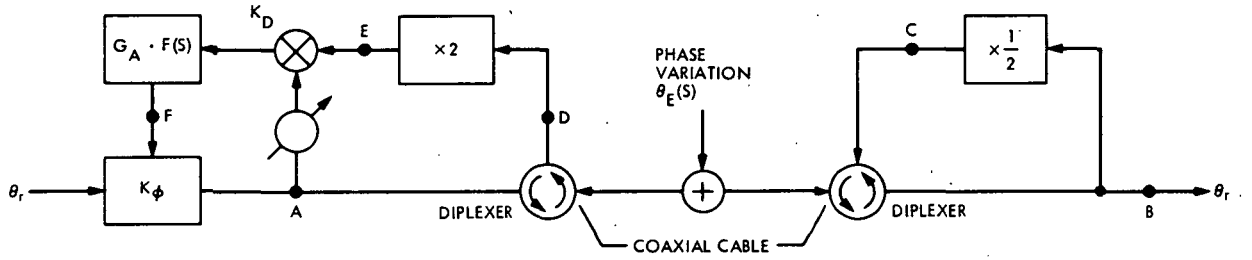


NOMENCLATURE

$K_\phi$, VOLTAGE VARIABLE PHASE SHIFTER GAIN, deg/V

G · F(S), ACTIVE LOW-PASS FILTER WITH DC GAIN

$K_D$, PHASE DETECTOR GAIN, V/deg

$\theta_r(S)$, INPUT/OUTPUT REFERENCE PHASE

$\theta_E(S)$, SIGNAL PHASE VARIATION DUE TO CABLE

K, TOTAL LOOP GAIN = $K_D \cdot G_A \cdot K_\phi$

LOOP SIGNAL PHASES

A. $-\theta_E(S)$, PHASE CORRECTING SIGNAL

B. $\theta_r(S)$, SIGNAL INPUT/OUTPUT PHASE

C. $\frac{\theta_E(S)}{2}$, $\frac{1}{2}$ SIGNAL PHASE VARIATION

D. $\theta_E(S)$, RETURNED SIGNAL PHASE

E. $2\theta_E(S)$, 2 × RETURNED SIGNAL PHASE

F. $\theta_E(S)$, DC CORRECTING ERROR/$K_\phi$

**Fig. 4. Type 2 phase-correcting loop, signal phases**

# Computer Modeling of a Single-Stage Lithium Bromide/Water Absorption Refrigeration Unit

F. L. Lansing
DSN Engineering Section

*Solar-assisted refrigeration systems have been proposed for application in Goldstone energy conservation projects. This article describes and analyzes the dynamic simulation and the computer modeling procedure of one of these systems, namely a lithium bromide/water absorption refrigeration system. A new analytical expression that fits the three-dimensional surface of LiBr concentration, refrigerant temperature and solution temperature in the range of interest from 0.50 to 0.65 kg LiBr/kg solution is presented with a standard deviation of ±0.2 percent. This will save considerable computing time and effort required for evaluation of system performance. A numerical example from typical running conditions is added to show the relative weight of each parameter used together with the sequence of program steps followed. The results from this simulation are heat rates, line concentrations, pressures and the overall coefficient of performance.*

## I. Introduction

In recent years, the lithium bromide/water absorption system has become prominent in refrigeration for air conditioning. It possesses several advantages over the other types of absorption systems, such as:

(1) It has the highest coefficient of performance (COP) compared to other single-stage absorption units at the same cycle temperatures.

(2) It is composed of simpler components since it can work efficiently without the need of rectification columns. A basic generator is sufficient due to the nonvolatility of the absorbent (LiBr), allowing only water vapor to be driven off the generator.

(3) Less pump work is needed compared to other units due to operation at vacuum pressures.

On the other hand, the lithium bromide/water absorption system has some drawbacks such as:

(1) It is limited to relatively high evaporating temperatures since the refrigerant is water. This means that evaporation temperature above 0°C must generally be satisfied to prevent flow freezing.

(2) Crystallization of LiBr salt at moderate concentrations (>0.65 kg LiBr/Kg solution) will tip off the cycle range of operation.

(3) The systems have to be designed in hermetically sealed units since they operate at vacuum pressures. Improper operation would result if leakage of air into the system occurred.

Irrespective of its drawbacks, the LiBr/water unit is still considered the most economical for this kind of refrigeration technique. It has been selected as a candidate refrigeration system in connection with a proposed solar assisted equipment for application in Goldstone energy conservation projects.

This article describes and analyzes the computer modeling of such units. The modeling procedure is generalized to enable those concerned with use or evaluation of cycles employing this material to save considerable time and effort required for calculations.

## II. Thermodynamic Cycle

The system components and the working fluid states are shown in Figs. 1 and 2. There are four basic heat exchanger surfaces: the evaporator, the absorber, the generator, and the condenser, in addition to a liquid-liquid heat exchanger. Lithium bromide is, basically, nothing more than salt water. However, lithium bromide is a salt with an especially strong attraction for water.

The cycle of operation may be started as shown in Fig. 1, from the evaporator. The refrigerant (water) is evaporated while it is taking heat from the fluid being chilled (air for instance). The water vapor (state 10) is then sucked up by lithium bromide spray injected into the absorber, thus the name absorption system. Due to the exothermic reaction taking place in the absorption process, heat has to be removed, and the mixture of lithium bromide and refrigerant vapor at this stage is called the "strong solution" (state 1). "Strong" and "weak" refer to the amount of refrigerant present. The strong solution is then pumped (state 2) through a liquid-liquid heat exchanger (state 3) to the generator. This heat exchanger will improve the cycle performance, as will be shown later. In the generator (sometimes called the concentrator) the strong solution is heated and boiled by an external heat source to release the refrigerant vapor (state 7), leaving behind a concentrated LiBr/water solution (state 4). The latter is called "weak solution" since it contains a smaller amount of refrigerant. The refrigerant vapor leaving the generator is condensed (state 8) in the condenser and is directed to the evaporator through an expansion valve (state 9). The weak solution flows back to the absorber through the liquid-liquid heat exchanger as a spray (state 6) to complete the cycle.

The thermodynamic cycle is sketched on the equilibrium temperature-pressure-concentration chart as shown in Fig. 2. It is bounded by two constant concentration lines: $X_1$ and $X_4$ for the absorber and generator concentration, respectively, and two constant pressure lines: $P_e$ and $P_c$ for the evaporator and condenser pressures, respectively.

For an efficient air conditioning application, the evaporator temperature $t_e$ should be low enough to dehumidify the air. In practice, it ranges from 4.5 to 10°C according to the load conditions. The heat rejection temperatures $t_a$ and $t_c$ for the absorber and the condenser, respectively, vary according to the type of cooling medium (air, water), ambient conditions of dry and wet bulb temperatures, and whether their cooling lines are connected in series or parallel with each other.

The generator temperature $t_g$ depends on the source of heat available, i.e., solar, gas or steam. However, a minimum temperature of 80°C should be maintained to provide efficient operation.

The operational function of the liquid-liquid heat exchanger in the cycle will be the reduction of the weak solution temperature $t_4$, leaving the generator and increasing the strong solution temperature $t_1$ leaving the absorber. The result is that it reduces the heat input necessary to the generator while reducing the heat rejected from the absorber by heat exchanging between the two solutions. This heat exchanger does increase the coefficient of performance of the system and is, therefore, always desirable.

## III. Thermodynamic Properties

Enthalpies of the water (refrigerant) and LiBr (absorbent) solutions were calculated with reference temperature at 25°C (Refs. 1–4). The following expressions were found essential to the calculation of the cycle performance:

(1) The enthalpy of pure water liquid at temperature $t$°C

$$= (t - 25) \quad \text{kcal/kg} \qquad (1)$$

(2) The enthalpy of saturated water vapor at temperature $t$°C

$$= (572.8 + 0.417\,t) \quad \text{kcal/kg} \qquad (2)$$

(latent heat $= 597.8 - 0.583\,t \pm 0.4$ kcal/kg)

(3) The enthalpy of superheated steam at temperature $t$°C and at a pressure equal to the saturation pressure of steam at temperature $t_s$°C

$$= (572.8 + 0.417\,t_s) + 0.46\,(t - t_s)$$

$$= 572.8 + 0.46\,t - 0.043\,t_s \quad \text{kcal/kg} \qquad (3)$$

by taking the specific heat of water vapor = 0.46 kcal/kg°C at very low pressures (0.01 to 0.1 atm).

(4) The specific heat of lithium bromide/water solution of concentration $X$ kg LiBr/kg solution is given by

$$C_s = 1.01 - 1.23\,X + 0.48\,X^2 \quad \text{kcal/kg solution} \qquad (4)$$

(5) The enthalpy of LiBr/water solution of concentration $X$ kg LiBr/kg solution at 25°C is

$$H_{X,25} = 68.06 - 456.67\,X + 416.67\,X^2 \quad \text{kcal/kg solution} \qquad (5)$$

(6) The enthalpy of LiBr/water solution of concentration $X$ kg LiBr/kg solution at temperature $t$°C is given by

$$H_{X,25} + C_X(t - 25)$$

or

$$= (42.81 - 425.92\,X + 404.67\,X^2) + (1.01 - 1.23\,X + 0.48\,X^2)\,(t) \qquad (6)$$

(7) In the range of concentration from 0.50–0.65 kg LiBr/kg solution, the author found that it is possible to fit the refrigerant temperature $t_R$, the saturated solution temperature $t_m$, and the concentration $X$ by the relation

$$(t_R\text{°C}) = (49.04 - 134.65\,X) + (1.125 - 0.47\,X)\,(t_m\text{°C})$$

with a standard deviation ±0.2%. This may be rewritten as

$$X = \frac{49.04 + 1.125\,t_m - t_R}{134.65 + 0.47\,t_m} \qquad (7)$$

i.e., $X$ is completely defined by the set $\{t_R, t_m\}$.

(8) The saturated vapor pressure $P$ in mm Hg corresponding to saturation temperature $T$°K for pure water is given by (Ref. 5)

$$\log_{10} P \text{ mm Hg} = 7.8553 - \frac{1555}{T} - \frac{11.2414 \times 10^4}{T^2} \qquad (8)$$

## IV. Performance Calculations

The determination of the thermodynamic properties of each state in the cycle, the amount of heat transfer in each component, and the flow rates at different lines depend on the following set of input parameters:

Generator temperature $t_g$, °C

Evaporator temperature $t_e$, °C

Condenser temperature $t_c$, °C

Absorber temperature $t_a$, °C

Liquid-liquid heat exchanger effectiveness $E_L$

Refrigeration load $Q_E$, tons

The above set can be determined from actual running measurements or assumed by a first reasonable estimate to cycle performance.

Together with the assumptions of neglecting the pumpwork and neglecting the pressure drop in components and lines and assigning saturation conditions to states numbers 1, 4, 8, and 10 in Fig. 1, the properties are determined as follows:

### A. Absorber Concentration

This is determined by Eq. (7) using $t_a$ for the solution temperature and $t_e$ for the water temperature corresponding to the evaporator pressure $P_e$:

$$X_1 = X_2 = X_3 = X_{\substack{strong \\ solution}} = \frac{49.04 + 1.125\,t_a - t_e}{134.65 + 0.47\,t_a} \quad \text{kg LiBr/kg solution} \qquad (9)$$

### B. Generator Concentration

This is evaluated, from Eq. (7), using $t_g$ for the solution temperature and $t_c$ for the refrigerant temperature corresponding to the condenser pressure $P_c$

$$X_4 = X_5 = X_6 = X_{\substack{weak \\ solution}} = \frac{49.04 + 1.125\,t_g - t_c}{134.65 + 0.47\,t_g}$$

kg LiBr/kg solution (10)

It may be noted that $X_4$ is always larger than $X_1$, and

$$X_7 = X_8 = X_9 = X_{10} = \text{zero} \quad \text{kg LiBr/kg solution} \tag{11}$$

for the pure water flow in the condenser and evaporator.

### C. Pressure Limits in the Cycle

Using Eq. (8), it is possible to evaluate the pressure in every line as follows:

$P_{evaporator}$, $P_e = P_1 = P_6 = P_9 = P_{10}$ in mm Hg is given by

$$\log_{10} P_e = 7.8553 - \frac{1555}{t_e + 273.15} - \frac{11.2414 \times 10^4}{(t_e + 273.15)^2} \tag{12}$$

and the condenser pressure, $P_c = P_2 = P_3 = P_4 = P_5 = P_7 = P_8$ in mm Hg is given by

$$\log_{10} P_c = 7.8553 - \frac{1555}{(t_c + 273.15)} - \frac{11.2414 \times 10^4}{(t_c + 273.15)^2} \tag{13}$$

### D. Flow Rates

Enthalpy of saturated liquid water, state 8, is given by Eq. (1) at the condenser temperature $t_c$ as

$$H_8 = (t_c - 25) \quad \text{kcal/kg} \tag{14}$$

The throttling processes from 8 to 9 and that from 5 to 6 give

$$\left.\begin{aligned} H_8 &= H_9 \\ H_5 &= H_6 \end{aligned}\right\} \tag{15}$$

Enthalpy of saturated water vapor, state 10, is given by Eq. (2) at the evaporator temperature $t_e$ as

$$H_{10} = 572.8 + 0.417\,t_e \tag{16}$$

Applying the first law of thermodynamics to the evaporator will give

$$Q_E = m_R\,(H_{10} - H_9)$$

where $m_R$ is the refrigerant flow rate, equals the difference between the strong and weak solution rates. By using Eq. (15)

$$m_R = \frac{Q_E}{H_{10} - H_8} \tag{17}$$

On the other hand, the lithium bromide mass balance in the absorber gives

$$m_W X_6 + m_R X_{10} = m_s X_1 = (m_w + m_R) X_1$$

and by using Eqs. (11) and (17), then

$$m_W = \left(\frac{Q_E}{H_{10} - H_8}\right)\left(\frac{X_1}{X_4 - X_1}\right), \tag{18}$$

$$m_s = \frac{Q_E}{(H_{10} - H_8)}\left(\frac{X_4}{X_4 - X_1}\right) \tag{19}$$

Since the concentrations $X_1$ and $X_4$ are restricted not to exceed certain limits to avoid crystallization problems, and if the temperatures of the cycle are set to vary according to ambient and load conditions, the mass flow rates in the different lines will be varied accordingly. This necessitates the existence of LiBr and water solution inventories to be used for flow compensation, especially at times when variations of load, hot water temperature, and cooling water temperature do occur.

### E. Liquid-Liquid Heat Exchanger Temperatures

Once the heat exchanger effectiveness $E_L$, the mass flow rates ($m_W$,$m_s$) and the concentrations ($X_1$,$X_4$) are given, it is possible to determine the solution temperatures $t_3$ and $t_5$ from Fig. 3 as follows:

Based on the weak solution side, which has the minimum heat capacity, the effectiveness $E_L$ is defined by (Ref. 6)

$$E_L = \frac{t_g - t_5}{t_g - t_a} \tag{20a}$$

or based on the strong solution side

$$E_L = \frac{(m_s \cdot C_{X1}) \cdot (t_3 - t_a)}{(m_W \cdot C_{X4}) \cdot (t_g - t_a)} \tag{21a}$$

where $C_{X1}$ is specific heat of the strong solution whose concentration is $X_1$, and $C_{X4}$ is the specific heat of the weak solution whose concentration is $X_4$. Both $C_{X1}$, $C_{X4}$ are determined from Eq. (4) as

$$\left.\begin{aligned} C_{X1} &= 1.01 - 1.23\,X_1 + 0.48\,X_1^2 \\ C_{X4} &= 1.01 - 1.23\,X_4 + 0.48\,X_4^2 \end{aligned}\right\} \tag{22}$$

Equations (20) and (21) are rewritten using Eqs. (18) and (19) to give the temperatures $t_3$ and $t_5$ as:

$$t_5 = t_g - E_L(t_g - t_a) \tag{20b}$$

and

$$t_3 = t_a + \left[E_L \cdot \left(\frac{X_1}{X_4}\right)\left(\frac{C_{X4}}{C_{X1}}\right)(t_g - t_a)\right] \tag{21b}$$

The enthalpies $H_1$ and $H_5$ are then calculated using Eq. (6) as follows:

$$H_1 = (42.81 - 425.92\,X_1 + 404.67\,X_1^2) + (1.01 - 1.23\,X_1 + 0.48\,X_1^2)\cdot(t_a) \tag{23a}$$

$$H_5 = (42.81 - 425.92\,X_4 + 404.67\,X_4^2) + (1.01 - 1.23\,X_4 + 0.48\,X_4^2)\cdot(t_5) \tag{23b}$$

### F. Heat Transfer in Condenser, Generator, and Absorber

The enthalpy of water vapor leaving the generator and entering the condenser (state 7) is determined by Eq. (3) as

$$H_7 = 572.8 + 0.46\,t_g - 0.043\,t_c \tag{24}$$

The heat balance of the condenser gives

$$Q_C = m_R(H_7 - H_8) \tag{25a}$$

or using Eq. (17) for $m_R$ expression, it becomes

$$Q_C = \frac{Q_E}{(H_{10} - H_8)}\cdot(H_7 - H_8) \tag{25b}$$

Heat balance for the combined generator and heat exchanger control volume gives

$$Q_G = m_w H_5 + m_R H_7 - m_s H_2 \tag{26}$$

Since the pumpwork is negligible, then

$$H_1 \simeq H_2 \tag{27}$$

Using Eqs. (17), (18), (19), and (27), it is possible to write $Q_G$ as

$$Q_G = \frac{Q_E}{(H_{10} - H_8)}\left[\frac{X_1 H_5}{(X_4 - X_1)} + H_7 - \frac{X_4 H_1}{(X_4 - X_1)}\right] \tag{28}$$

Heat balance of the absorber gives $Q_A$ as

$$Q_A = m_w H_6 + m_R H_{10} - m_s H_1$$

Using Eqs. (15), (17), (18), and (19), $Q_A$ is rewritten as

$$Q_A = \frac{Q_E}{(H_{10} - H_8)}\left[\frac{X_1 H_5}{(X_4 - X_1)} + H_{10} - \frac{X_4 H_1}{(X_4 - X_1)}\right] \tag{29}$$

Equations (25b) and (29) are governed by the first law of thermodynamics in the form

$$Q_C + Q_A = Q_G + Q_E \tag{30}$$

### G. Coefficient of Performance (COP)

This is defined as

$$\text{COP} = \frac{\text{refrigeration effect}}{\text{external heat input}} = \frac{Q_E}{Q_G}$$

It is simply derived from Eq. (28) as

$$\text{COP} = \frac{(H_{10} - H_8)(X_4 - X_1)}{[X_1 H_5 + (X_4 - X_1)H_7 - X_4 H_1]} \tag{31}$$

### H. Ideal Coefficient of Performance

The maximum coefficient of performance of the above absorption cycle is given by:

$$(\text{COP})_{max} = \frac{T_e(T_g - T_a)}{T_g(T_c - T_e)} \tag{32}$$

where $T_e$, $T_a$, $T_c$, and $T_g$ are the absolute temperatures of the evaporator, absorber, condenser, and generator, respectively.

The ratio

$$\frac{(\mathrm{COP})_{actual}}{(\mathrm{COP})_{max}}$$

is called the 'relative performance ratio," to show the deviation from reversible cycle operation.

## V. Main Components Modeling

Each of the four basic heat exchangers (condenser, absorber, generator and evaporator) is considered as a "constant temperature heat exchanger" as shown in Fig. 4. This is due to the fact that the heat transfer mechanism involves a change in phase while the temperature of one of the heat transfer fluids is kept constant.

There are two basic approaches to determine the heat transfer characteristics of each heat exchanger, namely,

(1) Using the conventional logarithmic mean temperature difference expression.

(2) Using the combined effectiveness/number of exchanger heat transfer units $N_{tu}$, the latter defined as (Ref. 6).

$$N_{tu} = \frac{UA}{\textit{Smaller heat capacity of the two heat transfer fluids}} \tag{33}$$

Both approaches give a straightforward solution and there exists a one-to-one correspondence between the two sets of parameters in each case.

Because of lack of sufficient and reliable information about the overall conductance coefficient $U$ for a LiBr-water solution, an approximate modeling trial was made by Wilber et al. (Ref. 7) in terms of a "characteristic product" ($UA$) associated with each heat exchanger. The latter was determined from the temperature pattern at nominal design conditions, in spite of the fact that the conductance $U$ is a dominant function of flow rates and fluid properties for a laminar flow.

On the other hand, Lackey (Ref. 2) indicated that an increase of LiBr-water flow rate by as much as 350 percent resulted in a change of the overall temperature pattern of only 6 percent and the product ($UA$) was no longer considered to be a fixed property at all operating conditions. The above suggests that the main components modeling procedure would be best characterized by fixed temperature differences $\Delta T_i$ and $\Delta T_0$, as shown in Fig. 4, rather than a fixed ($UA$) product. Consequently, the flow rates of the externally heating or cooling fluids would be self-controlled to suit the variations in heat transfer rates. A good practical estimate of the inlet temperature difference $\Delta T_i$ and the outlet temperature difference $\Delta T_0$ is 10°C and 3°C, respectively, each for the generator, absorber and condenser and 20°C and 6°C, respectively, for the air-cooled evaporator.

## VI. Liquid-Liquid Heat Exchanger Modeling

This is considered as an "unbalanced counter flow heat exchanger," since the two relevant streams possess unequal heat capacities. The exact effectiveness expression (Ref. 6) as applied to LiBr-water solutions indicated that extreme off-design changes of flow rates or concentrations can change the design effectiveness value of $E_L$ by only ±5 percent. The consequent effect on the solution enthalpies leaving the heat exchanger, Eq. (23), is negligible. This suggests that the effectiveness $E_L$ may be taken as a constant in the analysis without great loss of accuracy.

## VII. Summary

The sequence of program calculations is summarized as follows:

*Input Data*

(1) $t_g$, °C, generator temperature

(2) $t_e$, °C, evaporator temperature

(3) $t_c$, °C, condenser temperature

(4) $t_a$, °C, absorber temperature

(5) $E_L$, exchanger effectiveness

(6) $Q_E$, kcal/hr, load

*Steps of Analysis*

(1) $X_1 = \dfrac{(49.04 + 1.125\,t_a - t_e)}{(134.65 + 0.47\,t_a)}$ kg LiBr/kg solution

(2) $X_4 = \dfrac{(49.04 + 1.125\,t_g - t_c)}{(134.65 + 0.47\,t_g)}$ kg LiBr/kg solution

* IF $0.5 < (X_1 \text{ and } X_4) < 0.65$ proceed, else stop.

(3) $H_8 = (t_c - 25)$ kcal/kg

(4) $H_{10} = (572.8 + 0.417\,t_e)$ kcal/kg

(5) $m_R = \dfrac{Q_E}{(H_{10} - H_8)}$ kg/hr

(6) $m_s = m_R \cdot \dfrac{X_4}{(X_4 - X_1)}$ kg/hr

(7) $m_w = m_R \dfrac{X_1}{X_4 - X_1}$ kg/hr

(8) $t_5 = t_g - E_L(t_g - t_a)$ °C

(9) $C_{X_1} = 1.01 - 1.23\,X_1 + 0.48\,X_1^2$ kcal/kg°C

(10) $C_{X_4} = 1.01 - 1.23\,X_4 + 0.48\,X_4^2$ kcal/kg°C

(11) $t_3 = t_a + \left[ E_L \cdot \dfrac{X_1}{X_4} \cdot \dfrac{C_{s_4}}{C_{s_1}} \cdot (t_g - t_a) \right]$ °C

(12) $H_1 = (42.81 - 425.92\,X_1 + 404.67\,X_1^2) + (1.01 - 1.23\,X_1 + 0.48\,X_1^2) \cdot (t_a)$ kcal/kg

(13) $H_5 = (42.81 - 425.92\,X_4 + 404.67\,X_4^2) + (1.01 - 1.23\,X_4 + 0.48\,X_4^2) \cdot (t_5)$ kcal/kg

(14) $H_7 = (572.8 + 0.46\,t_g - 0.043\,t_c)$ kcal/kg

(15) $Q_C = m_R(H_7 - H_8)$ kcal/hr

(16) $Q_G = (m_w H_5 + m_R H_7 - m_s H_1)$ kcal/hr

(17) $Q_A = (m_w H_5 + m_R H_{10} - m_s H_1)$ kcal/hr

(18) $COP = Q_E/Q_G$

(19) $(COP)_{max} = \dfrac{(t_e + 273.15)\,(t_g - t_a)}{(t_g + 273.15)\,(t_c - t_e)}$

(20) relative performance ratio $= COP/(COP)_{max}$

(21) $P_e = \text{antilog}\left[ 7.8553 - \dfrac{1555}{t_e + 273.15} - \dfrac{11.2414 \times 10^4}{(t_e + 273.15)^2} \right]$ mmHg

(22) $P_c = \text{antilog}\left[ 7.8553 - \dfrac{1555}{t_c + 273.15} - \dfrac{11.2414 \times 10^4}{(t_c + 273.15)^2} \right]$ mmHg

## VIII. Numerical Example

The following numerical example presents the performance characteristics of a typical running condition:

*Input Data*

$t_g = 90°C$

$t_e = 7°C$

$t_c = 40°C$

$t_a = 40°C$

$E_L = 0.8$

$Q_E = 1$ ton of refrigeration $= 3024$ kcal/hr

Cooling fluid lines to the condenser and absorber are in parallel.

*Calculation Steps*

$X_1 = 0.5672$, kg LiBr/kg solution

$X_4 = 0.6233$, kg LiBr/kg solution

$H_8 = 15$, kcal/kg

$H_{10} = 575.72$, kcal/kg

$m_R = 5.3931$, kg/hr

$m_s = 59.9199$, kg/hr

$m_w = 54.5268$, kg/hr

$t_5 = 50$, °C

$C_{X_1} = 0.46677$, kcal/kg°C

$C_{X_4} = 0.42982$, kcal/kg°C

$t_3 = 73.52$, °C

$H_1 = -49.9124$, kcal/kg

$H_5 = -43.9594$, kcal/kg

$H_7 = 612.48$, kcal/kg

$Q_C = 3222.3$, kcal/hr

$Q_G = 3896.9$, kcal/hr

$Q_A = 3698.6$, kcal/hr

$COP = 0.776$

$(COP)_{max} = 1.1689$

relative performance ratio $= 0.664$

$P_e = 7.45$ mmHg

$P_c = 55.37$ mmHg

The temperature profile of each heat exchanger is sketched as shown in Fig. 5. Having established an analytical procedure for the performance characteristics of a lithium bromide/water absorption system enables the study of further changes in the thermodynamic cycle. Examples of these changes are the temperature of entering heating fluid to the generator, the cooling load at the evaporator, and the temperature of entering cooling fluid at the condenser or absorber.

## Definition of Symbols

$A$ heat exchanger surface area, $m^2$

$C_x$ specific heat of solution of concentration X, kcal/kg solution °C

$E_L$ effectiveness of liquid/liquid heat exchanger

$H$ specific enthalpy, kcal/kg

$m$ mass flow rate, kg/hr

$p$ pressure, mm Hg

$Q$ rate of heat transfer, kcal/hr

$t$ temperature, °C

$U$ overall conductance coefficient, kcal/(hr-$m^2$-°C)

$X$ solution concentration, kg LiBr/kg solution

*Subscripts*

$a,A$ absorber

$c,C$ condenser

$e,E$ evaporator

$g,G$ generator

$s$ "strong" solution

$w$ "weak" solution

## References


1. Ellington, R. T., Kunst, G., Peck, R. E., and Reed, J. F., "The Absorption Cooling Process." Institute of Gas Technology Research Bulletin No 14, Chicago, Ill., Aug. 1957.
2. Lackey, R. S., "Solar Heating and Cooling of Buildings," Westinghouse Electric Corporation Report to the National Science Foundation, NSF-74-C584-1-2, Appendix J., May 1974.
3. Threlkeld, J. L., *Thermal Environmental Engineering*, Prentice Hall, 1970.
4. San Martin, R. L., and Couch, W. A., "Modeling of Solar Absorption Air Conditioning," Institute of Environmental Science Proceedings, Vol. 1, 1975, pp. 186–189.
5. Pennington, W., "How to Find Accurate Vapor Pressures of LiBr-Water Solutions," *Refrigeration Engineering*, May 1955.
6. Kays, W. M., and London, A. L., *Compact Heat Exchangers*, McGraw Hill Book Co., Inc., 1958.
7. Wilbur, P. J., and Mitchell, C. E., "Solar Absorption Air Conditioning Alternatives," *Solar Energy*, Vol. 17, 1975, pp. 193–199.

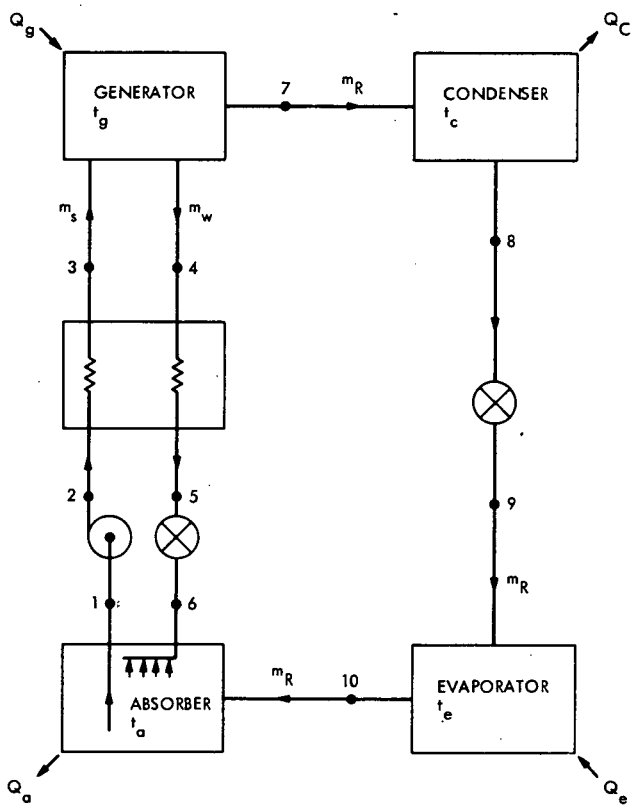


**Fig. 1. Flow diagram for a lithium bromide/water absorption system**

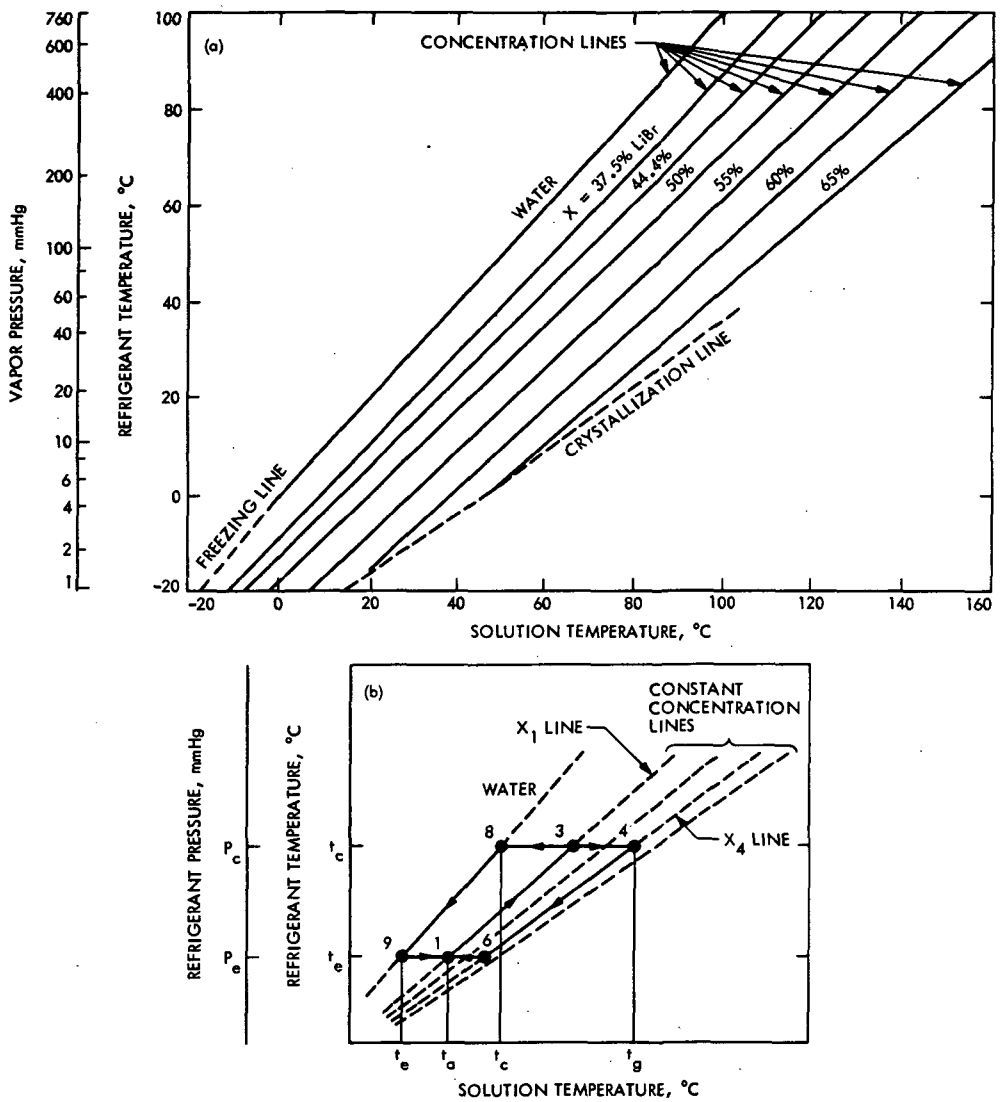


*Fig. 2. Equilibrium chart for lithium bromide/water solution*

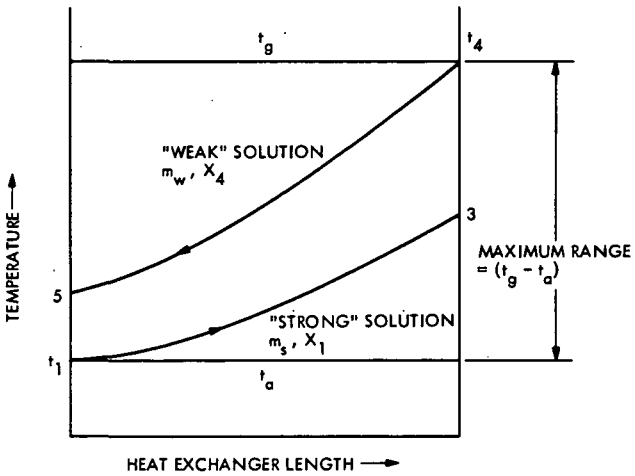


Fig. 3. Effectiveness of liquid-liquid heat exchanger

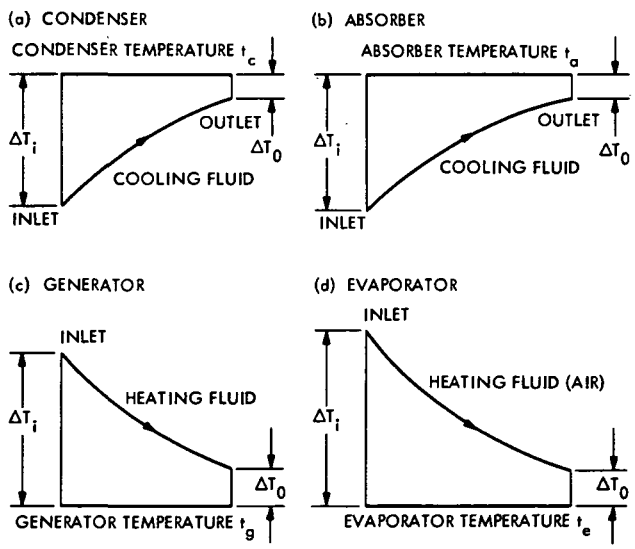


Fig. 4. Temperature profiles along the four main components: condenser, absorber, generator and evaporator

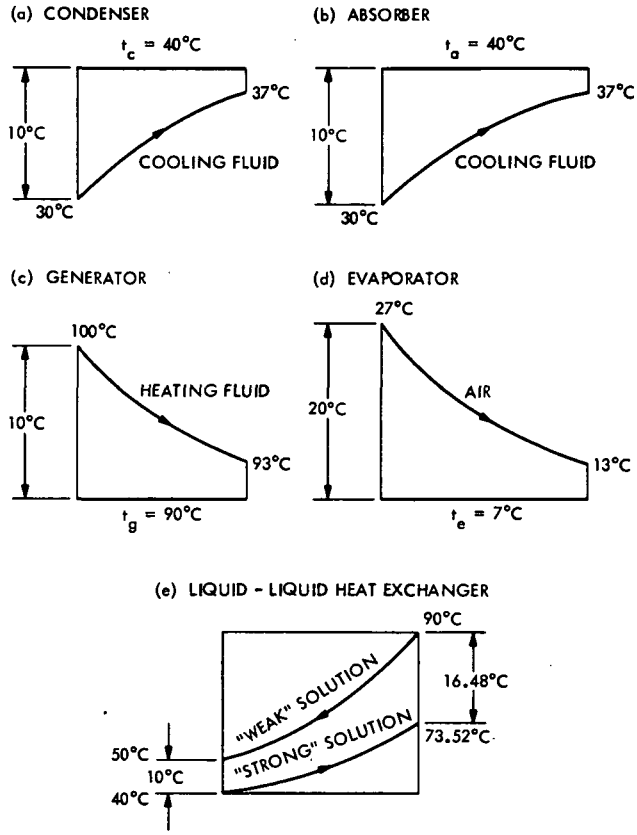


Fig. 5. Temperature patterns along the heat exchangers for the numerical example

# DSN Research and Technology Support

E. B. Jackson
RF Systems Development Section

*The activities at the Goldstone Venus Station (DSS 13) and the Microwave Test Facility (MTF), during the period Dec. 8, 1975 through Feb. 15, 1976, are discussed and progress noted. Continuing testing and refinement of the remote controlled automated pulsar observing station is noted, along with routine pulsar observations of 22 pulsars. Automatic stability-reliability testing of the station receiver/maser noise-adding radiometer (NAR) combination is described. An updated discussion of the data being collected by the 24-hour-per-day, seven-day-per-week Solar and Microwave Data Acquisition System (SAMDAS) is presented in which currently available data types are tabulated.*

*Supporting research activities in support of the X-band radar and stability tests on semirigid coaxial cables are discussed along with preparations for testing of a new design diplexer for future DSN use. The activities of the DSN High-Power Transmitter Maintenance Facility are discussed, and continuing observations of Jupiter at 2295 MHz are reported along with the radio calibration sources used in this program. Routine clock synchronization transmissions are noted along with some engineering measurements and changes directed toward energy conservation.*

During the period Dec. 8, 1975 through Feb. 15, 1976, the Development Support Group, in operating the Venus Station (DSS 13) and the Microwave Test Facility (MTF), supported various programs as discussed below.

## I. Station Automation

In support of RTOP 70 "Network Monitor, Control & Operations Technology," demonstration of a remotely operated automated station is planned using DSS 13 as the test station. A successful demonstration has been conducted (*DSN Progress Report 42-30*, pp. 214–221), and refinement of software and equipment reliability testing is continuing.

Including automated tracking, 38.5 hours of station support have been provided. The automated tracking has been directed from the on-site computer rather than the JPL-located computer. An unsuccessful remote-controlled test was terminated after computer communications problems.

## II. Pulsar Observations

In support of the radio science experiment "Pulsar Rotation Constancy," DSS 13 provided 61.25 hours of observations during which the emissions from the pulsars listed in Table 1 were recorded. These data, recorded at 2388 MHz, left circular polarization (LCP), are used to determine precise pulse-to-pulse spacing, pulse shape, and pulse power content of the signals emitted by these pulsars.

## III. Maser/Receiver/NAR Reliability-Stability Testing

Reliability and stability testing of the DSS 13 receiving system is conducted automatically during nonoperational station periods. The 26-m antenna is prepositioned to a fixed azimuth and elevation, and the noise adding radiometer (NAR) automatically records total receive system temperature as a function of time. The rotation of Earth sweeps the fixed antenna beam across the sky, resulting in generation of a radio brightness temperature sky map in addition to collecting data on stability and reliability of the system. During this reporting period, 659.5 hours of such data were automatically collected with the 26-m antenna at 360 deg Az and progressively positioned from 52.6 to 51.5 deg El. This testing is done at 2295 MHz, using right circular polarization (RCP) on the 26-m antenna.

## IV. Solar & Microwave Data Acquisition System (SAMDAS)

Continuous operation of the data collection system continued. Tape changes and emergency corrective maintenance were provided by the Development Support Group. At the end of the reporting period, substantial maintenance had been performed by the Communication Elements Research Section, and the system was again functioning and collecting data shown in Table 2.

## V. Microwave Power Transmission

The Venus Station provided eight hours of testing at various output powers up to 250 kW, during which tests were performed on reflected power vs subreflector position with the antenna at zenith, and various measurements were made while illuminating the rectenna arrays. The system was also operated and exercised in support of a NASA-directed film crew.

Near the end of this period the first shipment of magnetrons arrived for the investigation into the feasibility of obtaining inexpensive phased array power by using commercially available oven magnetrons in a phase-locked mode. The large power supplies with which to conduct this investigation have arrived and are being put into operation.

At the end of the reporting period, a total of 500 kWh of energy has been transmitted from the 26-m antenna and converted to direct current by the rectenna array.

## VI. X-Band Radar

Although plagued with various problems, operation with two klystrons continued, with available power gradually being increased until, at the end of the period, 300 kW was available with good reliability.

A spare VA-949J klystron, S/N 33R1, was received, partially tested and returned to Varian upon request because of possible improper focusing. Klystron S/N 31R4 was received, and vacuum and filaments were tested after being assembled into a magnet and support.

Among the problems encountered were multiple failures of the Logimetrics traveling wave tube (TWT) power supplies and improper operation of the master combiner control panel. The Varian TWT was replaced with the ITT TWT, and the system was operational at the end of the reporting period.

## VII. Block IV Receiver-Exciter Stability

Preparatory to making an extensive investigation into the phase stability of the Block IV receiver-exciter, preliminary measurements were made on the phase stability vs temperature of semirigid cables at DSS 13. Measurements were made at 2388 MHz on a coaxial cable loop 610 m in length. Techniques and results are described elsewhere in this issue (article by Buchanan and Price).

## VIII. DSN High-Power Transmitter Maintenance Facility

The DSN High-Power Transmitter Maintenance Facility (HPTMF), located at DSS 13 and the MTF, continued to support the 10-, 20-, 100- and 400-kW transmitters used in the DSN, with particular emphasis on the 100- and 400-kW transmitters and the 20-kW transmitter



C.4

klystrons. Klystron 5KM70SG, S/N H1-32, was tested for its ability to develop 20-kW output RF power. Additionally, bandpass curves were obtained and confirmation of the manufacturer's test data was obtained.

Klystron X-3060, 100 kW, S/N A617R2, which had been returned from Spain, DSS 63, was assembled and tested, and discovered to have excessive body current. However, klystron S/N J524R2 was assembled, tested, found to be fully operational, and successfully completed a 12-hour test at 100-kW RF output power.

Two complete dual ignitron decks (one spare) were assembled for installation into the Goldstone Mars Station, DSS 14, and tested at operational voltages in the HPTMF. Development of a complete Engineering Change Order (ECO) kit is underway. Additionally, a kit is being developed to expedite replacement of a 400-kW klystron with a 100-kW klystron if the DSN 400-kW transmitter at DSS 14 should suffer a klystron failure.

## IX. Diplexer Testing

The RF Systems Development Section has a new design diplexer which should be less prone to generation of noise in DSN use. In preparation for testing of this diplexer at 100 kW, the diplexer has been assembled into the S-band megawatt transmit (SMT) feedcone which was removed from the DSS 14 64-m antenna. This feedcone has been installed into the cone testing area of Building G-53 at DSS 13. A Block II DSN maser has been connected and cooled and the waveguide has been connected with which to provide 100 kW of RF at 2115 MHz. Testing is expected to commence during the week ending Feb. 22, 1976.

## X. Planetary Radio Astronomy

In support of the radio science experiment "Planetary Radio Astronomy," the Venus Station measures and records radiation received at 2295 MHz from the planet Jupiter and various radio calibration sources. These measurements use the 26-m antenna, the maser/receiving system, and the NAR. During this period 73.25 hours of observations were provided during which the radiation from Jupiter and the calibration sources tabulated in Table 3 were measured.

## XI. Clock Synchronization System

Although failure of a transmitter phase modulator forced postponement of a scheduled transmission to Spain, DSS 63, operation was otherwise uneventful, with nine transmissions being made as scheduled by DSN scheduling, five to Australia, DSS 43, and four to DSS 63.

Insulated cover panels were installed on the antenna-mounted heat exchanger to minimize conduction heat losses and reduce power required to prevent distilled water freezing. A 15-channel temperature recorder was installed and temperatures were monitored throughout the system. With these data, including ambient temperature, heat loss rates, heat flows, etc., can be calculated and a different operational mode can be devised for the winterization control system. Although temperatures have not been extreme, it is interesting to note that, subsequent to installation of the insulating panels, the system electrical heaters have not been necessary. The energy input to the water from the circulating pump alone has been adequate to keep the water temperature above the heater thermostat setting.

**Table 1. Pulsars observed at DSS 13, Dec. 8, 1975, through Feb. 15, 1976**

| | | | |
|---|---|---|---|
| 0031 − 07 | 0823 + 26 | 1706 − 16 | 2021 + 51 |
| 0329 + 54 | 0833 − 45 | 1749 − 28 | 2045 − 16 |
| 0355 + 54 | 1133 + 16 | 1818 − 04 | 2111 + 46 |
| 0525 + 21 | 1237 + 25 | 1911 − 04 | 2218 + 47 |
| 0628 − 28 | 1604 − 00 | 1929 + 10 | |
| 0736 − 40 | 1642 − 03 | 1933 + 16 | |

**Table 2. Data being acquired by SAMDAS as of 15 Feb. 1976**

| Environmental | Solar | Microwave |
|---|---|---|
| Air temperature | Tracking pyroheliometer (2) | X-band radiometer (8 GHz) |
| Soil temperature | Pyranometer (3) | Antenna temperature |
| Humidity | | Azimuth |
| Pressure | | Elevation |
| Rainfall | | |
| Wind | | |
| Speed, 30-m (100-ft) tower | | |
| Direction, 30-m (100-ft) tower | | |
| Peak, 30-m (100-ft) tower | | |
| Mean-110 sec, 30-m (100-ft) tower | | |
| Instantaneous, atop G-51 | | |

**Table 3. Radio calibrations sources observed at DSS 13, Dec. 8, 1975, through Feb. 15, 1976**

| | | |
|---|---|---|
| 3C17 | 3C286 | NRAO 530 |
| 3C48 | 3C309.1 | PKS 2134 |
| 3C123 | 3C345 | Virgo A |
| 3C273 | 3C348 | VRO 4222 |
| 3C274 | 3C353 | |
| 3C279 | 3C454.3 | |

# Analysis of Solar Effects Upon Observed Doppler Noise During the Helios 1 Second Solar Conjunction

A. L. Berman
Network Operations Office

*This report analyzes observed doppler noise during the Helios 1 second solar conjunction with the previously presented $NOISE_p$ solar noise model. It is concluded that the $NOISE_p$ model continues to adequately predict "average" solar corruption of observed doppler noise, and that deviations from the $NOISE_p$ model continue to appear to correlate in some fashion with fluctuations in observed solar activity.*

## I. Introduction

During August 1975, the Helios 1 spacecraft underwent its second solar conjunction. Previous to this event, this author and S. T. Rockwell, using doppler noise data gathered during the first Helios 1 solar conjunction (May 1975) and the 1975 Pioneer 10 (April) and Pioneer 11 (March) solar conjunctions, derived a geometrical parameter ($ISI$) which could be used to model solar corruption of doppler noise (Ref. 1). The model developed ($NOISE_p$) is as follows:

$\alpha$ = Sun-Earth-probe angle (SEP), deg

$\beta$ = Earth-Sun-probe angle (ESP), deg

$$ISI = \frac{\beta}{\sin \alpha}$$

and:

$$NOISE_p\,(\text{Hz}) = \begin{cases} 0.003 & ; \quad ISI \leq 223 \\ K_1\,(ISI)^{1+K_2}; & ISI > 223 \end{cases}$$

where

$$K_1 = 2.8 \times 10^{-6}$$

$$K_2 = 2.9 \times 10^{-1}$$

Although the $NOISE_p$ model fit the early 1975 Helios 1, Pioneer 10 and Pioneer 11 solar conjunction doppler noise data in a reasonable fashion, it might be considered with some suspicion since the quantities $K_1$ and $K_2$ were empirically determined from the data. Therefore, the second 1975 Helios 1 solar conjunction represented the first

opportunity to test the $NOISE_p$ model against a solar conjunction data base entirely disassociated from the original derivation of the model. Obviously, a successful prediction of the Helios 1 second solar conjunction by the $NOISE_p$ model would auger well for the basic validity of the model.

Additionally, this author and S. T. Rockwell (Ref. 2) concluded that deviations from the $NOISE_p$ model could be explained by short-term fluctuations in solar activity; certainly one would be interested in again attempting to correlate solar activity with deviations from the $NOISE_p$ model. The main thrust of this report will hence address the following questions.

(1) How well does the $NOISE_p$ model fit the Helios 1 second solar conjunction doppler noise data?

(2) During the Helios 1 second solar conjunction, can deviations from the $NOISE_p$ model be correlated with observed fluctuations in solar activity?

## II. Helios 1 Second Solar Conjunction Doppler Noise Data Base

The Helios 1 second solar conjunction phase climaxed with solar occultation on August 30 and 31, 1975. To substantially bracket this event, doppler noise data were accumulated from July 29, 1975 (DOY 210) to October 2, 1975 (DOY 275), inclusive. The data consist of an "average doppler noise" value for each pass (tracked) during the above period. Obviously, then, each "average doppler noise" value is completely specified by two parameters:

(1) Deep Space Station (DSS).

(2) Pass (actual starting DOY of pass).

The method used to select a "pass average" was changed slightly from Ref. 1 (p. 232) in an attempt to insure greater objectivity. The method used here was to record a doppler data running standard deviation each half hour throughout a track, from the Network Operations Control Center (NOCC) pseudoresidual program output. The six lowest values from each track were then averaged to produce the "pass average." Data were, of course, restricted to good, two-way, 60-second-sample-rate doppler data.

The accumulated data comprise Table 1. Presented in this table are the following parameters:

(1) Station (DSS).

(2) DOY (day of year of start of pass).

(3) Average noise (Hz).

(4) $\alpha$ (degrees).

(5) $\beta$ (degrees).

(6) ISI (unitless).

## III. Comparison of the $NOISE_p$ Model With Observed Doppler Noise During the Helios 1 Second Solar Conjunction

Figure 1 presents the $NOISE_p$ model and the observed doppler noise ($NOISE_A$) as a function of day of year (DOY), while Fig. 2 presents the same quantities as a function of SEP. Finally, Fig. 3 presents the observed doppler noise vs integrated solar intensity (ISI). Since the observed data show a pronounced positive bias when compared to the $NOISE_p$ model (which will be considered in Section IV to follow), the quantity

$$1.5 \times NOISE_p$$

has additionally been included in Figs. 1, 2, and 3. Examination of Figs. 1, 2, and 3 would certainly lead one to conclude in a qualitative sense that the $NOISE_p$ model is a good representation for the very disparate doppler noise data base accumulated during the Helios 1 second solar conjunction. However, it would be useful to attempt to make a more quantitative statement in regard to the efficacy of the $NOISE_p$ model as applied to the aforementioned data base. To this end, residuals were formed as follows:

$$\text{Residual} = 10 \log_{10}\left(\frac{NOISE_A}{1.5 \times NOISE_p}\right)$$

Residuals computed in the above manner for the Helios 1 second solar conjunction yielded the following standard deviation:

$$1\sigma = 2.15$$

which is to say that approximately 67% of the observed doppler noise values was constrainted to:

$$0.61\,[1.5 \times NOISE_p] < \text{Observed Noise} < 1.64\,[1.5 \times NOISE_p]$$

In consideration of the above, it is important to remember that the data base spans more than three orders of magnitude (0.0018 Hz to 5.000 Hz), or in logrithmic form:

$$10 \log_{10} \left\{ \frac{5.000}{0.0018} \right\} = 34.4$$

This author considers the $NOISE_p$ model performance creditable when the $1\sigma$ value of 2.15 is compared to a total range of 34.4, particularly in light of the nonexistence of any solar noise models prior to $NOISE_p$.

An allied subject invites comment at this time. B. Madsen (Ref. 3, p. 28) comments on the possibility of discrete solar events which might cause doppler noise at a SEP = 15 deg to increase to values expected at a SEP = 1 or 2 deg. At least as far as "pass average doppler noise" is concerned, this effect is not borne out by the data accumulated so far in Refs. 1 and 2 and this report. For instance, the residual of $NOISE_p$ at SEP = 1 deg compared to $NOISE_p$ at SEP = 15 deg is:

$$10 \log_{10} \left\{ \frac{NOISE_p(1°)}{NOISE_p(15°)} \right\} = 15.1$$

No residuals of this size have been observed for data in the region:

$$\text{SEP} \gtrsim 15 \text{ deg}$$

Finally, to further illustrate this point, Fig. 4 indicates the equivalent SEP angles for $1\sigma$ deviations from the $NOISE_p$ model, where

$$1\sigma = 2.15$$

## IV. Correlation of $NOISE_p$ Residuals With Fluctuations in Solar Activity

In Ref. 2, it was concluded that deviations from the $NOISE_p$ model are primarily due to fluctuations in solar activity as seen along the signal path, these fluctuations being a result of

(1) Radial asymmetry of solar activity combined with solar rotation.

(2) Variation with time of solar activity for any region of the solar surface.

A particularly dramatic example of Item (1) can be seen in Fig. 5. Prior to DOY 084 (Pioneer 11 solar conjunction) both Pioneer 10 and Pioneer 11 signal paths were to the left (or east, as viewed from Earth) of the Sun; between DOY 084 and DOY 094 (Pioneer 10 solar conjunction), the Pioneer 10 signal path was to the left of the Sun and the Pioneer 11 signal path to the right (west) of the Sun; finally, after DOY 094, both Pioneer signal paths were again on the same side of the Sun (the west). Figure 5 shows the correlation to be very strong when both spacecraft signal paths are on the same side of the Sun, and little or no correlation when the spacecraft signal paths are on opposite sides of the Sun. Additionally, Fig. 5 indicates observed sunspot activity (Zurich, $R_Z$) which has been retarded 10 days for signal paths east of the Sun and advanced 10 days for signal paths west of the Sun. As was mentioned in Ref. 2, all indices of solar activity move somewhat in unison; Ref. 2 used Ottawa measured solar flux to indicate possible correlation with solar activity; this report will use $R_Z$ for the same purpose.

Figure 6 shows the Helios 1 second solar conjunction $NOISE_p$ residuals plotted with $R_Z$ (advanced 16 days for west signal paths and retarded 16 days for east signal paths) vs day of year. As in Ref. 2, strong similarities are seen between the residuals and solar (sunspot) activity.

It was noted in Section III that the Helios 1 second solar conjunction noise data were biased upward from the $NOISE_p$ model, and that a model equal to

$$1.5 \times NOISE_p$$

gave a more reasonable fit to the data. This can be explained by the overall increase in solar activity between the early 1975 data to which $NOISE_p$ was originally fit and the August–October 1975 period of the second Helios 1 solar conjunction. During the earlier period, the flux and sunspot activity averaged

$$\text{Ottawa flux} = 71.1$$
$$R_Z = 8.3$$

while during the latter period, the average indice values were

$$\text{Ottawa flux} = 85.0$$
$$R_Z = 26.7$$

This increased activity affords the opportunity to make some very gross conjectures for the Mariner Jupiter/Saturn (MJS) period and the Pioneer 11 Saturn Encounter.

Figure 7 shows the past 12 years of solar activity in terms of $R_Z$, and B. Madsen in Ref. 3 indicates that the prediction for the next solar cycle calls for a maximum smoothed sunspot number of approximately 100. Considering that during July and August 1975 the sunspot activity quickened to an average of about

$$R_Z \sim 34$$

with a maximum of

$$R_Z = 104$$

and based on the Helios 1 observed doppler noise during this period, one might tentatively consider the following to be very approximate upper bounds to the expected doppler noise during the active portion of the next sunspot cycle:

| $R_Z$ average | Expected noise |
|---|---|
| 50 | $\lesssim 2.0 \times NOISE_p$ |
| 100 | $\lesssim 4.0 \times NOISE_p$ |

## V. Summary

This report analyzes the solar effects on the doppler data during the second Helios 1 solar conjunction. The doppler noise is shown to fit the previously presented $NOISE_p$ model, although at an elevated level

$$\text{Observed doppler noise} \propto 1.5 \times NOISE_p$$

This results from the fact that the average solar activity during July and August 1975 was considerably higher than the level in effect during the early 1975 solar conjunctions—the earlier data being those to which the $NOISE_p$ model was originally scaled. From this change in average level of solar activity, one can make some extremely tentative guesses as to the magnitude of solar corruption of doppler data during the next solar cycle, these being

| $R_Z$ average | Expected noise |
|---|---|
| 50 | $\lesssim 2.0 \times NOISE_p$ |
| 100 | $\lesssim 4.0 \times NOISE_p$ |

Finally, strong similarities are seen between observed solar activity (in this case, $R_Z$) and deviations from the $NOISE_p$ model.

## References


1. Berman, A. L., and Rockwell, S. T., "Analysis and Prediction of Doppler Noise During Solar Conjunctions," in *The Deep Space Network Progress Report 42-30*, pp. 231–263, Jet Propulsion Laboratory, Pasadena, Calif., Dec. 15, 1975.
2. Berman, A. L., and Rockwell, S. T., "Correlation of Doppler Noise During Solar Conjunctions With Fluctuations in Solar Activity," in *The Deep Space Network Progress Report 42-30*, pp. 264–272, Jet Propulsion Laboratory, Pasadena, Calif., Dec. 15, 1975.
3. Madsen, B., "Predicted Effect of the Solar Corona on MJS Telecommunications Performance," IOM 3396-75-171, Jet Propulsion Laboratory, Pasadena, Calif., Oct. 14, 1975 (an internal document).

## Bibliography

Winn, F. B., et al., "Corruption of Radio Metric Doppler Due to Solar Plasma Dynamics: S/X Dual Frequency Doppler Calibration For These Effects," in *The Deep Space Network Progress Report 42-30*, pp. 88–101, Jet Propulsion Laboratory, Pasadena, Calif., Dec. 15, 1975.

## Acknowledgments

The author would like to acknowledge S. T. Rockwell, who processed the data, and M. F. Cates, who executed the illustrations.

Table 1. Heilos 1 second solar conjunction 1975

| Deep Space Station (DSS) | Day of year (DOY) | Average doppler noise, Hz | Sun–Earth–probe angle, deg | Earth–Sun–probe angle, deg | Integrated solar intensity (ISI) |
|---|---|---|---|---|---|
| 11 | 215 | 0.0573 | 7.130 | 163.911 | 1321 |
| 11 | 216 | 0.0462 | 7.052 | 163.998 | 1336 |
| 11 | 219 | 0.0323 | 6.757 | 164.393 | 1397 |
| 11 | 220 | 0.0350 | 6.638 | 164.571 | 1424 |
| 11 | 223 | 0.0525 | 6.198 | 165.286 | 1531 |
| 11 | 224 | 0.0792 | 6.030 | 165.581 | 1576 |
| 11 | 225 | 0.0455 | 5.839 | 165.923 | 1631 |
| 11 | 226 | 0.0304 | 5.647 | 166.280 | 1690 |
| 11 | 235 | 0.1964 | 3.147 | 171.642 | 3127 |
| 11 | 274 | 0.0033 | 20.612 | 47.014 | 133 |
| 11 | 276 | 0.0037 | 20.743 | 40.222 | 114 |
| 12 | 228 | 0.0603 | 5.234 | 167.077 | 1832 |
| 14 | 210 | 0.0290 | 7.375 | 163.751 | 1276 |
| 14 | 212 | 0.0282 | 7.301 | 163.766 | 1289 |
| 14 | 213 | 0.0295 | 7.250 | 163.799 | 1298 |
| 14 | 214 | 0.0220 | 7.191 | 163.849 | 1309 |
| 14 | 217 | 0.0718 | 6.962 | 164.111 | 1354 |
| 14 | 221 | 0.0455 | 6.501 | 164.784 | 1455 |
| 14 | 222 | 0.0342 | 6.345 | 165.038 | 1493 |
| 14 | 227 | 0.0537 | 5.432 | 166.691 | 1761 |
| 14 | 231 | 0.0725 | 4.434 | 168.730 | 2182 |
| 14 | 234 | 0.7752 | 3.548 | 170.702 | 2758 |
| 14 | 239 | 1.4350 | 1.502 | 175.783 | 6706 |
| 14 | 241 | 5.0200 | 0.590 | 178.300 | 17,315 |
| 14 | 244 | 0.9230 | 0.989 | 177.006 | 10,255 |
| 14 | 246 | 0.3180 | 2.171 | 173.183 | 4572 |
| 14 | 247 | 0.1915 | 2.831 | 170.928 | 3461 |
| 14 | 248 | 0.0870 | 3.435 | 168.783 | 2817 |
| 14 | 250 | 0.0423 | 4.895 | 163.270 | 1913 |
| 14 | 251 | 0.0328 | 5.482 | 160.906 | 1684 |
| 14 | 252 | 0.0255 | 6.327 | 157.375 | 1428 |
| 14 | 254 | 0.0240 | 7.954 | 150.045 | 1084 |
| 14 | 255 | 0.0178 | 8.705 | 146.403 | 967 |
| 14 | 256 | 0.0168 | 9.542 | 142.154 | 857 |
| 14 | 257 | 0.0107 | 10.410 | 137.512 | 761 |
| 14 | 258 | 0.0137 | 11.433 | 131.734 | 665 |
| 14 | 259 | 0.0225 | 12.166 | 127.330 | 604 |
| 14 | 260 | 0.0140 | 13.003 | 122.057 | 542 |
| 14 | 261 | 0.0127 | 13.846 | 116.454 | 487 |
| 14 | 262 | 0.0163 | 14.806 | 109.687 | 429 |
| 14 | 264 | 0.0088 | 16.306 | 98.075 | 349 |
| 14 | 265 | 0.0072 | 17.006 | 92.148 | 315 |
| 14 | 266 | 0.0055 | 17.746 | 85.444 | 280 |
| 14 | 267 | 0.0063 | 18.263 | 80.384 | 256 |
| 14 | 269 | 0.0043 | 19.270 | 69.349 | 210 |

Table 1 (contd)

| Deep Space Station (DSS) | Day of year (DOY) | Average doppler noise, Hz | Sun–Earth–probe angle, deg | Earth–Sun–probe angle, deg | Integrated solar intensity (ISI) |
|---|---|---|---|---|---|
| 14 | 270 | 0.0037 | 19.713 | 63.680 | 189 |
| 14 | 271 | 0.0033 | 20.001 | 59.464 | 174 |
| 14 | 273 | 0.0022 | 20.470 | 50.831 | 145 |
| 14 | 275 | 0.0028 | 20.698 | 43.629 | 123 |
| 14 | 277 | 0.0020 | 20.735 | 36.728 | 104 |
| 42 | 210 | 0.0353 | 7.368 | 163.749 | 1277 |
| 42 | 212 | 0.0242 | 7.288 | 163.773 | 1291 |
| 42 | 214 | 0.0683 | 7.178 | 163.862 | 1311 |
| 42 | 216 | 0.0295 | 7.021 | 164.035 | 1342 |
| 42 | 227 | 0.0413 | 5.377 | 166.798 | 1780 |
| 42 | 228 | 0.0387 | 5.152 | 167.240 | 1862 |
| 42 | 233 | 0.1988 | 4.061 | 169.542 | 2394 |
| 42 | 234 | 0.2502 | 3.401 | 171.044 | 2883 |
| 42 | 237 | 0.5162 | 2.310 | 173.695 | 4309 |
| 42 | 249 | 0.2225 | 3.663 | 167.945 | 2629 |
| 43 | 224 | 0.0507 | 6.158 | 165.356 | 1541 |
| 43 | 225 | 0.0493 | 5.982 | 165.666 | 1590 |
| 43 | 225 | 0.0390 | 5.783 | 166.027 | 1648 |
| 43 | 249 | 0.2470 | 3.591 | 168.209 | 2686 |
| 43 | 250 | 4.7112 | 4.224 | 165.860 | 2252 |
| 43 | 255 | 0.0178 | 8.215 | 148.782 | 1041 |
| 43 | 256 | 0.0142 | 8.128 | 149.207 | 1055 |
| 43 | 257 | 0.0133 | 9.812 | 140.739 | 826 |
| 43 | 258 | 0.0143 | 10.701 | 135.897 | 753 |
| 43 | 260 | 0.0158 | 12.403 | 125.871 | 586 |
| 43 | 261 | 0.0182 | 13.310 | 120.060 | 522 |
| 43 | 262 | 0.0180 | 14.164 | 114.266 | 467 |
| 43 | 263 | 0.0137 | 14.992 | 108.310 | 419 |
| 43 | 264 | 0.0098 | 15.833 | 101.878 | 373 |
| 43 | 265 | 0.0085 | 16.520 | 96.305 | 339 |
| 43 | 266 | 0.0063 | 17.300 | 89.529 | 301 |
| 43 | 267 | 0.0052 | 17.909 | 83.871 | 273 |
| 43 | 268 | 0.0042 | 18.481 | 78.146 | 247 |
| 43 | 269 | 0.0045 | 18.940 | 73.205 | 226 |
| 43 | 270 | 0.0046 | 19.401 | 67.739 | 204 |
| 43 | 271 | 0.0042 | 19.782 | 62.690 | 185 |
| 43 | 272 | 0.0043 | 20.100 | 57.867 | 168 |
| 43 | 273 | 0.0048 | 20.353 | 53.294 | 153 |
| 43 | 274 | 0.0035 | 20.514 | 49.770 | 142 |
| 43 | 275 | 0.0033 | 20.641 | 46.032 | 130 |
| 43 | 276 | 0.0028 | 20.716 | 42.643 | 121 |
| 43 | 277 | 0.0028 | 20.747 | 39.323 | 111 |
| 44 | 229 | 0.0468 | 4.902 | 167.945 | 1963 |

Table 1 (contd)

| Deep Space Station (DSS) | Day of year (DOY) | Average doppler noise, Hz | Sun–Earth–probe angle, deg | Earth–Sun–probe angle, deg | Integrated solar intensity (ISI) |
|---|---|---|---|---|---|
| 61 | 210 | 0.0282 | 7.386 | 163.756 | 1274 |
| 61 | 213 | 0.0230 | 7.269 | 163.786 | 1294 |
| 61 | 215 | 0.0450 | 7.151 | 163.889 | 1317 |
| 61 | 216 | 0.0763 | 7.079 | 163.967 | 1330 |
| 61 | 218 | 0.1342 | 6.903 | 164.188 | 1366 |
| 61 | 219 | 0.0478 | 6.785 | 164.353 | 1391 |
| 61 | 220 | 0.0363 | 6.666 | 164.529 | 1417 |
| 61 | 221 | 0.0655 | 6.551 | 164.705 | 1444 |
| 61 | 222 | 0.0320 | 6.412 | 164.929 | 1477 |
| 61 | 223 | 0.0495 | 6.251 | 165.197 | 1517 |
| 61 | 225 | 0.0420 | 5.928 | 165.763 | 1605 |
| 61 | 226 | 0.0387 | 5.709 | 166.165 | 1670 |
| 61 | 227 | 0.0475 | 5.520 | 166.521 | 1731 |
| 61 | 228 | 0.0482 | 5.291 | 166.966 | 1811 |
| 61 | 229 | 0.0435 | 5.056 | 167.435 | 1900 |
| 61 | 232 | 0.0783 | 4.265 | 169.096 | 2274 |
| 61 | 234 | 0.3895 | 3.672 | 170.419 | 2661 |
| 61 | 250 | 0.0443 | 4.626 | 164.312 | 2037 |
| 61 | 272 | 0.0037 | 20.206 | 56.041 | 162 |
| 61 | 274 | 0.0025 | 20.578 | 47.959 | 136 |
| 61 | 275 | 0.0025 | 20.684 | 44.211 | 125 |
| 61 | 276 | 0.0027 | 20.735 | 40.895 | 115 |
| 61 | 277 | 0.0022 | 20.747 | 38.207 | 108 |
| 63 | 254 | 0.0380 | 7.681 | 151.306 | 1132 |
| 63 | 258 | 0.0173 | 10.994 | 134.232 | 704 |
| 63 | 262 | 0.0177 | 14.511 | 111.791 | 446 |
| 63 | 266 | 0.0052 | 17.503 | 87.672 | 292 |
| 63 | 269 | 0.0038 | 19.138 | 70.891 | 216 |
| 63 | 270 | 0.0037 | 19.585 | 65.346 | 195 |

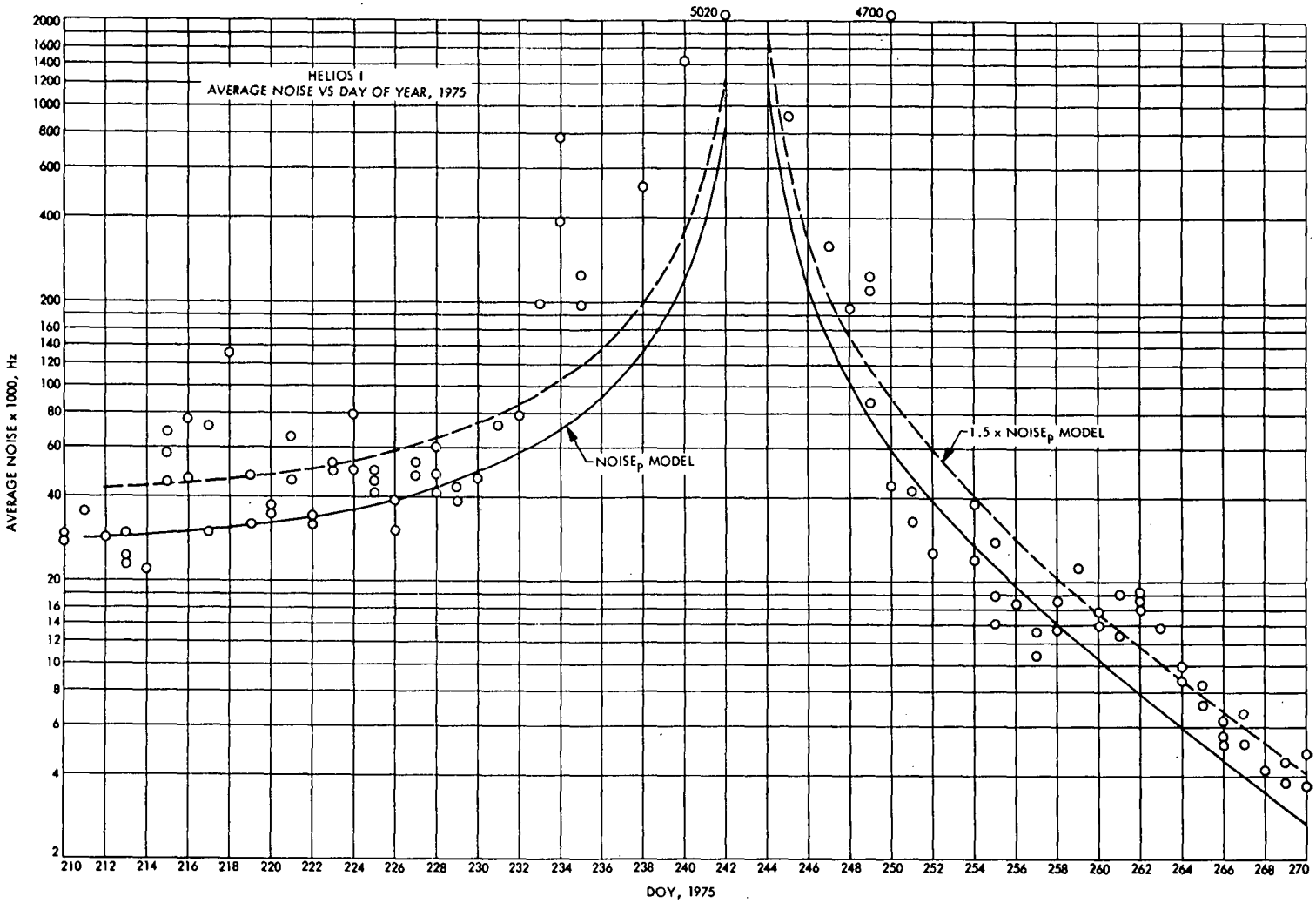


**Fig. 1. Average noise vs day of year, 1975**

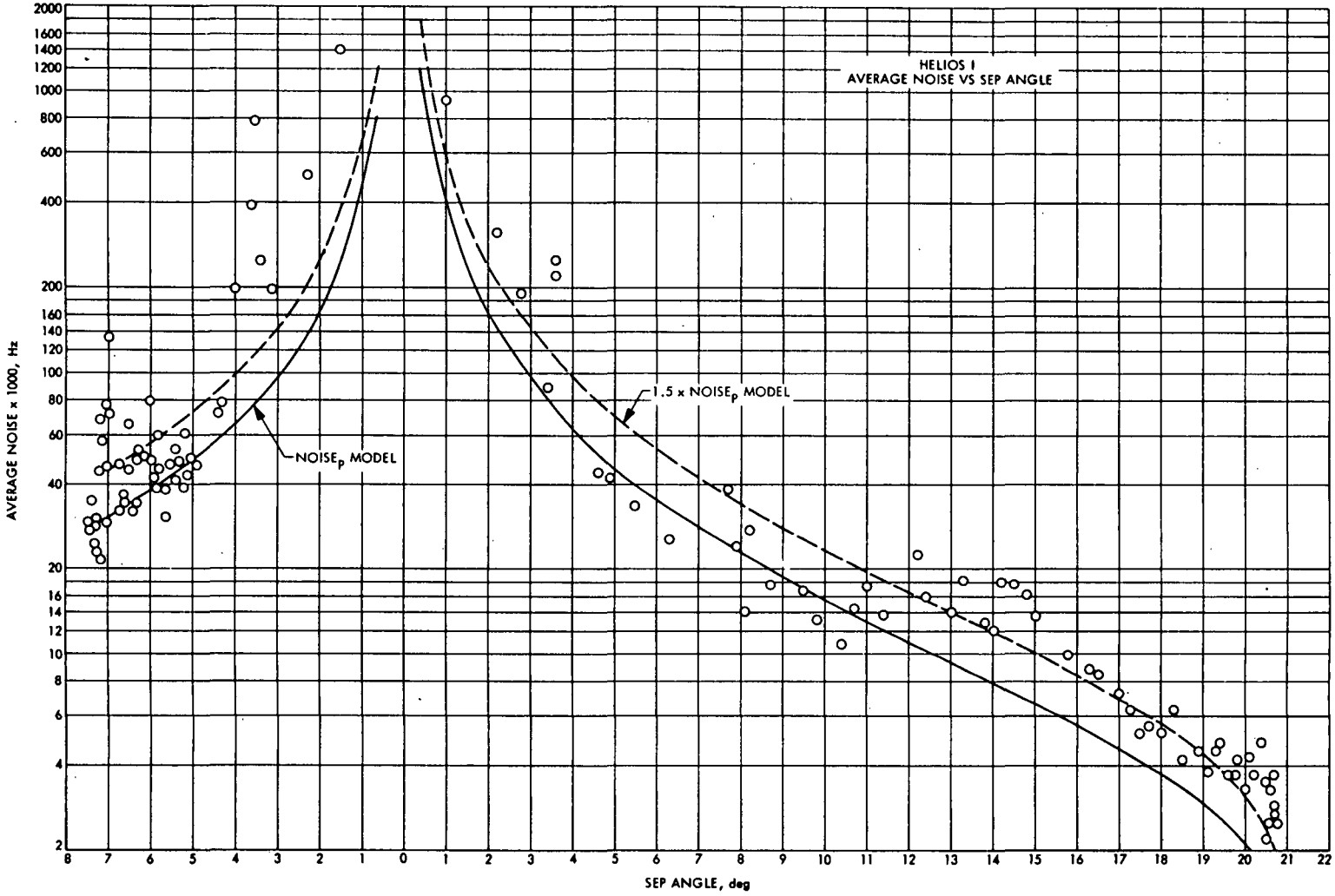


**Fig. 2. Average noise vs SEP angle**

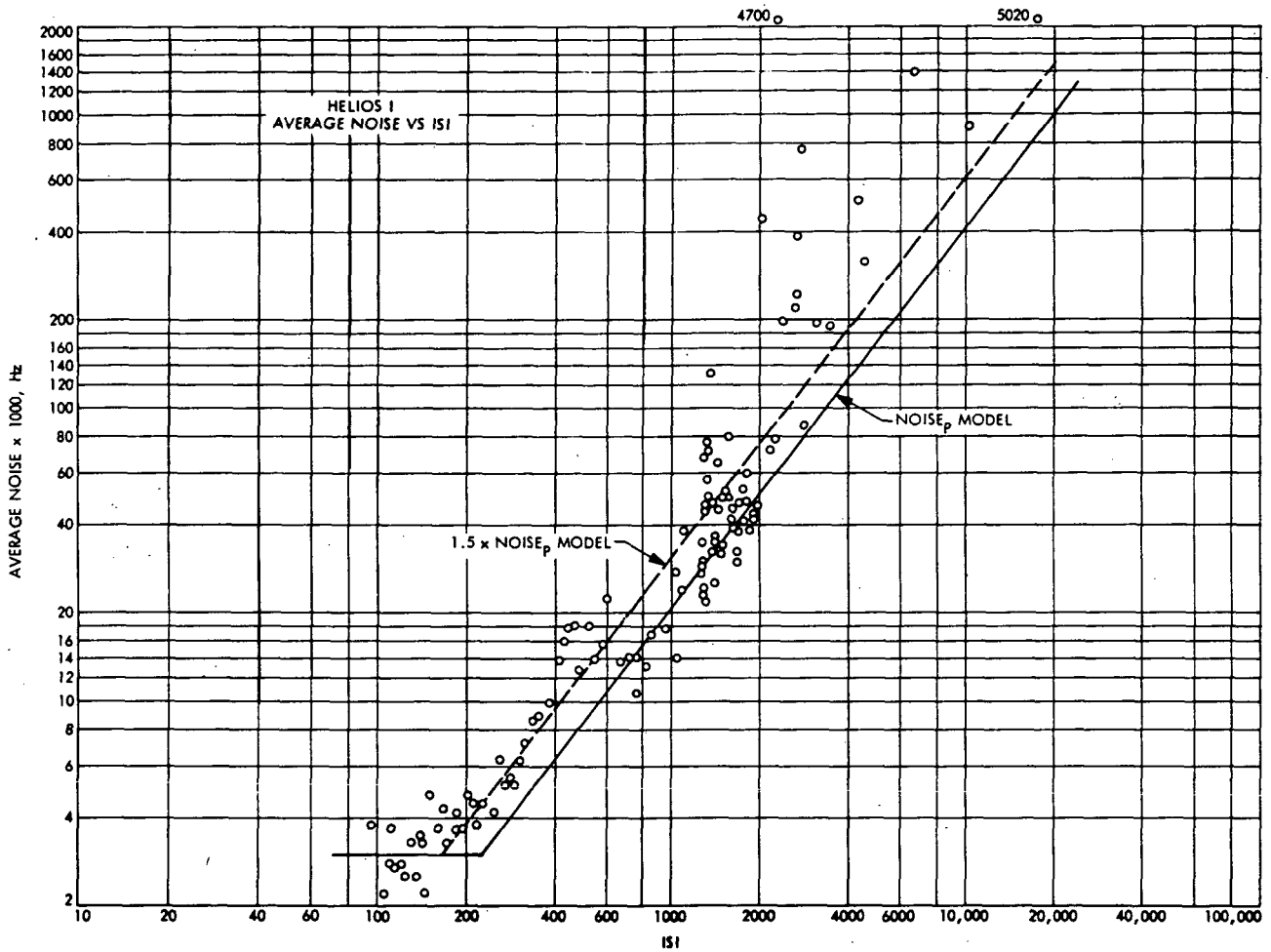


Fig. 3. Average noise vs ISI

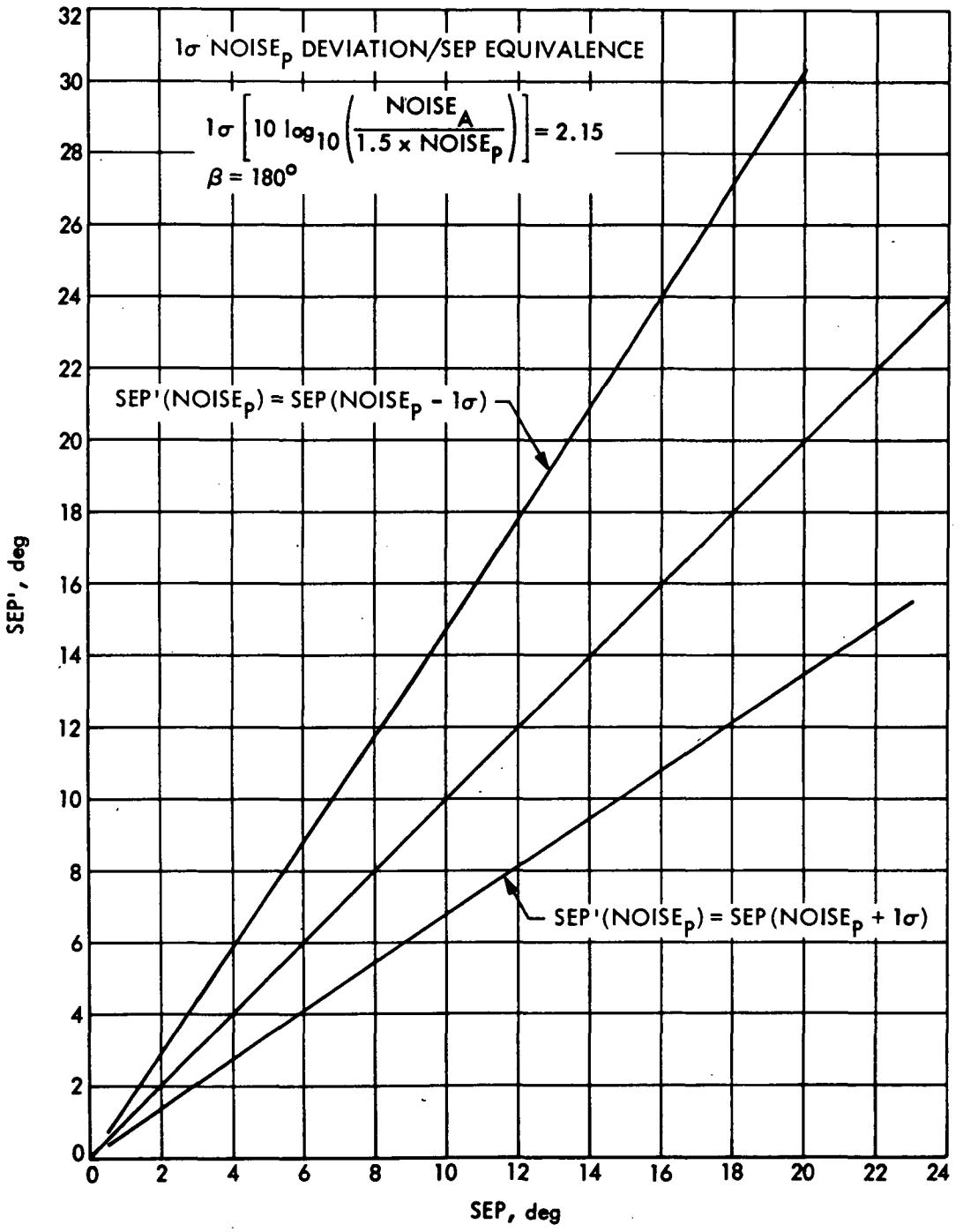


Fig. 4. Equivalent SEP angles for 1σ *NOISE$_p$* deviations

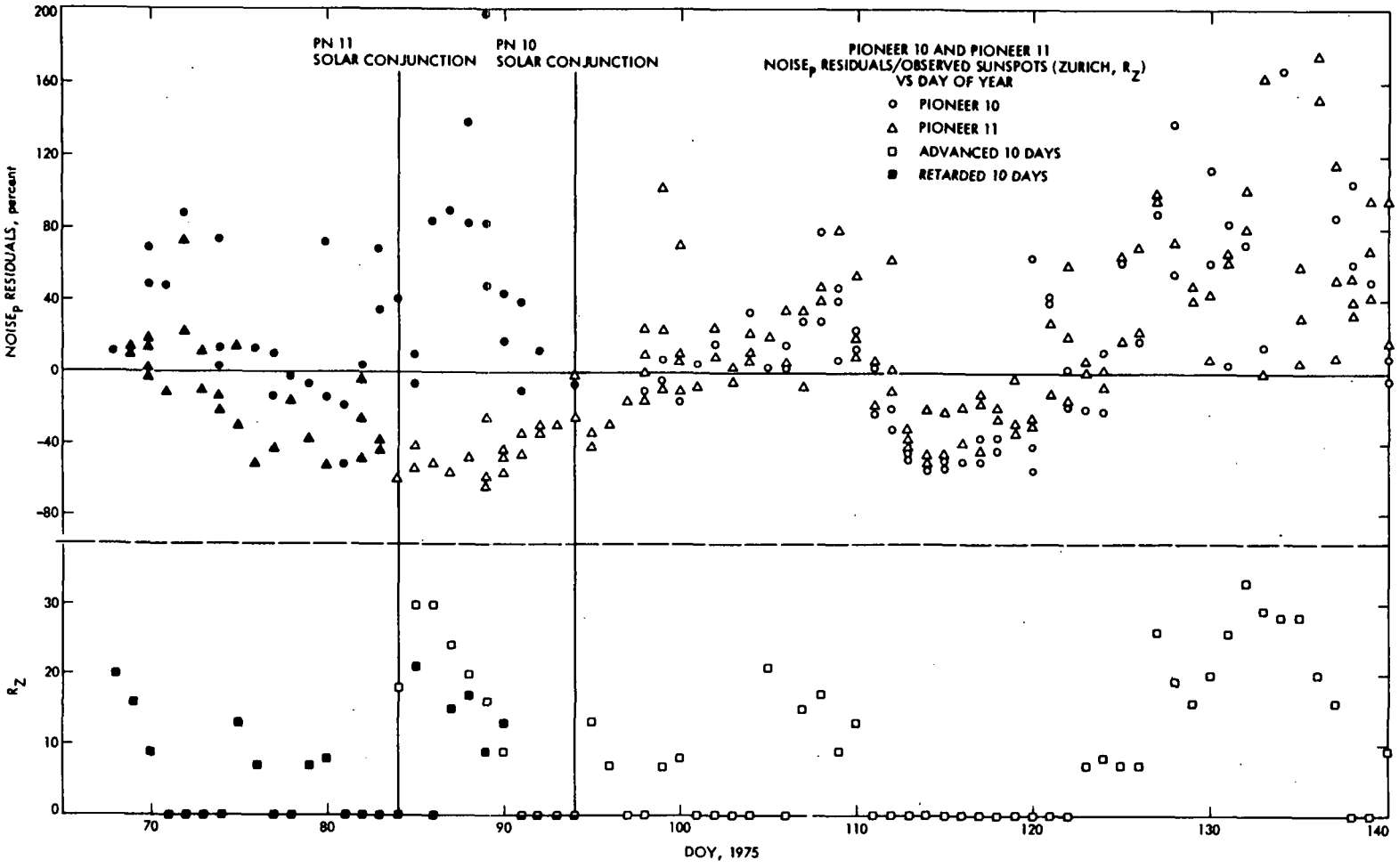


Fig. 5. Pioneer 10/11 *NOISE$_p$* residuals and observed sunspots vs day of year

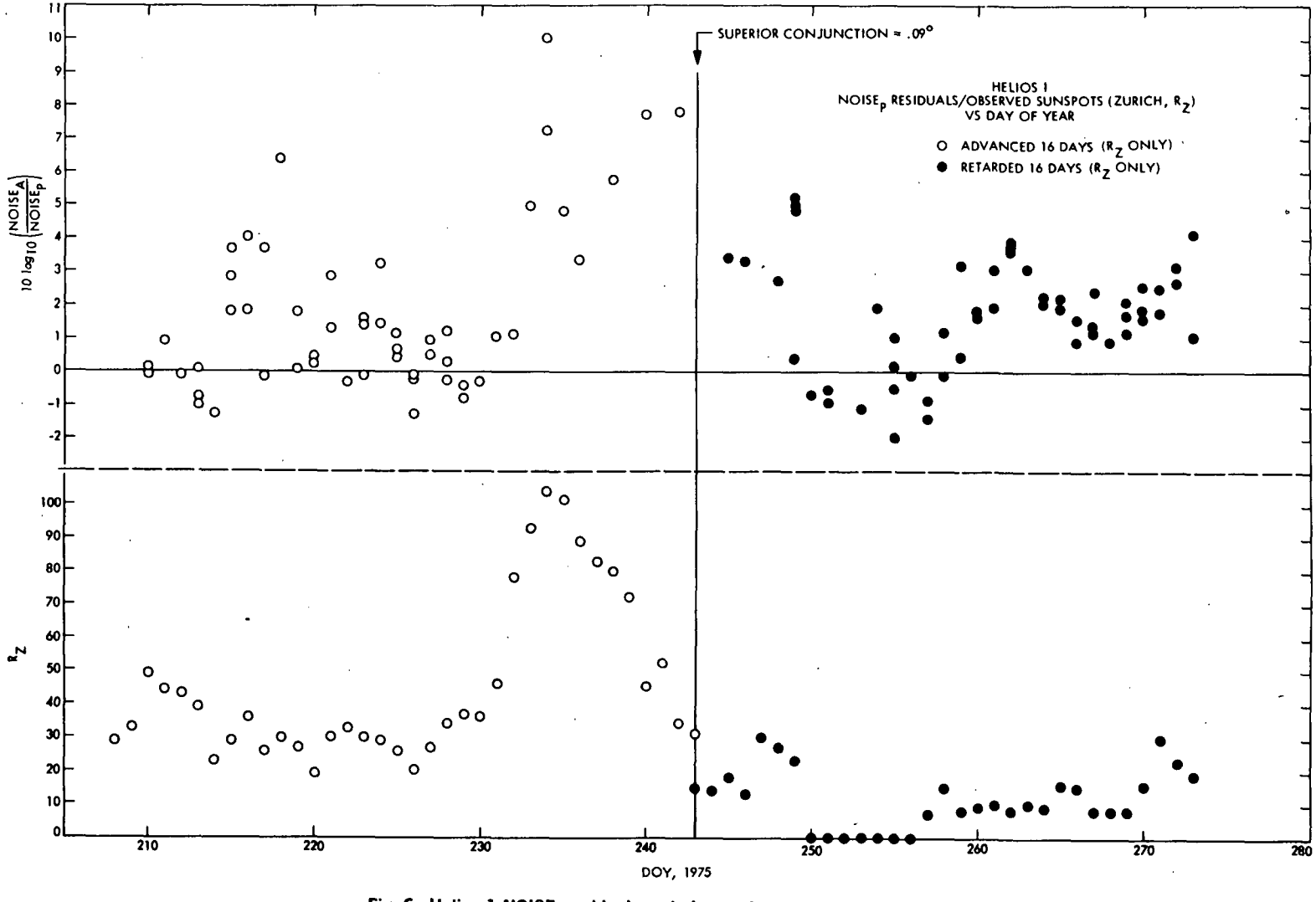


Fig. 6. Helios 1 *NOISE$_p$* residuals and observed sunspots vs day of year

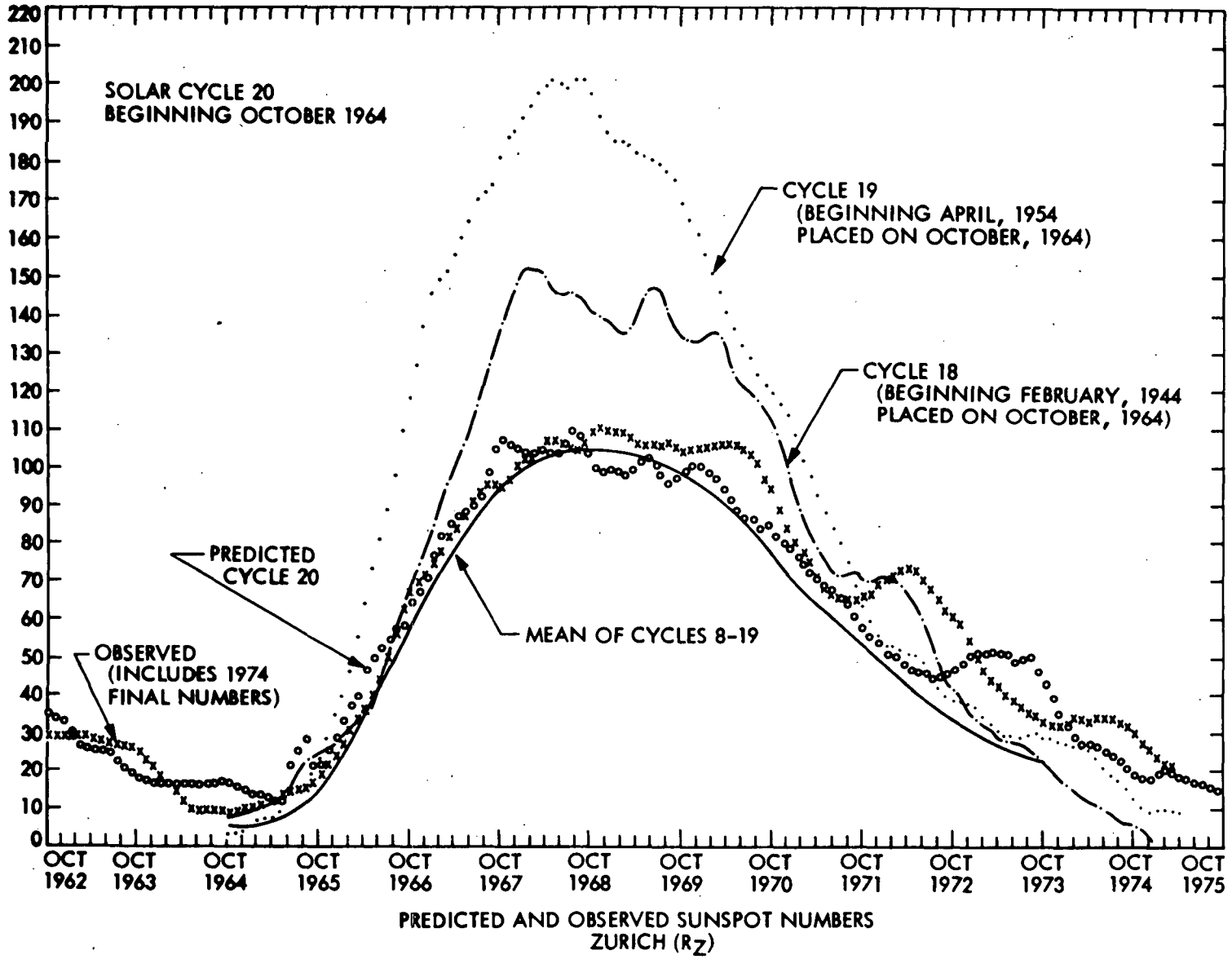


Fig. 7. Predicted and observed sunspot activity, 1962–1975

# Tracking Operations During the Helios 2 Launch Phase

L. E. Bright
Network Operations Section

*The prelaunch planning for the DSN's participation in the launch of the Helios 2 spacecraft is reviewed from the point of view of the tracking function. The actual events of the initial acquisition are discussed and analyzed in relation to prelaunch plans. In addition, an analysis of the effects of the Helios 2 spacecraft's spin on doppler data is provided.*

## I. Introduction

The relative infrequency of launches of deep space probes and the uniqueness of the demands they place on the DSN for an initial acquisition make it essential that the experience gained in each launch phase be carefully preserved and documented so that it may be applied to best effect in future launches. With this in mind, the present report summarizes the DSN's planning for and operations during the Helios 2 launch phase from the viewpoint of the tracking function. (The Helios-2 liftoff occurred at the open window launch time of 05:34:00.8 GMT on January 15, 1976. All GMT event times in this report unless otherwise stated are on January 15, 1976.)

Section II covers the planning activities for the launch and initial acquisition while Section III discusses and analyzes the actual launch phase operations at the Network Operations Control Center (NOCC) and at the Australian Deep Space Stations, DSSs 42 and 44, the prime and backup initial acquisition stations, respectively. A summary and conclusions are offered in Section IV.

## II. Prelaunch Planning

Planning for the initial acquisition of a new spacecraft begins many months before the actual launch. In the case of Helios 2, of course, most of the planning for and all of the experience gained in the Helios 1 launch were directly applicable. The Viking launches between the two Helios launches also provided valuable experience to personnel at the DSSs and at JPL.

For the tracking function, the "on paper" phase of preparation for launch culminated with an Initial Acquisition Plan for Helios 2 issued by the Tracking Element of the Network Operations Analysis Group (NOAG). Prepared by the present author with the generous assistance of other members of the NOAG and DSN Operations, the

plan defined a baseline strategy for the initial acquisition to which minor refinements were made as a result of operational testing and other preparatory activities. That plan is summarized in the following paragraphs.

### A. Features Peculiar to the Helios Spacecraft

Several unique features of the Helios spacecraft had a significant impact on initial acquisition planning. The first of these was the so-called "silent spacecraft mode," a spacecraft configuration in which the transmitter has been automatically switched off due to a momentary drop in spacecraft power. To reactivate the transmitter, it is necessary to acquire the uplink "in the blind" and subsequently command the transmitter back on. Obviously, this adds a new element of uncertainty into the initial acquisition process: does a failure to detect the spacecraft signal result from erroneous ground receiver settings or from mispointing of the station's antenna (frequency and angle uncertainties are always high during a launch phase), or is the spacecraft simply not transmitting a signal?

Another special consideration was the "interference zone." The changing aspect angle of the ground station as viewed by the spacecraft carries the radio line-of-sight through a region where the dual elements of the spacecraft low-gain antenna interfere destructively. This, combined with the fact that the spacecraft is spinning rapidly while transmitting through an antenna that is offset from the spin axis, produces a very complex amplitude and frequency modulation of the downlink signal. Consequently, the possibility of losing lock on the downlink during this period had to be allowed for in the acquisition procedures.

A final point that had to be considered was that the downlink signal is not automatically switched to coherent mode when the uplink is acquired. The coherent mode is brought about only by ground command. Consequently, there is no change in downlink frequency (with the resulting receiver-out-of-lock condition) that normally accompanies a successful uplink acquisition. Moreover, station and Network Operations Control Team (NOCT) personnel must be prepared for a change in frequency when the downlink *is* switched to coherent.

### B. Trajectory Considerations

The tracking parameter rates seen by DSS 42 in the Helios launch phase trajectories could only be considered extreme when compared to the rates seen in previous launch passes. For example, during the launch opportunity period January 15–February 7, 1976, a typical Helios 2 two-way doppler (D2) rate might reach 500 Hz/s, which would be among the highest D2 rates seen in any launch phase and nearly twice the highest rate observed during the Helios 1 launch. Angle rates would also be extreme. (These trajectory features may be seen in Figs. 1 and 2, which depict the DSS 42 pass in terms of a stereographic projection of apparent spacecraft motion and nominal best-lock frequency curve, respectively.) Other general observations of interest were:

(1) The Helios 2 trajectory rates would be highest at the open window of any given launch date, and would diminish monotonically as the launch time progressed into the (daily) window.

(2) Trajectory rates would increase from day to day throughout the launch opportunity, reaching their extreme values the last day of the opportunity.

(3) The launch pass at DSS 42 would have a duration of from 5½ to 7 hours, with the retrograde point occurring at about 1½ hours after rise.

For the actual Helios 2 launch date and time the resulting tracking rates were typical of the range of possible values through the entire launch opportunity. Actual peak values were:

$$\text{Hour angle rate} = 0.157 \text{ deg/s}$$

$$\text{D2 rate} = 549 \text{ Hz/s}$$

This D2 rate does not include spin modulation effects which can, under the worst conditions (see Section III-G), more than double the instantaneous rate. Still a D2 rate of 1200 Hz/s is quite tolerable under high signal level conditions, giving a phase-locked-loop phase error of only about 6 degrees. The angle rates were also well within tracking capabilities.

Based on Helios 1 experience, the following $3\sigma$ uncertainties in tracking observables were assumed for the Helios 2 launch pass:

$$\Delta\text{Hour Angle} \approx 1.2 \text{ deg}$$

$$\Delta\text{Declination} \approx 0.8 \text{ deg}$$

$$\Delta\text{Uplink (XA)} \approx 17 \text{ Hz (Voltage-controlled oscillator (VCO) level)}$$

These were the same uncertainties assumed for the Helios 1 launch based on estimated $3\sigma$ injection condition perturbations. Since new estimates for Helios 2 in-

dicated improved launch vehicle performance, and since Helios 1 and Viking launch pass residuals were orders of magnitude smaller than the above uncertainties, these estimates were considered to be reasonable. However, they were incomplete in the sense that there are "failure modes" of launch vehicle performance which would result in grossly larger errors than those above. Bearing this in mind, the initial acquisition was designed to accommodate possible trajectory uncertainties far in excess of the "nominal" launch vehicle performance induced uncertainties.

### C. Prediction Strategy

In order to assure the availability of the best possible predictions in any of the possible launch contingency situations, the following plan for generation of up to eight different predicts sets was adopted:

(1) $L - 7$ days: Approximately seven days before launch three predicts sets would be generated. These sets would be the open, mid and close window cases (designated H15O, H15M, H15C) for the nominal launch date and time. These prelaunch nominal sets would be generated with time from launch (TFL) time and two different sample rates: 20 s/sample until $L + 75$ min and 300 s/sample after that time. (The high angle and frequency rates occur during the first half-hour of the pass.) These sets would be transmitted to DSS 42 and DSS 44 in both text and binary form to serve as backup to the predicts generated on launch day.

(2) $L - 90$ min: At launch minus 90 minutes, a polynomial coefficient tape (PCT) based on the latest launch time would be generated. This PCT combined with the latest available spacecraft frequencies would then be input to the predict run (set H15U) from which the (nominally) prime drive tape would be punched. These predicts would serve in the tracking Real-Time Monitor (RTM) for pseudoresidual calculations as well as for reference as frequency predictions. With a GMT time field, they would have the same sample rates as the $L - 7$ days predicts and reflect the tuning pattern to be used in the uplink acquisition.

(3) $L - 10$ min: In case of a hold during the countdown, generation of a PCT based on the latest estimate of the launch time would commence at about launch minus 10 minutes. The predicts (H15E) generated from this tape and incorporating the latest frequencies would be identical in format to the $L - 90$ min set.

(4) $L + 5$ min: By about launch plus 5 minutes, generation of a PCT based on the actual liftoff time would begin. The "actual launch time" predicts (H15A) produced from this PCT would be identical in format to the "U" and "E" predicts above.

(5) $L + ?$ min: If the solar orbit injection burn did not occur, generation of a parking orbit PCT would start at an appropriate time to allow tracking by the first DSS that would come into view. (There would be a long time span before the spacecraft would come into view of a DSS should it remain in the parking orbit.) The corresponding predicts would be in GMT at a nominal sample rate of 10 s/sample. The set designation would be H15N.

(6) $L + 180$ min: Approximately three hours after launch a PCT based on the Real-Time Computer System (RTCS) estimate of the solar orbit injection state vector would be produced. Predicts from this PCT would have GMT time and a sample rate of 300 s/sample. This set, designated H15I, would extend to approximately launch plus 14 hours.

(7) $L + 9$ h: By launch plus 9 hours the spacecraft is, for most tracking purposes, in "cruise phase." The set of predicts generated at this time would therefore be in a more or less standard multistation format (but extend to only about $L + 30$ hours). Input would be a PCT based on the first orbit solution using S-band radio metric data from DSS 42.

In addition to the JPL predicts, Air Force Eastern Test Range (AFETR) predicts would be generated by the Real-Time Computer System (RTCS), using JPL frequency inputs and ETR trajectory data with three sets to be transmitted during the launch period: a preflight nominal set at launch minus 45 min, a set based on Vanguard C-band data at about launch plus an hour, and a set at launch plus 190 min based on S-band data from DSS 42.

For a nominal or near-nominal launch trajectory, JPL predicts would be prime for all uses and ETR predicts prime only in case of a non-nominal trajectory or when use of JPL predicts was precluded by hardware or software failures.

### D. Angle Drive Strategy

The relevant considerations in formulating the angle drive strategy at DSS 42 for the Helios 2 launch phase were the following:

(1) In the silent spacecraft mode, the antenna must be

driven in the blind for a period long enough to acquire an uplink and subsequently to command the spacecraft on.

(2) The low signal strength and signal-to-noise ratio (SNR) characteristic of the interference zone makes it improbable that autotrack can be maintained through the first ~8 minutes of the track (i.e., through the end of the interference zone). If autotrack is broken, the ground antenna begins to drive away from the spacecraft, risking the loss of downlink lock.

(3) Under strong signal conditions, the preferred tracking mode is autotrack.

(4) The uplink should be acquired as quickly as possible after the end of the interference zone (at about rise + 8 m).

(5) The antenna must be on Antenna Pointing Subsystem (APS) drive tape during the switch to two-way coherent (in autotrack the antenna could drive off point when the noncoherent–coherent link switch causes the receivers to drop lock).

Consistent with the above requirements, the basic angle drive strategy was defined:

(1) Computer drive from the best available predicts until downlink lock is established (the spacecraft may be silent) but in any case through the end of the interference zone; then,

(2) As soon as criterion 1 allows, switch to autotrack.

(3) Return to computer drive for the noncoherent–coherent downlink transition, then back to autotrack.

Where this basic strategy called for computer drive, the choice of an appropriate drive tape would be according to the following procedure:

If a verified GMT drive tape based on a launch time that is accurate to ±5 seconds is available, it is used. A time bias correction is applied if the launch time error is greater than 1 second. (The corresponding predict set might be any of the following, depending on the circumstances: H15U, H15A, H15E.) If none of the available (verified) drive tapes satisfies the launch time accuracy criterion, the plan calls for use of a verified H15A or H15E drive tape with a time bias applied so as to correct the launch time to within a second of actual launch time.

Either of these situations would allow use of a drive tape with (at most) a small time bias (a few seconds perhaps). If, however, no GMT tape were available with the desired launch time accuracy and neither the "A" nor "E" drive tape had been punched and verified, it would be necessary to use a preflight nominal verified drive tape in TFL format (H15O, H15M, H15C). The time offset used in this case would be the actual launch time in GMT, a somewhat more risky procedure.

In general, use of a prelaunch nominal drive tape would also require angle offsets. These would be computed from H15E or H15A *page print* predicts, if available; otherwise the Tracking Network Operations Analyst (NOA) would provide angle biases based on the known variation of launch trajectory characteristics with launch time.

The above launch time accuracy criterion may seem overly stringent, but consider that a 5-second error translates to about 1600 Hz error in one-way doppler frequency (D1) and an angular error (0.93 deg) of almost 5 times the offset beamwidth of the S-band cassegrain monopulse (SCM) antenna!

If it should be necessary to use AFETR predicts, it would not be possible to perform the highly automated and optimized initial acquisition strategy that is possible with JPL predictions. The initial acquisition strategy in the event of prime AFETR predicts would be similar to those in the era previous to Pioneer 10, Pioneer 11, Mariner Venus Mercury, Helios 1, and the Vikings. In this case the antenna would be manually driven to the AFETR predictions until it was possible to autotrack on the S-band acquisition antenna (SAA), i.e., at least through the end of the interference zone.

### E. One-Way Downlink Acquisition

The one-way downlink acquisition would be relatively less complicated than the uplink and coherent downlink acquisitions, and in the past the DSSs have very rapidly and routinely locked the one-way downlink according to standard procedures; hence, no special procedures were required. However, the following estimates of downlink prediction uncertainty were provided (at S-band):

$$3\sigma \text{ D1 TFREQ} \approx 2500 \text{ Hz}$$

$$3\sigma \text{ D1 Trajectory} \approx 850 \text{ Hz}$$

In addition, it was recognized, an uncertainty in D1 would be introduced by the possibility that actual launch time could differ from the expected time (for which pre-

dicts are generated) by up to 5 seconds (see Section II-D on angle drive strategy). This could affect the D1 value by up to 1650 Hz. In the worst case this would be added to the $3\sigma$ uncertainties to give a D1 total uncertainty $\approx$ 4300 Hz.

### F. Uplink Acquisition Strategy

The impact of the possible silent spacecraft mode and the antenna interference zone on the uplink acquisition strategy was considered in the decision to wait until the end of the interference zone before attempting the uplink acquisition. Otherwise, the plan called for an uplink acquisition that would be quite routine, particularly since the $3\sigma$ frequency uncertainties were small. The uncertainties assumed were (at VCO level):

$$\Delta\text{Uplink (trajectory)} \approx 17 \text{ Hz}$$

$$\Delta\text{Uplink (best lock)} \approx 12 \text{ Hz}$$

$$\Delta\text{Uplink (temperature)} = \Delta T \cdot \frac{\partial}{\partial T}(\text{Uplink}) \approx 10 \text{ Hz}$$

To allow for an error of up to 5 seconds in predicted launch time, another 4 Hz was added to the root-sum-square of the probabilistic uncertainties, giving:

$$\text{Total uplink uncertainty} \approx 27 \text{ Hz}$$

These frequency uncertainties were relatively small, and tended to counterbalance the difficulties posed by the possible silent spacecraft mode and the antenna interference zone.

To be extremely conservative (and hence accommodate some of the "non-nominal" launch vehicle performance modes alluded to previously) the above $3\sigma$ XA[1] uncertainty was generously padded, resulting in an uplink acquisition search of approximately XA $\pm$100 Hz.

For this acquisition, a sweep rate of +3 Hz/s was selected because:

(1) A rate of +3 Hz/s would result in an effective rate at the spacecraft of about +150 Hz/s (S-band), which is reasonably close to the geometric mean of the upper and lower sweep limits (200 Hz/s).

(2) It was felt that 3 Hz/s would be close to the limit at which the site could no longer accurately tune the exciter (a manual operation).

Finally, the uplink acquisition would consist of a single uplink frequency sweep in the direction of XA change, placing the ending tracking synthesizer frequency (TSF) near the XA frequency to satisfy a command capability requirement that the difference between TSF and XA be no greater than 110 Hz at VCO level. No additional tuning would be required.

If the first sweep were not successful, a second, contingency sweep was planned. This sweep would be at the same rate as the prime sweep, but would cover a region approximately 50 percent greater (XA $\pm$150 Hz). It would start about 3½ min after the end of the first sweep, and include a downleg, an upleg, and then a downleg back to TSF.

### G. Possible Misacquisitions

The misacquisitions considered were of two kinds: acquisition of a spurious signal in the spacecraft transmitter power spectrum or acquisition of the main carrier on a *ground antenna* sidelobe.

The acquisition plan included a table of possible spurious signals, all about 30 dB below the power level of the main carrier and at various frequency offsets from about 3.5 to 26.5 kHz from the carrier. "The necessary steps to be taken to insure that the locking to a spurious signal, should it occur, be quickly identified and remedied" were specified as follows:

*Detection of Spurious Signals*

(1) The NOCT and station personnel will be familiar with the possibility of occurrence of a spurious signal lockup and, specifically, with the frequency offsets at which this can occur.

(2) The NOCT (primarily the telemetry and monitor NOAs) will observe and interpret actual vs predicted signal strength.

(3) The NOCT (primarily the track NOA) will observe and interpret pseudoresidual output.

*Corrective Action*

Break receiver lock on spurious signal and reacquire on carrier.

Concerning the second kind of misacquisition the plan stated: "The possibility exists of locking on a (ground)

[1]"XA" denotes the VCO-level frequency at which the DSS must transmit in order that the doppler-modified S-band uplink at the spacecraft will equal the spacecraft receiver's best-lock frequency.

antenna sidelobe while in autotrack. The following information concerning antenna sidelobes is available:

| Angular offset | Loss, dB |
|---|---|
| N/A (SAA) | −36 |
| 0.50 deg (SCM) | −20 |
| 1.20 deg (SCM) | −27 |
| 1.80 deg (SCM) | −37 |

If it is suspected (from the above data) that antenna sidelobe lock has occurred, autotrack should be broken and the antenna manually driven to antenna mainbeam lock."

All of the foregoing plans and procedures applied to DSS 42 as the prime initial acquisition station. For DSS 44 as backup station the same strategies applied with the following exceptions:

The uplink acquisition would be performed at DSS 44 only if there should be a failure that would preclude performing the acquisition from DSS 42. Since the acquisition aid antenna at DSS 44 is receive only, the SCM must be used for the uplink acquisition. The narrow halfpower offset of the SCM (0.18 deg) requires very accurate pointing for successful acquisition of the uplink. Thus, it was considered advantageous to go to autotrack on the SCM prior to turning on the transmitter. Finally, because of the higher gain of the SCM and in order to use a familiar power of 1 kW, the uplink acquisition might have to be delayed for several minutes after spacecraft rise so as not to exceed the uplink signal level constraint of −70 dBm.

## III. Analysis of Launch Phase Operations

### A. Predicts Generation

A basic *sine qua non* for a successful initial acquisition is the availability of tracking predictions incorporating the most current possible knowledge of the spacecraft's trajectory and frequency characteristics. Accordingly, much of the activity of DSS, NOCT and supporting advisory personnel prior to spacecraft rise centers on the generation, validation, transmission and revalidation of various predicts sets.

The first set of predictions generated during the Helios-2 launch countdown was the set designated H15U. The generation process began with delivery by the Helios navigation team of a polynomial coefficient tape (PCT) describing the nominal spacecraft trajectory as viewed at the Australian tracking complex. Frequencies were unchanged from the nominal values supplied earlier by project telecommunications analysts. Transmission of the predicts in both text and binary form and punching and verification of the prime antenna drive tape also proceeded smoothly. The whole process was complete by 04:28:00 GMT, just over an hour before launch.

The launch minus 35 minutes update of spacecraft frequencies showed a change of about 20 Hz in the transmitter reference frequency. This prompted a decision to run the predict set H15E (provided for in acquisition plans in case of a slip in the launch time) even if the launch should occur on time. The new frequency information would be used in this set. When the launch did in fact occur on time (at 05:34:00.8 or 0.8 sec late, actually) this procedure was implemented and the predict set H15E was declared prime for frequency information. Set H15U naturally remained prime for antenna drive. The fact that launch occurred within a second of open window alleviated the need for the set H15A, which was therefore cancelled.

### B. Summary of Operations at DSS 42

1. **One-way downlink acquisition.** No information was received from the down-range AFETR stations that the Helios 2 spacecraft was in the silent mode, and in fact, this was apparent when, within seconds of the predicted spacecraft rise time, DSS 42 routinely acquired a one-way downlink. (Obviously, this condition vastly reduced the uncertainties heretofore inherent to the initial acquisition procedure at DSS 42.) Signal levels, however, were about 30 dB lower than expected and the station concluded that they were on an antenna sidelobe. Antenna pointing, on drive tape control because of the interference zone, was manually adjusted and offsets were entered, bringing the signal level to a near-nominal value. The station reported that they were "on the main beam now." With this assurance and once safely out of the interference zone, DSS 42 switched antenna drive to autotrack for the brief period of noncoherent tracking to follow.

2. **Interference zone.** The effect of the interference zone on signal levels was minor. The degradation of about 8 or 9 dB that did occur (as seen in the SAA receiver) was completely masked in the SCM receiver by losses due to pointing error (since the SCM antenna has a very narrow beamwidth). Neither receiver lost lock during the interference zone although spin modulation effects resulted in a very high doppler noise level.

3. **Uplink acquisition.** Uplink tuning began on schedule while, coincidentally, antenna pointing was being manually adjusted. Despite the fact that the pointing adjustment involved some rather large antenna excursions (up to 0.8 deg from nominal), pointing errors had no impact on the uplink acquisition since uplink transmission was through the broadbeam SAA antenna. Telemetry data confirmed that nominal uplink acquisition had occurred when the spacecraft receiver's automatic gain control reading dropped precipitously in response to DSS 42's powerful S-band signal.

4. *Two-way noncoherent tracking.* The brief period (about 12 min) of two-way noncoherent tracking following the uplink acquisition proceeded routinely up to the time of the command that would cause the spacecraft to shift its downlink signal to coherent with the uplink. In preparation for this command and the resulting receiver-out-of-lock condition, DSS 42 returned antenna drive to computer mode (drive tape) with offsets to compensate for the angle biases observed during the autotrack period.

5. **Reacquisition of (coherent) downlink.** After dropping lock due to the coherent command, receivers were in lock again only 20 seconds later, but at a signal level some 30 dB below the predicted value. The low signal level evoked some discussion among Network Operations Control Team (NOCT) and advisory personnel and between DSS 42 and the tracking controller at JPL as to whether a sideband (i.e., a spurious signal) acquisition or a sidelobe acquisition had occurred. Finally, after locking up and retuning receivers twice and after performing manual adjustments to antenna pointing angles, DSS 42 obtained solid receiver lock on the spacecraft's carrier signal, at normal levels. The period from first receiver-out-of-lock condition (due to switch in downlink frequency) until receiver lockup on the coherent downlink carrier was about 6 min 15 s. Quantitative details of the reacquisition may be seen in the graph of hour angle residuals and doppler residuals in Figs. 3 and 4, respectively.

The remainder of the DSS 42 pass, for most tracking purposes a routine cruise-phase operation, proceeded smoothly and without incident.

### C. Summary of Operations at DSS 44

The one-way downlink signal was acquired less than 20 s after the predicted rise time. (Network Control System Block II Real Time Monitor data show receiver lock was sustained from 06:24:15 GMT. The station reported (presumably intermittent) lock as early as 06:23:52.) Two-way coherent downlink was acquired on the main carrier just 17 s after loss of lock occurred as a result of the spacecraft's switch to a coherent downlink. (Receiver out-of-lock (ROL) was at 06:46:43 and receiver in-lock (RIL) was at 06:47:10.) In another 20 seconds, data from DSS 44 was being correctly flagged as three-way. Autotracking was resumed and the pass continued to spacecraft set without event.

One anomaly during the pass was quickly noticed and corrected by alert DSS 44 personnel. Moments after spacecraft rise and a flawless acquisition of the downlink, the station reported a problem with the X-angle antenna drive. The erratic behavior of the drive can be clearly seen in the graph of the pseudoresidual for the X-angle shown in Fig. 5. The dramatic effect of the station's corrective action—manual peaking of the signal and subsequent switchover to autotrack—is equally clear in the plot of signal level from the SCM antenna (Fig. 5).

It is worthy of note that the forced switch to autotrack occurred before the interference zone and hence DSS 44 tracked throughout the zone in autotrack mode with no harmful results!

### D. Prediction Accuracy

It is always of interest to compare the preflight estimates of uncertainties in tracking observables with the pseudoresiduals that result from differencing predicts and actual radio metric data.

In the case of the angle residual, the first point of interest occurred only after antenna drive was switched to autotrack at 06:33:30. After a brief transient in antenna drive response the hour angle residual was 0.30 degrees. Since the preflight uncertainty estimates are estimates of the *maximum* $3\sigma$ deviations from nominal (which typically occur at spacecraft rise), it is necessary to extrapolate the angle residuals back to the rise time in order to make a meaningful comparison. From Fig. 3, which presents a profile of the hour angle residual for the first half-hour, a rough graphical extrapolation yields for the hour angle residual at rise (i.e., at ~06:24):

$$\Delta\mathrm{HA} \approx 0.95 \text{ deg}$$

(The first two points occur during the antenna drive transient mentioned above and should not be used in the extrapolation.) Of this total "error," about 0.13 deg is accounted for by the fact that the actual launch time was 0.8 s later than the nominal time, on which tracking

predicts were based. Making a liberal allowance of 0.05 deg for possible antenna misalignment leaves 0.77 deg as an indicated trajectory-dependent error. Based on the assumed $3\sigma$ hour angle uncertainty of 1.2 deg from Section II, a statistical table assigns a probability of only 5 percent to the class of errors of this size or larger. Thus if the trajectory uncertainty estimates are realistic, the Helios-2 trajectory was a one-in-twenty case. (The somewhat remote possibility that antenna pointing inaccuracies exceeded the 0.05 deg quoted above will be routinely pursued.)

By contrast to the hour angle residual, the declination angle residual held close to an average of

$$\Delta\text{DEC} \approx 0.11 \text{ deg}$$

a value that is in no way remarkable: statistically speaking, about 2 out of 3 cases can be expected to have a trajectory-dependent declination angle residual of this magnitude or greater.

The one-way doppler residual represents an intermediate case. The probability associated with the peak value of

$$\Delta\text{D1} \approx (-)\,783 \text{ Hz}$$

at rise is about 25 percent after adjusting for the launch time discrepancy of 0.8 s. Here it is impossible to separate the distinct components of the residual which arises in part from uncertain knowledge of the spacecraft's auxiliary oscillator frequency (which provides a reference for generation of the noncoherent downlink frequency) and in part from uncertain knowledge of the spacecraft's radial velocity (which determines the amount of doppler shift on the downlink).

### E. Uplink Acquisition at DSS 42

Based on guidelines as summarized in Section II, the instructed uplink acquisition sweep was defined as:

| | |
|---|---|
| Ramp start time | 06:31:00 GMT |
| Starting frequency | 22.017880 MHz (VCO) |
| Frequency rate | 3 Hz/s (VCO) |
| Ramp end time | 06:32:20 GMT |
| Ending frequency | 22.018120 MHz (VCO) |
| Sweep duration | 80 s |

The instructed sweep and the sweep actually executed by DSS 42 can be seen in Fig. 6. The station tuned manually at a remarkably constant rate of about 2.5 Hz/s or about 85 percent of the instructed rate. Due to a late start (about 10 s late) and the slow tuning rate, the final tracking synthesizer frequency (TSF) was achieved some 25 s late. These minor departures from the nominal sweep parameters had no effect on the success of the acquisition.

### F. Comments on the Interference Zone

A number of observations on the interference zone, theory and practice, are in order. First, this author's own Initial Acquisition Plan implies that the principal feature of the interference zone is low signal levels. This is inaccurate. The "low signal level" feature per se is insignificant—just an hour after the zone, the spacecraft's signal level is lower than the minimum value reached during the zone, this being due merely to space loss. (Ground receiver automatic gain control (AGC) data show a maximum interference zone degradation of about 10 dB.) The interference zone is characterized, theoretically at least, by a rapidly changing signal level or, in effect, amplitude modulation. This could (in theory) make autotracking marginal or impossible; in point of fact, however, DSS 44 autotracked through the entire zone without difficulty!

The most noticeable effect on tracking data shows in the extreme degree of corruption to doppler data that results from the very heavy spin (frequency) modulation of the spacecraft's downlink. This assumes that receiver lock is maintained throughout the period of severest modulation, as was indeed the case with receivers at both DSS 42 and DSS 44.

### G. The Effects of Spin Modulation on Doppler Data

Although experience in two Helios initial acquisitions has shown that the spin modulation effects of the offset low-gain antenna are not severe enough to disrupt a carefully planned acquisition procedure, it would be helpful to be able to predict the effects of spin modulation on observable tracking quantities. If the maximum effects are known in advance, it is possible to identify at least any anomaly that is not masked by spin modulation effects and to take appropriate steps to determine the source of such an anomaly.

It is in fact quite easy to derive a theoretical expression for the maximum effect of spin modulation on doppler data. A simplified derivation of the effect is presented below, on the assumption that what is measured by the DSS doppler system is the real doppler shift of the space-

craft's downlink frequency. A more complete derivation yields the same result up to an (uninteresting) additive constant in the indicated one-way doppler frequency.

Let $\omega$ denote the spacecraft's spin vector in rad/s, and let $\hat{L}$ be a unit vector along the line of sight from the spacecraft to DSS 42. Now define an orthogonal coordinate system as follows: let $\hat{l}$ denote the unit vector perpendicular to $\omega$ that lies in the plane of $\omega$ and $\hat{L}$. Let $\hat{n} = \omega/|\omega|$ and choose the unit vector $\hat{m}$ to complete the right-handed orthogonal system $\hat{l}$, $\hat{m}$, $\hat{n}$ (Fig. 7). Now since the velocity vector $\mathbf{v}_s$ of the horn antenna is orthogonal to $\omega$ it has no $n$ component. Furthermore, we have chosen our coordinate system so that $\hat{L}$ has no $m$ component. Consequently the component of antenna velocity along the line-of-sight, $\mathbf{v}_s \cdot \hat{L}$, is just the product of the $l$ components of $\mathbf{v}_s$ and $\hat{L}$ (the products of the $m$ and $n$ components each involve a factor zero):

$$\mathbf{v}_s \cdot \hat{L} = v_{s_l} L_l + v_{s_m} \cdot 0 + 0 \cdot L_n$$

or

$$\mathbf{v}_s \cdot \hat{L} = v_{s_l} L_l \tag{1}$$

Now $\mathbf{v}_s$ is just the velocity vector of a point in uniform circular motion in the $lm$ plane so its $l$ component varies sinusoidally. We may then write

$$v_{s_l} = v_s \cos \omega t = 6\lambda\omega \cos \omega t \tag{2}$$

where $\lambda$ is the wavelength of the spacecraft's S-band downlink signal and $6\lambda$ is the distance of the horn antenna from the spin axis (a convenient relationship designed into the spacecraft).

Now if $\theta$ is the angle between $\hat{L}$ (line-of-sight vector) and $\hat{n}$ (or $\omega$), the $l$ component of $\hat{L}$ is just (recall that $\hat{L}$ is in the $ln$ plane):

$$L_l = \sin \theta$$

Putting this result and Eq. (2) into (1), we have

$$\mathbf{v}_s \cdot \hat{L} = v_{s_l} L_l = 6\lambda\omega \sin \theta \cos \omega t \tag{3}$$

for the component of the antenna's spin velocity along the line-of-sight to the ground station. We will call this the radial spin velocity component:

$$\dot{r}_s = \mathbf{v}_s \cdot \hat{L} = 6\lambda\omega \sin \theta \cos \omega t \tag{4}$$

Now, defining the following additional symbols:

$c$ = speed of light *in vacuo*

$f_{s/c}$ = spacecraft's S-band downlink frequency (Hz)

$f_{dop}$ = change of downlink frequency due to the doppler effect

$\dot{r}$ = antenna's total line-of-sight (radial) velocity

$\dot{r}_{cm}$ = radial velocity of spacecraft center of mass

$\Delta t$ = doppler sampling interval

we can write (noting that $\lambda = c/f_{s/c}$):

$$f_{dop} = f_{s/c} \frac{\dot{r}}{c} = \frac{\dot{r}}{\lambda} = \frac{1}{\lambda} (\dot{r}_{cm} + \dot{r}_s)$$

$$= \frac{\dot{r}_{cm}}{\lambda} + \frac{1}{\lambda} (6\lambda\omega \sin \theta \cos \omega t)$$

where we have used the expression (4) for $\dot{r}_s$. Thus

$$f_{dop} = \frac{\dot{r}_{cm}}{\lambda} + 6\omega \sin \theta \cos \omega t \tag{5}$$

The first term $\dot{r}_{cm}/\lambda$ represents the usual doppler shift of a nonrotating spacecraft while the term $6\omega \sin \theta \cos \omega t$ is the spin modulation term that is superimposed when the spacecraft is rotating. (The time derivative of the second term gives the instantaneous rate of change of the downlink frequency due to the spacecraft rotation:

$$\dot{f}_s = -6\omega^2 \sin \theta \sin \omega t$$

This formula was used to estimate the receiver stress that could be expected due to the high rate of change of the spacecraft's signal in Section II-B.)

Now the instantaneous doppler frequency is not directly observable in the DSS instrumentation. What is displayed in near-real-time, and recorded for later analysis, is the difference (called a pseudoresidual) between an average doppler frequency, periodically determined at intervals $\Delta t$, and the predicted doppler frequency for the corresponding time. The average frequency is measured by continuously counting doppler cycles (extracted from the downlink signal by a method that need not concern us here), differencing successive sampled counts $C_i$ and dividing by the time interval $\Delta t$ between samples: symbolically

$$\Delta C_i = C_{i+1} - C_i$$

and

$$\bar{f}_{dop} = \frac{\Delta C_i}{\Delta t}$$

Then clearly

$$\begin{aligned}\Delta C &= \int_t^{t+\Delta t} f_{dop}\, dt \\ &= \int_t^{t+\Delta t} \frac{\dot{r}_{cm}}{\lambda}\, dt + \int_t^{t+\Delta t} (6\omega \sin\theta \cos\omega t)\, dt \\ &= \frac{\Delta r_{cm}}{\lambda} + 6\omega \sin\theta \int_{\omega t}^{\omega(t+\Delta t)} \cos\phi \frac{d\phi}{\omega} \\ &= \frac{\Delta r_{cm}}{\lambda} + 6 \sin\theta \text{ “}\Delta \sin\phi\text{”}\end{aligned}$$

where $\phi = \omega t$ and

$$\begin{aligned}\text{“}\Delta \sin\phi\text{”} &= \sin(\omega t + \omega\Delta t) - \sin\omega t \\ &= \sin(\phi + \Delta\phi) - \sin\phi\end{aligned}$$

(Note that we have used the fact that $\theta$ is slowly varying to bring sin $\theta$ out of the integrand: over the sample intervals of interest (1 sec to 10 sec) the spacecraft DSS line-of-sight may be considered fixed, hence $\theta$ is constant.)

Now we can write an expression for the computed estimate of the doppler frequency:

$$\bar{f}_{dop} = \frac{\Delta C}{\Delta t} = \frac{1}{\lambda}\frac{\Delta r_{cm}}{\Delta t} + \frac{6\sin\theta}{\Delta t} \text{“}\Delta \sin\phi\text{”} \qquad (6)$$

Since the “center-of-mass” doppler shift $(1/\lambda)(\Delta r_{cm}/\Delta t)$ can be predicted to a high degree of accuracy, the pseudoresidual (measured doppler less predicted center-of-mass doppler) may be written as

$$\text{Doppler residual} = \frac{6\sin\theta}{\Delta t} \text{“}\Delta \sin\phi\text{”} + \text{linear bias term} \qquad (7)$$

for small sample intervals. The “linear bias term” can be easily removed by a linear regression over a number of successive samples. Such a “detrending” of the doppler residual is in fact performed by the Real Time Monitor (RTM) so that the term

$$\bar{f}_s \equiv \frac{6\sin\theta}{\Delta t} \text{“}\Delta \sin\phi\text{”} \qquad (8)$$

may be observed directly in near-real-time.

The first thing we may say about this spin modulation residual is that the maximum possible value for a given $\theta$ is

$$\frac{12\sin\theta}{\Delta t}$$

since the factor “$\Delta \sin\phi$” can be at most 2. Let us write out the term in full:

$$\begin{aligned}\text{“}\Delta \sin\phi\text{”} &= \sin(\phi + \Delta\phi) - \sin\phi \\ &= \sin(\omega t + \Delta\phi) - \sin\omega t\end{aligned}$$

We have written $\Delta\phi$ instead of $\omega\Delta t$ to emphasize that $\Delta\phi$ is a constant (for given sample interval $\Delta t$). The actual maximum depends on the instantaneous value of $\phi = \omega t$ at the sample time. Thus we wish to determine

$$\max_{\phi} [\sin(\phi + \Delta\phi) - \sin\phi].$$

The value $\phi_0$ of $\phi$ that gives this maximum value may be determined by equating the derivative of “$\Delta \sin\phi$” with respect to $\phi$ to zero and solving for $\phi = \phi_0$. This gives

$$\begin{aligned}\frac{d}{d\phi} \text{“}\Delta \sin\phi\text{”} &= \cos(\phi + \Delta\phi) - \cos\phi \\ &= \cos\phi\cos\Delta\phi - \sin\phi\sin\Delta\phi - \cos\phi \\ &= (\cos\Delta\phi - 1)\cos\phi - \sin\phi\sin\Delta\phi = 0\end{aligned}$$

which implies that

$$\begin{aligned}(\cos\Delta\phi - 1)\cos\phi &= \sin\phi\sin\Delta\phi \\ \tan\phi &= \frac{\cos\Delta\phi - 1}{\sin\Delta\phi} \\ &= \tan(-\Delta\phi/2)\end{aligned}$$

This last line may be obtained by writing $\Delta\phi$ in the preceding line as $2(\Delta\phi/2)$ and applying the double angle formulas for $\cos\Delta\phi$ and $\sin\Delta\phi$.

Then, of course,

$$\phi_0 = -\frac{\Delta\phi}{2}$$

and

$$\begin{aligned}\text{“}\Delta \sin\phi_0\text{”} &= \sin(\phi_0 + \Delta\phi) - \sin\phi_0 \\ &= \sin\frac{\Delta\phi}{2} - \sin\left(-\frac{\Delta\phi}{2}\right) \\ &= 2\sin\frac{\Delta\phi}{2}\end{aligned}$$

This formula actually gives the maximum or minimum value of "$\Delta \sin\phi$" depending on the sign $\Delta\phi$ (minimum if $\Delta\phi < 0$, maximum if $\Delta\phi > 0$) but note that

$$\min(\text{"}\Delta \sin\phi\text{"}) = -\max(\text{"}\Delta \sin\phi\text{"})$$

and we are really interested only in the *magnitude* of "$\Delta \sin\phi$." Hence

$$\max_{\phi}|\bar{f}_e| = \frac{6\sin\theta}{\Delta t}\max_{\phi}|\text{"}\Delta \sin\phi\text{"}|$$

$$= \frac{6\sin\theta}{\Delta t}\left(2\sin\frac{\omega\Delta t}{2}\right) \text{ for one-way doppler} \quad (9)$$

It is easily shown that the spin modulation effect on two-way doppler is just twice the effect on one-way doppler (except for the turnaround ratio, which for our purposes is negligible). Hence

$$\max_{\phi}|\bar{f}_e| = \frac{12\sin\theta}{\Delta t}\left(2\sin\frac{\omega\Delta t}{2}\right) \text{ for two-way doppler} \quad (10)$$

Table 1 shows these expressions evaluated for several combinations of $\omega$, $\Delta t$ and $\theta$ that are of interest.

A comparison of the above prediction to reality may be made by consulting Fig. 8. It shows the one-way doppler residuals seen during the Helios 2 launch pass over a brief period just after the uplink tuning. As can be seen, the maximum deviation of the samples from the detrender line is very nearly the value predicted by the above theory, namely 6.3 Hz (see Table 1).

## IV. Summary and Conclusions

Tracking operations during the Helios 2 launch phase proceeded smoothly with two exceptions: (1) an antenna drive component failure at DSS 44 necessitated a brief departure from the planned antenna drive scheme, and (2) spurious signal acquisitions slightly delayed the carrier reacquisition after the transition from noncoherent to coherent downlink. Neither of these problems had a serious effect on the DSN's ability to provide good tracking data and reliable telemetry and command links to the spacecraft. On the whole, planning and preparation for the launch were thorough and sound, and as a result the launch phase operations may be judged a solid success.


## Acknowledgments

The author is grateful to the following persons for their assistance in the preparation of this report: A. Berman and R. Schlaifer, who checked for technical accuracy and made a number of helpful suggestions; M. Humnicky, R. Brady and G. Hiendlmeier, who provided valuable data; M. Cates and C. Darling who are responsible for the fine graphical illustrations; and F. Almon for her very fast and accurate typing support.

**Table 1. Maximum spin modulation effects on doppler**

| RPM[a] | $\Delta t$, s | $\Delta\phi$, deg | $\theta$, deg | Doppler mode | Max $f_s$, Hz | GMT[b] |
|---|---|---|---|---|---|---|
| 96.00 | 1 | 216.0 | 90 | 1-way | 11.4 | – |
| 87.95 | 1 | 167.7 | 90 | 1-way | 11.9 | – |
| 87.95 | 1 | 167.7 | 32 | 1-way | 6.3 | 06:33:00 |
| 50.34 | 10 | −58.0 | 90 | 2-way | 2.2 | – |
| 50.34 | 10 | −58.0 | 10 | 2-way | 0.4 | 08:00:00 |

[a]RPM = spacecraft spin rate in revolutions per minute.

[b]GMT (on January 15, 1976) at which the condition actually applied during the Helios 2 launch phase.

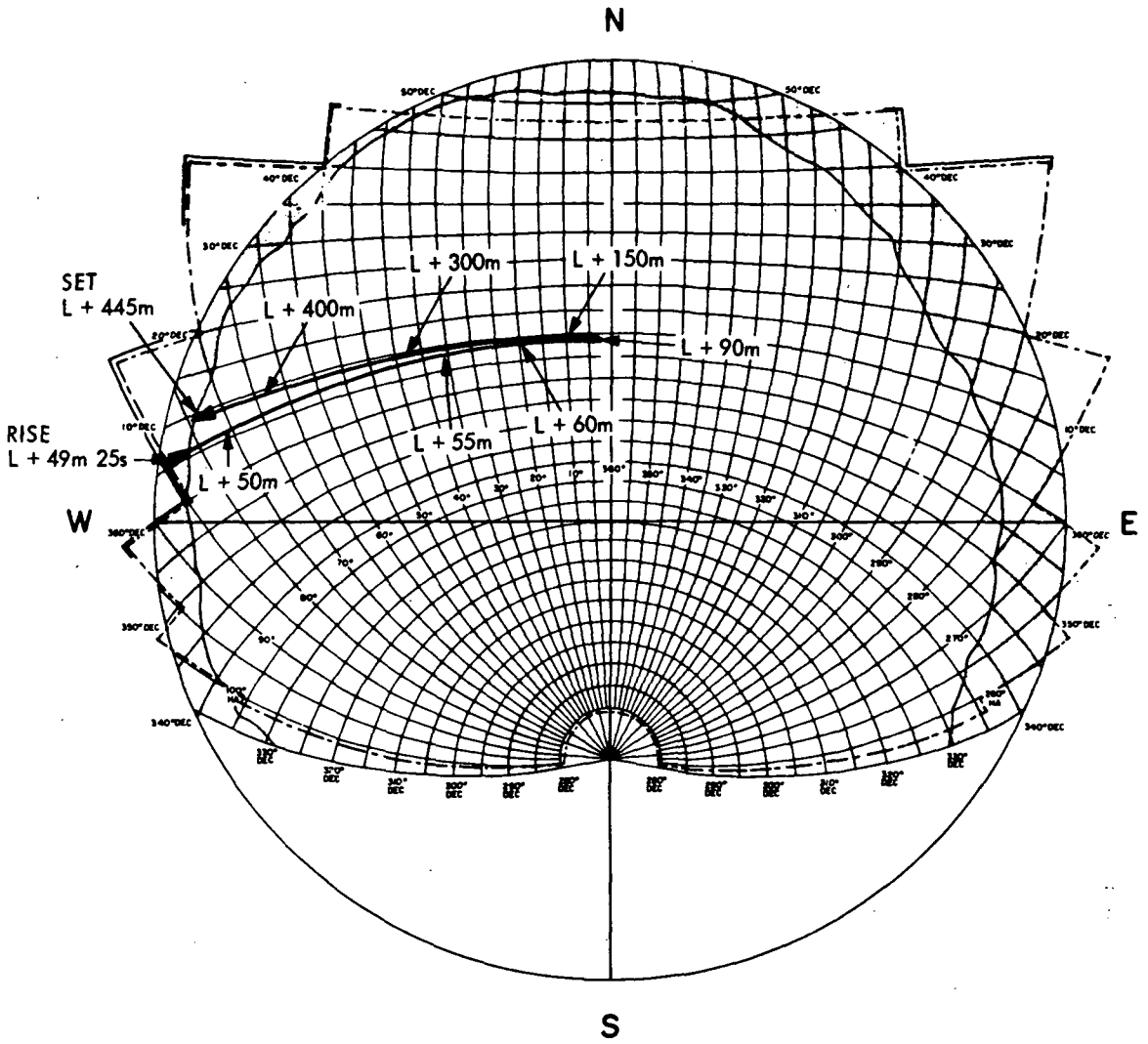


| ANTENNA LIMITS | | | | | |
|---|---|---|---|---|---|
| DEC | PRE | FINAL | HA | PRE | FINAL |
| DN | 047.400 | 047.992 | H1E | 305.400 | 304.886 |
| D2E | 039.540 | 040.404 | H2E | 285.280 | 284.850 |
| D3E | 019.520 | 020.432 | H3E | 275.250 | 274.788 |
| D4E | 359.530 | 000.320 | H4E | 265.450 | 264.840 |
| D5E | 349.630 | 350.376 | H5E | 260.160 | 258.876 |
| D6E | 336.550 | 337.440 | H6E | 257.600 | 257.264 |
| D2W | 39.500 | 040.374 | H1W | 054.450 | 055.175 |
| D3W | 019.500 | 020.414 | H2W | 074.500 | 075.314 |
| D4W | 359.500 | 000.314 | H3W | 084.750 | 085.290 |
| D5W | 349.600 | 350.370 | H4W | 094.220 | 094.918 |
| D6W | 336.550 | 337.434 | H5W | 099.320 | 100.262 |
| DS | 280.480 | 279.916 | H6W | 101.780 | 102.428 |

TIDBINBILLA STATION DSIF 42
HA-DEC COORDINATES
STEREOGRAPHIC PROJECTION
REV-1 JPL 3109 MARCH 69

Fig. 1. Stereographic projection of Helios-2 launch pass at DSS 42

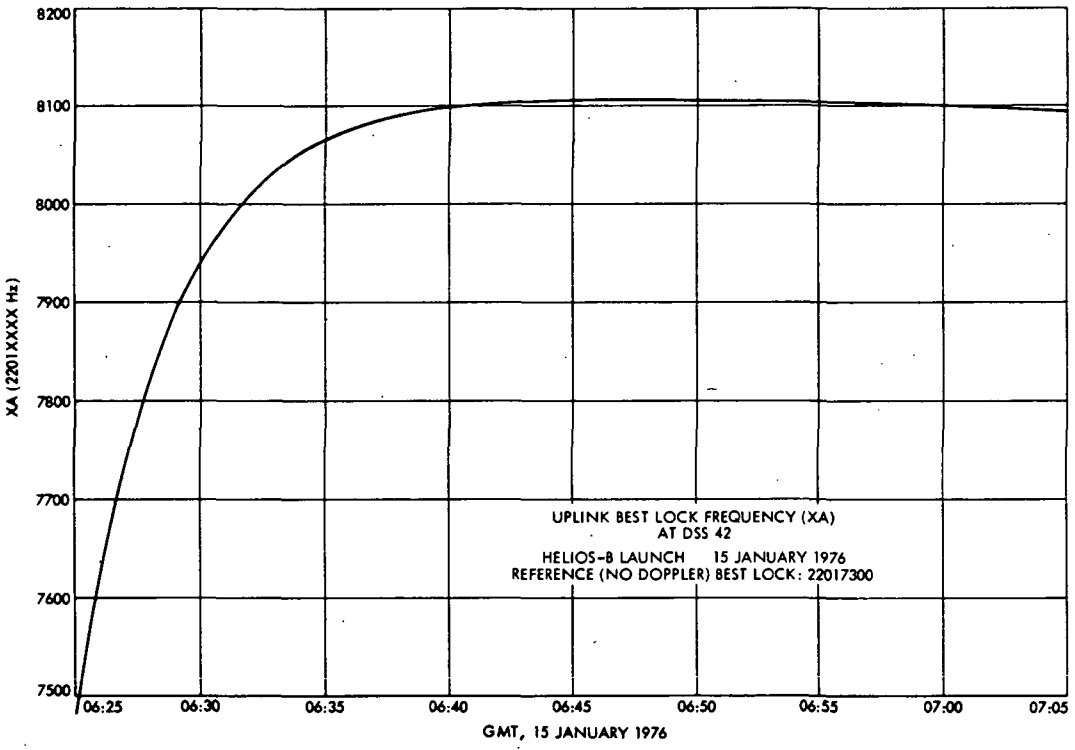


**Fig. 2. Uplink best-lock frequency (XA) at DSS 42**

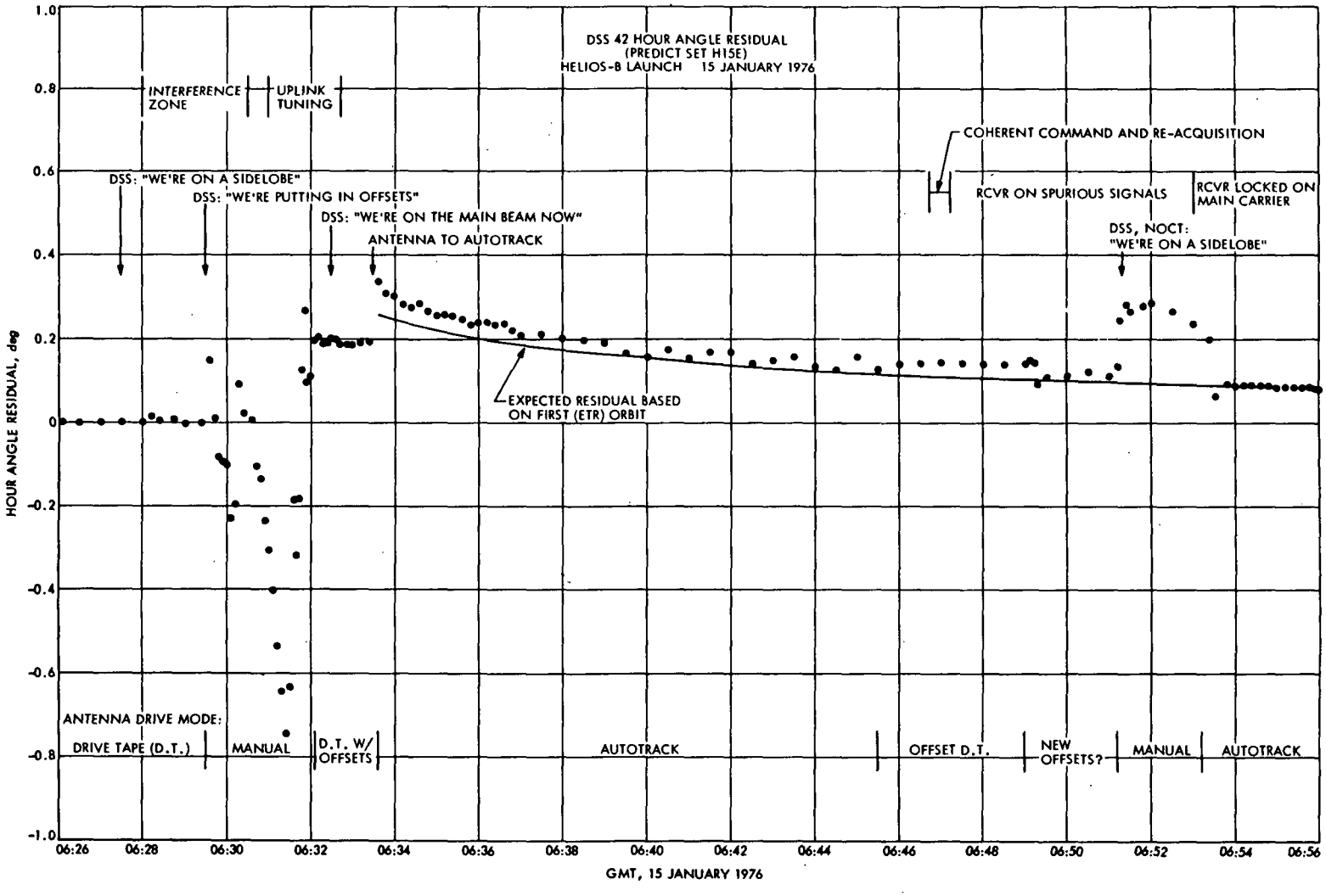


**Fig. 3. DSS 42 hour angle residual**

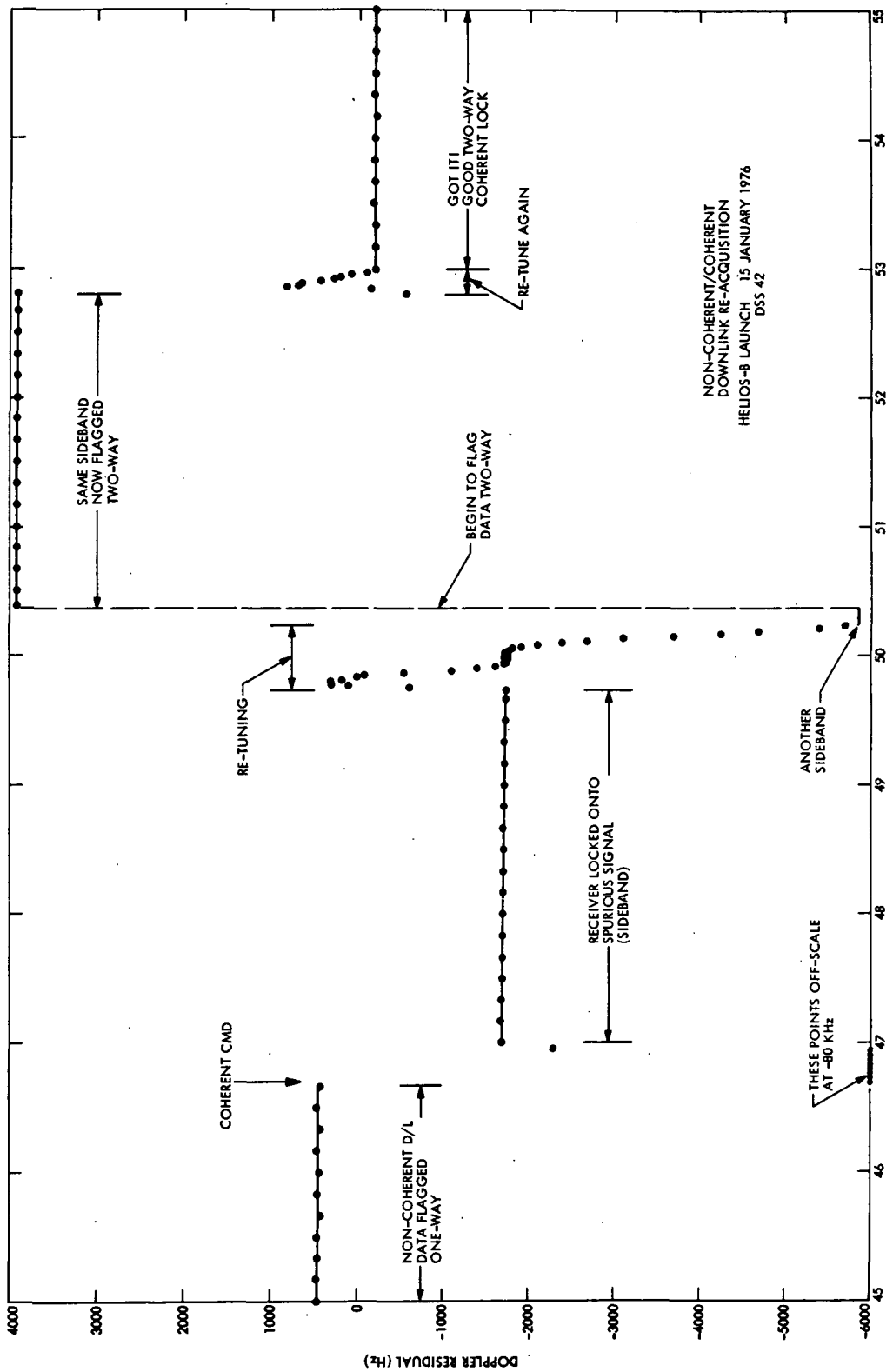


Fig. 4. Noncoherent/coherent downlink reacquisition at DSS 42

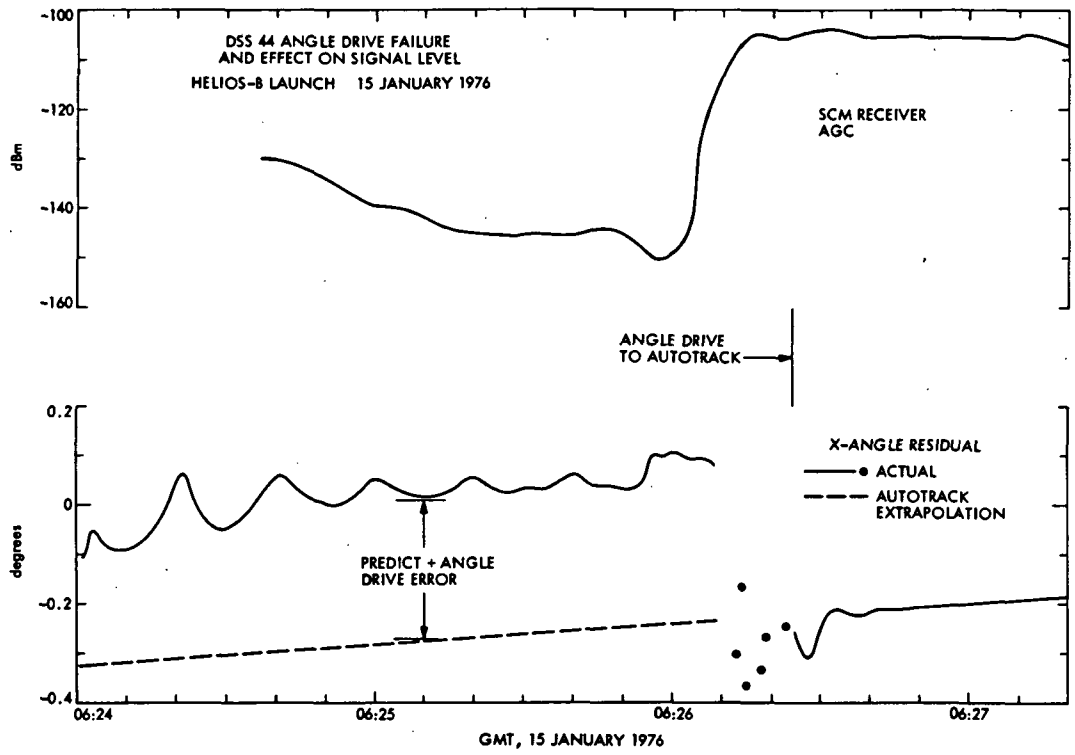


**Fig. 5. DSS 44 angle drive failure and effect on signal level**

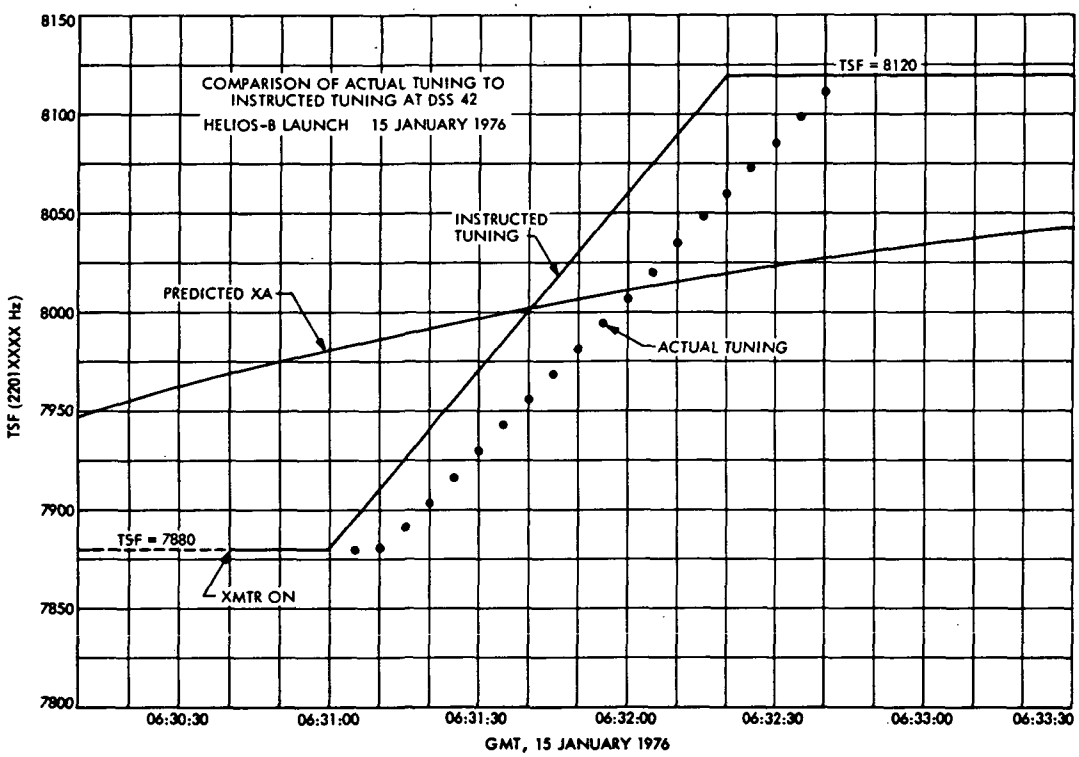


**Fig. 6. Comparison of actual tuning to instructed tuning at DSS 42**

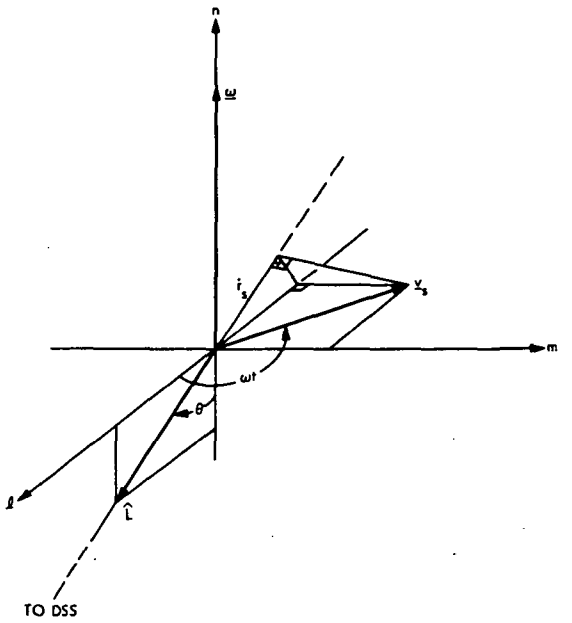


Fig. 7. Spin-modulation geometry

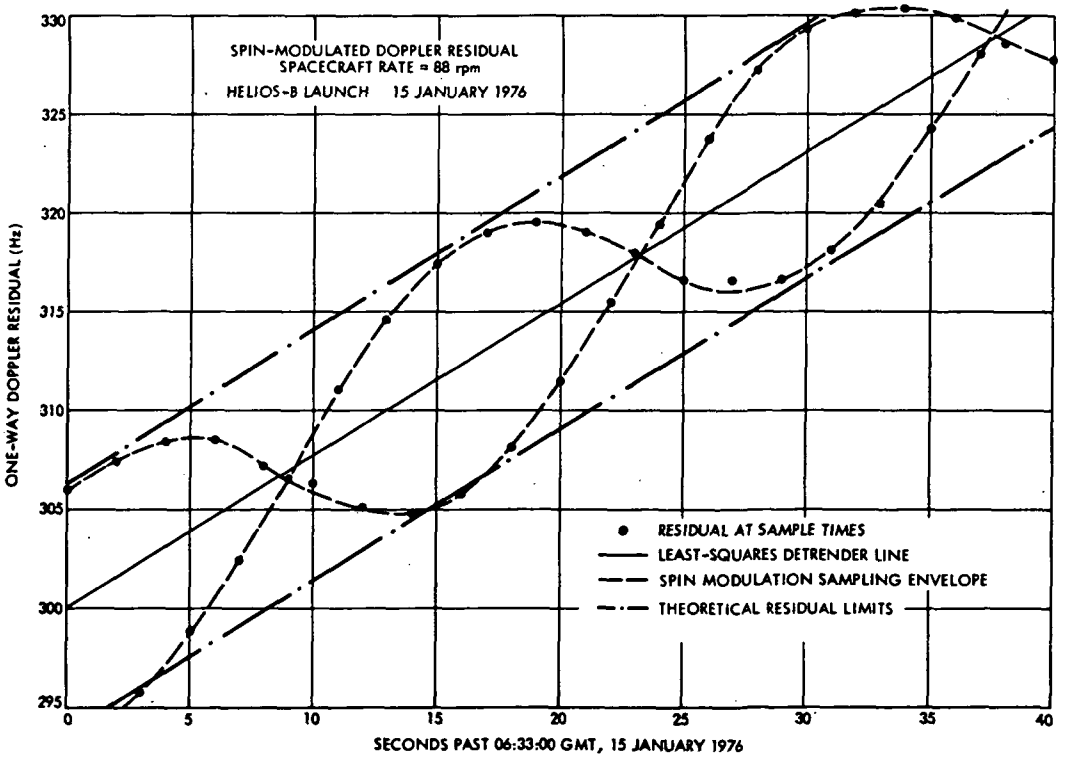


Fig. 8. Spin-modulated doppler residual

# Temperature Effects on Transmission Line Phase and Group Delay

H. R. Buchanan and A. L. Price
R. F. Systems Development Section

*An investigation of the phase and group delay stability of various coaxial and waveguide transmission lines has been initiated. The purpose of the test is to determine the feasibility of separating the receiver-exciter equipment from the tricone area of the 64-meter antenna.*

*Initial test results are reported from both controlled environment and field operating environment experiments.*

## I. Introduction

The increase in volume of electronic equipment mounted in the tricone area of the 64-meter antennas has led to a congested situation which calls for remedial action. Moving the Block IV Receiver-Exciter to a location remote from the tricone would be beneficial to this problem if the phase and group delay in the receiving system were not degraded. This current investigation relates to the phase and group delay thermal stability of various transmission lines that could be used for such a move.

## II. Test Plan

The investigation was planned in two phases: (a) a controlled temperature investigation of relatively short lengths of commonly used transmission lines, and (b) field measurements on relatively long lengths of semi-rigid coaxial cable exposed to the external environment.

The controlled temperature tests are being conducted by Western Automatic Test Services (WATS) of Sunnyvale, California, on approximately 30-meter lengths of the following transmission lines:

1/2-inch Spir-O-Line semi-rigid coax

SF 214 coax

F545-AA Flexco coax

41656 Heliax semi-rigid coax

EW71 elliptical semi-flexible waveguide

In this series of tests, the sample is placed in an environmental chamber whose temperature is raised in 5.5°C steps from -18°C to 66°C. At each temperature, the sample is left for one hour to stabilize and then phase, attenuation and voltage standing wave ratio (VSWR) are measured over a programmed frequency range using the network analyzer technique. Group delay is calculated. All data are recorded.

In addition, an improvised thermal chamber has been set up at JPL to test a series of seven-meter lengths of rigid transmission lines. The following lines will be tested:

WR112 waveguide

WR430 waveguide

7/8 EIA rigid coax

The test arrangement is shown in Figure 1, with WR112 waveguide as the test sample. As shown in Figure 1, the length (approximately 13 meters) of the reference path is equivalent to the test sample path so that differential phase measurements have a good resolution. Again, in this test, phase vs. frequency measurements are plotted on an X-Y recorder after the sample temperature has stabilized at each new temperature setting.

The field tests were conducted at DSS 13, the Venus Station, at Goldstone, California. A bundle of four 305-meter lengths of 1/2-inch Spir-O-Line, which has been in use for approximately six years, was selected for S-band testing. This bundle of four cables, fastened together with cable ties, was removed from the cable tray and placed atop the tray where solar heating could give a wider temperature variation. The far ends of two of the cables were connected together with a short length of RG-214, a solid dielectric, flexible coaxial cable, with double braid shields.

The looped back cables, a stable-frequency S-band source, temperature monitoring, and a Hewlett Packard Network Analyzer were interconnected as shown in Figure 2. This 610-meter length of Spir-O-Line, with a propagation constant of 0.83, contains approximately 5846 wavelengths at 2388 MHz, the test frequency. This corresponds to $2.1 \times 10^6$ electrical degrees. To reduce apparent phase changes due to frequency changes in the test source, the frequency stability should be high. (A stability of $2 \times 10^{-6}$ would limit errors from this source to approximately 1 degree.) The frequency source used was an exciter multiplier chain whose input frequency was derived from a rubidium frequency standard. Since all elements of the multiplier chain are mounted on a stabilized temperature cold plate, it is estimated the frequency stability of the source is better than $1 \times 10^{-6}$.

The temperature measurement was performed by a thermistor inserted into the cable bundle approximately 12 meters from the test position. This ensures that the thermistor records temperature rise due to solar heating.

## III. Test Results

The controlled temperature tests at WATS are being conducted. Some of the test results received thus far are shown in Figures 3, 4, 5 and 6 for 1/2-inch Spir-O-Line and SF 214 coax. The phase and group delay characteristics of 1/2-inch Spir-O-Line vs temperature are shown for S and X-band in Figures 3 and 4 respectively. In both cases, the group delay variation is less than 0.5 nanosecond over the -18° to 66°C temperature range. The average phase shift variation with temperature is -2.7 and -8.3 electrical degrees per degree Centigrade at 2.3 and 7.2 GHz respectively. This represents a temperature coefficient of 23.6 parts per million (ppm)/°C.

Of particular interest however is an anomaly which is evident in Figures 3 and 4 in the 27° to 32°C range. This appears to be related to a transient phase characteristic also noted in the field tests. The preliminary conclusion is that some type of significant physical change occurs in the Spir-O-Line cross-section over certain transient temperature conditions.

Test results for SF 214 coax at S-band are given in Figure 5. The average group delay over the -18° to 66°C temperature range is 153.5 nanoseconds with a maximum variation of two nanoseconds. The phase shift variation with temperature is -47.3 degrees electrical per °C at 2.3 GHz. This represents a temperature coefficient of 326 ppm/°C.

The variation of attenuation with temperature of the Spir-O-Line and SF 214 cables is given in Figure 6.

The field tests were conducted at DSS 13. After several day-night cycles of continuous recording, observation of the data points to several conclusions: (1) Over a very limited temperature range (2.5 - 7.5°C), the phase stability of the cable appears to be approximately 8 parts per million per degree Celsius; (2) At temperatures near 0°C, the rate of differential phase change increases dramatically with changes as great as 255 degrees of phase for a decrease in temperature from 7.5 to 0°C. This "transition" temperature was approximately repeatable with some hysteresis being observed; (3) As the cable is

cooled from approximately 25°C, a reversal in the direction of changes in the electrical length occurs at approximately 9°C, with reversal recurring at approximately 9°C as the cable is warmed from near 0°C. Figures 7, 8 and 9 illustrate the data from which these three conclusions were drawn.

The two principal components of the differential phase changes in this coaxial cable appear to be the physical differential length changes caused by the different thermal coefficients of expansion of the copper inner and aluminum outer conductor and the changes in the dielectric constant of the high density polyethylene inner conductor support. It is theorized that the reversals are caused by one of the principal contributors, probably the physical changes, overpowering the other and reversing the slope. The "transition" phenomena could well be caused by changes in characteristic impedance as the stress is relieved either by transverse or longitudinal movement of the center conductor.

Spir-O-Line semi-rigid coaxial cable is constructed with a copper inner conductor supported by a bundle of six semi-ellipsoidal hollow high density polyethylene tubes. Around the tube bundle is an outer conductor of aluminum with a black polyethylene jacket over all. The recommended connectors for this cable grip the outer conductor firmly while allowing the inner conductor to slip in a basket arrangement. Calculations indicated that, if the differential expansion stress were all relieved by longitudinal movement, the differential physical length of the cable would change approximately 0.5 cm/°C for the 610-meter length. The connector was removed from one end of the cable and a dial indicator was affixed in such a manner as to grip the outer conductor firmly while bearing on the inner conductor. After several day–night cycles, the total differential movement observed was 0.01 cm. Apparently stress is relieved by transverse as well as longitudinal movement, with transverse movement representing almost all the movement.

Another pair of cables, with similar lengths, were tested in an identical test set-up to check for uniqueness in the first pair. This second test disclosed that the "transition" phenomena noted with the first pair did not occur with the second pair. However, the phase reversal noted at approximately 9°C on the first pair was observed on the second pair although not at the same temperature. The average phase stability of the second pair of cables was also superior to the first pair.

The different test results indicate that the manner in which connectors are installed, and the past operational history of the cable, are also factors in differential phase stability.

## IV. Future Plans

Further testing of other cable and waveguide types is in process and will be reported on at a later date. Additional tests at DSS 13 are planned to ascertain what performance can be expected from typical cables assembled in the field in accordance with the manufacturer's instructions.

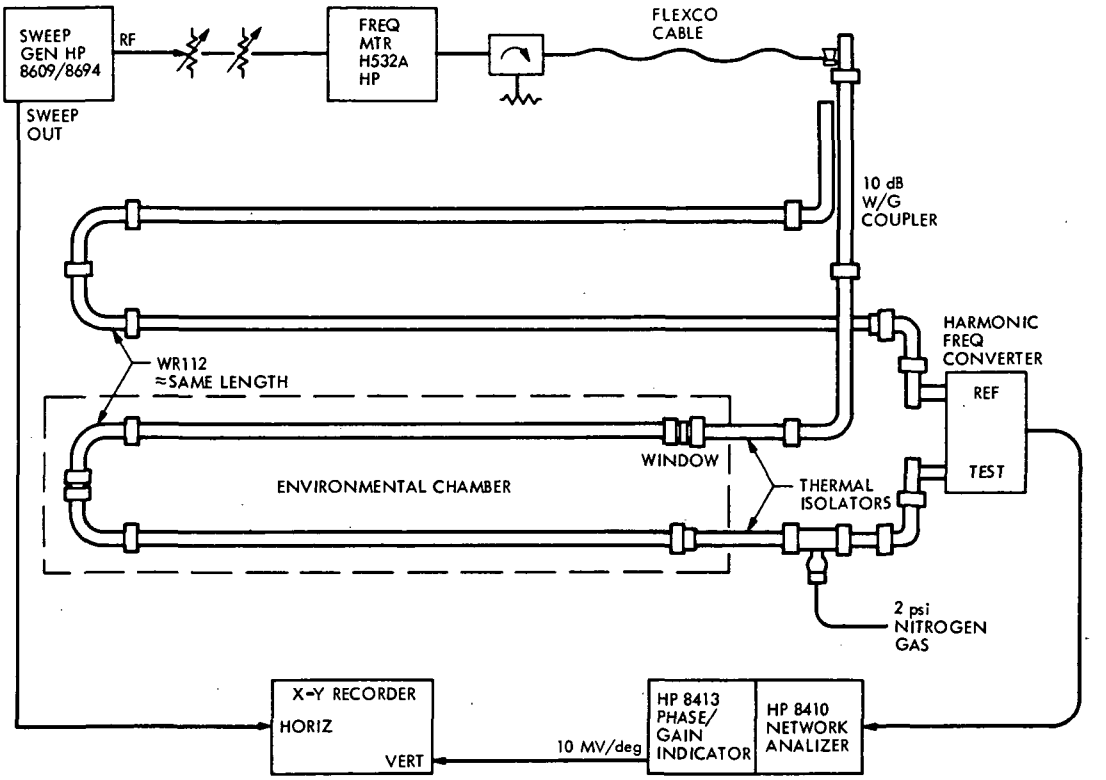


Fig. 1. Test configuration phase stability vs. frequency/temperature

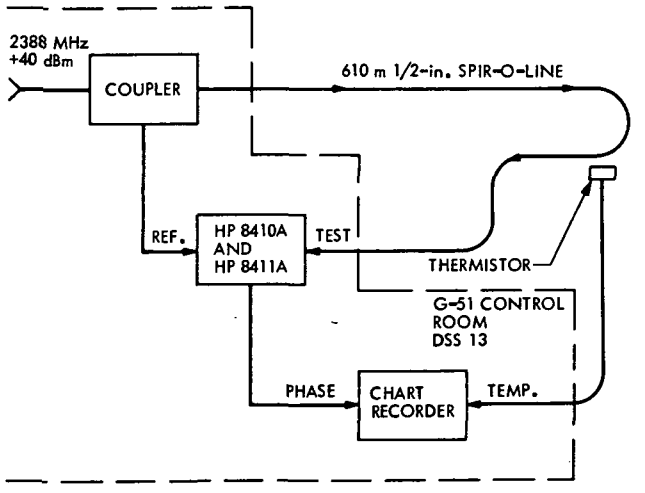


Fig. 2. Field test set-up, differential phase vs. temperature

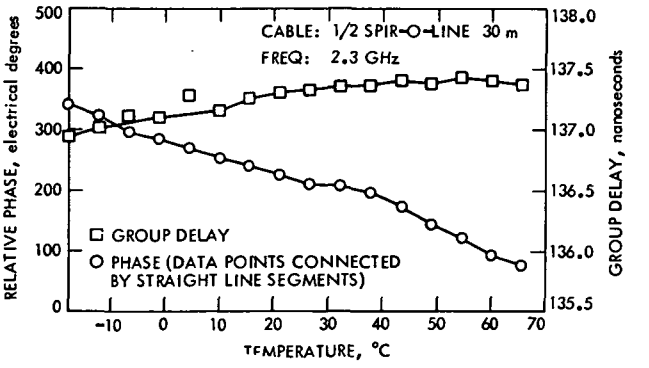


Fig. 3. Phase and group delay vs. temperature (cable: ½ Spir-O-Line; frequency: 2.3 GHz)

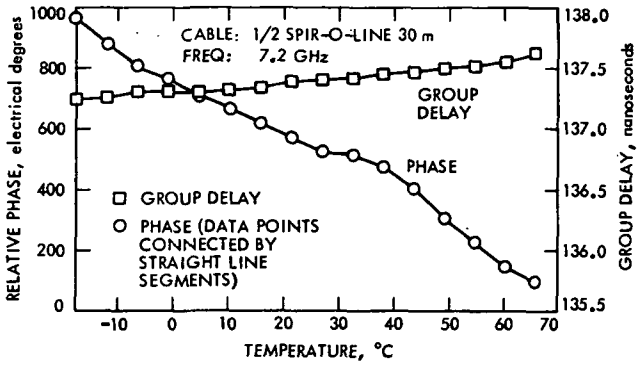


**Fig. 4. Phase and group delay vs. temperature (cable: ½ Spir-O-Line; frequency: 7.2 GHz)**

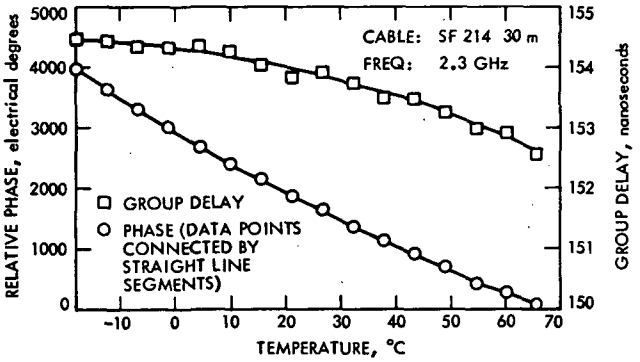


**Fig. 5. Phase and group delay vs. temperature (cable: SF 214; frequency: 2.3 GHz)**

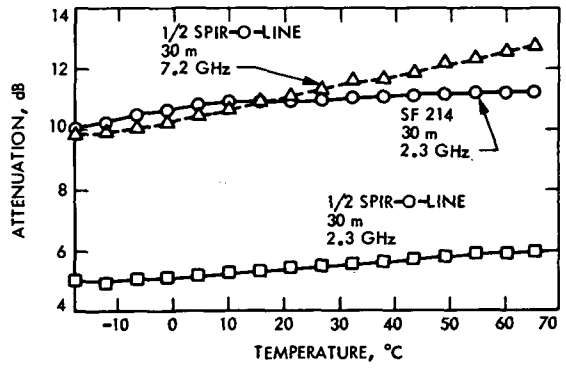


**Fig. 6. Attenuation vs. temperature**

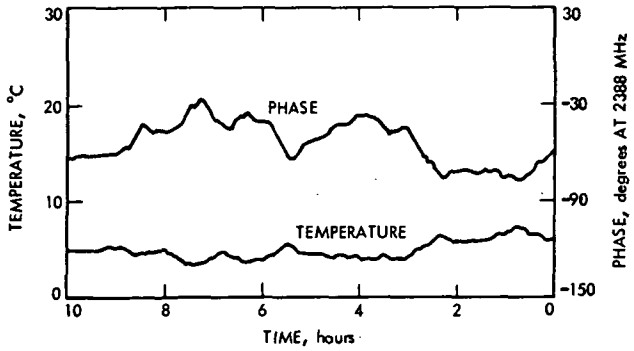


**Fig. 7. Differential phase, illustrating anticipated phase vs. temperature**

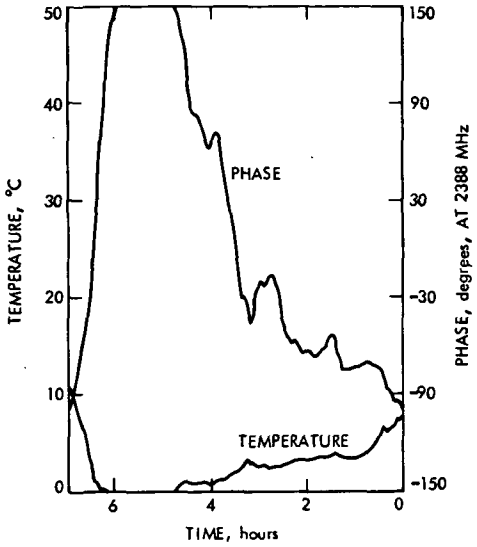


**Fig. 8. Differential phase, illustrating "Transition" phenomena at temperatures near 0°C**

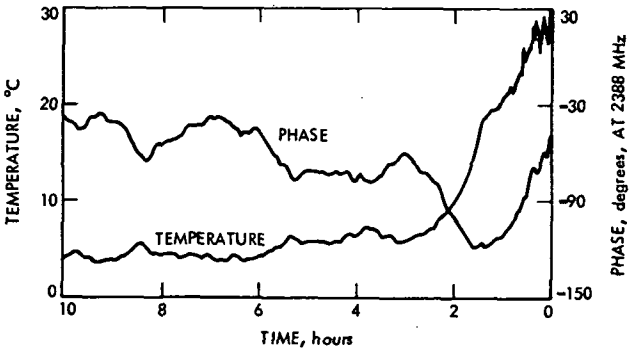


**Fig. 9. Differential phase, illustrating phase reversals with temperature changes**

# Life Cycle Costing of Long-Term Capability With a Discount Rate

E. C. Posner
TDA Planning Office

*This article studies life-cycle costing for a capability needed for the indefinite future. The two costs considered are reprocurement cost and maintenance and operations (M&O) cost. The reprocurement price is assumed known, and the M&O costs are assumed to be a known function of the time since last reprocurement, in fact an increasing function. The problem is to choose the optimum reprocurement time so as to minimize the quotient of the total cost over a reprocurement period divided by the period. Or one could assume a discount rate and try to minimize the total discounted costs into the indefinite future. It is shown that the optimum policy in the presence of a small discount rate hardly depends on the discount rate at all, and leads to essentially the same policy as in the case in which discounting is not considered. An algorithm for finding the optimum reprocurement time is presented as implemented in an MBASIC program.*

## I. Introduction

Suppose that one is planning to provide a capability into the indefinite future. The initial procurement cost is given. In addition, the annual maintenance and operations costs are known and are a nondecreasing function of the time since the initial procurement. One has the option of replacing the equipment at the original price at any time, thus reverting to lower maintenance costs. However, costs in the future are discounted at a constant nonnegative rate. The total discounted cost of future procurements and maintenance and operations costs is called the Life-Cycle Cost Increment. The idea is to choose the reprocurement time so as to minimize this Life-Cycle Cost Increment. It is shown that as the discount rate approaches zero, the optimum reprocurement time approaches a limit, as does the minimum Life-Cycle Cost Increment divided by the discount rate. This ratio is shown to be a decreasing function as the discount rate increases. The procurement time limit is the optimum reprocurement time for zero discount rate, where the goal is to minimize the Life-Cycle Cost Rate, the average future expenditure per year. Finally, the limit of the minimum Life-Cycle Cost Increment divided by the discount rate is the minimum of the Life-Cycle Cost Rate. An MBASIC program has been designed and used to define optimum policies when one has the option of procuring "better" equipment, which perhaps costs more

but results in lower maintenance and operations costs. The purpose of this article, then, is to create a framework for considering life-cycle costing with a discount rate, and, specifically, to show that the choice of discount rate does not materially affect optimum policy, but rather affects only the figure computed for discounted future costs. This latter cost is essentially given in arbitrary units, however, and we shall show how the proper units of life-cycle cost can be found.

The model of this paper is not overly typical of the DSN, which operates in an atmosphere of changing technology and new capability. Instead, we assume that we must provide a capability "forever." That capability is provided by a subsystem which costs $P$ dollars to procure, and will always cost $P$ dollars to procure. (The effect of inflation will be discussed shortly.)

Now comes the least certain assumption of this article. We assume that we know the M&O (maintenance and operations) cost rate for the subsystem (and assume this cost is independent of any other decision made). More particularly, the M&O cost rate in dollars/year depends on the age of the subsystem, i.e., the time since it was last reprocured. This function $M(t)$ is assumed to be nondecreasing with time, certainly a reasonable assumption. When $M(t)$ starts getting too large, we would reprocure at price $P$ and start off again at the initial low M&O cost $M(0)$.

Now consider the discount rate $\alpha$, a nonnegative number. Our model is built so that $\alpha = 0$ corresponds to not having a discount rate, and the definition of life cycle cost must then change. The discount rate $\alpha$ should represent the "social discount rate," the value of money for social investment. Thus, $\alpha$ might be, say, 2%, but should not be nearly as high as the inflation rate; that is, it should not be near 8%. We have assumed the reprocurement price $P$ is constant forever, and also that $M(t)$ starts off again at the old $M(0)$, no matter how long we wait to reprocure. In other words, we have removed inflation from the picture, which explains the small values of $\alpha$. Those who do not like to discount at all will be pleased to learn that the value of $\alpha$ in the problem considered here hardly matters (once $\alpha$ is small), and leads to the same policies as in the case of no discounting.

For mathematical convenience, and because the money market works that way, we are using "continuous compound interest." That is, the value of $P$ dollars discounted time $t$ years in the future is $Pe^{-\alpha t}$. For integer $t$, "classical" discounting would use $P/(1+\alpha)^t$ instead, which is "annual discrete discounting." The relevant comparison is thus $e^{\alpha t}$ vs $(1+\alpha)^t$. If discrete discounting is the policy, but continuous is used for mathematical convenience, a small discrepancy results. For example, for $\alpha = 2\%$ discrete, the correct continuous discount rate, say $\alpha'$, to use would be 1.98%. For $\alpha = 20\%$, the highest rate considered in this article, $\alpha' = 18.2\%$. We shall ignore this distinction from now on, but have mentioned it because of the Truth in Lending Act.

We assume that we have just paid $P$$ for a new subsystem. Let us also assume that we have decided to buy an identical replacement subsystem every $T$ years; thus $T$ determines the policy. Note that we can restrict ourselves to considering only such periodic policies, since if it is wise to replace after the first $T$ years it is always wise to do so because every reprocurement starts the same process over.

When $\alpha > 0$, the Life-Cycle Cost Increment for policy determined by $T$ is the total future costs, reprocurement plus M&O. But when $\alpha = 0$, we define instead the Life-Cycle Cost Rate (the other would be infinite) as the total cost (M&O plus reprocurement) over period $T$, including the reprocurement at price $P$ at time $T$ but excluding the original procurement. This number is then made into a cost rate by dividing by the period $T$. It will turn out that the minimum Life-Cycle Cost Increment, when multiplied by the discount rate $\alpha$, approaches the Life-Cycle Cost Rate as $\alpha$ approaches 0. Thus, the proper units when discounting should be dollars per year, using the above normalization. Even though the Life-Cycle Cost Increment itself is in dollars, those dollars are really in a sense arbitrary units. This will be made more believable by our convergence results, to be given below.

## II. Determining Life Cycle Cost

We first need the equation which displays the fact that if we reprocure at time $T$, we start over with $M(0)$ as the maintenance rate. Let $C_\alpha(T)$ be the Life-Cycle Cost Increment when $\alpha > 0$. Then

$$C_\alpha(T) = \int_0^T e^{-\alpha t} M(t)dt + e^{-\alpha T}[P + C_\alpha(T)], \alpha > 0 \tag{1}$$

(the "Renewal Equation"). The $e^{-\alpha t}$ term in the integral discounts the M&O cost. After one period of length $T$, we reprocure at price $P$ and start over (renew) at Life-Cycle Cost Increment $C_\alpha(T)$. However, the cost $P + C_\alpha(T)$, be-

ing deferred $T$ years, is discounted by $e^{-\alpha T}$. We solve for $C_\alpha(T)$ to find

$$C_\alpha(T) = \left[\int_0^T e^{-\alpha t} M(t)\, dt + e^{-\alpha t} P\right] \Big/ (1 - e^{-\alpha t}),\ \alpha > 0. \tag{2}$$

When $\alpha = 0$, let $C_{(0)}(T)$ be the Life-Cycle Cost Rate. Then straightforward calculation produces

$$C_{(0)}(T) = \frac{1}{T}\left(P + \int_0^T M(t)dt\right). \tag{3}$$

Equation (1) shows that $C_\alpha(T)$ and $C_{(0)}(T)$ are differentiable functions of $T$ in $T > 0$:

$$C'_\alpha(T) = \frac{M(T) - \alpha\,[P + C_\alpha(T)]}{e^{\alpha T} - 1},\ \alpha > 0. \tag{4}$$

Likewise, from Eq. (3),

$$C'_{(0)}(T) = \frac{M(T) - C_{(0)}(T)}{T}. \tag{5}$$

Thus, if $C_\alpha(T)$ and $C_{(0)}(T)$ have a minimum in $T > 0$ (note that both are $+\infty$ when $T = 0$), then the minimum occurs at a stationary point, one where the derivative is 0. Thus, at a minimum,

$$C_\alpha(T) = \frac{M(T)}{\alpha} - P,\ \alpha > 0; \tag{6}$$

$$C_{(0)}(T) = M(T). \tag{7}$$

Define $C_{(\alpha)}(T)$ as $\alpha C_\alpha(T)$ for $\alpha > 0$, and call it the "Normalized Life Cycle Cost Increment." Then (6) and (7) become

$$C_{(\alpha)}(T) = M(T) - \alpha P,\ \alpha \geqq 0. \tag{8}$$

It will be shown in the next section that either $C_{(\alpha)}$ has no stationary point in $T > 0$ because it decreases forever, or else has a unique stationary point which is the minimum sought for.

Let us stop to study an example, which illustrates the results of the next section. Let $M(T) = kt$ for $t \geq 0$ ($k$ in dollars/yr$^2$). Then we can evaluate $C_\alpha(T)$ and $C_{(0)}(T)$ exactly:

$$C_\alpha(T) = \frac{(k/\alpha^2)\,(1 - e^{\alpha T} - \alpha T e^{-\alpha T}) + e^{-\alpha T} P}{1 - e^{-\alpha T}}, \tag{9}$$

$$C_{(0)}(T) = \frac{1}{T}\left(P + \frac{kT^2}{2}\right). \tag{10}$$

Then $C_{(0)}(T)$ has zero derivative, and thus its minimum, at

$$T_{(0),min} = \sqrt{\frac{2P}{k}}, \tag{11}$$

with associated Minimum Life Cycle Cost Increment

$$C_{(0),min} = \sqrt{2Pk}. \tag{12}$$

For $\alpha = 0$, we find, differentiating (9), that the minimum Life Cycle Cost Increment $C_{\alpha,min}$ is achieved at $T_{\alpha,min}$, where

$$\alpha T_{\alpha,min} + e^{-\alpha T_{\alpha,min}} = 1 + \frac{\alpha^2 P}{k}. \tag{13}$$

Equation (13) does indeed have a unique solution in $T > 0$, since the function $\alpha T + e^{-\alpha T}$ is increasing in $T > 0$. For $\alpha \to 0$, we can show

$$T_{\alpha,min} = \sqrt{\frac{2P}{k}} + \frac{P\alpha}{3k} + O(\alpha^2), \tag{14}$$

so that $T_{\alpha,min} \to T_{(0),min}$ as $\alpha \to 0$.

And

$$C_{\alpha,min} \sim \frac{\sqrt{2Pk}}{\alpha}, \tag{15}$$

so $\alpha C_{\alpha,min} = C_{(\alpha),min}$ (definition) does indeed converge to $C_{(0),min}$. More tedious analysis would even show that $C_{(\alpha),min}$ is $C_{(0),min}$ plus $\alpha$ times a negative constant plus terms in $\alpha^2$ or higher, as $\alpha \to 0$, since in fact $C_{(\alpha),min}$ is shown in the next section to be a decreasing function of $\alpha$ as $\alpha$ increases, for all $\alpha$.

## III. Key Results

This section lists key results without proof; proofs are found in Ref. 1. The proofs are not esoteric, merely using the fact that $e^{\alpha t} - 1$ looks like $\alpha t$ as $\alpha \to 0$. It is assumed that the maintenance cost rate function $M(t)$ (dollars/yr) is continuous nondecreasing. Also, $P$, the purchase price, is greater than 0. The results below are true for all $\alpha \geq 0$, including $\alpha = 0$, the case of no discounting.

*Result 1:* $C_{(\alpha)}(T)$ is either decreasing for all $T$ ("minimum at $\infty$") or has a unique minimum $T_{\alpha,opt}$, with

minimum $C_{(\alpha)}(T_{opt}) = C_{(\alpha),min}$, which is positive. For convenience of writing, we allow $\infty$ to be a minimum to avoid having to separately consider the special case in which $C_{(\alpha)}(T)$ decreases forever.

*Result 2:* $C_{(\alpha)}(T)$ is decreasing to the left of its minimum and increasing to the right of it.

*Result 3:* $C_{(\alpha)}(T)$ approaches $\infty$ as $T$ decreases to 0. As $T \to \infty$, $C_{(\alpha)}(T)$ may or may not be bounded.

The next result is useful in obtaining a convenient algorithm for finding $T_{\alpha,opt}$.

*Result 4:* $C_{(\alpha)}(T)$ is convex upward to the left of $T_{\alpha,opt}$.

*Result 5:* $T_{\alpha,opt}$ is increasing in $\alpha$ as $\alpha$ increases, when $T_{\alpha,opt}$ is finite. When it is infinite for one $\alpha$, it is infinite for larger $\alpha$.

*Result 6:* $C_{(\alpha),min}$ is decreasing in $\alpha$ as $\alpha$ increases, and approaches $M(0)$ as $\alpha \to \infty$, where $M(0)$ is the maintenance cost rate at time 0.

The following are the two key results of this article. Result 7 shows that the optimum reprocurement time for small discount rate $\alpha$ is close to the optimum reprocurement time for zero discount rate. Result 8 shows that the minimum Normalized Life-Cycle Cost Increment $C_{(\alpha),min}$ for $\alpha > 0$ approaches the minimum Life-Cycle Cost Rate $C_{(0),min}$ as the discount rate $\alpha$ decreases to 0. Result 8 is the hardest result of this article to prove.

*Result 7:* $T_{\alpha,opt} \to T_{0,opt}$ as $\alpha \to 0$.

*Result 8:* $C_{(\alpha),min} \to C_{(0),min}$ as $\alpha \to 0$.

In fact, $T_{\alpha,opt}$ and $C_{(\alpha),min}$ are continuous functions of $\alpha$ in the region $\alpha \geq 0$, and Results 7 and 8 are the important special cases. What they mean is that the optimum policies for small $\alpha$ are close to the optimum policy for those who do not discount. The "discounters" get different answers from the "nondiscounters" only because they have failed to normalize $C_\alpha(T_{\alpha,opt})$ into $C_{(\alpha)}(T_{\alpha,opt})$ by failing to multiply by $\alpha$. This normalization brings the minimum Life-Cycle Cost Increment to the more real units of dollars/year. The unnormalized Life-Cycle Cost Increment in dollars is really in arbitrary "$\alpha$-money units," even though the same word "dollars" is used. The results will be numerically illustrated in a particular instance in the next section.

## IV. Computing the Optimum

An interactive structured program for demonstration purposes has been produced in MBASIC according to the methodology of DSN Standard Practice 810-13, "Software Implementation Guidelines and Practices." The procedure to find $T_{\alpha,opt}$ first finds two times on either side of the optimum. This is easy to do because of Result 2, since we need only check the slopes—positive slope of $C_{(\alpha)}(T)$ means $T > T_{\alpha,opt}$, negative slope means $T < T_{\alpha,opt}$. Once we have "trapped" $T_{\alpha,opt}$, we converge to it (more precisely, we find a cycle time which is guaranteed to produce a cost within 0.5% of $C_{(\alpha),min}$) by taking advantage of the convexity Result 4. Full details on the procedure can be found in Ref. 1.

Figure 1 shows an exact output of the program. The variable TMAX is the largest cycle we are willing to consider, in this case 12 years—if $T_{\alpha,opt} > 12$ years, we use 12 years as the cycle (as a change from the value 50 years as declared before changes). The variable FINE is the quantization, for integration purposes, set as 1/4 year both for numerical reasons and because 3 months is considered the minimum time to which such life cycle policies can respond. This variable is not changed in the run shown. The variable BUMP is used in the sensitivity check within the format within the *'ed box—it is 1 year, unchanged by the user in this run. The variable DELTA, set at 2% (.02) in the program, is changed in this run to 0.5% (.005); it is the fractional accuracy we guarantee in $C_{(\alpha),min}$. The purchase price is $\$P$, entered as 12. Zero discount rate ALPHA was input. The maintenance cost rate $M(t)$ in \$/yr is entered as $1 + (X/24) \cdot [1 + (X/32)] = 1 + X/24 + X^2/(24 \cdot 32)$. (Here $X$ is time $t$ divided by FINE (FINE was 1/4) in order to agree with the definition of the array variable $M$ as indexed from 0 to TMAX/FINE.) This quadratic function was used as being possibly typical of the as yet untested real world.

The answer then is TOPT = 8 years, with minimum Life-Cycle Cost Rate \$3.61/yr. This value is accurate to 0.5%, but the accuracy of $T_{0,opt}$ is neither specified nor relevant —we are trying to control costs, not times. We also find that if we increase the reprocurement time from 8 years to 9 years, the cost rate goes up only 4¢/yr, to 3.65 \$/yr. Decreasing the cycle to 7 years raises the cost rate only 3¢/yr. Thus, the optimum is rather broad, which is a useful property. We also print the percent of the cycle costs that are M&O costs, in this case 58.5%. For the example under discussion, Fig. 2 graphs $C_{(0)}(T)$ vs $T$ to show this broad minimum. The graph was obtained from a modification

of the program under discussion. Figure 3 graphs $C_{(\alpha),min}$ for the above parameters, but with ALPHA varying from 0 up to an outrageous 20% per year. Note that $C_{(\alpha),min}$ decreases from 3.61 \$/yr at zero discount rate down to 2.34 \$/yr at 20% discount rate. At the more reasonable 2% discount rate, $C_{(.02),min}$ is 3.50 \$/yr, only 14¢/yr different. More important, the optimum cycle time $T_{\alpha,opt}$ produced by the program is 8 years, from ALPHA = 0 up to ALPHA = 0.1, and then fluctuates near 8 years (see Table 1). If the 8 years of 0 discount rate were used for 2% rate, the $C_{(.02),min}$ would be within 1% of the true minimum. Even at 20% discount rate, the use of 8 years instead of the 10.25 years of Table 1 produces an increase in cost of only 2%, as a run of the program with BUMP = 2.25 shows. Thus, there appears to be little reason to use positive discount rates for the particular infinite-horizon life cycle problem considered in this article.

## V. Allowing Purchase Price to Vary

There are of course situations where one has the option to lower M&O costs by paying more for the initial procurement (and thus for the reprocurements). Unfortunately, we don't always know exactly what the tradeoff is, but, in this section, we shall create an illustration in which we do know the tradeoff. We then find the best price $P$ to pay so that when we subsequently minimize the Life-Cycle Cost Rate, we obtain the overall minimum Life-Cycle Cost Rate. (But for $\alpha > 0$, the proper cost to minimize is $P + C_\alpha(T)$, or, what gives the same choice of $P$ and $T$, $\alpha P + C_{(\alpha)}(T)$.)

Suppose the tradeoff of purchase price $P$ vs maintenance cost rate $M(t)$ is given by

$$M(t) = t\left(1 + \frac{1}{P^2}\right). \tag{16}$$

For very low $P$, $M(t)$ is outrageous. As $P$ gets large, $M(t)$ settles down to $t$, so that very expensive "models" are not a good buy either. "Freshman Calculus" techniques show that $T_{0,opt}(P)$ is given, for a fixed $P$, by

$$T_{0,opt}(P) = P\left(\frac{2P}{P^2+1}\right)^{1/2} \tag{17}$$

with associated $C_{(0),min}(P)$ given by

$$C_{(0),min}(P) = \left[\frac{2(P^2+1)}{P}\right]^{1/2} \tag{18}$$

We seek the minimum of (18) as $P$ varies. It is readily shown to occur at $P = 1$ with value $C_{(0),best}$ given by

$$C_{(0),best} = 2. \tag{19}$$

From Eq. (17) with $P = 1$, we find that the best reprocurement time, $T_{0,best}$, is

$$T_{0,best} = 1. \tag{20}$$

In other words the best overall policy, the one resulting in minimum Life-Cycle Cost Rate when $P$ is allowed to vary, is to purchase units costing \$1 every (one) year.

We also used the computer program to vary $P$ and find the overall minimum of $C_{(0),min}(P)$. We found that $C_{(0),best}$ was 2 to within 5 decimal places, occurring at $P = 1$ to within 3 decimal places. It took 11 uses of the original program to obtain the answer, varying $P$ each time. Details are omitted.

## VI. Future Work

Future areas for investigation suggest themselves from the preceding sections. The most important is the problem of how to learn what the maintenance cost rate function $M(t)$ is. This problem can be considered a sequential estimation problem, as in Ref. 2.

Unfortunately, the use of a similar approach is currently hampered by the fact that it is difficult to assign M&O costs to particular subsystems or assemblies. Equally important, it is very difficult to tell what the tradeoff is between procurement price and M&O costs. For example, we don't yet know how much to pay for increased semiautomatic operability of DSN subsystems, because we do not know in enough detail how the M&O cost rate function $M(t)$ is built up.

In another vein, a rational policy on life cycle costing ought perhaps to take into account availability of the tracking station or Network. Thus, we could decide to lower $M(t)$ by increasing the probability of downtime. Or, for a given acceptable downtime, there would be a combined procurement specification and reprocurement time which results in lower overall costs.

Another area of investigation that could prove fruitful for the DSN involves modeling the M&O cost interactions

of the various subsystems at a tracking station, acting in concert. It seems clear that costs of maintenance and operations are not actually additive by subsystem. Thus, one may wish to consider a combined policy on procurement intervals that takes total station or network costs into account. The techniques could even be statistical in nature for a system the size of a DSN tracking station.

The various problem areas above are indicative of the kinds of things one might want to know when adopting a life cycle cost policy, whether for the "infinite horizon" idealization of this paper or for the case more typical of much of the DSN, the fixed life cycle case (usually defined as initial procurement cost plus 10-year undiscounted M&O cost).

## References


1. Posner, Edward C., "Life Cycle Costing with a Discount Rate," submitted to *Management Science*.
2. Lorden, G., "Sequential Tests for Exponential Distributions," in *The Deep Space Network*, Technical Report 32-1526, Vol. 5, pp. 82–90, Jet Propulsion Laboratory, Pasadena, Calif., Oct. 15, 1971.

Table 1. $T_{\alpha,\,opt}$ vs $\alpha$

| $\alpha$, % | $T_{\alpha,opt}$, years |
|---|---|
| 0 | 8.00 |
| 0.5 | 8.00 |
| 1 | 8.00 |
| 1.5 | 8.25 |
| 2 | 8.00 |
| 3 | 8.25 |
| 5 | 8.00 |
| 7.5 | 8.25 |
| 10 | 9.00 |
| 15 | 9.25 |
| 20 | 10.25 |

```
 LOAD 'MAINTLFCY'
>RUNH
MBASIC 12/10/75   17:25:37


ENTER CHANGES TO TMAX,FINE,BUMP,AND DELTA,IF ANY. THEN TYPE  CON
>TMAX=12,DELTA=.005
>CON

ENTER PURCHASE PRICE P:12

ENTER DISCOUNT RATE ALPHA:0

ENTER MAINTENANCE COSTS INTO ARRAY FROM 0 TO TMAX/FINE;USE M( )=
THEN TYPE  CON
>M(X)=1+(X/24)*(1+(X/32)) FOR X=0 TO 48
>CON


*****************************************************************************
*                                                                           *
* TOPT= 8.00 YRS                                                            *
* MIN COST: C(TOPT)= .361E+01 $                                             *
*                                                                           *
*                                                                           *
*  C(TOPT+1.00)= .365E+01 $                                                 *
*  C(TOPT-1.00)= .364E+01 $                                                 *
*                                                                           *
* 58.5 % OF LIFE CYCLE COST IS MAINTENANCE COST                             *
*                                                                           *
*****************************************************************************


MAINTLFCY OVER
```

**Fig. 1. Sample run**

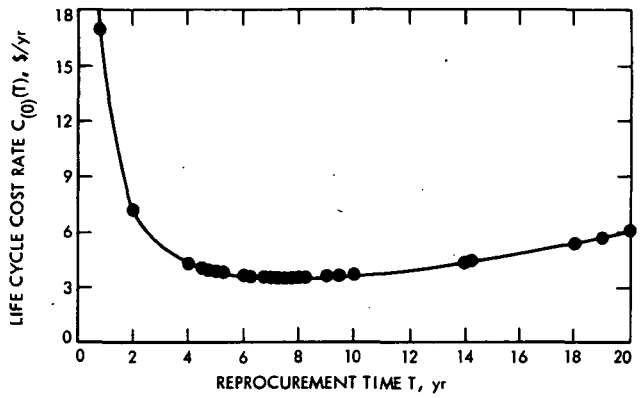


**Fig. 2. Life-Cycle Cost Rate vs cycle length**

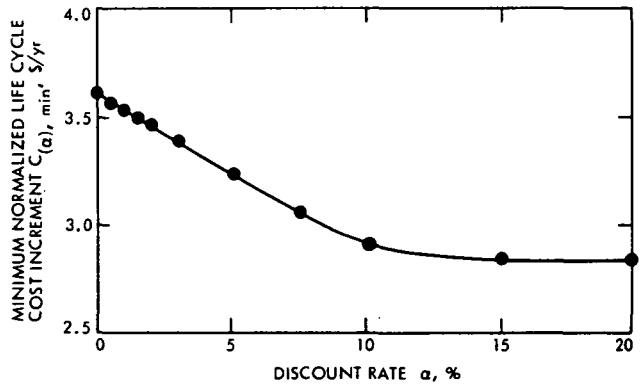


**Fig. 3. $C_{(\alpha),\,min}$ vs α**

# Computerizing Goldstone Facility Maintenance Data for Management Decisions

F. R. Maiocco and J. P. Hume
DSN Facility Operations Office

*This article is the result of a study done with a view to computerizing the facility maintenance management operations at the Goldstone Deep Space Communications Complex (GDSCC). It briefly describes the Data Management system in existence at the time the study was initiated and a proposed Automated system. Further, it gives results of development work to date, provides a few sample results and identifies other areas of work, some of which are currently in progress or in the planning stage.*

## I. Background

Several attempts were made in the past to improve the operational efficiency of the Goldstone Facility Maintenance (GFM) Work Control Center (WCC). Visits to other facilities and plant operations in the Southern California area were made. Management audits were conducted to identify information flow, functions performed, and various tasks required to coordinate and schedule the preventive maintenance, corrective maintenance and special work activities performed under direction of the GFM plant engineer.

## II. Justification of Recent Management Audits

The Deep Space Network (DSN) Facility Operations Manager is responsible for providing day-to-day support to facility installations and for providing special support to spacecraft missions and research and development (R&D) activities throughout the DSN. During the past few years DSN Management has been compelled to provide this support with reduced resources. Current indications are that this mode of operation will continue.

In addition to the above trend, one of JPL's long-range goals is to implement a Centralized Management Data Base system. The GFM support unit will be a user of this Data Base system and has recently provided to the Data Base designers estimates of GFM data requirements.

A further justification is to permit analytical assessment of manpower planning and budget estimating as demands for services vary in Cost Centers over a given planning horizon time. Such analyses will permit Cost Center managers to utilize modern management science techniques in arriving at efficient decisions.

## III. Existing GFM Data System

The current data system is a manual data acquisition, information handling, and processing system. The GFM data system consists of a preventive and corrective maintenance operation, a Maintenance Work Order system and a Work Request system.

The Preventive Maintenance (PM) file, which consists of approximately 1,500 line items, is maintained in a Cardex file system located in the WCC. Figure 1 depicts the Cardex file system, and Figure 2 is a sample card upon which is recorded both the static history information about a unique PM item and the transaction information which includes Maintenance Man-Hours (MMH), material costs and any special comments noted by the technician. In addition to the PM work, the WCC maintains a Maintenance Work Order (MWO) and a Work Request (WR) data system for approximately nine shops. This information is manually recorded on individual shop ledgers, 3 × 5 card files, personal ledger files in addition to the shop ledger files, a suspense file and a centralized secretarial file system. The MWO system encompasses corrective maintenance for those items which have PM numbers, and other minor maintenance jobs. The WR system is designed to handle major and expensive maintenance jobs or those jobs resulting in subcontracts. Figure 3 depicts a MWO form and Figure 4 is a WR form.

The current Data Base System is encumbered with a superfluous amount of paper work, a multiplicity of data recording which results in time delays for report generation, excessive man-hours spent in data recording, a higher potential for data errors, and inefficient data management, to name a few areas for improvement.

Once the assigned jobs are accomplished by the shop personnel, the shop leadman prepares a summary of activities performed by his shop and submits a report to the WCC on a Work Report form (Figure 5).

The data recorded on the forms, as shown in Figures 2–5, are manually transcribed to the various shop ledgers, card files and personal files prior to preparing any shop, material or management report required for decision making.

## IV. A Proposed Computerized System for the GFM Data Base

The overview of the GFM computerized Data Base System is shown in Figure 6. It basically indicates that all work scheduling, computations, and report generation will be performed by the computer with data input, work planning and job estimating done by the WCC personnel. One Data Base will be maintained rather than a multiplicity of data files. Key job statistics and transaction information will be entered into the computer by WCC personnel via a remote computer terminal (see Figure 7). All processing and report generation will be automated to provide near-real-time management reports.

The GFM Data Base which is currently being designed for computer implementation will serve two major users. One of the users will be JPL management personnel and the other group includes Goldstone Facility supervision, WCC planners and shop leadmen.

The type of data provided and information processing requirements of the two groups are somewhat diverse. Management on the one hand requires information about current operations and expenses; on the other hand, it requires information pertinent to workload and manpower planning for both short-term and long-term projects. The WCC planners and shop management personnel are more concerned with the daily, weekly, and monthly job scheduling, outstanding purchase requests, backlog of jobs and availability of craftsmen for workload planning.

Typical management reports required are as follows:

(1) Shop Work Schedules.

(2) Weekly Workload Summaries.

(3) Shop Backlog.

(4) Subcontractor Status Report.

(5) Material Budget Account.

(6) Monthly/Quarterly Expenditure Reports.

(7) Shop Workload Experience Report.

(8) Equipment History Report.

(9) Workload and Manpower Planning.

Computer input requirements necessary to facilitate the above reports are exhibited in Figures 8–12. The essential statistics of each maintenance activity, i.e., job number, man-hours and material costs, are input to unique computer files via the appropriate file format, for example, on a weekly basis. Once these basic data are stored in the computer, WCC or management reports can be generated by utilizing the special-purpose application programs to summarize, by shop, over a given time period, the man-hours and material costs expended, number of jobs completed, number of jobs in the shop backlog, etc.

As the GFM Data Base expands, statistical analysis can be performed on certain data in order to:

(1) Detect the expected number of emergency calls per shop.

(2) Detect abnormalities in types and frequency of repairs.

(3) Provide essential statistics to permit cost trade-offs on repair or buy decisions.

(4) Estimate trends in demands for services per shop.

(5) Estimate workload and manpower requirements.

(6) Determine energy consumption and other types of analyses normally not apparent in a manual Data Base System.

These types of features are desirable for DSN Facility Operations and substantial cost savings could be realized by improvements in the GFM operational efficiency.

Additional potential areas for improvement in facility operations are scheduling, manpower utilization, organization of data files, timeliness of management reports, accuracy of the data base, and planning and availability of more useful and pertinent information on overall facility operations.

## V. Status of the GFM Data Base

To minimize transition problems during the conversion to a Computerized Management Data Base System, implementation is taking place in phases.

The GFM automated system entails providing the computer with major blocks of information which contain a comprehensive set of data about Goldstone buildings, equipment, meters, type of maintenance activities, personnel, budgetary information, and the necessary application software required to process the Facility Data into meaningful Management Reports.

An input file generator program is required to input data to computer-generated files; housekeeping routines are necessary for file updating and querying the GFM data base files; and special-purpose application programs are necessary for generating management reports and analyses.

The File Generator Program is currently the GFM data base workhorse as it permits the user to create preventive maintenance files, maintenance work order files, work request files, an index file, utility meter static history files and meter transaction data files. History files maintain static information, whereas the transaction data files maintain data which change as a function of time.

Editor, edit-aid and sort programs assist the user in performing limited housekeeping, updating, and modifications of existing GFM files.

Application programs generated to date include a Utility Report program, an Energy Consumption Report and a Plot Routine. The Utility Report program provides monthly, last 3 months, last 6 months, last 12 months and year-to-date reports of electrical, liquified petroleum gas (LPG) and water usage. A plot option exists in the Utility Report program when the user requests a 6-month, 12-month or year-to-date report. As of 1 March 1976 the diesel fuel (DF) meters will be installed, software changes as required will be updated and the Utility Report will then include diesel fuel usage.

Recent interest by NASA resulted in a GFM Energy Consumption program being generated. This program allows the user to select an interval of time for which data are to be extracted from existing data files and then summarizes all utility consumption of electrical, LPG and DF in thermal units for a consolidated Energy Consumption Report.

## VI. Results of Development Work

Figure 13 is a monthly Utility Usage Report for December 1975. It identifies the power, water, LPG and diesel fuel meter location, meter number, monthly usage of the appropriate parameter being monitored and the percent change from the previous month for each meter.

Figure 14 is a 6-month report of total usage for each meter. It represents the period of July 1975 through December 1975 and identifies the meter location, meter

code, percent change during the two quarters, and total semi-annual consumption. During the generation of this latter report, but prior to printout, the user is questioned by the computer as to whether a plot of monthly usage is required. If the user responds by typing "yes," the computer automatically stores the monthly results for each meter in a temporary file. After printing the report as denoted in Figure 14, the computer informs the user that the data for plotting are stored in a temporary file and the user is instructed to load the plot routine for plotting the meter data.

The plot routine queries the user, meter by meter, by asking if the respective meter data are to be plotted. Figure 15 is a plot of the monthly electrical usage for the meter titled "Main Sub SCE" over the 6-month period noted above.

The annual (last 12 months) and year-to-date reports are similar in format, i.e., a two part report is generated. The first part of the report summarizes by meter the consumption during both the first half and second half of the year, and the total annual consumption for each parameter monitored. The second part of the report generates for the respective meters the quarterly consumption for the respective parameters. Should the user at the appropriate time inform the computer that monthly data should be saved for plotting, the computer, after printing the Annual Report, informs the user to load the Plot Routine to obtain plots of the appropriate meter's monthly trends. Figures 16 and 17 are respectively Part I and Part II of the Annual Utility Usage Report.

The DSN tracking facilities in general consume a considerable amount of energy, and since the recent energy crisis, it has become mandatory that JPL provide NASA with a report of Goldstone monthly energy consumption for the previous quarter.

Figure 18 is a copy of the Energy Consumption Report generated by the GFM Energy Consumption Program. Part I represents the monthly consumption in LPG, DF, and electrical power with the total monthly consumption converted to megawatt hours thermal units (MWHT). Column totals are presented for LPG, DF, electrical power and total MWHT. A second total in thousands (kilo) of dollars is displayed for the cost of electrical power. No costs are included for LPG or DF.

As a result of the above work, the following improvements in the Work Control Center's efficiency have been achieved:

(1) The Monthly Utility Usage Report, which consisted of approximately 15 pages, has been reduced to a maximum of 2 pages and a cover letter.

(2) Report preparation time, which took from 2 to 4 weeks, has been significantly reduced to basically computer access time.

(3) A reliable Energy Consumption Data Base has been established.

(4) Computation errors are basically non-existent and the accuracy of the reports is dependent on the accuracy of the data input to data files.

(5) Expanded capability exists in energy reporting not previously available in the manual recording system.

## VII. Planned Activities

There are a number of tasks either in the development or planning stage which are to be completed this fiscal year. The major tasks are identified as follows:

(1) Create Preventive Maintenance Static History and Transaction Data Files, Maintenance Work Order Files and Work Request Files for calendar years 75 through 76.

(2) Extend the capability of the File Generator Program to allow WCC users to create building, budget, procurement and personnel files.

(3) Develop and implement a scheduling algorithm that will establish optimum weekly and monthly shop schedules for Preventive Maintenance, Maintenance Work Orders and Work Requests.

(4) Develop and implement an updating algorithm for the Maintenance Work Order and Work Request Files.

(5) Investigate the application of Relational Data Base capabilities to the GFM Data Base System.

(6) Extend development work of the preliminary workload and manpower planning model to accommodate time-varying demand statistics and manpower constraint in order to estimate budgetary requirements for management decisions.

(7) Develop procedures and algorithms for estimating parameters utilized in the workload and manpower planning model.

(8) Develop and implement a preliminary budget planning model.

(9) Develop and implement the GFM Expenditure Report.

(10) Provide consulting support to GFM personnel with respect to the above procedures.

## VIII. Conclusion

The GFM on-line computerized management system is an important technique for increasing the Goldstone Facility Maintenance Work Control Center efficiency and will play a vital role in the plant engineering and facilities management at Goldstone. In the near future, we expect optimal scheduling, improved facilities management by exception and objective planning, better manpower utilization, workload analysis and budget planning.

At this point in time of reducing DSN resources, rising labor and material costs, the DSN manager and GDSCC facilities supervision must use every management science tool available. By taking advantage of advances in computer technology and utilizing special-purpose GFM application programs as previously noted, the GDSCC Facility Support Unit will improve its operational efficiency.

Fig. 1. Cardex file of PM data

**ELECTRICAL DEPARTMENT SWITCH GEAR MAINTENANCE RECORD**

| | | |
|---|---|---|
| LOCATION | MOTOR STARTER | FUSE SIZE |
| I D NO. | NEMA SIZE | CONTROL TRANS. |
| L A NO. | COIL CAT. NO. | KVA VOLTAGE |
| MANUFACTURE | COIL VOLTAGE | MAKE |
| CAT. NO. | LINE VOLTAGE | |
| SERIAL NO. | BREAKER SIZE | TRANSITION |
| STYLE | BREAKER TYPE | HEATER SIZE |
| MODEL | TRIP DEVICE | |
| TYPE | | |
| NEMA CL. | | |
| DESIGN | | |
| DATE INSTALLED | | |
| DRAWING NO. | | |

JPL 5118-s/DSIF(8/69)

ITEM: COST MAINTENANCE RECORD

| DATE | LABOR | MAINT | DATE | LABOR | MAINT | DATE | LABOR | MAINT |
|---|---|---|---|---|---|---|---|---|
| | | | | | | | | |
| | | | | | | | | |
| | | | | | | | | |
| | | | | | | | | |
| | | | | | | | | |
| | | | | | | | | |
| | | | | | | | | |
| | | | | | | | | |
| | | | | | | | | |
| | | | | | | | | |
| | | | | | | | | |

PM # GOVT # BLDG #

Fig. 2. Cardex file card

**MAINTENANCE WORK ORDER**

| | | | |
|---|---|---|---|
| EQUIPMENT # | LA # | DATE | TIME RECEIVED |
| EQUIPMENT NAME | | HP | REPORTED BY |
| DEPARTMENT | SECTION # | | ASSIGNED BY |
| BUILDING | ROOM | | DATE TIME |
| OTHER LOCATION | | | ASSIGNED TO |
| SCHEDULED WORK M Q SA A | | UNSCHEDULED WORK | JOB # |
| ORIGINATOR | | | APPROVED BY |
| WORK PERFORMED | | | |

TOTAL TIME REQUIRED _____

JPL 1013 DEC 62

Fig. 3. Maintenance work order form

NO. 9432

GOLDSTONE DEEP SPACE COMMUNICATION COMPLEX

**WORK REQUEST**

ACCOUNT NO. TO BE CHARGED

**INSTRUCTIONS**

ORIGINATOR COMPLETE ALL INFORMATION NOT ENCLOSED WITHIN HEAVY LINES AND FORWARD WORK REQUEST TO MAINTENANCE OFFICE.

DATE _____

| ORIGINATOR | STATION | BLDG. | EXT. |
|---|---|---|---|
| | | | |

REASON FOR REQUEST (JUSTIFICATION)

DESCRIPTION OF REQUEST (INCLUDE SKETCHES, DWGS., ETC.)

| REQUISITION NO. | PURCHASE ORDER |
|---|---|
| | |
| | |
| | |
| | |
| | |

| SERVICE | ESTIMATE | | ACTUAL COST | |
|---|---|---|---|---|
| | MATERIAL | LABOR | MATERIAL | LABOR |
| AIR COND. | | | | |
| CARPENTER | | | | |
| CONCRETE | | | | |
| CONTRACT | | | | |
| DRAFTING | | | | |
| ELECTRIC | | | | |
| ENGINEER | | | | |
| GRADING | | | | |
| MATERIAL | | | | |
| PAINTING | | | | |
| PHOTO | | | | |
| PLUMBING | | | | |
| SHEET MT. | | | | |
| WELDING | | | | |
| | | | | |
| TOTAL | | | | |

| DATE REQUIRED | PREPARED BY |
|---|---|
| | |

SUPERVISOR SIGNATURE

| | |
|---|---|
| ENGINEER APPROVAL | DATE |
| MAINTENANCE APPROVAL | DATE |
| AUTHORIZATION TO PROCEED | DATE |

ACKNOWLEDGEMENT

| TO | DATE |
|---|---|
| | |

| ANTICIPATED COMPLETION DATE | ESTIMATED COST |
|---|---|
| | |

REMARKS

MAINTENANCE OFFICE

**Fig. 4. Work request form**

WORK REPORT DATE _____

NAME _____ SHIFT ____ CRAFT _____

| WORK DESCRIPTION | START TIME | STOP TIME | HOURS |
|---|---|---|---|
| | | | |
| | | | |
| | | | |
| | | | |
| | | | |
| | | | |
| | | | |
| | | | |
| | | | |
| | | | |
| | | | |
| | | | |
| | | TOTAL | |

F-030

Fig. 5. Work report form

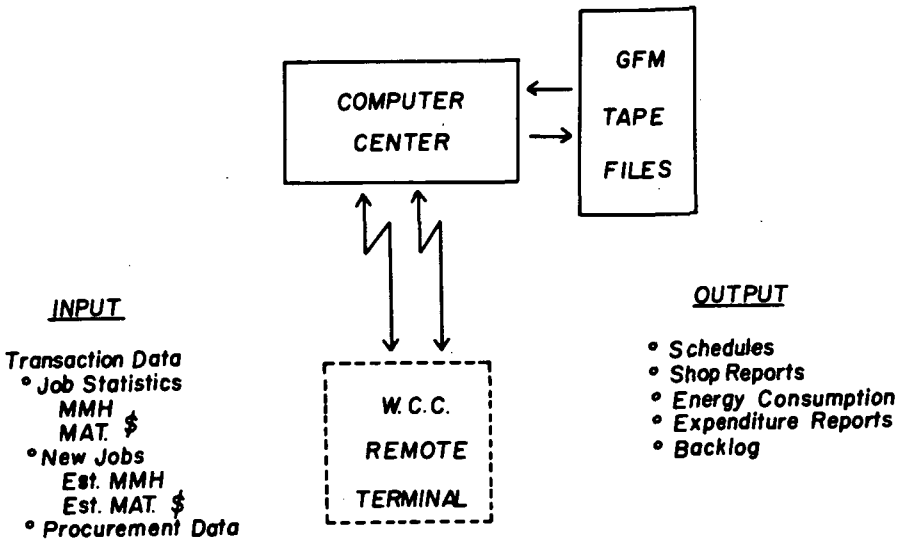


Fig. 6. Overview of GFM data base system

Fig. 7. Remote computer terminal

Preventive Maintenance (PM)

PM History File - Record Layout

| Item | Field Size | Format |
|---|---|---|
| Shop Code[1] | 1 | A |
| PM Number | 5 | N |
| Item Name | 15 | A |
| Serial Number | 15 | A/N |
| Government Number | 10 | A/N |
| Model Number | 15 | A/N |
| Building Number | 3 | A/N |
| Room Number | 5 | A/N |
| Date of Purchase | 6] (MMDDYY) | N |
| End of Warranty Period | 6] | N |
| MMH - Monthly Std. | 4 | N |
| MMH - Quarterly Std. | 4 | N |
| MMH - Overhaul Std. | 4 | N |
| Special Comments | 55 | A/N |

*MMH = Maintenance Manhours.

A = Alpha-characters.

A/N = Alphanumeric characters.

[1]See Fig. 12.

Fig. 8. PM history file record



PM Data - Record Layout

| Item | Field Size | Format |
|---|---|---|
| Shop Code[1] | 1 | A |
| PM Number | 5 | N |
| Maintenance Code[1] | 2 | A |
| Status Code[1] | 1 | A |
| Date of Action (MMDDYY) | 6 | N |
| MMH | 5 | N |
| Material Cost | 7 | N |
| Work Description | 50 | A/N |

[1]See Fig. 12.

Fig. 9. PM data file record

WORK REQUEST (WR) - RECORD LAYOUT

| ITEM | FIELD SIZE | FORMAT |
|---|---|---|
| Shop Code[1] | 1 | A |
| WR Number | 5 | N |
| WR (Maint.) Code[1] | 2 | A |
| Originator | 15 | A |
| Date Required (MMDDYY) | 6 | N |
| Est. Number of Craftsmen | 1 | N |
| Est. MMH (XXX.X) | 5 | N |
| Est. Material Cost | 6 | N |
| Est. Completion Date | 6 | N |
| Date Received (MMDDYY) | 6 | N |
| Actual Start Date (MMDDYY) | 6 | N |
| Actual Completion Date (MMDDYY) | 6 | N |
| Actual Number of Craftsmen | 1 | N |
| Actual MMH (XXX.X) | 5 | N |
| Actual Material Cost | 6 | N |
| Status[1] | 1 | A |
| Priority[1] | 1 | N |
| Building Code | 3 | A/N |
| Room Number | 5 | A/N |
| Task Description | 50 | A/N |

[1]See Fig. 12.

Fig. 10. Work request (WR) record

MAINTENANCE WORK ORDER (MWO) - RECORD LAYOUT

| ITEM | FIELD SIZE | FORM FORMAT |
|---|---|---|
| Shop Code[1] | 1 | A |
| MWO Number | 5 | N |
| MWO (Maint.) Code[1] | 2 | A |
| Originator | 15 | A |
| Date of Request (MMDDYY) | 6 | N |
| Date Required (MMDDYY) | 6 | N |
| Est. Number of Craftsmen | 1 | N |
| Est. MMH (XXX.X) | 5 | N |
| Est. Material Cost | 6 | N |
| Status[1] | 1 | A |
| Est. Completion Date (MMDDYY) | 6 | N |
| Priority[1] | 1 | N |
| Actual Number of Craftsmen | 1 | N |
| Actual MMH (XXX.X) | 5 | N |
| Actual Material Cost | 6 | N |
| Building Code | 3 | A/N |
| Room Number | 5 | A/N |
| Task Description | 50 | A/N |

[1]See Fig. 12.

Fig. 11. Maintenance work order (MWO) record

## CODES FOR COMPUTER INPUTS

1. Shop Codes (Cost Center) ---- one (1) alpha-character.

| Code | Shop Description |
|---|---|
| C | Carpenter & Paint |
| E | Electrical |
| M | Machine |
| G | Engraving |
| P | Photolab |
| H | Heavy Equipment (mechanical) |
| D | Drafting & Engineering |
| K | Contracts |
| A | A/C, Heating, Plumbing (Refer Shop) |
| S | Security |

2. Maintenance Codes ---------- two (2) alpha-characters, maximum.

| Code | Description |
|---|---|
| W | Weekly |
| M | Monthly |
| Q | Quarterly |
| SA | Semi-annual |
| AN | Annual |
| U | Unscheduled |
| S | Scheduled |
| E | Emergency |
| K | Contractor |
| P | Philco |

3. Status Codes ---------- one (1) alpha-character.

| Code | Description |
|---|---|
| C | Complete |
| P | Work in Progress |
| M | Material Delay |
| D | Delay Other Than Material |
| N | Work Not Started |
| A | Awaiting Approval |
| X | Cancelled, Not Approved |

4. Priority ----------(To be attached)

Fig. 12. Sample codes for computer input

GOLDSTONE MONTHLY UTILITY USAGE REPORT DATE:01-27-76

| LOCATION | METER NUMBER | MC | BEGINNING DATE:12-28-75 TOTAL KWH X10**3 | ENDING DATE:12-28-75 KW DEMAND X10**3 | TOTAL KVAR X10**3 | % CHG |
|---|---|---|---|---|---|---|
| MAIN SUB S.C.E. | 180-724 | 01 | 795.000 | 1.830 | | 21.0 |
| MAIN SUB S.C.E. | 179-673 | 02 | | | 66.00 | 0.0 |
| ECHO SITE | 60-085-004 | 03 | 530.400 | .696 | | 248.0 |
| ECHO SITE | 60-085-005 | 04 | 0.000 | 0.000 | | 0.0 |
| ECHO SITE | DELETED*** | 05 | 0.000 | 0.000 | | 0.0 |
| FORT IRWIN INTERSECTION | U-301-21477 | 06 | .293 | 0.000 | | 561.4 |
| PUMP STATION | 48-591-353 | 07 | 15.500 | 0.000 | | 252.3 |
| PIONEER SUB | 43-897-195 | 08 | 241.200 | .384 | | 48.9 |
| PIONEER SITE | 46-493-495 | 09 | 0.000 | 0.000 | | 0.0 |
| PIONEER SITE | 46-493-496 | 10 | 0.000 | 0.000 | | 0.0 |
| VENUS SUB #1 | 24-900-394 | 11 | 1585.600 | 0.000 | | 0.0 |
| VENUS SUB #2 | 13450 | 12 | 66.240 | .480 | | 4.6 |
| VENUS SUB #3 | 111C275G33 | 13 | 32.400 | .120 | | 145.5 |
| ANTENNA RANGE | 27-298-726 | 14 | 4.480 | .080 | | 55.6 |
| MARS SITE S.C.E. | F-264-128 | 15 | 841.600 | 1.920 | | 39.9 |
| MARS SITE | RP-14-856 | 16 | | | 304.00 | -61.1 |
| MARS SITE | 308-73320 | 17 | 0.000 | 0.000 | | 0.0 |
| GOLDSTONE TOTAL USAGE | | | 1636.60 | | 3.75 | |

WATER, LPG & DIESEL USAGE REPORT OF GALLONS DISPENSED X10**3

| | | | | | | |
|---|---|---|---|---|---|---|
| GOSCO WATER MAIN | N/A | 18 | 740.700 | 0.000 | | -64.9 |
| LPG-ECHO | N/A | 19 | 6.010 | 0.000 | | 11.3 |
| LPG-PIONEER | N/A | 20 | 1.053 | 0.000 | | 28.2 |
| LPG-VENUS | LP & 15 | 21 | .673 | 0.000 | | -27.6 |
| LPG-VENUS | 2 | 22 | .610 | 0.000 | | -37.1 |
| LPG-ANT. RANGE | N/A | 23 | .173 | 0.000 | | -35.8 |
| LPG-MARS | N/A | 24 | .033 | 0.000 | | -80.8 |
| ECHO DFG | NONE | 25 | 0.000 | 0.000 | | 0.0 |
| MARS DFG | NONE | 26 | 0.000 | 0.000 | | 0.0 |
| PIONEER DFG | NONE | 27 | 0.000 | 0.000 | | 0.0 |

Fig. 13. Monthly utility usage report

GOLDSTONE SEMI-ANNUAL SUMMARY OF UTILITY CONSUMPTION DATE:01-28-76

BEGINNING DATE:0775 ENDING DATE:12-28-75

| LOCATION | NO | PERCENT CHANGE THIS QUARTER KWH | KVAR | SEMI ANNUAL CONSUMPTION X10**3 KWH | DEMAND | KVAR |
|---|---|---|---|---|---|---|
| MAIN SUB S.C.E. | 01 | -10.30 | | 4695.00 | 13.17 | |
| MAIN SUB S.C.E. | 02 | | -59.63 | | | 918.00 |
| ECHO SITE | 03 | 19.65 | | 2092.80 | 3.01 | |
| ECHO SITE | 04 | -100.00 | | 95.20 | .60 | |
| ECHO SITE | 05 | -100.00 | | 95.20 | .48 | |
| FORT IRWIN INTERSECTION | 06 | 30.95 | | .07 | 0.00 | |
| PUMP STATION | 07 | -2.92 | | 60.50 | 0.00 | |
| PIONEER SUB | 08 | -11.44 | | 1685.20 | 2.30 | |
| PIONEER SITE | 09 | -100.00 | | 11.32 | .25 | |
| PIONEER SITE | 10 | -100.00 | | 14.08 | .33 | |
| VENUS SUB #1 | 11 | 19920.00 | | 1609.60 | 0.00 | |
| VENUS SUB #2 | 12 | 800.33 | | 238.32 | 1.60 | |
| VENUS SUB #3 | 13 | 8.16 | | 122.40 | .50 | |
| ANTENNA RANGE | 14 | 23.00 | | 16.56 | .21 | |
| MARS SITE S.C.E. | 15 | 5.26 | | 4116.40 | 9.95 | |
| MARS SITE | 16 | | -6.51 | | | 3456.00 |
| MARS SITE | 17 | -100.00 | | .00 | 0.00 | |
| GOLDSTONE TOTAL USAGE | | | | 8813.40 | 23.12 | |

WATER: LPG & DIESEL USAGE REPORT OF GALLONS DISPENSED X10**3

| | | | | | |
|---|---|---|---|---|---|
| GDSCC WATER MAIN | 18 | -41.51 | 9023.70 | 0.00 | |
| LPG-ECHO | 19 | 142.96 | 30.71 | 0.00 | |
| LPG-PIONEER | 20 | 79.08 | 3.84 | 0.00 | |
| LPG-VENUS | 21 | 230.97 | 3.18 | 0.00 | |
| LPG-VENUS | 22 | 1955.56 | 6.18 | 0.00 | |
| LPG-ANT. RANGE | 23 | 325.86 | .69 | 0.00 | |
| LPG-MARS | 24 | 70.00 | .14 | 0.00 | |
| ECHO DFG | 25 | 0.00 | 0.00 | 0.00 | |
| MARS DFG | 26 | 0.00 | 0.00 | 0.00 | |
| PIONEER DFG | 27 | 0.00 | 0.00 | 0.00 | |

Fig.14. Semi-annual summary of utility consumption

```
DO YOU WANT PLOTS OF METER  1 DATA?  Y=YES,N=NO
?Y

DATA HAS YMIN = 657  YMAX = 852
ENTER YMIN,YMAX FOR PLOT:
650,900
```

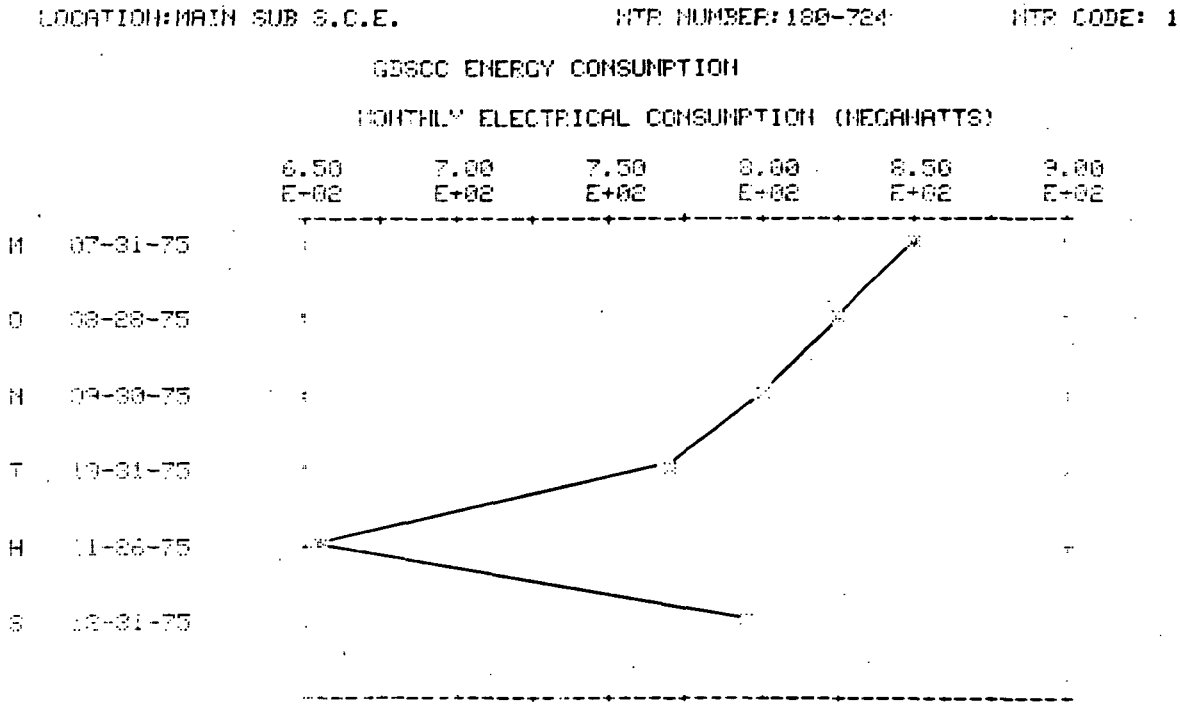


**Fig. 15. Computer generated plot of monthly electrical consumption (megawatts)—6-month plot**

GDSCC ANNUAL FACILITY USAGE X10**3 DATE:01-28-76

BEGINNING DATE:0175 ENDING DATE:12-28-75

PART I: ANNUAL CONSUMPTION SUMMARY

| LOCATION | NC | 1ST-HALF KWH | 1ST-HALF DEMAND | 2ND-HALF KWH | 2ND-HALF DEMAND | TOTAL KWH | TOTAL DEMAND |
|---|---|---|---|---|---|---|---|
| MAIN SUB S.C.E. | 01 | 4554.00 | 12.21 | 4695.00 | 13.17 | 9249.00 | 25.38 |
| MAIN SUB S.C.E. | 02 | 636.0 * | | 918.0 * | | 1554.0 * | |
| ECHO SITE | 03 | 3.00 | 0.00 | 2092.80 | 3.01 | 2092.80 | 3.01 |
| ECHO SITE | 04 | 0.00 | 0.00 | 95.20 | .20 | 95.20 | .20 |
| ECHO SITE | 05 | 0.00 | 0.00 | 0.00 | 0.00 | 0.00 | 0.00 |
| FORT IRWIN INTERSECTION | 06 | .87 | 0.00 | .87 | 0.00 | 1.75 | 0.00 |
| PUMP STATION | 07 | 38.90 | 0.00 | 60.50 | 0.00 | 99.40 | 0.00 |
| PIONEER SUB | 08 | 1119.60 | 1.30 | 1285.20 | 2.30 | 2404.80 | 3.60 |
| PIONEER SITE | 09 | 31.84 | .54 | 11.52 | .25 | 63.36 | .79 |
| PIONEER SITE | 10 | 61.44 | .66 | 14.08 | .33 | 75.52 | .99 |
| VENUS SUB #1 | 11 | 19.20 | 0.00 | 1609.60 | 0.00 | 1628.80 | 0.00 |
| VENUS SUB #2 | 12 | 235.68 | 2.83 | 232.32 | 1.60 | 522.00 | 4.44 |
| VENUS SUB #3 | 13 | 242.40 | 9.91 | 122.40 | .50 | 364.80 | 10.42 |
| ANTENNA RANGE | 14 | 43.20 | .23 | 18.56 | .20 | 61.76 | .44 |
| MARS SITE S.C.E. | 15 | 3846.40 | 8.26 | 4118.40 | 9.95 | 7964.80 | 18.21 |
| MARS SITE | 16 | 2092.8 * | | 3456.0 * | | 5548.8 * | |
| MARS SITE | 17 | .88 | 0.00 | 0.00 | 0.00 | .88 | 0.00 |
| GOLDSTONE ANNUAL USAGE | | | | | | 17213.80 | 43.59 |

*=QUAR MEASUREMENT

WATER, LPG & DIESEL USAGE REPORT OF GALLONS DISPENSED X10**3

| | | | | | | | |
|---|---|---|---|---|---|---|---|
| GDSCC WATER MAIN | 16 | 6351.30 | 0.00 | 9023.70 | 0.00 | 15375.00 | 0.00 |
| LPG-ECHO | 19 | 102.76 | 0.00 | 30.71 | 0.00 | 133.49 | 0.00 |
| LPG-PIONEER | 20 | 25.62 | 0.00 | 3.84 | 0.00 | 29.46 | 0.00 |
| LPG-VENUS | 21 | 10.65 | 0.00 | 3.18 | 0.00 | 13.83 | 0.00 |
| LPG-VENUS | 22 | 8.04 | 0.00 | 2.18 | 0.00 | 10.22 | 0.00 |
| LPG-ANT. RANGE | 23 | 3.50 | 0.00 | .63 | 0.00 | 4.13 | 0.00 |
| LPG-MARS | 24 | .10 | 0.00 | .13 | 0.00 | .23 | 0.00 |
| ECHO DFO | 25 | 0.00 | 0.00 | 0.00 | 0.00 | 0.00 | 0.00 |
| MARS DFO | 26 | 0.00 | 0.00 | 0.00 | 0.00 | 0.00 | 0.00 |
| PIONEER DFO | 27 | 0.00 | 0.00 | 0.00 | 0.00 | 0.00 | 0.00 |

**Fig. 16. Part I: Annual utility usage report**

GDSCC ANNUAL FACILITY USAGE X10**3 DATE:01-28-76

BEGINNING DATE:0175 ENDING DATE:12-28-75

PART II: QUARTERLY BACK-UP OF ANNUAL REPORT

| MC | KWH (KVAR*) QUARTERLY CONSUMPTION 1-QTR | 2-QTR | 3-QTR | 4-QTR | ANNUAL | QUARTERLY DEMAND CONSUMPTION 1-QTR | 2-QTR | 3-QTR | 4-QTR | ANNUAL |
|---|---|---|---|---|---|---|---|---|---|---|
| 01 | 2154.0 | 2400.0 | 2475.0 | 2220.0 | 9249. | 3.3 | 6.9 | 7.2 | 6.0 | 23.4 |
| 02 | 228.0 | 408.0 | 654.0 | 264.0 | 1554 * | | | | | |
| 03 | 0.0 | 0.0 | 952.8 | 1140.0 | 2093. | 0.0 | 0.0 | .8 | 2.2 | 3.0 |
| 04 | 0.0 | 0.0 | 95.2 | 0.0 | 95. | 0.0 | 0.0 | .5 | .1 | .6 |
| 05 | 0.0 | 0.0 | 0.0 | 0.0 | 0. | 0.0 | 0.0 | 0.0 | 0.0 | 0.0 |
| 06 | .4 | .5 | .4 | .5 | 2. | 0.0 | 0.0 | 0.0 | 0.0 | 0.0 |
| 07 | 15.7 | 23.2 | 30.7 | 29.8 | 99. | 0.0 | 0.0 | 0.0 | 0.0 | 0.0 |
| 08 | 504.0 | 615.6 | 681.6 | 603.6 | 2405. | .5 | .8 | 1.2 | 1.1 | 3.6 |
| 09 | 31.2 | 20.6 | 11.5 | 0.0 | 63. | .2 | .3 | .3 | 0.0 | .8 |
| 10 | 37.1 | 24.3 | 14.1 | 0.0 | 76. | .3 | .3 | .3 | 0.0 | 1.0 |
| 11 | 4.8 | 14.4 | 8.0 | 1601.6 | 1629. | 0.0 | 0.0 | 0.0 | 0.0 | 0.0 |
| 12 | 193.9 | 101.8 | 23.0 | 209.3 | 528. | 1.4 | 1.4 | .6 | 1.0 | 4.4 |
| 13 | 130.8 | 111.6 | 58.8 | 63.6 | 365. | 7.2 | 2.7 | .3 | .3 | 10.4 |
| 14 | 28.2 | 15.6 | 8.3 | 10.2 | 62. | .1 | .1 | .0 | .2 | .4 |
| 15 | 1744.0 | 2102.4 | 2006.4 | 2112.0 | 7965. | 3.4 | 4.8 | 5.0 | 5.0 | 18.2 |
| 16 | 950.4 | 1142.4 | 1804.8 | 1651.2 | 5549 * | | | | | |
| 17 | .5 | .4 | 0.0 | 0.0 | 1. | 0.0 | 0.0 | 0.0 | 0.0 | 0.0 |
| GOLDSTONE ANNUAL USAGE | | | | | | | | 172 | 13.80 | 43.59 |

*=KVAR MEASUREMENT

WATER, LPG & DIESEL USAGE REPORT OF GALLONS DISPENSED X10**3

| | | | | | | | | | | |
|---|---|---|---|---|---|---|---|---|---|---|
| 18 | 2386.8 | 3964.5 | 5693.6 | 3330.1 | 15375. | 0.0 | 0.0 | 0.0 | 0.0 | 0.0 |
| 19 | 87.6 | 13.2 | 9.0 | 21.8 | 133. | 0.0 | 0.0 | 0.0 | 0.0 | 0.0 |
| 20 | 22.1 | 3.6 | 1.4 | 2.5 | 29. | 0.0 | 0.0 | 0.0 | 0.0 | 0.0 |
| 21 | 3.7 | 2.1 | .7 | 2.5 | 14. | 0.0 | 0.0 | 0.0 | 0.0 | 0.0 |
| 22 | 6.3 | 1.7 | .1 | 2.1 | 10. | 0.0 | 0.0 | 0.0 | 0.0 | 0.0 |
| 23 | 3.0 | .6 | .1 | .6 | 4. | 0.0 | 0.0 | 0.0 | 0.0 | 0.0 |
| 24 | .0 | .1 | .1 | .1 | . | 0.0 | 0.0 | 0.0 | 0.0 | 0.0 |
| 25 | 0.0 | 0.0 | 0.0 | 0.0 | 0. | 0.0 | 0.0 | 0.0 | 0.0 | 0.0 |
| 26 | 0.0 | 0.0 | 0.0 | 0.0 | 0. | 0.0 | 0.0 | 0.0 | 0.0 | 0.0 |
| 27 | 0.0 | 0.0 | 0.0 | 0.0 | 0. | 0.0 | 0.0 | 0.0 | 0.0 | 0.0 |

*=KVAR MEASUREMENT

Fig. 17. Part II: Annual utility usage report

```
WHAT IS TODAYS DATE?    MM-DD-YY = 01-18-76
BEGINNING DATE OF INTEREST IS:    MMYY = 0975
ENDING DATE OF INTEREST IS:    MMYY = 0176
DATA FILES REQUESTED ARE MISSING FOR YEAR 1976
```

DATE: 01-18-76

ENERGY CONSUMPTION AT GDSCC

BEGINNING DATE:0975 ENDING DATE:0176

PART I: SUMMARY

| DATE | LPG K-GAL | MMHT | D.FUEL K-GAL | MMHT | POWER MMH | MMHT | TOTAL MMHT |
|---|---|---|---|---|---|---|---|
| 975 | 3.625 | 101 | 18.390 | 747 | 1377.923 | 4684 | 5532 |
| 1075 | 9.231 | 258 | .375 | 15 | 1325.964 | 5187 | 5460 |
| 1175 | 10.197 | 285 | .250 | 10 | 1367.958 | 4650 | 4945 |
| TOTALS | 23.053 | | 19.015 | | 4271.845 | | 15938 |
| TOTAL KILO DOLLARS | | | | | 116.88 | | |

PART II: SUMMARY

| DATE | TOTAL MMHT | CUM MMHT | POWER COST(NO.) | CUM COST(KILO.$) | CUM POWER(MMH) | CUM LPG K-GAL | CUM D.F.K-GAL |
|---|---|---|---|---|---|---|---|
| 975 | 5532 | 5532 | 30162.89 | 38.16 | 1377.923 | 3.625 | 18.390 |
| 1075 | 5460 | 10993 | 43914.97 | 79.08 | 2703.887 | 12.856 | 18.765 |
| 1175 | 4945 | 15938 | 37797.66 | 116.88 | 4271.845 | 23.053 | 19.015 |

**Fig. 18. Energy consumption at GDSCC**





NASA—JPL—Coml., L.A., Calif.